New Sol-Gel Coatings to Improve Casting Quality

Nwaogu, Ugochukwu Chibuzoh

Publication date:
2011

Document Version
Publisher's PDF, also known as Version of record

New Sol-Gel Coatings to Improve Casting Quality

A PhD Thesis

By

Ugochukwu Chibuzoh Nwaogu

Supervisor: Niels Skat Tiedje, PhD.
(Associate Professor)

Department of Mechanical Engineering,
Technical University of Denmark.

December, 2011.

To my humble family

"My interest is in the future because
I am going to spend the rest of my life there"

Albert Einstein

Preface

This is a PhD Thesis on "New Sol-Gel Coatings to Improve Casting Quality" which was carried out and submitted to the Department of Mechanical Engineering at the Technical University of Denmark (DTU), in partial fulfillment of the requirements for the award of the degree of Doctor of Philosophy (PhD). The work presented herein was supervised by Associate Professor Niels Skat Tiedje within the period of November, 2008 to December, 2011. The expertise of the nine industrial partners and one research institute was reasonably harnessed for the success of this work.

In view of the large amount of data collected from all the experiments performed at the DTU foundry and laboratories, and the industrial tests in the companies, the most significant results and analyses along with a rich literature survey are presented.

I will not say it was an easy task to come this far, however, determination coupled with a very friendly working environment was the driving force. Being a member of the Casting research group at DTU MEK, under Niels Skat Tiedje has been a source of inspiration and motivation. The exposure was inestimable and working with industrial partners exposed me to a high calibre brain-storming.

Coming back to Denmark from Germany after my Masters Degree in Materials Science at Technical University of Hamburg, Germany (after being an exchange student at Aalborg University, Denmark in 2007) was a decision I needed no guidance to make for several reasons. Again, the site of liquid metal for the very first time at Funfrap foundry in Aveiro, Portugal, during the early part of my Masters study in Materials Science at University of Aveiro, Portugal, was amazing. That also enhanced my decision to take up the PhD in Casting Technology at DTU, among three other PhD offers in different countries in Europe. I wanted to be part of the group working with liquid metals and associated areas.

Having reached this stage of my studies and looking back from a vantage position, the path was rigorous, I must say. Amidst challenges, I acquired lots of knowledge and skills, I had to learn effective time management and team work. Working smartly and systematically, I overcame lots of the challenges. Effective literature study and ideas from the industrial partners, opened my thoughts to the direction of the project coupled with the guidance of my supervisor. Innovative and creative thinking became part of the success story.

Today, I am happy I have come this far.

Ugochukwu Chibuzoh Nwaogu.

Acknowledgements

I want to thank in a special way, my supervisor, Dr. Niels Skat Tiedje, for granting me this rare opportunity to carry out this PhD studies with him at DTU. Your understanding, consistent motivation, unflinching support and encouragement, excellent directives and the creation of a friendly and humorous working environment, are second to none. I enjoyed working with you.

I remain grateful to the following people - Professor Jesper Hattel, Dr. Jesper Thorborg, Dr. Cem Tutum, Jakob Skov Nielsen, Nikolaj Kjelgaard Vedel-Smith, Jens Ole Frandsen, Anette Fournais kaltoft, Ole Munch, Peter Sanderhoff, Michael Wenani Nielsen and Elham Moumeni and other PhD students in the Modelling and Casting Technology groups, who have contributed in one way or the other to make this work a reality. I say thank you! I am also grateful to Pia Holst Nielsen, the MPP secretary, for her express handling of my official affairs.

Many thanks to my partners at Danish Technological Institute, Aarhus, Thomas Poulsen and Claus Bischoff, for their total devotion to this project and for ensuring that it got to completion with their experimental and administrative supports.

These acknowledgements will not be complete if I do not express my profound gratitude to the many people employed in the nine industrial partners whom I have worked with. I thank them for their expertise discussions and constructive criticisms, which helped in no small measures to improve the quality of the work. In another context, I want to specially thank Frese Metal- og Stålstøberi A/S for always providing my working materials and also for granting me days of industrial visit which exposed me well. In a similar notion, I also want express my gratitude to the following foundries for also granting me days of industrial visit. They are Johan Jensen & Søn Metalstøberi, Dania A/S, Vald Birn A/S and Vestas Castings Kristiansand, Norway.

With inestimable happiness and joy that knows no bounds, I appreciate my parents and siblings for their encouragements and moral support. I remain highly indebted to my beautiful and lovely wife, Evelyn, for her love, devotion and for being with me through thick and thin since we got married, five years ago. The men of the house, my sons, Toby and Niels (Niels came within the period of the PhD studies, hence he got my supervisor's first name) are my source of joy and the quest to make them happy all the time keeps me going. I love you boys!

Last but not the least, I would like to express my appreciation to Technical University of Denmark, for offering me employment throughout this PhD studies and also for providing a very friendly and flexible working environment.

Contents

List of Figures

List of Tables

Abstract

Sand casting is one of the oldest casting methods. The greatest advantage of sand casting is that almost any metal can be poured in the sand and there is almost no limit on the size, shape, or weight of the part. Sand casting provides the most direct route from pattern to casting. Among the limitations involved in sand casting is the need for fettling and machining in order to finish the castings, especially castings having rough surfaces, veinings, or finnings, and other surface defects. In this regard, this project deals with the understanding and reduction or elimination of the occurrence of these mentioned defects on the castings made in sand moulding materials by use of novel refractory coatings.

The project involves the development of novel foundry coatings using the SOL-GEL Technology. The idea was to harness the possibilities offered by this technology to produce environmentally-friendly refractory foundry coatings. This process is a novel application for foundry coating development.

In the approach for this research project, intensive efforts were made to understand casting technology, the behaviour (mechanical and thermal) of moulding materials (at ambient and elevated temperatures), foundry coating technology and purposes, mould-metal reactions, metallurgy, modelling and simulations of casting processes, and surface metrology of castings.

In the experimental approach, several coating formulations were prepared both with nanoparticle refractory materials (TiO_2, ZnO) and microparticle refractory materials (filter dust, zircon, china clay, olivine, aluminium silicates). However, the nanoparticle refractory materials proved incompatible with the sand grains for foundry coating production. Therefore, the bulk of the work was centred on the micro-sized refractory materials which showed positive results.

The coatings were extensively characterized experimentally. The wet properties (density, ^{o}Baumé parameter, viscosity) and dry properties (penetration, coverage, layer thickness, moisture, permeability) as they apply to foundry industry, were measured and presented. The results show that the particle size, the particle size distribution, and the percentage solid content play a significant role in the rheology of the coatings. The percentage solid content is directly proportional to the density, ^{o}Baumé parameter, viscosity, coverage, layer thickness and inversely proportional to the penetration, moisture content and permeability.

In this project, a new Strength Testing Machine (STM) for moulding materials was built and calibrated in-house for the determination of the mechanical properties of moulding materials. Coated moulding materials were tested for strengths (tensile, bending and compression) using the new STM, to determine the effect of the

coatings on the strengths of the moulding materials. The results reveal that the coatings degrade the strengths in the tensile and bending modes, but not significantly, while the compression strength was increased using the coatings. Thermal degradation examinations were performed on cores coated with sol-gel containing coatings and those coated with the same coating without sol-gel component to understand the effect of the sol-gel component on the thermal stability. The observations made lead to the conclusion that lower amounts of sol-gel component will enhance the thermal stability of the moulding material.

Numerical modelling and simulations of the casting processes were performed to understand and predict defect areas in the castings. The coating layer thickness was modelled for simulation purposes. The thermal behaviour of the moulding materials was also simulated. The simulation results show that the effect of the coating on the moulding materials is thermal insulation. The simulation results agree with the experimental results. In another context, the likely surface reactions of the moulding materials and the metal were predicted and these depend on the free energy of formation of the products, CO_2/CO ratio and the temperature.

Many casting experiments were performed in both horizontally- and vertically-parted moulds using coated cold box and furan cores with uncoated cores as control. Many industrial tests were also performed. The cores were coated by dipping at different times in filter dust sol-gel coating with different solid contents, commercial coatings, and commercial coatings containing various amounts sol-gel component as additive. The coating application on moulds was by spraying. The surface quality of the castings shows that the filter dust sol-gel coating improved the surface quality of the castings and the results are comparable with the investigated commercial coatings. However, this coating formulation was dropped due to the fact that the filter dust is not a conventional material and it is not in continuous supply. The surface of the castings made with cores coated with the commercial coatings containing sol-gel component as an additive shows that better surface quality of castings were obtained with lower amount of sol-gel additive. In another context, the casting surface quality obtained by spraying the vertically-parted mould reveals that the coatings can enhance the surface quality and also influence the metallostatic pressure effects. Multilayer application by spraying proved more satisfactory. The thermal measurements during the casting experiments shows that the coatings have a thermally insulating effect on the cores, in concordance with the numerical results.

The surface metrology applied on the surface of the castings shows that the castings made with coated cores have lower surface roughness than the castings made with uncoated cores. In this project, it was also shown that optical metrology with white light is applicable to the evaluation of the surface texture of castings with a medium magnification, say $5\times$.

Finally, this project has successfully applied sol-gel technology in the development of foundry coatings and the results show positive potentials.

Chapter 1

Introduction

1.1 Background

Castings can be produced in either permanent metal or expendable refractory moulds. The use of metal moulds is limited to metals with low melting points. Thus, the greater part of the output of the foundry industry consists of castings made in refractory moulds, mainly sand castings. Silica sand is the mainstay of that part of foundry industry that uses expendable moulds. The reasons are: silica sand is cheap, available, often occurs together with its own binder (clay), is naturally round-grained, packs well, and is refractory enough to be used for all common metals and alloys [1]. However, casting defects that are a result of the thermal expansion of silica sand have always posed problems for the foundry industry. The phenomenon is caused by the rapid thermal expansion of the sand systems[1] during the casting process, resulting in the core failing due to cracking. The molten metal then flows into these cracks, creating a thin fin of metal, which is referred to as a veining or finning defect. Other related casting defects occurring as a consequence of the expansion effect of silica sand include scabs, rat-tails, and castings out of dimensional tolerances [2, 3]. Apart from these defects associated with silica sand expansion, there are other defects which occur when the melt subject the sand to thermal distortion. These include metal penetration, sand burn-on, sand inclusion and erosion, etc. Some of these defects are shown in Figure 1.1.

The use of refractory coatings on cores and moulds is fundamental to obtaining acceptable casting surface quality. Refractory coatings are used on green sand moulds and resin bonded cores in foundries to aid surface finish improvements, reduce thermal expansion defects such as veining, metal penetration, and unbonded sand defects such as erosion. Fetling[2] and casting inspection often contribute a very significant percentage to the total production cost in foundries. Therefore, there is a strong need for the reduction of the production cost. As the need for more complex, critical castings and higher quality standards grows, the function and quality of the core coatings utilized in the process becomes important [4].

[1] Sand systems refer to sand moulds and cores.

[2] Cleaning of castings after shot-blasting.

(a) Veining defect (b) Penetration and veining defect

Figure 1.1: Some castings with defects after shot-blasting .

Some are more successful than others [3]. The castings shown in Figure 1.1 are made with coated sand moulds and cores, but the castings still have these defects.

The question that has remained unanswered is what can be done to reduce the tendency of occurrence of these defects? Or better still, eliminate them completely?

Therefore, the project innovation consortium was formed to develop and test a novel Eco-friendly coating based on Sol-Gel Technology for foundry applications. The other members of the consortium apart from DTU are briefly introduced in Section 1.4.

The novel coatings were extensively characterized experimentally and tested with casting experiments. The surface quality defined by the roughness parameter of the castings made with these coatings were measured with a 3D optical microscope to establish a novel application of this measurement method in the foundry industry. This is a non contact scanning process based on focus variation. In most foundries, surface quality of castings is measured by using roughness comparators which are highly operator dependent and therefore subject to variation. Most importantly, this method is only qualitative and lacks reproducibility. Therefore, it is imperative to find a method that is quantitative and highly reproducible for surface quality measurement of castings. The results are correlated with the series of characterization results of the coatings and the conditions of casting using some statistical models. In this project, it was also found out from our measurement trials, that most sand castings are out of stylus instruments measuring range, especially the profilometers. Furthermore, a mechanical testing machine was developed and used for measuring the tensile and flexural strengths of chemically bonded core materials. This is a novel application for chemically bonded core materials since the traditional strength machines are used for green sand materials. Moreover, this system shows the loading profile, unlike the existing machines, which measure the maximum strengths.

In chapter 2, a detailed discussion of mould and core dynamics emanating from the contact of the mould or core with the liquid metal will be given. Furthermore, the concept of order-packing of granular materials as it affects sand grains is discussed. Most of the physical phenomena occurring during the casting process and the associated casting surface defects as a results of the mould/core and molten metal

interaction, will be discussed. Chapter 3 will briefly discuss Surface Technology. The parameters for the characterization of surface roughness and ISO standards dealing with surface texture characterization according to literature are presented. Chapter 4 deals with the modelling and simulations of casting processes, elucidating anticipated defect areas in the model. Chapter 5 covers materials and approach adopted in the execution of the research. In this chapter, different areas of the project and methods of investigation are presented. Chapter 6 presents the summary of the results from different areas of the project. Chapter 7 shows the results from industrial trials as case studies. Chapter 8 deals with the discussion of the results, findings of this research, and further knowledge. Chapter 9 presents the summary of the work by showing the important deductions from the research as conclusions while also providing the lead for future work. Another important section of this thesis is the supplements part. The supplements present the different publications of the results from the various areas of the research.

1.2 Scope of Thesis

The scope of this thesis is to enhance surface quality of castings using novel sol-gel coatings on moulds and cores thereby saving energy and cost in the fetling shops of the foundries.

The main idea is to develope a novel foundry coating using the sol-gel process. This process has been applied in different areas of coating production for various applications such as membrane application, thermal barrier, corrosion and wear resistant coatings, self cleaning, etc. but has not been applied in the development of foundry coatings. Therefore, this is a novel application of this process in foundry coating production. The sol-gel process has an advantage that the system can easily be controlled to get a tailored microstructure. The coatings investigated in this study were produced by the Sol-Gel group in the Materials Testing Division at Danish Technological Institute, Aarhus, Denmark. Therefore, this study concentrates on investigating and understanding the behaviour of the coatings on the cores and making castings with the coated cores to elucidate the performance of the coating in improving the surface quality of the castings.

1.3 Goals

The goals of the project include:

- To analyse how sol-gel coatings adhere to the surface of cores produced with different binder systems.
- To analyse how the coatings behave when subjected to the heat treatment resulting from direct contact with liquid metal during casting.
- To describe surface reactions between the coatings, cores, and castings during mould filling and solidification.

- To suggest model equations for the surface reactions.
- To determine the mechanical properties of core materials onto which the coatings are applied.
- To propose mode of fracture of the cores and coatings.
- To characterize the surface quality of the castings made with cores coated with sol-gel coatings and to quantify the surface roughness of some standard surface comparators.
- To investigate the interfacial microstructure of the casting in contact with the coated moulding materials.

1.4 Project Partners

This project, apart from being hosted and carried out at Technical University of Denmark, DTU, Mechanical Engineering laboratories, has other partners that have in one way or the other contributed immensely with their foundry expertise to the milestone so far reached in the research. A brief introduction of each is provided below.

1.4.1 C. C. Jensen A/S

C. C. Jensen A/S is a family-owned international company, established in 1953, and based in Denmark. Their uniqueness is based on combination of tradition, innovation, and technical expertise. C. C. Jensen has a global network of 9 subsidiaries, 5 affiliate companies, 1 joint venture partner and more than 40 distributors [5].

1.4.2 Dania A/S

Dania A/S was established in 1947. Dania manufactures and supplies series produced machine moulded components in grey iron and nodular iron with weights ranging from 0.5 to 60 kg, preferably complex and core intensive castings. Dania also offers surface treatment and machining services [6].

1.4.3 Danish Technological Institute (DTI)

The Danish Technological Institute (DTI) applies and disseminates research- and technologically-based knowledge for the Danish and international business sectors. They provide consultancy and standardisation services [7]. The coatings being investigated in this project are produced by the Sol-Gel group at DTI.

1.4.4 DISA Industries A/S

DISA Industries is a complete foundry supplier and provides cutting edge moulding technology, core solutions, and global technical services. DISA Industries is popularly known for the production of the automatic moulding machine, DISAMATIC, for vertically-parted green sand moulds [8].

1.4.5 Frese Metal- og Stålstøberi A/S

Frese Metal- og Stålstøberi A/S has more than 65 years of foundry experience and specialises in making complicated, core intensive, single or series production of quality castings in corrosion resistant materials such as bronze, aluminium bronze and stainless steel using an automatic moulding No-bake process [9].

1.4.6 Johan Jensen & Søn Metalstøberi

Johan Jensen & Søn Metalstøberi was established in 1892. This means that they have more than a century's worth of experience in the area of grouting[3] and casting equipment for all purposes. Their customer base ranges from large cement factories, shipyards, and large machinery factories to small local blacksmiths [10].

1.4.7 Nordsjællands Metalstøberi

Nordsjællands Metalstøberi A/S is the largest aluminium sand-casting foundry in Denmark. This foundry produces castings in any kind of standardized aluminium alloys suited for sand forms. They produce items from 1 gram to several hundred kilos [11].

1.4.8 Sibelco Nordic A/S (formerly PV Sand)

The company was founded in 1971. From middle of June 2010, the company name was changed from PV Sand A/S to Sibelco Nordic A/S. Sibelco Nordic A/S is a leading manufacturer and supplier of many products for foundries, the offshore-industry, surface treatment, construction industry and sport & leisure [12]. This company participated in the development of the coatings being investigated.

1.4.9 Vald. Birn A/S

Birn provides optimum manufacturing process for a broad spectrum of machine-moulded castings weighing up to approximately 80 kg in medium and large volumes with and without cores. Birn produce a wide range of standard cast materials in grey iron and nodular iron. Apart from manufacturing cast components, Birn offers machining, surface treatment, and assembly services [13].

[3] To fill or finish with a thin mortar or plaster.

1.4.10 Vestas Castings Group A/S

Vestas Castings Group A/S under Vestas Nacelles A/S is a subsidiary of Vestas Wind Systems A/S. In Vestas Casting Group A/S, the weight of the castings ranges from 100 kg to 20 tonnes. The main activity of Vestas Castings Group is the casting of items in high strength ductile iron and grey cast iron for wind turbines. The components cast are primarily rotor hubs, blade hubs, main beams, bearing houses, base frames, stiffeners, and torque arms. These components are cast in moulds of furan resin bonded sand [14].

Chapter 2

Mould and Core Dynamics

2.1 Concept of Order-Packing of Granular Materials

Packing can be defined as any manner of arrangement of solid units, in which each constituent unit is supported and held in position in the earth's gravitational field by tangential contacts with its neighbours. The packing of aggregate materials affects their physical properties such as bulk density, porosity, pore size distribution, pore shape, aggregate strength, and tortuosity[1] [15]. The concept of order-packing embraces the manner in which the sizing and shaping of aggregate particles contribute to the orderly packing in a refractory matrix. By promoting the orderly packing, it is possible to obtain an improvement of density and stability from the physical arrangement of aggregate particles, as well as, from the addition of binders to fill the voids and cement the particles [16, 17, 18]. The packing of aggregate materials is influenced by particle size, particle size range, sphericity[2], roundness[3] and surface roughness of the aggregate materials, cementing materials (binders), moisture content, and water surface tension [15, 19]. Particles have a certain geometric form or shape with varying degree of roundness. It is generally accepted that the sphericity and roundness of particles are significant factors in determining the physical properties of aggregate materials. The properties which are likely to be influenced by particle sphericity and roundness include the void ratio, pore size distribution, number of points of contact, compressibility, cohesion, friction, and strength. Void ratio of sands increases with decreasing sphericity and usually with decreasing roundness [15].

It has been discovered that factors such as grain shape and distribution, rammed densities, and surface stabilities, do influence the casting results obtained with foundry sands. Formerly, it was assumed that the order-packing is established within a mould by ramming forces. The more modern concept holds that through the dynamic grouping and packing of compatible particle sizes during mulling, an

[1] Tortuosity is a term used to describe diffusion in porous media.

[2] Sphericity is a measure of the degree to which the shape of a particle approaches that of a sphere.

[3] Roundness is basically a measure of angularity of the particle corners regardless of shape.

aggregate is predisposed toward orderly packing before it is ever discharged from a Muller and placed in a mould [16]. However, particle size has no influence on packing behaviour of large particles, but this is not the case with finer particles. Particle size affects packing, only when particles are less than 50 µm [15].

Bulk density (γ_d), porosity (ε), void ratio (e) and packing density (Ω), which are commonly used as a measure of packing, are related to one another by the following relationship:

$$\varepsilon = 1 - \frac{\gamma_d}{\gamma_s} = \frac{e}{1+e} = 1 - \Omega \tag{2.1}$$

where γ_s is the density of solids [15, 18, 20, 21]. Most measurements of packing are expressed in terms of bulk density; however, it is better when comparing materials to use e or Ω which is independent of the density of solids [15].

2.1.1 Some Theoretical Relationships

To develop the application of this concept for dynamic orderly packing during mulling, the packing potentialities of true spheres such as glass beads are considered since this is a simpler system even than the granular materials, and provides a framework within which the packing of less uniform particles can be understood [16, 22].

With a mass composed of uniform spheres, or beads, of a certain sieve size (a 1-component system), one can visualize the beads as packing to create either a simple cubic or rhombic formations (Figure 2.1). By placing a layer of four beads in true vertical alignment above another layer of four beads, one secures an example of a simple cubic packing (Figure 2.1a). This type of packing is physically unstable in that the natural tendency is to shift from cubic to rhombic. If one shifts the upper layer so that one of its components rests in the pocket common to the four beads in the lower layer, an example of simple rhombic packing is created (Figure 2.1b).

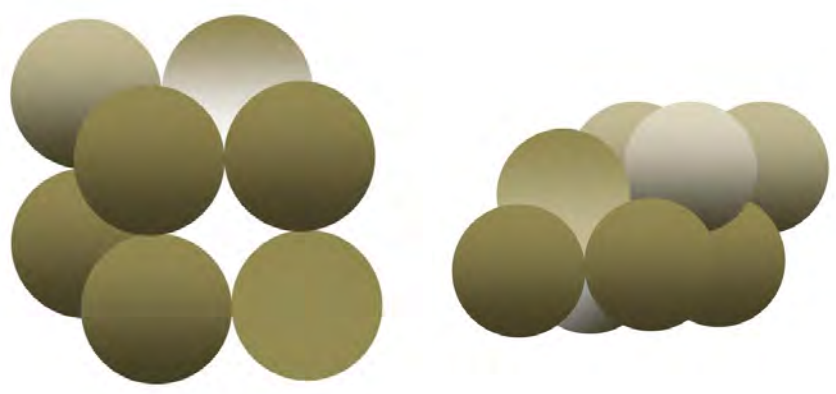

(a) Simple cubic (b) Simple rhombic

Figure 2.1: Types of packing uniform spheres from one sieve (1-component system) [16].

Considering cubic packing, one perceives that there is a space within the centre of the formation into which a smaller sphere can be fitted. If a sphere of proper size is inserted into this cavity, it can contact all of the eight larger spheres without distorting the geometrical perfection of the cubic structure; and a 2- component system has been created (Figure 2.2). Similarly, the simple rhombic type of formation is capable of including a sphere within an internal cavity enclosed by the larger spheres. However, in comparison the included sphere in the rhombic formation is smaller than the included sphere within the cubic formation.

If we assume we are dealing with perfect spheres of diameters equal to standard sieve openings, the forgoing can be restated in a more practical terms. With a cubic formation composed of large spheres, a sphere from the next smaller sieve will just fit into the cubic cavity. With a rhombic formation created from the same large-size spheres, a sphere from the second smaller sieve will just fit into the rhombic cavity.

These discussions could be extended to the more complex orderly packing arrangements peculiar to 3-, 4-, 5-, and 6-component systems. However, it is believed orderly formations from 2-component systems predominate when mixing and mulling is applied to foundry sands. Further explanation of Figure 2.2, (assuming we are still dealing with spheres from No. 70 and No. 80 sieves), we find that placing a No. 80 sphere within the cubic cavity formed by the No. 70 spheres technically transforms the formation from simple cubic to a body-centred-cubic type of formation (Figure 2.2b).

It can be noted that the rigidity and stability of the formation has been increased because the smaller sphere serves as a “key” between the two layers of larger spheres. A shift from simple cubic to simple rhombic alignment is no longer possible. Furthermore, the small sphere is occupying the space that could be filled by ineffective bond. Maximum efficiency and economy requires that binders be present as coatings on aggregate components, and not be wasted in filling void spaces. Finally, it should be evident that the points of sphere-to-sphere contact (the areas where the bond of adhesion is most effective) have been increased from 12 in the simple cubic formation to 20 in the body-centred cubic formation.

Assuming that increasing contact points between the spheres promotes better adhesion throughout a mass as a whole, it can be postulated that the creation of the body-centred cubic formation has contributed a 66.6% increase in strength potentials with respect to improving bond efficiency [16].

In another context, since the small spheres are of such size that they can fit into the existing pores without disturbance, then the pore space is reduced. If it is continued to put in small spheres in pores without any distortion in the geometrical system formed, all the pores will be filled when the permeability of the system is zero. In view of the influence of pore space on permeability, it is important to know the size of the largest sphere which can be accommodated within the cavities of close-packed uniform grains. This can be calculated and if the diameter of the original spheres is “d”, the largest inclusive sphere has a diameter of ($\sqrt{(2)}$ – 1)d or 0.4d. The next largest sphere which can fit into the remaining pores has a diameter of 0.2d [17]. However, it is mentioned in [23], that a few researchers

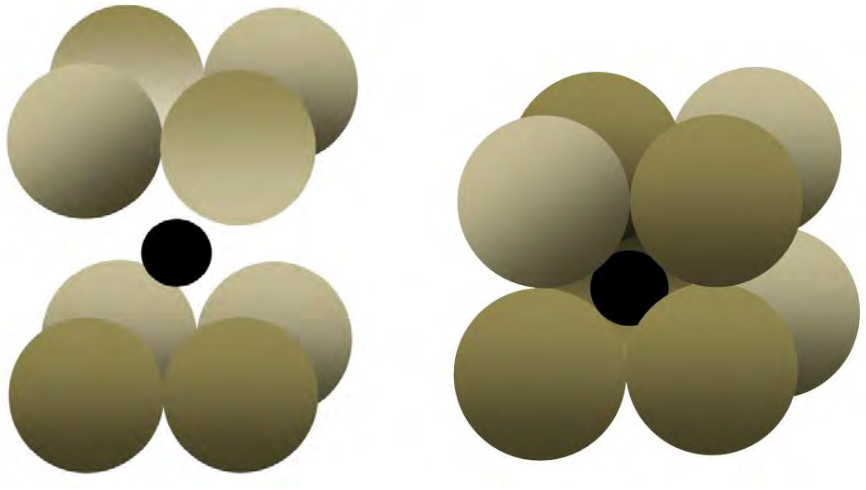

(a) Expanded formation (b) Compact formation

Small size diameter = 0.732 R and Large size diameter = R

Figure 2.2: Types of packing uniform spheres from one sieve (2-component system) [16].

reported that porosity for fine particles packing is higher than that of coarse particles and the proposed mechanism suggested that increasing the inter-particle forces increases porosity. Table 2.1 summarizes important characteristics of pore structures designed by different degrees of mono-size spheres packing.

Table 2.1: Important characteristics of some mono-size sphere packing.

Packing type	**CN**	**Porosity, %**	**R of sphere inscribed in cavities**	**R of sphere inscribed in Throats**
Hexagonal close-packed	12	25.95	0.2247R-octahedral	0.154R
			0.4142R-tetrahedral	
Tetragonal	10	30.19	0.2910R	0.1547R
				0.26497R
Body-centred cubic	8	31.98	0.2910R	0.2247R
Orthorhombic	8	39.54	0.5275R	0.1547R
				0.4142R
Cubic	6	47.64	0.732R	0.4142R
Tetrahedral	4	66.00	1.00R	0.732R

2.1.2 Practical Applications

The concept for dynamic orderly packing is not applicable to natural sands. Most natural sands contain a high percentage of clay and silt-like materials; and mulling is used to plasticize the clay and create rather thick coatings upon individual grains. Upon being rammed together, portions of the clay coatings are forced into the voids between adjacent sand grains. As a generalization, one can state that the density and stability of natural sand is more dependent upon the bond than distribution of sand grains; synthetic sands, being the most used moulding sand, are more dependent upon distribution of sand grains than bond. However, mulling is required to develop the characteristics of both.

2.1.3 Grain Distribution – Laws of Probability

It is generally assumed that a sieve analysis sharply defines between the different sizes of grains comprising a sand base. According to [16], such is not the case. On any particular sieve one finds grains ranging from those just able to pass through the preceding sieve to those just unable to pass through to the following sieve. Because of this lack of sharp differentiation between the grains on adjacent sieves, it is impossible to simply screen a sand and secure grains of uniform size on each of two successive sieves (Figure 2.3).

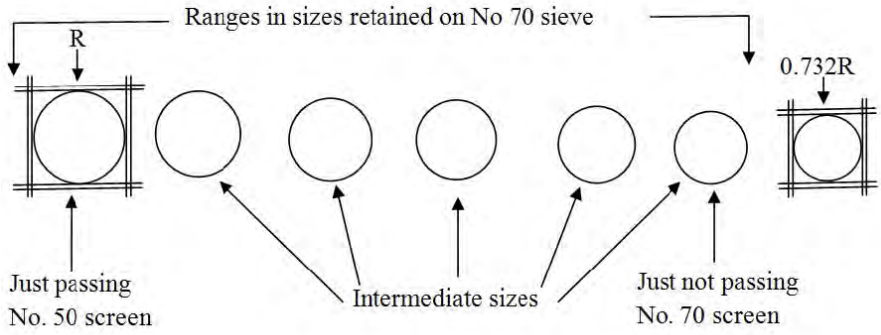

Figure 2.3: Schematic portrayal of range in sizes retained on No. 70 sieve demonstrate non-uniformity on any sieve [16].

2.1.4 Influence of Particle Geometry

The theoretical discussion dealt with true spheres – geometric shapes that facilitate fast distribution and easy packing. This is not the case with foundry sand [16, 24]. Most possess non-uniform shapes and can be classified as being rounded, sub-angular, angular and compounded types [15, 25] as shown in Figure 2.4.

- Rounded grains have the least contact with one another in a rammed structure, thereby making the sand highly permeable to gases. Sand having

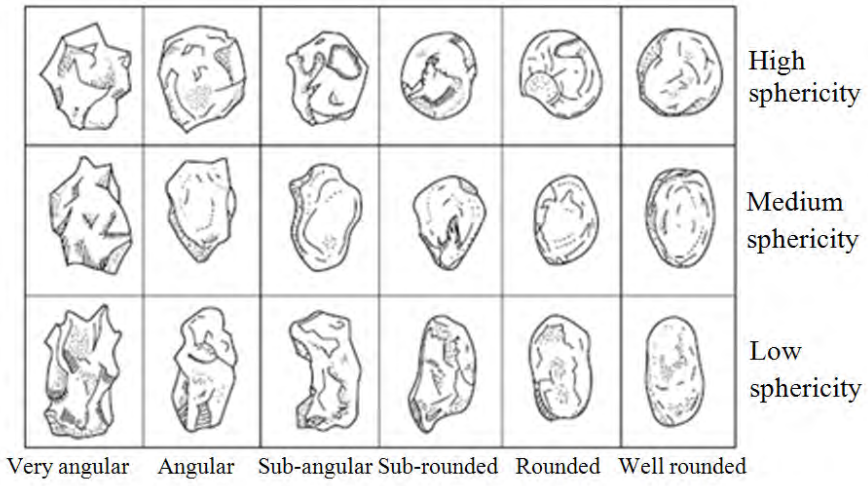

Figure 2.4: Classification of sand grain shapes.

rounded grains, however, lack strength and do not pack up to the optimum extent. The binder requirements are minimal and they have higher flowability.

- Sub-angular grains have comparatively lower permeability and greater strength than the rounded ones.

- Angular grains have defined edges, and the surfaces are nearly flat. They produce higher strength and lower permeability in the mould than sub-angular grains. The binder consumption is likely to be higher and they have lower flowability.

- Compounded grains are cemented together such that they fail to separate when screened. They may consist of rounded, sub-angular or angular grains or a combination of the three. These are the least desirable due to their tendency to breakdown at high temperature.

Obviously the well rounded types should be more compatible with promoting orderly packing than the angular or sub-angular types. Investigations have revealed that round grains are usually found on the No. 6 to No. 40 sieves; sub-angular grains upon the No. 50 to No. 140 sieves; and angular grains upon the No. 200 and finer sieves. In practice, sand grains contain mixed grain shapes, depending on origin. A sub-angular-to-rounded grain mixture would be the best combination [26].

Ranges of grain size, shapes and condition of grain surface all have their effect on mould and core performances. Grain sizes are measured by means of DIN and AFS standard screen analyses. Particles of 0.02 mm to approximately 2.0 mm mean diameter are usually considered as sand grains. Smaller particles down to 2 μm are silt and particles smaller than 2 μm are clay. Those larger than 2 mm may be considered as gravel [16]. The finer the grains, the more intimate will be the

Table 2.2: Calculation of Grain Finesness Number (GFN) [27]

Sieve No. British Stand.	Sand Retained on the Sieve (g)	Multiplied by Prev. Sieve No	Product
+10	Nil	-	-
+16	Nil	-	-
+22	0.2	0.2 × 16	3.2
+30	0.8	0.8 × 22	17.6
+44	6.7	6.7 × 30	201.0
+60	22.6	22.6 × 44	1104.4
+100	48.3	48.3 × 60	2898.0
+150	15.6	15.6 × 100	1560.0
+200	1.8	1.8 × 150	270
Through 200	4.0	4 × 200	800
		Product = 6854.2	
AFS Fineness No. $= \frac{Product}{Weight\ of\ sample} = \frac{6854.2}{100} = 68$ AFS			

contact and the lower the permeability. However, fine grains tend to fortify the mould and lessen its tendency to get distorted [26].

The analysis of particle sizes of sand substance, spread as they are over a range extending from about 1 mm to 0.1 mm (1000 to 100 µm), forms a major method of assessment of the suitability for moulding purposes. This test reveals both the coarseness and fineness of the aggregate material, which may be summarized as "grain fineness number" (GFN) based upon either B.S. or I.S.O. sieve apertures [26]. The GFN is obtained from a nest of standard laboratory sieves on a vibrating mechanism with a sensitive balance (± 0.5 accuracy) [27]. 100 g of sample of perfectly dry sand is placed on top (coarsest) sieve. The system is vibrated for 15 minutes. The content of each of the sieves is weighed starting with the top sieves and the weights are recorded against the corresponding sieve mesh number (either the British standard sieve numbers or the AFS American standard sieves). The weight of each separate sieve is multiplied by the preceding sieve mesh number. The total product is divided by the total sample weight and this gives the AFS Fineness Number. This is exemplified in Table 2.2.

Appreciable percentages of coarse grains should be avoided because of their adverse effect on casting surface finish. The finer the grain sizes are the better the opportunity to achieve smooth finishes of the castings. However, only fine grain sands do not guarantee smooth castings as thermal instability, inadequate mould density, poor flowability, and chemical activity, all affect the casting surface. The variation of size, shape, and distribution results in significantly different properties when the aggregates are mixed with binder and rammed into shape. The large grain size sand has a relatively low specific surface area, so requiring a small binder addition for a given mechanical strength, while small grains with higher specific

area need a larger binder addition to achieve the same strength [28]. Furthermore, the distribution of grain sizes in a sand has a strong influence on their ease of bonding. A narrow or very broad range of grain sizes will require larger percentages of binders than will a moderate screen-spread sand to develop a given level of green strength. Fines, silt, and clay are to be avoided or kept to a minimum in this case. Liquid binders, when properly mixed with sand, form a very thin coating on the grains [16].

2.2 Phenomena Affecting Mould and Core Dynamics

2.2.1 Heat Transfer

The rate of heat removal from the cast component during casting is important as it determines the solidification rate and time, temperature distribution in the material, and in the sand systems. The understanding of the heat transfer into the sand systems is also important as it affects the surface finish of the castings, depending on the behaviour to the heat. Heat transport and solidification processes in various casting processes are generally complex as illustrated in Figure 2.5.

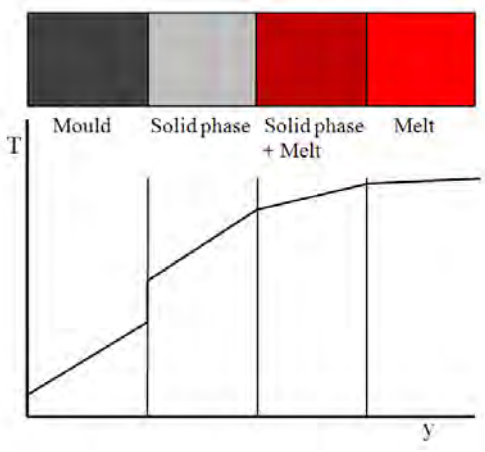

Figure 2.5: Temperature distribution in a cast, solidifying metal melt [29].

From Figure 2.5, the important identifiable resistances to heat extraction flow from the melt to the mould include the melt, the solid phase + melt, the solid phase, the metal/mould interface and the mould and the surrounding of the mould. However, the resistances from the melt and the solid phase + melt (two-phase region) are negligible. Nothing is normally known about the state of solidification, in the two-phase region [29]. And in the melt and the mould surrounding, the turbulent flow and mixing balance the temperature gradients rapidly as the bulk flow of the liquid is fast and the mould is hardly heated up on the outside during solidification [30].

The temperature of the melt is generally higher than the solidus during casting. However, the mould material cools the cast metal. The melt is cooled more rapidly

at the surface, which is in contact with the sand system. Consequently, solidification starts at this surface and the solidification front moves inwards into the melt.

2.2.1.1 Resistance from the Solid Phase

For heat flow from a liquid metal poured at its melting point T_m against a mould wall with initial temperature T_0, the transient[4] heat problem can be described by the partial differential equation for heat conduction in 1-D, given by Fourier's second law,

$$\frac{\partial T}{\partial t} = \alpha_s \frac{\partial^2 T}{\partial x^2} \tag{2.2}$$

Fourier's 3-D form of the heat conduction equation is given by

$$\frac{\partial T}{\partial t} = \alpha_s \left(\frac{\partial^2 T}{\partial x^2} + \frac{\partial^2 T}{\partial y^2} + \frac{\partial^2 T}{\partial z^2} \right) \tag{2.3}$$

α_s is the thermal diffusivity of the solid and it is expressed as

$$\alpha = \frac{k_s}{\rho_s c_p^s} \tag{2.4}$$

where

k_s is thermal conductivity

ρ_s is density

c_p^s is heat capacity at constant pressure.

The boundary conditions in Eq. 2.2 are $x = 0$, $T = T_0$; at $x = S$, $T = T_m$ and at the solidification front the rate of heat evolution must balance the rate of conduction down the temperature gradient [30, 31, 32]. The relationship is given by:

$$H\rho_s \left(\frac{\partial S}{\partial t} \right) = k_s \left(\frac{\partial T}{\partial x} \right) \tag{2.5}$$

H is the latent heat of solidification.

However, if the rate of evolution of heat is faster than the rate of conduction, there will be local overheating of the mould leading to production of castings with surface defects [33].

2.2.1.2 Resistance from the Mould/Metal Interface

It is reported in [30] that in many casting processes, heat flow is controlled to a significant extent by the resistance of the mould/metal interface. This occurs when both the metal and the mould have reasonably good thermal conductivity,

[4]The temperature is a function of both position and time.

therefore the resistance is dominated by the heat transfer between them. This is mostly the case when an insulating coating is applied to the mould or when the solidifying casting shrinks away from the mould (conversely, the mould heats up and expands away from the metal). The result is creation of an air gap between the two. The contact between metal and sand mould is not ideal, therefore the temperature at the interface becomes important for predicting the thermal shock that the mould can be subjected to. In [29], it was reported that during sand casting process, the temperature at the interface between the metal and the mould is approximately equal to the liquidus temperature of the liquid metal. However, the following assumptions are considered:

- The thermal conductivity of the metal is very large compared to that of the sand mould.
- During casting the temperature of the mould wall immediately becomes equal to the temperature T_L of the liquid metal and maintains this temperature throughout the whole solidification process.
- At large distances from the interface the temperature of the mould is equal to the room temperature T_0

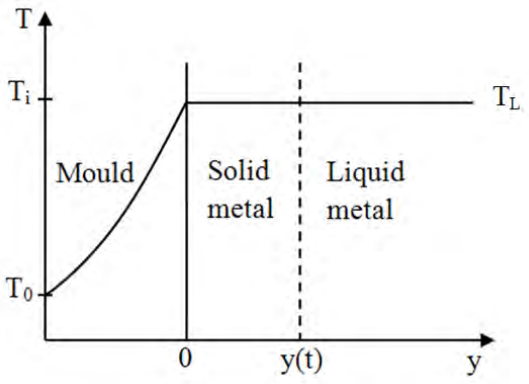

Figure 2.6: Sketch of the temperature profile during casting in a sand mould [29].

As can be seen in Figure 2.6, sand has a poor thermal conductivity. The heat transport through the sand mould is always a "bottle neck". Consequently, the solidification process is completely controlled by the thermal conduction through the sand mould.

There is a temperature difference across the interface between two different materials. The larger the difference the more heat is transferred per unit time from the hotter to the colder one. Under stationary condition, this is expressed as

$$\frac{dQ}{dt} = -h\,A\,(T_2 - T_1) \tag{2.6}$$

where h is the heat transfer coefficient expressed in J/m^2sK or W/m^2K.

Poor contact between the materials will result in a poor response time [34] and a thin layer of air between them. Air is a poor conductor and heat transfer is significantly reduced [29].

The amount of heat per unit area, which is transported into the mould per unit time in the negative direction through the interface between the mould and the metal is given by

$$\frac{\partial q}{\partial t} = -\sqrt{\frac{k_{mould}\,\rho_{mould}\,c_p^{mould}}{\pi t}}(T_i - T_0) \tag{2.7}$$

where T_i is the interface temperature.

This amount of heat consists of only solidification heat because the temperature in the liquid phase (T_L) is constant in the solid phase and the melt. The solidification heat per unit area and unit time is given by

$$\frac{\partial q}{\partial t} = -\rho_s(-\triangle H)\,\frac{dy_L}{dt} \tag{2.8}$$

where dy_L/dt is the solidification rate, i.e. the velocity of the solidification front in the melt. The thickness of the solidifying layer as a function time is given by Eq. 2.9:

$$y_L(t) = \frac{2}{\sqrt{\pi}}\,\frac{T_i - T_0}{\rho_s(-\triangle H)}\,\sqrt{k_{mould}\,\rho_{mould}\,c_p^{mould}}\,\sqrt{t} \tag{2.9}$$

In Eq. 2.9, the second factor describes the metal while the third factor describes the mould. It can also be seen from this equation that the thickness of the solidifying layer is a parabolic function of time. The solidification rate is rapid initially but decreases successively when the solidified layer grows.

The geometry of the mould wall has influence on the ability to extract the heat from the melt. Heat is transferred more rapidly in a concave mould area than in a planar surface because in a planar surface, heat spreads into a larger volume. Conversely, heat is transferred more slowly into a convex mould/casting area than in a planar one, because the heat spreads into a smaller volume than in a planar case [29].

2.2.1.3 Resistance from the Mould

The rate of solidification of castings made in silica sand moulds is generally controlled by the rate at which heat can be absorbed by the mould. The sand mould acts as an insulator, keeping the casting warm. Ceramic, investment and plaster moulds are even more insulating, preventing premature cooling of the melt, enhancing fluidity to give adequate ability to fill thin sections for which these casting processes are renowned. Unfortunately, the extremely slow cooling can lead to poor mechanical properties.

The product ($k_{mould}\,\rho_{mould}\,c_p^{mould}$) in Eq. 2.7 is a useful parameter to assess the rate at which various moulding materials can absorb heat [30]. This $(k_{mould}\,\rho_{mould}\,c_p^{mould})^{\frac{1}{2}}$ is defined as the cooling power of the moulding material.

2.2.2 Pressure from Metal

2.2.2.1 Pressure from Melt

The pressure from the melt is observed in three different forms namely static pressure due to depth, dynamic pressure due to flow and buoyancy forces. In the static condition, the expected linear increase in the size of a casting as the feeder height is increased is evident from the expression of pressure, p; density, ρ; height, h and acceleration due to gravity, g:

$$p = \rho g h \tag{2.10}$$

The effect of density is also noteworthy. The air gap seems sensitive to the hydrostatic pressure. Generally, the air gap is reduced as the hydrostatic pressure is increased with depth [30].

In the dynamic situation, the flow in the liquid is driven by the difference in pressure, p between two points. This is given by Bernoulli's equation (Eq. 2.11) according to the principle of continuity (Eq. 2.12) for an incompressible liquid:

$$p_1 + \rho g h_1 + \left(\frac{\rho v_1^2}{2}\right) = p_2 + \rho g h_2 + \left(\frac{\rho v_2^2}{2}\right) \tag{2.11}$$

$$A_1 v_1 = A_2 v_2 = A v \tag{2.12}$$

where A is the area of surface [29].

The pressure p, of the impact of a free jet of metal against a mould wall is given by

$$p = \rho v^2 \tag{2.13}$$

where v is the velocity of the incoming melt. This is the pressure experienced by the mould if impacted by a stream of metal jetting from an ingate. From Eq. 2.13, the dependence on squared velocity entells the need to keep the velocity through the ingates low. The effect of density is also clear and emphasizes the problem for the heavier alloys compared to the lighter alloys.

The buoyancy effect is very important, because liquid metals are so dense, and therefore exert buoyancy force that makes it difficult for internal cores to remain submerged in the liquid metal. This becomes important in the design of core prints for cores that will be completely submerged in the melt. Thin long cores with high ratio of length to diameter may buckle if its expansion is not accommodated at the ends. The high floatation force will ensure that the buckling is in the upward direction. Silica sand cores in liquid magnesium are almost as dense as the melt, and therefore experience little or no buoyancy. Zircon sand core in liquid aluminium is even closer to neutral buoyancy coupled with its low thermal expansion [30].

2.2.2.2 Pressure due to Casting Expansion/Contraction on Solidification

The expansion/contraction of most metals during solidification generate high pressure that expands and deforms the moulds. This expansion is homogeneous[5] and any internal holes will also enlarge in proportion.

However, if the mould is rigid and able to withstand this pressure, then the expansion/contraction of the cast material will no longer be homogeneous. At least part of the expansion will be forced to occur inwards, largely closing any internal porosity present in the casting. By this mechanism, rigid moulds produce sounder cast iron castings. The expansion of the iron is the result of the precipitation of graphite during solidification. Ductile iron is more demanding for rigid moulds than grey iron. Thus, general experience is that ductile iron is more difficult to cast sound.

Considering the fact that grey iron exhibits coupled growth of the eutectic. This means that the austenite and the graphite phases grow together, and the expansion of the graphite and the shrinkage of the austenite approximately cancel. On the other hand, ductile iron exhibits divorced growth of the eutectic phases, with significant shrinkage due to the freezing of austenite, preceding the expansion due to the formation of graphite [30, 35].

2.2.3 Gas Pressure in Moulds and Cores

There is a vigorous evolution of volatile materials from moulds and cores when they come in contact with the liquid metal. In green sand moulds and many other binder systems the main component of this volatilization is water. In other moulds, the gases generated diffuse away through the bulk of the mould. In green sand moulds, due to the presence of clay and other fines, the permeability of the gases becomes difficult. The venting of the moulds was done by needling with wires.

In cores, however, the escape of gases is limited to the area of the core prints to prevent the metal being damaged by passage of gas bubbles through it because the cores are usually covered by the liquid metal. Furthermore, the rate of heating of the core is greater than that of the mould because the core is much smaller in size and it is usually surrounded on several sides by hot metal. All these factors contribute to the internal pressure within the cores rising significantly [30]. Two groups of researchers have done much work on gas evolution from green sand moulds [36, 37], chemically bonded sand cores [37, 38, 39] and shell cores [40]. As a fact, they did not measure the pressure due to these gases in the sand systems. However, Winardi et al. [36], concluded that green sand produces a greater volume of gases at higher rates than any other bonded sand in the foundry due to its high moisture and combustible concentrations while Tiedje et al. [39], quantified the amount of each identified compound evolved from the respective binders investigated. The rate of out-gassing or gas evolution is very different for different binders as shown in Figure 2.7.

[5] i.e. takes place uniformly throughout the material.

Sand cores are generally made from clean, washed and dried silica sand which is closely graded in size to maintain adequate permeability. They are bonded with chemical binders which are rigidized by heat or chemical reactions to produce a strong, easily handled shape. The numerous different systems in use have different responses to the heat of the casting process, and produce gases of different kinds, in different amounts, at different times, and at different rates [30, 39]. At present the phenolic isocyanate-urethane systems are among the lowest overall producers of volatiles as can be seen from Figure 2.7.

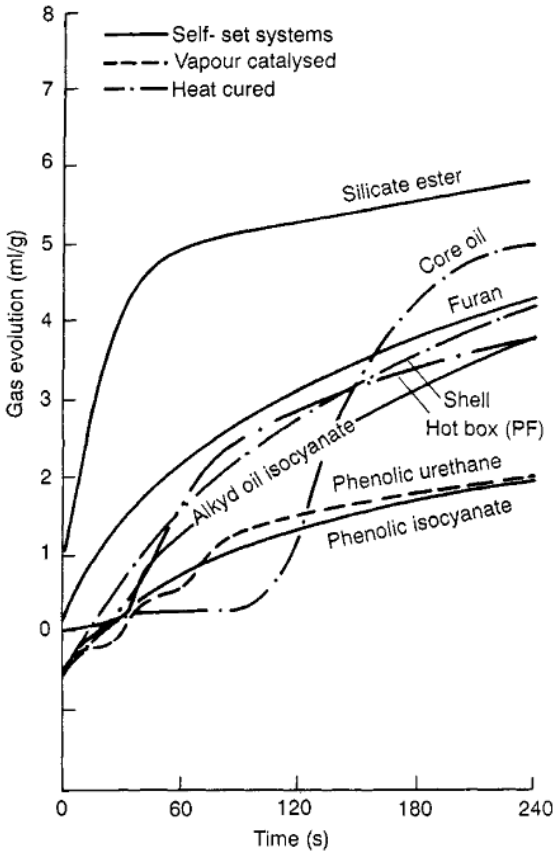

Figure 2.7: Gas evolution from various binder systems [30].

2.2.4 Explosive Reactions

2.2.4.1 General Mould Gas Explosions

General mould gas explosions occur as a result of the reaction of the molten metal and the volatile constituents from the mould, especially water. In most cases, the reactions are dampened by the sand which has high thermal inertia[6]. However, out-gassing reactions are steady and sustained. The content of the out-gassing may be flammable or explosive gases. These include hydrocarbons and other organics

[6]The degree of slowness with which the temperature of a body approaches that of its surroundings.

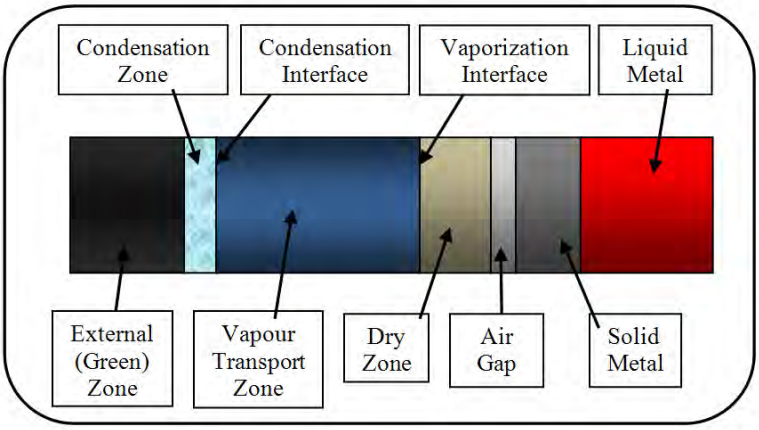

Figure 2.8: The schematic structure of the transformation zones in a green sand mould during casting [36].

such as methane, alcohol, and reaction products like hydrogen, carbon monoxide etc. [30, 37, 38, 39]. Explosion occurs when there is proper mixing of the oxygen of the air with the flammable components. This implies that turbulence enhances these explosions, therefore should be minimized as much as possible during filling. Explosions are common with moulds open to air through the feeders or over sized sprues. Filling from the bottom upwards and properly calculated single sprues can help eliminate such explosions. It is also important to keep moisture content as low as possible while venting the moulds.

2.2.4.2 Water Explosions

This is mainly applicable to green sand moulds. At the completion of filling in a mould, the metal increases its local rate of heat transfer to the mould due to the pressure pulse accompanying the final stage of filling. The enhanced heat transfer causes the water in the mould to evaporate explosively. Subsequently, the high local pressure results in the metal penetrating deeper into the sand [30].

2.2.5 Transformation Zones

When the hot metal heats the surface of the mould, the water will be boiled off, migrating away from the mould face, only to condense again in the deeper, cooler parts of the mould. As the heat continues to diffuse in, the water migrates further. Dry and wet zones travel through the mould [30]. The evaporation of water in green sand produces four distinct zones: dry zone, vapour transport zone (VTZ), condensation zone and external green zones [36] as shown in Figure 2.8.

The dry zone is the closest to the solidifying metal and is separated from the metal by a narrow air gap. This layer has a high temperature resulting in the evaporation of all the moisture in this zone. For silica sand in this zone, some of the quartz is shattered due to rapid heating and some is partially transformed into Tridymite and Crystobalite which have a lower density. The sand in the dry

zone can expand up to 1.5% and has higher compressive strength than the green sand. The steam generated in the dry zone at the vaporization interface flows into a constant temperature zone, called the vapour transport zone. The vapour transport zone has a uniform temperature of 100 °C and uniform moisture content across the whole zone. The vaporization interface moves away from the mould-metal interface with a speed of about 1 mm/s while the condensation interface moves away with a speed of 3 mm/s. Therefore, the vapour transport zone moves deeper into the mould and grows larger with time. The sand strength in the vapour transport zone is much lower than the bulk strength of the sand. Failure of the mould starts with the vapour transport zone. The transported vapour condenses over a narrow zone next to the vapour transport zone. This zone is called the condensation zone. The external zone is the farthest part from the mould-metal interface where the temperature and water content are not affected by the heat [30, 36].

The thickness of the vapour transport zone as a function of time can be determined from the movement of vaporization and condensation interfaces. The depth and the size of the dry zone can also be predicted at any time once the thickness of the vapour transport zone is determined. The movement of the interfaces can be calculated using the rate equation,

$$d = (Dt)^{\frac{1}{2}} \tag{2.14}$$

where

d is distance from the core-metal interface (cm)

D is coefficient of diffusion (cm^2/s)

t is time (s).

The pressure that develops in the vapour transport zone in a green sand mould is given by

$$\triangle P = \frac{Q\, A_C\, L_P\, \mu}{A_P\, P_e} \tag{2.15}$$

where

$\triangle P$ is pressure gradient inside the vapour transport zone (Pa)

Q is gas flow rate ($m^3/m^2/s$)

A_C is core-metal contact area (m^2)

L_P is distance for gas to flow in the vapour transport zone (m)

μ is gas viscosity (kg/m-s)

A_P is gas flow area (m^2)

P_e is permeability coefficient of the vapour transport zone (m^2)

Eq. 2.15 can also be used to determined the pressure in the sand.

As soon as the melt is in contact with the sand mould, the water at the surface of the mould is vaporized and the sand is dry. The instantaneous thickness of dry sand during immersion in a particular geometry can be calculated [36] using:

$$r = R - \left[\frac{L_{Water}\, W_{Water}}{Q\, \rho\, \pi\, l_{Sand}}\right] \tag{2.16}$$

where

r is instantaneous depth of dry sand (m)

R is total sand radius (m)

L_{Water} is heat of vaporization of water (J/kg)

W_{Water} is amount of water in the sand (kg)

Q is heat from melt (J/kg)

ρ is density of sand (kg/m^3)

l_{Sand} is area of the core (m^2)

It is important to note than the rate of advance of the evaporation front is dependent on the amount of water present in the mould. Higher water content makes slower progress. This is because more heat is required to move the front and this extra heat will require extra time to arrive. The extra ability of the mould to absorb heat is also reflected in the faster cooling rates of castings made in moulds with higher water content. Furthermore, measurements of the thermal conductivity of various moulding sands have confirmed that the apparent thermal conductivity of the moisture-condensation zone is about three or four times that of dry sand [30]. Vapour transport zones are present in various degrees in chemically bonded sands [41].

2.2.6 Metal-Mould Reactions

The feasibility of a chemical reaction to occur is based on the free energy change of the system. This energy is referred to as Gibb's Free Energy (G) and is defined as the energy associated with a chemical reaction that can be used to do work. The free energy (G) of a system is the sum of the its enthalpy[7] (H) and the product of the Kelvin temperature (T) and the entropy[8] (S) of the system (Eq. 2.17)[42, 43]:

$$G = H - TS \tag{2.17}$$

Chemical reactions involve a change in free energy $\triangle G$ [44, 45] given by

$$\triangle G = \triangle H - T\triangle S \tag{2.18}$$

In the standard state conditions, the result is the standard-state free energy change ($\triangle G^0$) given by

$$\triangle G^0 = \triangle H^0 - T\triangle S^0 \tag{2.19}$$

The standard conditions referred to here are ambient temperature and atmospheric pressure. The definition of the free energy change of a system as seen in equations

[7]Entalpy is the heat of the system.

[8]Entropy is a measure of the disorder in a system.

2.18 and 2.19 shows the relative importance of the enthalpy and entropy terms as driving forces behind a particular reaction. The change in the free energy of the system measures the balance between the two driving forces that determine whether the reaction is spontaneous. The enthalpy and entropy terms have different sign conventions [46].

Favourable	Unfavourable
$\triangle H^0 < 0$	$\triangle H^0 > 0$
$\triangle S^0 > 0$	$\triangle S^0 < 0$

The Gibb's Free Energy for the formation of products in the standard conditions is called the free energy of formation, $\triangle G^0_f$. The standard-state free energy of a reaction (r) can also be calculated from

$$\triangle G^0_r = \sum \triangle G^0_{f,\,Products} - \sum \triangle G^0_{f,\,Reactants} \tag{2.20}$$

Therefore, for a hypothetical reaction such as: a A + b B $\rightarrow$ c C + d D, the total free energy of reaction is given by

$$\triangle G^0_r = c\triangle G^0_{f,\,C} + d\triangle G^0_{f,\,D} - a\triangle G^0_{f,\,A} - b\triangle G^0_{f,\,B} \tag{2.21}$$

However, the following equation (Eq. 2.22) relates the standard-state free energy of reaction with the free energy of reaction at any moment in time during a reaction (not at standard conditions):

$$\triangle G = \triangle G^0 + RTlnQ \tag{2.22}$$

where

$\triangle G$ is free energy change at any moment

$\triangle G^0$ is the standard-state free energy change

R is the ideal gas constant = 8.314J/mol-K

lnQ is the natural log of the reaction quotient[9].

The net direction of a chemical reaction such as the one above will be from higher to lower energy [45]. Summing up the whole arguments, the following deductions were made on Gibbs Free Energy change as a measure of the driving force for a chemical reaction to occur:

$\triangle G^0 < 0$	$\rightarrow$	Reaction proceeds spontaneously
$\triangle G^0 = 0$	$\rightarrow$	System at equilibrium
$\triangle G^0 > 0$	$\rightarrow$	Reaction will not occur

[9]The reaction quotient is the mathematical product of the concentrations (or partial pressures) of the product of a reaction divided by the mathematical product of the concentrations (or partial pressures) of the reactants of a reaction at any moment.

The understanding of the relationship between the Gibb's Free Energy and Reactions will be valuable in the prediction of the reaction products during casting in green sand and chemically-bonded sand moulds. This is also applied in melt refining [28]. This approach was used by Celal Cingi in the study of Mould-Metal Reactions in Magnesium Investment Castings [47], where he investigated oxides formation in magnesium investment castings. Oxides formation is one of the most important metal-mould reactions. The standard free energies of formation of the simple oxides are given in Ellingham diagram (Figure 2.9) which plots $\triangle G^0$ against temperature. Other information seen in the figure is the partial pressure of oxygen at which it is in equilibrium with various oxides [48]. The temperature at which the oxygen dissociation pressure of various materials reaches a given value can also be obtained from the diagram as

$$-\triangle G = RTlnK_P \tag{2.23}$$

$$= 2.303RTlog\{P_{O_2}/atm\} \tag{2.24}$$

for the reaction considered. It follows that the line drawn from the point where $\triangle G = 0$, $T = 0$ to the appropriate scale mark on the right-hand side of the diagram intercepts the free-energy line for the element concerned at the required temperature. This means that the oxygen dissociation pressure of a given Metal-Metal Oxide system at a given temperature is obtained by joining the point ($\triangle G = 0$, $T = 0$) on the top left hand to the appropriate point (temperature) on the M-MO free energy line and extrapolating to the scale on the right hand ordinate for P_{O_2}(atmospheres). From Figure 2.9, the slope of most of the lines is similar and corresponds to the loss of 1 mol of gaseous O_2; small changes in the slope occur at the temperature of phase changes or the melting point of the metals, and a more dramatic increase in slope signals the boiling point of the metal [49]. The ratio CO/CO_2 can also be seen from the figure and it represents the measure of the oxygen activity at the mould/core-metal interface [48].

2.2.6.1 Mould Surface Reactions

At mould surfaces, pyrolysis[10] will take place. The various organic components in the binder for green sand and chemically bonded sand will decompose producing averagely hydrocarbons, CO, CO_2 which in turn will produce carbon. Carbon is poorly wetted by many liquid metals and therefore assist in improving the surface finish of castings. However, it is reported in [30] that for ductile iron, the solid magnesium oxide-rich film on the surface acts as a mechanical barrier that prevents penetration into the sand. And as such, coating is not required on the cores. This might not be completely true because foundries use coatings on cores for ductile iron castings. They further reported for grey iron, that the melt surface grows a film of liquid silicate, as a result of the oxidizing atmosphere in green sand moulds. This silicate is highly wetting to sand grains therefore, coatings are required on the cores and moulds to prevent metal penetration.

[10]Pyrolysis is the decomposition of organic compounds by the action of heat

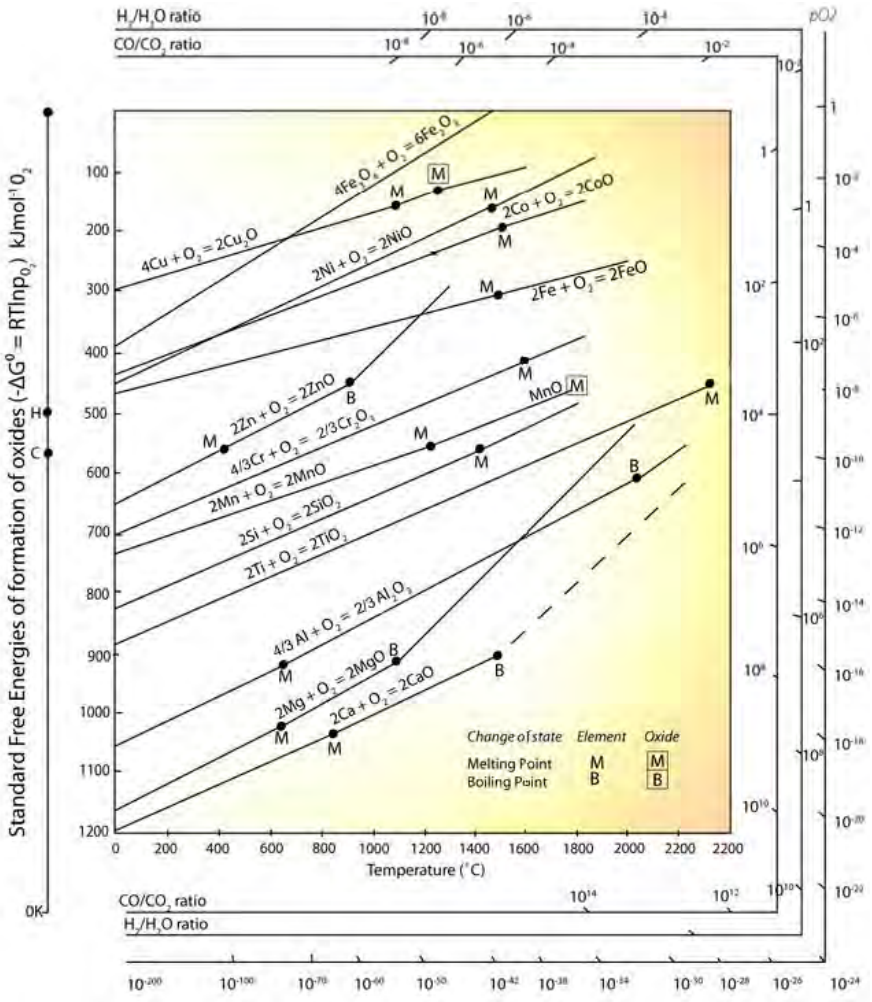

Figure 2.9: Ellingham diagram - change in standard free energy of reaction versus temperature diagram for various oxidation reaction.

Other reactions on the mould surface occur with the sand grains. The most common is the reaction of silica (SiO_2) and iron oxide (wustite, FeO) to produce fayalite (Fe_2SiO_4).

$$2\ FeO + SiO_2 \rightarrow Fe_2SiO_4$$

Fayalite causes the grains to fuse and collapse as they melt into each other, since its melting point is only 1205 °C. This low-melting-point liquid acts as a glue adhering sand grains to the surface of the casting, to form burn-on [30].

2.2.6.2 Metal Surface Reactions

The most common and important mould/metal reaction is the reaction of the metal with water vapour to produce a surface oxide and hydrogen. Another metal surface reaction is carburization, which is more severe in low carbon content steel because of carbon pick-up. This is the reason why low carbon steel is not produced by lost foam process. The carbon atoms most probably adsorb in interstitial sites on the surface, each embedded between four iron atoms [50].

In iron castings, decarburization creates a layer free from graphite. This affects machinability. It is possible that the carbon is oxidized by the water vapour thereby depleting the carbon. Hydrogen decarburizes steel at 925 °C. This reaction is very important in the casting of steel in green sand and resin bonded sand moulds. Strongly surface-active elements such as sulphur retard carburization and nitrogenation by site blocking thereby interfering with the adsorption of carbon [50, 51, 52]. However, sulphur has its own associated limitations in Ductile iron.

The use of furan and phenolic resin-bonded moulds made with catalysts such as sulphuric and/or sulphonic and phosphoric acids, cause problems in ferrous casting because of sulphur and phosphorus pick-up respectively. In ductile iron, sulphur pick-up reverts the graphite from spheroidal to flake form [30, 53], reducing the fatigue resistance. In grey iron, the presence of the hard phosphide phase as a result of phosphorus pick-up creates machining problems [30].

2.3 Defects Associated with Mould and Core Dynamics

During casting, as the molten metal enters the mould or hits the cores, the contact triggers off lots of activities as discussed in Section 2.2 above. The effects of these activities result in changes in the size and shape of moulds and cores. These effects lead to defects, some of which are described below.

2.3.1 Expansion related defects

The expansion of the moulding materials and its magnitude depends on the type of sand and binder systems used. Temperature-expansion curves for various mould materials are shown in Figure 2.10.

Most sand moulds and cores are based on silica sand since it is the most readily available and the cheapest moulding material [27, 54]. Silica sand has a high, non-linear thermal expansion. This expansion is around 1.3 to 1.9% [27]. During casting there is a phase transformation from α- to β-quartz at 573 °C [24, 55, 56, 57, 58]. This is because the α-phase is stable at lower temperatures and has smaller volume than the β-phase which stable at higher temperatures. This takes place by an increase in the dimensions of the a and c axes of the quartz crystal [58]. When the molten metal come in contact with the mould material, a rapid thermal expansion of the sand core occurs as a result of the phase transformation from low volume α-phase to high volume β-phase. This rapid expansion causes core failure due to crack formation. If the metal is still liquid, the metal runs into the cracks in the cores forming fins, or in foundry terms, veins as the metal solidifies [59]. Another group of researchers [60] are of the opinion that immediately after the sand had reached its peak volume, it starts to contract. This contraction ranges from as much as 1% to as low as 0.3%. They concluded that the contraction of the silica sand that occurred after the initial α to β expansion is the cause of the

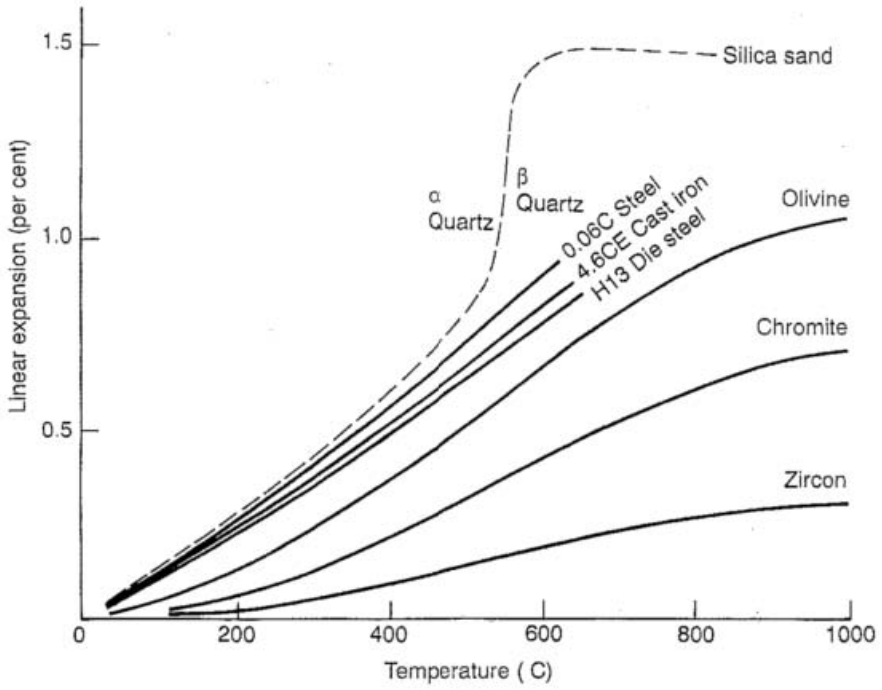

Figure 2.10: Linear expansion - Temperature curves for mould materials [30].

veining defects. Any expansion of the mould results in the demand for extra feed metal otherwise the shrinkage pipe will extend into the casting.

Apart from veining, other defects associated with expansion include rat tails, buckles, and scabs as described below.

2.3.1.1 Veins/Fins

Veins appear on castings surfaces as irregular protrusions with sharp edges as a result of molten metal flowing into cracks on the moulds or cores. They mostly occur in sharp corners, thin sand sections, etc. Thin cores surrounded by heavy metal sections are also prone to cause veining defects [61]. In high production iron foundries worldwide, silica sand is commonly used for making cores due to its availability and relatively low cost compared to other refractory sands. Despite advancement in core technology for improved core production, certain fundamental deficiencies still remain. These include:

- Poor refractoriness of silica sand
- Non-linear thermal expansion of the bonded core sand

Poor refractoriness of the silica sand can lead to sand burn-in/on and/or metal penetration defects. These defects can be controlled by the use of refractory core coatings. However, conventional refractory coating is not enough to overcome the synergistic effects of the non-linear thermal expansion of silica sand and low hot strength of the binders used. This leads to the formation of sand expansion defect

Figure 2.11: Veining or finning and sand burn-on defects on casting surface.

known as "veins" or "fins" [62]. A typical example of veining defect is shown in Figure 2.11.

As liquid iron surrounds an uncoated core during the casting process, the immediate surface temperature of the core rapidly increases - subsequently this heat diffuses deeper into the core substrate. The rate of heat transfer from the melt to the core is governed by several factors, which includes:

- Thermal conductivity of the core substrate
- Heat transfer between the liquid metal and the core surface

The rise in temperature on the core leads to thermal expansion of the core. However, physical stresses are developed in the core due to the fact that the expansion is non-linear across the cross-section, i.e. the core surface wants to expand more than the inner area of the core. During the period of temperature rise, there is little risk of crack formation because only compressive stresses are created. As the temperature at the metal/core interface exceeds 600 °C, the effect on the core is that thermally expanded core surface starts to contract while the material slightly below the surface is still expanding. This leads to the cracking of the substrate surface, if the hot strength of the binder cannot overcome the contractive forces. If the metal at the metal/core interface is still liquid and the substrate surface temperature is above the solidus of the metal, then the crack formed will be filled with liquid metal to form veins or fins [62].

2.3.1.2 Buckle, Scabbing and Rat-Tail

A surface layer of the mould may peel and bows away from the mould and subsequently pressed back against the mould by the arrival of the liquid metal, forming a **buckle.** Alternatively, if the peeled layer fractures, then metal can flow behind

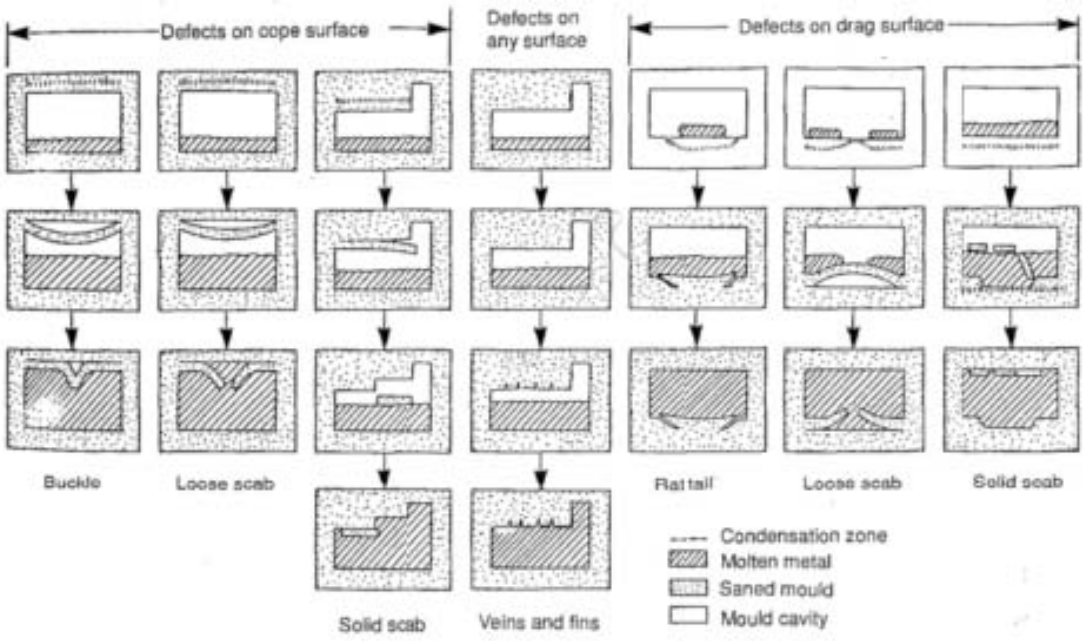

Figure 2.12: A schematic showing mould surface defects [30].

fractured surface, forming a **scab**. When no metal flows into the fractured surface, a **rat-tail** is formed. A schematic of these defects is illustrated in Figure 2.12

2.3.2 Adherence Sand Defects

These defects have to do with combination of moulding material and the metal. There are different types of such defects with different mechanisms of occurrence. The defects include metal penetration, Burn-on, Burn-in, surface roughness, etc.

2.3.2.1 Metal Penetration

According to I. L. Svensson et al. [63], Draper and Gaindhar proposed a general definition of metal penetration accepted by the foundry industry, as the condition in which cast metal has entered into the inter-granular spaces of the moulding material beyond the first layer of sand grains. Many research [64, 65, 66, 67] have been carried out on this type of defect because of the high demand for quality surface finish. Syvestro [64] identified and described different types of metal penetration namely, mechanical penetration, chemical (reaction) penetration, vapour penetration, water explosion penetration, and eutectic exudation penetration depending on the nature of their causes.

The requirements for penetration to occur are described by Eq. 2.25 [67].

$$P_{pen} = -\frac{2\sigma cos\theta}{r_p} \tag{2.25}$$

where,

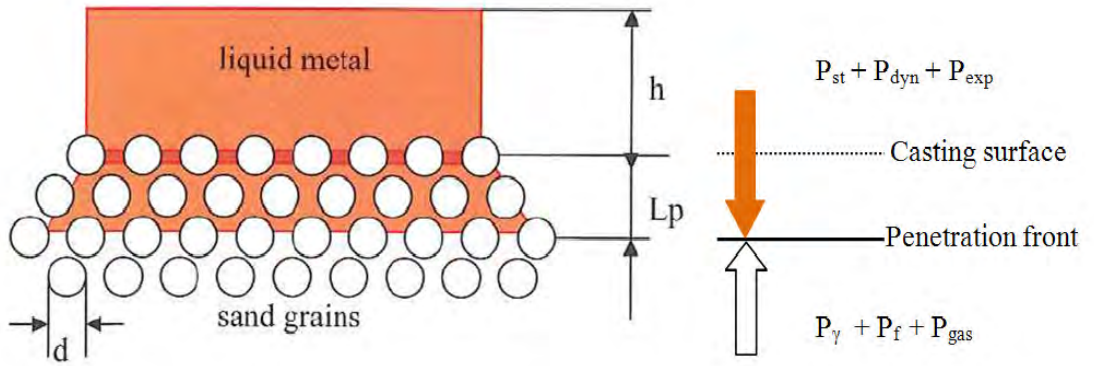

Figure 2.13: Pressure balance during metal penetration in moulding aggregates [66].

P_{pen} is the penetration pressure (N/cm^2)

σ is the surface tension of the liquid metal (N/cm)

θ is the contact angle between the liquid metal and the substrate material used for the mould (degrees)

r_p is the pore size of the mould material (cm)

From this equation, it can be seen that the causes of penetration can include too large grain fineness number GFN, loosely packed sand, or impurities in the metal that lower the contact angle. Therefore, if $P_{pen} > 0$, there will be no penetration but if $P_{pen} < 0$, there will be penetration. However, Piwonka [68] reported that most penetration defects are caused by poor casting design, not poor moulds. His argument is based on the observation that most penetration problems in cast iron are found in corners where heat is concentrated (i.e. a hot spot).

Two major types of penetration will be described further - mechanical penetration and chemical penetration. Mechanical penetration is the transport of metal into the inter-granular spaces between the sand grains as a result of excessive metallostatic pressure without displacing the sand grains [61]. The mechanism of mechanical penetration is shown as a pressure balance at the mould-metal interface and a schematic illustration is shown in Figure 2.13:

The liquid metal exerts a static pressure; P_{st}, a dynamic pressure; P_{dyn}, and pressure due to expansion during solidification, P_{exp}. All these pressures favour penetration. However, capillary pressure; P_{γ}, from the wetting of the sand grains, gas pressure from expanding mould gases; P_{gas}, and frictional pressure P_f between the liquid metal and sand grains oppose it. The balance of these pressures is given as an equation:

$$P_{st} + P_{dyn} + P_{exp} = P_{\gamma} + P_f + P_{gas} \tag{2.26}$$

When the left-hand side of the Eq. 2.26 is greater than the right-hand side, liquid metal is likely to penetrate into the inter-granular spaces of the sand grains, leading to penetration. The equivalent capillary diameter; d_e for sand moulds with refractory coatings, is given by

$$d_e = 0.702d \tag{2.27}$$

where d is the average coating particle diameter.

Chemical penetration can occur when a chemical reaction produces a change in one of the variables in Eq. 2.25, leading to penetration. The reaction of liquid metal with oxygen (in the air in the mould, or in the moisture in the sand) to form iron oxide; FeO which has a lower contact angle (21 °) than Fe on silica substrate. This change in the value of θ in Eq. 2.25 may cause penetration to occur depending on the values of the other variables. FeO can wet silica and penetrate, followed by iron which wets iron oxide. Furthermore, FeO can also react with the silica to form fayalite (Fe_2SiO_4). The dissolution of silica from the sand grains increases the pore size which also enhances penetration. The reaction sequence is given below.

$2Fe + O_2 \rightarrow 2FeO$

$2FeO + SiO_2 \rightarrow Fe_2SiO_4$

Fayalite is often found on the surface of castings with penetration defects, and its presence is taken as a sufficient evidence that the penetration is chemical in nature. Oxides of other metals may also be formed on the casting surface depending on the composition of the metal cast. Alloys of high Mn content pose problem due to preferential oxidation of Mn leading to a low melting point silicate which produces a casting with strongly adhering sand. These silicates have been identified as $MnSiO_3$ and $MnSiO_4$ [67]. A typical metal penetration is shown in Figure 2.14 and a typical penetration microstructure is shown in Figure 2.15.

2.3.2.2 Burn-On and Burn-In

Burn-on is a thin sand crust firmly adhering to the casting surface. The defect occurs to a greater extent in the case of thick-walled castings and at high temperatures. The defect indicates that the mould and the metal were overheated causing a mould-metal reaction resulting in oxides and silicates covering the metal surface. According to Kruse et al. [69], the causes of these defects have been a subject of research for many years quoting Asanti 1966 and Chernogorov 1970. They attributed the defects to vapour penetration, liquid iron silicate formation, and mechanical penetration mechanisms. They occur in the hottest locations of the casting. The most distinguishing feature of burn-on is that it never penetrates further than one or two grains of surface moulding sand deep on the mould-metal interface. Sylvestro [64] claims that it is easily removed. His studies showed that the sand grains are held on the surface of the casting by oxide adhering agent.

The burn-in indicates that it is more severe than burn-on and more difficult to remove. More sand grains are held on the surface of the casting by more oxide adhering agent. A typical example of burn-on is shown in Figure 2.16.

Figure 2.14: Metal penetration.

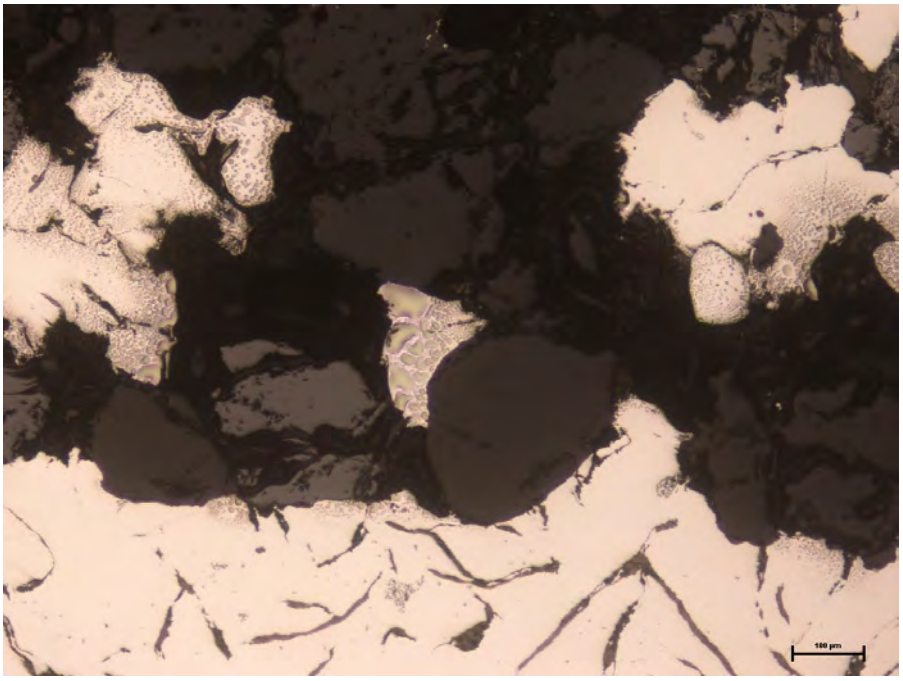

Figure 2.15: Metal penetration micrograph showing the metal (light area) and sand (dark area).

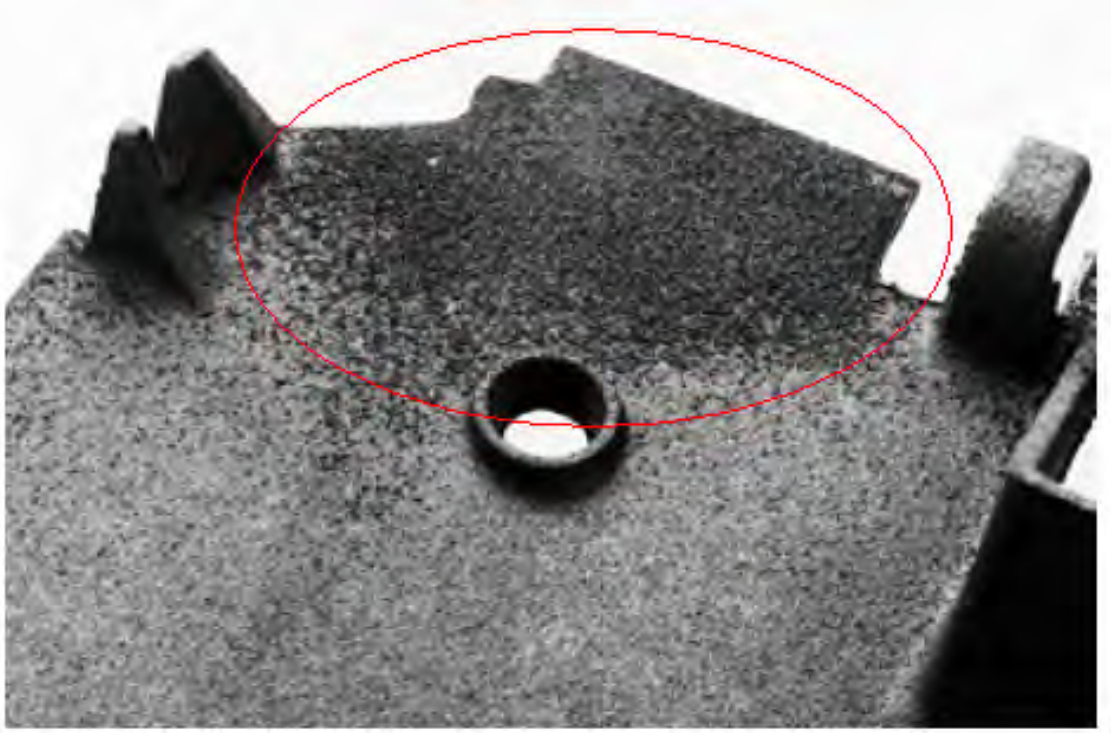

Figure 2.16: A casting with closely adhering sand layer [70].

2.3.3 Gas Related Defects

Gas related defects include pin holes, blow holes, etc. These are smooth walled, nearly spherical cavities often not contacting the surface. Smaller cavities appear in groups while larger cavities seem to be isolated. These are produced by gas entrapped in the metal during solidification. These defects are due to lower gas passing tendency of the mould which is caused by poor venting, lower permeability of the mould, and improper casting design. The lower permeability of the mould is due to use of finer grains, higher percentage of clay and moisture and excessive ramming of mould. Often, they are only exposed after light machining [71].

2.3.3.1 Pin Holes

These are small holes created when expelled gases are escaping as the molten metal solidifies which decreases the solubility of gases. In other words, these are very small diameter and long pin holes showing the path of escape. The high pouring temperature which increases the gas pick-up is the main reason for this defect. An example of a pin holes is shown in Figure 2.17.

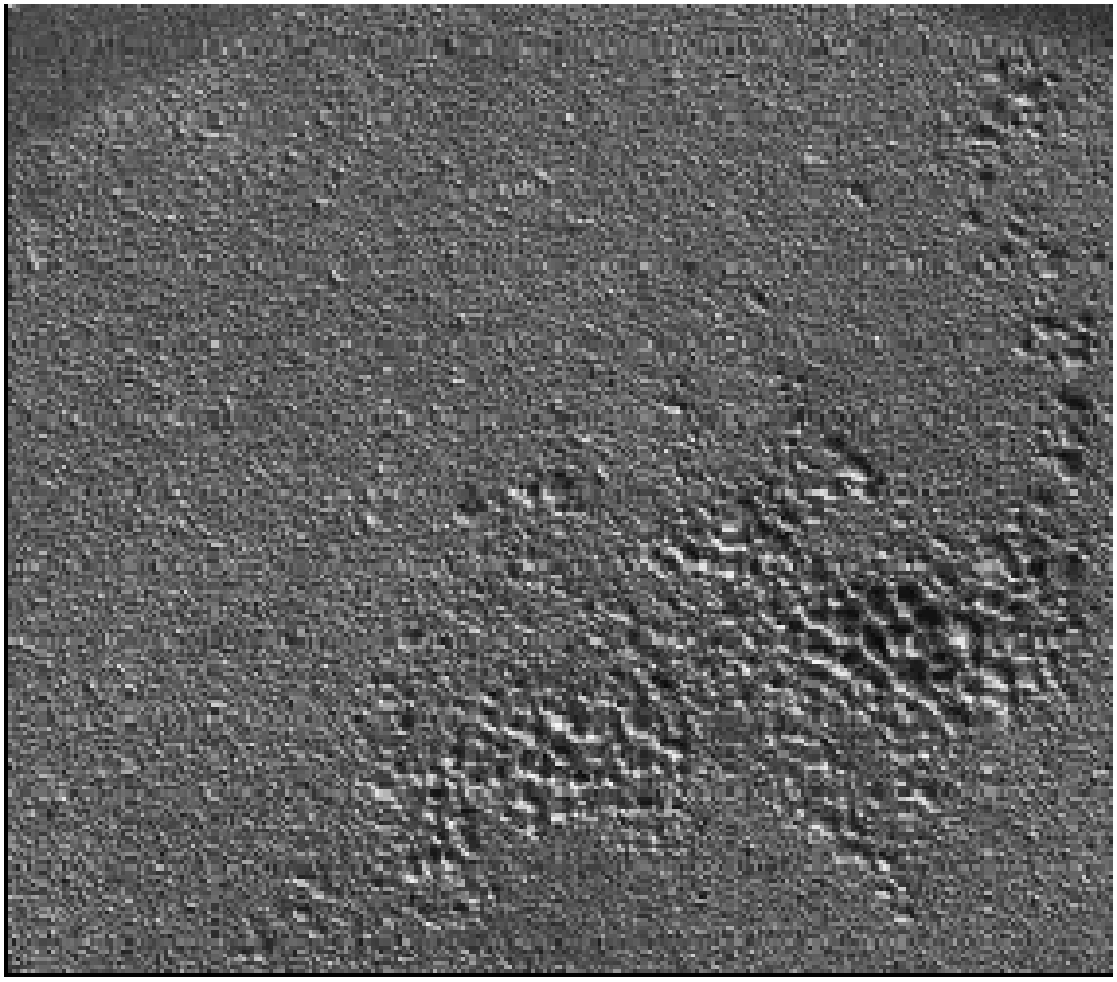

Figure 2.17: Pin holes defect [70].

2.3.3.2 Blow Holes

These are spherical, flattened or elongated cavities present inside the casting or on the casting surface. When present inside the casting they are called blow holes while they are called open blows if they appear on the surface of the castings. If the gas pressure in the core/mould increases to the point at which it exceeds the pressure in the surrounding liquid, then gas will force its way out of the core and into the liquid.

If the mould is filled quickly, then the hydrostatic pressure due to depth in the liquid metal is built up more rapidly than the pressure of gas in the core/mould. The higher metal pressure effectively suppresses any bubbling of gas through the casting. If the mould is filled slowly, the gas pressure in the core/mould exceeds the metal pressure and remains higher during most of the filling of the mould. Gas escapes through the metal during the late stage of the filling [30]. Figure 2.18 shows a casting with blow holes exposed after machining.

Figure 2.18: Blow holes defects [70].

Chapter 3

Surface Technology

Surface technology is concerned with: (1) defining the characteristics of a surface, (2) surface texture, (3) surface integrity, and (4) the relationship between manufacturing processes and the characteristics of the resulting surface [72]. However, in this project the primary concern is mainly with surface texture (surface topography).

The main goal of this project is to use the novel coatings to improve the surface quality of the castings. The coatings are applied to the cores to produce a smooth surface finish, free from veining defects, metal penetration, burn-on/in, scabs, buckles, etc., and with very low surface roughness. Therefore, it is very important to make surface characterization of the surface of the castings. The parameters of interest in the assessment of the quality of the surface of castings are the surface texture and microstructural evolution around the metal-mould interface for both grey iron and ductile iron followed by the expected reactions taken place at the casting surface during the casting process.

All surfaces have their own characteristics, which collectively are referred to as surface texture. Surface texture is identified in terms of well defined and measurable quantities such as flaws[1], lay[2], roughness, and waviness[3]. Roughness is defined as closely spaced, irregular deviations on a small scale; it is expressed in terms of its height, width, and distance along the surface [73]. Surface roughness is described by various parameters which include maximum profile peak height, Rp; maximum profile valley depth, Rv; maximum height profile, Rz; mean height of the profile elements, Rc; and total height of the surface, Rt. All these are referred to as amplitude profile parameters (peak to valley). The other group is referred to as amplitude parameters (average of ordinates) and includes the arithmetic mean value, Ra; and the root-mean-square roughness, Rq [74]. The Ra and Rq parameters are generally and commonly used to describe the surface roughness of a substrate. For its simplicity, the arithmetic mean value (Ra) was adopted internationally in the mid-1950s and used widely in engineering practice. The units used for surface roughness are micron (µm) or µin (1 µm = 40 µin or 1 µin = 0.025 µm) [73]. In this project, the Ra values will be considered as the parameter to

[1]Random irregularities such as scratches, cracks, holes, depressions, tears or inclusions.

[2]Direction of the predominant pattern.

[3]Deviation from a flat surface.

assess the quality of the surface of the castings while introducing areal (surface) parameters (Sa and Sq).

3.1 Surface Topography

3.1.1 Surface Topography Measuring Instruments

Line profiling methods produce a topographic profile, z(x). This measurement is commonly performed with a stylus instrument (Figure 3.1a). A typical stylus instrument gives height information and it consists of a stylus that is in physical contact with the surface being measured and a transducer that converts the vertical movement of the stylus into an electrical signal. The electrical signal is amplified and processed or converted into a digital signal via an A/D converter and then analysed using a computer. The part of the stylus in contact with the surface is usually a diamond tip with a radius of curvature ranging from 2 µm to 10 µm. The major disadvantages of using a stylus instrument is that it requires direct physical contact with the specimen, which limits the measuring speed [74, 75].

There are also non contact optical instruments that measure the actual surface topography by either scanning a beam or using the field of view (profile and areal methods), and those that measure a statistical parameter of the surface, usually by analysing the distribution of scattered light (area integrating methods). Many optical instruments use a microscope objective to magnify the features on the surface being measured. Magnification varies from 2.5× to 100× depending on the application and the surface of the specimen. Instruments using a microscope objective have two identified fundamental limitations [74]. Firstly, the numerical (or angular) aperture (NA) determines the largest slope angle on the surface that can be measured and also has effects on the optical resolution. The NA of an objective is given by

$$NA = n \sin \alpha \tag{3.1}$$

where n is the refractive index of the medium between the objective and the surface (usually air, so n is approximated to 1) and α is the acceptance angle of the aperture. The acceptance angle determines the slopes on the surface of the specimen that can physically reflect back into the objective lens and hence be measured. The second limitation is the optical resolution of the objective. The resolution determines the minimum distance between two lateral features on a surface that can be measured. The resolution is approximately given by

$$r = \frac{\lambda}{2\,NA} \tag{3.2}$$

where λ is the wavelength of the radiation. For a theoretically perfect optical system (i.e. aberration free), the optical resolution is given by Rayleigh criterion, where the $\frac{1}{2}$ in Eq. 3.2 is replaced by 0.61 [74]. A stylus instrument and an optical instrument are presented in Figure 3.1.

(a) A stylus instrument (b) Alicona InfiniteFocus microscope

Figure 3.1: Surface topography measurement instruments.

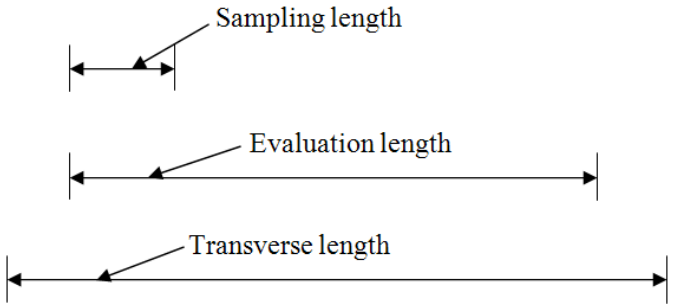

Figure 3.2: Length measures on a profile [76].

3.1.2 Surface Profile Measurement

This is the measurement of a line across the surface that can be represented mathematically as a height function with lateral displacement, z(x). Profile measurement is performed with a stylus or optical scanning instrument, by transversing the stylus across a line on the surface in a perpendicular direction of the lay unless otherwise stated [76]. The conditions are defined in ISO 4287 and 4288 [77].

3.1.2.1 Evaluation Length

This is the total length along the surface (x axis) used for the assessment of the profile under investigation. ISO 4287, advocates the use of five sampling lengths for roughness evaluation of surface roughness, the sum of which gives the evaluation length.

3.1.2.2 Total Transverse Length

The total length of the surface transversed in making a measurement is the total transverse length. It is usually greater than the evaluation length in order to allow mechanical and electrical transients to be excluded from the measurement. The length measured is shown in Figure 3.2.

3.1.2.3 Profile Filtering

This is a means for selecting a range of structure in the total profile for analysis. On the other hand, it may be thought of as a means of rejecting information considered irrelevant, for example noise from the instrument. A filter that rejects short wavelengths while retaining longer ones is referred to a low-pass filter. A filter that preserves short-wavelengths while rejecting long wavelengths is referred to as a high-pass filter. The combination of a low-pass and a high-pass filter to select a restricted range of wavelengths with both high regions and low regions rejected is called a band-pass filter. The wavelength at which the transmission (and also the rejection) is 50% is called the cut-off of that filter [74].

The transmission characteristics of a filter are determined by its weighting function[4]. The weighting function, standardized by ISO 11562, in the form of Gaussian probability function is described mathematically by

$$s(x) = \frac{1}{\alpha\lambda} exp\left(\frac{x}{\alpha\lambda}\right)^2 \tag{3.3}$$

where α is a constant designed to provide 50% transmission at a cut-off wavelength of λ, and is equal to

$$\sqrt{\frac{ln2}{\pi}} \approx 0.4697 \tag{3.4}$$

The filter effect of the weighting function, $s(x)$, is exclusively determined by the constant, α. A surface filter separates the profile into long wave and short wave components. The roughness profile is the profile derived from the primary profile by suppressing the long-wave component using a short-wavelength (high-pass) filter, with a cut-off, λc. The roughness profile is the basis for the evaluation of the roughness profile parameters [74, 76]

3.1.2.4 Surface Profile Parameters

These are amplitude profile parameters (peak to valley), amplitude parameters (average of ordinates) and spacing parameters. However, two amplitude parameters (average of ordinates) are discussed because these are the most commonly used parameters in the industries and in research.

Arithmetic mean value, Ra

The Ra parameter is the arithmetic mean of the absolute values of the ordinate, z(x), within the sampling length, L, [74, 79, 80] given by

$$Ra = \frac{1}{L}\int_0^L \mid z(x) \mid dx \tag{3.5}$$

[4]A mathematical device used when performing a sum, integral, or average in order to give some elements more "weight" or influence on the result than other elements in the same set.

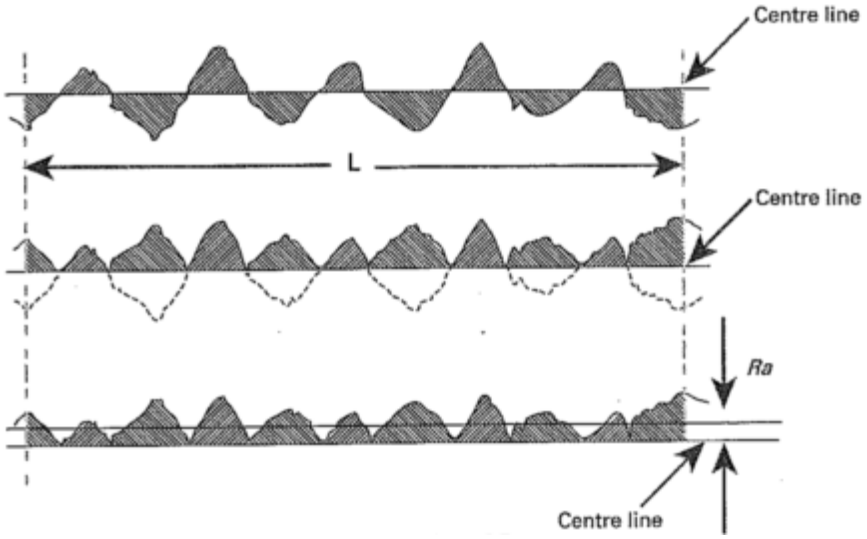

Figure 3.3: A graphical representation of the derivation of Ra [74].

Eq. 3.5 is for a continuous z(x) function. L is the sampling length. However, when making surface texture measurements, z(x) is generally determined over a discrete number of measurement points. In this case, the equation is written as

$$Ra = \frac{1}{N} \sum_{i=1}^{N} \mid Z_i \mid \tag{3.6}$$

where N is the number of measured points in the sampling length [74, 81].

The Ra is derived by placing the areas of the graph below the centre line within the sampling length above the line (Figure 3.3). The Ra value is the mean height of the resulting profile [74]. The Ra value over one sampling length is the average roughness; therefore, the effect of a single non-typical peak or valley will have only a small influence on the value. Ra value assessment is made over a number of consecutive sampling lengths and the average value obtained is accepted.

The root-mean-square roughness, Rq

The Rq parameter is defined as the root mean square value of the ordinate values, z(x), within the sampling length [74, 82],

$$Rq = \sqrt{\frac{1}{L} \int_0^L z^2(x) dx} \tag{3.7}$$

The discretized form which is normally used is

$$Rq = \sqrt{\frac{1}{N} \sum_{i=1}^{N} Z_i^2} \tag{3.8}$$

Table 3.1: ISO specification standards [74, 83].

ISO standard	**Brief description**
ISO 3274	Describes a typical stylus instrument and its characteristics
ISO 4287	Gives the definitions of the surface profile parameters and how to calculate them
ISO 4288	Describes the various default values, and basic rules and procedures for surface texture analysis
ISO 11562	Describes the phase correct Gaussian filter that is applied for various cut-off filters used for surface profile analysis
ISO 12179	Presents the methods for calibrating contact stylus instruments for profile measurement
ISO 5436 P1	Describes the artefacts that are used for calibrating stylus instruments
ISO 5436 P2	Describes the concepts and use of software measurement standards
ISO 1302	Provides the rules for the indication of surface texture in technical product documentation such as drawings, reports etc

Rq is always 11% larger than Ra for a given surface. However, this is only true of a sinusoidal surface, although Rq is always larger than Ra. The Rq parameter is used in optical applications where it is more directly related to the optical quality of a surface. Also, Rq is directly related to the total spectral content of a surface [74]. Eqs. 3.7 and 3.8 show that there is a relationship between Rq and Ra, as shown by the ratio Rq/Ra [73].

3.1.2.5 Profile Specification Standards

According to [74, 83] there are nine ISO specification standards relating to the measurement and characterization of surface profile. These standards only cover the use of stylus instruments and are presented in Table 3.1.

3.1.2.6 Symbols for Surface Texture

Designers specify surface texture on an engineering drawing by means of symbols as shown in Figure 3.4. The symbol designating surface texture parameters is a check mark, with entries as indicated for average roughness, waviness, cutoff, lay, and maximum roughness spacing.

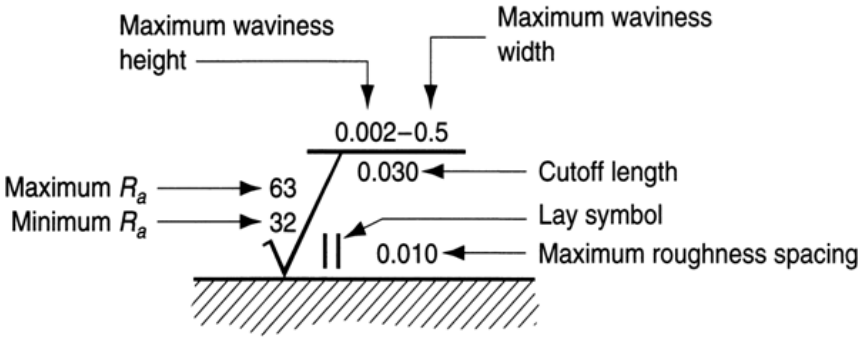

Figure 3.4: Surface texture symbol with identification labels in engineering drawings [72].

Table 3.2: Comparison of profile and areal analyses [84].

Criterion	**Profile analysis**	**Areal analysis**
Popularity	Well known	New
Background	ISO 4287, 4288	Surfstand book
Repeatability	Medium	High
Analyzed area	Small	Large
Result values	Ra, Rq, Rz	Sa, Sq, Sz
Surface structure	With direction	Without direction

3.1.3 Area Surface Texture Characterization

Due to increasing need to relate surface texture to surface function, it becomes pertinent to adopt a three-dimensional, or "areal", measurement of the surface. A 2D profile measurement has inherent limitations. It does not indicate functional aspects of the surface. Again, with profile characterization it is often difficult to determine the exact nature of a topographic feature. Areal measurements provide a more realistic representation of the whole surface and have more statistical significance [74]. A comparison of the profile and areal profile analyses is presented in Table 3.2.

3.1.3.1 Areal Filtering

The current standardized approach for the separation of the roughness and waviness components from a primary surface is a Gaussian filter. The weighting function of an areal filter is the Gaussian function defined by

$$s(x,y) = \frac{1}{\alpha^2 \lambda cx \lambda cy} exp\left[-\frac{\pi}{\alpha^2}\left(\frac{x^2}{\lambda cx^2} + \frac{y^2}{\lambda cy^2}\right)\right] \tag{3.9}$$

$$-\lambda cx \leq x \leq \lambda cx, \;\; -\lambda cy \leq y \leq \lambda cy \tag{3.10}$$

where x, y are the two-dimensional distance from the centre of the weighting function, λc is the cut-off wavelength, α is a constant, to provide 50 % transmission characteristic at the cut-off λc, and $\alpha = 0.4697$.

3.1.3.2 Areal Parameters

There are two classes of areal parameters, namely field and feature parameters. However, two field parameters with direct application to the investigation will be discussed for this project.

The root-mean-square value of the ordinates, Sq

This is the root-mean-square value of the surface departures, z(x,y), within the sampling area

$$Sq = \sqrt{\frac{1}{A} \iint_A z^2(x,y)\, dxdy} \tag{3.11}$$

where A is the sampling area, xy. This equation is for a continuous z(x,y) function. For a sampled definition,

$$Sq = \sqrt{\frac{1}{MN} \sum_{j=1}^{M} \sum_{i=1}^{N} Z_{i,j}^2} \tag{3.12}$$

The arithmetic mean of the absolute height, Sa

The Sa parameter is the arithmetic mean of the absolute value of the height within a sampling area,

$$Sa = \frac{1}{A} \int_A \mid z(x,y) \mid dxdy \tag{3.13}$$

For a discrete data,

$$Sa = \frac{1}{MN} \sum_{i,j=1}^{MN} Z_{i,j} \tag{3.14}$$

The Sa parameter is the closest relative to the Ra parameter, however, they are fundamentally different because areal, Sa parameters, use areal filters whereas profile, Ra parameters, use profile filters [74]. Deviations on the surface structure can be detected with the Sa value. A change in the Sa value suggests a change in the production process [84].

3.1.3.3 Area Specification Standards

The areal specification standards are at various stages of development. The idea is to have the profile standards as a subset of the areal standards. All the areal standards are part of ISO 25178.

Chapter 4

Simulations

Computerized simulation programmes for casting processes have been developed since the early 1980s. These simply reproduce the trial-and-error methods previously applied on real casting processes on a computer. This is both quicker and cheaper, and also enables a better understanding of metal behaviour to be obtained [85, 86].

A series of casting processes were simulated using a commercial software, MAGMASOFT®, in order to predict the temperature distribution around the cores, sand penetration, burn-on, and hot spot areas including other relevant criteria in the study of casting defects such as pressure distribution during pouring. The influence of coating layer deposit on the cores was also elucidated with respect to thermal behaviour of the cores. The simulation included both filling and solidification so that it is possible to assess how the melt flow and the heat transfer interaction with the mould and core surfaces.

4.1 Mesh Generation

Mesh are small volumes in which calculations are performed. Complex geometries are divided into these small volumes. Fluid flow and heat transfer is calculated using Navier-Stokes equation and the heat transfer equation respectively. In combination with mass and energy balances, these equations describe fluid flow and heat transfer in and out of individual volumes. Thermal fields and flow velocities can be used in various criteria functions to describe the risk of mould erosion, formation of shrinkage porosity, local microstructure, etc. A fine mesh is divided into many elements while a coarse mesh has few elements. The finer the mesh the more accurate the results and the longer the simulation time. In the simulation of the casting processes, MAGMA 5.1 version was used and it has the ability to generate mesh automatically while maintaining the accuracy and simulation time. The Magma 5.1 mesh generation creates the mesh of the geometry using one of the following four modes [87]:

- Number of Elements
- Minimal Wall Thickness

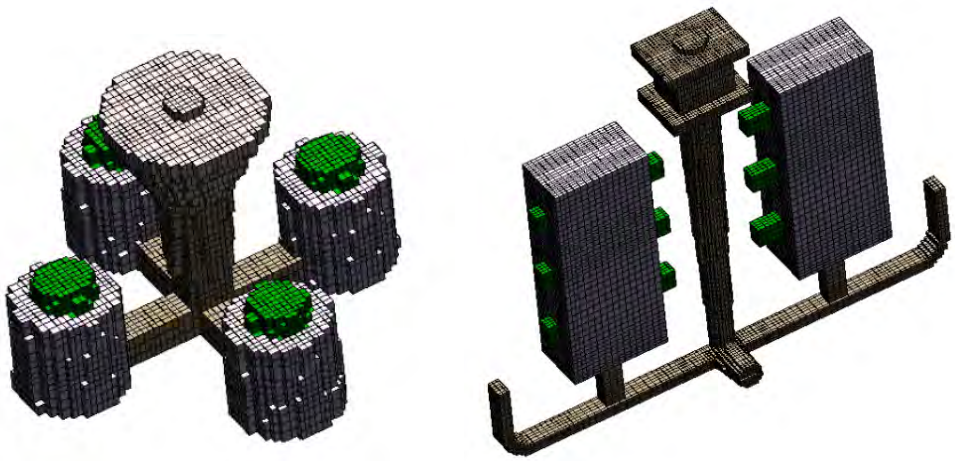

(a) Horizontally-parted mould - casting (b) Vertically-parted mould - casting

Figure 4.1: Enmeshment of the geometries.

- Single Parameter Set
- Multiple Parameter Set

However, in the mesh generation used for these simulations, the number of elements was specified and the mesh was automatically generated. Figure 4.1 shows the enmeshed version of the geometries.

4.2 Simulations

A casting process simulation requires the definition of both geometry and process parameters. MAGMA 5.1 can simulate both sand and permanent mould processes. In the sand mould process used for this project simulations, the definition of the required process parameters input is managed through the following main functions: Materials Definitions, Heat Transfer Definitions, Casting Processes, and Treatment after Casting. There are two solvers for the calculation of mould filling, the standard solver and solver 5. Solver 5 gives more accurate results, but needs more computer capacity than the standard solver [87]. Solver 5 is used for this project simulations.

After the coating layer deposit was measured from the image analysis using the Image Pro Plus software for the sol-gel coatings containing 0, 40, 50 and 60% solid contents, the coating layer was modelled in each case by adding the layer thickness obtained from the measurements to the core dimensions. Simulations were carried out considering mould filling and solidification sequences. In the simulations performed, efforts were made to replicate the conditions used or intended to be used for the physical experiments in the foundry. These include the melt temperature, filling time, the pouring temperature, casting size, core size, metal, initial and boundary conditions.

4.2.1 Horizontally-Parted Moulds

The model used for the simulations in horizontally-parted moulds is shown in Figure 4.2. This model contains four casting cavities with a central downsprue. Each casting cavity contains a core with an embedded thermocouple at the centre of the core. This model helps to eliminate the effect of variation in melt temperature, filling time and pouring temperature. It also enhances effective and comparative studies of different coatings, different dipping times, different core systems, and measurement of different temperatures in the cores.

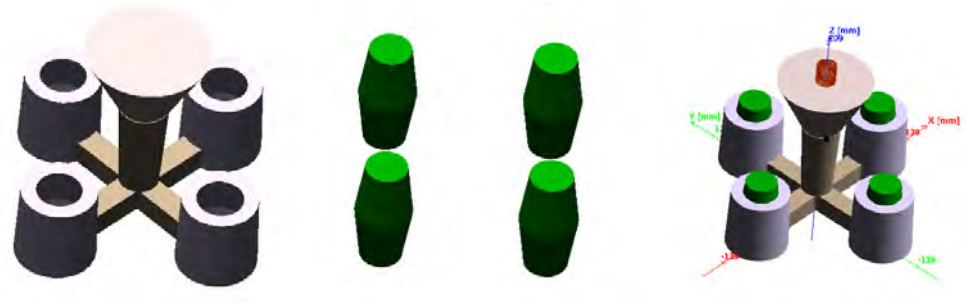

(a) The casting (b) The cores (c) Casting and cores

Figure 4.2: CAD model for the horizontally-parted mould.

4.2.2 Vertically-Parted (DISA) Moulds

The pattern used for vertically-parted moulds is illustrated in Figure 4.3. This pattern contains two heavy casting cavities with positions for three cores horizontally placed. The downsprue is in the middle of the two cavities as shown in Figure 4.3a. The model helps in the investigation of the influence of pressure height on the surface quality of the castings. The position of the three cores in the casting enables the investigation of the surface of quality of castings around the cores relative to the heights of their locations.

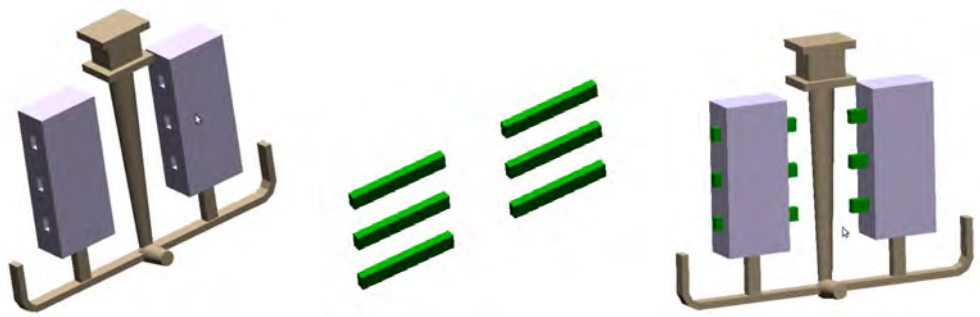

(a) The castings (b) The cores (c) Casting and cores

Figure 4.3: CAD model for the vertically-parted mould.

4.2.3 Temperature Distribution in the Cores

In these simulations the cores are produced using silica sand with cold box process. Silica sand has a critical temperature at which it expands rapidly because of the transformation from α-quartz to β-quartz as shown in Figure 2.10. This critical temperature is 573 °C. Therefore, it is expected that when the cores are heated up to this temperature, they will expand rapidly causing thermal stresses in the core due to non uniform expansion. This will in turn lead to cracking of the cores. The temperature distribution fields from simulations are shown in Figure 4.4 for horizontally-parted moulds. Figure 4.4(a) shows the temperature distribution at completion of filling, it can be seen from the figure that the maximum temperature reached at the surface of the cores, at the end of filling, is between $300 - 400$ °C. As solidification progressed, the heat diffused more into the bulk of the core raising the temperature as shown in Figure 4.4b-f. This simulation shows that if at all there will be crack formation in the cores, it will occur during solidification and not during filling, which only took 5 s. Therefore, to avoid the defects formed as a result of cracking of the core, the solidification should start along with filling and continue after filling in order to form the first solidified metal skin before cracking occurs.

The temperature distribution fields for the vertically-parted mould are shown in Figures 4.5 and 4.6 for filling and solidification respectively. The simulation results during filling shows that the down core is most liable to crack during the filling process because its temperature rose above the silica sand critical temperature. Consequently, veining defects are likely to occur in the lowest core. However, it should be observed that the middle and top cores are subjected to high temperature radiation from the incoming melt, especially, the top core before the melt reaches it since the mould is filled from the bottom. It is suggested that this condition will get the cores completely fried or roasted by the radiation in that they are weakened before the melt gets to them. The binder at the surface of these cores, particularly the top cores may be destroyed thereby exposing the inter-granular pores in these cores. This will lead to high surface roughness of the casting in contact with these top cores.

The temperature distribution fields in the cores during solidification (Figure 4.6) show that the cores are subjected to high thermal distortion as we can see from the temperature gradient. From Figure 4.6b-f, it is obvious that the simulation predicts that the cores are completely destroyed by the heat from the melt, as it shows that the core temperature is equal to that of the melt (this means that the core binder breaks down completely). This suggests that there will be greater tendency for the formation of sand burn-on and metal penetration.

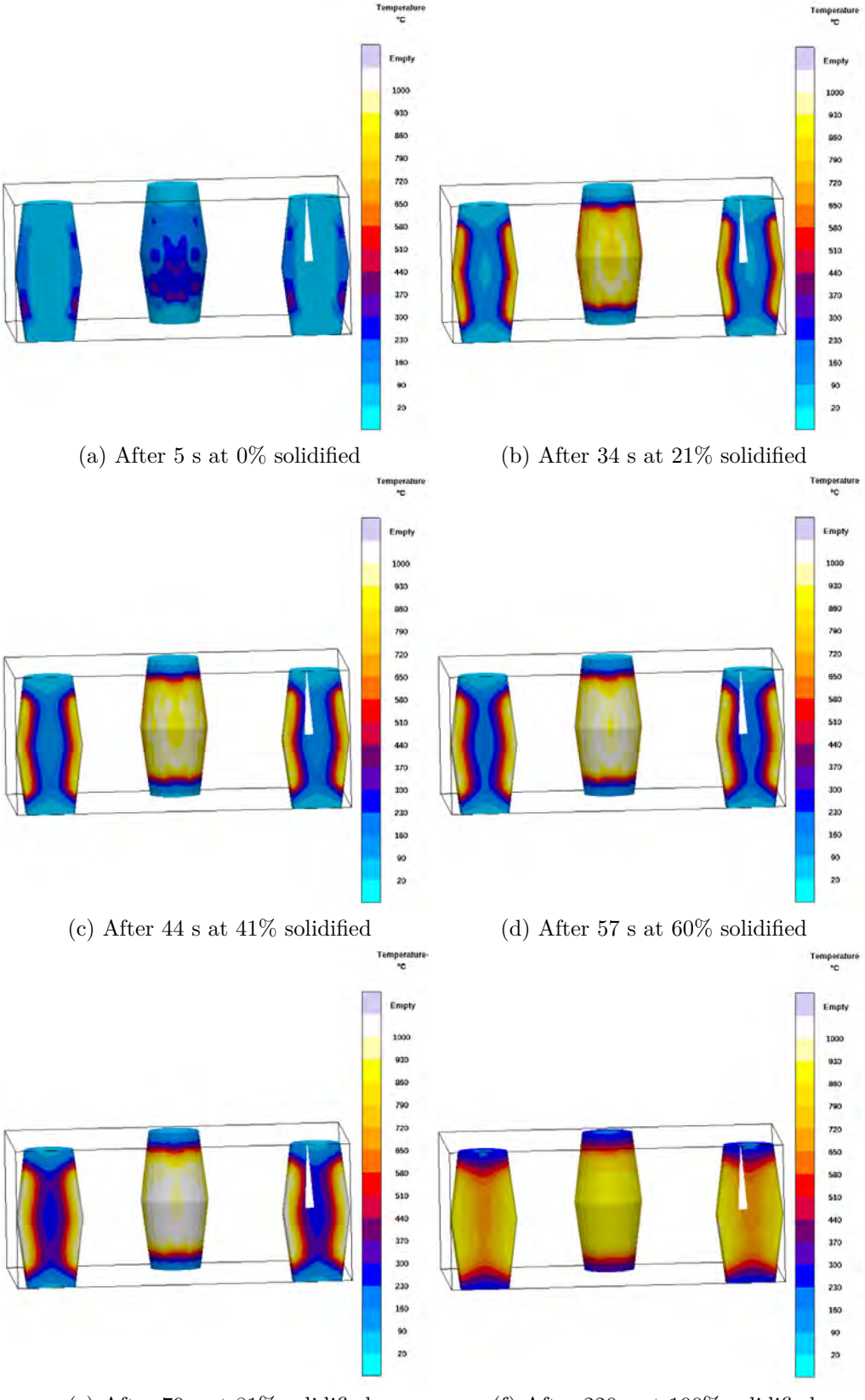

(a) After 5 s at 0% solidified

(b) After 34 s at 21% solidified

(c) After 44 s at 41% solidified

(d) After 57 s at 60% solidified

(e) After 79 s at 81% solidified

(f) After 220 s at 100% solidified

Figure 4.4: Temperature distribution in the cores during solidification.

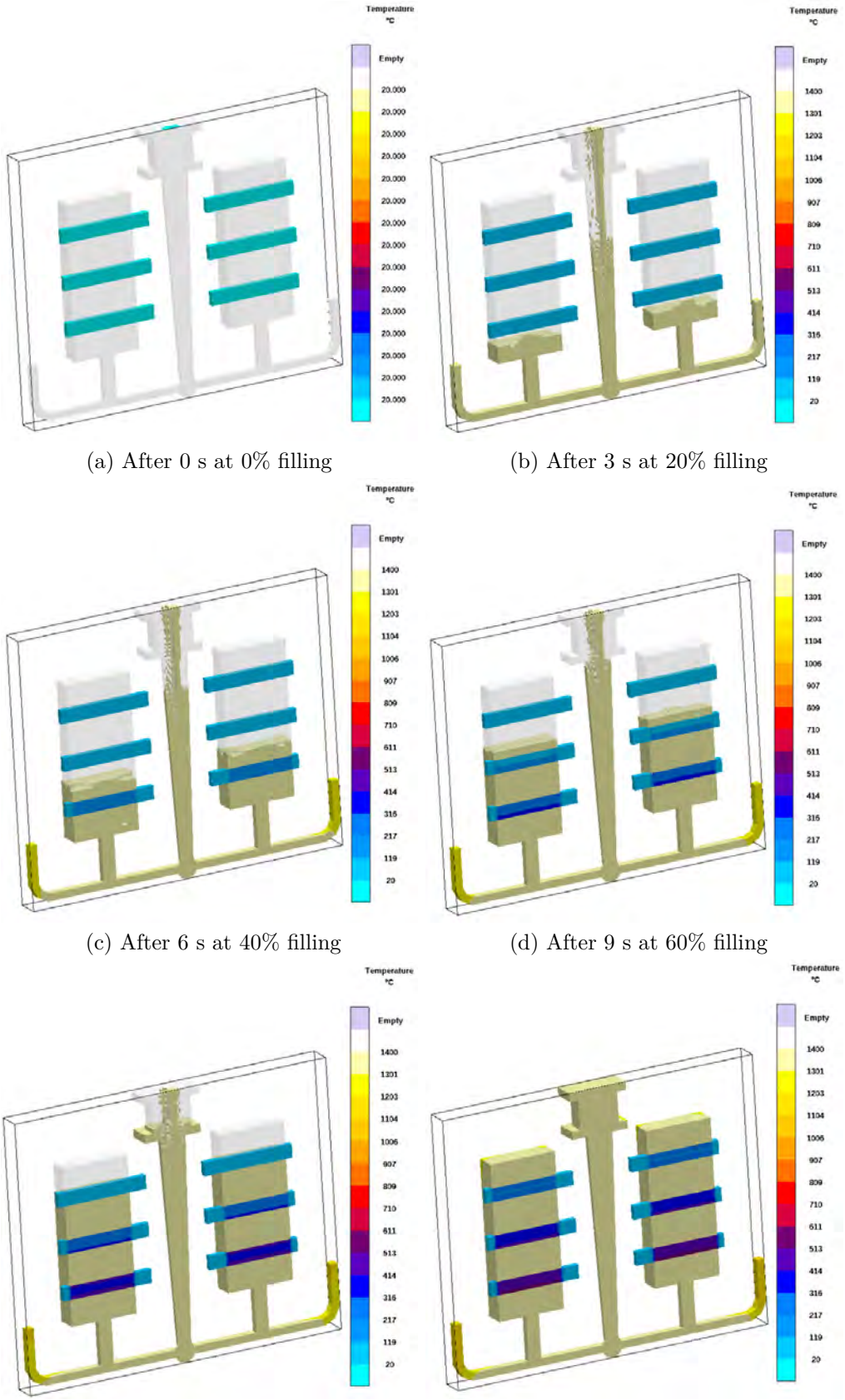

(a) After 0 s at 0% filling

(b) After 3 s at 20% filling

(c) After 6 s at 40% filling

(d) After 9 s at 60% filling

(e) After 12 s at 80% filling

(f) After 15 s at 100% filling

Figure 4.5: Temperature distribution in the cores during filling.

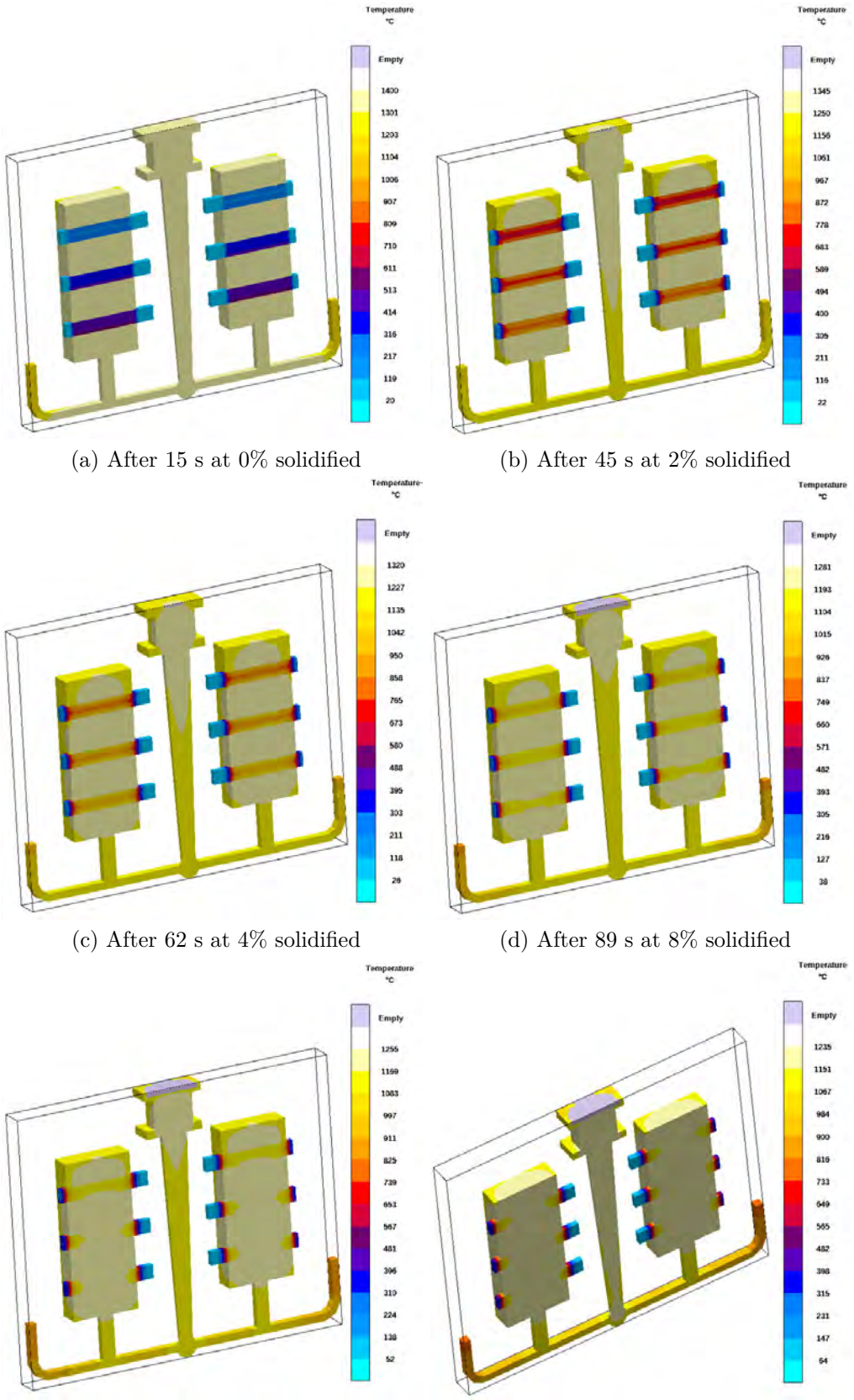

(a) After 15 s at 0% solidified

(b) After 45 s at 2% solidified

(c) After 62 s at 4% solidified

(d) After 89 s at 8% solidified

(e) After 110 s at 12% solidified

(f) After 119 s at 16% solidified

Figure 4.6: Temperature distribution in the cores during solidification.

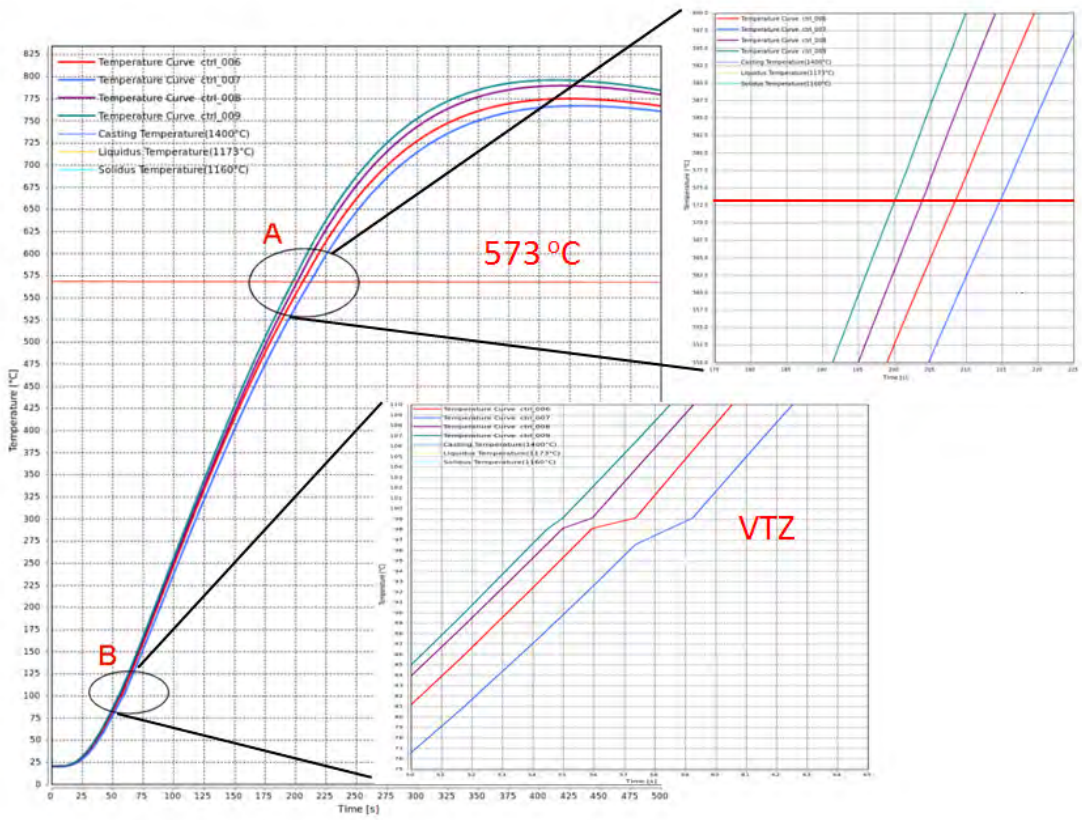

Figure 4.7: Temperature profiles in the cylindrical cores of varying thicknesses showing critical temperature of silica sand and VTZ.

The temperature profile in the cylindrical cores with varying thicknesses are shown in Figure 4.7. The effect of increasing the thickness of each core by coating it, is clearly seen in these profiles. It takes longer time for the centre-line temperature to go through the vapour transport zone and to reach the phase transformation temperature of the silica sand. This trend continues until the lowest thickness, showing the shortest time as shown by the enlargement of the region A at 573 °C. The time delay to reach this critical temperature is an advantage because it will allow for the first solidified skin of the casting to form before the critical temperature is reached, thereby creating a solid barrier between the crack formed at the critical temperature and unsolidified liquid metal. Therefore, the liquid metal cannot flow back into the crack thereby eliminating the formation of veining defects.

At region B of the profile in Figure 4.7, it can be seen from the enlargement of that region that the larger the thickness of the core the larger the vapour transport zone (VTZ). This suggests that the moisture in each of the cores increases with thickness as more inter-granular pores are created and more moisture occupies the pore spaces.

Temperature profiles when the three thermocouples are located at different distances from the core-metal interface is presented in Figure 4.8. These profiles show that the thermocouples at location 1 are rapidly heated as expected because they are closest to the core-metal interface. There is a significant delay before the

thermocouple in location 2 is reached. However, there is no significant delay in reaching the thermocouple in location 3, after reaching the one in 2, as can be seen from the profile. This could be as a result of complete destruction of the core binder system thereby enhancing thermal diffusion by radiation and convection. This simulation confirms that there can be gained time by increasing the thickness of the cores by using thermally insulating refractory materials in the foundry coatings.

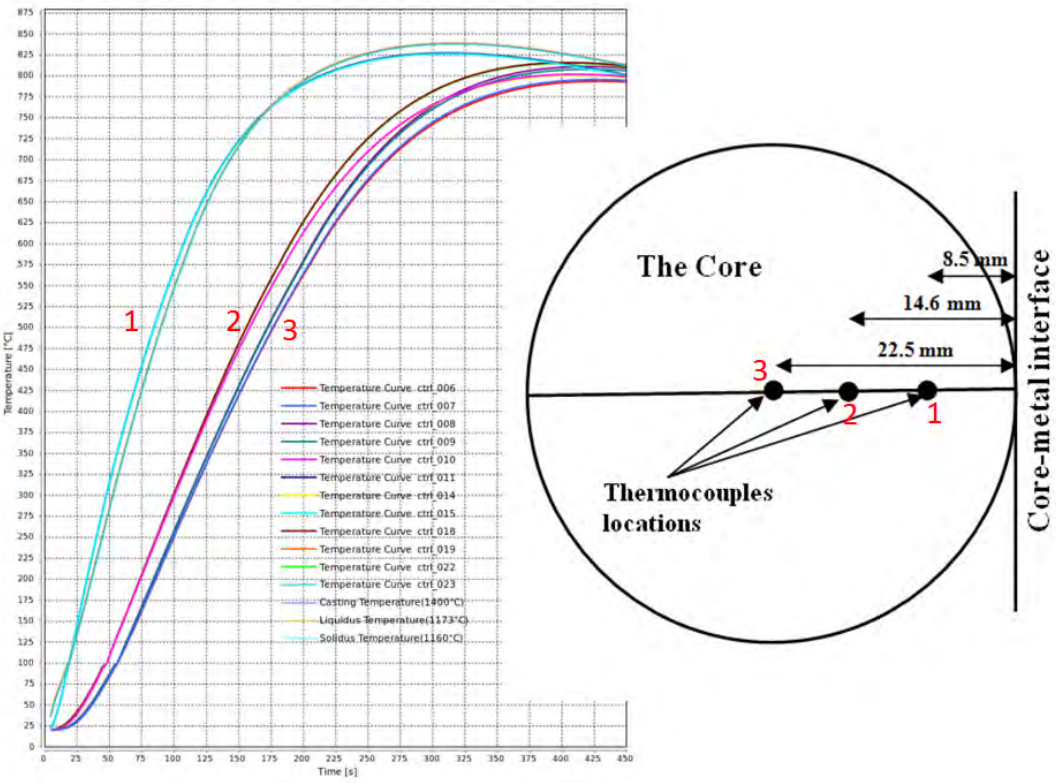

Figure 4.8: Temperature profiles in cylindrical cores at different thermocouple locations.

The temperature profiles in the cores used in the vertically-parted moulds are shown in Figures 4.9 and 4.10. From Figure 4.9, the temperature at which the lowest core thermocouple (ctrl 004) was reached is 442 °C. This confirms the suggestion that the lowest core is likely to crack and form veining defects. This is followed by the middle core thermocouple (ctrl 005) which was reached at 342 °C. The top core thermocouple (ctrl 006) recorded an initial temperature at 203 °C. The cores were heated up rapidly above the liquidus temperature(1173 °C), evidently shown in Figure 4.10. This suggests that the simulations predict complete destruction of the core binder materials by the melt and penetration occurs leading to the unique solidification plateau observed during cooling as shown in Figure 4.10. This shows that the core temperature is equal to the melt temperature. This is in agreement with the results presented in the temperature distribution during solidification in Figure 4.6.

In order to confirm the prediction of the simulations about the core temperature being equal to the temperature of the metal, a careful look at the profiles reveals that the solidification plateau lies between the liquidus (1173 °C) and solidus (1160 °C) temperatures as clearly seen in Figure 4.10. From Figure 4.10, the middle core thermocouple showed the longest plateau followed by the lowest core thermocouple and finally the top core thermocouple. This suggests that the melt at the middle core thermocouple is the last to freeze, followed by the down core thermocouple and then the top core thermocouple.

These observations are made and attributed to the fact that the cores are relatively smaller than the casting, therefore, large melt surrounds the cores. This will lead to rapid burn out of the binder. From this, it can be deduced that when the core is heated above the liquidus temperature, there is a greater tendency for sand burn-on and metal penetration to occur.

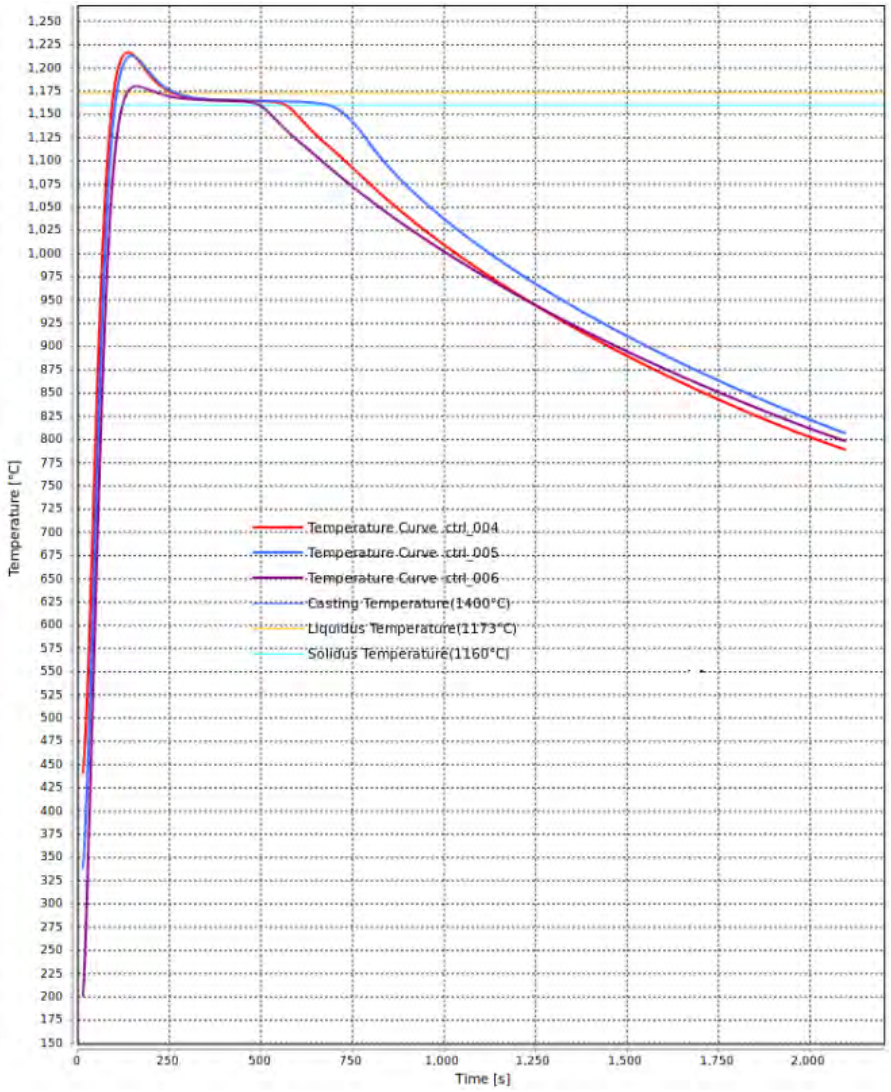

Figure 4.9: Temperature profiles in the rectangular cores in vertically-parted moulds.

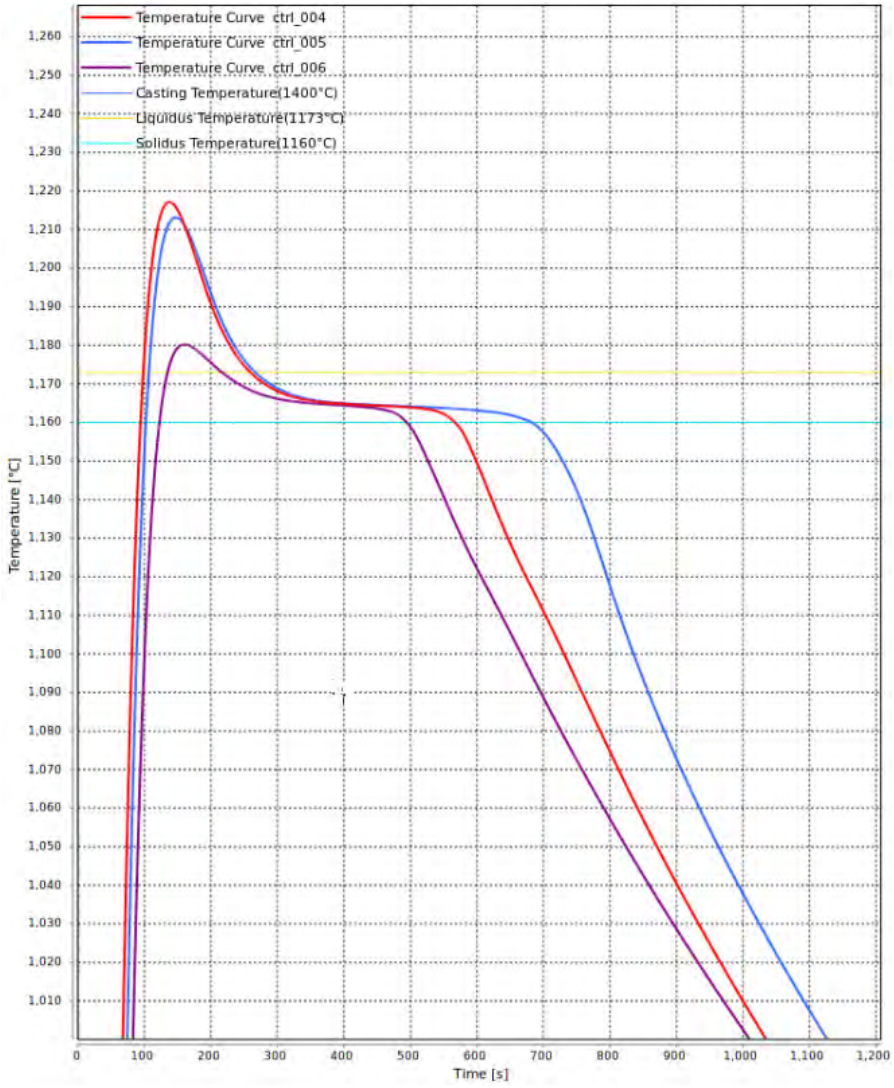

Figure 4.10: Scaled temperature profiles in the rectangular cores in vertically-parted moulds

4.2.4 Metallostatic Pressure Distribution

Metallostatic pressure has a significant effect in large castings. Its effect in small castings is not quite pronounced. The tendency of metal penetration increases with metallostatic pressure at constant average grain sizes of the moulding sand [88]. As a result of this, the surface quality of the lower part of large castings differ from the upper part of the same casting. The simulated metallostatic pressure distribution in the cylindrical castings during filling is shown in Figure 4.11. It can be seen that as the mould is being filled, the metallostatic pressure keeps changing and increasing, reaching highest pressure at the bottom at completion of filling. This is why it is sometimes referred to as pressure height effect, because it depends on the height involved and melt density. Due to the small size of this castings, the metallostatic pressure did not increase significantly as illustrated in Figure 4.11 and may not have any adverse effect on the surface quality of the castings.

However, for the pressure distribution presented in Figure 4.12, it is evident that the metallostatic pressure increases significantly with filling and reaches highest at the bottom of the casting at completion of filling. This effect continues to be more pronounced as the height of the casting increases thereby subjecting the lower part of the casting to metal penetration. Another important effect of metallostatic pressure in large castings is the dilation of the mould walls causing the formation of wedge-shaped castings [30]. From the simulation results, it is expected that the surface quality of the casting around the lowest core will be worse than the surface quality around the middle and top cores due to the influence of the increasing metallostatic pressure.

4.2.5 Predicted Defects Associated with Moulding Materials

Defect prediction is one area of casting process simulation that is very important because it provides information that will help in the optimization of the process to reduce or eliminate the defects in castings. This saves money, time, and energy for foundries. From the simulated results presented for the cylindrical castings in Figure 4.13, there is absence of porosities in the castings. However, the results showed sand burn-on tendency and hot spot areas which also enhance sand burn-on defect formation (Figure 4.13b and c). Sand burn-on is caused by localized overheating of the mould or core, causing liquid metal at the mould-metal interface to penetrate shallowly into the mould or core. When the metal at the mould-metal interface stays hot enough to partially decompose the binder or coating material, while still remaining fluid, burn-on will occur [89]. Considering the size of these castings sand burn-on may not be a problem since it is more severe in the downsprue.

However, with relatively large castings, the tendency or occurrence of sand burn-on defects and other defects such as porosities and metal penetration, becomes imperative. The predicted defects on the castings made in the vertically-parted mould are shown in Figure 4.14. Areas of porosity are shown on the top of the castings in Figure 4.14a. This means that to make sound castings, feeders may be required. From Figure 4.14b, it can be seen that the predicted hot spot areas are the same with the last-to-freeze zones in the castings (Figure 4.14c). This means that the middle cores are subjected to higher thermal load. High tendency of sand burn-on and metal penetration occurrence in these castings is predicted around the cored areas as shown in Figure 4.14d and e. Metal penetration is considered a more severe form of sand burn-on, and penetrated sand is generally chipped or ground off the surface of the casting in the fetling shop.

Penetration requires the presence of partial liquid metal at the mould-metal interface and local overheating of the surface of the moulding material, to occur. Penetration goes deeper into the moulding materials and it is limited by the temperature of the moulding material away from the interface. The temperature of the moulding materials usually decreases away from the mould-metal interface, therefore the flowing metal will solidify, and penetration will stop [89].

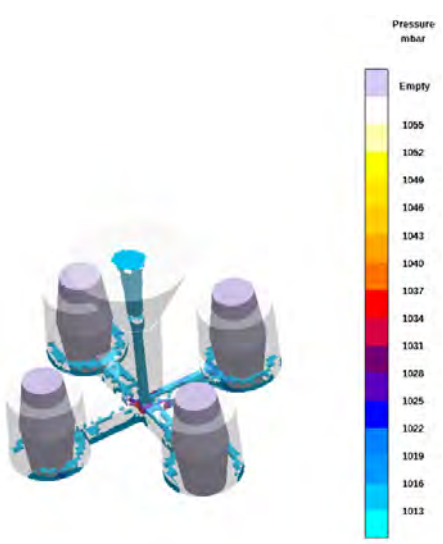

(a) After 0.5 s at 10% filling

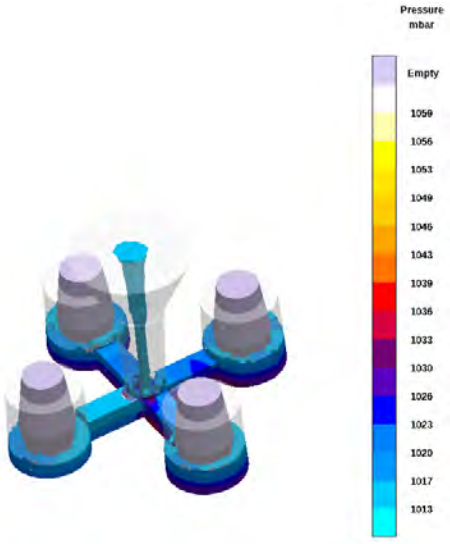

(b) After 1.5 s at 30% filling

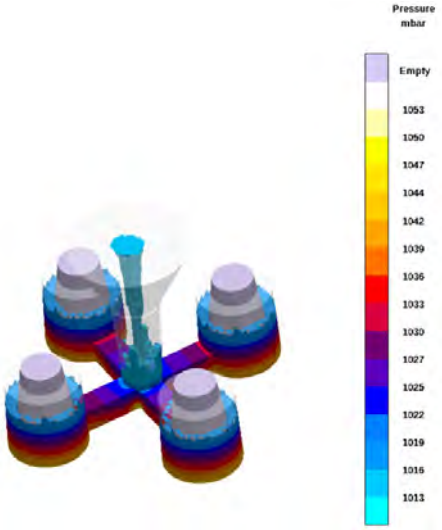

(c) After 2.5 s at 50% filling

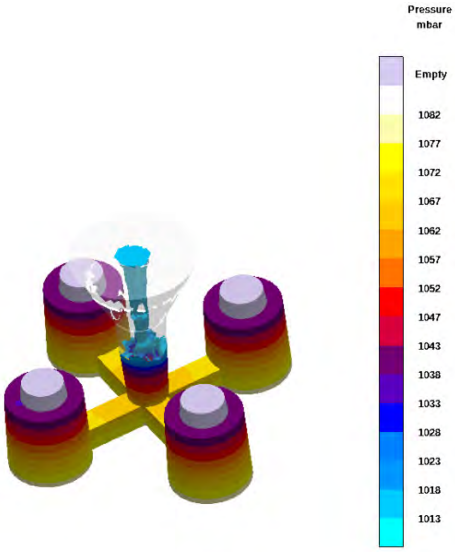

(d) After 3.25 s at 65% filling

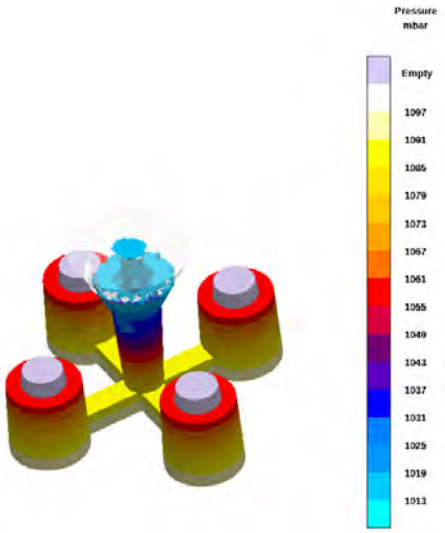

(e) After 4 s at 80% filling

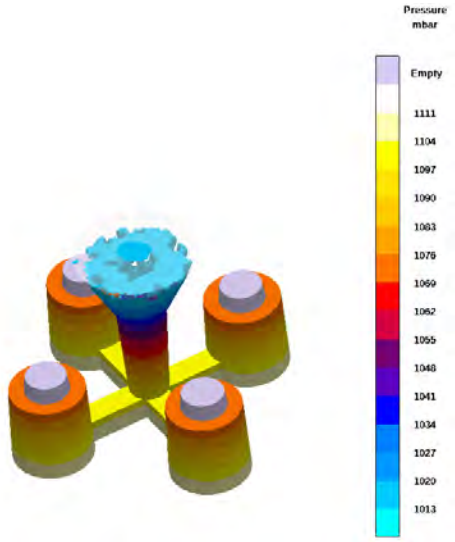

(f) After 4.5 s at 90% filling

Figure 4.11: Pressure distribution in the melt during filling.

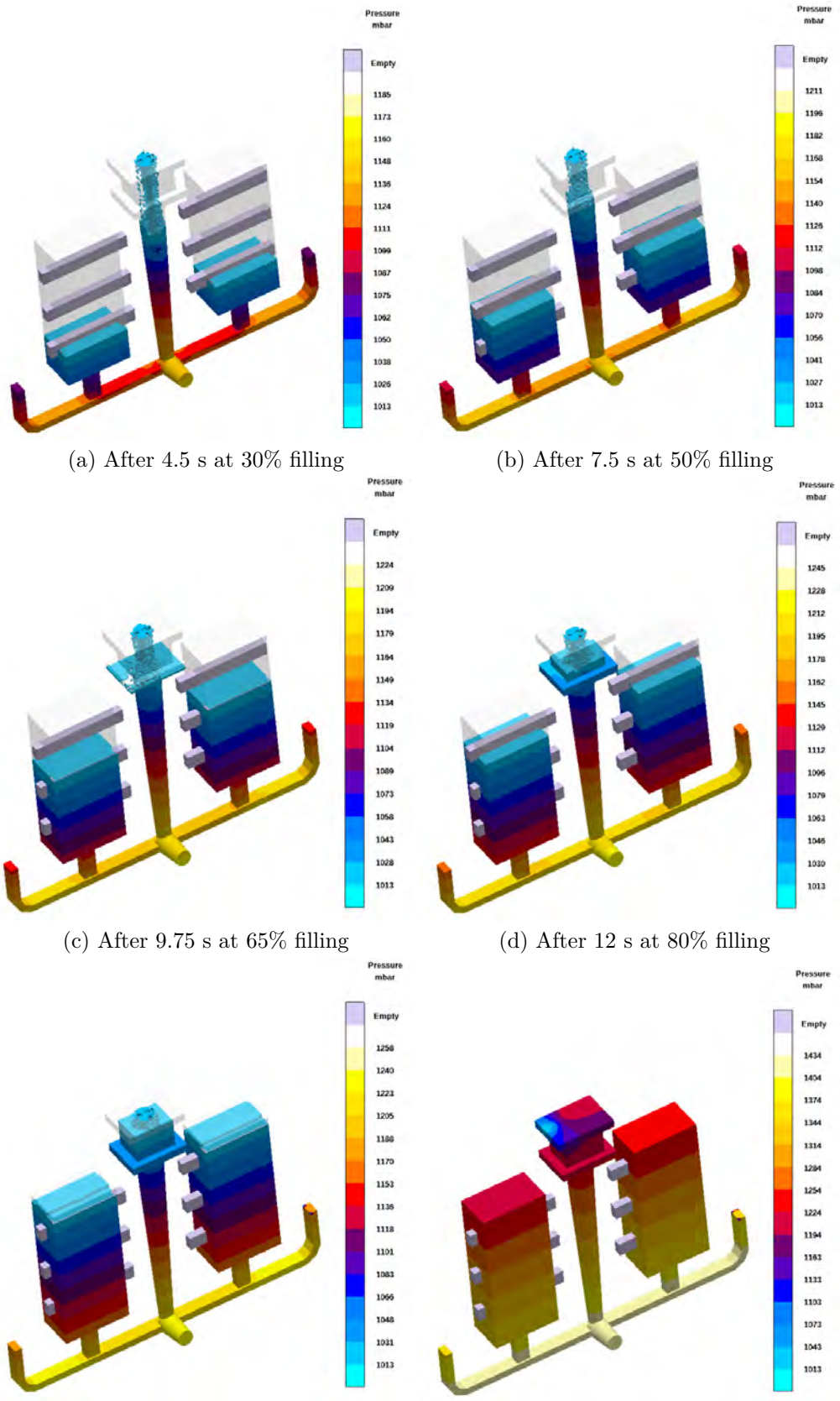

(a) After 4.5 s at 30% filling

(b) After 7.5 s at 50% filling

(c) After 9.75 s at 65% filling

(d) After 12 s at 80% filling

(e) After 14.25 s at 90% filling

(f) After 15 s at 100% filling

Figure 4.12: Pressure distribution in the melt during filling.

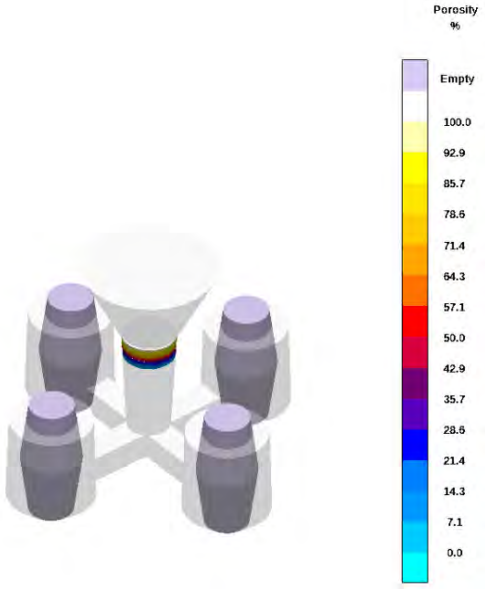

(a) Porosity

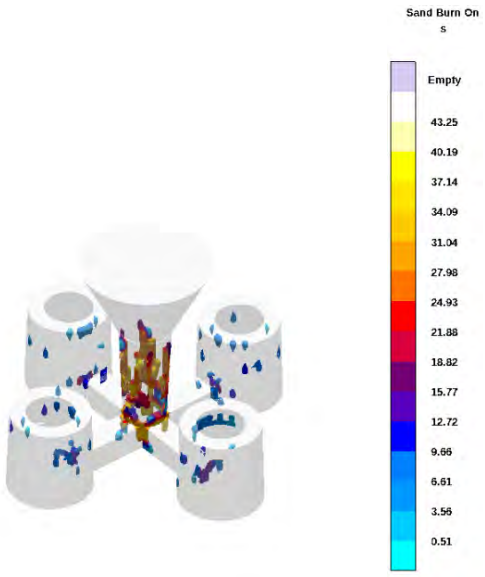

(b) Sand burn-on

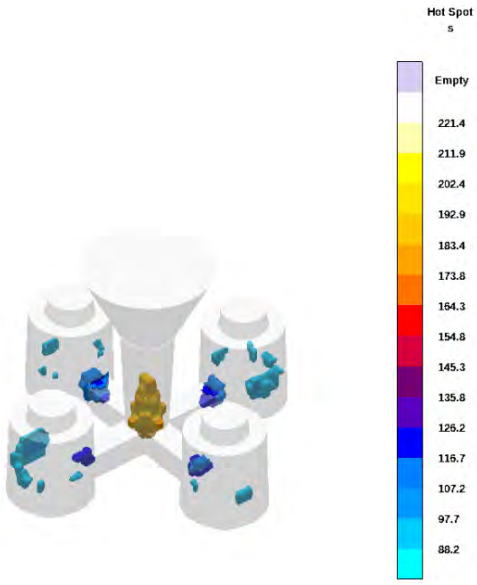

(c) Hot spot

Figure 4.13: Predicted defect locations in the horizontally-parted moulds.

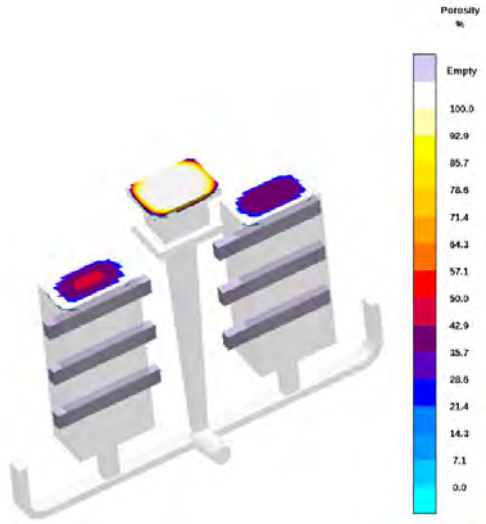

(a) Porosity

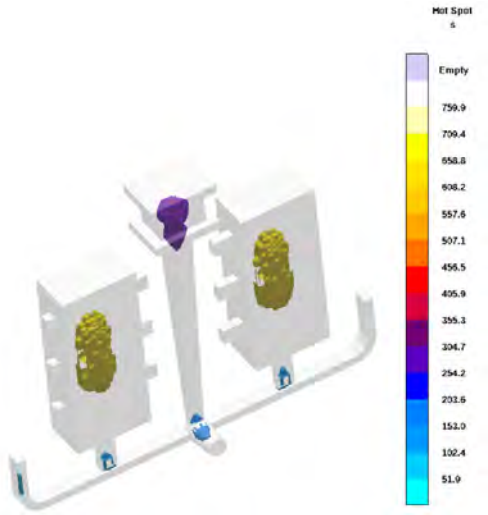

(b) Hot spot

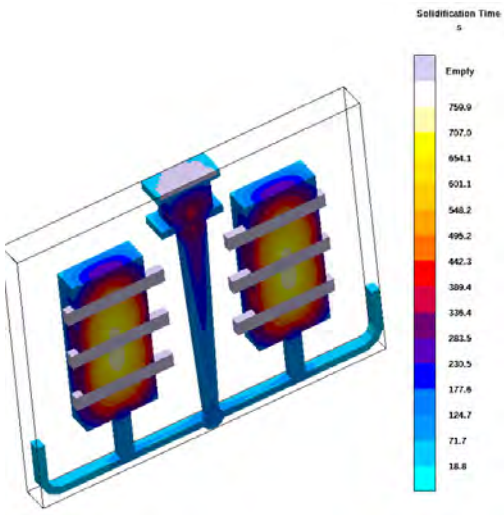

(c) Solidification time

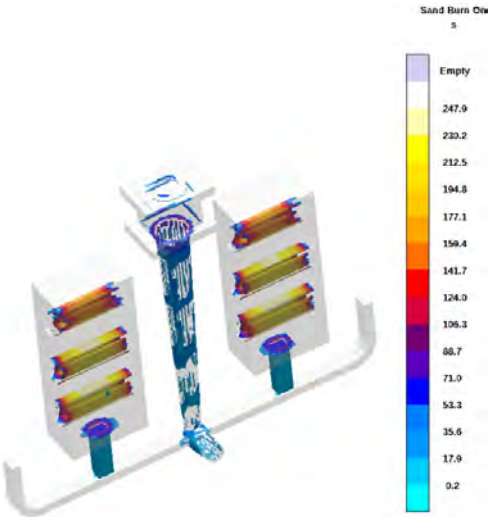

(d) Sand burn on

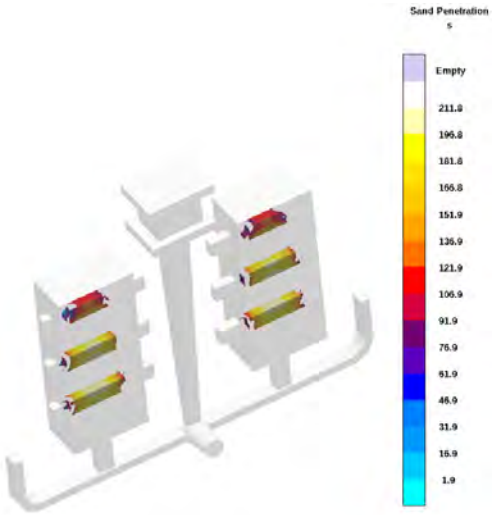

(e) Sand penetration

Figure 4.14: Predicted defect locations in the vertically-parted moulds.

Chapter 5

Materials and Approach

5.1 Coating Production and Formulations

5.1.1 Sol-Gel Process

The basic sol-gel process involves the sequential hydrolysis and polycondensation of inorganic or metal organic precursors in aqueous acid or base with a mutual co-solvent with the formation of colloids or clusters [90]. Sol-gel chemistry is the process in which a sol[1] agglomerates to form a gel[2]. This process is driven by the van der Waals forces. In the sol-gel process two distinct reactions take place: hydrolysis of the alkoxy groups and condensation of the resulting hydroxyl groups. The relative rates of these two reactions are governed by the concentration of the reagents and the presence of acidic or basic catalysts. The process takes place by dissolving the alkoxide in alcohol and hydrolyzing the solution by adding water under acidic, basic, or neutral conditions as shown in the hypothetical reaction equation below:

$M(OR)_Z + H_2O \rightarrow M(OR)_{Z-1}(OH) + ROH$

The hydrolyzed species then condenses as shown in the following reaction equations:

When the hydrolyzed species react amongst themselves in a process called oxolation, water is released,

$M(OR)_{Z-1}(OH) + M(OR)_{Z-1}(OH) \rightarrow (RO)_{Z-1}M\text{-}O\text{-}M(OR)_{Z-1} + H_2O$

When the hydrolyzed species react with another alkoxysilane in a process called alkoxolation, alcohol is released

$M(OR)_{Z-1}(OH) + M(OR)_Z \rightarrow (RO)_{Z-1}M\text{-}O\text{-}M(OR)_{Z-1} + ROH$

In these reactions, metal-organic precursors are used. The most commonly used metal alkoxides are represented by $M(OR)_Z$, where R represents an organic (typically alkyl) group and M represents a metal.

[1]Sol is defined as dispersions of solid particles having at least one dimension in the range of 1-100 nm in liquid media.

[2]Gel is defined as a 3-dimensional network of the dispersed solid particles in a liquid medium.

The unique property of the sol-gel process is the ability to allow a better control of the whole process and synthesis of tailor-made structures from the molecular precursors to the products. Table 5.1 shows commonly accepted rules of thumb used as starting point in sol-gel chemistry and material development based on relative hydrolysis and condensation rates [91].

Table 5.1: Expected product of sol-gel process depending on the rates of hydrolysis and condensation [92].

Hydrolysis	**Condensation**	**Results**
Slow	Slow	Colloids/sols
Fast	Slow	Polymeric sols/gels
Fast	Fast	Colloidal gels or precipitates
Slow	Fast	Controlled precipitation

If the stoichiometry of water to alkoxide ratio is changed, this leads to a change in sol concentration and pH affecting the sol reaction conditions. These inter-related parameters are type of precursor, hydrolysis ratio, catalyst type/amount, and type of solvent.

5.1.1.1 Precursors

In order to gain control over the hydrolysis-condensation process, the precursor reactivity which comes from the nature of metal or metalloid, during the process has to be decreased. Electronegativity or degree of unsaturation in a metal or metalloid alkoxide leads to different reactivities in these materials. As the orbital size increases, the valence electrons become less tightly bound, which leads to a lower electronegativity, ionization potential, and higher reactivity. Another property of the metal alkoxide that has to be taken into account is its molecular structure. The full coordination of many metals often cannot be satisfied in metal alkoxides $M(OR)_n$. This is due to the fact that the oxidation state Z of the metal is lower than its usual coordination number N which defines the degree of unsaturation. Higher degree of unsaturation results in higher reactivity [91]. It is established that the hydrolysis rate of metal alkoxides decreases with increasing size of the alkoxy group (e.g. ethoxide > propoxide > butoxide). This is a consequence of steric hinderance and overcrowding of the transition state, thus leading to slower reaction rates [93].

5.1.1.2 Hydrolysis Ratio

The hydrolysis ratio is expressed by the molar ratio of water to metal alkoxide. The stoichiometrically needed ratio of H_2O:$Si(OR)_4$ for complete hydrolysis of the

alkoxide is 2:1 [90, 91, 94]. Increasing the water content above the stoichiometric value favours the condensation reaction through oxolation[3] and results in particulate sol [91]. However, at hydrolysis ratio lower that stoichiometric value, the polymeric sol may form as a result of the dominant hydrolysis reaction.

5.1.1.3 Catalyst Type/Amount

Hydrolysis is performed with a catalyst. Three procedures are proposed: acid catalysis, base catalysis, and two-step catalysis. Catalyst type and pH of the reaction determine the resulting morphology. Acid catalysis is performed with HCl, H_2SO_4, HNO_3, HF, oxalic acid, formic acid, and acetic acid. Base catalysis involves dilute ammonia (10^{-2} M). Gelation are generally longer when the pH of the sol is low. Slow hydrolysis and fast condensation rates lead to the formation of colloidal structures that is characteristic of base catalyzed systems to form a network of uniform particles in the sol and the resulting pore volume is large. Fast hydrolysis, and slow condensation rates characterize an acid catalyzed system, which produces linear like polymeric clusters or randomly branched chains. The associated elemental units either particulate or polymeric cluster allow to define the membrane pore structure. Accessible micro-pores[4] could be obtained by packing of polymeric clusters while the packing of colloidal particles enables the formation of meso-porous[5] structures [90, 91, 93].

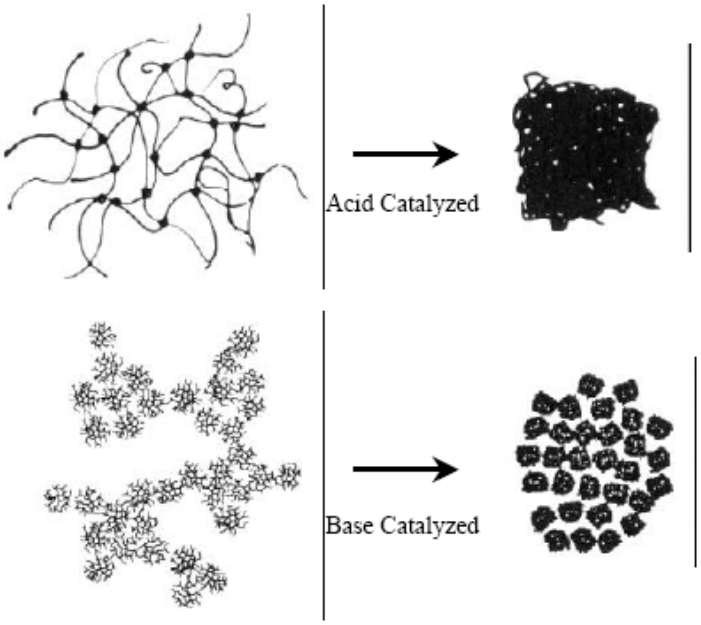

Figure 5.1: Schematic representation of gel densification for (a) acid and (b) base catalyzed systems [91].

[3]Condensation process with the production of water.
[4]Have pore diameters of less than 2 nm.
[5]Containing pores with diameters between 2 and 50 nm.

5.1.1.4 Solvent Type

Metal alkoxides are often dissolved in organic solvents to homogenize the reaction mixture before hydrolysis can take place. The most often used solvents are parent alcohols, which have the same number of carbon atoms in the alkyl group as in the alkoxy group of the metal alkoxide (for example, ethanol is the most suitable solvent for a metal ethoxide). However, solvents are often not chemically inert towards metal alkoxides and the metal alkoxide reactivity can be easily modified by changing the solvent. Solvent type and concentration have significant effect on gelation kinetics and sol-gel reaction mechanisms [91].

5.1.1.5 Sol → Gel → Film Transformation

During sol-gel processing, sols and gels evolve in a different way depending on precursors used. Two main structures of gels can form depending on the method used for processing (colloidal or polymeric) including;

1. Physical (colloidal) gels in which steric effect in the sol dominates gel formation. These gels are concerned with aqueous media
2. Polymeric gels in which the relative rates and extent of reactions are critical for gel formation. In this case organic media are preferred.

The final porous microstructure in the system is established during drying that accompanies the process of film formation by dip or spin coating. For the purpose of this study dip coating is the application process adopted because it is a commonly used method in the industry. In the dipping process, a porous support like chemically-bonded sand core is brought into contact with the coating suspension for a few seconds, resulting in film formation. The dip coating parameters, such as sol viscosity and dipping time, as well as the withdrawal speed, play a significant role in determining the thickness of the wet coating layer and consequently, the thickness of the final ceramic dry layer [95]. Figure 5.2 shows the steady state film deposition profile during dip coating of a porous support with sequential stages of structural development that result from the draining accompanied by solvent evaporation, continued condensation reactions, and capillary collapse. The entrained sol concentrates by gravitational draining of the suspension and evaporation of the solvent accompanied by flow into or out of the porous support. Increasing sol concentration due to the continued condensation reactions leads to aggregation and gelation. At the final stage of the deposition, the gel film is collapsed by capillary pressure that establishes the final pore size because of drying. During drying, there is a tendency for the formation of cracks, therefore, it becomes important to control the drying rate. The extent of shrinkage of the solid network at the critical point has a determining role on the final pore volume-size distribution in the dried gel. This in turn depends on a balance between the capillary pressures that tries to collapse the gel and stiffness of the gel that is controlled by the condensation reaction. There is little time for network formation during film deposition and the structure of the film is largely controlled by the structure of the clusters in the sol [96].

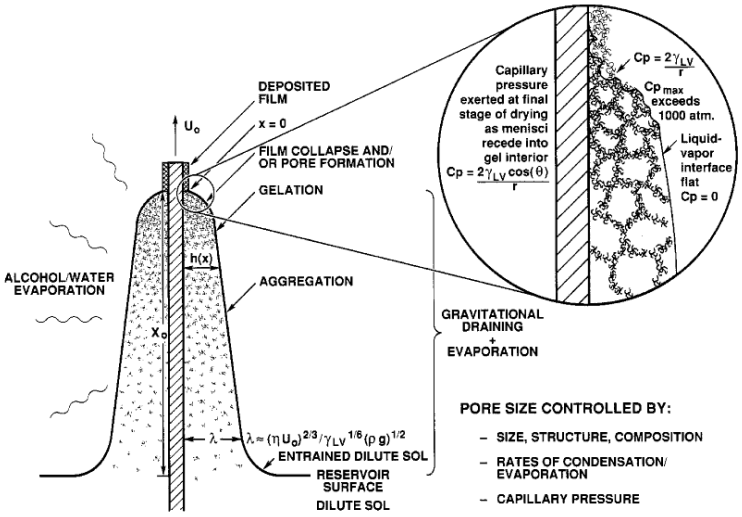

Figure 5.2: Schematic of the steady state dip-coating process [95].

Drying accompanies both the dip and spin-coating processes and largely establishes the shape of the liquid profile and is governed by capillary pressure. The increase in concentration leads to the formation of a gel-like structure. Further evaporation gives rise to capillary tension in the liquid and that tension is balanced by compressive stresses on the solid phase causing it to contract. The drying process has two successive stages; constant rate period (CRP) and falling rate period (FRP). The initial period of drying is called the constant rate period due to the constant evaporation of the solvent. During the constant rate period, the loss of pore fluid is accommodated by the shrinkage of the gel surface. In other words, the volume shrinkage will be equal to the volume of the pore fluid lost by evaporation. The driving force for this shrinkage is the capillary tension P developed in the liquid, which can be correlated to the pore radius through the Kelvin equation [90, 94]:

$$P = \frac{2\,\gamma_{LV}\,cos\theta}{r_p} \tag{5.1}$$

where; γ_{LV} is liquid-vapour interfacial energy, θ is contact angle, and r_p is pore radius. This tension in the liquid causes the gel network to contract. Further shrinkage and condensation continue up to the critical point, as the reactive terminal hydroxyl species are brought into closer contact. At this point shrinkage stops and tension is maximised. Contracting network is stiff and resists further compaction. Further evaporation of the pore fluid causes the suspension meniscus to go into the gel interior, which is the beginning of the second stage of drying, the falling rate period. The remaining liquid can escape only by evaporation from the pores and diffusion of vapour to the surface without further dimensional changes.

As the film dries, it shrinks in volume. Because of the presence of the rigid support, the reduction in volume is accommodated completely by a reduction in thickness. When the film has solidified and stresses can no longer be relieved by flow, tensile

stresses develop in the plane of the substrate that nearly equals to the stress in fluid;

$$\sigma = \left[\frac{E}{(1-\upsilon)}\right]\left[\frac{(f_s - f_r)}{3}\right] \tag{5.2}$$

where E is Young's modulus, υ is Poissons ratio of the coating suspension, f_s is the volume fraction of solvent at the solidification point, and f_r is the volume fraction of residual solvent in the dry film. Although, large stress occurs in the film, it is commonly observed that cracking of films does not occur if the film thickness is below a certain critical thickness [95].

5.1.2 Sol-Gel Reaction Mechanism Involved in this Study

In the sol-gel coating formulations, the sol-gel solution stock is produced by hydrolysis and condensation reactions. This is done by controlled acid (HCl) catalyzed hydrolysis with water of (3-glycidyoxypropyl)trimethoxysilane (GLYMO, Degussa) and aluminium (III)-s-butoxide, in 75% solution of s-butanol (AL, ABCR) as the mutual co-solvent to form the silanol group (Si-OH). The pH of this sol-gel solution is about 5. The hydroxide (≡Si-OH) from the hydrolysis is condensed with another silane, propyltrimethoxysilane (PTMO, Evonik/Degussa) in a process called alkoxylation[6] to form the siloxane bonds (≡Si-O-Si≡). The molar composition of the sol-gel solution stock is expressed by GLYMO:AL:HCl:PTMO as 385:3:1:95. The structure of the precursors are shown in Figure 5.3 while the properties are presented in Table 5.2.

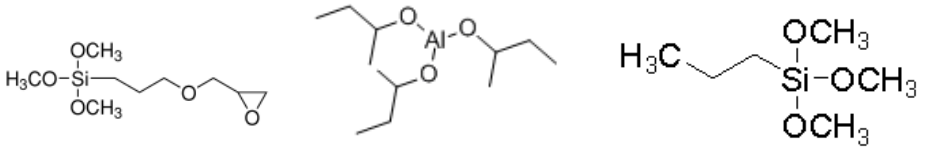

(a) GLYMO (b) AL, ABCR (c) PTMO

Figure 5.3: The structure of the precursors.

Trialkoxysilanes are well known coupling agents and are readily available with different functional groups [97]. They react readily with themselves and other metal alkoxides to form hybrid inorganic/organic polymers as shown in the following reaction equations. These equations typifies the sol-gel stock solution reaction equations for hydrolysis and condensation (alkoxolation). The R´ represents a functional group such as alkyl chains containing epoxy, amine, chloro, or vinyl group.

$R´Si(OR)_3 + H_2O \rightarrow R´Si(OR)_2(OH) + ROH$ (hydrolysis)

$Al(OR)_3 + H_2O \rightarrow$ HO-$Al(OR)_2$ + ROH (hydrolysis)

$\sim\sim R´Si(OR)_2(OH)$ + HO-$Al(OR)_2\sim\sim \rightarrow \sim\sim R´Si(OR)_2$-O-$Al(OR)_2\sim\sim$

[6] condensation under release of alcohol.

Continued hydrolysis and condensation of the reactive M-OR groups with PTMO will lead to a polymer that can be applied to a substrate by spin, dip, or spray methods.

Table 5.2: Properties of the Sol-gel stock precursors.

Properties	**GLYMO**	**AL, ABCR**	**PTMO**
Refractive index	1.429	1.439	1.391
Boiling point	120 °C	40 °C	142 °C
Density	1.07 g/mL	1.237 g/mL	0.932 g/mL

5.1.3 Novel Sol-Gel Foundry Coatings Investigated

New sol-gel foundry coatings, here referred to as **S**ol-g**e**l **S**and coatings (SeS) were formulated according to the components shown in Table 5.3 for the screening tests. The coating components include sol-gel component as the binder, nanoparticles (TiO_2, ZnO) as the refractory filler material, sulphuric acid as the hardener, and water as the liquid carrier. Water is used as the liquid carrier due to its non-toxicity, availability, low price and ease of adjustment of rheological properties. The coating mixing set up is shown in Figure 5.4. Both water and other components are varied in order to determine the optimal composition. In SeS_4, another hardener was introduced in the form of aluminium complex in place of sulphuric acid (H_2SO_4). These are trial formulations which were used for screening tests and to elucidate the performance of sol-gel coatings on chemically-bonded sand cores and in improving the casting surface quality.

Another formulation SeS_5 was made. In this formulation, the nanoparticle refractory filler materials were replaced with filter dust from Vald Birn A/S. The filter dust particles size is of micron range [107]. The amount of filter dust used vary from 20 - 60% relative to the liquid amount in the coating. Stable suspension of the refractory filter dust in the coating matrix was difficult, consequently bentonite was introduced as a suspension agent. Both hardener types (sulphuric acid and aluminium complex) were also alternatively used. Water was used as the liquid carrier while sol-gel component was added as the binder. From the various amounts (20 - 60%) of the solid content in the coating matrix, 40, 50, and 60% solid content coatings were selected based on the coverage of the sand grains on the core.

Some comparative studies were also performed with commercial coatings to assess the performance of the sol-gel coatings relative to the conventional coatings in improving the surface quality of the castings.

In a further development, the sol-gel component was increased to further study its effect on the mechanical properties of chemically-bonded sand materials.

In the light of the shortage and non-continuous availability of the filter dust coupled with its inconsistent composition, other common refractory materials such as zircon, olivine, china clay, and aluminium silicates were investigated with the sol-gel component. This means, in these formulations, the filter dust was replaced

with each of these refractory materials. The density of the refractory materials follows this trend: Zircon > Olivine > China clay > Aluminium silicate. Three different coating compositions consisting of water with respectively 10, 25, 50% sol-gel stock were prepared. To each of these compositions, 50% of each refractory material was added. All prepared samples were left standing for a period of time and then the precipitates were scraped to determine the ease of mixing each into suspension again.

Table 5.3: Different sol-gel coatings investigated in the preliminary tests.

Sol-gel coating	**Components**	**Types**
SeS_1	sol-gel component	
	50% wt. water	
	1 and 10% nanoparticles	TiO_2, ZnO
	hardener	H_2SO_4
SeS_2	sol-gel component	
	water	
	1 and 10% nanoparticles	TiO_2, ZnO
	hardener	H_2SO_4
SeS_3	sol-gel component	
	60 and 65% wt. water	
	50 and 150% nanoparticles	TiO_2, ZnO
	hardener	H_2SO_4
SeS_4	sol-gel component	
	85% wt. water	
	nanoparticles	TiO_2, ZnO
	hardener	H_2SO_4, Al (III)-s-butoxide, 75 % in s-butanol

5.1.4 Sol-Gel Coating as Additive to Existing Foundry Coatings

The sol-gel component was tested as an additive to existing foundry coatings. In this experiment, various amount of sol-gel component was added to existing foundry coatings. Due to the number of coated cores involved, Taguchi approach to experimental design was applied to reduce the number of experimental runs for casting purposes and analysis.

(a) mixing sol-gel component and bentonite (b) mixing after adding filter dust

Figure 5.4: Coating making process, the mixing.

Table 5.4: The parameters and levels for the investigation.

Factors	**Units**	**Level**		
		1	2	3
Sol-gel component	%	10	25	50
Viscosity	s	11	13	15
Dipping time*	s	S	L	10

* S = short (1-2 s), L = long (3-5 s)

5.1.4.1 Experimental Design using Taguchi Approach

Sol-gel component was added to a commercial (W254 6 Micro) coating as an additive, and the resulting coating was applied to the cores made with cold box and furan binders. The conditions of coatings and application are given in Table 5.4.

From Table 5.4, there are three parameters and each parameter has three levels. Following full factorial design of experiments, the experimental design is 3^3 Factorial designs i.e. 27 experimental runs for one of the core groups. The Taguchi approach was adopted to reduce the number of experimental runs. Using Taguchi L_9 (3^3) orthogonal array [98], the experimental design is give in Table 5.5. The response from the factors in this experimental design is the surface roughness value of the castings made with these selected cores. The smaller surface roughness value is an indication of better performance.

Table 5.5: The L_9 orthogonal array of experiments for the parameters and their levels.

No. of Expts.	**Factors**		
	Sol-gel component	**Viscosity**	**Dipping**
1	10	11	S
2	10	13	L
3	10	15	10
4	25	11	10
5	25	13	S
6	25	15	L
7	50	11	L
8	50	13	10
9	50	15	S

5.1.4.2 Data Analysis from Taguchi Experimental Design

Taguchi recommends that the data can be analyzed through the mean response for each experimental run. It was also suggested for analysis of variation, an appropriately chosen signal-to-noise ratio (SN) is used. These signal-to-noise ratios are derived from the quadratic loss function. A key component of Taguchi's philosophy is the reduction of variability. Each product or process performance will have a target or nominal value. It is the objective of this experimental design to reduce the variability around this target value. Taguchi models the departure from this target value with a loss function. The loss refers to the cost that is incurred by society when the consumer uses a product whose quality characteristics differs from the nominal. The concept of society loss is a departure from traditional thinking. Taguchi imposes a quadratic function of the form

$$L(y) \;=\; k(y \,-\, T)^2 \tag{5.3}$$

shown in Figure 5.5. Obviously, this type of function penalizes even small departures of y from the target T . This function attaches penalties only to cases where y is outside of the upper and lower specifications (say $y > USL$ or $y < LSL$)
Having given a brief description of the loss function, there are three signal-to-noise ratios derived from the quadratic loss function which are considered to be standard and widely applicable. They are

1. Nominal is best:

$$SN_T \;=\; 10\,log\left(\frac{\bar{y}^2}{S^2}\right) \tag{5.4}$$

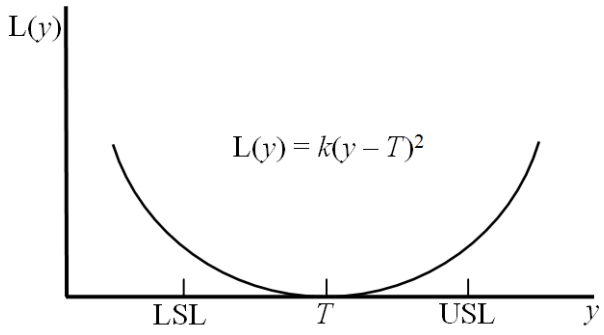

Figure 5.5: Taguchi's quadratic loss function.

2. Larger the better:

$$SN_L = -10\,log\left(\frac{1}{N}\sum_{i=1}^{N}\frac{1}{y_i^2}\right) \tag{5.5}$$

3. Smaller the better:

$$SN_S = -10\,log\left(\frac{1}{N}\sum_{i=1}^{N}y_i^2\right) \tag{5.6}$$

where $\overline{y}$ is sample mean, S is sample standard deviation (S^2 is the sample variance), y_i is the sample, and N is the number of observations in a sample.

The SN ratios are expressed in a decibel (dB) scale. SN_T is used if the objective is to reduce variability around a specific target, SN_L if the system is optimized when the response is as large as possible, and SN_S if the system is optimized when the response is as small as possible. Factor levels that maximize the appropriate SN ratio are optimal [98]. Therefore, smaller the better i.e Eq. 5.6 for the surface roughness will be selected for obtaining the optimum combination of the parameters and their levels.

Descriptive statistics and analysis of variance (ANOVA) were also applied to distinguish the means of the target response (surface roughness, Ra value).

5.2 Wet Coating Characterization

5.2.1 Specific Gravity

The specific gravity of the sol-gel coating slurry was measured with a picnometer. This measurement was also performed on the commercial coatings. This parameter gives an idea of the solid content of the coating which determines the coating density.

5.2.2 Viscosity

The viscosity of the coating determines how the coating will penetrate into the cores and moulds and the thickness of surface layer deposit on the cores or moulds. Viscosity is also used to assess the level of solid content in the coating and to predict the rheology of the coating. In spray application, there is a limit to the viscosity of the coating that can easily be applied. Too high viscosity, will block the nozzle of the spray gun or atomization will be difficult. In the case of dip coating application, this is not the case, it has a wider application tolerance. In sol-gel process, there are two main reactions, hydrolysis and condensation. The condensation reaction is a network formation reaction which leads to the gellation of the coating. The gelling of the coating significantly increases the viscosity of the coating at the right amount of sol-gel component [Supplement 3].

The Ford flow cup was used to measure the viscosity of the sol-gel and commercial coating slurries according to ASTM D1200 standard. A flow cup, sometimes called an efflux cup or viscosity cup, is a simple gravity device that measures the timed flow of a known volume of liquid passing through an orifice located at the bottom of the shaped cup as shown in Figure 5.6. Under ideal conditions, this rate of flow would be proportional to the kinematic viscosity (expressed in stokes and centistokes) that is dependent upon the specific gravity of the draining liquid [99]. The rate of flow (T) in seconds (efflux time) can be converted to centistokes viscosity (V) using the following equation,

$$V = 9.14T - \frac{226}{T} \tag{5.7}$$

while if the centistokes viscosity is known, the following equation is used [100].

$$T = \frac{\left(V + \sqrt{V^2 + 8263}\right)}{18.28} \tag{5.8}$$

The efflux times measured with the flow cup for some of the coatings were converted to centistokes viscosity using Eq. 5.7 and presented in the result section.

5.2.3 ^{o}Baumé Parameter

The ^{o}Baumé test was performed with a hydrometer. The hydrometer is floated in the sol-gel coating slurry and the ^{o}Baumé reading is taken directly from the hydrometer scale, when it has stopped sinking. This measurement was also performed on water and alcohol-based commercial coatings. The ^{o}Baumé parameter is commonly used in the foundries today to control the coating consistency for various sizes of foundry applications because it is quick and easy. Higher ^{o}Baumé number indicates higher viscosity.

Figure 5.6: Measurement of viscosity by efflux time [99].

5.3 Coating Application on Cores and Moulds

The cold box and furan cores were dip-coated with different times at all stages of the experiments in order to replicate the foundry applications.

The green sand moulds were spray-coated. The distance from the spray gun to the mould was 10-15 cm. Some mould cavities were given single layer spray-coating while some were given multilayer spray-coating. The spray coating process is shown in Figure 5.7.

(a) Grill (b) Vice

Figure 5.7: The spray-coating process of green sand moulds.

5.4 Core-Coating Interaction and Analyses

5.4.1 Weight of Wet and Dry Coating on Cores

The cores were weighed before dip-coating, W_1, after dip coating, W_2, and after curing at 110 °C for 1 hour, W_3.

Weight of wet coating on cores = $W_2 - W_1$

Weight of dry coating on cores = $W_3 - W_1$

These parameters can be used to determine the economics of the coating.

5.4.2 Moisture Content

The moisture content was determined by first measuring the weight of each core. The cores were respectively heated at a temperature between $105 - 110$ °C until its weight is constant. The loss in weight, expressed as a percentage of the initial weight of the cores, is the moisture content. It is important to know the moisture content of the cores and moulds in order to avoid gas defects in castings.

5.4.3 Core Surface Coverage

The coverage of the surface of cores by the coating is elucidated by using a stereomicroscope - ZEISS Stereo CL1500 ECO. Knowing the coverage ability of the coating will help to assess and prevent the occurrence of metal penetration, sand burn on/in defects and improvement of the surface quality of the casting made with the cores.

5.4.4 Coating Penetration into the Cores

The coating penetration into the cores after sectioning was obtained by using a stereomicroscope - ZEISS Stereo CL1500 ECO. The penetration depth on the images obtained with the stereomicroscope was determined by several distance measurements using an image analysis software - Image-Pro Plus Version 6.1. The average values were presented. This test is very important because it will determine the extent to which the pores in the sand cores are filled with the refractory material of the coating and their anchorage on the sand grains.

5.4.5 Core-Coating Refractory Material Interaction

The dried coated core materials were sectioned and the areas of the core where the coating refractory materials are, were carbon-sputtered to make it conductive. The prepared samples were examined using the Scanning Electron Microscope (SEM), JOEL JSM-5900 with LaB6 – Filament equipped with INCA X Oxford Instruments EDS to elucidate the interaction of the core and the refractory materials.

5.4.6 Permeability

The ambient-temperature permeability of the cores was determined as an average of three measurements using a permmeter as shown in Figure 5.8a. The sample holder (Figure 5.8b) was adapted to fit the geometry of the core to enable reliable measurements. This test is very important because it will determine the ease with which the gas in the sand bodies can be vented to avoid gas related defects on the castings and to assess the effect of the coatings on the permeability of the core materials.

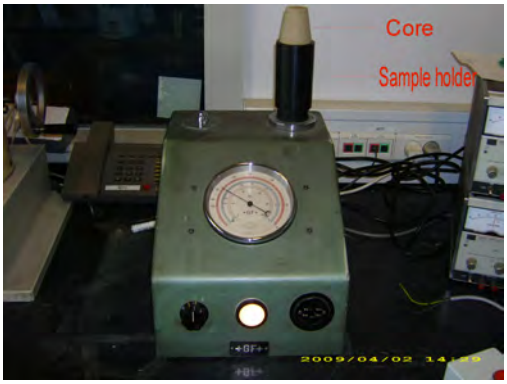

(a) A permmeter

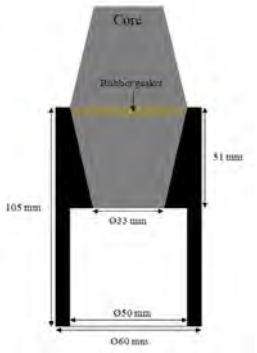

(b) Sample holder with a core

Figure 5.8: A permmeter and sample holder for measuring the permeability of the cores.

5.5 Mechanical Properties of Coated Core Materials

The mechanical properties of the coated core materials were determined. This tests highlighted the effects of the coating on the mechanical properties of chemically-bonded sand materials. For the process, a new strength testing machine (STM) was built for the measurement of tensile and flexural strengths of the coated core materials [Supplement 4]. This machine loads the specimens uniformly (at a constant strain rate) using a user defined specifications. The operating systems of the machine are interfaced with a computer using labview software in order to measure the loading and the corresponding displacements and presenting the results as load-displacement curves. From this plots, the maximum strength and stiffness of the chemically bonded sand materials were determined [Supplement 5]. The new STM and the specimens with the adaptive specimen plugs are shown in Figure 5.9. The core materials coated with filter dust coating and coatings with more sol-gel base were investigated. The results of the mechanical properties of core materials coated with coatings containing more sol-gel stock is presented in this section and for the core materials coated with filter dust coating, the results are reported in Supplement 5.

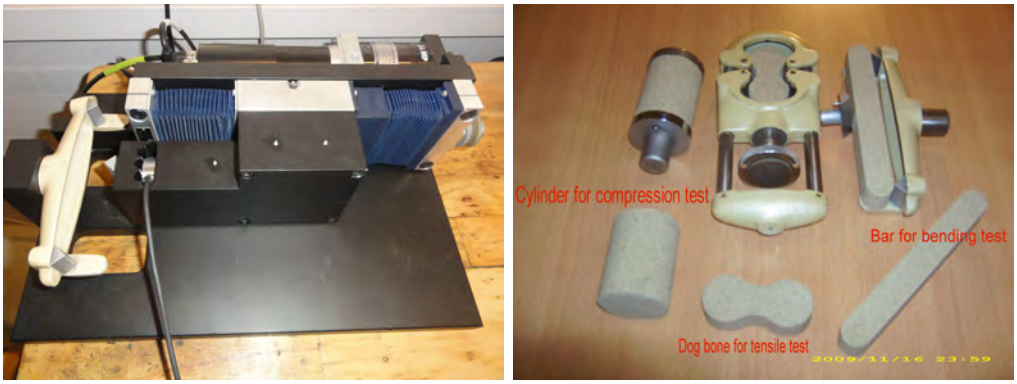

(a) The new STM (b) The specimens and adaptors

Figure 5.9: Measurement of the mechanical properties of chemically bonded sand materials.

5.5.1 Tensile Test

The "dog bone" specimens were used for the tensile test experiment using the new STM with proper adaptor for the tensile test (Figure 5.9b). Three specimens treated with the same conditions were tested and the results were averaged and standard deviations were determined. The dimensions of the specimen are shown in Figure 5.10.

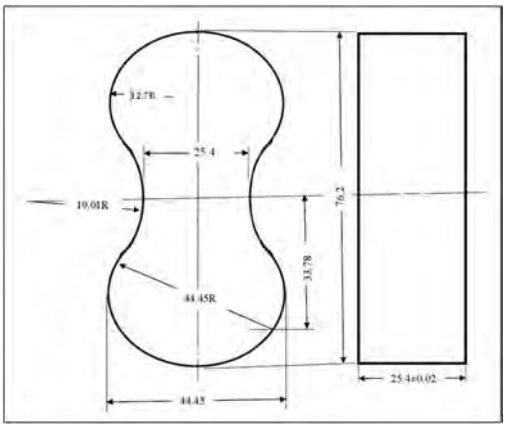

Figure 5.10: Standard tensile test specimen (dog bone) for sand materials (dimensions in mm).

5.5.2 Bending or Flexural Test

The bar specimens were used for the bending or flexural test using the new STM with the right adaptor for the bending test (Figure 5.9b). Three specimens of the same treatment were also used for the test. The dimensions of the specimen is 172 mm $\times$ 22 mm $\times$ 22 mm with a curvature radius of 11 mm at both ends. The set up is shown below.

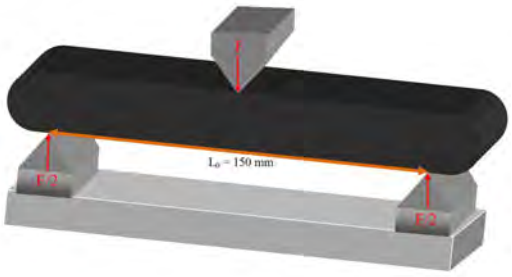

Figure 5.11: A schematic showing the bending test set-up.

5.5.3 Compression Test

The compression test is performed on three cylindrical core material specimens using Amsler Hydraulic Test Press. This instrument measures the maximum compressive loading at breakage point. The specimen dimensions and the direction of loading are shown in Figure 5.12.

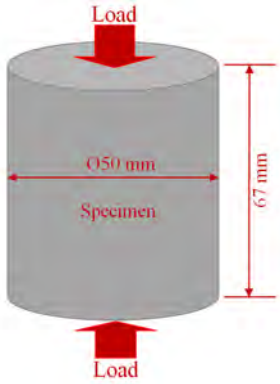

Figure 5.12: A schematic of the compression test specimen and set-up.

5.5.4 Statistical Evaluation of Mechanical Properties

Descriptive statistics was applied to the measured strength values to determine the means and the standard deviations. Analysis of variance (ANOVA) was used to determine the significance of the measured strength means. All statistical analysis was performed at 95% confidence interval. Weibull statistical distribution was used to analyze the strength of the chemically-bonded sand core materials to determine the materials' reliability, or in other words, the probability distribution according to which the material will fail will be obtained.

5.5.4.1 Theory of Weibull Distribution

Weibull distribution function is used to model fracture strength data of brittle materials to determine the strength reliability, which is one of the factors limiting the wider use of these materials in various structural applications [101, 102, 103].

Two popular forms of this distribution are two- and three- parameter Weibull distributions. The cumulative distribution function (CDF) of the three-parameter Weibull distribution is given as follows

$$F_f\,(x;\,\gamma,\,\alpha,\,\beta)\;=\;1\;-\;exp\left[-\left(\frac{x\;-\;\gamma}{\alpha}\right)^{\beta}\right] \tag{5.9}$$

$\gamma \geq 0$, $\alpha \geq 0$, $\beta \geq 0$

where γ, α and β are the locations, scale, and shape parameters respectively. When $\gamma = 0$, Eq. 5.9 becomes the CDF of two-parameter distribution, Eq. 5.10.

$$F_f\,(x;\,\alpha,\,\beta)\;=\;1\;-\;exp\left[-\left(\frac{x}{\alpha}\right)^{\beta}\right] \tag{5.10}$$

$\alpha \geq 0$, $\beta \geq 0$

This CDF equation is the most known definition of two-parameter Weibull distribution and it is mostly applied in the modeling of the fracture strength of brittle materials. In the context of this investigation, $F_f\,(x;\,\alpha,\,\beta)$, represents the probability that the fracture strength is equal to, or less than x. In probability, the sum of probability of failure and probability of survival or reliability $R_s\,(x;\,\alpha,\,\beta)$, is unity [102, 104]. Therefore,

$$F_f\,(x;\,\alpha,\,\beta)\;+\;R_s\,(x;\,\alpha,\,\beta) = 1 \tag{5.11}$$

The reliability is the probability that the fracture strength is at least x and it is defined as

$$R_s\,(x;\,\alpha,\,\beta)\;=\;exp\left[-\left(\frac{x}{\alpha}\right)^{\beta}\right] \tag{5.12}$$

$\alpha \geq 0$, $\beta \geq 0$

In Eqs. 5.9-5.12, α and β are estimated from the observations. The methods usually applied in the estimation of these parameters are method of linear regression [102, 105, 106], and method of maximum likelihood [103]. The most widely used is the linear regression method due to its simplicity [106]. This method is based on the fact that Eq. 5.10 can be transformed into a linear regression model of the form, Y = m X + c, when the natural logarithm of both sides is taken twice [102, 105, 106] given Eq. 5.13,

$$ln\left[ln\left(\frac{1}{1\;-\;F_f\,(x;\,\alpha,\,\beta)}\right)\right]\;=\;\beta ln(x)\;-\;\beta ln(\alpha) \tag{5.13}$$

The measured fracture strength are ranked in ascending order, and a probability of failure $F_i\,(x;\,\alpha,\,\beta)$ is assigned to each strength, x_i. The Weibull modulus, β can be determined directly from the slope term in Eq. 5.13. And the scale parameter, α, can be determined from the intercept term and is given by;

$$\alpha = exp\left(-\frac{c}{\beta}\right) \tag{5.14}$$

The following probability estimators (median ranks) are quoted in [106] to have been used as the Fi(x;α,β)$F_i(x;\ \alpha,\ \beta$ in different literature. These include

$$F_i = \frac{i - 0.5}{n} \tag{5.15}$$

$$F_i = \frac{i}{n + 1} \tag{5.16}$$

$$F_i = \frac{i - 0.3}{n + 0.04} \tag{5.17}$$

$$F_i = \frac{i - 0.375}{n + 0.25} \tag{5.18}$$

where F_i is the probability of failure for the i^{th} –ranked n strength datum [106]. A. Saghfi et al. [106], stated that Eq. 5.15 gives the least bias and is therefore preferred for the purpose for probability estimation. In Eq. 5.10, when $x = \alpha$,

$F_f\,(x;\ \alpha,\ \beta) = 1 - exp\left[-(1)^{\beta}\right]$

$F_f(x) = 1 - 0.368 = 0.632$

This implies that according to Eq. 5.14 characteristic strength (α) is the time or the number of cycles at which 63.2% of the data is expected to fail [106]. The characteristic life, α is a measure of the scale, or spread, in the distribution of the data. A $\beta < 1$ indicates that the material has a decreasing failure rate. This rarely happens. Similarly, a $\beta = 1$ indicates a constant failure rate, and a $\beta > 1$ indicates an increasing failure rate [102] as the load is increased.

5.6 Casting Process

Sand casting process was used. The defects to be addressed are more common with castings made by sand casting process.

At Frese Metal, Slagelse, Denmark, the cores are made from silica sand with the chemical composition given in Table 5.6 and two different binder systems were used. The regenerated sand cores are made from furan resin binders of phenol formaldehyde/furfuryl alcohol (PF/FA) type. PF/FA has FA contents in the region of 30 and 70%. The cold box cores are made using the Amine/Phenol Urethane Process. The bond is based on the use of a two part isocyanate, part one being a phenolic resin, and the second part an isocyanate contained in a solvent. The result, promoted by a reaction with Triethylamine (TEA) or dimethylethylamine (DMEA) vapour, is the formation of a solid polyurethane resin. The cores are coated for 1, 3, and 5 s with the new sol-gel coating produced at the Technological Institute, Aarhus, Denmark, by a dipping method.

Table 5.6: Chemical composition of the core sand.

Compounds	**SiO_2**	**Al_2O_3**	**K_2O**	**Fe_2O**	**CaO**	**TiO_2**	**Na_2O**
Composition (%)	98.61	0.69	0.51	0.05	0.01	0.07	0.05

The melt composition is shown in Table 5.7. The charge was melted in an Inducto induction furnace operated at a frequency of 1000 Hz and a power of 125 kW. The casting was carried out when the temperature of the melt in the furnace was above 1465 °C, measured with a thermocouple.

Table 5.7: The melt composition.

Composition (wt. %)	**C**	**Si**	**Mn**	**P**	**Mg**	**Fe**
Grey Iron	3.5	2.6	0.2	0.02	-	Bal.
Ductile iron	3.8	2.3	0.39	0.04	0.06	Bal.

5.6.1 Horizontally-Parted Moulds

The moulds for the castings were prepared by the sodium silicate-CO_2 process. The mould pattern is presented in Figure 5.13. The layout contains four mould cavities with four cylindrical cores sitting right at the centre of each mould cavity. The core and casting dimensions are shown in Figure 5.14. The casting from each mould weighs between 4 - 4.5 kg depending on the downsprue. Some of the cores have k-type thermocouple inserted to the mid section of the cores, as shown in Figure 5.15, to measure the temperature in order to assess the thermal behaviour of the cores during casting.

(a) The cope pattern (b) The drag pattern

Figure 5.13: The mould pattern used for the horizontally-parted moulds.

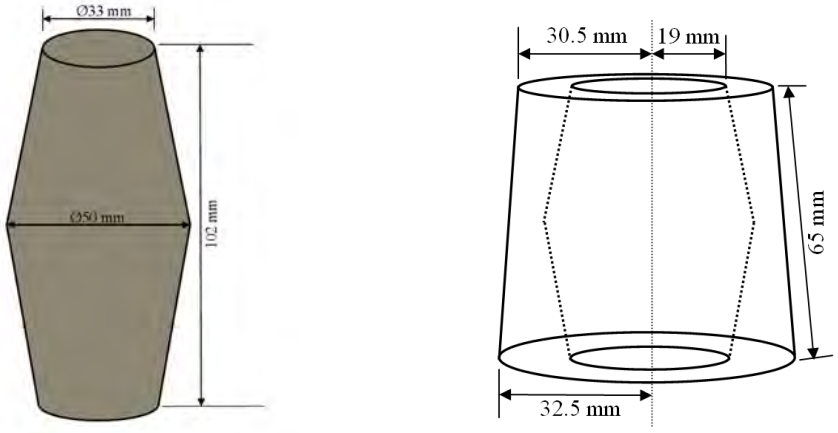

(a) The core dimension (b) The casting dimension

Figure 5.14: The core and casting dimensions for the horizontally-parted moulds.

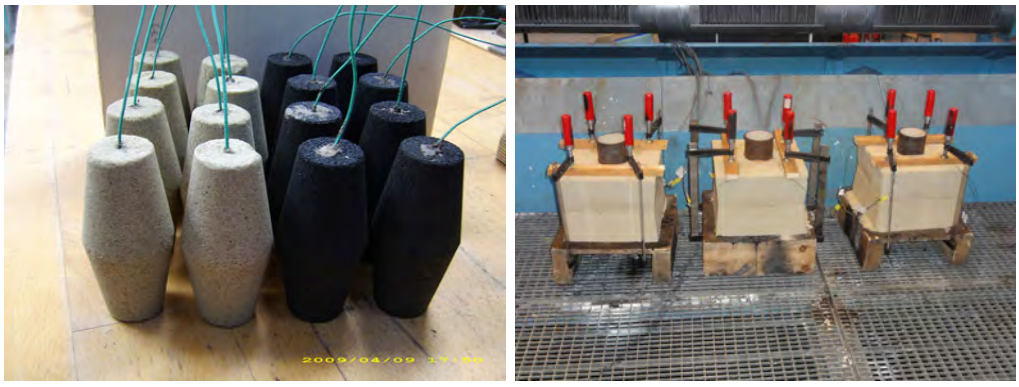

(a) The cores with k-type thermocouples (b) Moulds ready for pouring

Figure 5.15: The horizontally-parted moulds experimental set-up.

5.6.2 Vertically-Parted (DISA) Moulds

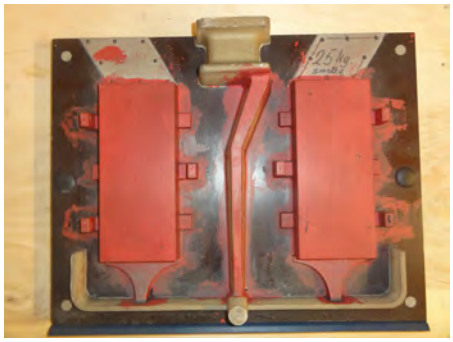

(a) The mould pattern plate1 (PP)

(b) The mould pattern plate2 (SP)

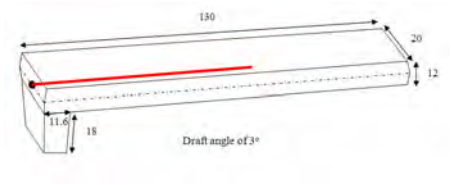

(c) The core dimension

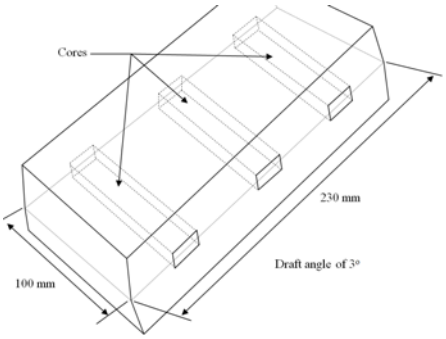

(d) The casting dimension

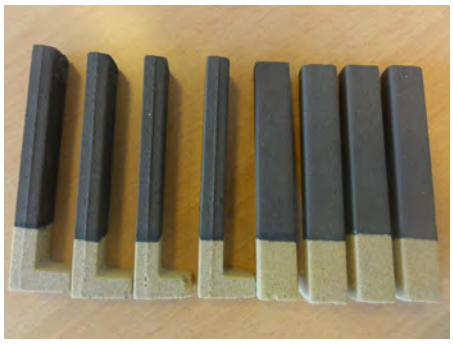

(e) The coated cores

(f) The mould cavity with six cores

Figure 5.16: The casting layout for the vertically-parted moulds.

The moulds used for these tests were made from green sand using DISAMATIC 2110 moulding machine at DTU foundry shop. The casting layout is presented in Figure 5.16. The mould contains two castings alongside the gating system in between them. Each casting has locations for three cores as shown in Figure 5.16. From the layout, the distance between the down core and the middle core is 54 mm, with the top core, 111 mm and the distance between the middle and the top core is 57 mm. The distance of each of the cores from the top of the casting is 46, 115, and 181 mm for the top, middle and down cores respectively. The cores

are surrounded by large amount of liquid metal in order to provoke surface defects around the casting interface with the cores, so that the performance of the coatings on the cores can be assessed. Due to the geometry of the castings, only one of the cores has a k-type thermocouple inserted to its mid section, to assess the level of thermal shock on the core.

5.6.3 Data Acquisition

The temperature profiles in the cores, when they are in contact with the melt, was measured by using TIG welded k-type thermocouples (Ø= 0.2 mm) embedded in the cores up to the mid section. These thermocouples were connected to the DASYLab data acquisition system laboratory software, version 8.

5.7 Analyses of the Surface Quality of Castings

5.7.1 Prediction of Surface Reactions

Reactions take place when the liquid metal comes in contact with the mould materials. Considering the fact that the moulds may contain oxygen (from moisture) and sulphur, these elements will enhance oxidation and sulphurization while the metal may undergo decarburization and/or sulphurization with the elements. These reactions can affect the properties of the cast components. The Web Tool software is used to predict the likely surface reactions and to construct the corresponding Ellingham diagrams.

5.7.2 Surface Roughness Measurement

Surface roughness of various castings were measured. The performance of the coatings in improving the surface quality of castings will reflect on the surface roughness of the castings. The lower the surface roughness values the better the coatings performance. However, castings free from veining, scabs and metal penetration defects are also indications of the coatings positive performance. For detailed surface roughness measurement, both profile and areal measurements were made using the 3D Alicona "InfiniteFocus" microscope (IFM) G4 to build a true 3D colour images of surfaces and microscopic structures. It was also used to make extensive surface characterization of the standard surface comparators, used in the foundries, to enhance comparison with the cast component surfaces obtained. This is a novel application in foundry applications and a detailed Technical Report on this approach for foundry application is provided in Supplement 7. The system is shown in Figure 3.1b. The operating principle combines the small depth of focus of an optical system with vertical scanning to provide topographical and colour information from the variation of focus. This non-destructive method uses white light which is delivered through a beam splitter to a series of selectable, infinity-corrected, high-Numerical Aperture (NA) objectives contained in a six-place nosepiece (2.5×, 5×, 10×, 20×, 50× and 100×). The specimen's reflected

light is projected through the beam splitter onto a colour digital sensor. The variation of sharpness is now utilized for extracting depth information. The operating principle, Focus-Variation, has been added to the latest ISO standard for classifying surface texture methods. The new draft of ISO norm 25178 for the first time includes standardized parameters to classify optically area based measurements [84]. In this project, for consistency, the measurement conditions are maintained.

5.7.3 Surface and Interfacial Microstructural Examination

The microstructure of the cast components at the interface between the casting and the coated cores or moulds were examined using an optical microscope. The specimens were ground and polished accordingly to mirror surface. A set of the specimens were etched with Nital solution while the other set were left unetched. The etched specimens were used to study the effect of the coating on the matrice of the cast components while the unetched specimens were used to study the effects on the graphite flake and nodule size and distribution around the interface in grey and ductile iron respectively.

Chapter 6

Results

The results will be presented according to the following schematic showing the flow of the work (Figure 6.1).

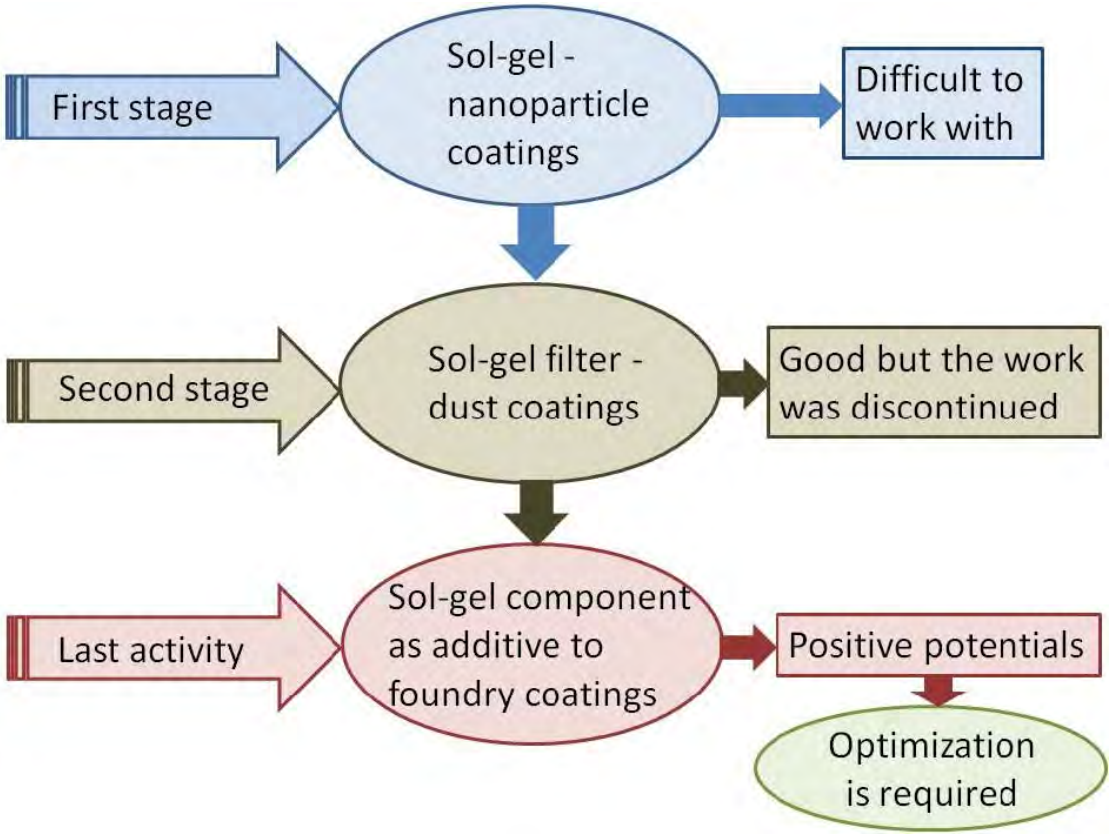

....

Figure 6.1: A schematic showing the flow of the work.

6.1 Screening Tests Results with Nanoparticle SG Coatings

The results from the screening test with nanoparticle Sol-Gel (SG) are summarily presented. The surface of the core specimens were not covered by the refractory coating as can be seen in Figure 6.2 and the penetration of the coatings into the core substrate was not uniform and also penetration was deeper as shown in Figure 6.3. The observed effects were attributed to the difference in the particle sizes of the granular materials - sand and refractory filler materials. The sand grain particle sizes are in the micron range while the refractory filler particle sizes are in the nano range. Therefore, during the dip coating process, the nanoparticles could not get deposited on the sand core surface rather they penetrated non uniformly and deeply into the cores depending on the dipping times.

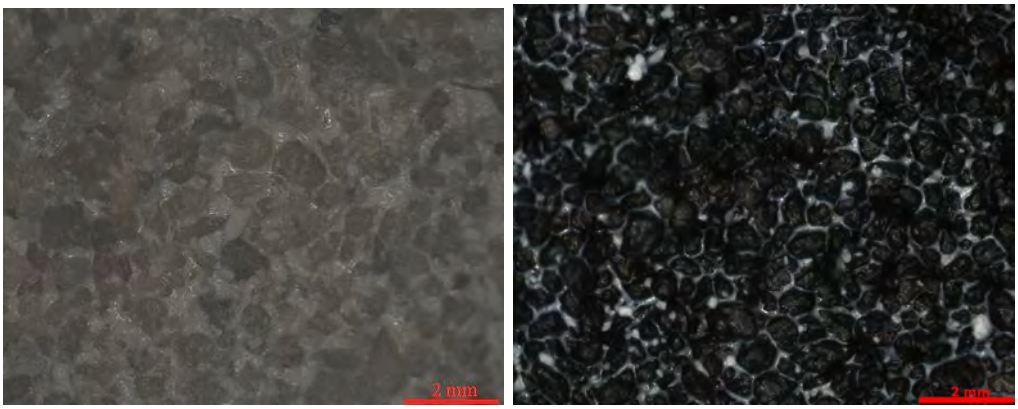

(a) Cold box core dip-coated for 5 s (b) Furan core-dip coated for 5 s

Figure 6.2: Poor surface coverage of sol-gel coatings containing nanoparticles.

The pore spaces between the sand grains are in several orders of magnitude larger than the nanoparticles consequently, the nanoparticles flowed with the liquid carrier into the bulk of the substrate without sealing the pore spaces. The part of the core that entered the coating suspension first (lower part) absorbed more of the coating than the part (upper part) that entered the coating later. This means that the penetration of the coating into the core is time-dependent. This is clearly seen in Figure 6.3 with the difference in colours. The nanorefractory particles agglomerated as they penetrate into the bulk of the core. The agglomeration of the nanoparticles (the white powder in the marked area) is quite obvious and it is also clear that the pore spaces are not sealed as can be seen from Figure 6.4. The particle size difference between the sand grains and the nanoparticles is also clearly seen from the figure.

(a) Cold box core dip-coated for 1 s

(b) Furan core dip-coated for 1 s

(c) Cold box core dip-coated for 3 s

(d) Furan core dip-coated for 3 s

(e) Cold box core dip-coated for 5 s

(f) Furan core dip-coated for 5s

Figure 6.3: Non uniform nanoparticles sol-gel coating penetration into the cores.

Figure 6.4: Agglomeration of the nanoparticles in the bulk of the core.

Furthermore, due to the nature of the coating, the core materials act like a sponge to the coating because they are porous. Therefore, diffusion and capillarity are the mechanisms of the penetration process. Most importantly, since there is no coverage of the core materials, the castings made with these cores will have poor surface finish. The castings with the best surface finish in this series are shown in Figures 6.5 and 6.6 for cast iron and aluminium alloys respectively. From Figures 6.5 and 6.6, it is very clear that there is no striking difference between the surface of the castings made with the uncoated cores and the surface of the castings made with coated cores. This is because the coating refractory filler did not cover the sand grains on the surface of the cores as shown in Figure 6.2. As a result, the sand grains will reproduce their features on the surface of the castings thereby producing casting with rough surfaces as observed. From the figures, the different dipping times did not make outstanding improvements for either cold box or furan cores. However, considering the casting temperature of aluminium alloys ($700 - 750\,^{\circ}\mathrm{C}$), it is evident that the moulding materials did not suffer much thermal shock like they did with the casting of iron at about $1430\,^{\circ}\mathrm{C}$. The surfaces of the aluminium alloy castings showed better surface quality. A comparison of the castings made with cold box and furan cores reveals that the surface quality of castings from furan cores is much better than those made with cold box cores. This is attributed to the fact that cold box cores are made with 100% fresh sand unlike furan cores which are made with only 20% fresh sand and 80% from regenerated sand which has undergone thermal shock already. Therefore, with the bulk of furan core system being regenerated, furan core materials have higher thermal integrity than the cold box materials. From these results, it implies that to obtain an improved surface finish of the castings, the sand grains will be completely covered by the finer refractory fillers of the coating to a certain surface layer deposit [107]. From the results obtained, the nanoparticle refractory fillers are not suitable for foundry coating formulation considering the particle size difference with the sand grains. Consequently, micron range particle sizes were used in place of the nanoparticles in the subsequent formulations.

(a) Uncoated cold box core

(b) Uncoated furan core

(c) Cold box core dip-coated for 3 s

(d) Furan core dip-coated for 3 s

(e) Cold box core dip-coated for 5 s

(f) Furan core dip-coated for 5 s

Figure 6.5: Surface of iron castings made with nanoparticle sol-gel coatings.

(a) Uncoated cold box core

(b) Uncoated furan core

(c) Cold box core dip-coated for 3 s

(d) Furan core dip-coated for 3 s

(e) Cold box core dip-coated for 5 s

(f) Furan core dip-coated for 5 s

Figure 6.6: Surface of aluminium alloy castings made with nanoparticle sol-gel coatings.

6.2 Wet Coating Characterization

The results of some of the wet coating characterization are presented in this section. Details of the coating characterization techniques are presented in on one of the supplements [108]. The results presented in Figure 6.7 show the anomaly between

density, viscosity, and °Baumé parameters which are measured for two different commercial coatings; water-based, and alcohol-based coatings.

Density results show that the water-based coating has twice the density of alcohol-based coating. This means that the water-based coating has double of the solid content as the alcohol-based coating [109]. But it is also clear that there is no significant difference in their respective viscosity values. However, the °Baumé of the water-based coating with higher density is significantly higher than that of the alcohol-based coating. It was reported in [110] that higher °Baumé number indicates higher viscosity. However, from the results presented here, higher °Baumé rather indicates higher density. Therefore, it is possible °Baumé tracks the density (solid content) of the coating and not the flow properties of the coatings or probably, the °Baumé parameter do not correlate the properties of two coatings with different formulations. This may mean that the °Baumé parameter only tracks the properties of coatings with same formulation. In other words, comparing the properties of the water-based coatings and that of the alcohol-based coatings is not proper.

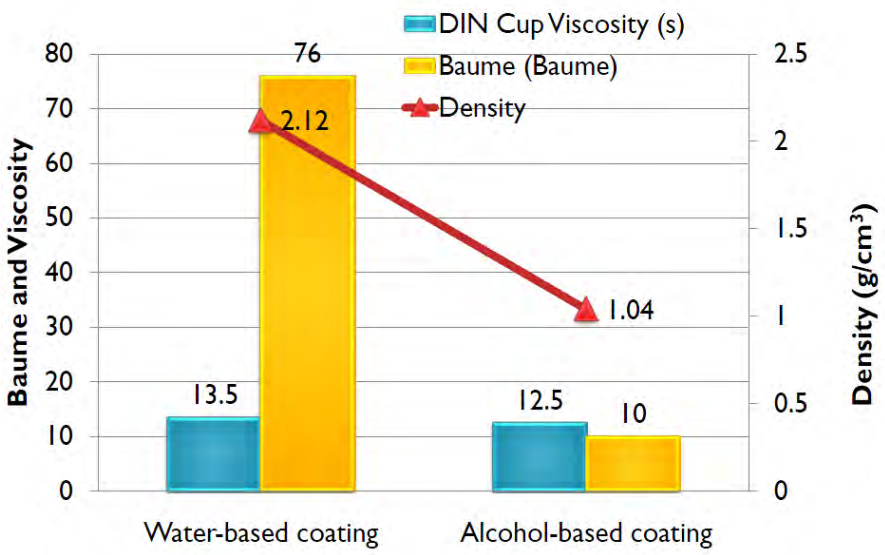

Figure 6.7: Mystery of °Baumé parameter as the only coating quality control parameter.

6.3 Core-Coating Interaction Results and Analyses

This section will present and discuss results obtained after coating and curing the coating on the cores.

6.3.1 Mass of Wet and Dry Coating on Cores

The results from the tests give an idea of the amount coating that can be taken up by a specific area of the core. The mass of the dry coating is relative to the mass of the wet coating. The masses of the wet and dry coating increases with dipping time as can be seen in Figure 6.8. The introduction of more finer particles into the a particulate system increases its moisture holding capacity. Therefore, it is expected that the mass of wet coating will also increase with the percentage of solid content in the coatings. However, a variation is observed with the coating containing 50% solid content showing a mass lower than those of 40 and 60% solid content coatings. This could be regarded as an experimental outlier[1]. This is evident in the results obtained from the mass of dry coating showing increasing mass of dry coating with increasing dipping time and the percentage solid content for all the coatings. Therefore, the consistency of the coating suspension becomes an important factor during coating application.

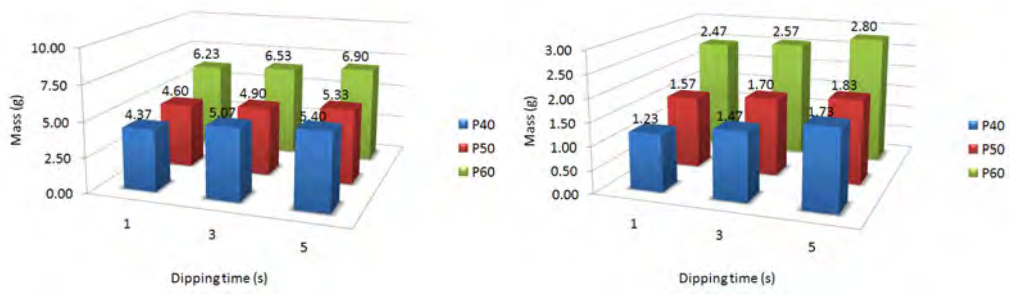

(a) Mass of wet coating (b) Mass of dry coating

Figure 6.8: Variation of mass of wet and dry coating with dipping time and percentage solid content.

6.3.2 Moisture Content

The difference between the mass of wet coating and that of dry coating expressed as a percentage could invariably be taken as the moisture content of the coating. However, a more detailed moisture test between the two core systems investigated showed a reverse trend as can be seen from Figure 6.9. This reverse variation in trend of the moisture content of both cold box and furan cores is attributed to the reaction products in the two different systems having opposite affinity for moisture. A critical examination of one of the experimental thermal profiles around the vapour transport zone (VTZ) of the two binder systems as shown in Figure 6.10, reveals a uniform temperature of 100 °C and uniform moisture content across the whole zone for each of the treatments. The VTZ moves deeper into the cores and grows larger with time as can be seen in the figure (Figure 6.10). When examining the VTZ temperature profile of cold box cores, it can be seen that the core coated for 1 s (CG1) reached 100 °C faster, followed by 3 s (CG3) coated core, and finally 5 s (CG5) coated core.

[1]An observation that is numerically distant from the rest of the data.

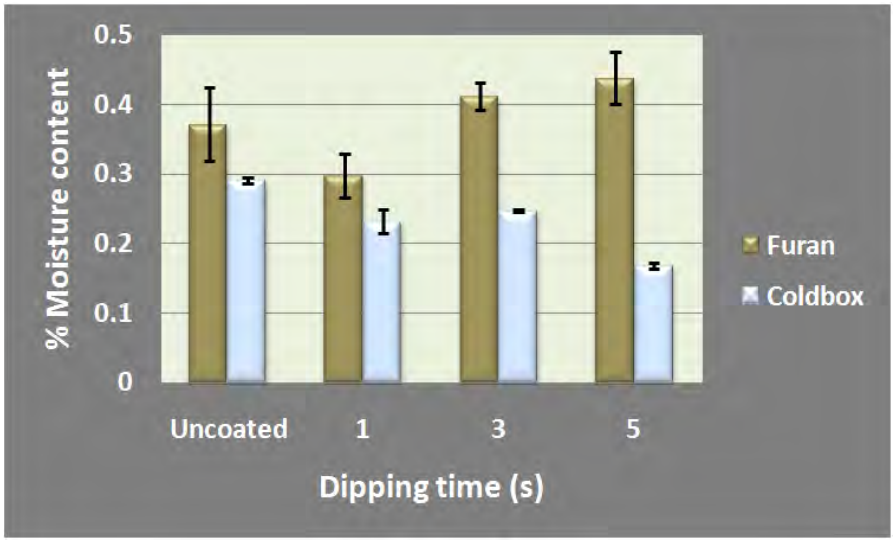

Figure 6.9: Moisture content of each of the cold box and furan core with similar treatments.

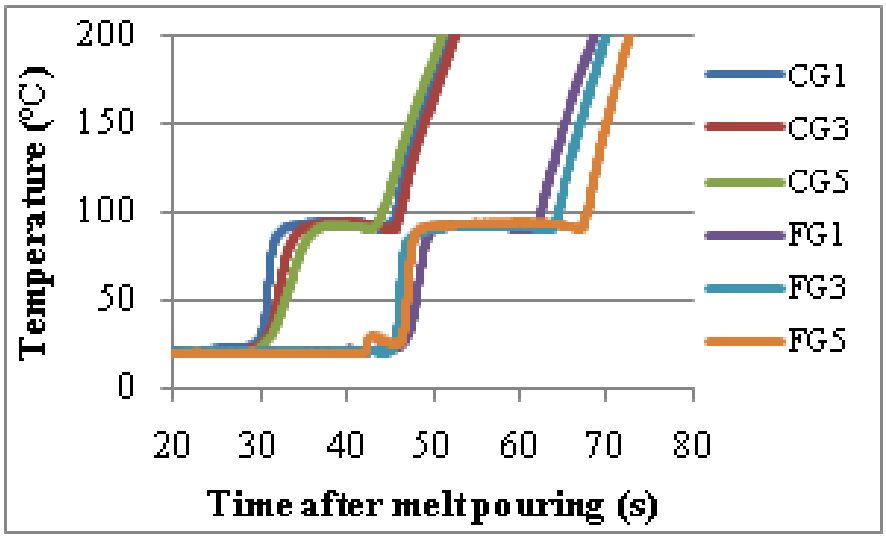

Figure 6.10: Heating curves of each of the treatments showing the vapour transport zones for cold box (CG) and furan (FG) cores.

This is because the heat from the melt was transferred both conductively through the sand grains and filler particles contact and convectively through mass flow of water vapour in the cores [36]. This suggests that for the cores investigated, CG1 has the highest moisture content followed by CG3 and lastly CG5. This is also clearly seen in the length of each of the VTZs: CG5 is shortest followed by CG3 while CG1 presumably with the highest moisture has the longest VTZ. The VTZ for furan cores is larger which suggests that it has higher moisture content than the cold box cores. For the furan cores, the VTZ temperature profiles, shown in the figure show an observable reverse trend. These observation supports the results obtained in the moisture test for the same reason. The reaction products

formed in the case of furan may be described as hydrophilic while the reaction products formed in cold box cores are hydrophobic in nature hence the decreasing affinity for moisture with increasing dipping time. It is also reported in [111] that the water retention in this type of system depends on inter-granular, grain surface morphology and on the pore network formed.

6.3.3 Core Surface Coverage

The coatings containing filter dust and the coatings with sol-gel additive showed good surface coverage relative to the uncoated cores. The filter dust coating also completely covered the sand grains on the cores, however there are presence of cracks (Figure 6.11b). This is attributed to the increasing amount of solid content and use of bentonite as the binder [107]. The sand grain in the cores were completely covered and free from cracks when sol-gel component is added as additive to a water-based commercial coating. The coating with sol-gel component additive showed increasing glassy ceramic nature with increasing sol-gel component amount [Supplement 3] (Figure 6.11b).

(a) Uncoated core (b) Coated core with Filter dust sol-gel coating (P40D3) (c) 50% sol-gel additive coating

Figure 6.11: Core surface coverage by different coatings.

6.3.4 Coating Penetration into the Cores

Apart from the nanoparticle coatings, the latest formulations showed uniform penetration as can be seen from Figure 6.12 for the filter dust sol-gel coating. The coating in all the cases penetrated around 2 mm into the core. The penetration shown in Figure 6.13 is typically required compared to that observed for the nanoparticle coatings which showed no uniform penetration as presented in Figure 6.3. This uniform penetration is consistent for all the subsequent formulations, which implies that to obtain the expected uniform coating penetration, the refractory particles must be in micro-range sizes and distribution relative to the sand grain sizes, as is the case with the filter dust. The filter dust coating is more compact and seems to provide a more protective layer (Figure 6.13a). However, the amount of the sol-gel component in the coating significantly affected the rheological properties when the sol-gel component is used as additive (Figure 6.13b). A much closer examination on the penetrated area showed two advancing fronts into the bulk of the core, the carrier liquid front and the refractory material front tagging behind [107].

For good surface finish of castings, it is expected that the coating should be able to have a dry proud layer thickness between 0.3-0.6 mm [107, 112]. Although this will reduce the permeability of the cores, but the coatings are also porous, however, the presence of the glassy ceramic formation has significant reducing effect on the permeability of the coating. It should also be noted that increasing the surface layer deposit also increases the tendency for cracking of the coating during drying, therefore, an optimum layer thickness that is free from cracks after drying is proposed. This is dependent on several factors such as refractory material particle size, coating viscosity, the solid content, the dipping time, the drying time, and the drying temperature.

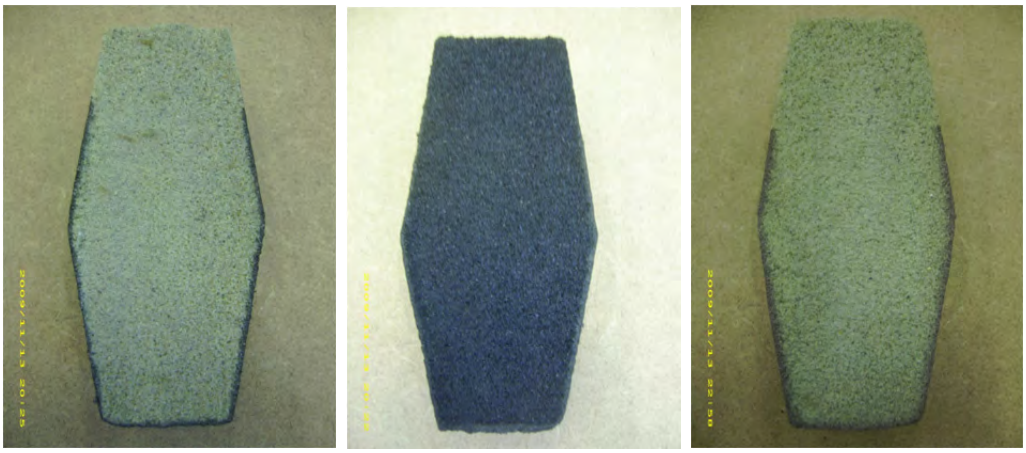

(a) Cold box; sol-gel coating (b) Furan; sol-gel coating (c) Cold box; commercial coating

Figure 6.12: Uniform coating penetration into the cores from the filter dust coating.

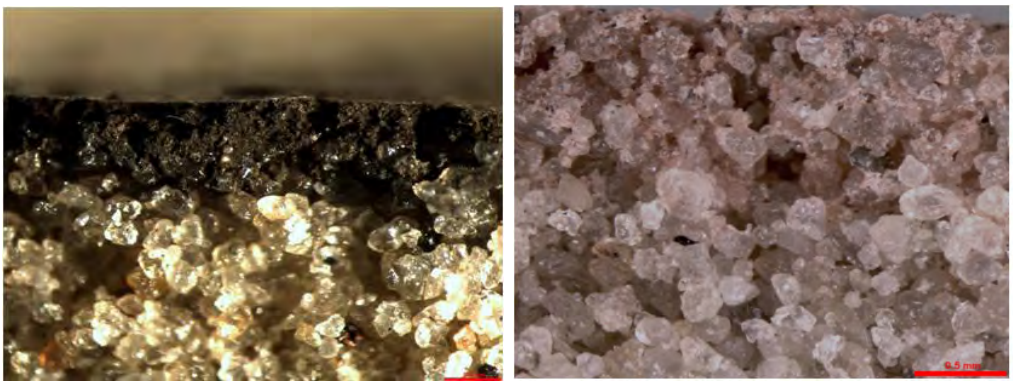

(a) Filter dust sol-gel coating (b) 50% sol-gel additive coating

Figure 6.13: Micrographs of coating penetration in cold box by coatings.

6.3.5 Core-Coating Refractory Material Interaction

The deposition and penetration of refractory filler materials on a dip coated core is shown in Figure 6.14a. As the cores are made with a binder before the application

of the coatings, the binder has already cured. In this situation, the sand grains are covered by the binder material. The sand grains are held together by bonding bridges formed by the binder as shown in Figure 6.14b. The bonding bridges are only formed where the sand grains touch one another. These are at selected points and in-between the bonding bridges are voids. This is due to the sand grains are not perfectly packed due to the variation in shapes and sizes as can be seen in Figure 6.14c. When the coating applied on the core material is dried, the refractory materials are deposited in the pores or voids in the penetrated area and depending on the viscosity, solid content of the coating and dipping time, the refractory materials may be deposited on the surface of the cores as the proud layer. The refractory materials are held together by the coating binder. However, these deposited refractory materials are just sitting in the voids with only physical connection with the binder material covering the sand grains. A closer look at Figure 6.14d, reveals that the powdery refractory filler material is only sitting on the sand grains without any evidence of bonding (physical adsorption). However, it can be clearly seen from the figures that the density of the penetrated area is increased by filling up the pore volume. This will definitely reduce the permeability of the cores while enhancing the thermal capacity.

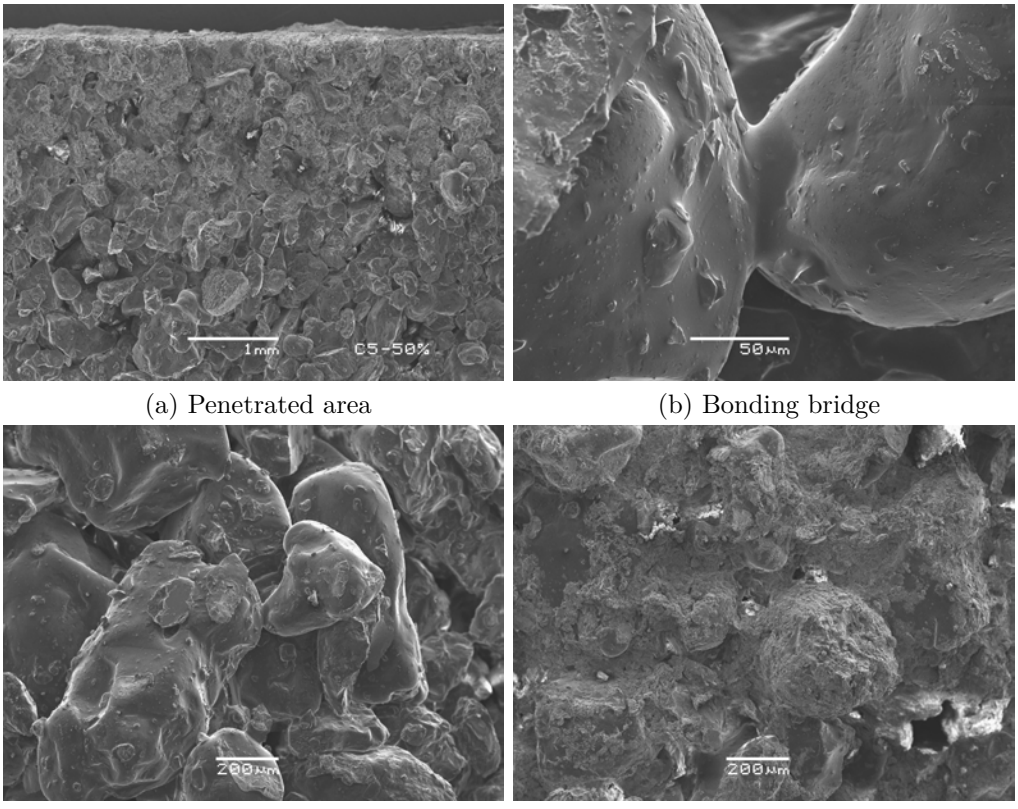

(a) Penetrated area (b) Bonding bridge

(c) Coating-free area (d) Powdery filler deposits

Figure 6.14: Core-coating interaction.

6.3.6 Permeability of Coated Cores

It is a well known fact that the permeability of coated cores is significantly reduced by the coating [41, 107, 108, 112]. This is due to the filling of the intergranular pore spaces between the sand grains with the refractory materials with several orders of magnitude lower than the sand grain sizes. The ambient-temperature permeability of the coated cores is affected by several factors including the solid content, particle size, shape, and distribution and coating layer thickness. The ambient-temperature permeability is inversely proportional to the coating layer thickness [107]. In foundries, in order to enhance venting in big cores, holes are drilled into the cores, to avoid the tendency of formation of gas porosities and other gas-related defects in the castings. For smaller cores, foundries rely on the core print for venting of the cores. So, for the filter dust sol-gel coatings and sol-gel additive coatings, their cases will not be exceptions. The permeability of the cores are significantly reduced due to the formation of a glass ceramic matrix with very low porosity with sol-gel coatings. The is evident from the permeability results presented in Figure 6.15 for the uncoated and coated cores. The coatings significantly reduced the permeability of the cores, even more with the coatings containing sol-gel component compared to the coating without sol-gel component additive, shown by the markings in the figure below.

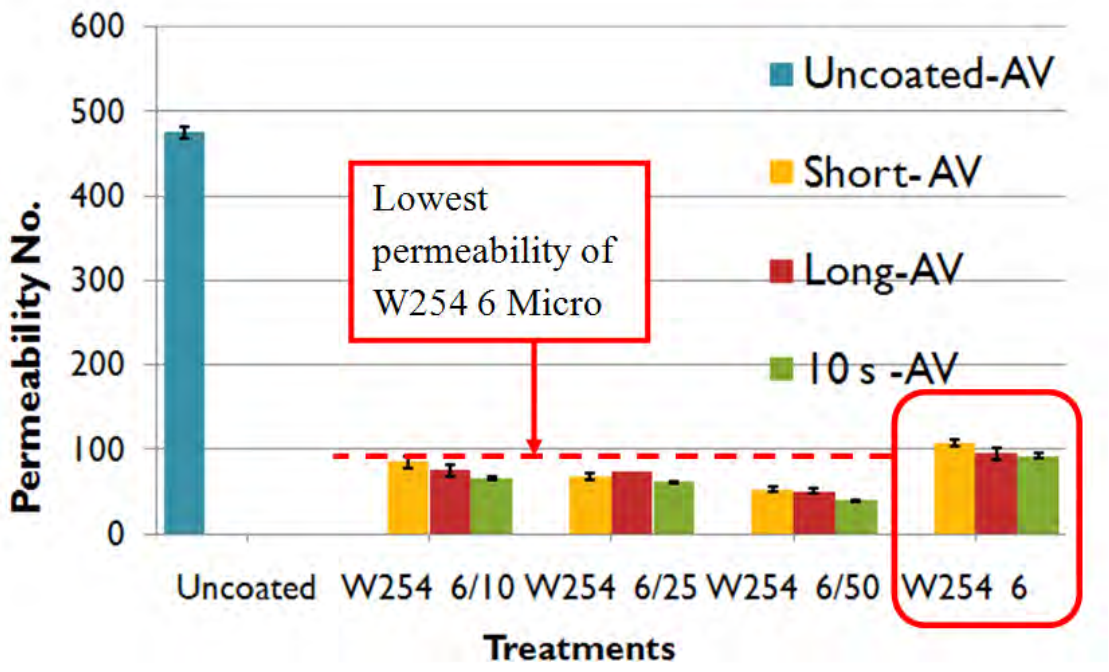

Figure 6.15: Permeability of uncoated and coated cores.

6.4 Behaviour of Sol-Gel Material with other Refractory Materials

Table 6.1: Observations of first-time and direct mixing of sol-gel stock with refractory materials.

Test	**Refractory filler/50%**	**Observations on mixing**
1	Zircon	Poor mixing
2	Olivine	Bubble formation probably due to the reaction of alkaline olivine with acid sol-gel stock
3	China clay	Viscosity gradually increases with increasing amount of sol-gel stock
4	Aluminium silicate	Poor mixing

Table 6.2: Observations in remixing coating precipitates after standing for a period of time.

Test	**Refractory filler/50%**	**Standing time/h**	**Scrapping and mixing**
1	Zircon	1.5	Easy to mix into suspension. Increasing sol-gel stock increases hardness of precipitate.
2	Olivine	2	Easy to mix into suspension. Precipitate harder than in the case of Zircon with increasing amount of sol-gel stock.
3	China clay	2.5	Easy mixing into suspension. No precipitate was observed.
4	Aluminium silicate	2	Easy to mix into suspension. Precipitate hardness comparable to Zircon.

The results of the sol-gel compatibility test with other refractory materials are presented in Table 6.1. The results show that first time/direct mixing of sol-gel stock with refractory materials such as Zircon, Olivine, China clay and Aluminium silicate does not produce homogeneous coating suspension. This is a set-back for this technology. However, there may be need for strong dispersants and stabilizing agents to enhance homogenization of the coating components. After the coatings were allowed to stand for a period of time, the coating precipitates were scraped and remixed into suspension. The following observations presented in Table 6.2 were made. These observations seem positive but the time involvement in the remixing becomes an issue.

6.5 Sol-Gel Stock as Additive to other Foundry Coatings

As additive to existing foundry coatings, 10, 25 and 50% sol-gel components compared to the total coating formulation was added to each formulation. The properties of the foundry coatings investigated with sol-gel component additive are presented in Table 6.3. All the coatings showed complete mixing with the various percentages of sol-gel component. No sign of reactions were observed. The coating suspensions were allowed to stand for a period of time at room temperature to elucidate the sedimentation of the refractory particles. The observations presented in Table 6.4 were made.

Table 6.3: Properties of the various foundry coatings.

Coating	**Liquid carrier**	**Refractory filler**
W200	Water	Zircon
S103	Alcohol	Zircon
S160	Alcohol	Olivine
W225	Water	Aluminium silicate
S120R	Alcohol	Aluminium silicate with iron oxide (Fe_2O_3)

The coatings containing 10% sol-gel component additive was diluted to a viscosity of 13-14 s (DIN viscosity) using the corresponding carrier liquid for each coating. Cold box cores were dip-coated in each of the diluted coating for 1 s, cured for 1 h at 110 °C. The homogeneity of the various coating suspensions is evident on the cured coated cores by uniform colour of the coatings on the cores as shown in Figure 6.16. The coated cores have no evident drippings or runnings.

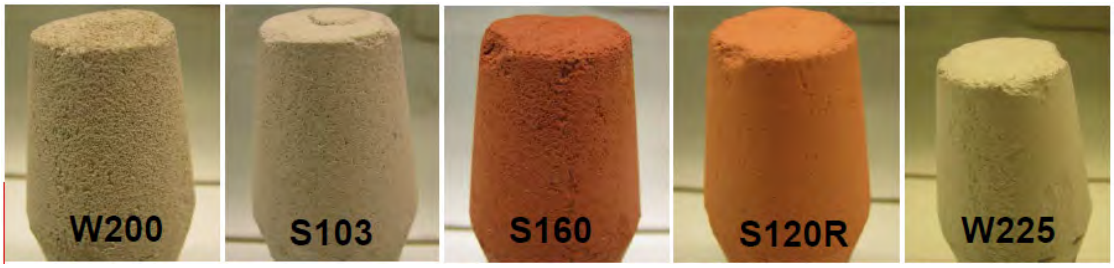

Figure 6.16: Uniform colour of various coatings on the cured cold box cores.

Table 6.4: Observations after allowing coating suspensions to stand for a period of time.

Coating	**Standing time/h**	**Observations on sedimentation**	**Remixing after 5 days**
W200 (Zircon)	1.5	For 25 and 50% sol-gel component the filler felt heavier when mixed into suspension.	Good mixing into suspension. Precipitate hard.
S103 (Zircon)	1.5	No sedimentation	Easy to mix. No precipitation.
S160 (Olivine)	1.5	No sedimentation	Good mixing into suspension. No precipitation.
W225 (Al silicate)	1.5	No sedimentation	Easy to mix into suspension. No precipitation.
S120R (Al silicate + Fe_2O_3)	1	No sedimentation	Easy to mix into suspension. No precipitation.

6.6 Mechanical Properties of Core Materials at Ambient Temperature

The results of the mechanical properties of core materials coated with coatings containing increased amount of sol-gel stock is presented in this section. Three different amounts of sol-gel component (35, 51 and 65%) were used in the coating formulation with filter dust filler material.

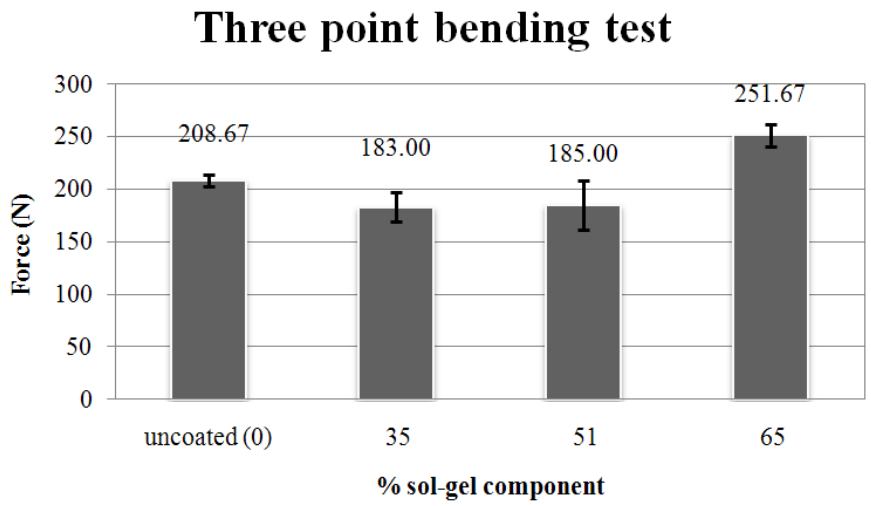

Figure 6.17: Flexural strength of cold box core materials coated with filter dust coating containing various amounts of sol-gel components.

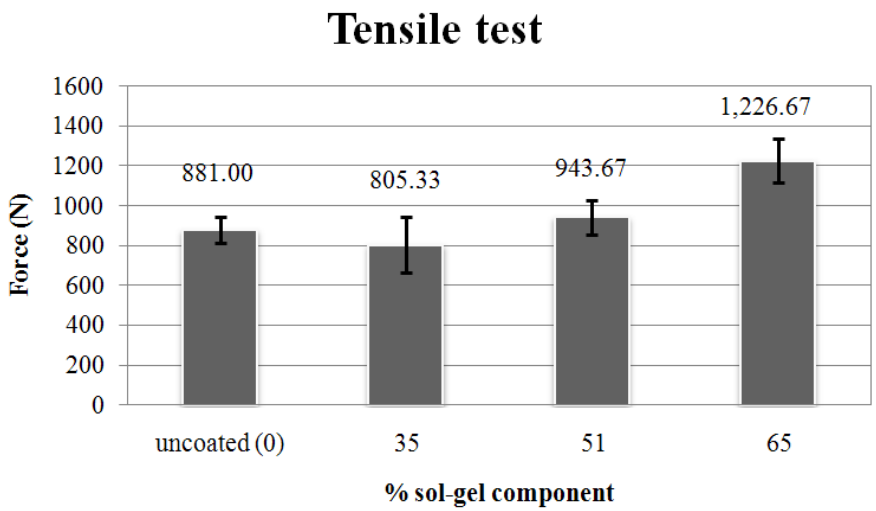

Figure 6.18: Tensile strength of cold box core materials coated with filter dust coating containing various amounts of sol-gel components.

From the results presented in Figures 6.17 and 6.18, it can be seen that at 35% sol-gel component, the strength of the moulding material seems to decrease in both flexural and tensile modes. This may be attributed to the effect of the moisture of the coating dominating the effect of the sol-gel component. However, with increasing amount of sol-gel component the strength of the moulding material increases. This may be due to the availability of the proper concentration of sol-gel component for the formation of a gel network which enhances the strength of the moulding materials. In this situation, the sol-gel effect dominates in the system. On the other hand, the effects of this increasing amount of sol-gel component on the ease of shakeout of the moulding materials was not investigated. But it is opined that since the coating penetration into the moulding materials is small

compared to the volume of the moulding materials, this may not be a problem. Detailed analyses of the mechanical properties of moulding materials of cold box and furan origin coated with filter dust coating are provided in [Supplement 5] accordingly.

6.7 Thermal Behaviour of Moulding Materials

A core coating can be designed to be either more insulating or more conductive depending on the requirement. The coating layer's thermal properties will affect the heat transfer from the molten metal to the core and consequently, the temperature gradient within the core and microstructural evolution at the casting interface. This, in turn, can affect core binder pyrolysis rate and related gas evolution characteristics. The thermal profiles of the heat distribution in the cores measured during casting of metals in both the horizontally- and vertically-parted moulds are presented. The effects of various coating formulations on the thermal profiles were elucidated. In the horizontally-parted moulds, the thermal profiles in cold box cores coated with Coating 1 (40% solid content and 9% sol-gel content), Coating 2 (50% solid content and 9% sol-gel content), and Coating 3 (40% solid content and 50% sol-gel content) relative to the uncoated cold box core are presented in Figure 6.19. From the figure, it can be seen that the coating provided an insulating effect to the surface of the core to reach the silica sand Transformation Temperature Zone (TTZ) of 573 °C. This means the coating reduces the thermal shock experienced by the mould materials. The mechanism of this effect is by filling the pore space with finer particles, thereby creating a greater thermal resistance barrier between the particles. This, consequently, increases the heat capacity of the individual particles, thereby slowing down heat transport. Coating 2 delayed the time to heat up the core to 573 °C by 27 s relative to the uncoated core. This is followed by Coating 3 by 22 s, and finally Coating 1, by 15 s (Figure 6.19b).

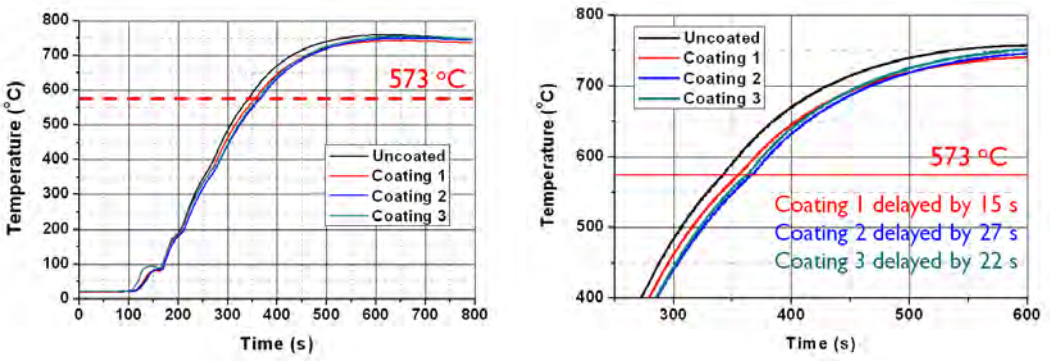

(a) Full profile (b) Scaled profile

Figure 6.19: Thermal profiles in cold box cores coated with different sol-gel filter dust coatings showing the silica sand TTZ.

This means that these coating formulations can render adequate protection to the

core giving room for the solidification of the metal to start before cracking and complete degradation of the cores occur. This will eliminate surface defects such as veinings, sand burn-on, metal penetration, etc.

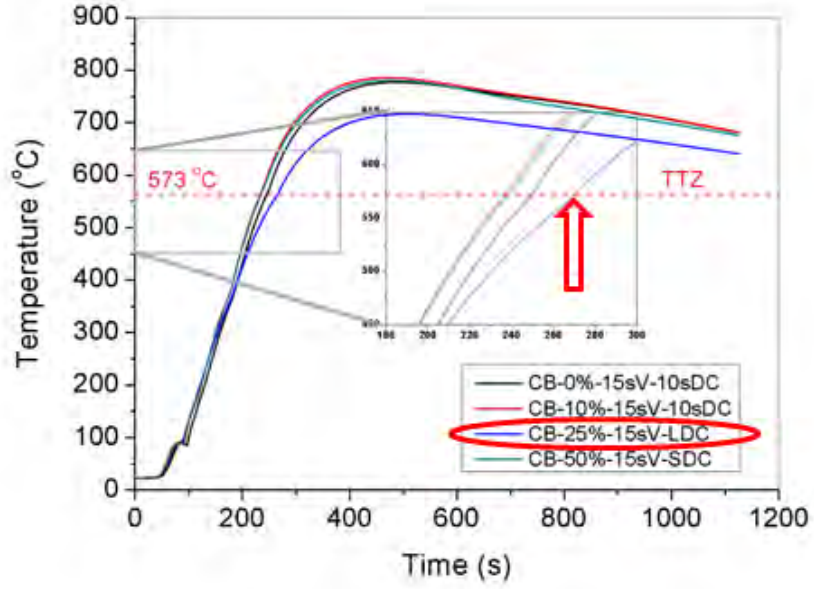

(a) Cold box - TTZ

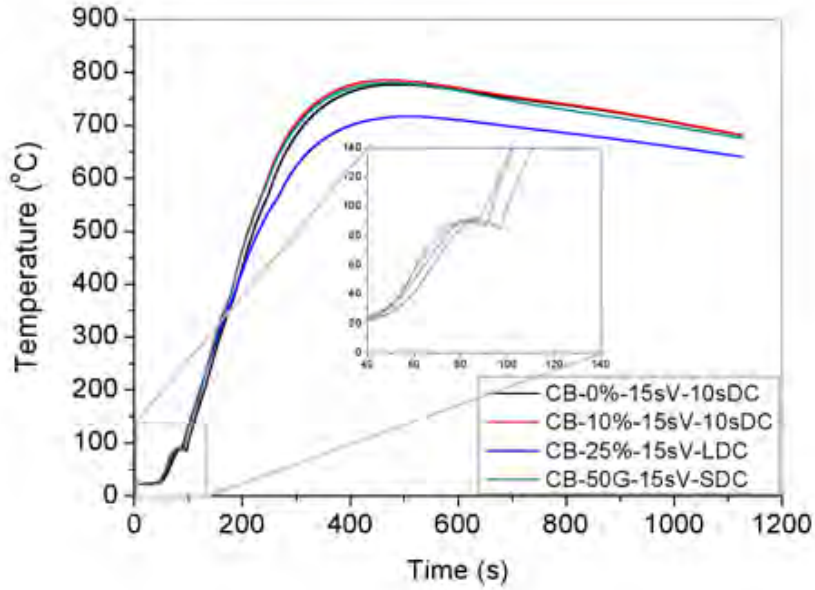

(b) Cold box - VTZ

Figure 6.20: Thermal profiles in coated cold box cores.

This is attributable to the thickness of the proud layer deposit of the coating material which in turn is due to the amount of solid content, insulating nature and the viscosity of the coating. The higher the viscosity the higher the proud

layer deposit and the better the protection.

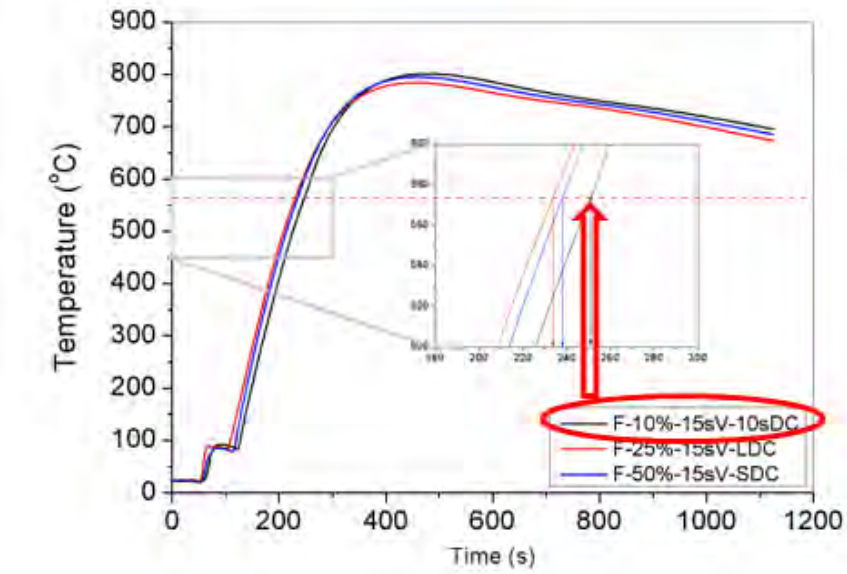

(a) Furan TTZ

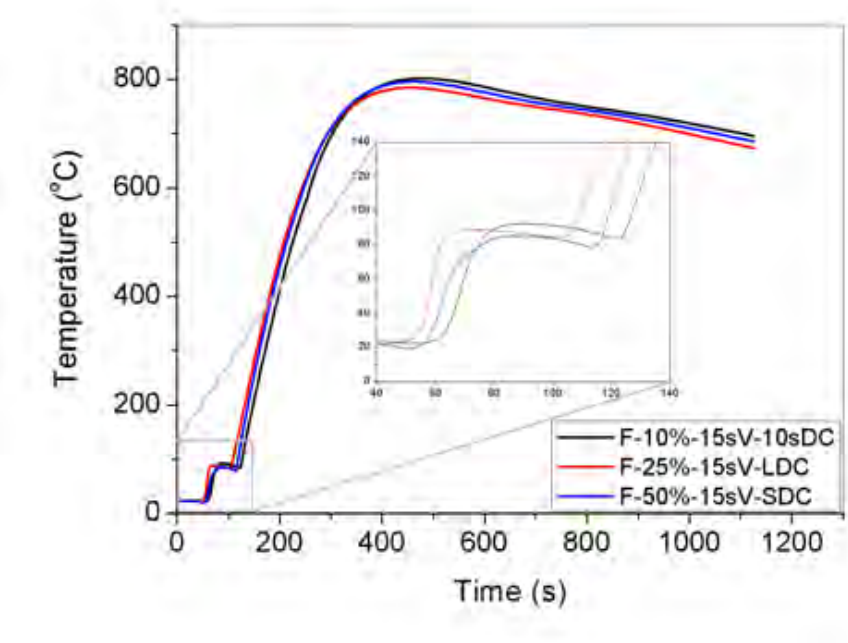

(b) Furan VTZ

Figure 6.21: Thermal profiles in coated furan cores.

Also in using sol-gel component as additive to foundry coatings on cold box and furan cores, the effects of the coatings on the heat distribution in the cores are presented in Figures 6.20 and 6.21 respectively. The Transformation Temperature Zone (TTZ) shows the effect of the coating in providing insulation effect to the cold box and furan cores, while the Vapour Transport Zone (VTZ) shows the effect

of the heat on the moisture in the core around the core-metal interface (Figures 6.20 and 6.21). The larger the VTZ, the more the moisture content [36, 41].

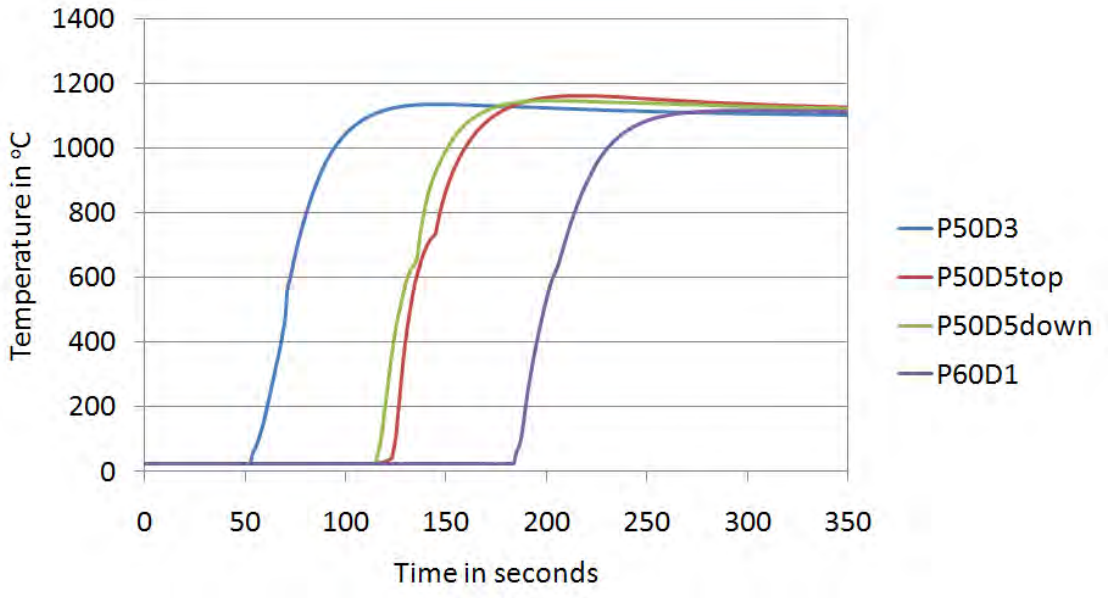

Figure 6.22: Thermal profiles in cold box core used in the vertically-parted moulds.

In a similar context, the thermal profiles of the core materials were also measured during casting in the vertically-parted moulds (DISA moulds). The thermocouples were placed in the two cores (top and down) on one side of the mould. Due to the small nature of the cores and the large metal mass surrounding them, the cores were heated above 1000 °C as shown in Figure 6.22. It is evident that the VTZ is not clearly identifiable in these profiles due to the rapidity of the degradation. Consequently, the moisture is rapidly burnt out. In these profiles, it is expected that the high thermal shock experienced by the cores will provoke surface defects. The idea is to see how the coatings will protect the cores from the thermal shock. This will be seen on the surface quality of the castings accordingly.

In another investigation to understand the effect of addition of sol-gel component to commercial coatings, the thermal degradation behaviour of coated furan and cold box core materials were monitored in a preheated furnace (temperature - above 700 °C). Three different amounts (5, 10, and 20%) of sol-gel component were added to a commercial coating and applied to both cold box and furan cores and also their counterparts without sol-gel component was applied to other set of cores with same conditions as control. The coated cores with sol-gel containing coating and the coated cores with sol-gel free coating were degraded in the furnace for at least 30 minutes while holding the furnace temperature between 760−875 °C. The observations made lead to the conclusion that the smaller amount of sol-gel component enhanced the thermal integrity of the cores. Higher amounts of sol-gel component forms more glass ceramic matrix that becomes very brittle at elevated temperatures due to development of thermal stresses in the system. Typical core specimens subjected to thermal degradation tests are shown in Figure 6.23 for

furan and cold box cores, coated with a coating containing 5% sol-gel component and the one without sol-gel in the coating.

(a) Furan

(b) Cold box

Figure 6.23: Thermal degradation of furan and cold box cores.

6.8 Analyses of the Surface of Castings

6.8.1 Prediction of Surface Reaction Products

The components of cast iron include Iron (Fe), Carbon (C), Silicon (Si), Manganese (Mn), Phosphorus (P), Sulphur (S), Magnesium (Mg); (more in ductile cast iron), Aluminium (Al), and Calcium (Ca). Considering the fact that the moulding material and mould cavity may contain oxygen, carbon, and sulphur, the elements in cast iron will undergo oxidation, carburization, and/or sulphurization. Therefore, the knowledge of the standard free energies of such reactions is important and can be calculated with The Web Tool software [113]. This software was also used to construct the Ellingham diagrams for the oxides, carbides, and sulphides. All calculations were based on the following equation.

$$\triangle G^o\,(T) \;=\; 8.314 \;\times\; T ln P_{O_2} \tag{6.1}$$

The partial pressures of oxygen; P_{O_2}, carbide; P_C, and sulphur; P_{S_2} used was 10^{-15} atmospheres. The temperature range within the casting temperature of cast iron (298 to 1750 K).

When values of $\triangle G^o_f$ for oxides are displayed, the Ellingham Diagram offers a useful way to estimate the equilibrium oxygen partial pressure as a function of temperature. Thus, it is used to predict the temperatures at which a metal is stable and the temperatures over which it will spontaneously oxidize (Figure 6.24), carburize or decarburize (Figure 6.25), or sulphurize (Figure 6.26). Since $\triangle G^0$ is a measure of the driving force behind the reaction and the more negative the value the greater the driving force, the lower the reaction line the more stable the products as they are associated with a more negative $\triangle G^0$ [28]. For temperatures at which the free energy of formation of the forward reaction products (for example oxides, carbides, sulphides, etc.) is positive, the reverse reaction is favoured and the products will spontaneously decompose to the metal.

The oxidation of C by H_2O is strongly endothermic

$C \;+\; H_2O \;\rightarrow\; CO \;+\; H_2$; $\triangle H^o = +131.3\,kJmol^{-1}$, $\triangle S^o = +133.7\,JK^{-1}mol^{-1}$

At high temperatures, CO undergoes a reversible disproportionation

$2CO \;\rightleftharpoons\; C + CO_2$; $\triangle H^o = -172.5\,kJmol^{-1}\,CO_2$, $\triangle S^o = -176.5\,JK^{-1}mol^{-1}$

The equilibrium concentration of CO is 10% at 550 °C and 99% at 1000 °C. Below 710 °C (983 K) carbon is a stronger reducing agent when it is converted into CO_2 rather than CO; whereas above this temeperature the reverse is true [49]. Therefore, at casting temperatures, the ratio CO/CO_2 is likely to be greater than unity, this will hinder penetration.

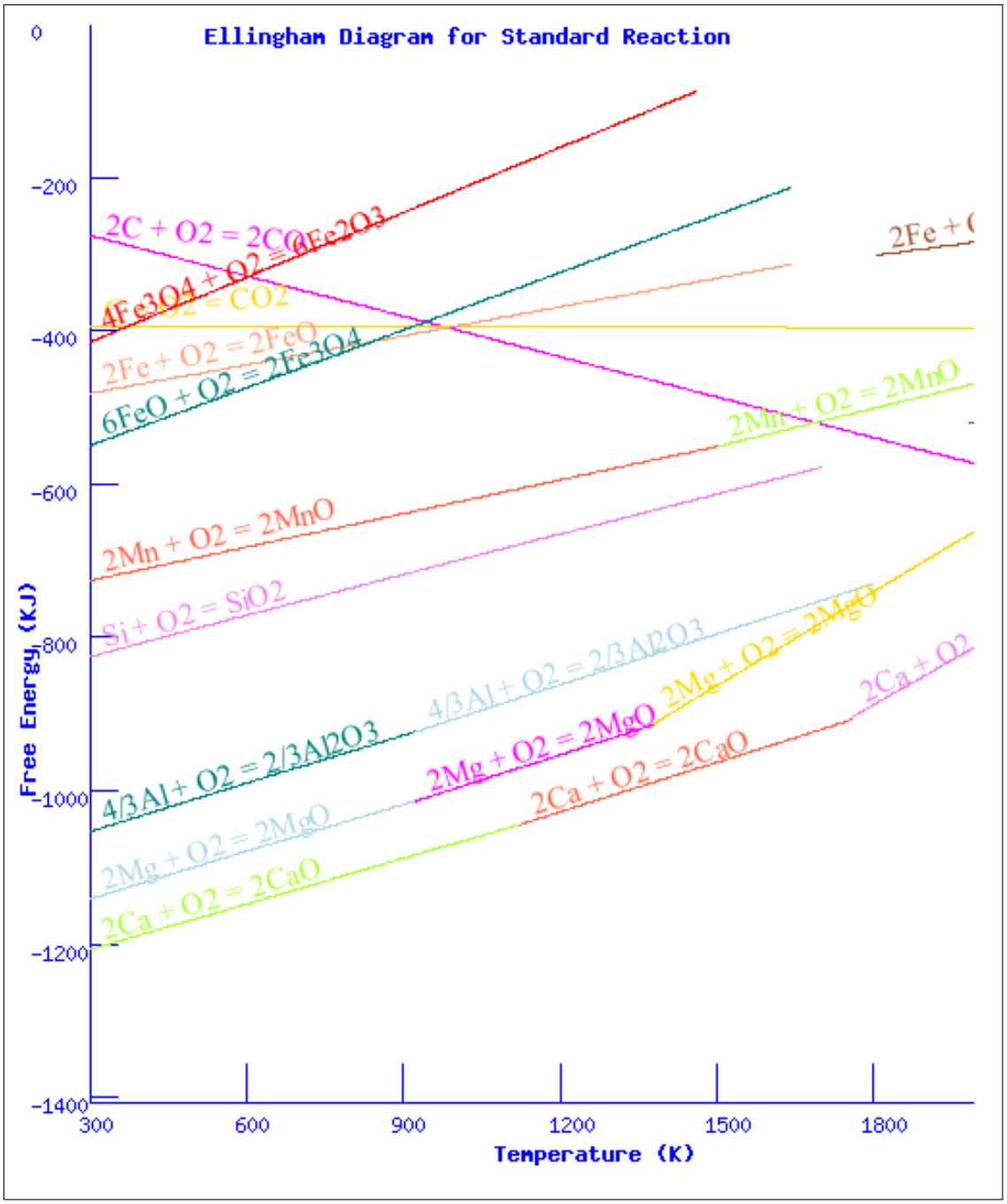

Figure 6.24: Predicted oxidation reactions likely to occur in the mould with liquid metal.

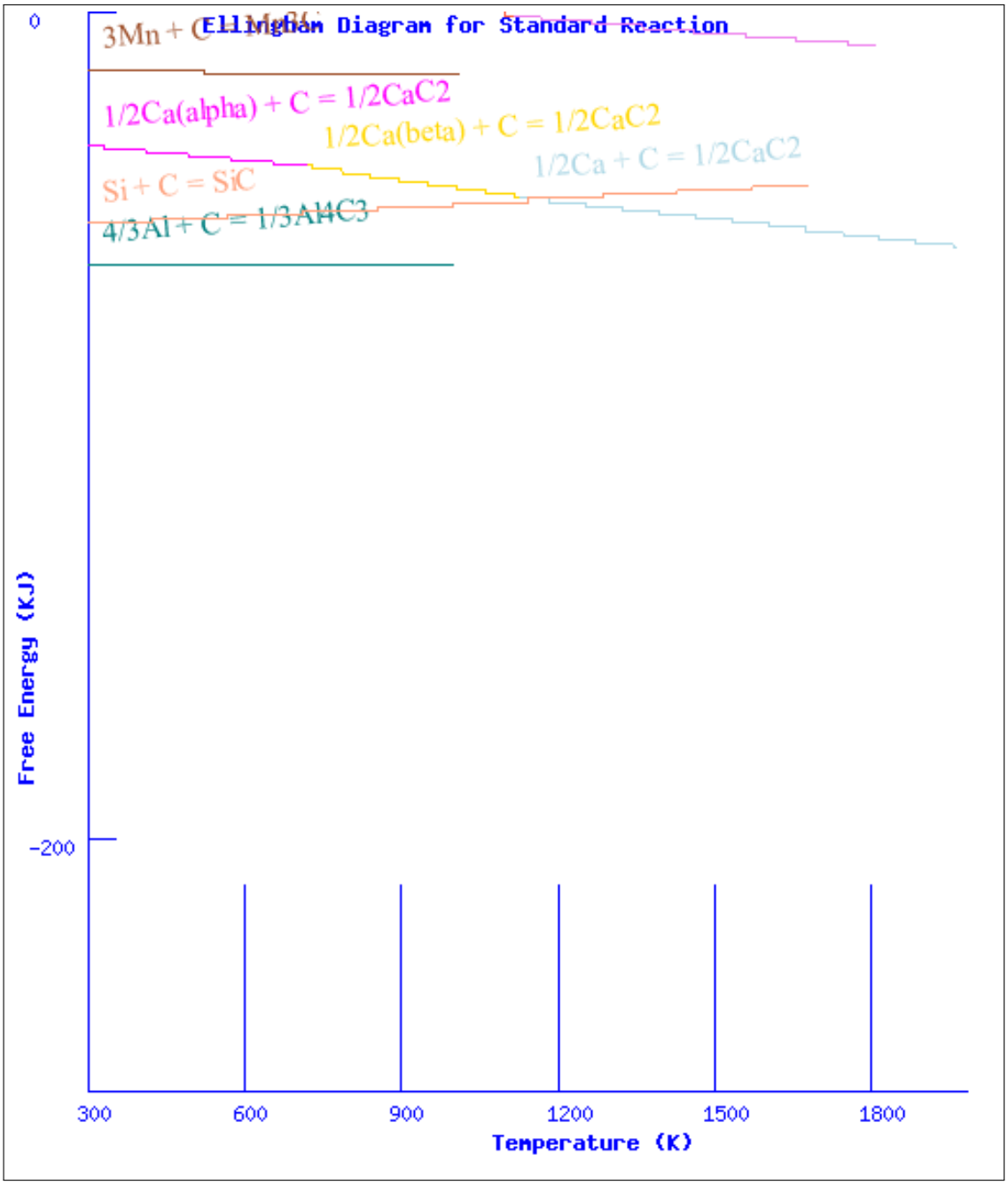

Figure 6.25: Predicted carburization reactions likely to occur in the mould with liquid metal.

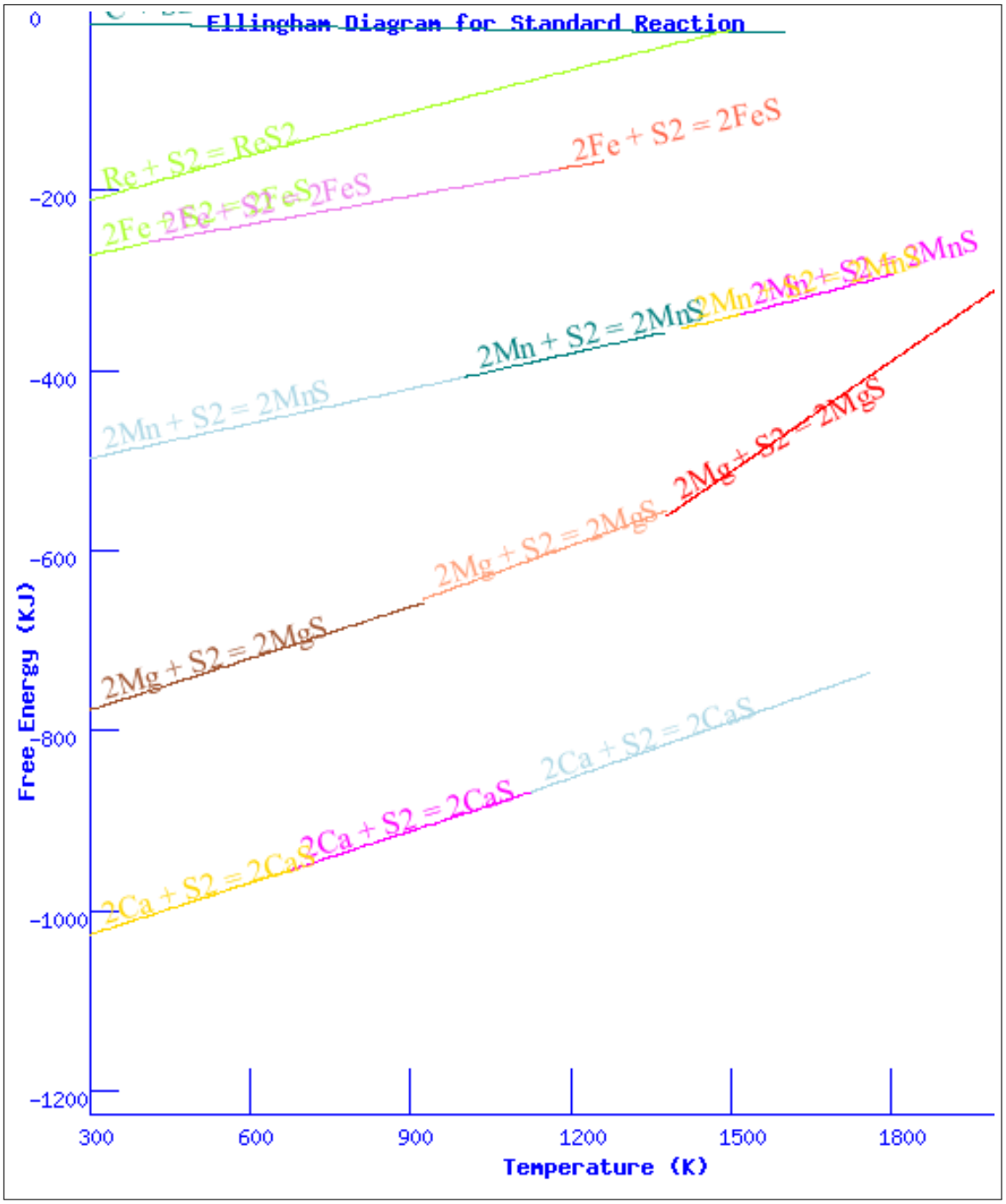

Figure 6.26: Predicted sulphurization reactions likely to occur in the mould with liquid metal.

6.8.2 Surface Quality of Castings

The improvement of the surface quality of castings by use of novel sol-gel coatings is the main objective of this research. The use of high thermal resistant coating refractory materials of micron-size range relative to the sand grains used for producing the moulding materials, has a significant impact on the performance of foundry coatings. The fine details of the refractory materials deposited as surface layer on the moulding materials will reflect on the surface quality of the castings. This gives improved surface finish of the cast components by reducing roughness, metal penetration, veining defects, etc. The photographs of the surface of castings produced with various sol-gel coating formulations with micron-size refractory materials, in horizontally-parted and vertically-parted moulds, are presented for visual examination. Some comparisons with commercial foundry coatings are also provided. On seeing the improvement achieved by the sol-gel filter dust coating, the surface quality of the casting surfaces was estimated by measuring the surface roughness for subsequent approaches.

6.8.2.1 Sol-Gel Filter Dust Coating on Cold Box and Furan Cores

The cores for these castings were not completely coated in order to allow for venting. However, the cores were not uniformly coated to a particular height either (the coated heights are not the same) as shown in Figure 6.27. The coated part of the cores is on the lower part of the castings. Therefore, for some castings the effect of the part of the core without coating may be seen. This part of the castings should be ignored in the assessment of the surface quality of these castings where they occur. But, it can serve as a control to check the performance of the coating on the coated part over uncoated part.

Figure 6.27: The coated cores with random coating heights.

The castings made with uncoated and 1 s dip-coated cold box and furan cores

in 40% solid content and 9% sol-gel content coating are presented in Figure 6.28. From this figure, it is evident that the coatings on both cold box and furan cores improved the surface finish of the castings. This shows that there is a positive potential in using sol-gel process for foundry coating production. It can also be seen that the surfaces of castings made with furan cores seem better than the surfaces of castings made with cold box cores. This is believed to be due to the fact that furan cores have higher thermal resistance than the cold box core materials due to the minimal level of fresh sand present in the core material [41].

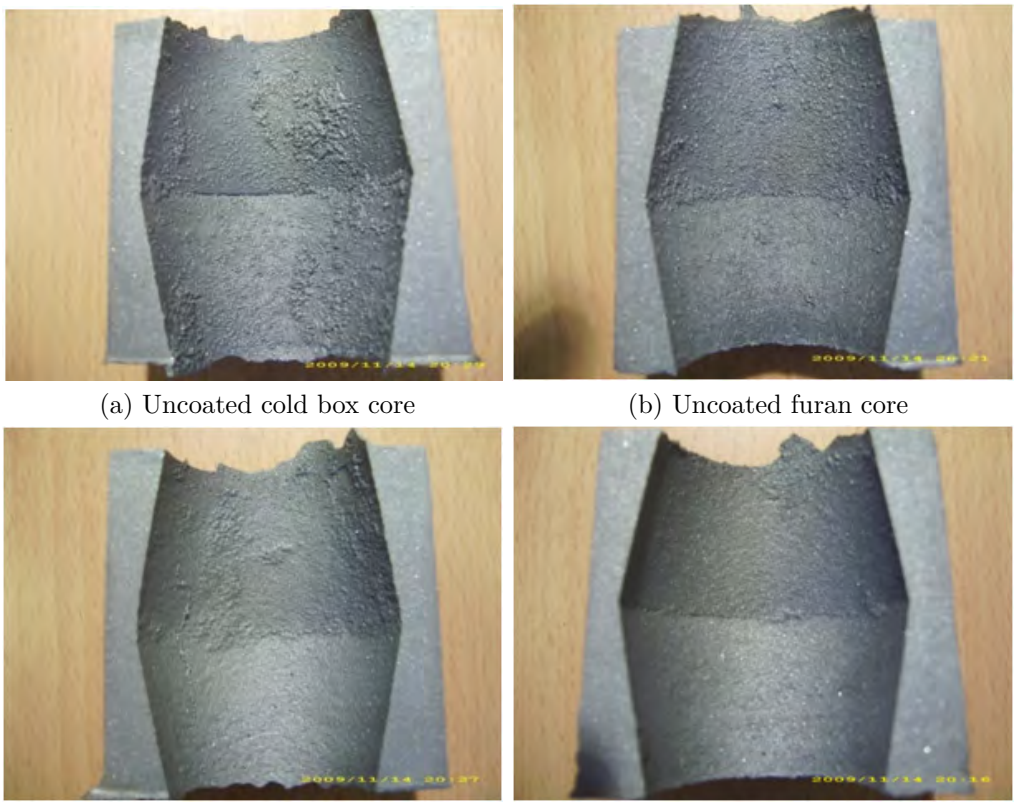

(a) Uncoated cold box core (b) Uncoated furan core

(c) Cold box core coated for 1 s (d) Furan core coated for 1 s

Figure 6.28: Surface quality of castings made with uncoated and cores coated with sol-gel filter dust coating.

Also, the castings made with cold box and furan cores dip-coated for 1 s in two other commercial coatings are compared with castings produced with cold box and furan cores dip-coated for 1 s in sol-gel filter dust coating. The results are presented in Figures 6.29 and 6.30 for cold box and furan cores respectively. From Figure 6.29, it can be seen that the coatings on the cold box cores improved the surface quality of the castings relative to the casting made with uncoated core. Some veining defects are observed on the surface of casting made with the water-based coating (Figure 6.29c), this is attributed to the higher viscosity of this coating during processing, which lead to higher surface layer deposit thickness.

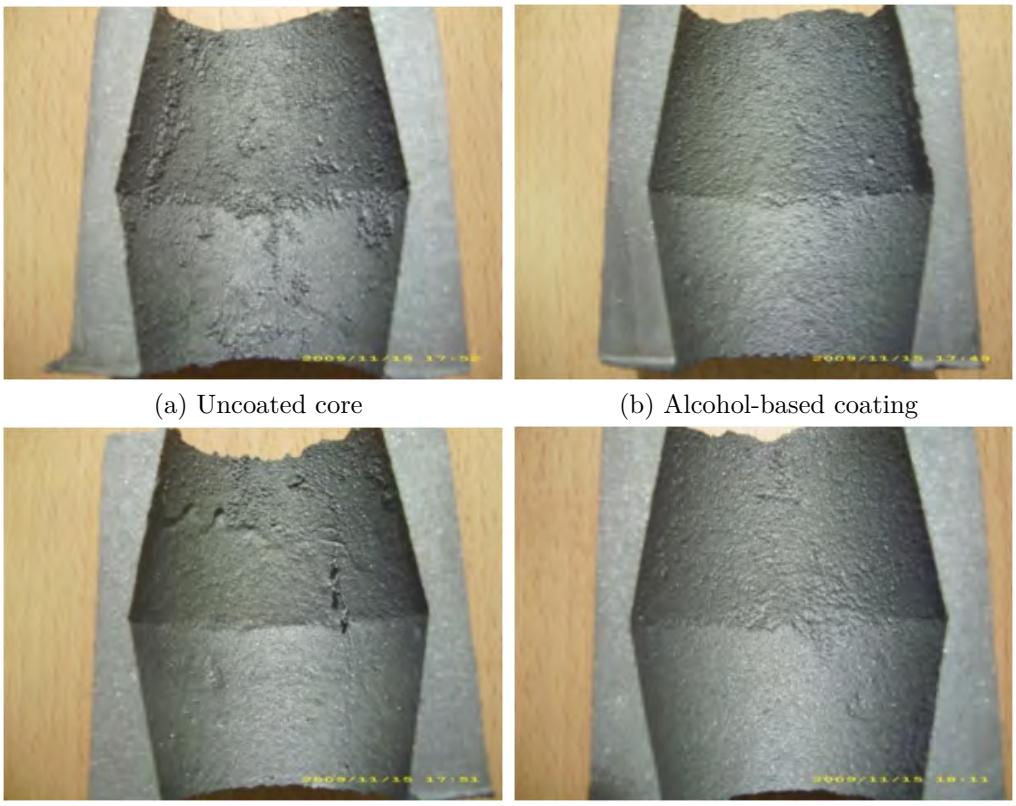

(a) Uncoated core (b) Alcohol-based coating

(c) Water-based coating (d) Sol-gel-based coating

Figure 6.29: Comparison of surface quality of castings made with uncoated and coated cold box cores.

From Figure 6.30, a similar observation is made for the furan core system. The coatings on the cores improved the surface quality of the castings when compared with the surface of casting produced with uncoated core. Generally, from these visually observed surface qualities of castings, it can be proposed that the filter dust sol-gel dust coating has comparable performance with the commercial coatings in improving the surface quality of castings.

According to the simulation results in Figure 4.13, it is suggested that porosity and sand burn-on defects may not be a problem with these castings considering their small sizes. From Figure 4.13, these defects are limited to the downsprue and this is in agreement with the experimental casting shown in Figure 6.31.

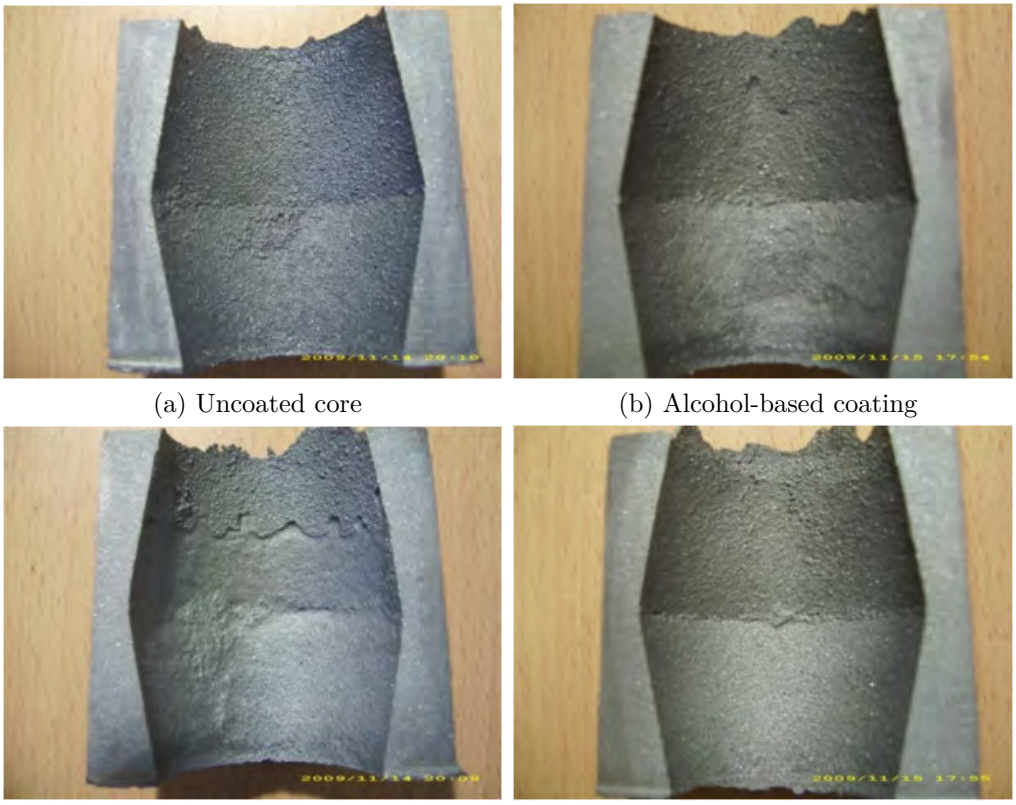

(a) Uncoated core (b) Alcohol-based coating

(c) Water-based coating (d) Sol-gel-based coating

Figure 6.30: Comparison of surface quality of castings made with uncoated and coated furan cores.

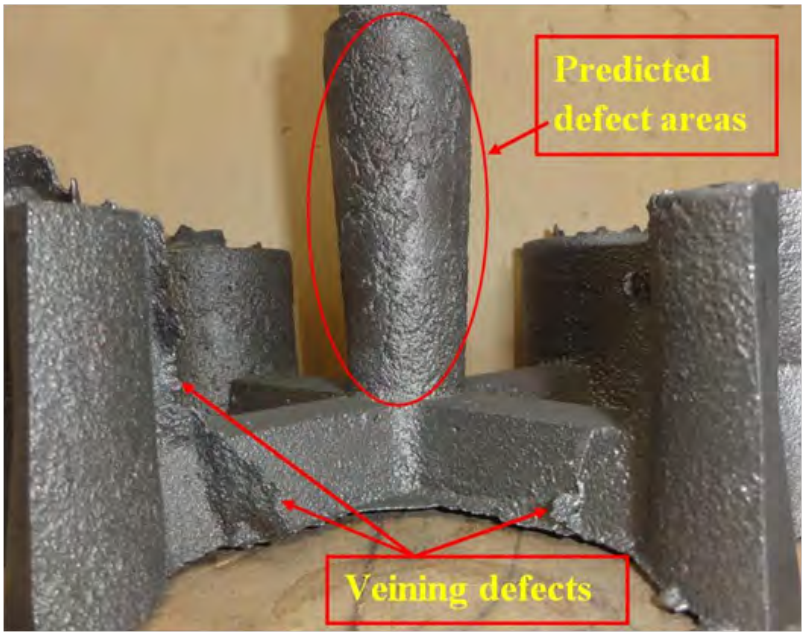

Figure 6.31: Experimental casting showing areas of defects in agreement with numerical simulations in the horizontally-parted mould.

The sol-gel coating with 40, 50, and 60% filter dust (solid content) and 9% sol-gel content was applied to cold box cores by dip-coating for 1, 3, and 5 s for vertically-parted moulds (DISA moulds) to investigate the influence of pressure height of the melt on the surface quality of the castings around the cores. The system was also studied to see how the coatings on the cores will effect enhancement of the surface quality of the castings. The casting surfaces made with the cores coated with 40% solid content coating and core dipping time of 1, 3, and 5 s are presented in Figure 6.32. The castings are filled from the bottom (the bottom of each casting is where the scale (ruler) is placed). The casting made with uncoated cores is shown in Figure 6.32a. The identification and description of the core locations in the castings is shown in Figure 6.32b and the label P40D1 means 40% solid content and 1 s dipping time. As can be seen at the down channel of the casting produced with uncoated cores, there is evident veining defect of about 85 mm long. This is due to the cracking of the core around that area before solidification started. The castings produced with coated cores shows surfaces without veining defects.

An observation was made during the estimation of the surface roughness of each channel in the castings, that the top channels have higher roughness than the other lower channels as shown in Figure 6.33. It is expected that, due to the influence of metallostatic pressure as shown in the simulation results presented in Figure 4.12, the casting surfaces at the down channels will have the highest surface roughness followed by the mid channel, then the top channel will have the lowest roughness. However, this was not the case because the top core seem to be fried by the radiation heat from the incoming melt, thereby getting the surface destroyed before the melt reaches the core. This caused the casting surfaces at the top cores to have higher surface roughness as can be seen from Figure 6.33. Again, the mid core is surrounded by the last-to-freeze metal from the simulation results (Figure 4.14b and c), therefore the mid core is subjected to extreme thermal shock and distortion. This can lead to metal penetration.

For the sol-gel filter dust coatings containing 50 and 60% solid content, the proud layer on the cores suffered severe cracks during curing. This was reproduced in the surface of the castings made with these cores. The surface roughness estimation of the casting surface around the core coated with 50% solid content coating is presented in Figure 6.34, while the photographs of the surfaces of castings made with cores coated with 60% solid content coating is presented in Figure 6.35. The network of cracks on the castings made with coated cores is obvious. This is attributed to the growing proud layer thickness with increasing solid content or to the presence of bentonite in the coating formulation. Bentonite is known to swell on absorption of water and shrinks on the release of the water during drying. This shrinkage leads to stress development in the coating then causing it to crack. The effect of the radiation from the incoming melt was also observed on the surface quality of the castings around the mid and top coated cores, with metal penetration on the mid channel for uncoated core (Figure 6.35a), but there is only minimal metal penetration with coated cores as shown in Figure 6.35b-d. This shows that the sol-gel coating may have a good thermal stability to withstand the effect of the heat from the metal.

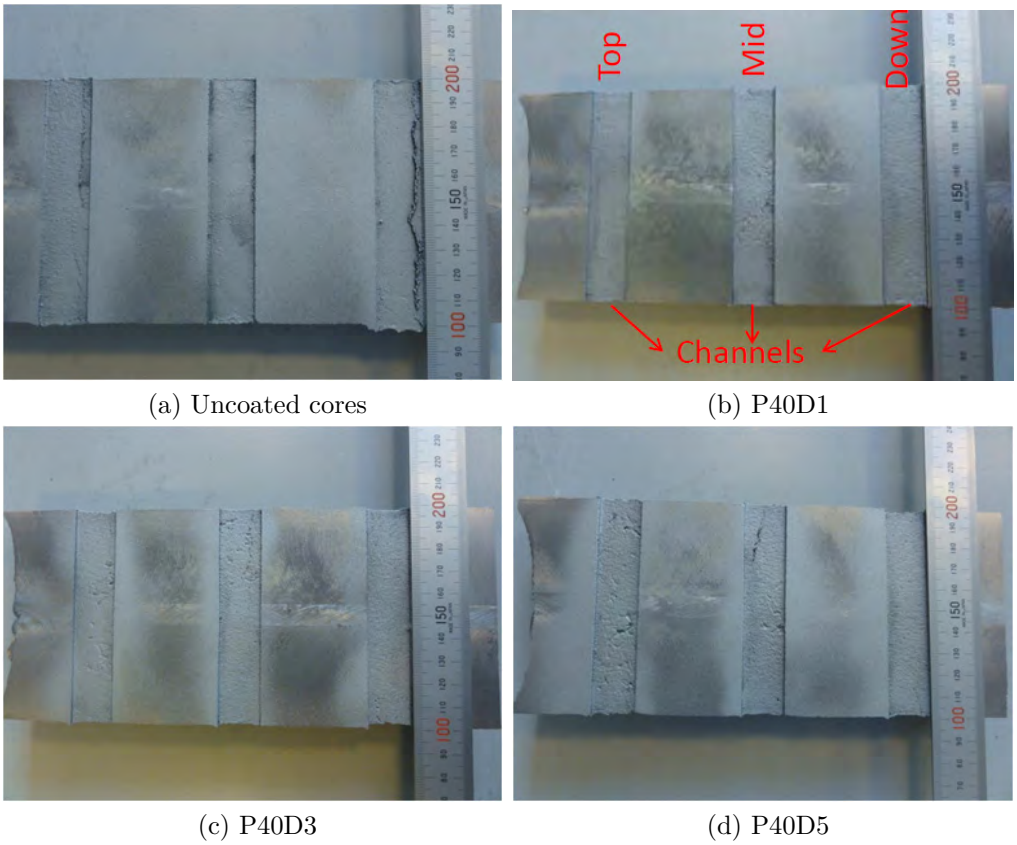

(a) Uncoated cores (b) P40D1

(c) P40D3 (d) P40D5

Figure 6.32: Sol-gel filter dust coating containing 40% solid content and 9% sol-gel content.

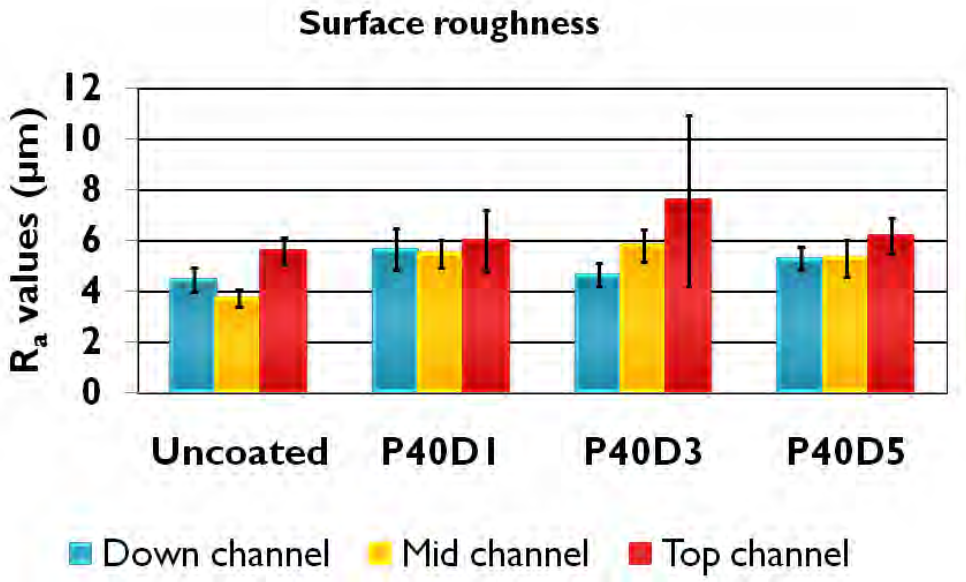

Figure 6.33: Surface roughness estimation of the casting surface around the cores coated with 40% solid content sol-gel coating.

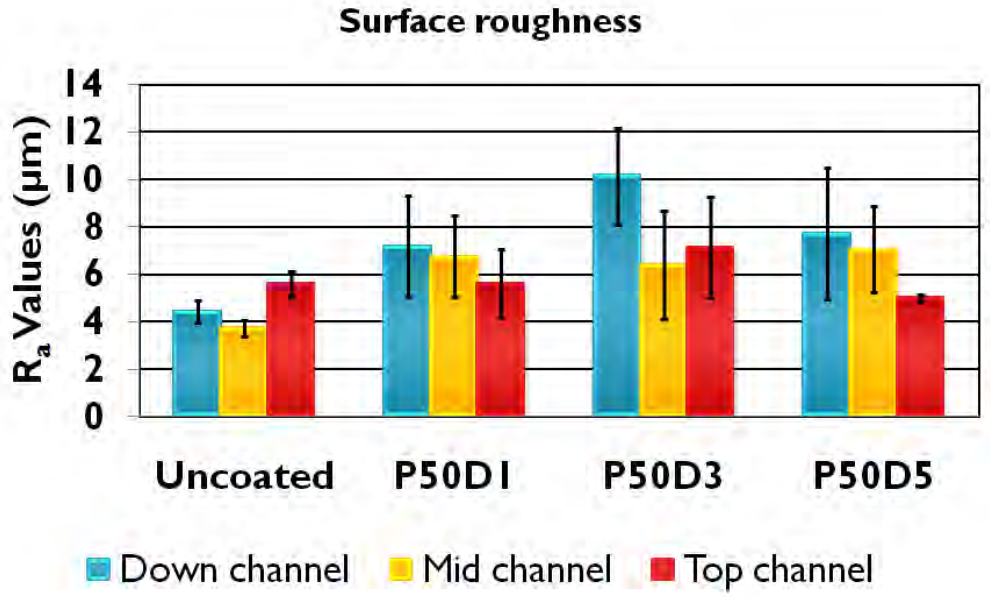

Figure 6.34: Surface roughness estimation of the casting surface around the cores coated with 50% solid content sol-gel coating.

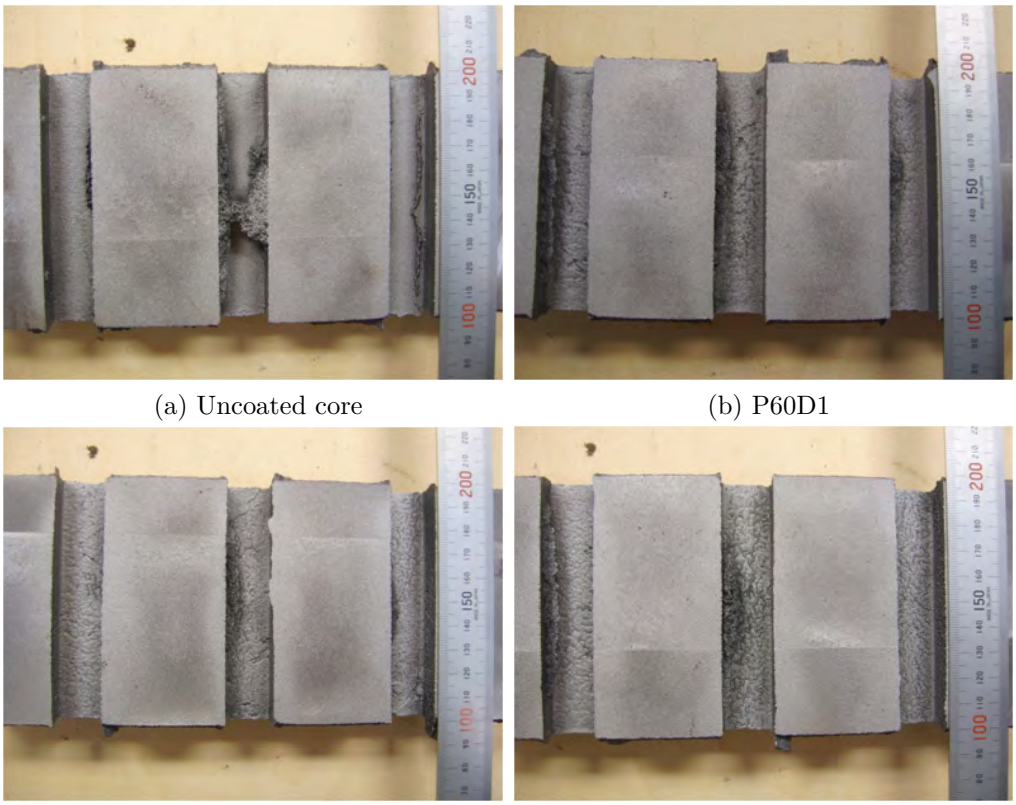

(a) Uncoated core

(b) P60D1

(c) P60D3

(d) P60D5

Figure 6.35: Sol-gel filter dust coating containing 60% solid content and 9% sol-gel content.

Figure 6.36: Experimental casting showing areas of defects in agreement with numerical simulations in the vertically-parted mould.

Furthermore, the predicted defect areas shown in Figure 4.13 agree with the defect areas from experimental castings as shown in Figures 6.35a and 6.36 for penetration in the mid channel and shrinkage porosity on the top of the castings respectively.

6.8.2.2 Varying Sol-Gel Content and Solid Content to get Three Different Formulations

The castings made with cold box cores dip-coated for 3 s in Coating 1 (40% solid content and 9% sol-gel content), Coating 2 (50% solid content and 9% sol-gel content), and Coating 3 (40% solid content and 50% sol-gel content) for horizontally-parted moulds are presented in Figure 6.37. The surfaces show that the coated cores improved the surface quality of castings with Coating 3 showing the best surface quality. This is attributed to the high amount of sol-gel component (50%) in the coating forming glass ceramic surface which provided high thermal stability and smoothness which reflected on the surface of the casting.

The influence of dipping time is also shown with castings made with cores coated with Coating 2 containing 50% solid content and 9% sol-gel content. The longer the dipping time the more coating refractory material is deposited on the surface of the cores. This enhances surface coverage and protective barrier to the core substrates [107]. Therefore, it is expected that 5 s dipping will produce the best casting surface. This is confirmed, as obviously seen in Figure 6.38d.

For the vertically-parted mould, 3 s dipping time in each coating was used to show the effect of the coating type on the surface quality of the castings around the coated cores. The casting surfaces are shown in Figure 6.39. The poor surface of the casting (Figure 6.39a) made with uncoated cores is obvious with almost 100 mm crack length in the down channel, 75 mm crack length in the top channel and evidence of metal penetration in the mid channel. The metal penetration in the mid channel and the crack in the top channel (Figure 6.39b) were eliminated with

coating 1 (40% solid content and 9% sol-gel content), but the crack on the down channel could not be removed by the coating, probably because the coating is not thick enough to withstand the thermal shock from the metal.

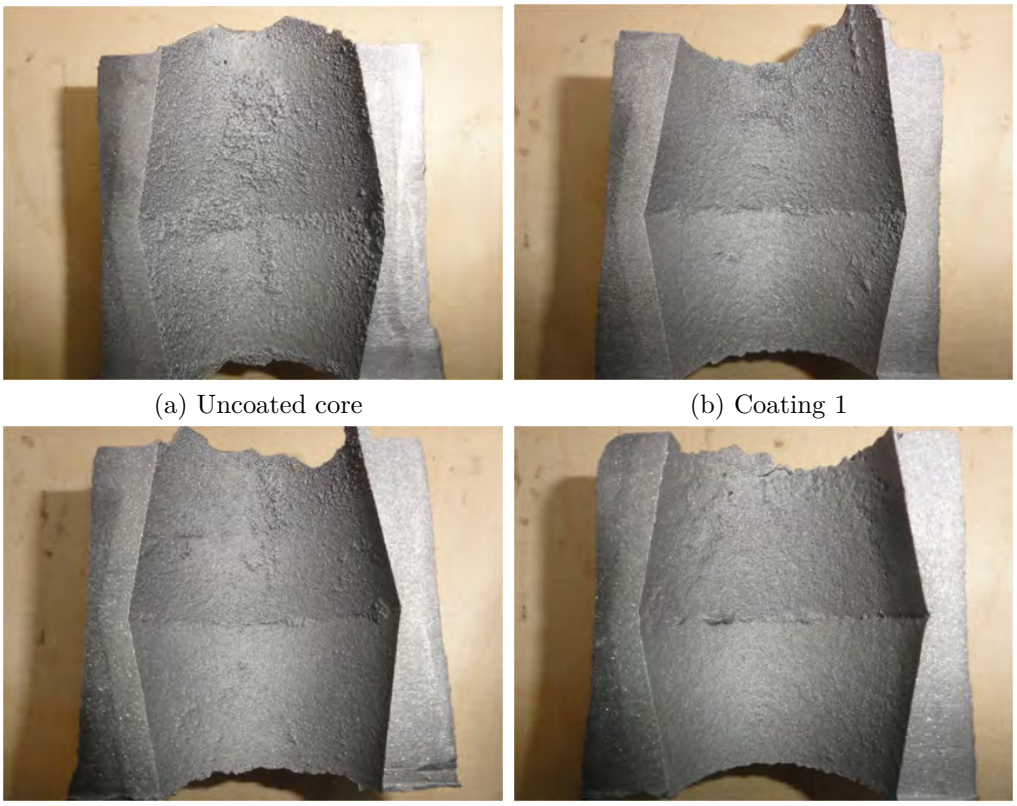

(a) Uncoated core (b) Coating 1

(c) Coating 2 (d) Coating 3

Figure 6.37: Surface quality of castings showing the influence of sol-gel coating type on 3 s dipping of cold box cores.

However, with Coating 2 containing 50% solid content and 9% sol-gel content and Coating 3 containing 40% solid content and 50% sol-gel content, all the surface defects were removed giving better casting surfaces as can be seen in Figure 6.39c and d. This means that, increasing the amount of solid content from 40% in Coating 1 to 50% in Coating 2, provided a layer deposit that can withstand the thermal shock from the metal. In a similar context, increasing the sol-gel amount from 9% in Coating 1 to 50% in Coating 3, enhanced the formation of a thermally stable glass ceramic surface which improved the surface finish of the castings. An estimation of the surface roughness of the castings is presented in Figure 6.40.

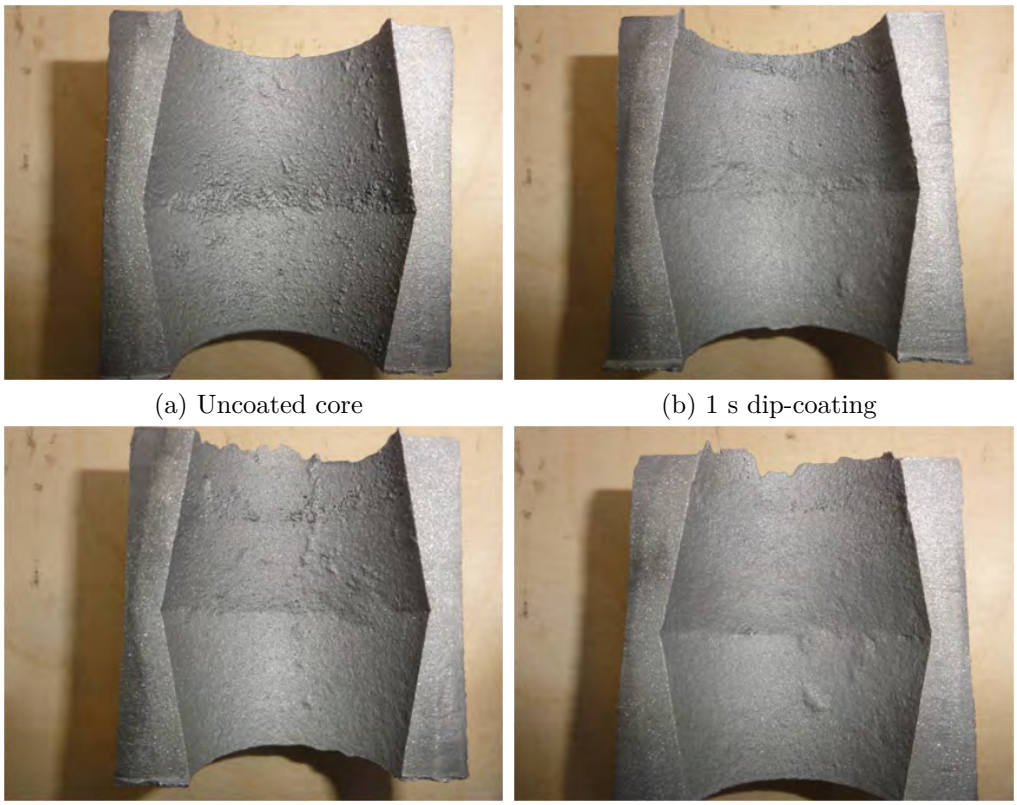

(a) Uncoated core (b) 1 s dip-coating

(c) 3 s dip-coating (d) 5 s dip-coating

Figure 6.38: Surface quality of castings showing the influence of dipping time in Coating 2 on surface quality of castings.

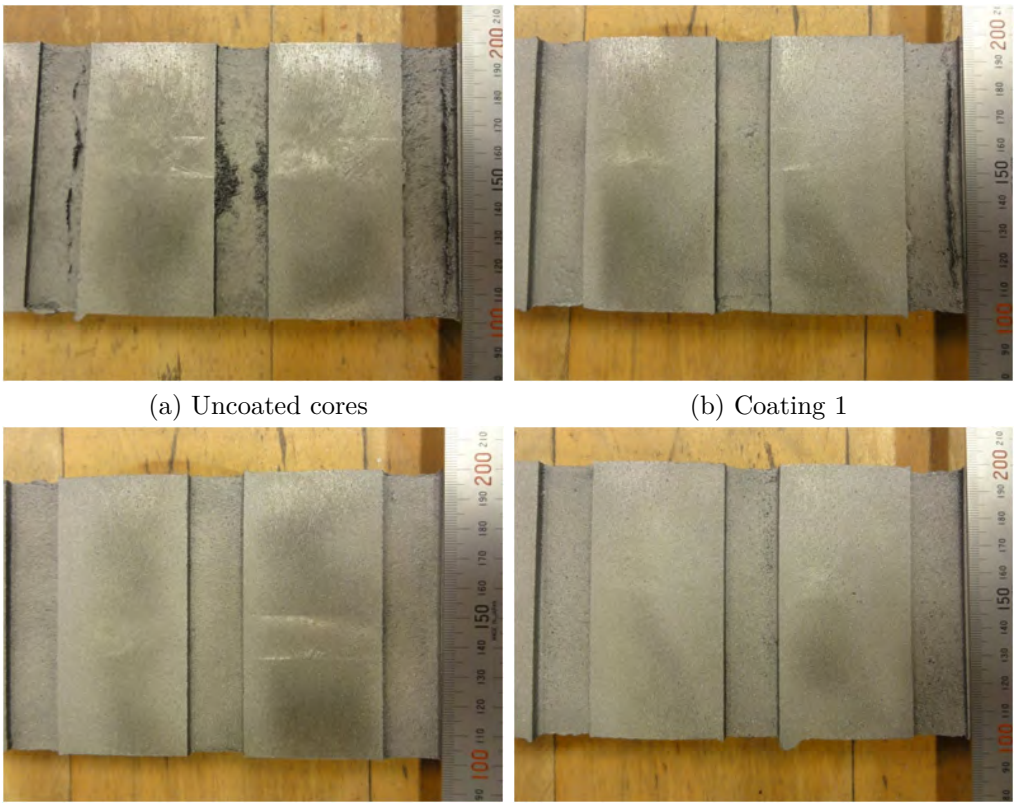

(a) Uncoated cores (b) Coating 1

(c) Coating 2 (d) Coating 3

Figure 6.39: Influence of sol-gel coating type on the surface quality of castings with different location of coated cores.

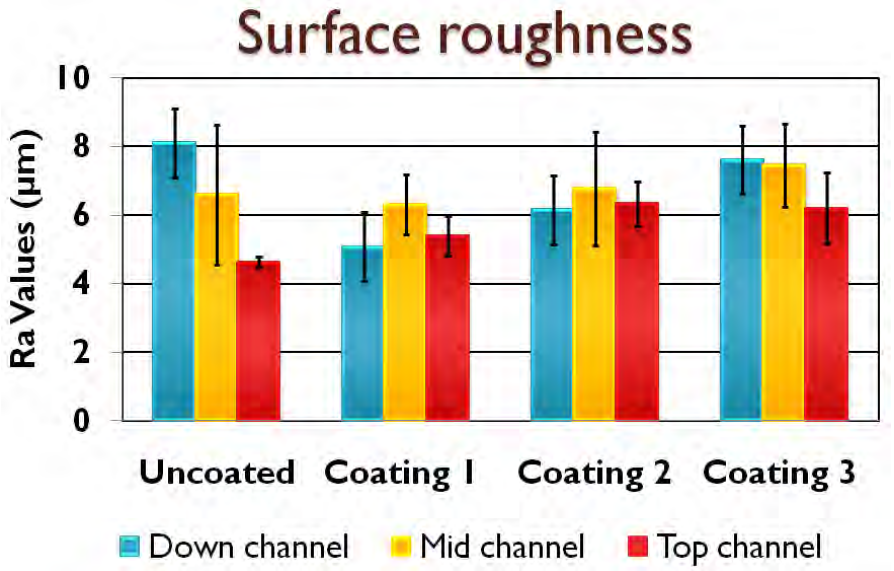

Figure 6.40: Surface roughness estimation of the casting surface around the cores coated with three different sol-gel coatings.

6.8.2.3 Using Sol-Gel Component as Additive to Foundry Coatings with Cold box and Furan Cores

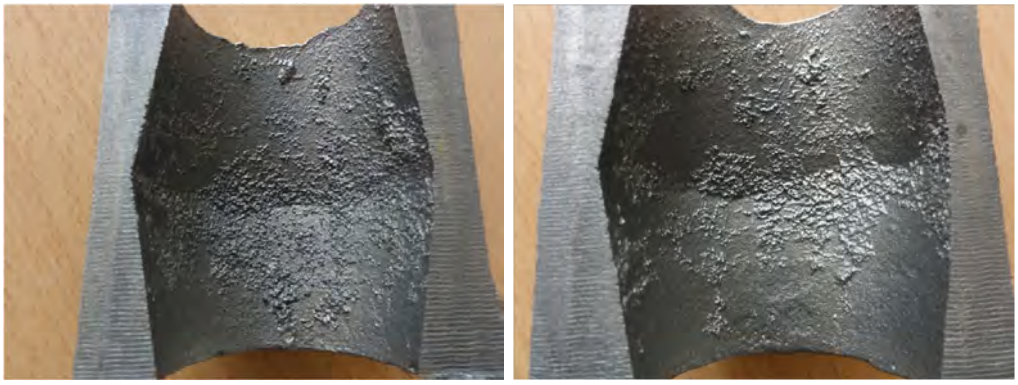

(a) Cold box core (b) Furan core

Figure 6.41: The surface of castings made with uncoated cold box and furan cores.

(a) W254.6M + 0%SG-15 s V-10 s DC (b) W254.6M + 10%SG-15 s V-10 s DC

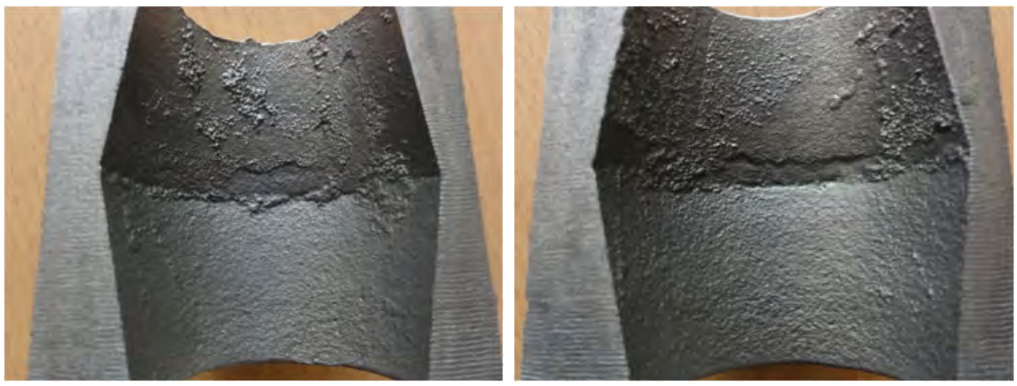

(c) W254.6M + 25%SG-15 s V-L DC (d) W254.6M + 50%SG-11 s V-L DC

Figure 6.42: The effect of addition of sol-gel component to a commercial coating on surface quality castings made with cold box cores.

The poor surface quality of castings made with uncoated cold box and furan cores are shown in Figure 6.41. The castings made with cores dip-coated in a foundry coating (W254.6M) containing sol-gel component as an additive are shown for both cold box (Figure 6.42) and furan (Figure 6.43) core systems in a horizontally-parted mould. From Figure 6.42, the results show that there is no significant effect of adding sol-gel component to the coating for cold box cores. The surfaces of the castings produced with coating containing no sol-gel component and with coating containing sol-gel component are comparable. This implies that adding sol-gel component to this coating for cold box cores may be an economic waste. However, for furan cores as shown in Figure 6.43, it is obvious that there is observed improvement on the surface quality of the castings made with the coating containing sol-gel component relative to the surface of the casting produced with coating containing no sol-gel component. The casting surface produced with the coating containing no sol-gel additive showed evidence of surface reaction products while the surface of castings produced with the coating containing different amounts of sol-gel additive improved the surface quality significantly. Therefore, for furan cores, the addition of the sol-gel additive to the coating may make the coating applicable to the core system.

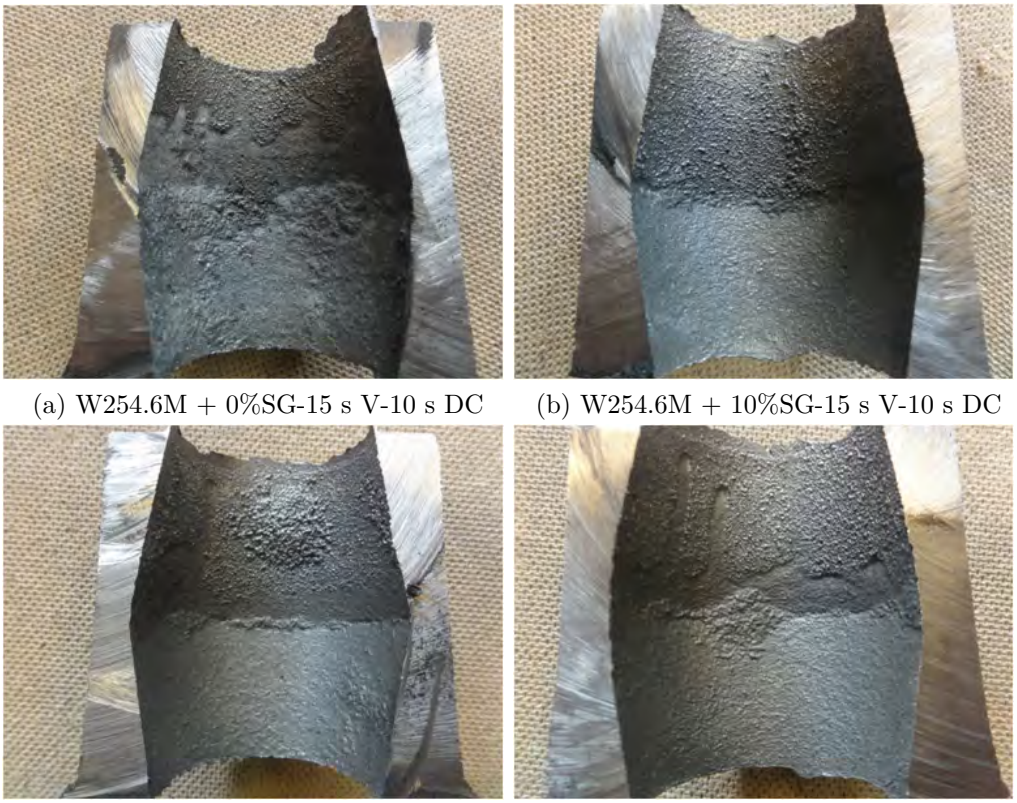

(a) W254.6M + 0%SG-15 s V-10 s DC (b) W254.6M + 10%SG-15 s V-10 s DC

(c) W254.6M + 25%SG-15 s V-L DC (d) W254.6M + 50%SG-15 s V-S DC

Figure 6.43: The effect of addition of sol-gel component on surface quality of castings made with furan cores.

6.8.2.4 Using Sol-Gel Component as Additive to Foundry Coatings with Green Sand Moulds

The castings made in vertically-parted moulds are vice casting made by spraying foundry coatings containing sol-gel component as additive. The castings examined are castings identified with the mould numbers as 10, 11, 14, 20, and 22. The description of the treatments given to the prints in the mould is as follows:

- Mould no.10: Print 1+3: No coating, Print 2+4: W230, dilution of W230: 30% addition of water.
- Mould no. 11: Print 1+3: No coating, Print 2+4: W230 + 4% Sol-Gel, dilution of W230: 25% addition of water.
- Mould no. 14: Print 1+3: No coating, Print 2+4: W230 + 20% Sol-Gel, dilution of W230: 25% addition of water with multilayer application. Moulds poured after 1 hour extra waiting time.
- Mould no. 20: Print 1+3: No coating, Print 2+4: W226 + 4% Sol-Gel, dilution of W226: 30% addition of water.
- Mould no. 22: Print 1+3: No coating, Print 2+4: W226, dilution of W226: 30% addition of water with multilayer application .

From visual examination of the surfaces, the surface quality of the castings could not be distinctly distinguished. The only improvement visually observed was with the multilayer application from mould No. 14 as can be seen from Figure 6.44.

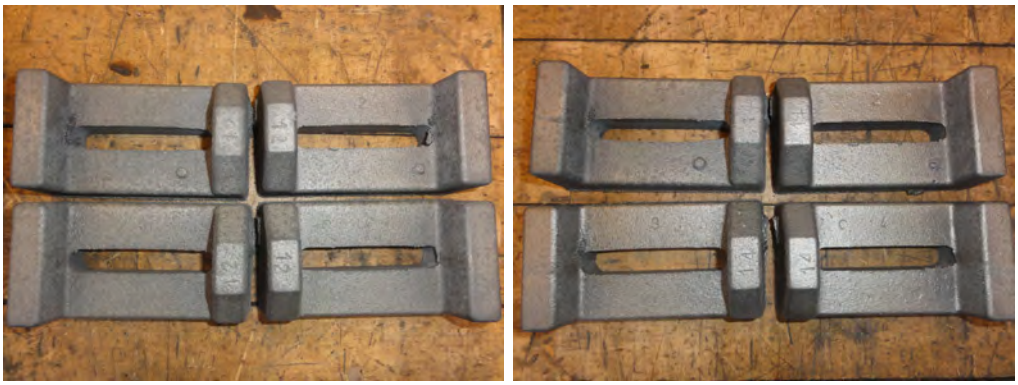

(a) W230 + 4% SG (b) W230 + 20% SG-Multilayer

Figure 6.44: Vice castings .

A detailed surface texture measurement and analysis of the casting surfaces was made using the Alicona microscope and Scanning Probe Image Processor (SPIP) software respectively. Areal surface analysis is performed in order to distinguish the surfaces. A description of the casting geometry is provided in Figure 6.45. Prints 2 and 4 were spray-coated while prints 1 and 3 are left uncoated. This pattern also helps in the investigation of the influence of metallostatic pressure on the surface finish of the vice castings. For each of the prints in a mould, the top

and down of the front face (Figure 6.45c) and top and down of the reverse face (Figure 6.45d), were scanned for roughness measurement. Six measurements were made on each face and then averaged. The parameter used for the description of the surface roughness is the Sa value which is synonimous to Ra value. The only difference is that the Ra value gives profile (2D) detail which is regarded as not being representative of the surface texture, especially in unpatterned surfaces (random texture) like those of castings, while Sa value gives areal (3D) detail which covers more area of the surface thereby providing a more representative information. The roughness results presented here are average of the measurements made on the front face of the top and down arms of the vice castings along with the reverse face.

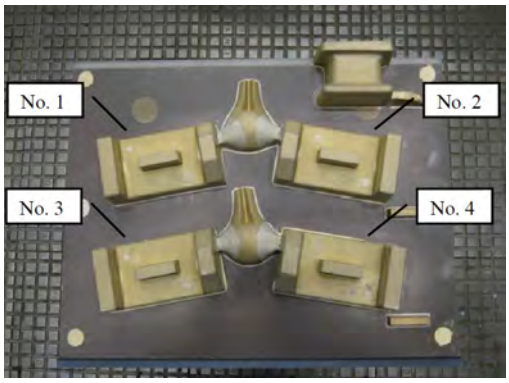

(a) Casting layout-SP-showing the Prints

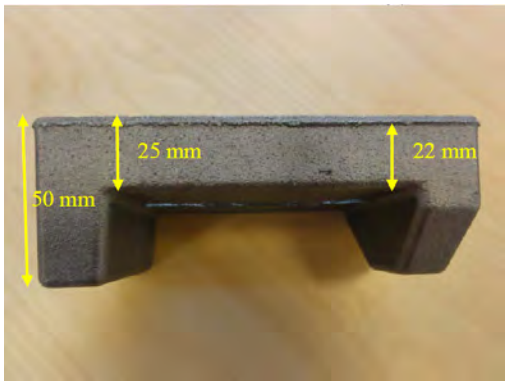

(b) Vice - side view

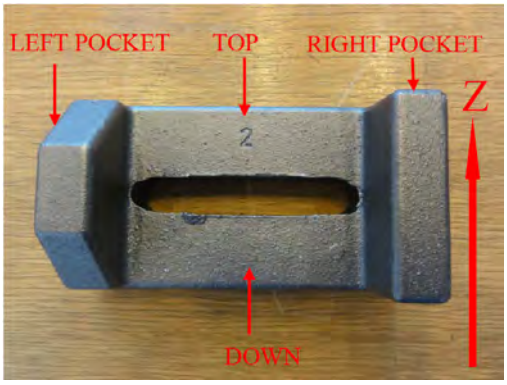

(c) Vice-front face

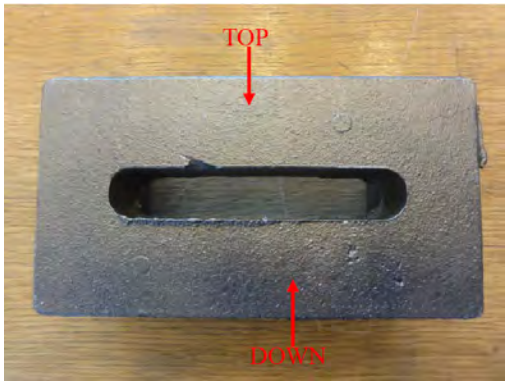

(d) Vice-reverse face

Figure 6.45: Casting layout and descriptions.

The objective used is 5× giving a vertical resolution of 410 nm and a working distance of 23.5 mm. For this objective, the XY range is 2.8392 mm × 2.1538 mm and a light beam spot diameter of 6 mm. After data acquisition with Alicona "InfiniteFocus" Microscope, the image was analysed with Scanning Probe Image Processor (SPIP) software. Plane correction was performed on the entire image to level the surface (assuming it is not level) and to remove the primary profile. However, the measurements were done on flat surfaces, therefore, there was no significant difference. The surfaces were filtered to remove waviness using Gaussian filter according to ISO 11562. This sequence of operations was followed consistently for all the measurements. Typical example of processed surfaces are shown in

Figure 6.46.

The reason for filtering the surfaces is to remove the dominance of waviness over the surface roughness. This reason is shown in Figure 6.47. As can be seen, the actual surface roughness is obvious in Figure 6.47d. A typical 3D surface texture of an analyzed surface is presented in Figure 6.48.

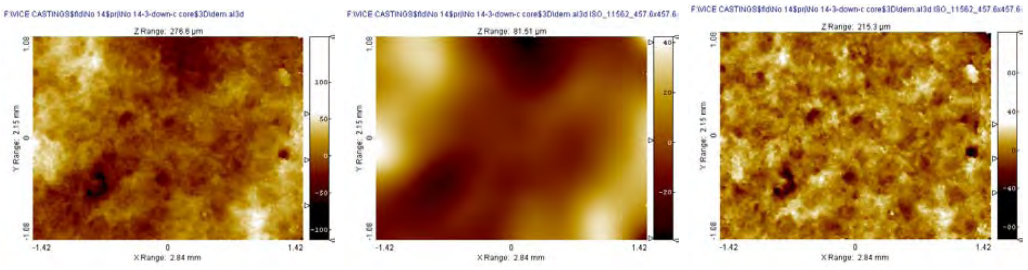

(a) Original surface (b) Filtering-waviness (c) Filtering-roughness

Figure 6.46: Surface processing in Scanning Probe Image Processor (SPIP).

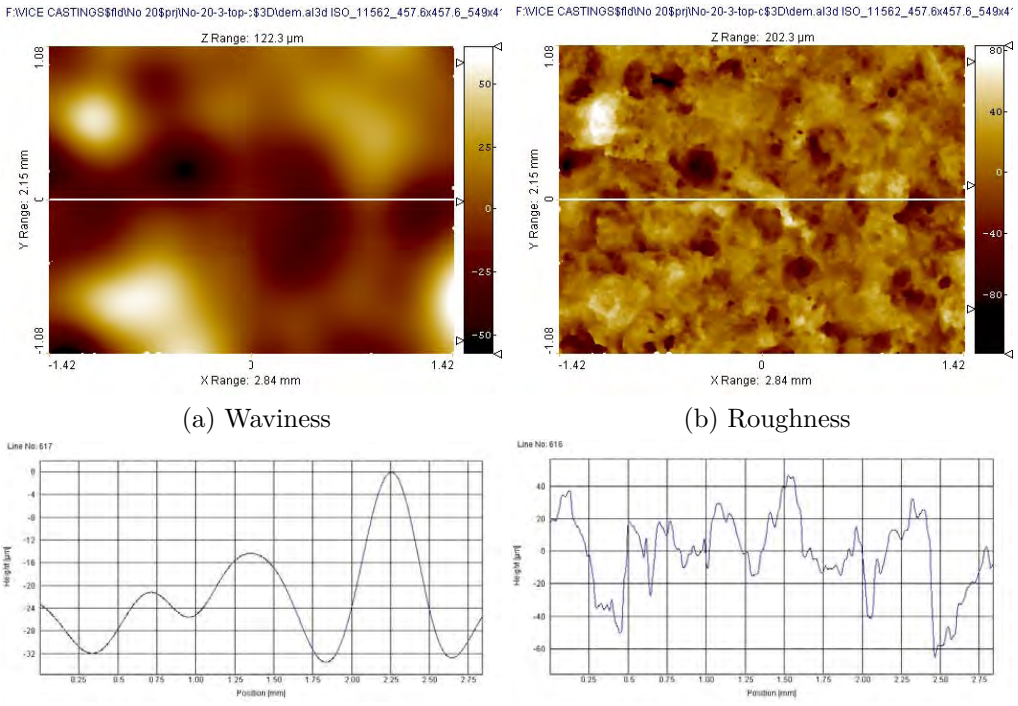

(a) Waviness (b) Roughness

(c) Waviness profile (d) Roughness profile

Figure 6.47: The difference between waviness and roughness. The reason for filtering.

The surface roughness estimation of the multilayer application of spraying of mould No. 14 with W230 containing 20% sol-gel component gave the castings with the best surface finish. The results are presented in Figures 6.49 - 6.51.

In the investigation of the influence of metallostatic pressure on the surface quality of the castings, from Figure 6.49, a comparison of the top and down arms of the

vice castings shows that the down arm has higher roughness than the top arm. Comparing Prints 1 and 3 for the uncoated mould cavity it is also evident that Print 3 has higher roughness than Print 1, being lower in the mould where the effect of metallostatic pressure is higher. However, with Prints 2 and 4, a clear distinction is not observable because the coating probably modified or eliminated the influence of the metallostatic pressure. This implies that with effective coating, the surface quality of the castings can be significantly improved.

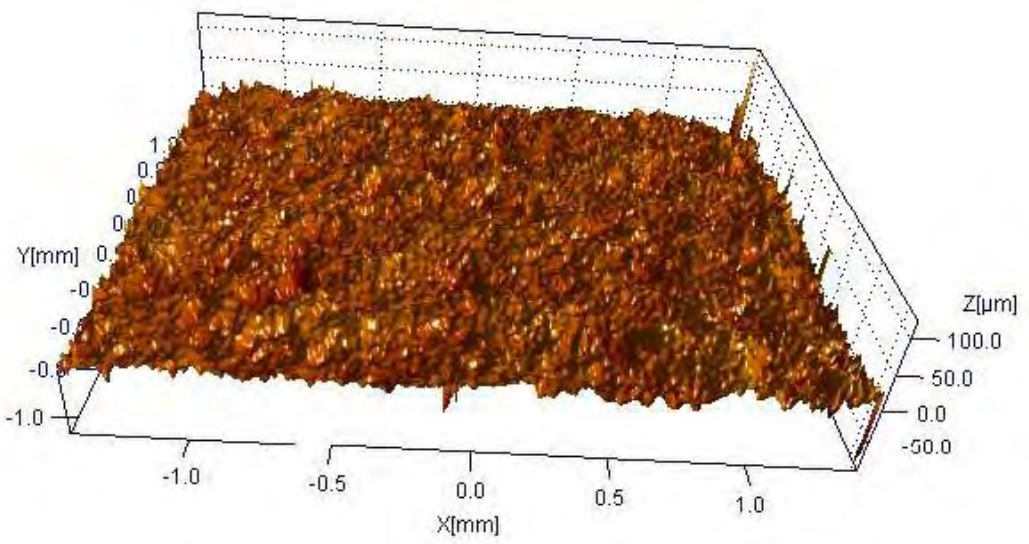

Figure 6.48: A typical 3D surface texture of a processed casting surface for roughness measurement in SPIP.

Prints 2 and 4 have lower roughness as expected, but the reverse face showed a much lower roughness. This is due to the fact that the reverse face was much more effectively coated as it is only 3 mm into the mould unlike the front face which is about 22 mm into the mould (see Figure 6.45b). This is clearly shown in Figure 6.50. From this figure, it can be seen that the reverse faces for the coated prints have lower surface roughness than the front face of the same prints. This is the same for both the top and down arms of the prints. This confirms the effectiveness in the coating of the reverse face relative to the front face. This is because it is difficult to coat deeper and narrow recesses in mould cavities with spraying due to the back pressure of air preventing the deposition of the refractory materials of the coating [108].

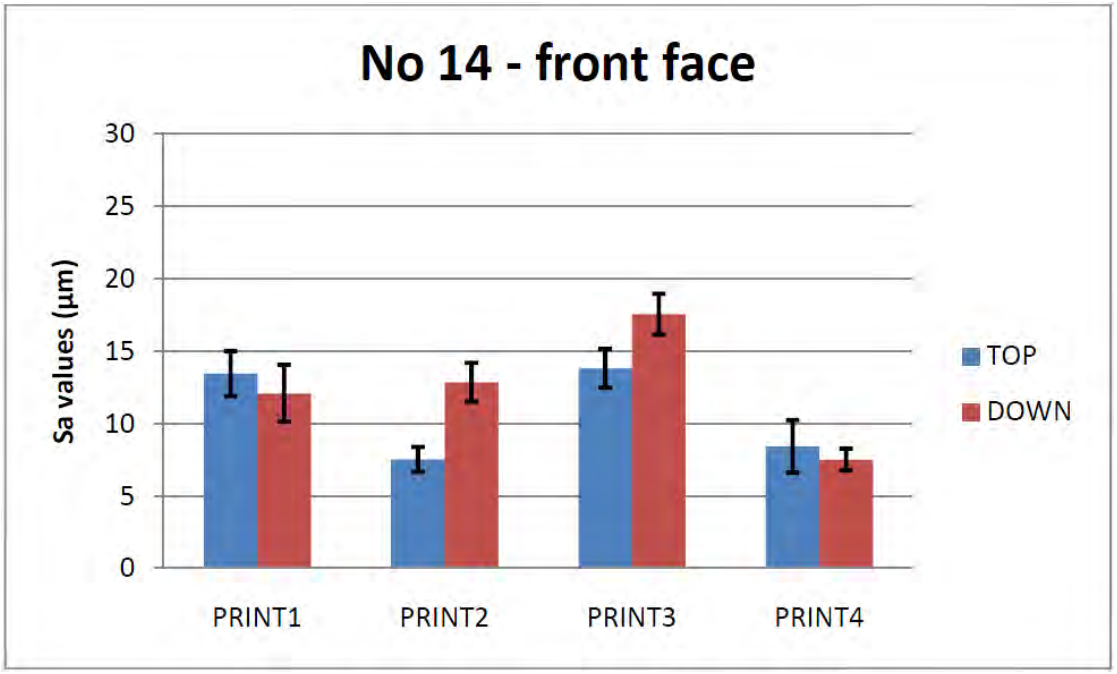

(a) Front face

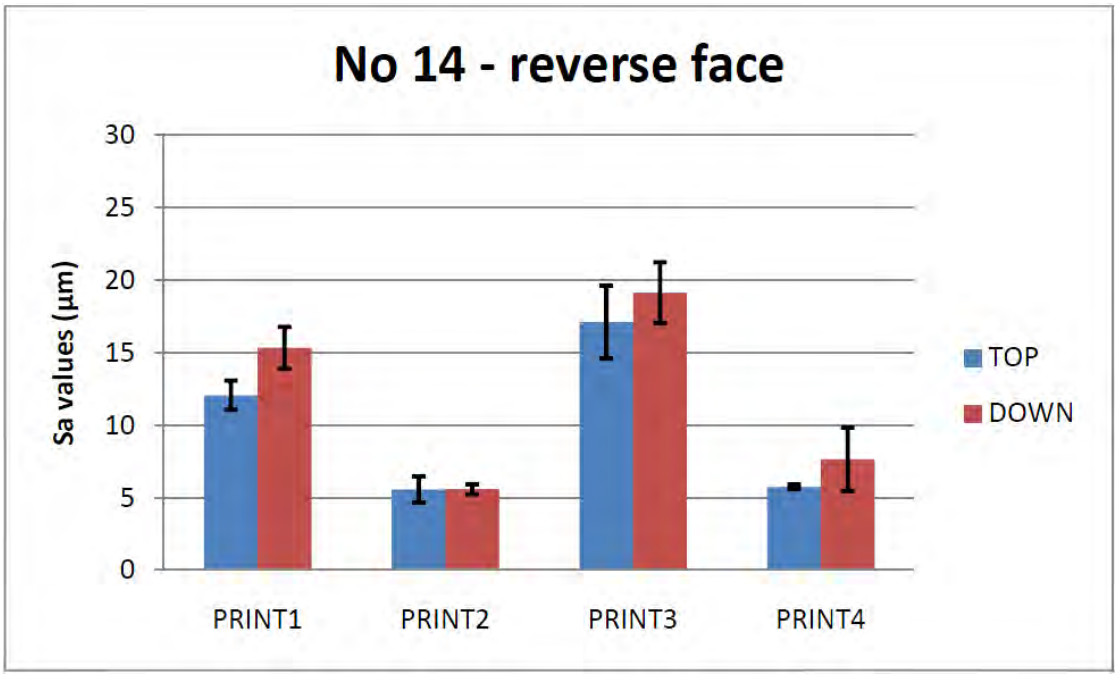

(b) Reverse face

Figure 6.49: Surface roughness results described by Sa values for multilayer application of W230 + 20% sol-gel component.

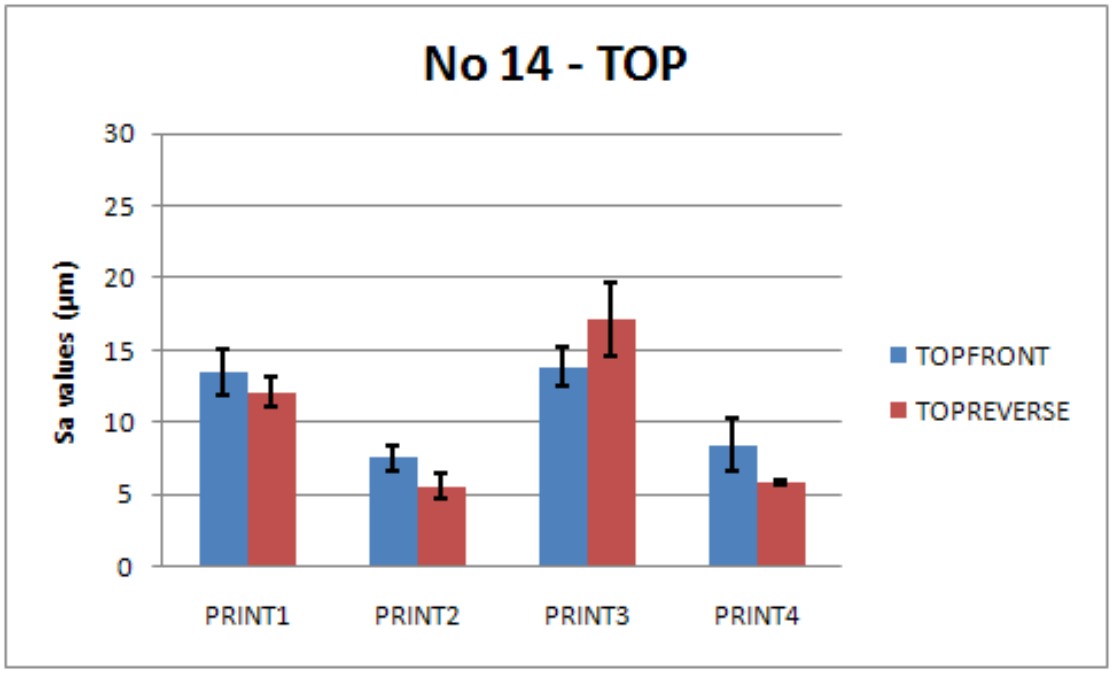

(a) Top

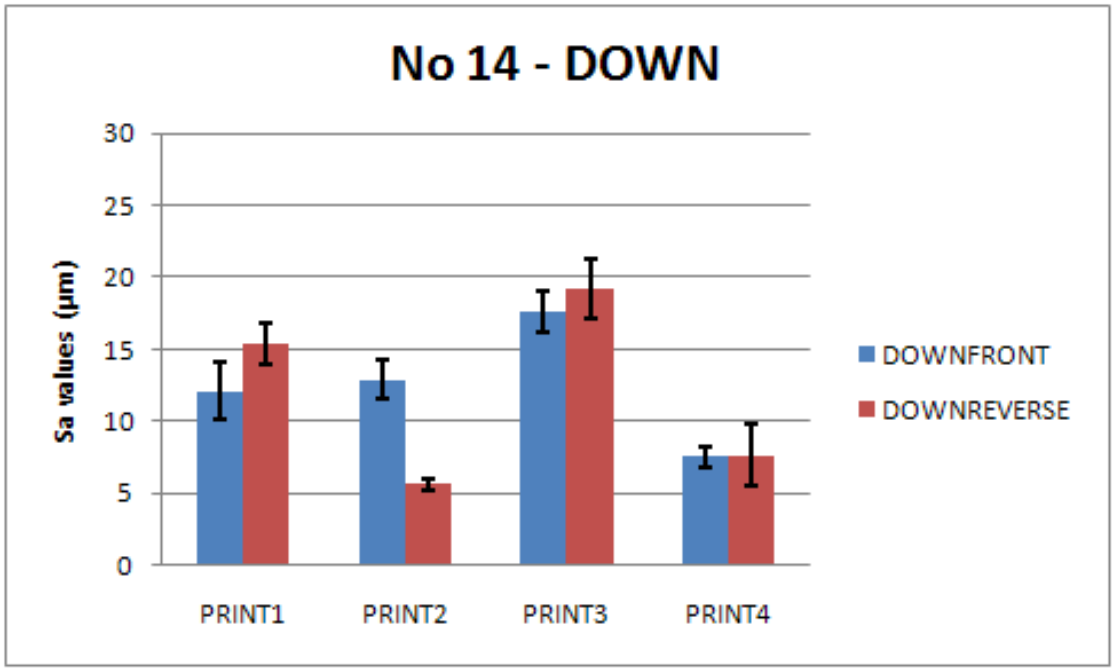

(b) Down

Figure 6.50: A comparison of the front and reverse faces of the castings in the coated prints.

A clear separation from the different measurements for Prints 1 and 2, and Prints 3 and 4 as shown in Figure 6.51a and b is obvious. This indicates that the multilayer coating has a positive potential in improving the surface quality of casting in the green sand mould. Similar plots were made for the other castings but a distinct separation was not observed, but in most cases the average showed the expected

difference [Supplement 7].

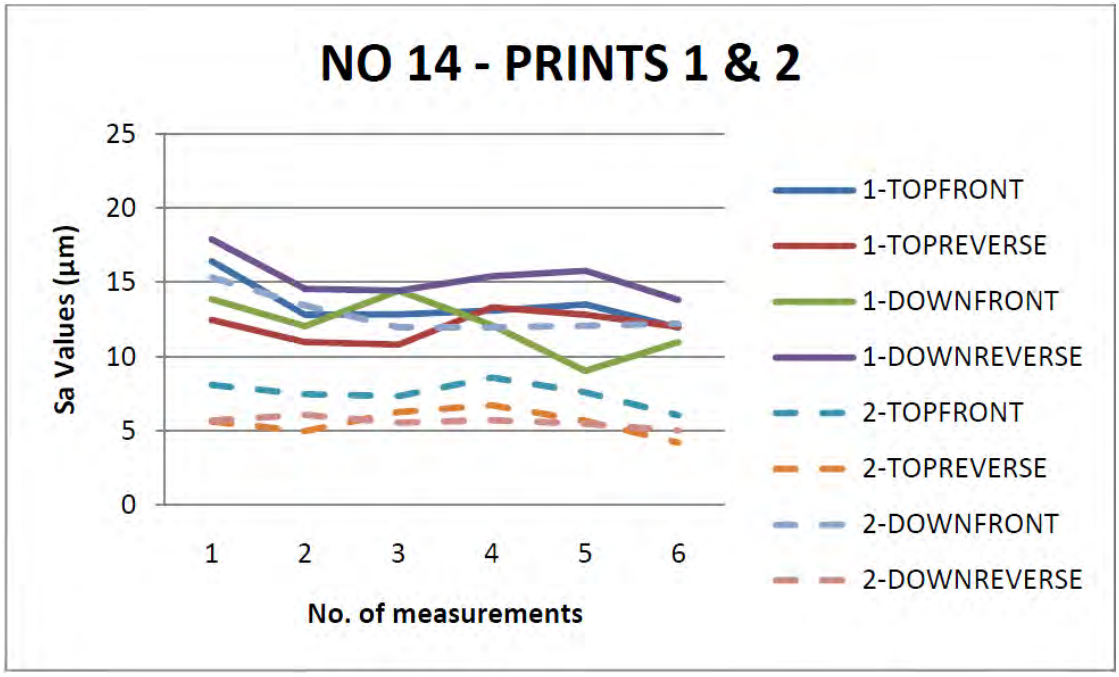

(a) Prints 1 and 2

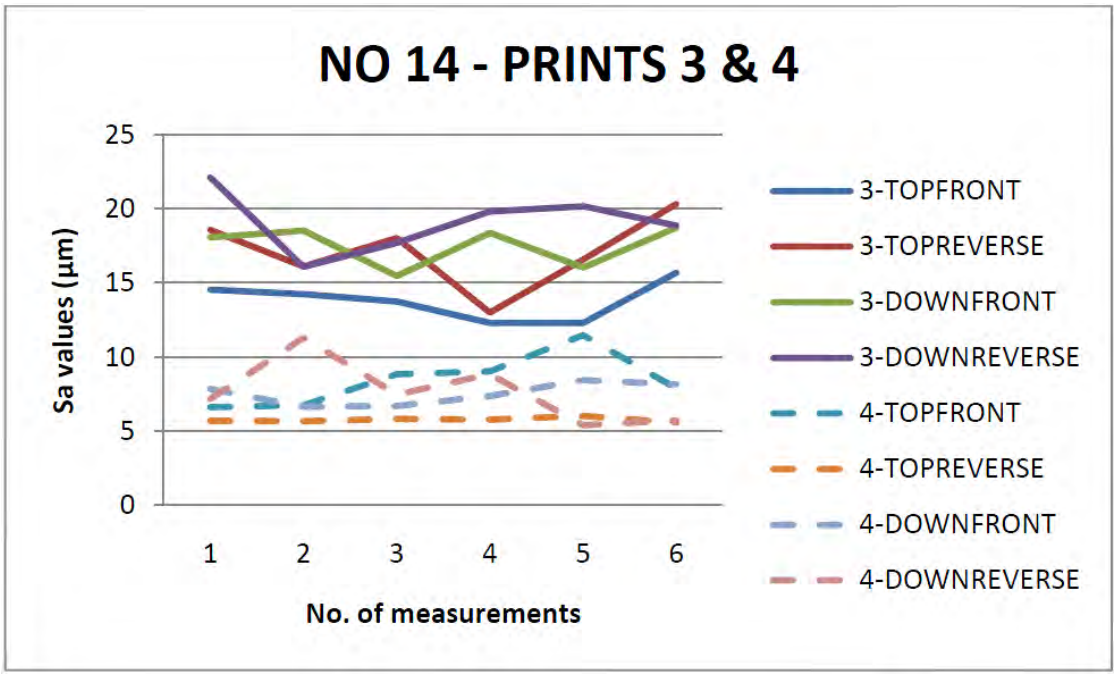

(b) Prints 3 and 4

Figure 6.51: Plots of the various measurements comparing two prints at the same height in the mould.

As a reference, a comparison is made by measuring the roughness of the casting surface around the coated core areas and the results are presented in Figure 6.52. The results show that the roughness of the castings around the core areas is comparable and also lower than most of the surface roughness obtained from

the coated front and reverse faces of the castings. However, the multilayer coated reverse side of the casting (Figure 6.49b) showed a better result when compared with the roughness of the casting around the core area. This confirms that the multilayer coating application will be effective in improving the surface quality of castings in green sand moulds.

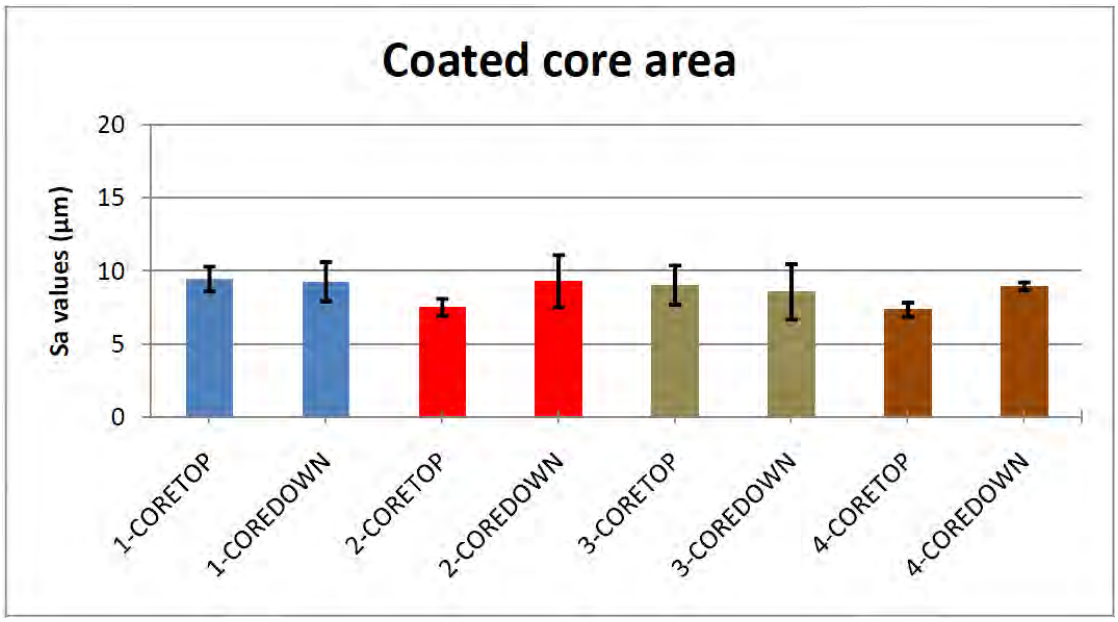

(a) Roughness

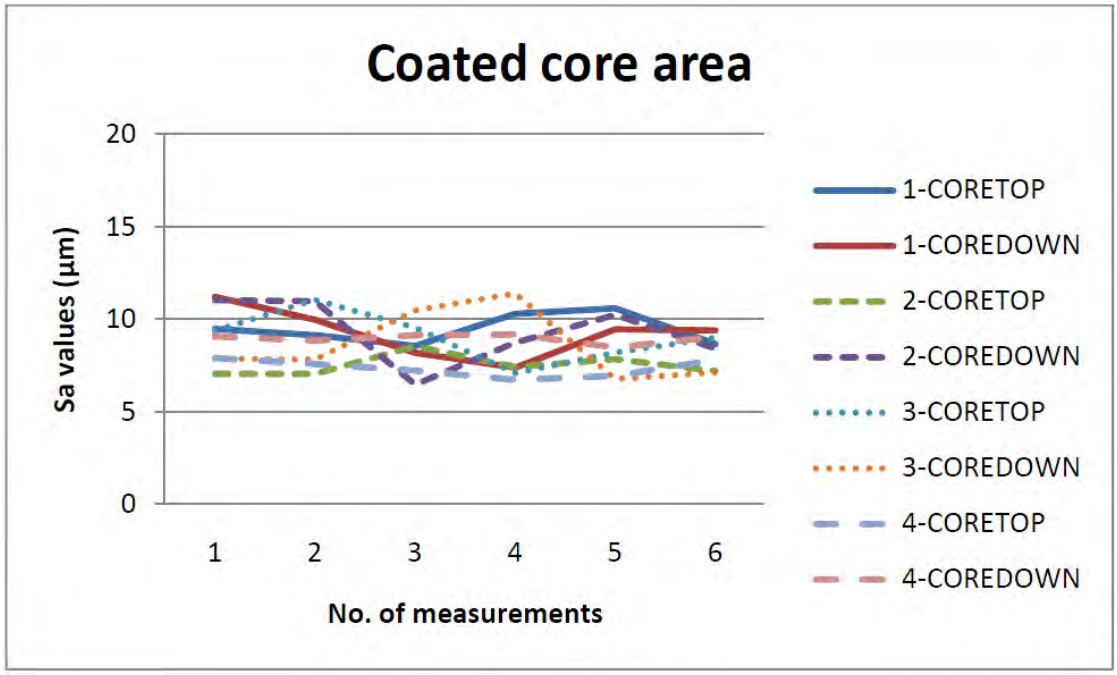

(b) Measurements

Figure 6.52: Surface roughness of the castings around the coated core area.

It is also note-worthy that there is no mechanical effect forcing the refractory materials in-between the pore spaces of the sand grains in the mould during spraying.

Consequently, in some foundries they apply brushing on the moulds or cores after spraying. Spraying is sensitive to the viscosity of the coating, therefore the coating has to be thin in order to be easily atomised by the spray gun, otherwise the spray gun will be clogged. This means that the coating will not properly cover the sand grains with one-time spraying of the moulds or cores. From the summary of the results presented in Table 6.5, spraying W230 and W230 containing sol-gel component was consistent in reducing the roughness of the castings. Multilayer coating with W230 + 20% sol-gel seems more positive in reduction of the surface roughness of the castings. W226 seems to create rather higher roughness than reducing it in general terms. This could be as a result of reaction products adhering to the surface of castings, making the surface rough. This is observed when the surface of the castings was felt (tactile examination).

Table 6.5: Summary of percentage roughness reduction with coating Prints 2 and 4 relative to the uncoated Prints 1 and 3 for front and reverse faces.

	Percentage reduction with coatings				
	W230	**W230+ 4% SG**	**W230+20% SG-Multi**	**W226+ 4% SG**	**W226-Multi**
Front face	NO 10	NO 11	NO 14	NO 20	NO 22
Prints 1 & 2	24	17	20	13	9
Prints 3 & 4	26	12	49	-5	-17
Reverse face					
Prints 1 & 2	26	3	59	-4	-6
Prints 3 & 4	35	36	63	39	-5
Average	27.8	17.0	47.8	10.8	-4.8

The negative numbers indicate that the uncoated Prints have lower roughness by these negative %.

6.8.3 Interfacial Microstructure

In cast iron, the properties of the material depends on the matrix structure and the shape of the graphite precipitated. These are determined by the composition, solidification, and suitable heat treatment [114]. The carbon precipitated in the eutectic reaction is not a major contributor to mechanical strength. The mechanical properties of cast iron are derived mainly from the matrix [114].

Ductile iron, also known as nodular or spheroidal iron, is produced with a total of 3.4 to 3.8 wt % carbon and 2 to 2.8 wt % silicon. In as-cast condition, the matrix will consist of varying proportions of pearlite and ferrite (Figure 6.53a), and as the amount of pearlite increases, the strength and hardness of the iron also increase, while the ductility decreases. The matrix structure can be changed by heat treatments, and those often carried out are annealing to produce a fully

ferritic matrix, and normalizing to produce a substantial pearlitic matrix [115]. The properties of ductile iron are significantly affected by the graphite nodules, in particular the roundness (referred to as nodularity) but also the number of graphite nodules per unit area and the volume fraction. In addition, the carbide content should be controlled to avoid detrimental effects on the fracture toughness. Magnesium is added to attain high nodularity but it may also result in slag defects when it reacts with oxygen and other products such as silica and increase the tendency for carbide formation during solidification [116, 117].

Grey irons are iron-carbon-silicon alloys containing small amounts of other elements. Most grey irons are produced with a total carbon of 3 to 3.5 wt % and normal silicon level vary from 1.8 to 2.4 wt %. The properties of grey iron depend on the size, amount and distribution of the graphite flakes and the matrix (Figure 6.53b). Flake iron microstructure and mechanical properties depend on cooling rate which makes them particularly section sensitive [114, 118]. As the section size increases, the solidification rate decreases with an accompanying increase in grain size and subsequent decrease in tensile strength. This is the result of the mechanism of solidification [118].

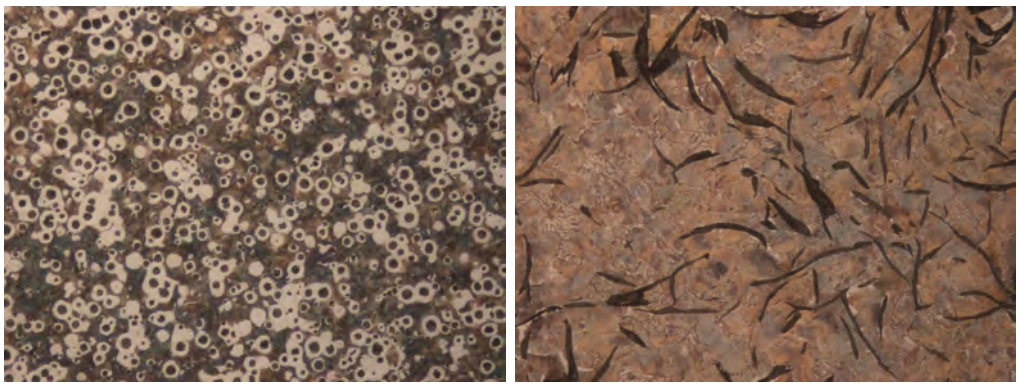

(a) Ductile iron (b) Grey iron

Figure 6.53: Typical microstructure of cast iron.

As the castings are in contact with the coated cores, the influence of the coating on the solidification conditions can be elucidated by examining the casting microstructural evolution at the mould/core-metal interface. The results of the microstructure evolution at the interface of the castings and the coated cold box and furan cores are presented in this sub-section. A comparison is made with the bulk microstructure and the microstructure of subsurfaces of the castings made with uncoated cores, in order to deduce the possible effects of the coating on the interface microstructure of the castings (ductile and grey iron). The microstructure evolution of ductile and grey iron castings at the interface with uncoated and sol-gel coated cold box cores are presented in Figure 6.54. From the figure, it can be seen that both the graphite nodules (in the case of ductile iron) and graphite flakes (in the case of grey iron) are uniformly distributed in the matrices of all the microstructures for both uncoated and coated cold box cores. This suggests that the sol-gel coating has no negative effect on the distribution of the graphite structure at the interface.

In Figure 6.55, from the microstructure at the interface of ductile and grey iron castings with uncoated and coated furan cores, similar observations were made as with cold box cores (Figure 6.54). Both the graphite nodules and the graphite flakes are uniformly distributed and are comparable with microstructures obtained with uncoated furan cores.

A detailed examination of the microstructures presented in Figures 6.54 and 6.55, reveals that the graphite nodules are of form VI as reported in [119], while the graphite flakes are of Type C (Kish graphite), mainly found in hyper-eutectic composition [119, 120]. This is caused by a condition of very slow cooling rate and near eutectic compositions, or under inoculation [120]. Considering the slow cooling rate this could be associated with the insulating nature of the moulding materials as the extraction of heat from the metal is slow.

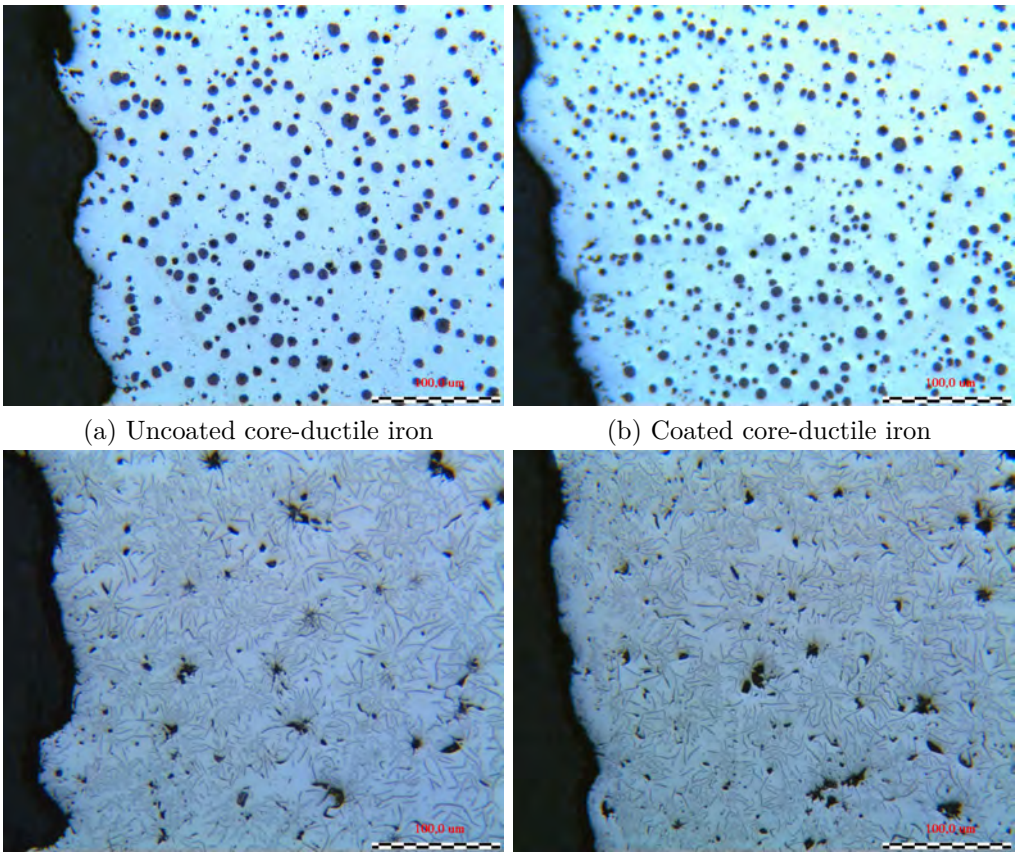

(a) Uncoated core-ductile iron (b) Coated core-ductile iron

(c) Uncoated core-grey iron (d) Coated core-grey iron

Figure 6.54: Interface microstructure of ductile and grey iron castings with cold box cores-unetched.

However, there are some observations made along the interface of the castings made with coated cores. These are presented in Figure 6.56 as representative images showing the different types of effects observed and the type of core systems where they occurred. In Figure 6.56a, it can be seen that there are graphite nodule-free areas at the interface with coated cold box core which was not observed at the interface of the castings made with uncoated cold box core (Figure 6.54a). The graphite nodule-free areas look like stain-front as if the nodules dissolved. This

graphite nature is referred to as chunky graphite. It also looks as if there is edge effect on the sample. Further investigation at higher magnifications is required to confirm these.

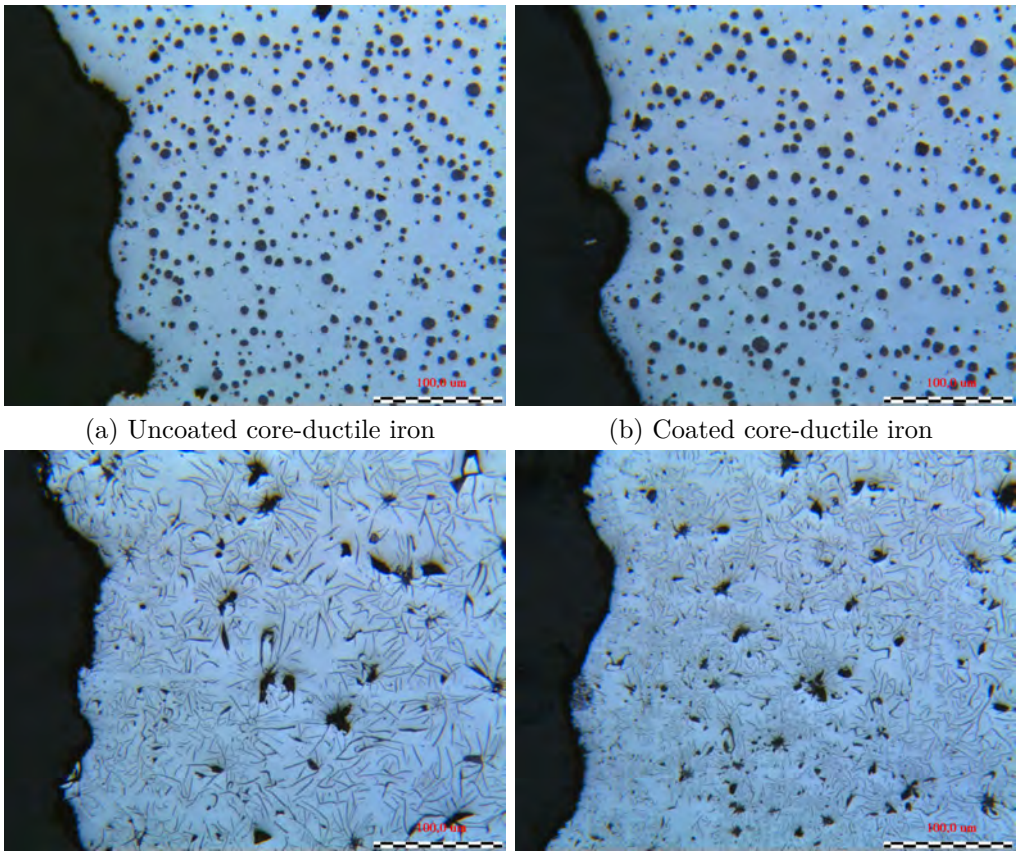

(a) Uncoated core-ductile iron (b) Coated core-ductile iron

(c) Uncoated core-grey iron (d) Coated core-grey iron

Figure 6.55: Interface microstructure of ductile and grey iron castings with furan cores-unetched.

Again, Figure 6.56b shows a clear reversion of the graphite nodules to graphite flakes at the interface of ductile iron casting with coated furan core. This is usually attributed to excess sulphur build-up in moulding sand, in this case, core sand. This causes reversion to flakes as the magnesium in the iron reacts with oxygen and/or sulphur forming MgO and/or MgS (Figures 6.24 and 6.26) thereby depleting the magnesium available for nodularization [121]. Boonmee et al. [122] proposed a mechanism for the degeneration of graphite at the interface as occurring because of: 1. loss of Mg or Ce - possible causes are fading or chemical reaction with O or S; 2. poisoning by deleterious elements such as Te, Sb, As, etc. Their conclusion in this case is that Mg from the melt is tied by the O or/and S diffusing from the mould. This defect was observed on the casting made with furan system and therefore agrees with the report in [53] that it is common with furan and phenolic resin-bonded moulding sand, where P-toluene sulphonic acid (PTSA) is used as catalyst. In the furan system, the sulphur content in the sand should not exceed 0.15% for up to 25 mm thick sections and approximately 0.7% for up to 75 mm thick sections. High density coatings are particularly effective in reducing the

defect. Coatings with a CaO/MgO/talc composition are regarded as most effective [123].

Furthermore, Figure 6.56c reveals a ferritic rim at the interface of the casting and the coated cold box core. According to Narasimha and Wallace in [122], a ferritic layer is to be expected in commercial grey iron castings. However, the probable causes of this defect are under inoculation, slow pouring rate, and low pouring temperature [120]. From the mentioned possible causes, it can be inferred that the formation of the defect is not associated with the coating. Sea coal in the green sand was found to reduce the ferritic rim in grey iron casting [122].

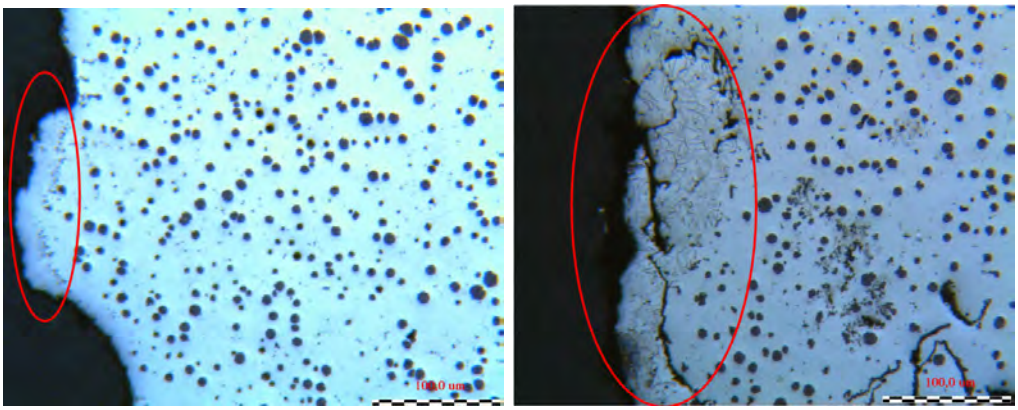

(a) Cold box (b) Furan

(c) Cold box

Figure 6.56: Observed defects at castings interface with coated cores-unetched.

The microstructures of grey iron castings from different areas of the castings making contact with commercially-coated core, green sand mould, sol-gel-coated core, and the bulk of the metal in each case are shown in Figure 6.57. The microstructure are obtained by etching the polished surfaces with Nital solution in order to reveal the details of the matrix of the castings.

Figure 6.57a and b show the interface microstructures of a grey iron casting with commercially-coated cold box core and the bulk of the casting respectively. There is presence of islands of ferrite (light colour) in the microstructure from the inter-

face.

Figure 6.57c and d show the microstructures of a grey iron casting at the interface with uncoated green sand mould and the bulk microstructure of the same casting respectively. The observed difference can be considered not to be significant.

Figure 6.57e and f show the microstructures of a grey iron casting at the interface with sol-gel coated-cold box core and that of the bulk of the metal respectively. However, the microstructure at the interface with sol-gel-coated cold box core, as can be seen in Figure 6.57e, reveals a clear ferritic rim. There is obvious depletion of the pearlite at the interface around a depth of about 200 µm. The occurrence of decarburized skin on grey cast iron was reported as early as 1962. This phenomenon was attributed by Reisener in [122] to the interaction of the casting surface layer with the moisture of the mould, which results in the formation of carbon dioxide and hydrocarbon gases at the metal-mould interface. These gases escape through the moulding material. These chemical reactions could lead to the depletion of carbon in the casting skin. A comparison with the interface microstructure of the casting surface with green sand mould (Figure 6.57c), which is generally believed to have higher moisture content than cold box core material, showed a significantly lower level of decarburization. But green sand moulds also have a very high carbon content, therefore, the effect of the moisture could have been compensated by the carbon content. The effect of moisture is minimized by using pyrophyllite (an aluminium silicate hydroxide - $Al_2O_3.SiO_2.H_2O$) as a mould coating. Pyrophyllite expands at high temperature to a dense interfacial barrier layer [122]. Yamada et al. [124], reported that decarburization occurs at a critical temperature of 930 K, below which decarburization does not occur. They said that the rate controlling process for the formation of decarburized layer is the diffusion of carbon atoms towards the interface where they get oxidized.

It is note-worthy that these microstructural defects are commonly associated with moulding materials and as such could not be attributed to the presence of the coatings alone. Mould and core making technologies have significant roles in the development of these defects. The effect of liquid metal processing (such as poor inoculation, high contaminant concentrations, etc) is not left out too. Therefore, a detailed investigation of interfacial microstructure and the evolutionary history becomes a subject for further studies.

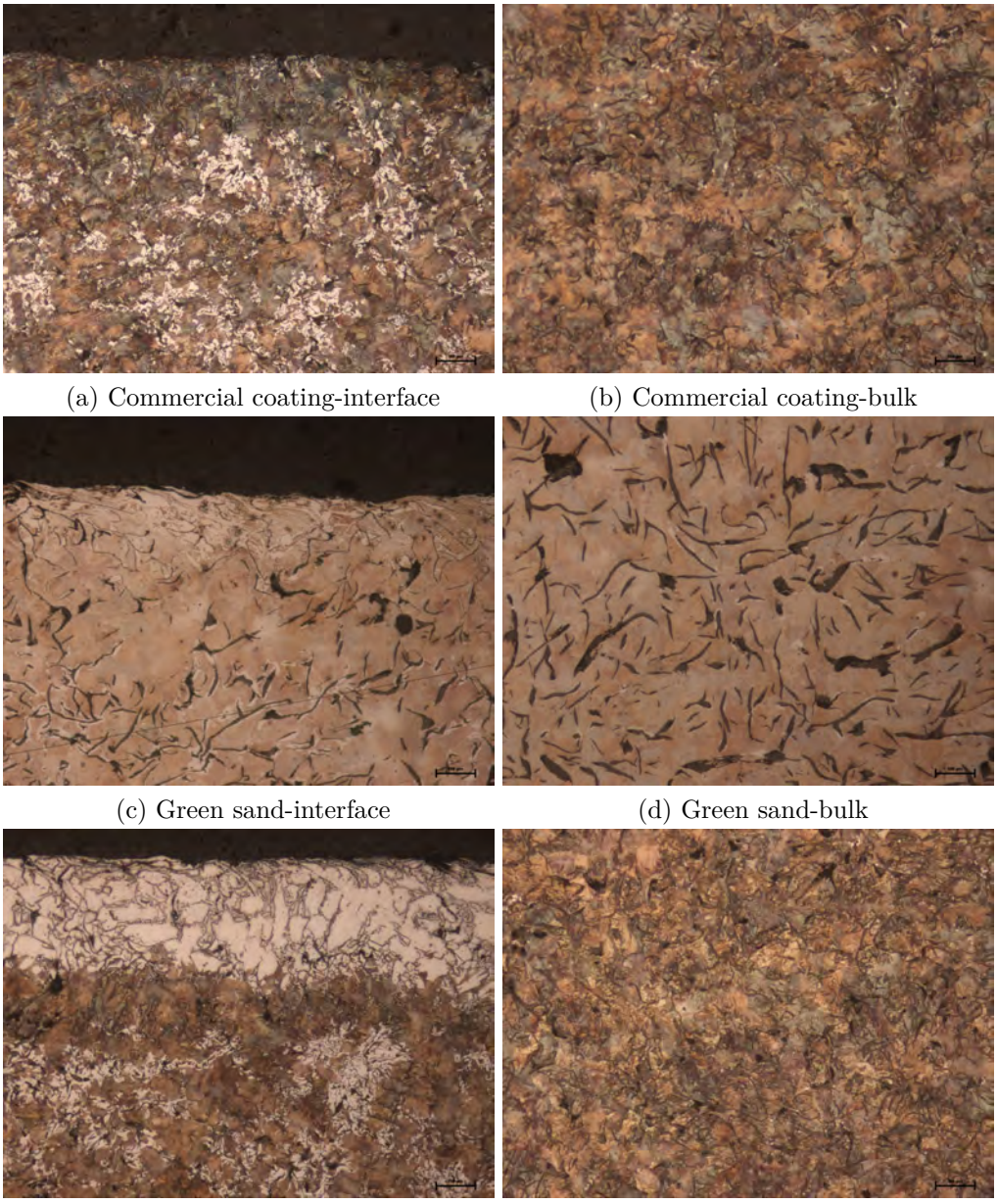

(a) Commercial coating-interface (b) Commercial coating-bulk

(c) Green sand-interface (d) Green sand-bulk

(e) Sol-gel coating-interface (f) Sol-gel coating-bulk

Figure 6.57: Interfacial microstructure of grey iron casting in contact with different surfaces-etched with Nital solution.

Chapter 7

Case Studies

Objective

- Testing coating formulations to assess their performance.
- Elimination of surface defects to improve the surface quality of the castings.

7.1 Casting: Part for X-Ray Detector, Hospital Equipment.

Foundry: Johan Jensen & Søn Metalstøberi

Table 7.1: Casting conditions at Johan Jensen & Søn Metalstøberi.

Alloy	CuSn6Pb22 (Bronze)
Casting size	800 × 800 × 400 mm
Wall thickness	10 mm
Casting weight	124 kg
Poured weight	165 kg
Pouring temperature	1120 °C
Pouring time	15 - 20 s
Mould	Horizontally-parted furan sand mould
Cores	Furan sand cores

7.1.1 First Trials

7.1.1.1 Coatings Used

1. Traditional coating (Zirconia)
2. W 235.1 (aluminium silicate)
3. W 235.1 + 5% sol-gel component

(a) Traditional coating (Zirconium)

(b) W 235.1 (aluminium silicate)

(c) W 235.1 + 5% sol-gel component

Figure 7.1: Castings from first trials.

7.1.1.2 Conclusions from First Trials

- Sol-gel modified coating performs better than reference coating.
- Traditional coating preforms better than sol-gel modified coating.

7.1.2 Second Trials

7.1.2.1 Coating Used

1. Traditional coating + 5% sol-gel component
2. Traditional coating + 10% sol-gel component

(a) Traditional coating + 5% sol-gel component

(b) Traditional coating + 10% sol-gel component

Figure 7.2: Castings from second trials.

7.1.2.2 Conclusions from Second Trials

- 10% sol-gel component addition appears as good as traditional coating.
- 5% sol-gel component addition deemed better than traditional coating after cleaning.

7.2 Casting

Foundry: Vald. Birn A/S

Table 7.2: Casting conditions at Vald. Birn A/S.

Alloy	GG250
Pouring temperature	$1370 - 1390\,^{\circ}\mathrm{C}$
Mould	Vertically-parted green sand mould
Core	Cold box sand core

7.2.1 First Trials

1. Traditional coating
2. Filter dust sol-gel coating

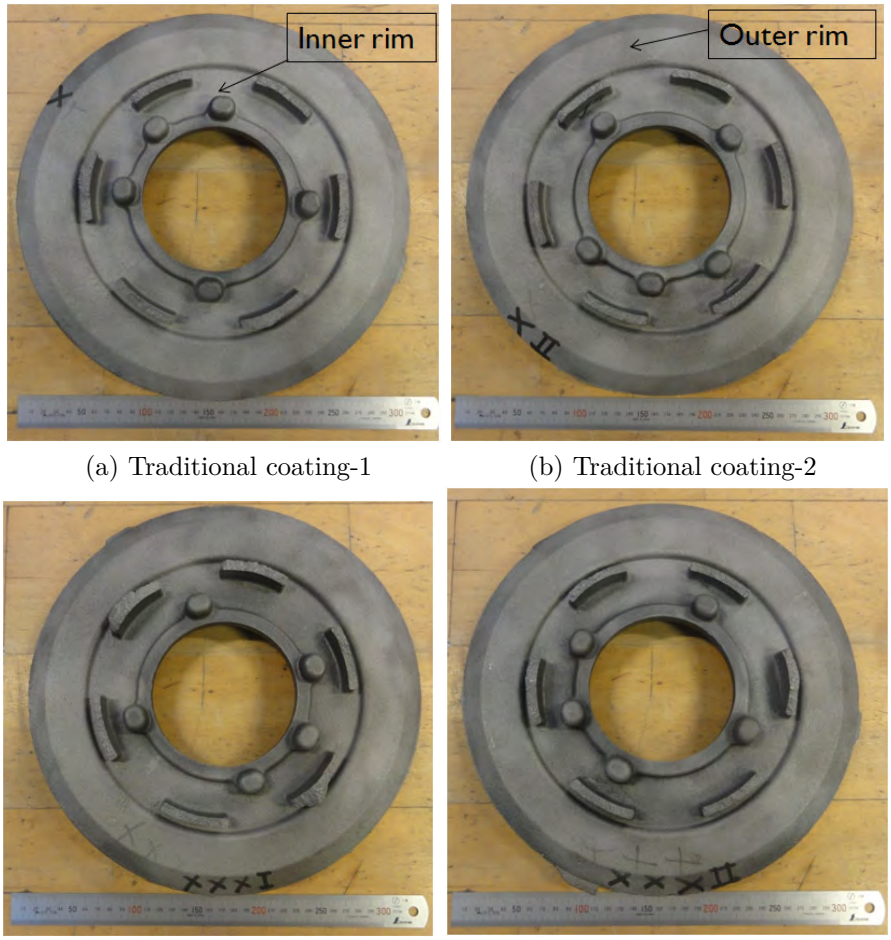

(a) Traditional coating-1 (b) Traditional coating-2

(c) Filter dust sol-gel coating-1 (d) Filter dust sol-gel coating-2

Figure 7.3: Castings from first trial.

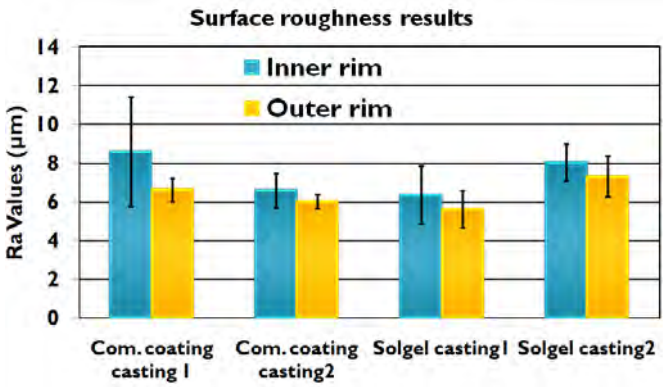

Figure 7.4: Summary of surface quality of castings from first trial by roughness evaluation.

7.2.1.1 Conclusion from First Trials

Castings made with the filter dust sol-gel coating showed comparable surface roughness, Ra values with casting made with traditional (conventional) coating.

7.2.2 Second Trials

7.2.2.1 Coating Used

1. Traditional Coating (36 ^{o}Baumé)
2. W254.6 Micro (40 ^{o}Baumé)
3. W 254.6 Micro + 10% sol-gel component (40 ^{o}Baumé)

(a) Traditional coating (b) Traditional coating-dry

(c) Reference coating (d) Reference coating-dry

(e) Reference coating + sol-gel (f) Reference coating + sol-gel-dry

Figure 7.5: The coated cores for the second trial casting at Vald. Birn.

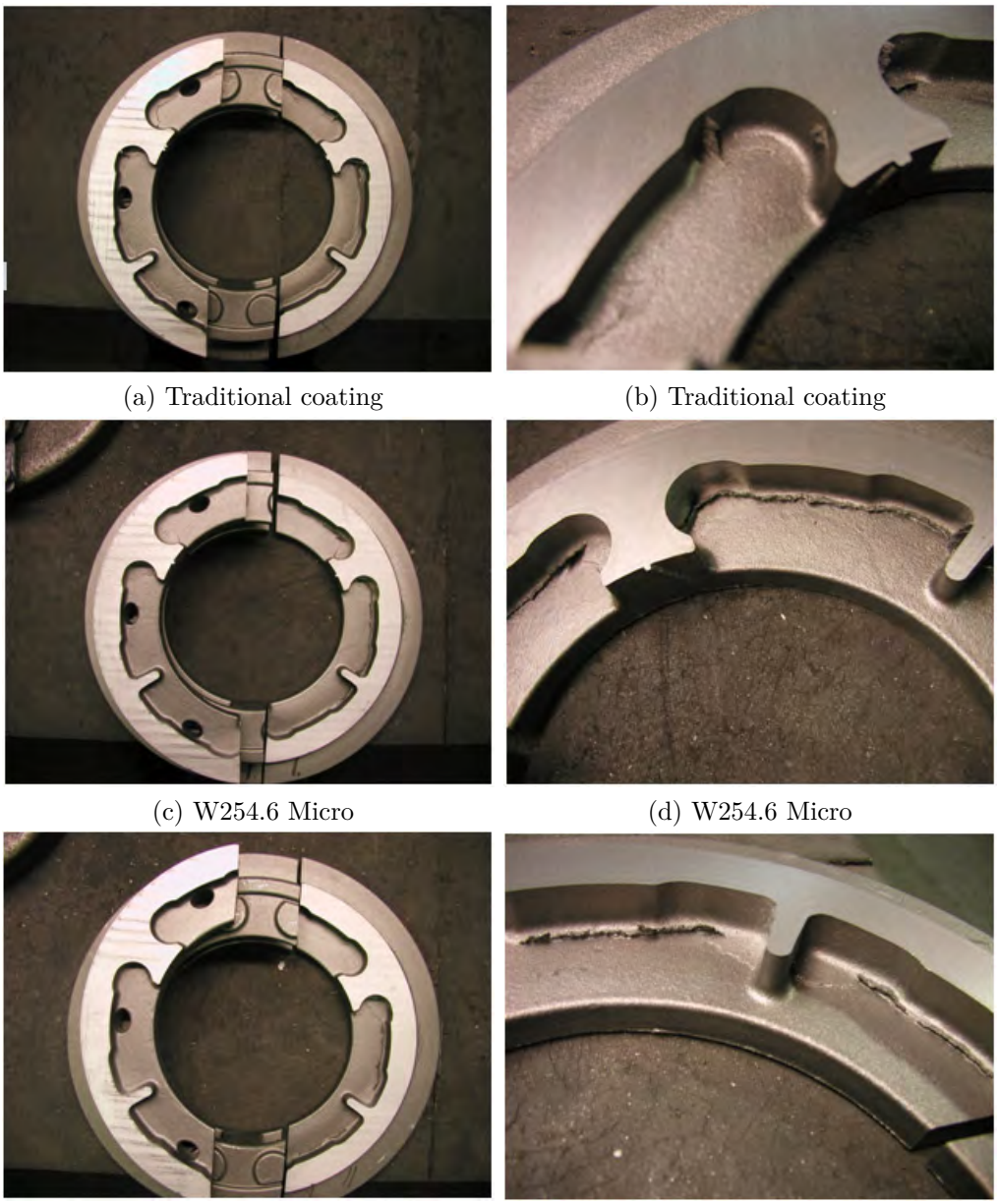

(a) Traditional coating (b) Traditional coating

(c) W254.6 Micro (d) W254.6 Micro

(e) W254.6 Micro + 10% sol-gel component (f) W254.6 Micro + 10% sol-gel component

Figure 7.6: Castings from second trial.

Table 7.3: Summary of casting defects (veinings) assessment for different coatings

Category (veining defects)	**Traditional coating**	**Reference coating**	**Reference coating + 10% sol-gel additive**
0-none	-	-	2
1-very few	5	-	5
2-few	7	3	7
3-some	8	8	5
4-many	-	9	-
5-very many	-	-	-

7.2.2.2 Conclusions from Second Trials.

- Tendency for runners and drips – only few drips remain after curing of traditional coating.
- Tendency to form drips and runners – also present upon drying of reference coating.
- Reference with sol-gel component seems visually to flow differently on the cores.
- Addition of sol-gel component seems to greatly decrease veining defects compared to the reference coating.

Chapter 8

Discussion

8.1 Refractory Coatings

The foundry industry is under pressure to produce cleaner, thinner and better tolerance castings. Despite the tolerances achieved in the core shop at room temperature, the distortion of the core upon exposure to molten metal and rapid heating may introduce additional variances to the finished castings. New resins and sand systems are being developed to meet these requirements, however, the foundry has pressed refractory coating manufacturers to produce coatings capable of enhancing the performance of chemically-bonded sand systems. To date, refractory coating's primary function has been to enhance casting surface finish and minimise metal penetration defects by reducing the capillary dimensions of the substrate and by changing the surface tension of the substrate surface [125]. In the US, most core applications limited the dry coating deposit to 0.1-0.25 mm. In Europe, dry coating deposits on sand cores are much heavier ranging from 0.25-0.40 mm and have shown some anti-veining properties. This means that coating deposits can reduce the thermo-mechanical stress development in resin bonded sand core systems [126].

The formulations of foundry coatings involves the dispensing and mixing of a particulate refractory material or a blend of particulate refractory materials and a carrier liquid for the particulate refractory materials and other additives. A detailed review of foundry coatings technology provided the different types of refractory materials for foundry coatings, binders, carrier liquids, and other additives alongside different characterization parameters for coatings [108]. The discussion presented here will deal with the observations from the results obtained from the sol-gel coating project carried out. Other knowledge-based arguments which emphasize the enhancement of foundry coating performance from literature will be provided.

Hollow parts of sand castings are formed by disposable cores. The most common type is the resin-bonded sand cores, in which the resin is designed to break down after casting, allowing the sand to flow out of the cored cavity. When the metal first enters the mould, the mould and cores experience lots of activities. They heat up and expand while the core also experiences buoyancy forces which will

tend to make it float. This is not a problem with liquid magnesium where the density difference with silica sand is near zero. Similar neutral buoyancy applies to aluminium vs. zircon sand system [127]. Buoyancy becomes a problem for the common systems such as aluminium vs. silica sand and liquid iron (or other dense metals such as copper and steel) vs. silica sand. This is particularly so for the later metals because of their high casting temperatures and high density. Floatation forces have to be withstood by adequate mechanical support of the cores, usually by good print design and location. Furthermore, the heating up and expansion of the mould and core lead to distortion and also thermal stress development in the mould and core, leading to cracking. This is followed by the occurrence of a series of defects which can be arrested by the application of refractory coatings which form a physical and thermal barrier to the metal poured. As a physical barrier, the coating can prevent the diffusion of liquid metal into the moulding materials. The permeability of the coating also plays a role in the elimination of the evolved gases. Coatings for high temperature casting production should have good permeability for gas and good thermal resistance to avoid expansion related defects. Both parameters depend directly on the coating thickness: it has to be thick enough to provide the needed thermal protection and thin enough as to allow diffusion of gas for escape if applied on the mould [128]. If it is suspected that the path of evolved gas exit will be through the molten metal, a coating with high permeability would be preferred to allow evolved gases from the core and coating to pass more easily through the coating layer. Conversely, if it is found that the gas must pass through the core print to vent to the atmosphere, then a relatively low-permeability core coating with high core sand permeability would be more advantageous [129].

8.1.1 Nanoparticle Sol-Gel Coatings

The quality and performance of a coating is directly related to the stability of the coating suspension, rheological behaviour, and the materials of the coating. From the preliminary investigations of the first formulated sol-gel coating containing nanoparticle refractory materials (TiO_2 and ZnO), the behaviour of the nanoparticle sol-gel coatings when applied on core materials revealed the significance of particle size (PS) and particle size distribution (PSD). It is seen that if the PS and PSD of the refractory materials are not compatible with the PS of the sand grains, the coating cannot cover the surface of the cores. In this situation, the nanorefractory materials just penetrated into the core material with the carrier liquid, obeying capillary effect. The sand grains of the core were not covered by the coating. Therefore, there was no refractory deposit on the surface of the cores. The surface quality of the castings made with these cores is poor. This implies that the use of nanorefractory materials for coating development requires high mass of the refractory materials-to-volume of carrier liquid ratio, in order to build up a high solid content and high viscosity to reduce the level of penetration and make a surface deposit of the refractory materials to cover the surface of the cores. This means producing expensive coatings. The PS and PSD of the refractory fillers for foundry coatings are typically in the range of 49-75 µm (200-300 mesh) [130].

Therefore, the use of nanorefractory particles is not suitable for foundry coating production.

8.1.2 Filter Dust Sol-Gel Coatings

The nanorefractory materials were replaced with filter dust. The filter dust refractory materials had a bulk average particle size of about 15 µm [107]. This PS seems also fine compared to the expected range given in literature. With the use of filter dust, the rheology of the sol-gel filter dust coating changed significantly. This was observed from the uniform penetration into the cores and complete surface coverage of the cores by the filter dust coating. It was reported in [130] that if the coating contains high amount of bentonite or the refractory materials are excessively fine, an increased tendency to cracking on drying is encountered. This can be possible explanations to the appearance of cracks on the surface of the cores coated with filter dust coating [107]. In controlled investigations, it is suggested that 3-4% bentonite and 0.2-0.3% sodium alginate solutions proved most satisfactory as suspension agents. It is also reported that the bentonite can be replaced with cellulose compounds such as carboxymethyl cellulose [16, 130]. These compounds do not crack during curing.

Ideally, a coating should be mechanically stable, resistant to thermal shock, inert to liquid metal, harmless as a contaminant in the moulding sand, and safe in the working environment. It was expected that the filter dust from sand moulding lines would be particularly useful because it has already undergone a thermal treatment that makes it more stable and it has a particle size and particle size distribution that is useful for the foundry coatings. Most of the coating characterization techniques used in this study are the ones used in the foundry to control the consistency of finished coating products. The consistency needs to be controlled to suit the particular mode of application. Coatings are applied by brush or swab, by dipping, flow coating, or by spraying. In this study, the characterization parameters for monitoring the coating consistency include ^{o}Baumé parameter, viscosity and density (specific gravity). It was reported in [130] that thixotropic[1] properties of the coating are suitable for brushing, allowing free flow to avoid dragging of the sand surface, and enabling brush marks to disappear before the viscosity increases again and strengthens the film. Spray coating requires thinner consistency, more suited for atomization for the formation of fine droplets. This means that the spray method is viscosity-limited and would require multilayer application for good surface coverage [Supplement 7]. Dip coating requires pseudoplastic or shear thinning behaviour[2], which means rapid response to shear forces encountered as the core enters the bath. This is the most effective technique for rapid production, being widely employed for cores, including complex units and assemblies. Flow coating or overpour is more suitable for larger cores and moulds, the coating is pumped from a tank and discharged over the required surface through a fan-shaped nozzle.

[1]Fluids apparent viscosity decreases under stress, and recovers its initial viscosity with time when unloaded.

[2]Fluids show a large decrease in viscosity when the shear rate is increased.

It was observed from the results of the characterization of the coatings that the rheological properties control the coating penetration depth into the core substrate, the uniform coverage, drip, and running properties. The coating viscosity, surface tension, and thixotropic or pseudoplastic nature allowed for the constant/uniform coating thickness, uniform penetration, and complete surface coverage. The coating viscosity is determined by the amount of solid content in the coating which in turn determines the proud layer thickness on the substrate. The surface tension determines the ability of the coating to wet and adhere to a substrate. The conditions for good wetting are always fulfilled when the surface tension of the substrate is higher than that of the liquid coating material [131]. Therefore, the surfactants added to the coatings reduce the surface tension of the coatings enhancing wetting and penetration.

In this study, it was observed, that the application of the coatings to the core materials also reduces the permeability of the cores. This is expected because the pore spaces between the sand grains are filled by the refractory materials from the coating. Furthermore, coverage of the surface of the core by the refractory coating materials led to the reduction of the permeability of the core [41].

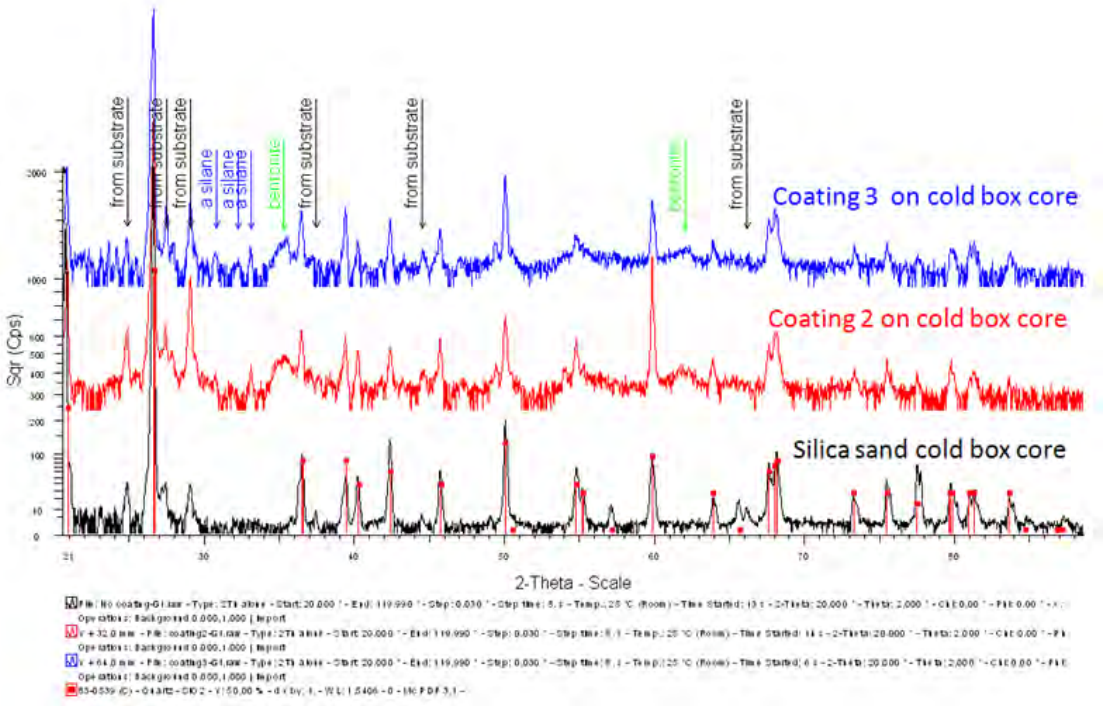

Figure 8.1: XRD micro-analysis on uncoated and coated silica sand cold box cores.

In a different context, the filter dust was assumed to be aluminium silicate. The filter dust coating was subjected to XRD analysis. The X-ray diffraction (XRD) micro-analysis of the uncoated silica sand cold box cores and silica sand cold box cores coated with Coating 2 (50% filter dust and 9% sol-gel content) and Coating 3 (40% filter dust and 50% sol-gel content) shows that the filter dust is mainly silica as shown in Figure 8.1. All the quartz peaks in the uncoated core appeared also in the coated core materials. There was no evidence of aluminium to confirm

the earlier assumption that the filter dust is mainly aluminium silicates. Without aluminium identified, the results confirm silica as being dominant.

Regardless of the good performance of the filter dust sol-gel coating in improving the surface quality of castings, the formulation was dropped due to the unavailability of the filter dust. The material is unconventional and inconsistent in composition, consequently, shows inconsistent and unpredictable properties. It will be emphasized here that the sol-gel filter dust coating showed strong positive potential in improving the surface quality of castings. However, this formulation was discontinued as a result of the undefined nature of the filter dust. This means that the filter dust requires a detailed characterization and proper processing, if it is to be used as a coating refractory material.

The formulation of sol-gel coatings with other conventional refractory materials proved difficult due to sedimentation and short shelf life. The short shelf life is as a result of the gelling of the system. This approach was not pursued further. However, the effect of sedimentation can be controlled by use of the right surface active agents to disperse the refractory materials in the coating matrix.

8.1.3 Sol-Gel Additive to Foundry Coatings

The use of sol-gel component as additive to existing foundry coatings became the latter research activity in the project. Different amounts of sol-gel component was added to selected foundry coatings and the effects on surface finish of castings [Supplement 3] and the strengths of moulding materials were investigated. The results showed that lower amount of sol-gel component proved significantly positive both in the improvement of surface finish of castings and in the strengthening of the moulding materials, especially with the thermal stability/resistance. When in contact with liquid metal, the glass ceramic nature of the surfaces with higher amounts of sol-gel component cracked rapidly, as a result of development of thermal stresses while with lower amount, both the strength and thermal stability were enhanced. This is seen from the results presented in one of the Case Studies and from the thermal degradation tests. The sol-gel addition changed the rheology of the coating matrix. From Figure 7.5, drips and runnings are observed on all the cores dipped in traditional, reference, and sol-gel coatings. Films and coatings represent one of the most important applications of sol-gel science and technology. The thickness of the sol-gel coatings is determined by the thickness of the parent film when it abruptly increases its viscosity during the sol-to-gel transformation. Sol-gel coatings are, after drying, generally amorphous and porous. Most of the drawbacks of the sol-gel method in the preparation of bulk materials include the cost of raw materials, cracking of the material during thermal treatment, etc. For the foundry coatings, the problem encountered with the sol-gel method is mainly with gellation on standing. With the level of penetration encountered with the addition of sol-gel component to the commercial coatings, it can be proposed that the sol-gel component lowered the surface tension of the system thereby increasing the wetting and adhesion on the substrate and consequently increasing the penetration.

8.1.4 Development of New Foundry Coatings

The formulation of a novel foundry coating requires several trials by varying the chemical compositions, concentrations of constituents, and studying the effects on the coating rheology and stability. Following this, the stability of the colloidal system is very important for coating performance. Hence, the problems encountered with the compatibility of sol-gel component with other conventional refractory materials, can be solved by enhancing the stability of the suspension. So, the knowledge of the zeta potential can reduce the time needed to produce trail formulations.

Zeta potential is a physical property which is exhibited by any particle in suspension. It can be used to optimize the the formulations of suspensions and emulsions. The particles in a dispersion may adhere to one another and form aggregates of successively increasing size, which may settle out under the influence of gravity. This was what happened with the conventional refractory materials during their dispersion in the sol-gel coating matrix.

An aggregate usually separates out either by sedimentation (if it is more dense than the medium) or by creaming (if it is less dense than the medium). In coatings, an in-between state of weak aggregation is satisfactory. The weak aggregation causes viscosity to be a function of shear rate. Stirring will produce enough shear to reduce the viscosity and promote blending [132, 133, 134]. It is important to know that there are electro-kinetic effects on the surface of particles in a liquid. Each colloid carries a "like" electric charge which produces a force of mutual electrostatic repulsion between adjacent particles. If the charge is high enough the particles will remain discrete, dispersed and in suspension. Removing or reducing the charge, the colloids will steadily agglomerate and settle out of suspension. Particle charge can be controlled by modifying the suspending liquid. Modifications include changing the liquid's pH or changing the ionic species in solution. This process is known as Electrostatic or Charge Stabilization. Another more direct technique is to use surface active agents which directly adsorb to the surface of the colloids and change its characteristics. This process is called Steric Repulsion [132, 134, 135]. Therefore, in the system where the refractory materials were not stable with the sol-gel component, any of this methods can be used to disperse the materials in the suspension depending on what suits the environment.

Zeta potential is a very good index of the magnitude of the interaction between colloidal particles and measurements of zeta potential are commonly used to assess the stability of colloidal systems. In an electrical double layer model (Figure 8.2), the potential between the stern layer and the diffuse layer (surface hydrodynamic shear[3]) is the zeta potential. The magnitude of the zeta potential gives an indication of the potential stability of the colloidal system. If all the particles in suspension have a large negative or positive zeta potential then they will tend to repel each other and there will be no tendency for the particles to come together. However, if the particles have low zeta potential values either way, then there will be no force to prevent the particles from coming together and flocculating.

[3]The microscopic shear force caused by the motion of different layers in a fluid, where the layers move at different velocities.

The dividing line between stable and unstable suspensions is generally taken at either +30 or −30 mV. Particles with zeta potentials more positive than +30 mV or more negative than −30 mV are normally considered stable [132, 136, 137]. There is a pH at which the zeta potential is zero, this is the point at which the suspension has the least stability and it is referred to iso-electronic point. The zeta potential parameter, can be applied in the formulation of the coatings to assess the stability of the coating suspension, especially with the conventional refractory materials in order to improve on the sedimentation effects by observing the effects of the addition of surface active agents on the zeta potential of the coating suspension. This will reduce the extra work encountered with preparation of many trials thereby saving time, energy and materials.

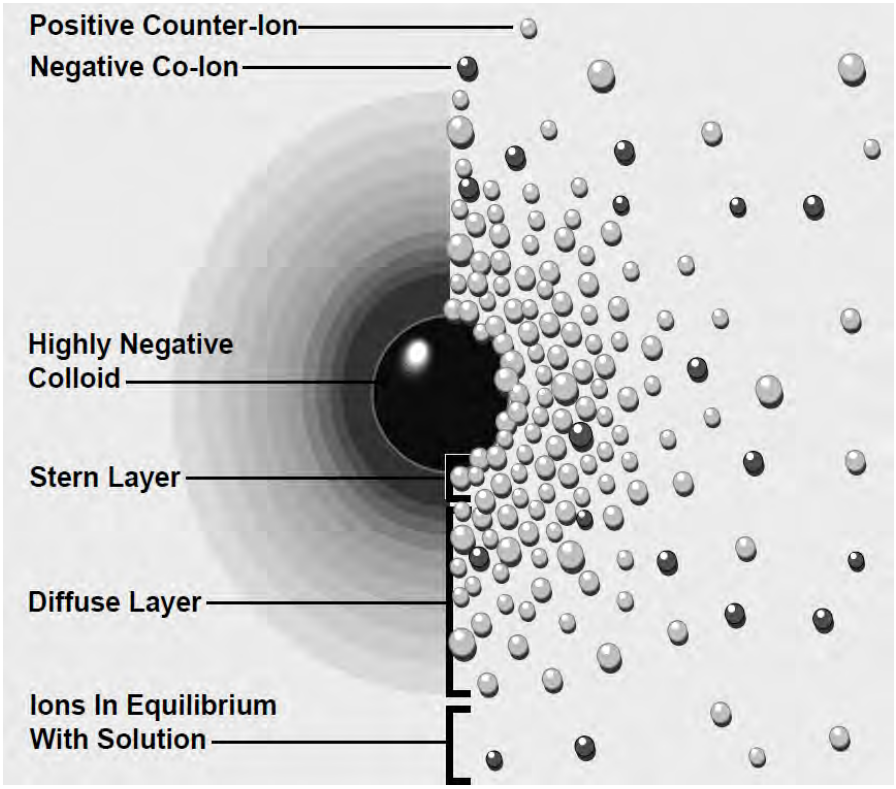

Figure 8.2: Electrical double layer model [134].

8.1.5 Conditioning of Coatings in the Foundry

Many foundries do not properly store, stir, or test their refractory coatings, and as a result they wind up with inconsistent castings. The formulation of the coating is the manufacturer's responsibility, but its homogeneity before application is the responsibility of the foundry. It is on this note that one of the Refractory Coating Manufacturers with their Engineering partners offers the foundries a state-of-the-art coating application control technology. The Coating Preparation Plant (CPP) automates the coating preparation from its as-supplied state to the density that delivers the desired wet layer thickness, with the various application methods like spraying, dipping and over-poring [138, 139]. Coating performance has a major

impact on casting quality. When coating preparation is not right, it will reflect on the surface quality of the castings. By understanding the basics of coatings and how to evaluate them, foundries are better prepared to recognize potential failure before it happens. For this reason, it makes sense to do some form of coating monitoring in the foundry shop. Based on the results from the investigations carried out in this research and information from literature, some of the following control measures described Tables 8.1-8.3 are recommended, to control foundry refractory coatings to enhance the quality and performance on castings.

Table 8.1: Measures to control coating consistency in the foundry shop [108, 139, 140].

Parameter	Description
Specific Gravity (SG)	To assure that the formulation is consistent, test SG regularly. The additives and binders may produce rheological effects or effects related to the surface energies of the liquid. The net effect is that the defining equation varies with each manufacturer and each coating formula, and therefore, it must be adjusted for each mixture: $SG = \frac{M}{M-D}$, where $M = 145$ and $D = {}^{o}Baumé$. The proper control strategy is to measure SG of the coating and occasionally estimate the rheological effects with careful ^{o}Baumé and/or viscosity measurements. Many foundries use ^{o}Baumé to control their coatings, but this test alone is not enough to maintain a coating consistency. The SG can be used to determine when the coating must be diluted or thickened.
Solids	The solid content of a coating should be checked occasionally, depending on usage. If a new drum is opened everyday, then it only needs to be tested once. If the use is one drum per week, it might be best to check the drum twice. For solids test, a clean watch glass is weighed , 20 mls coating sample is put in the glass, and it is then reweighed. The carrier (solvent) is driven off by drying at 102 °C. The watch glass is reweighed after the coating has dried, and the remaining percent solids is calculated. Some foundries use a "settling" or sediment test in which a graduated cylinder is filled with coating and the solid content is estimated by volume that settles to the bottom, usually for 24 hrs. This test does not yield a true volume or weight percent solids, however, the results should be reasonably reproducible, if compared at the same settling time.
Viscosity	Viscosity is a measure of a liquid's internal friction, or resistance to flow. For foundry applications, Ford flow cup or equivalent is a good measure. These cups hold a given volume and have carefully constructed drain holes at the bottom. The cup is dipped in the liquid and withdrawn. The drain time is measured and a chart is used to convert this time to centipoise. The viscosity will change (usually it decreases) while being stirred. For this reason, the mixer should always be turned off, prior to testing the coating. Also, temperature is a critical factor in determining viscosity. The results can indicate variations in the nature of the solvent due to aging, temperature, over-mixing, or some reactions with the container. It can also point towards a major problem with the binders or the suspending agents.
^{o}Baumé	The ^{o}Baumé test is the most common test used in foundries to control coatings because it is quick and easy. After mixing the coating sample thoroughly, immediately float the hydrometer in the coating slurry. When it stops sinking, read the ^{o}Baumé directly from the hydrometer scale. This relates to density and solid content of the coating.
pH	The pH indicates changes in the coating. This is measured using a pH meter or pH paper. It measures the acidity or alkalinity of the coating.
Runs and Drips	Runs and drips viscosity is measured by removing a hydrometer from the coating, holding it an angle of 45 ° and observing the way the coating runs off (stream, drip, or a combination of both).

Table 8.2: Measures for processing finished coating in the foundry shop [108, 140].

Activity	Description
Vendor certification	The first step in assuring the quality of the refractory coating is to make sure that they are certified by the manufacturer. The vendor should certify the chemical purity of the raw materials and should be contractually bound to inform you of any change in the formulation. One of the easiest incoming quality assurance check is to weigh the container (or check the manufacturer's recorded weight on the shipping invoice). If the wrong mineral was used, there usually will be a major discrepancy.
Reconstitution	Storage of coating allows time for its suspended refractory materials to settle out, and the vibrations during shipment accelerate this settling of minerals. Coatings should not be stored more than 30-90 days, depending on the formulation, without vigorous, complete remixing. Encountering any resistance along the sides, or the stirring rod cannot touch the bottom of the container, the solids in the coating may have settled, hence, the coating needs reconstitution.
Shop stirring	A cake of sediment at the bottom of a container can mean that the coating is not properly stirred. The binders and suspension agents in the coating may become more diluted in the coating used. This could mean that the moulds and cores may not receive the full benefit of the refractory coating. Operating a mixer continuously will cause a coating to lose solvent, since the internal friction actually heats up the liquid. Coatings should be stirred for 5 mins. in every 1 hr. The mixer can be shut off overnight or on weekends, and the drum properly covered to minimize evaporation. For next time use, the contents should be stirred continuously for 15-30 mins.
Consistent application	High solid coatings will change in viscosity and gel with prolonged over mixing. It is better to turn off the stirrer during spraying. As the solvent evaporates, a coating becomes stiffer and more likely to drag sand when brushed or swabbed on the core or mould surface.
Change over	The time when a new system has been tested successfully and replaces the old coating. When changing containers, there should be enough room in the new container to add and stir in the residual material from the old one. Refractory coatings should be stored inside, under moderate conditions. Coatings allowed to freeze may loose binder and exposure to direct sunlight may cause the coatings to loose solvent and cake.

Table 8.3: Measures to determine coating-core interaction in the foundry shop [108, 139, 140].

Parameter	Description
Core degradation	Core degradation varies from coating to coating. The longer a core stays wet, the more core degradation will take place, so it is key to put cores into an oven heat zone as quickly as possible after the core is dipped. Most coatings use surfactants as wetting agents to allow the coating to penetrate the proper depth. These surfactants change the surface tension of the water, making degradation worse.
Coating deposit	Once the optimum ^{o}Baumé level is defined to achieve a good surface finish to the castings, the amount of coating thickness can be determined. It can be Wet Layer Thickness (WLT) or Dry Layer Thickness (DLT). WLT is measured with the elcometer. It is always consistent with the DLT. For DLT, coating is removed from the flat surface on a core and the difference in the cored surface and the coated surface is measured. The amount of surface deposit can be used as a reference for future comparisons and making decisions about coating allowance in tooling design. Comparing test results with the coating thickness, among ^{o}Baumé, percent solids, and viscosity, viscosity shows the strongest correlation.
Coating penetration	The distance the coating penetrates the core is an important feature to a coating's success. A coating that lies entirely on the surface of the core is not anchored well and will most likely spall away. A coating that penetrates too much will over degrade the core. Coating penetration is also a function of core density. A core that is blown too tightly resists coating penetration while a core blown softly acts like a sponge and absorbs too much water. Any evaluation of coating penetration should be done on a core that is of normal production quality. Core release agents may waterproof the core and affect coating penetration. Penetration is evaluated by simply breaking or cutting a coated dried core and observing how far the coating penetrates the core.
Coating permeability	Coating permeability is the amount of gas that can pass through the coating. The level of permeability is dictated by both the type and amount of refractory materials that are used in the coating formula and the dry film thickness deposit on the core. The permeability of the coating on the core is measured using a laboratory permmeter. The permeability of the coating at the coating-metal interface may be different from that measured on the core. Some constituents of the coating may quickly thermally decompose, leaving voids that result in higher permeability. Some may soften and flux resulting in lower permeability.

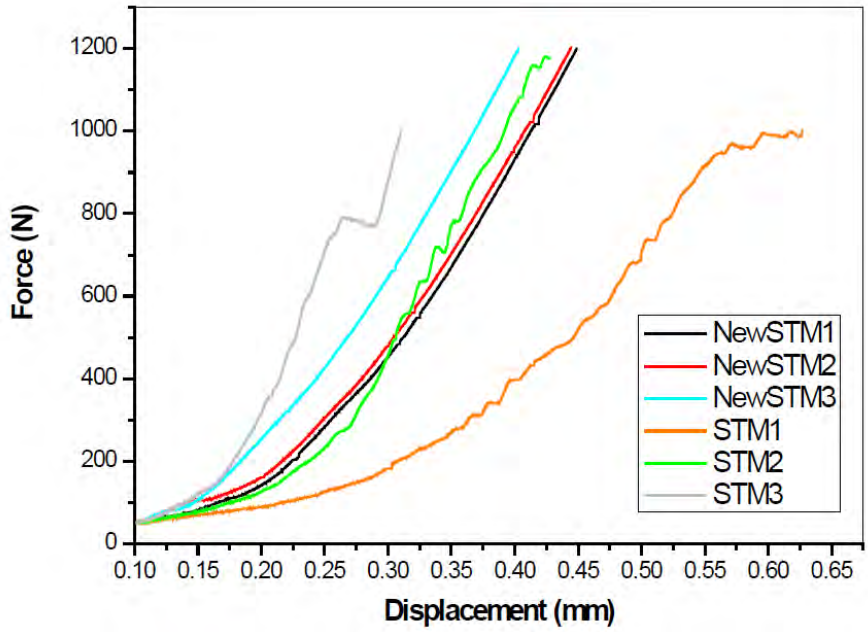

Figure 8.3: Higher precision of the new STM over the traditional STM.

8.2 Mechanical Properties of Moulding Materials

Lots of information about moulding materials are lost by neglecting to keep track of the properties of these materials. To draw attention to the fact that the properties of various moulding materials used in the foundry today, need to be tracked and properly documented, a new strength testing machine (STM) was built to measure the mechanical properties of moulding materials and also to monitor the behaviour of the moulding materials during loading [Supplement 4]. With traditional methods, the loading history to ascertain the deformation of the material is not available. This deficiency is the driving force for the development of the new STM. The force and displacement of the STM were calibrated to ensure reliability of the measurements. When taking elasticity and other linear measurement errors into account the system shows excellent precision in measuring the position and force, compared to the traditional STM as shown in Figure 8.3.

The controlling software is made to acquire and present data as Force (N) vs. Time (s) during measurement. It automatically converts the data as Force (N) vs. Displacement (mm) during data saving [Supplement 4]. The measurements with the new strength testing machine (New STM) was done at a constant loading rate of 0.5 mms^{-1}, which is one of the advantages of the new STM. This is very clearly shown in the figure above with the smoothness of the curves. In the measurements with the traditional STM, the controlling software still assumes uniform loading rate in the data acquisition during measurement, even at this situation, it is clearly seen that the loading is not uniform because it is manually loaded. Furthermore, the old STM does not measure displacement, which is another limitation. In the measurements presented in the figure above, three measurements were made for

both machines and the reproducibility of the New STM is obvious against the non reproducibility of the STM. This confirms the higher precision and reliability of the New STM over the old STM [73].

The new STM was used to measure the strength of the coated and uncoated moulding materials of cold box and furan origin. The results show that the coating slightly reduced the strength of the moulding materials in the tensile and flexural modes. This was due to the reaction of the coating liquid carrier with the moulding materials. This is in agreement with the observations of other researchers [141]. However, the claimed moulding materials strength reduction by the alcohol-based and water-based coatings of 30 and 50% respectively, seem too high from the observations made in the current study [Supplement 5]. In the compression mode, the coatings are seen to improve the compression strength of the moulding materials. In the analysis of the strength data obtained from the tensile, bending and compressive strengths, it was observed that there was a large scatter in the data obtained. The moulding materials are granular in nature and also brittle when bonded. Their behaviour is unpredictable due to the presence of many defects that can cause failure. Applying descriptive statistics to the data only provided us with the means and standard deviations, which invariably did not show any significant differences according to Null hypothesis. Therefore, the effects of moulding materials, dipping time and percentage solid contents were not ascertained. The information from the means and the standard deviations are purely statistical and may have limited practical implications in the foundry.

Weibull statistical distribution has been applied to brittle granular materials to model their strength data and to determine the reliability of these materials [102, 103, 104, 105, 106]. Bending strengths are used to assess brittle materials, therefore, moulding materials being granular in nature and brittle, their bending data is subjected to Weibull statistical analysis. In this study, the application of Weibull statistical distribution to foundry moulding materials is a novel one and proved to work well for the moulding materials [Supplement 5]. From the bending test data analysis, the strength limit of the moulding materials was found not to exceed 4 MPa and beyond this strength, the materials will fail. The determined strength limit is not the median value rather the value at which 63% of the materials will fail. This value is more reliable than the means because it provides the maximum limit without probability unlike the mean. J. Thole et al. [142] reported that weak moulds and cores can result in excessive casting distortion or warpage. Many casting defects, such as hot tears and veins, are also associated with the stiffness of the moulds and cores. In this respect, it is important to know the stiffness of the bonded sand materials. The determination of the stiffness of the moulding materials in this study was done at room temperature from the calculated stress-strain curves [supplement 5]. A straight line was fitted to the elastic portion of the stress-strain curves, with the slope representing the measured elastic modulus. The stiffness of the moulding materials at room temperature was found to be within the range, 1000-1600 MPa. The absence of a plastic behaviour in the moulding materials is a finding of the present study. This stiffness parameter can be used as a quality control means for the sand materials, because the particle size, particle size distribution, and binder strength will reflect in this parameter.

In other words, when new sand is introduced into the system, this parameter is determined and at a later stage of using the sand it is again measured and compared. The result is expected to reveal the state of the sand, although, binder consumption can also serve as an indicator for the state of the sand.

In another development in the study of the mechanical properties of the moulding materials, the fracture surfaces of the materials were subjected to microscopic examination. The results proved that the coating refractory materials do not contribute to the strength of the moulding materials. The microscopic studies also revealed that the strength of the moulding materials are determined by the bonding bridges between the sand grains and fracture mode is inter-granular through the bonding bridges. Therefore, the finer the sand grains, the more the bonding bridges and the stronger the moulding materials. This also means that more binder will be consumed due to larger surface area. The reverse will be the case with coarser grains. To improve the mechanical properties of moulding materials, camphor and castor oil can be added to the coating to promote film formation and improve its plasticity and strength [143].

8.3 Mass and Heat Transport at Core-Metal Interface

When the moulding materials come in contact with the liquid metal, lots of activities take place because they are typically capillary-porous bodies. There are mass and heat transports (diffusion), thermo-mechanical degradation of the moulding materials and chemical reactions, etc. The diffusion of heat in a capillary-porous body is complex. More especially, when the molten metal is put in contact with the mould which is very much colder, a contact is formed between the molten metal and the substrate only at the asperities protruding from the surface due to the effect of the surface tension of the molten metal [144, 145]. The quality of the contact between the liquid metal and the mould is largely determined by the surface micro-topography of the mould/core surface. Therefore, the surface tension of the liquid metal and the mould atmosphere play significant roles in determining the topographic contact. This non-perfect contact results in a thermal resistance to heat transfer known as Thermal Contact Resistance (TCR). TCR is equivalent to the inverse of the interfacial thermal conductance or heat transfer coefficient (h) at the interface. The occurrence of TCR at the interface is associated with the fact that the heat flux from the liquid metal to the cold mould/core wall needs to be constricted to pass through the micro-contact spots at the interface as illustrated in Figure 8.4. This may be modelled at a macroscopic scale by a temperature difference at the interface that characterizes the magnitude of the TCR according to Equation (8.1):

$$TCR = \frac{\triangle T}{q} \tag{8.1}$$

The significance of TCR in the mechanisms of heat transfer becomes more pronounced when the thermal properties of the contacting surfaces are high. If the

thermal conductivities of the contacting bodies are small, the TCR becomes very weak compared to the intrinsic thermal resistance of the bodies which depends on their thickness and thermal conductivities. Consequently, the TCR becomes negligible [145].

In the modelling of the coating layer on the silica sand cores for the simulations, the coatings refractory material is taken as silica from the XRD analysis. In this case, to model the coating layer on the cores was just to add the proud layer thickness of the coating on the cores, which was measured with an image analysis software [107]. However, the increased density of the penetrated area of the core could not be accounted for in the numerical calculations. This will introduce differences in the thermal profiles from the numerical simulations and the experiments. The coatings with thicker layers increase the heat capacity of the core material around the penetrated area and showed delayed heat transfer to the middle of the core materials where the thermocouple is located.

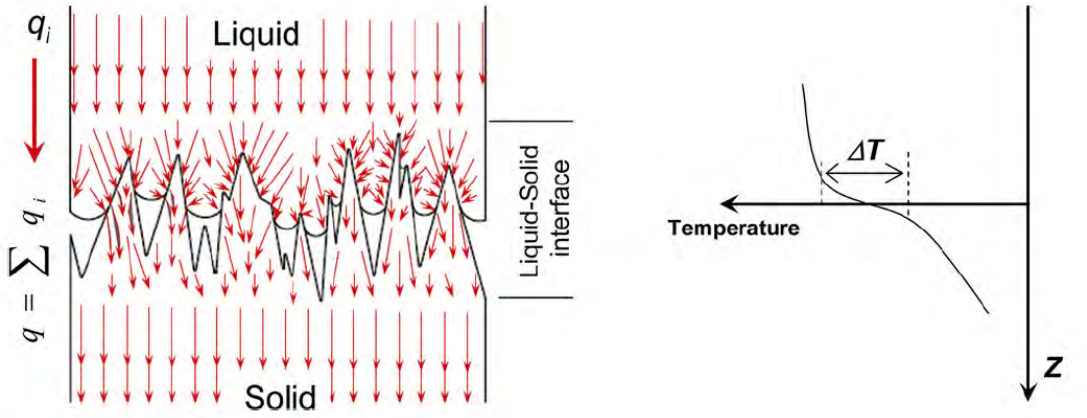

Figure 8.4: Schematic of the liquid solid contact (vertical scale exaggerated) showing the constriction of the heat flux as it passes through the microcontact area at the interface and the temperature profile at the interface [145].

In the moulding materials, heat is transmitted by conduction, radiation, and convection. In conduction, heat is transmitted through the points of contact of individual particles. Owing to the considerable thermal resistance of the contact zone, the coefficient of thermal conductivity of the body is many times smaller than that of the particles. Binding materials (including clay, water glass, water, cold box, furan, etc.) which bond together the moulding materials and thereby increase the area of mutual contact, raise the coefficient of thermal conductivity (k_s) and heat capacity (c_p) of the body. The gas filling the pores in moulding materials also take part in heat transfer. However, its thermal conductivity is ten times less than that of sand, and therefore, the effect in heat conduction can be disregarded. The fact is that gas transfers heat not only by conduction but also by contact (convection). The convection occurs both in the pores and between the pores [146]. Gas is transparent to heat rays, so heat migration in the pores results from radiation also. The amount of heat transferred by radiation depends on the geometric properties of the pores (sand grains), the degree of blackness of the surface, and the temperature.

Radiation depends mainly on temperature [146]. According to Stefan-Boltzmann law, heat flux is proportional to the difference of the fourth powers of absolute temperature [29, 31]. In this case, the primary concern is the temperature gradient on the surface of any given pore. This gradient results from the presence of a temperature gradient in the cross-section of the body (mould or core). The coefficient of radiation is proportional to the degree of blackness of the body and may vary from 0 (absolutely white body) to much higher for an absolutely black body. The general theory of radiation heat-exchange postulates that the amount of heat transmitted by radiation depends on both the shape and size of the pores. However, tracing the effect of the shape of the pores is difficult, but the effect of the size can be discussed on the basis of the theory of the action of screen for radiation heat-exchange. In this context, screens reduce heat exchange proportionally with the number of screens between two parallel surfaces. Bridges between pores may to some extent be regarded as a type of screen. Consequently, with increase in the dimensions of the sand grains (decrease in the number of bridges), heat-transfer must increase, and decrease with the reduction of the particle size. Therefore, with application of coating, it means that the density around the penetrated area is increased while introducing more bonding bridges which reduce the heat transfer thereby increasing the heat capacity accordingly. This, in effect, will increase the cooling power of the mould/core material. This could be one of the possible explanations to the delay observed in the thermal profiles during casting because the coating layer absorbs more energy before the temperature rises or the coating is thermally insulating. However, considering the small coating layer the explanation that the coating is thermally insulating becomes dominant.

In moulding materials, there are at least three identified types of convection currents of gas, resulting from different factors. The first type corresponds to normal convection arising from the difference in the specific gravities of gas particles heated to an uneven temperature. This type of convection occurs both in each individual pore and in the body as a whole, owing to filtration of the gas through its capillaries.

The second type of convection takes the form of forced directional filtration of the gas, caused by the pressure difference which arises near the casting owing to gas evolution from the liquid metal, combustion of coating and binding additives in the mould, evaporation of moisture, expansion of gas heated in the pores of the mould, etc.

The third type of convection is caused by thermodynamic factors, and always occurs when there is a gradient of temperature.

In moulding materials, there is also convection of the water, which generally circulates as both steam and liquid. The water and organic solvents evaporating in the heated parts of the capillary-porous body, is transferred as steam to the colder parts and condenses there. Volatilization is accompanied by heat absorption, therefore, the zone where evaporation takes place will thermally act as a heat sink, condensation is accompanied by heat evolution, because in the area where condensation takes place heat is generated. Migration of gas and liquid is accompanied by migration of heat together with their masses.

In the first period after the metal has been poured, a large amount of gas is evolved in the mould near the surface of the casting. The gas passes rapidly through the capillaries of the mould or core and considerably increases the intensity of heat-exchange. Such forced convection initially suppresses natural convection and completely determines the process. Then, as gas-evolution decreases, the forced convection weakens and the mechanism of diffusion resulting from the gradient of temperatures comes into action. In damp moulding materials, moisture is volatilized rapidly upon reaching the boiling point. The surface layer of the mould, in contact with the casting, dries, and a volatilization front moves inwards. As it passes through the capillaries and reaches a region of the mould having a temperature below the boiling point, the steam condenses. This involves the diffusion of a large amount of heat (at atmospheric pressure the volatilization of 1 kg of water is accompanied by the absorption of 2300 kJ of heat; the same amount of heat is liberated at the point of condensation of 1 kg of steam). The coefficient of thermal conduction is markedly higher in wet sand than in a dry one [146]. Based on the above discussions and deductions made, the following model shown in Figure 8.5 is proposed to explain mass and heat transport (diffusion) at the interface between the casting and the moulding material.

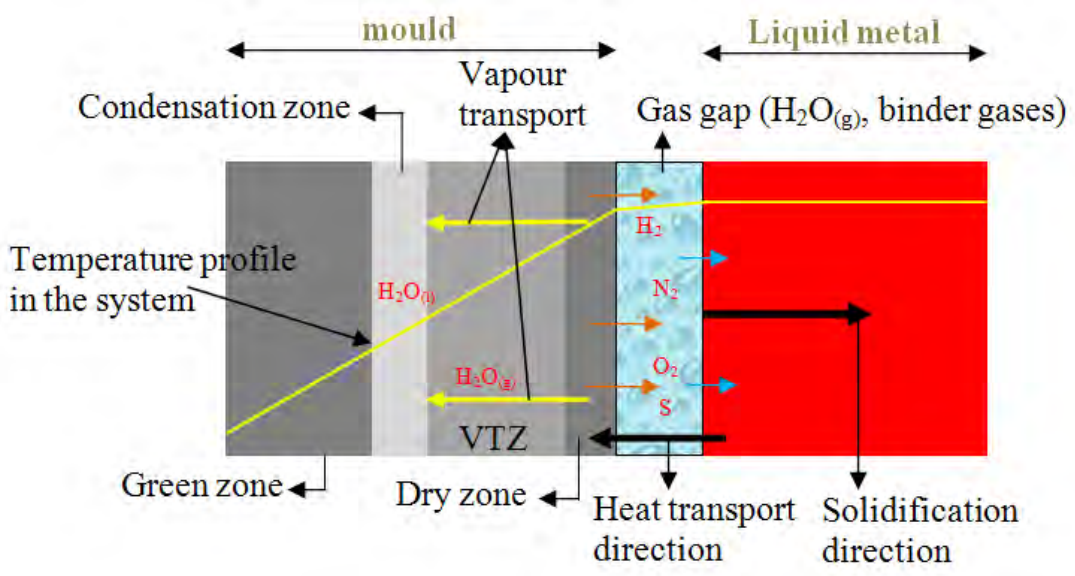

Figure 8.5: The model of the mass and heat transports at the mould/core-metal interface.

8.4 Mould-Metal Interaction

Furthermore, for liquid-solid contact, one can imagine two conditions of contact associated with either poor or good wettability between the solid and the liquid. These two situations of contact depends on the magnitude of the surface tension of the liquid metal, the nature of the solid surface and pressure. However, in both situations, the profile of the solid surface determines the topography of the interface.

As expendable moulds are being considered here, following the thermo-mechanical degradation of the moulding materials around the contact with the liquid metal, it is believed that the moulding materials will undergo thermal shock and in the process, thermal stresses build up leading to the cracking and breaking of the sand grains around the interface with liquid metal. Therefore, if a thermal protective coating is not applied, there will be presence of combination of finer grains and coarser grains at the interface as the binder is burnt out and penetration is occurring. This is shown in the modified model for the pressure balance for metal penetration presented in Figure 8.6. The modified model presents different sand grain sizes during metal penetration. Considering the dynamics, the kinetic condition that the molten metal penetrates the surface of the mould or core material is detailed as follows [143]:

$$P_s > P_r = P_g + P_c = -\frac{(2\sigma cos\theta)}{r} \tag{8.2}$$

where

P_s - pressure from molten metal

P_r - penetration resistance

P_g - gas pressure from expanding mould gases

P_c - capillarity resistance

σ - surface tension of the molten metal

θ - wetting angle

r - radius of pores between sand grains.

For molten metals of superior wettability, $\theta < 90^o$, $cos\theta > 0$ and for molten metals with inferior wettability, $\theta > 90^o$, $cos\theta < 0$. When the molten metals could not effectively wet the mould or core surface, then penetration is resisted. It is reported in [147] that penetration is responsible for major economic losses to the foundry. Most of the cost incurred is attributed to the rework in the fetling shop.

Thermal degradation test was performed on coated cores to elucidate the effect of the coating on the thermal stability of the cores. From the results presented in Figure 6.23, it was seen that the coating layer remained intact while the binder of the core is burnt out, evidenced by the free sand flowing out from the cracks. Therefore, the refractory coating on cores can actually protect the core material from thermal shock.

However, at the incidence of silica phase transformation and the occurrence of the associated defects when in contact with liquid metal, there has been lots of doubts with regard to what happens at the mould/core-metal interface at this transformation temperature. A brief explanation of what happens is presented in this discussion. At the mould/core-metal interface, the moulding material is rapidly heated up and due to the poor thermal conductance of the moulding materials, the surface of the moulding material is subjected to local overheating. This situation happens so fast and at a lower temperature than the TTZ. The consequence is burning out of the binder on the surface of the moulding materials. This leads to penetration, sand inclusion and rough casting surface defects.

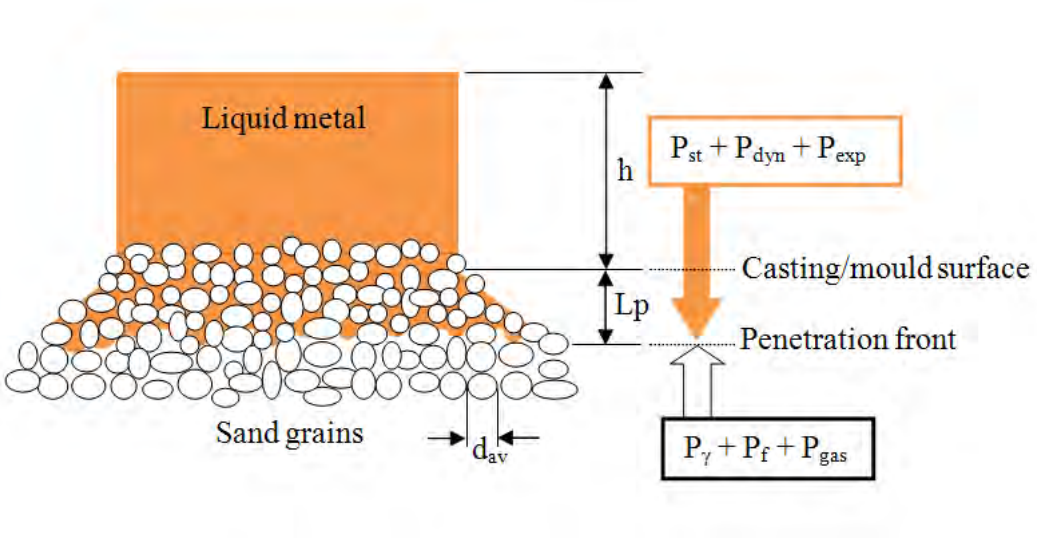

Figure 8.6: Proposed model for the thermo-mechanical degradation of the moulding materials at the core-metal interface during metal penetration.

When the surface temperature reaches 573 °C, α - β quartz phase transformation will occur with its associated rapid expansion. This expansion is non-uniform and consequently introduces thermo-mechanical stresses which lead to the cracking of the core/mould surface. If the metal temperature is still above the liquidus temperature, when the cracks occur, the melt will flow into these cracks forming veining or finning defects. However, with the application of refractory coatings, the rapidity of the heating of the moulding materials surface is significantly reduced and the binder around the surface of the moulding materials is protected from early burn-out, allowing the metal to start solidifying before the coating-core-binder failure. This will eliminate the the incidence of the defects (such as sand inclusion, penetration, roughness of casting surfaces, etc.) associated with the early burn-out of the binder. To a reasonable extent, the coatings also prevent the incidence of veining defects. This is particularly the case when the coating contains some additives that can enhance it thermal plasticity as mentioned earlier. The coating protective layer is clearly shown in Figure 6.23. From this figure, it can be seen that the coating remained intact even when the binder has completely burnt out. In the figure, what was observed is that the failure of the coating was by cracking, in this case the only likely defects to occur are veining defects if the temperature of the metal is above liquidus.

8.5 Casting Surface Quality

The quality of the surface as well as the dimensional accuracy of a casting depends on the extent of the reaction and interaction between the metal and the mould materials. Some of the variables affecting the reaction are the compositions of the metal and sand, pouring temperature, cooling rate, metal pressure, and the mould atmosphere. These reactions and interactions can lead to sand burn-on,

metal penetration, surface roughness, veinings, casting porosity, and dimensional inaccuracy [148]. In furtherance of the explanation of the interfacial interaction of the metal and the mould which determines the surface quality of the castings, cast iron can be used as an example. Iron is oxidized at the mould surface, forming an oxide liquid which wets the silica sand in the mould. This liquid phase penetrates into the pores of the mould. Silica is soluble in this oxide liquid to about of 50% by weight. The dissolution of silica enlarges the pores in the sand. This enlargement of the pores permits the molten iron to penetrate the mould/core at low pressures although iron does not wet the silica sand. The depth of penetration into the sand by the iron depends on the length of time the melt remains above the liquidus and the severity of the oxidation. At a very low CO_2/CO ratio, no penetration occurs because the atmosphere is reducing. This is why green sand contains carbon to avoid the risk of decaburization. At a higher CO_2 content, the iron will be oxidized. Slag formation depends on the time, temperature, and the oxidizing level at the mould-metal interface. The rate of oxidation and the amount of attack upon the sand increase under oxidizing environments [148]. All these affect the surface quality of castings produced under this situation. In the foundries, most of these effects are reduced by application of refractory coatings [149]. The activity at the mould/core-metal interface also have negative effects on the sub-microstructural evolution. If there is a change in the expected microstructure at the subsurface of the casting beyond machining allowance, the mechanical properties of the part will be affected. Therefore, the composition of the moulding materials and the coatings become very important to monitor. They should be inert to the molten metal. In this study, efforts were made to show some of the changes in the microstructure at the interface of castings with coated cores. This needs further investigation. Further work is necessary to show that the sol-gel additive has no negative effect on the casting microstructure.

The good surface quality of the castings obtained by application of coatings on the cores is attributed to the fact that the coating offers a protective barrier consequently stopping the reactions and interactions. Furthermore, the refractory filler materials in the coatings are very much smaller than the sand grains in sizes and at the right amount, offers the right surface coverage to the cores. The fine details of the refractory materials will be reproduced on the surface of the castings. Some of the coating also contain anti-veining substance such as Fe_2O_3 which prevents the occurrence of veining defects. This is the mechanism of surface improvement with coating application. From the results presented in the case studies, the sol-gel addition showed strong potential in enhancing the surface quality of the castings relative to the reference coating (the same coating but without sol-gel component). The addition of sol-gel to foundry coatings needs optimization for various coatings.

However, in this study, it was observed that the coatings improved the surface quality of the castings more in areas away from the parting-lines of the core box in both the cylindrical and flat cores. A closer observation shows that the parting-line area of the cores seem to be the weakest part. This emanates from the production process. These areas are mostly where penetration is largest especially in the castings made with smaller flat cores (Figure 6.35). Therefore, a complete surface quality of the castings can only be obtained by harnessing the synergy of the

expertise from the core shop and the quality of the refractory coatings. Some surface defects can be traced back to the core production process and poor sand compaction, while it may not be easy for one coating to take care of all surface defects on castings. Cores that come from the core shop with scars or other surface defects, and without proper care and storage, are more prone to produce defective castings.

The assessment of the surface quality of castings has been a difficult task. In the foundries, the measurement of surface roughness of castings has been neglected for decades, due to the inability of the mechanical surface roughness testing instruments such as stylus instruments, to reproduce the exact surface texture of cast surfaces. The roughness range of many cast surfaces is outside the capacity of these measuring instruments. It is also reported in [150] that since cast surfaces do not exhibit the same cyclic character as machined surfaces it is difficult to evaluate their roughness using conventional mechanical, optical, or pneumatic devices. Consequently, visual tactile standards are used to describe the surface of castings. Purchasers of castings specify and assess surface quality and surface texture more accurately and definitively using tactile comparators developed by Casting Technology International (CTI) [151]. These provide a practical and functional alternative to photographic representation of casting surfaces in standards such as MSS SP-55-2001 (Manufacturers Standardization Society Standard Practice-55-2001), Visual Method for Evaluation of Surface Irregularities. These comparators form the part of a larger set of comparators defining different surface defects of castings and apply to ISO 11971:2008 Steel and iron castings-visual examination of surface quality; BS EN 1370:1997 Founding - Surface roughness inspection by visual tactile comparators; BN EN 12454:1998 Founding - Visual examination of surface discontinuities. However, in this study, an evaluation of the surface roughness of the said standards proved that the standard with the lowest roughness in the series is higher in roughness than most of the cast surfaces, especially when coatings are applied to the cores or moulds used for making those castings.

An Optical 3D measurement system, Alicona "InfiniteFocus", based on Focus-Variation Technology, was applied in the measurement of surface roughness of castings and some standards. This technique was successfully used to quantify the surface roughness of cast components. In doing this, a moderate objective ($5\times$) was used because using higher objective will mean lower beam spot size which will give measurements values which are not a true representation of the texture of the cast surfaces. Surface parameters were used to describe the surface of the castings although average of profile parameters give similar results. Therefore, one time measurement with areal parameters saved at least 5 times the time required to make at least 5 profile measurements.

The measured data was analyzed using Scanning Probe Image Processor (SPIP), a 3D surface metrology software. In the data processing, filtering was used to separate the waviness and the roughness. The wavelength of primary concern are those associated with roughness. Roughness is a result of the manufacturing process, especially with sand casting, these include the uniformly distributed irregularities on the surface of the castings. If filtering was not performed, waviness will dominate the surface texture of the casting. In this situation, the effect of the coating and

moulding materials cannot be assessed. A typical effect of the filtering is shown in Figure 8.7. This figure emphasizes the need for filtering the surface in order to be able to measure the real surface roughness.

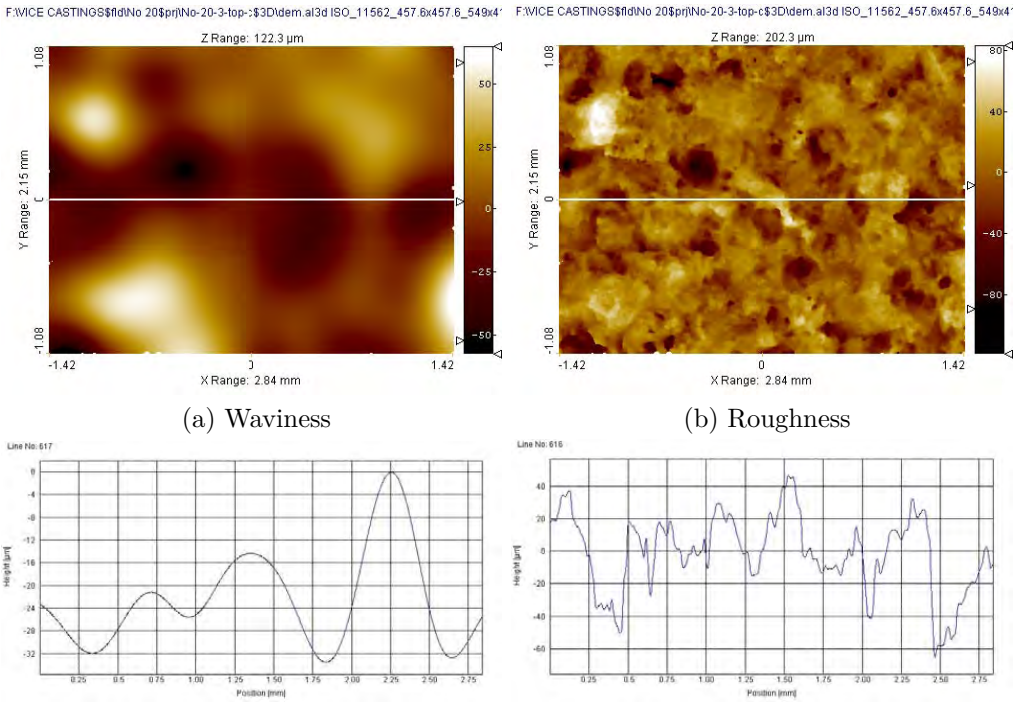

(a) Waviness

(b) Roughness

(c) Waviness profile

(d) Roughness profile

Figure 8.7: The difference between waviness and roughness.

Chapter 9

Summary

9.1 Conclusions

This PhD thesis addresses the development of a novel refractory foundry coating using the Sol-Gel Technology. The coatings were developed and applied on mould/core materials in order to enhance the surface quality of castings by reducing or eliminating the surface defects. From the detailed experiments performed, the following deductions are made.

Sol-gel refractory coatings for foundry applications are possible. However, the sol-gel stock is selective of particle size and particle size distribution, types of refractory materials and suspension agents. This selectivity has to be reduced for foundry coating development using sol-gel technology.

In the characterization of the coatings, the particle size and the particle size distribution of the refractory materials have significant roles to play in the performance of the coatings. Therefore, considering the sand grain sizes, nanoparticle refractory materials are not suitable for foundry coatings. The formulation of the sol-gel coatings with other refractory materials like zircon, olivine, china clay, and aluminium silicates did not prove workable as the refractory materials were flocculating in the systems. The rheological properties of coating such as viscosity and density are dependent on the solid content of the coating. From various characterization results, it can be concluded that the percentage solid content in the coating is directly proportional to the density, ^{o}Baumé, viscosity, coverage, and proud layer thickness, and inversely proportional to the penetration into the substrate, moisture content, and permeability. The characterization results of the coating emphasizes that ^{o}Baumé parameter be performed with additional tests such as viscosity, density, and surface tension, in controlling the consistency of foundry coatings. The coatings enhanced the thermal stability of the core materials in general, while with little amount of sol-gel additive, greater reinforcement to the stability of the core can be achieved.

Test casting of the coatings showed that the filter dust sol-gel coatings showed strong positive potential to enhance the surface quality of the castings. However, the development of this coating was discontinued as a result of non availability of the filter dust materials. The next activity was to add the sol-gel component as

an additive to commercial foundry coatings. The surface quality of the castings improved significantly with addition of certain amount of sol-gel component to some commercial coatings relative to the coating without sol-gel. Lower amounts of sol-gel components were observed to improve the thermal integrity/stability of the mould/core materials and consequently, enhance the surface quality and reduce veining defects.

During the application of the coating to the mould/core, the interaction of the coatings with the moulding materials leads to the lowering of the strength of the moulding materials. The mechanical property measurements of mould/core materials reveals that the strength of the moulding materials is determined by the binder and the fracture mode under loading is inter-granular through the bonding bridges between the sand grains. Sand moulds/cores are not fully compact with sand due to irregular particle shapes and sizes of the sand grains. Consequently, the mould or core has large amount of voids of different sizes determined by the sand grains and grain size distribution. Therefore, the cause of brittle failure of moulding materials is as a result of these voids. Chemically-bonded sand core materials have no specific strength but a range of strengths at ambient temperature. However, the knowledge of the mean strength is not much of technical use for the foundry rather, the strength at which the moulding materials can be reliably used. This is successfully determined by application of the Weibull Statistics on the measured strength data. From the Weibull statistical analysis, the reliability strength of the moulding materials is determined. The modulus of elasticity of the chemically-bonded sand core materials were determined in the range of 1000-1500 MPa for cold box and 1000-1600 MPa for furan core materials at ambient temperature. The binder remains the determinant contributor.

From the predicted reactions at the mould/core-metal interface, the metals get oxidized at very low free energy change within the casting temperature and also at very low CO/CO_2 ratio. The harder the oxide is to reduce, the greater the proportion of CO needed in the gases. This means that an oxidizing atmosphere should be avoided.

In this research, it has been established that optical system can be reliably used to characterize the surface texture of castings contrary to previous views. An optical 3D measurement system, Alicona "InfiniteFocus", based on Focus-Variation Technology, was applied successfully in the measurement of surface roughness of sand castings and some standards. Average parameters are more sensitive to changes in surface features than the extreme (peak-to-value height) parameters both in profile and surface measurements. Surface parameters are more precise and reliable and saves measurement time compared to the profile parameters. Parameter rash should be avoided in the foundry. Sa parameter from 3D surface measurement suffices for casting surface characterization. Bearing area curve parameters normalized to the core roughness can be used to determine the symmetry of the surface features.

9.2 Recommendations for Further Work

In view of the fact that the filter dust used as a refractory material for the sol-gel coating showed positive results with improving the surface quality of castings, probably due to the fact that it has already undergone thermal shock and has high thermal integrity, processing it and finding use for it in refractory linings for furnaces or as refractory fillers for foundry coatings will be favourable to the environment. This means recycling of a foundry waste.

Concerning the coating formulations where the sol-gel component was not compatible with many other refractory materials, this is a big limitation for the sol-gel application in foundry coating development. Therefore, it will be worth trying to apply surface active agents to get the refractory materials properly dispersed in the suspension and zeta potential measurements adopted to determine the stability of the coating suspensions. This approach will significantly reduce the number of trial formulations to be made thereby saving time, resources, and energy.

Having established that the sol-gel component shows positive results in enhancing the performances of commercial coatings, optimization of the amount of sol-gel component required for various commercial coatings and different moulding materials is required to be done. This will involve determining the viscosity, ^{o}Baumé, and the amount of commercial coating at each of the sol-gel component amount that shows good results. This will help in the formulation of a model for the addition for the right consistency for a particular commercial coating and moulding material. This will be done with a more automated production process like cold box core system to ensure reproducibility.

A detailed study of the subsurface microstructure of the castings at the interface with coated moulds/cores are recommended, accordingly.

Another area of interest that is worth developing further is to effectively utilize the capabilities of the new 3D optical measurement technique and make replicates of casting surfaces of interest without destroying the component. This will provide a non destructive novel technique of quantifying the roughness of cast components.

Bibliography

[1] K. P. Harris, Silica-free foundry sand at silica prices, Shape casting: The John Campbell Symposium, M. Tiryakioglu and P. N. Crepeau Eds. TMS, 2005.

[2] J. Thiel, M. Ziegler, P. D. Dziekonski, S. Joyce, Investigation of the Technical Limitation of Silica Sand to Thermal Expansion, AFS Transactions paper 07-145(04) (2007).

[3] S. G. Baker, J. M. Werling, Expansion Control method for Sand Cores, AFS Transactions paper 03-023(04) (2003).

[4] N. Hodgkinson, T. Birch, Improving Foundry Profitability through the use of RHEOTEC*XL Coating, Foseco Foundry Practice, 240 (2003)

[5] www.cjc.dk/profile

[6] www.dania-as.dk

[7] www.dti.dk

[8] www.disagroup.com

[9] www.fresemetal.dk

[10] www.johan-jensen-og-son.dk

[11] www.nord-metal.dk

[12] www.pvsand.dk

[13] www.birn.com

[14] Environmental statement 2005 – company site Vestas Castings Kristiansand AS, Norway.

[15] K.P. Panayiotopulos, Packing of Sands - A Review, Soil & Tillage Research 13 (1989) 101-121.

[16] The American Foundrymen's Society, Moulding Methods and Materials, 1st ed., Illinois, 1962.

[17] A. Raihane, O. Bonnefoy, J. –M. Chaix, J. –L. Gelet, G. Thomas, Analysis of the densification of a vibrated sand packing, Powder Technology (2010).

[18] Y. Peng, S. Hu, Q. Ding, Dense packing properties of mineral admixtures in cemetitious material, Particuology 7 (2009) 399-402.

[19] S. Shen, H. Yu, Characterize packing of aggregate particles for paving materials: Particle size impact, Construction and Building Materials. 25 (2011) 1362-1368.

[20] M. M. Monkul, G. Ozden, Compressional behaviour of clayey sand and transition fines content, Engineering Geology 89 (2007) 195-205.

[21] S. P. E. Forso, J. P Vuori, The determination of porosity of iron ore green pellets by packing in silica sand, Powder technology 159 (2005) 71-77.

[22] M. D. Webb, I. L. Davis, Random particle parking with large particle size variations using reduced-dimension algorithms, Powder Technology 167 (2006) 10-19.

[23] J. Xiang, The effect of air on the packing structure of fine particles, Powder Technology 191 (2009) 280-293.

[24] W. B. Parkes, Clay-bonded Foundry Sand, Applied Science Publishers, London, 1971.

[25] P. L. Jain, Principles of Foundry Technology, 4th ed. McGraw-Hill, New Delhi, 2006.

[26] T. S. Piwonka, Aggregate Moulding Materials, 15 (1988).

[27] Foseco, Ferrous Foundryman's handbook, Butterworth-Heinemann, Oxford, 2000.

[28] P.D. Webster, Fundamentals of Foundry Technology, Porticullis Press, Surrey, 1980.

[29] H. F., U. Åkerlind, Materials Processing during Casting, John Wiley, West Sussex, 2006.

[30] J. Campbell, The New Metallurgy of Castings, 2nd Edition, Burtterworth Heinemann, Oxford, 2003.

[31] J. Hattel Ed., Fundamentals of Numerical Modelling of Casting processes, Lyngby, 2005.

[32] S. N. Kulkarn, K. Radhakrishna, Evaluation of metal-mould interfacial heat transfer during the solidification of aluminium - 4.5% copper alloy castings cast in CO_2-sand moulds, Materials Science-Poland, Vol. 23, No. 3 (2005) 821-838.

[33] B. E. Brooks, C. Beckermann, Prediction of Burn-on and Mold Penetration in steel Casting using Simulation, in Proceedings of the 60th SFSA Technical and Operating Conference, Paper No. 5.3, Steel Founders' Society of America, Chicago, IL, 2006.

[34] K. M. Pedersen, N. Tiedje, Temperature measurement during solidification of thin wall ductile cast iron. Part 1: Theory and experiment, Measurement 41 (2008) 551-560.

[35] ASM International, Metals Handbook, Casting, 9th Ed. Vol. 15, metals park, Ohio, (1988)

[36] L. Winardi, H. E. Littleton, R. D. Griffin and J. A. Griffin, Gas from Green Sand Molds and Vapor Transport Zone, AFS Transaction 2008, vol. 49, pp. 381-398.

[37] L. Winardi, and G. Wilkinson, Comparison of Gas evolution and Permeability of Green Sand Molds and Chemically Bonded Sands, AFS Transaction 2008, vol. 50, pp. 399-412.

[38] L. Winardi, P. Scarber,Jr. and R. D. Griffin, Comparison of Gas evolution results from Chemically Bonded Cores in contact with Magnesium and aluminium Melts, AFS Transaction 2008, vol. 48, pp. 769-783.

[39] N. Tiedje, R. Crepaz, T. Eggert, N. Bay, Emission of organic compounds from mould and core binders used for casting iron, aluminium and bronze in sand moulds, Journal of Environmental Science and Health Part A, 45 (2010) 1866-1876.

[40] L. Winardi, H. Onda, S. Harada and A. Yoshida, Gas Evolution and Permeability of Shell Cores in Contact with Aluminum, AFS Transaction 2008, vol. 107, pp. 445-461.

[41] U. C. Nwaogu, T. Poulsen, C. Bischoff, N.S. Tiedje, Influence of New sol-Gel Refractory coating on the Casting properties of Cold Box and Furan Cores for Grey Cast Iron, Proceedings of the 69th World Foundry Congress, China (2010).

[42] D. A. Porter, K. E. Easterling, M. Y. Sherif, Phase Transformation in Metals and Alloys, 3rd Ed., CRC Press, Florida (2009).

[43] R. E. Smallman, R. J. Bishop, Modern Physical Metallurgy & Materials Engineering, 6th Ed. Butterworth-Heinemann, Oxford (2002).

[44] CliffsNotes, Chemistry: Gibbs Free Energy, www.cliffsnotes.com/study_guide/Gibbs-Free-Energy.

[45] Gibb's Free Energy and the Nature of Chemical Reactions: www.tiem.utk.edu/bioed/Webmodules/GibbsEnergy.htm

[46] Bodner Research Web, Gibbs Free Energy: www.chemed.purdue.edu./genchem/topicreview/bp/ch21/gibbs.php

[47] C. Cingi, Mould-Metal Reactions in Magnesium Investment Castings, PhD Thesis, Helsinki University of Technology Publications in Foundry Technology, 2006.

[48] R. W. Monroe, J. B. Andrews and J. Thiel, Iron Oxide in Molds and Cores for the production of Iron and Steel Castings, Paper 10-148.pdf, AFS Proceedings 2010.

[49] N. N. Greenwood, A. Earnshaw, Chemistry of the Elements, 2nd Ed., Butterworth-Heinemann, Oxford (1997).

[50] H. J. Grabke, Asorption, Segregation and Reactions of Non-metal atoms on Iron Surfaces, Materials science and engineering, 42 (1980) 91-99.

[51] H. G. Lee, Y. K. Rao, Rate of Decarburization of Iron-CarbonMelts: Part 1. Experimental Determination of the Effect of Sulphur, Metallurgical Transactions B, Vol. 13B (1982) 403-409.

[52] H. J. Grabke, W. Paulitschke, G. Tauber, H. Viefhau, Equilibrium Surface Segregation of Dissolved Nonmetal Atoms on Iron(100) Faces, Surface Science 63 (1977) 377-389.

[53] L. Riposan, M. Chisamera, S. Stan, T. Skaland, Surface Graphite Degeneration in Ductile Iron Castings for Resin Moulds, Tsinghua Science and Technology, Vol. 13, No. 2 (2008) 157-163.

[54] K. P. Harris, Silica-free foundry sand at silica prices, Shape casting: The John Campbell Symposium, M. Tiryakioglu and P. N. Crepeau Eds. TMS, 2005.

[55] F. Peters, R. Voigt, S. Z. Ou and C. Beckermann, Effect of mould expansion on pattern allowances in sand casting of steel, International Journal of Cast Metals Research, Vol. 20 No. 5 (2007) 275 – 287.

[56] R. B. Sosman, The phases of silica, 1965, New Brunswick, NJ, Rutgers University Press.

[57] F. M. Wahl, R. E. Grim and R. B. Graf, Phase transformations in silica as examined by continuous X-ray diffraction, The American Mineralogist, vol. 46 (1961)196 – 208.

[58] G.W. Moss, Mathematical Models of the Alpha-Beta Phase Transition of Quartz, PhD Dissertation, Blacksburg, Virginia, 1999

[59] S. G. Baker, J. M. Werling, Expansion Control method for Sand Cores, AFS Transactions paper 03-023(04) (2003).

[60] J. Thiel, M. Ziegler, P. D. Dziekonski, S. Joyce, Investigation of the Technical Limitation of Silica Sand to Thermal Expansion, AFS Transactions paper 07-145(04) (2007).

[61] AFS, Analysis of Casting Defects, 4th Ed., American Foundry Society, Illinois, 2007.

[62] T. Birch, D. Bell, Improved Iron Casting Quality through Application of Advanced Coating Technology, Foseco Foundry Practice, Vol. 243 (2005) 16-23.

[63] I. Dugic, A. Dioszegi, I. L. Svensson, The mechanism of metal expansion penetration during solidification of grey cast iron, Research Report, 1404-0018, 2006.

[64] G. D. Sylvestro, Experiences in Defect Diagnosis: Metal Penetration, Special Report AFS paper No. 89-07 (1989).

[65] J. O. Barlow, D. M. Stefanescu, A. M. Lane, W. C. Schreiber, M. Owens, T. S. Piwonka, Metal penetration in sand moulds for steel castings, Annual report, DOE/ID/13324-1

[66] I. Dugic, The mechanisms of metal expansion penetration during solidification of grey cast iron, PhD Thesis, Linkoping University, 2006.

[67] K. D. Hayes, M. Owens, J. Barlow, D. M. Stefanescu, A. M. Lane, T. S. Piwonka, Steel penetration in sand moulds, Final Technical Report, DOE/ID/13324-T1,1997.

[68] T. S. Piwonka, Understanding metal penetration in green sand: cast iron, Modern Casting (1996)

[69] B. L. Kruse, V. L. Richards, P. D. Jacksom, An Investigation of the Causes that Lead to Burn-in/Burn-on in Heavy Section Steel Castings, American Foundry Society, IL, 2006.

[70] www.ikominerals.com/upæoads/media/01_burn-on_sand.pdf

[71] T. L. Donohue, H. F. Frye, Characterization and correction of Casting Defects, The Ganoksin Project. www.ganoksin.com.

[72] M. P.Groover, Fundamentals of Modern Manufacturing: Materials, Processes and Systems, 3rd Ed. John Wiley & Sons, USA, 2002.

[73] S. Kalpakjian, S. R. Schmid, Manufacturing Engineering and Technology, 5th ed., Pearson Prentice Hall, New Jersey, 2006.

[74] R. K. Leach, Fundamental Principles of Engineering Nanometrology, Elsevier, London, 2010.

[75] P. Demircioglu, M. N. Durakbasa, Investigation on machined metal surfaces through the stylus type and optical 3D instruments and their mathematical modeling with the help of statistical techniques, Measurement 44 (2011) 611-619.

[76] D. J. Whitehouse, Handbook of Surface Metrology, IOP Publishing, London, 1994.

[77] Geometriske produckt-specifikationwe (GPS), DS-Håndbog 114.5:2006, Danske standard 2006.

[78] L. D. Chiffre, Geometrical Metrology and Machine Testing, A compendium for Course 41731, DTU Mechanical Engineering.

[79] I. Asiltürk, M. Cunkas, Modelling and prediction of surface roughness in turning operations using artificial neural network and multiple regression method, Expert systems with applications 38 (2011) 5826-5832.

[80] S. Derbyshire, Coating Compositions, United States Patent: 4,279,946, 1981.

[81] A. Larena, F. Millan, M. Verdu, G. Pinto, Surface roughness characterisation of multilayer polymer films for graphitic arts applications, Applied Surface Science 174 (2001) 217-224.

[82] J. Järnström, P. Ihalainen, K. Backfolk, J. Peltonen, Rougness of pigment coatings and its influence on gloss, Applied Surface Science 254 (2008) 5741-5749.

[83] B. Griffiths, Manufacturing Surface Technology, Butterworth Heinemann, 2001.

[84] Alicon Infintefocus, IFM Manual IFM 3.1.1.2 EN 26.02.2009.

[85] M. Jolly, Castings, University of Birmingham, UK.

[86] F. Bonollo, S. Odorizzi, Eds. Numerical Simulations of Foundry Processes, SGE, Podova, 2001.

[87] MAGMA5 Online Help

[88] DISA 231 B (2013-B Compatible), Moulding System Application Manual, Reg. No. 9157 H8610, Ed. 06-08.

[89] B. E. Brooks, C. Beckermann, Prediction of Burn-on and Mold penetration in Steel Casting Using Simulation, in Proceedings of the 60th SFSA Technical and Operating Conference, Paper No. 5.3, Steel Founders' Society of America, Chicago, IL, 2006.

[90] A. -M Siouffi, Silica gel-based monoliths prepared by the sol-gel method: facts and figures, Journal of Chromatography A, 1000 (2003) 801-818.

[91] B. Topus, Gas permeation through sol-gel derived alumina and silica based membranes, PhD Thesis, the Graduate School of Engineering and Sciences of İzmir Institute of Technology, 2009.

[92] A.C. Pierre, Introduction to Sol-Gel Processing; Kluwer Academic Publisher: Boston, 2002.

[93] J. D. Wright, N. A. J. M. Sommerdijk, Sol-Gel Materilas Chemistry Applications, CRC Press, Boca Raton, 2001.

[94] C. J. Brinker, G. C. Frye, A. J. Hurd, C. S. Ashley, Fundamentals of Sol-gel dip coating, Thin Solid Films, 201 (1991) 97-108

[95] C. J. Brinker, A. J. Hurd, P. R. Schunk, G. C. Frye, C. S. Ashley, Review of Sol-Gel Thin Film Formation, Journal of Non-Crystalline Solids, 147-148 (1992) 424-436.

[96] C. J. Brinker, R. Sehgal, S. L. Hietala, R. Deshpande, D. M. Smith, D. Loy, C. S. Ashley, Sol-Gel Strategies for Controlled Porosity in Inorganic Materials, Journal of Membrane Science 94 (1994) 85-102.

[97] E. P. Plueddemann, Silane Coupling Agents, 2nd Edition, Plenum Press, New York, 1990.

[98] D. C. Montgomery, Design and Analysis of Experiments, 3rd. John Wiley & Sons, New York, 1991.

[99] BYK Additives and Instruments: http://www.byk.com/physical-properties/viscosity-cups.html

[100] Gardco/DIN 4 mm Viscosity Cup: http://www.gardco.com/din_cups.cfm

[101] WTIA Technical note 10, WRC Bulletin No. 430; BS7910; AS/NZS 3788; API 579.

[102] M. H. Dirikolu, A. Aktas, B. Birgoren, Statistical Analysis of Fracture Strength of Composite Materials Using Weibull Distribution, Turkish J. Eng. Env. Sci., 26 (2002) 45-48.

[103] B. Basu, D. Tiwari, D. Kundu, R. Prasad, Is weibull distrubtion the most appropriate statistical strength distribution for brittle materials?, Ceramics International 35 (2009) 237-246.

[104] Y. Xu, L. Cheng, L. Zhang, D. Yan, C. You, Optimization of sample number for Weibull function of brittle materials strength, Ceramics International 27 (2001) 239-241.

[105] R. Sakin, I. Ay, Statistical analysis of bending fatigue life data using Weibull distribution in glass-fiber reinforced polyester composites, Materials and Design 29 (2008) 1170-1181.

[106] A. Saghafi, A. R. Mirhabibi, G. H. Yari, Improved linear regression method for estimating Weibull Parameters, Theoretical and Applied Fracture Mechanics 52 (2009) 180-180.

[107] U. C. Nwaogu, T. Poulsen, R. K. Stage, C. Bischoff, N.S. Tiedje, New sol-gel refractory coatings on chemically-bonded sand cores for foundry applications to improve casting surface quality, Surface & Coatings Technology 205 (2011) 4035-4044.

[108] U. C. Nwaogu, N. S. Tiedje, Foundry Coating Technology: A Review, Materials Science and Applications, 2 (2011) 1143-1160.

[109] Cast TIP, "Controlling refractory coatings," Modern Casting, 2010. http://www.thefreelibrary.com/Controlling+refractory+coatings.-a022.

[110] L. Winardi, R.D. Griffin, "Effects of Coating drying Methods on LOI, Gas Evolution and Core Permeability," AFS Transactions paper, Vol. 08-047, 2008.

[111] T. K. Tokunaga, K. R. Olsen, J. Wan, Moisture Characteristics of Hanford Gravels: Bulk, Grain-surface, and Intra-granular Components, Vadose Zone Journal 2 Soil Science Society of America (2003) 322-329.

[112] S. N. Ramrattan, M. K. Joyce, “Final Report - refractory Coating Control” http://amc.aticorp.org/reports/wmu2009.pdf

[113] Ellingham Diagram Web Tool, http://www.engr.sjsu.edu/ellingham

[114] R. Elliot, Cast Iron technology, Butterworths & CoLtd, 1988.

[115] Metals Handbook, 19th Ed. Volume 15, Casting, ASM International, Metals park, Ohio, 1988.

[116] N. S. Tiedje, 25 year Perspective: Solidification, processing and properties of ductile iron, Materials Science and Technology, Vol. 26 No. 5 (2010) 505-514.

[117] K. -F. Nilsson, D. Blagoeva, P. Moretto, An experimental and numerical analysis to correlate variation in ductility to defects and microstructure in ductile cast iron components, Engineering Fracture Mechanics, 73 (2006) 1133-1157.

[118] D. E. Krause, Gray Iron-A Unique Engineering Material, http://www.ironcasting.org/Gray%20Iron%20-%20A%20Unique%20Material.htm

[119] http://www.foundry.elkem.com/dav/b0beff04cb.pdf

[120] http://www.foundry.elkem.com/dav/47ef3df359.pdf

[121] http://www.foundry.elkem.com/dav/9ba90240eb.pdf

[122] S. Boonmee and D. M. Stefanescu, On the Mechanism of Casting skin formation in compacted graphite cast iron, Int. J. of Metalcasting, 3, 4 (2009) 19-24.

[123] J. Baier, C. Grefhorst, W. kleimann, M. Köppe and O. Podobed, Manual of Casting Defects. Incidence and avoidance of defects attributable to moulding sands. 3rd ed., IKO Marl, 2011.

[124] S. Yamada, T. Konno, S. Goto, S. Aso and Y. Komatsu, Some behaviors and Characteristics of Decarburized Layer in Spheroidal Graphite Cast Iron, Int. J. Soc. Eng. Resour.,Vol. 10, No. 1 (2002) 88-92.

[125] D. Stefanescu, S. Giese, T. P.iwonka and A. Lane, Cast Iron Penetration in sand Molds, Part1: Physics of penetration defects and penetration Model, AFS Transactions, Vol.104 (1996) 1233.

[126] M. K. Joyce, M. Rebros and S. N. Ramrattan, Comparing Alternate Foundry Refractory Coating Measurement Systems, AFS transactions Paper 08-126(04) (2008) 463-481.

[127] J. Campbell, The concept of net shape for castings, Materials and Design 21 (2000) 373-380.

[128] P. -M Geffroy, M. Lakehal, J. Goñi, E. Beaugnon and J. -F. Silvain, Thermal and mechanical behaviour of grey cast iron and ductile iron castings using magnetic molding and lost foam processes, Journal of Materials Processing Technology 209 (2009) 4103-4111.

[129] T. Penko, Ultra-Performance Core Coating For Mass Iron Production: Specialized Methods for Developing & Evaluating New Coating Technology, Foseco Metallurgy, Inc.

[130] P. Beeley, Foundry Technology, 2nd edition, Butterworth-Heinemann, Oxford, 2001.

[131] M. A. Butt. A. Chughtai, J. Ahmed, R. Ahmed, U. Majeed and I. H. Khan, Theory of Adhesion and its Practical Implications: A Critical Review, Journal of faculty of Engineering & Technology, (2008) 21-45.

[132] Malvern Instruments, Zeta Potential: An introduction in 30 minutes, Zetasizer nano series technical note MRK654-01.

[133] A. Sze, D. Erickson, L. Ren and D. Li, Zeta-potential measurement using the Smoluchowski equation and the slope of the current-time relationship in electro-osmotic flow, Journal of Colloid and Interface Science 261 (2003) 402-410.

[134] Zeta-Meter Inc, Zeta Potential: A Complete Course in 5 Minutes.

[135] M. Boström, D. R. M. Williams and B. W. Ninham, Specific Ion effects: Why DLVO Theory Fails for Biology and Colloid Systems, Physical Review Letters, Vol. 87, No. 16 (2001) 168103.

[136] B. J. kirby and E. F. Hasselbrink, Review -Zeta potential of micropfluidic substrates: 1. Theory, experimental techniques and effects on separations, Electrophoresis 25 (2004) 187-202.

[137] T. Missana and A. Adell, On the Applicability of DLVO theory to the Prediction of Clay Colloids Stability, Journal of Colloid and Interface Science, 230 (2000) 150-156.

[138] http://foseco.com/end-markets/foundry/products-services/coating-preparation-plant-1/

[139] Christoph Genzler, Coating application Consistency - The Total Coating Management Concept, Proceedings of the 69th World Foundry Congress, China (2010).

[140] http://www.thefreelibrary.com

[141] Gietech BV ir Henderieckx, coatings for chemically Bounded Sand, 2005.

[142] J. Thole, C. Beckermann, Measurement of Elastic Modulus of PUNB Bonded Sand as a Function of Temperature, International Journal of Metalcasting, 2010 AFS.

[143] D. Liao, Z. Fan, W. Jiang, E. Shen, D. Liu, Study on the surface roughness of ceramic shells and castings in the ceramic shell casting process based on expandable pattern, Journal of Materials Processing Technology 211 (2011) 1465-1470.

[144] G. -X. Wang, E. F. Matthys, Experimental determination of the interfacial heat transfer during cooling and solidification of molten

metal droplets impacting on a metallic substrate: effect of roughness and superheat, International Journal of Heat and Mass Transfer 45 (2002) 4967-4981.

[145] A. Hamsaiid, M. S. Dargusch, T. Loulou and G. Dour, A predictive model for the thermal contact resistance at liquid-solid interfaces: Analytical developments and validation, international Journal of Thermal sciences 50 (2011) 1445-1459.

[146] A. I. Veinik, Thermodynamics for the foundryman, Maclaren and sons, London, 1968.

[147] L. Tomek, K. Rusín, I. Stachovec, Influence of Cement Moulding Sand on the Structure of Castings, Proceedings of the 69th World Foundry Congress, China (2010).

[148] G. A. Colligan, L. H. VanVlack and R. A. Flinn, The effect of temperature and atmosphere on iron-silica interface reaction, TRANSACTIONS of the American Foundrymen's Society, Proceedings of the 62nd Annual Meeting May 19-23, 1958, Ohio.

[149] R. Stötzel, C. Koch, Z. Ze and H. Huang, High Performance Refractory Coatings - Markets and Requirements, Proceedings of the 69th World Foundry Congress, China (2010).

[150] British Standard-Founding-Surface roughness inspection by visual tactile comparators, BS EN 1370:1997. http://bbs.6jc.cn/pdf/o/EN%201370-1997.pdf

[151] http://www.castingstechnology.com/public/services

Supplements

SUPPLEMENT 1

U. C. Nwaogu, T. Poulsen, C. Bischoff, N.S. Tiedje, *“Influence of New sol-Gel Refractory coating on the Casting properties of Cold Box and Furan Cores for Grey Cast Iron”*, Proceedings of the 69th World Foundry Congress, Hangzhou, China (2010).

Proceedings of 69th World Foundry Congress
October 16 - 20,2010, Hangzhou China

Influence of New Sol-Gel Refractory Coating on the Casting Properties of Cold Box and Furan Cores for Grey Cast Iron

*U. C. Nwaogu[1] T. Poulsen[2] C. Bischoff[2] N. S. Tiedje[1]

1. Technical University of Denmark, Department of Mechanical Engineering, Institute of Production and Process Technology, DK-2800 Kgs. Lyngby, Denmark
2. Danish Technological Institute, Centre for Material Testing, Kongsvang Álle 29, 8000 Århus, Denmark
*E-mail: ugon@mek.dtu.dk

Abstract New Sol-Gel coated sand cores made from coldbox and furan binder systems were investigated. The idea of the coating was to improve the surface quality of castings. Grey iron was cast on the cores in a sand casting process. The effect of the high temperature of the melt on the cores was assessed by measuring the heating curves. The viscosity of the coating, moisture content and the permeability of the cores were evaluated. The surface quality of the castings was investigated using SEM and OM. The results show that the moisture content of the cores affected the permeability. In furan cores the vapour transport zone (VTZ) when in contact with the melt is larger than it is in a coldbox which means the furan cores have higher moisture content. The new sol-gel coating has the potential for improving the surface quality of castings without negative effects on the graphite distribution. The surface of castings made using the new sol-gel coated furan cores show better surface quality than those made using the coldbox.

Keywords heating curves; permeability; moisture content; coldbox; furan; casting surface quality

1 Introduction

In high production iron foundries everywhere, silica sand is predominantly used for core making due to its availability and because it is cheaper than other refractory sand such as Olivine or Zircon sand. In many foundries the silica sand is bonded using a phenolic-urethane binder system cured with a gaseous amine catalyst. This type of process is called the cold box process and it has become a common core production technique in many foundries because of its low operational and production cost compared to other processes such as hot box and shell processes[1].

Another type of resin commonly used by foundries is the so-called furan resin. This is a low productivity binder designed for manufacture of large moulds and cores[2]. This type of resin exhibits a lower performance in terms of "throughcure" and cold strength development. However due to the reduced nitrogen content they are more acceptable for reclamation purposes[3]. The use of synthetic resins is regarded as a promising area of development of the foundry process because it has a high drying strength, provides an excellent surface quality in castings and permits advanced techniques[2].

Nevertheless, there are still some fundamental deficiencies in these technologies, notably; poor refractoriness of silica sand, non-linear thermal expansion of the bonded core sand and inherent low hot strength of the binder systems. The poor refractoriness of the silica sand and non-linear thermal expansion of the bonded core sand can lead to some expansion defects on the surface of the castings such as sand burn-in, metal penetration and/or veining or scab[1].

Among the sand expansion defects mentioned above, veining or finning has been one of the most well-known and well-recognized casting defects for many years. It is a defect caused when sand grains on the surface of a mould or a core expand due to heat transfer from the molten metal[4]. Veining is associated with silica sand and results from the penetration of liquid metal into cracks formed during differential expansion of the core during heating. The differential expansion is linked to the $\alpha - \beta$ phase transition of quartz, which happens to be the main constituent of silica. The rapid expansion of silica sand up to 600 ℃ and especially at 573 ℃, where the $\alpha - \beta$ phase transformation occurs, is the cause of stresses in the binder structure. These stresses cause crack formation and liquid melt flows into the cracks causing finning or veining defects. The removal of these casting defects, called fettling, requires a lot of extra work, energy, time and money[4].

The use of refractory coatings on cores is fundamental to obtaining acceptable casting surface quality and is used on resin bonded cores in iron production foundries. As the need for more complex, critical castings and higher quality standards grows, the function of the core coatings utilized in the process becomes important[5].

In this study new sol gel-coated sand cores made from cold box and furan binder systems were investigated. The approach used was to make castings on these cores and then to evaluate the surface quality of the castings. Several other characterizations of the coated and uncoated cores were made such as temperature measurement, moisture and permeability tests and optical microscopy.

2 Experimental Procedure

At Frese metal-& stålstøberi A/S, Slagelse, Denmark, the cores are made from fine silica sand with the chemical composition given in Table 1 and furan and cold box binder systems are used. The cores have the following dimensions; length of 102 mm, diameter of 33 mm at both ends and a middle section diameter of 50 mm. The cores are made from regenerated silica sand with a Furan Resin Binder of Phenol Formaldehyde/Furfuryl Alcohol (PF/FA) type. PF/FA has FA contents in the region of 30 and 70%. The cold box cores are made using the Amine/Phenol Urethane Process. The bond is based on the use of a two part isocyanate, part one being a phenolic resin and the second part an isocyanate contained in a solvent.

Table 1 Chemical composition of the core sand

Compounds	SiO_2	Al_2O_3	K_2O	Fe_2O	CaO	TiO_2	Na_2O
Composition (%)	98.61	0.69	0.51	0.05	0.01	0.07	0.05

The result, promoted by a reaction with Triethylamine (TEA) or dimethylethylamine (DMEA) vapour, is the formation of a solid polyurethane resin[3]. The cores are coated for 1, 3 and 5 s with the new sol gel coating containing 40% refractory filler material of grain size 15 μm, produced at the Technological Institute, Århus, Denmark, by a dipping method. To assess the performance of the sol-gel coating in improving the surface quality of castings, commercial foundry water-based and alcohol-based coatings performances were compared with the sol-gel coating.

The viscosity of the coatings was tested according to ASTM D1200 standard using "Ford cup 4" having an orifice diameter of 4.0 mm at 20 ℃ environmental temperature. The Ford cup 4 is shown in Fig. 1.

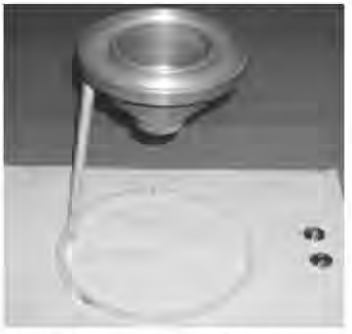

Fig. 1 Ford cup 4 used for measuring the viscosity of the coatings

The moisture test was performed on 5 pieces of each of the cores for each treatment time i. e. 0 (uncoated), 1, 3 and 5 s in an oven at 140 ℃ until constant weight was achieved. Five pieces of core were used to ensure the reliability of the data as variations might come from the core shooting and coating processes. The percentage average weight difference gives the moisture content.

The permeability test was also performed on 5 pieces of each of the cores for each of the treatment time as specified in the moisture test above, with a "GF" Electric Permeability Meter PED. The cell for the specimens was adapted to suit the geometry of the cores as shown by the schematic diagram in Fig. 2. The permeability testing machine gives direct permeability reading from the scale. Although, permeability is defined as the volume of air in cm^3 which passes in 1 min, under pressure of 1 g/cm^2 through a specimen of 1 cm^2 in cross sectional area and 1 cm high.

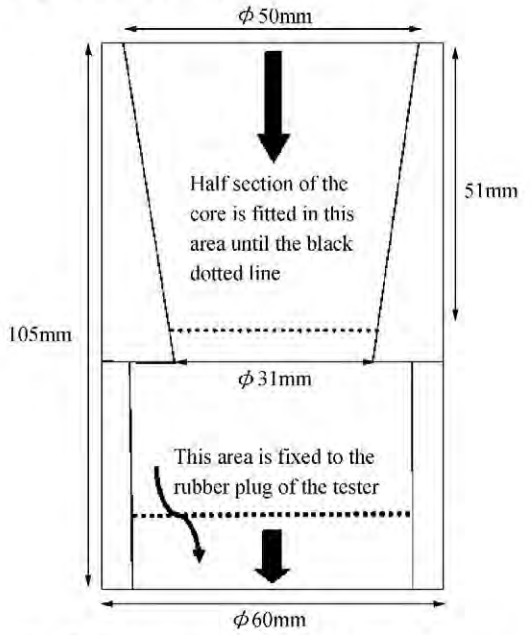

Fig. 2 The schematic diagram of the cell for core specimens for the permeability test

This is expressed mathematically as:

$$P = \frac{v \times h}{p \times a \times t} \quad (1)$$

where P is permeability number, v is the volume of air (cm^3) passing through the specimen, h is the height (cm) of the specimen, p is the pressure of the air (g/cm^2), a is the cross sectional area (cm^2) and t is time (min)[6].

The casting process used was a sand casting process with the layout shown in Fig. 3. The grey iron melt composition is provided in Table 2. The charge was melted in an Inductotherm induction furnace operated at a frequency of 1000 Hz and a power of 125 kW. The casting was carried out when the furnace temperature was 1 465 ℃, measured with a thermocouple.

Table 2 The melt composition

Composition	Haematite	Cast iron returns	Inoculant	Silica
Weight (kg)	20	40	0.012	0.3

The temperature profile in the cores when in contact with the melt was measured by using TIG welded k-type

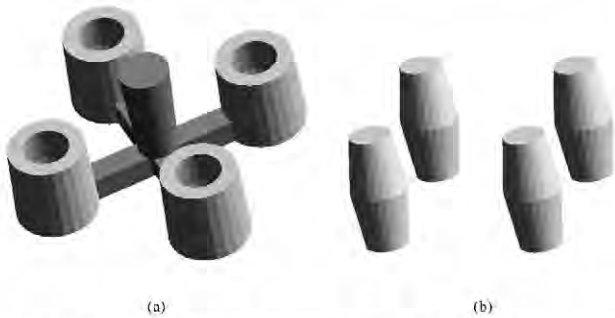

Fig. 3 The casting layout created with MAGMASOFT simulation software
(a) the casting with Down sprue and runners;
(b) the cores

thermocouples (ϕ = 0.2 mm) embedded in the cores up to the mid section. These thermocouples were connected to the DASYLab data acquisition system laboratory software, version 8.

The surface quality investigation of the castings after solidification and cleaning was performed on a scanning electron microscope (SEM), in order to elucidate the surface morphology due to the influence of the coating. The microstructure of the casting interface with the cores is examined with Olympus optical microscope (OM) with Infinity X Camera using Deltapix Camera software.

3 Results

3.1 Coating Viscosity

The viscosity test results showed that the sol-gel coating is less viscous compared to the two other commercial coatings (Fig. 4). The water-based coating has the highest viscosity and also penetrated less into the cores as shown in Fig. 5. However, the penetration of the sol-gel coating was uniform and comparable to the commercial coatings and the drip property was better than that of water-based coating due to water-based coatings have slow drying or curing rate, hence it is always baked to enhance drying.

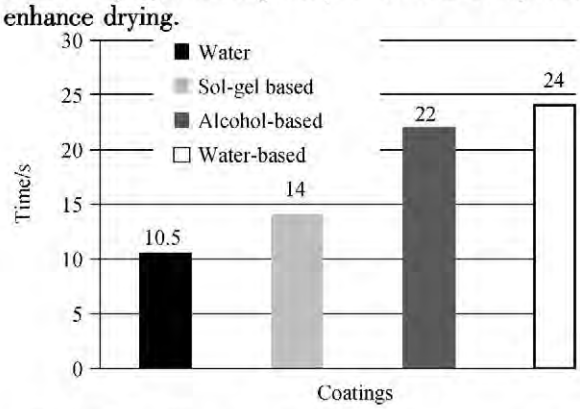

Fig. 4 The different coatings viscosity relative to the viscosity of water

3.2 Molsture Content

The moisture content results are presented in Fig. 6. The moisture content in the cold box cores reveals that the coated cores have lower moisture content compared to the uncoated cores.

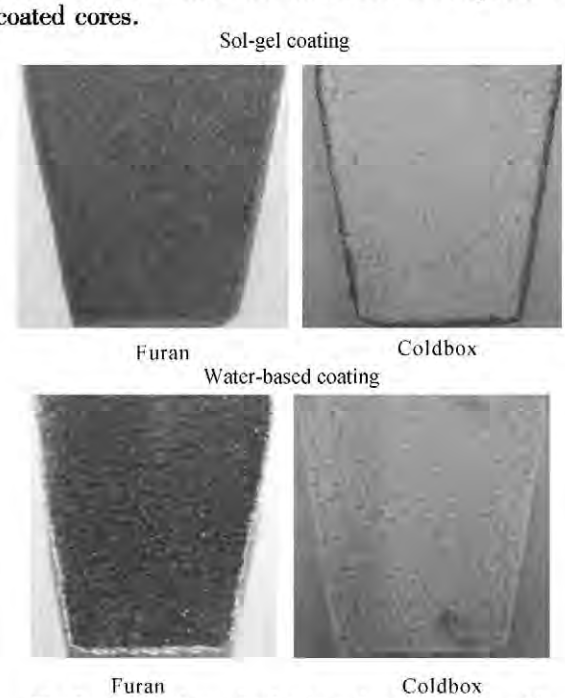

Fig. 5 Comparison of sol-gel coating penetration with water-based coating penetration into the cores

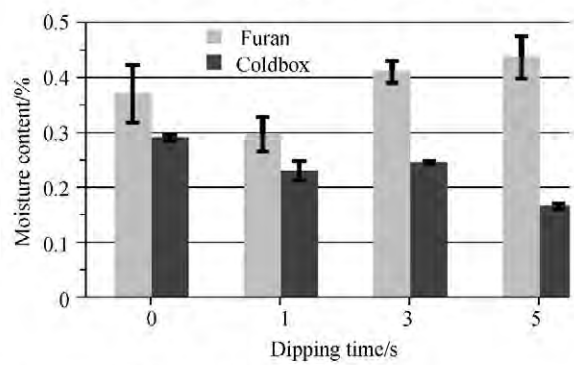

Fig. 6 Variation of % moisture content of furan and cold box cores with dipping time in sol-gel coating

The moisture content of the cores coated for 1 and 3 s is higher than that of the cores coated for 5 s. For furan cores the reverse trend was observed as can be seen from Fig. 6. The moisture content increased with the dipping time. This reverse variation in the moisture content of both cold box and furan cores with dipping time is attributed to the different products of the core-binder-coating reactions with different moisture affinity. From these results, it is suggested that the products from cold box reactions may be hydrophobic while those products from furan reactions are hydrophilic.

Examining the vapour transport zone (VTZ), the

temperature profile of the two binder systems showing the VTZ is shown in Fig. 7. The VTZ has essentially a uniform temperature of around 100 ℃ and uniform moisture content across the whole zone for each of the treatments. The VTZ moves deeper into the cores and grows larger with time for furan cores and thins down with time for cold.

Box cores as can be seen in Fig. 7. The VTZ for furan cores is larger which confirms that furan cores have higher moisture content than the coldbox cores. Furthermore, the trend observed in the moisture test is also the same with trend observed from the VTZ, which justifies the moisture test results.

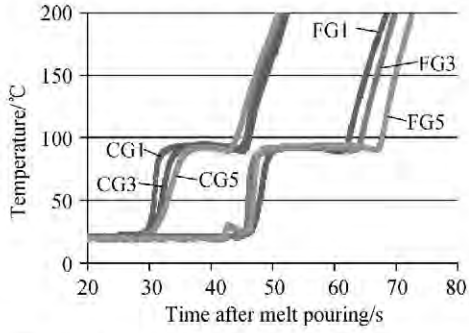

Fig. 7 Temperature profile of the vapour transport zone in cold box (CG) and furan (FG) cores dip-coated in sol-gel for 1, 3 and 5 s

3.3 Permeability Test

The permeability results presented in Fig. 8 show that the coating influenced the permeability of the coated cores. The various coatings have different levels of effects on the permeability of the coated cores. The coating reduced the permeability of both cold box and furan cores. The water-based coating reduced the permeability of both cores significantly followed by alcohol-based coating.

Sol-gel coating has medium permeability reduction effect on both cores. These results agree with what Winardi et. al[7] concluded: the higher the moisture content the lower the permeability. Also the permeability results are consistent with the viscosity results with water-based coating having the highest viscosity with lowest permeability for both cores.

Following the results obtained from the permeability test, it is expected that if the permeability of the coated cores is not drastically reduced; the castings from these cores may have good surface appearance. This is because as the permeability of the sand decreases, surface finish improves, provided that permeability is not so low that there are surface defects on the castings.

3.4 Casting Surface Quality

The surfaces of the castings in contact with uncoated and coated cold box and furan cores are shown in Fig. 9. By visual inspection, it can be seen that surfaces of the castings made with uncoated cores are poor in quality

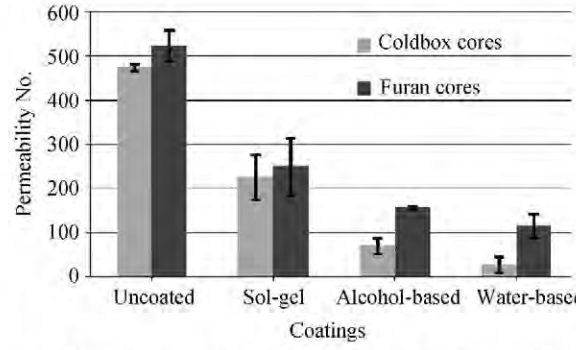

Fig. 8 The permeability of coated and uncoated coldbox and furan cores with different coatings

compared to the surfaces of casting made with coated cores. The casting made with uncoated cold box core showed extensive metal penetration compared to that of casting made with uncoated furan core. The reason for this may be due to that fact that furan core was made from more of regenerated sand which had already undergone severe thermal shock and therefore has higher resistance to thermal distortion than cold box cores which are made from fresh sand which higher expansion tendency. The surface of castings made with sol-gel coated furan and coldbox cores shows that the sol-gel coating has high and competitive potential for improving the casting surface quality relative to the commercial coatings. Their surfaces are smooth and free from metal penetration and veining tendency. The surface of the casting made with water-based coated coldbox core showed veining tendency (red mark, Fig. 9). Further the effect of coating layer thickness is also obvious on the surface of the castings made with water-based coating for both cold box and furan cores (red spotted mark, Fig. 9). This is due to high viscosity of this coating, consequently penetration becomes difficult leading to the deposition of more filler material on the surface of the core. The surface appearance of the castings where the castings made contact with 5 s sol-gel dip-coated cold box and furan cores are shown in Fig. 10. From the microstructure presented, the casting made with furan cores have better surface quality compared to those made with cold box cores. The reason is attributable to the use of regenerated sand with furan binder system, as previously mentioned, with higher resistance to thermal shock. The interfacial microstructure of the castings made with coated and uncoated cores are presented in Figs. 11 and 12 for both cores. From the figures, it can be seen that the distribution of the graphite flakes in the castings is uniform for both coated and uncoated coldbox and furan cores. Therefore the coating has no effect on the distribution of the graphite flakes. However, the graphite flakes in the castings made with coated cores are more refined than graphite flakes in the castings made with uncoated cores. This will enhance the strength of the casting around this region.

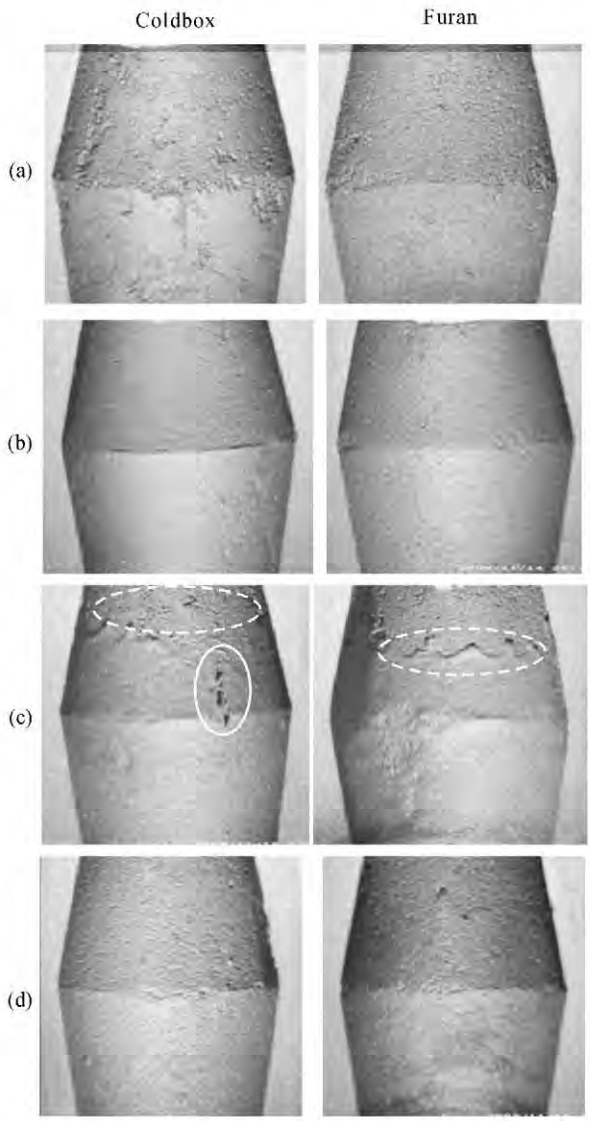

Fig. 9 The surface of the castings in contact with the cores after sand blasting (not to scale)
(a) uncoated; (b) sol-gel coating;
(c) water-baseol cating; (d) alcohol-based coating

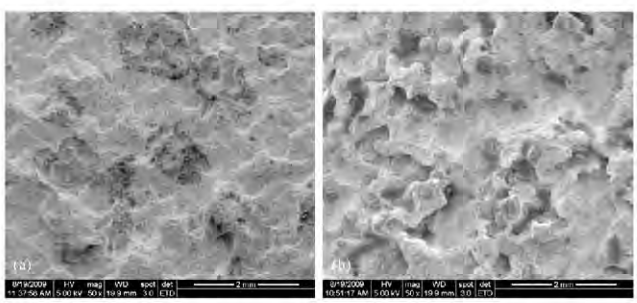

Fig. 10 The surface morphology of casting made with
(a) furan core; (b) cold box core dip-coated for 5 s with sol-gel coating

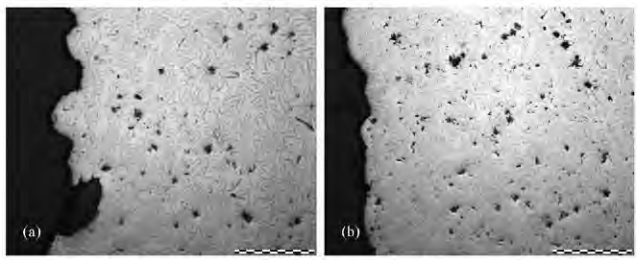

Fig. 11 Interfacial microstructure of castings made with
(a) uncoated; (b) 5 s sol-gel dip-coated cold box cores

4 Discussion

The fundamental purpose of this investigation was to understand the effect of coating on cores with particular focus on the use of coating to reduce or delay the expansion tendencies of cores when in contact with the melt. This is achieved by incorporating particles with a low coefficient of thermal expansion into the coating, as fillers.

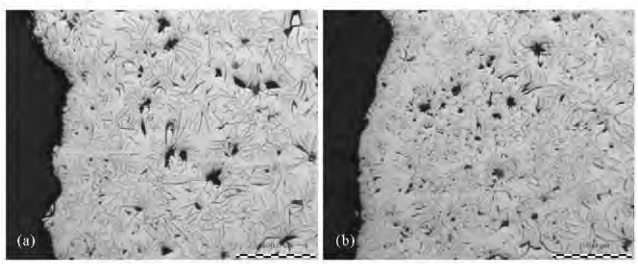

Fig. 12 Interfacial microstructure of castings made with
(a) uncoated; (b) 5 s sol-gel dip-coated furan cores

When this is done, the delay in the rapid expansion gives enough time for the melt to start solidifying from the melt/core interface such that when the associated crack due to the expansion occurs, the melt in the interface has solidified. Therefore, melt will not flow into the cracks to form fins or veins. On pouring the melt into the mould with cores during the casting process, the immediate surface temperature of the cores rapidly increases. Subsequently, this heat diffuses deeper into the core substrate. The rate of this heat transfer is governed by many factors including the thermal conductivity of the core substrate and the heat transfer between the melt and the core surface and the moisture content. The overall effect of this temperature rise on the cores is the thermal expansion of the substrate. However, this thermal expansion is not uniform across the cross section of the core, so thermal stresses are created as the core surface wants to expand more than the inner areas of the core. The risk of crack formation as the temperature rises is very high as only compressive stresses are in operation. These stresses are more common with silica sands than with any other refractory sand, due to the non linear thermal expansion of the silica sand as a result of the phase change from α-quartz to β-quartz at 573 ℃. As the

temperature of the melt/core interface exceeds 600 ℃, the surface of the core that has expanded starts to contract while the inner part of the core is still expanding.

At this point, the surface of the core can crack, because at this temperature the binder may have lost its hot strength and likely to break down. If the melt is still liquid and the core surface temperature is above the melt solidus temperature, the melt will flow into the crack causing finning or veining.

Therefore, by incorporating filter dust with low coefficient of thermal expansion as refractory filler material for the new sol-gel coating used for cores, it is expected that the expansion tendency will be reduced thereby eliminating the formation of vein or fin or metal penetration. The results presented for the surface quality of the castings show that the sol-gel coating has the potential for improving the casting surface quality.

5 Comclusion

From the results obtained, the following conclusions may be drawn:

❖ In both binder systems studied, the coating on the cores reduced the surface roughness of the castings relative to that of castings produced using the uncoated cores.

❖ Furan cores coated with the same treatment time as cold box cores have a higher moisture content.

❖ The coating reduced the permeability of cold box and furan cores.

❖ The vapour transport zones of the furan cores are larger than those of a cold box core receiving the same treatment.

❖ The new sol-gel coating containing filter dust as filler material has competitive potential relative to the two other commercial coatings.

Acknowledgement

This work was partly financed by Technical University of Denmark and partly by the Danish Research Council for Technology.

References

[1] T. Birch, D. Bell, Improved Iron Casting Quality through Application of Advanced Coating Technology, Foseco Foundry Practice, 243 (2005) :16 - 23.

[2] X. Zhou, J. Yang, G. Qu, Journal of Materials Processing Technology, Study on Synthesis and Properties of Modified Starch Binder for Foundry, 183 (2007) :407 - 411.

[3] T. A. Burns (Ed.), The Foseco Foundryman's Handbook, 9th ed., Staffordshire, 82 - 86.

[4] A. Schrey, NORACEL * W 100 - A new technology to prevent veining defects, Foseco Foundry Practice, 246 (2007) :1 - 7.

[5] N. Hodgkinson, T. Birch, Improving Foundry Profitability through the use of RHEOTEC * XL Coating, Foseco Foundry Practice, 240 (2003) :1 - 5.

[6] G. Casalino, L. A. C. De Felippis, A. Ludovico, Journal of Materials Processing Technology 166 (2005) 1 - 8.

[7] L. Winardi, H. E. Littleton, R. D. Griffin, J. A. Griffin, AFS.

[8] Transactions 2008 © American Foundry Society, Gas from Green Sand Molds and Vapour Transport Zone (2008) :381 - 391.

SUPPLEMENT 2

U. C. Nwaogu, T. Poulsen, R. K. Stage, C. Bischoff, N.S. Tiedje, "*New sol-gel refractory coatings on chemically-bonded sand cores for foundry applications to improve casting surface quality*", Surface & Coatings Technology 205 (2011)

DOI 10.1016/j.surfcoat.2011.02.042

Surface & Coatings Technology 205 (2011) 4035–4044

Contents lists available at ScienceDirect

Surface & Coatings Technology

journal homepage: www.elsevier.com/locate/surfcoat

New sol–gel refractory coatings on chemically-bonded sand cores for foundry applications to improve casting surface quality

U.C. Nwaogu [a,*], T. Poulsen [b], R.K. Stage [b], C. Bischoff [b], N.S. Tiedje [a]

[a] Technical University of Denmark, Department of Mechanical Engineering, Institute of Production and Process Technology, DK-2800 Kgs. Lyngby, Denmark
[b] Danish Technological Institute, Centre for Material Testing, Kongsvang Álle 29, Aarhus, Denmark

ARTICLE INFO

Article history:
Received 10 December 2010
Accepted in revised form 16 February 2011
Available online 26 February 2011

Keywords:
Sol–gel coating
Castings
Refractory filler
PUCB cores
Dip coating
Silica sand

ABSTRACT

Foundry refractory coatings protect bonded sand cores and moulds from producing defective castings during the casting process by providing a barrier between the core and the liquid metal. In this study, new sol–gel refractory coating on phenolic urethane cold box (PUCB) core was examined. The coating density, viscosity, moisture content and wet and dry weight of the coating were evaluated on cores that had been coated at three different dip-coating times. The coating coverage, surface appearance and depth of penetration into the cores were examined with a Stereomicroscope. Gray iron castings were produced with sol-gel coated and uncoated cores and the results were related to the coating properties. The casting results were also compared with castings made with cores coated with commercial alcohol-based and water-based foundry coatings. The analyses show that castings produced with sol–gel coated cores have better surface quality than those from uncoated cores and comparable surface quality with the commercial coatings. Therefore, the new sol–gel coating has a potential application in the foundry industry for improving the surface finish of castings thereby reducing the cost of fettling in the foundry industry since the raw materials and technology are easily affordable.

1. Introduction

Sol-gel coating technology [1,2] has been applied to various areas of coating production for corrosion protection [3,4], wear resistance [5], thermal barrier [6], anti-soiling [7], anti reflective [8,9] etc. but has so far not been applied to the foundry industry. In this regard, the coating being investigated is a novel application for the sol–gel coating technology. Owing to the intense developments in the field of sol–gel technology the availability of affordable sol–gel silane precursors present the technology as a suitable alternative/compliment to foundry refractory coatings. A number of advantages are affiliated with applying the technology. The inorganic ≡ Si-O-Si ≡ (siloxane) network that form the foundation of silica based sol–gel coatings provides a strong glass ceramic surface. By applying the coating to cores, cross binding of the sand grains with the sol–gel coating would induce a strengthening of the sand material resulting in a stronger protective barrier between the core and liquid metal. This added strength would prove valuable to reduce surface defects during casting. The inorganic nature of the sol–gel coating also has added environmental benefits by reducing undesired gaseous by-products from pyrolysis during casting. Finally, because a large number of precursors are available for manufacturing sol–gel coatings the technology presents the opportunity to chemically modify the coating to meet specific foundry demands.

Refractory coatings help foundries to protect chemically-bonded sand cores and moulds from producing castings with surface defects, such as metal penetration, veining, erosion etc. Metal penetration and veining defects are serious problems caused by the poor refractoriness of the silica sand and non-linear thermal expansion of the bonded sand core when in contact with the molten metal. The differential expansion is linked to the α–β phase transition of quartz, which is the main constituent of silica. The rapid expansion of silica sand up to 600 °C and especially at 573 °C, where the α–β phase transformation occurs, is the cause of thermal stresses in the core materials/binder structure. These stresses cause crack formation and liquid metal flows into these cracks, causing finning or veining defects. The removal of casting defects, called fettling, requires a lot of extra work, energy, time and money [10,11].

The use of refractory coatings on cores is fundamental to obtaining acceptable casting surface quality and is used on resin bonded cores in iron production foundries. As the need for more complex, critical castings and higher quality standards grows, the function of the core and mould coatings utilized in the process becomes important [12]. However, the understanding of the coating/core material interaction has been neglected for some decades. When applying a refractory coating on cores or moulds, it is important that a uniform coating layer free from surface imperfections such as runs, drips or cracks, is obtained. Otherwise, these features will reflect on the surface of the castings leading to defective castings.

* Corresponding author. Tel.: +45 45254737; fax: +45 45934570.
E-mail address: ugon@mek.dtu.dk (U.C. Nwaogu).

0257-8972/$ – see front matter © 2011 Elsevier B.V. All rights reserved.
doi:10.1016/j.surfcoat.2011.02.042

A literature survey reveals that surprisingly little research is carried out on a topic that is of great importance for the surface quality of castings. This has led to foundries loosing focus as to what parameters are to be considered in order to control foundry coatings applied on cores and sand moulds. In this study, it is our objective to redirect research into foundry coatings by developing a new sol–gel foundry coating for sand cores and investigating the performance in improving casting surface quality. It is also the objective of this study to analyze the coating/core material interaction and relate this to the surface quality of the castings obtained.

2. Material and methods

The refractory filler used in the preparing sol–gel coating is filter dust. The particle size and size distribution of the filter dust was measured by Malvern Mastersizer 2000 using laser diffraction with wet analysis.

All refractory sol–gel coatings were prepared from a sol–gel stock solution obtained by acid (0.1 N HCl) catalyzed hydrolysis with water of 3-glycidyloxypropyltrimethoxysilane (GLYMO, Degussa) and aluminium (III)-*s*-butoxide, 75% solution in *s*-butanol (AL, ABCR). After stirring the sol for 30 min., propyltrimethoxysilane (PTMO, Evonik/Degussa) was added and stirring continued for an additional 30 min. The molar composition of the stock sol–gel solution was GLYMO:AL:HCl:PTMO = 385:3:1:95. The stock solution was mixed with a 3% bentonite suspension in demineralized water for 30 min. affording a mixing ratio between sol–gel stock solution and bentonite suspension of 1:6.67. Refractory filter dust of average particle size of 15 μm (from analysis) was added and the blend was stirred for approximately 2 h until a homogeneous suspension was obtained. The coatings were prepared with 40, 50 and 60% by mass of filter dust (coatings referred to as P40, P50 and P60 respectively). Low percentages of the solid content did not provide surface coverage from our preliminary studies. The PUCB cores are produced from the Amine/phenol Urethane Process and silica sand of American Fineness Number (AFN) of 53 and mean grain size of 0.263 mm (information from the supplier, Dansand A/S). The bond is based on the use of a two part isocyanate, part one being a phenolic resin, and the second part an isocyanate contained in a solvent. The result, promoted by a reaction with triethylamine (TEA) or dimethylethylamine (DMEA) vapour is the formation of a solid polyurethane resin holding the sand grains. The cores are coated with the sol–gel based coating, and water-based and alcohol-based coatings by dipping method for 1, 3 and 5 s (D1, D3 and D5 respectively). These times were chosen because they cover the range of dipping times used by the foundries.

The coating density was determined by weighing 200 ml of coating in a suitable beaker. The density, ρ (g/cm^3) was calculated from the expression given in Eq. (1).

$$\rho = \frac{m}{V} \tag{1}$$

Where m = mass (g) and V = volume (cm^3).

The coating viscosity was determined using the flow cup method. The Ford Flow Cup with outlet orifice of 4 mm was filled with the coating to the brim (100 ml). A stop watch was used to measure the time it takes the coating to drain through the hole until the first drop appears. This time, called the efflux time is the viscosity in seconds. The Ford Flow Cup viscosity in seconds is converted into Stokes viscosity by interpolation using the Ford Flow Cup Viscosity Conversion Chart which plots centistokes viscosity values against efflux time for different Ford Flow Cup numbers (for this experiment Ford Cup #4 was used).

The core material moisture content test was performed on five cores for each treatment time i.e. uncoated (0 s), 1, 3 and 5 s in an oven at 140 °C until constant weight was achieved. The weight of each core was measured before and after oven-drying. The percentage average of the sum of the mass differences before and after oven drying for each time is taken as the moisture content. The use of five cores ensures the reliability of the data since variations might come from the core making and coating processes.

The wet weight of coating on cores was obtained by measuring the mass of five uncoated cores initially, then weighing the cores immediately after coating with different coatings for 1, 3 and 5 s. The average mass differences before and after wet coating gives the wet weight of the coating on cores. The dry weight is determined by drying the coated cores in an oven at 140 °C for 1 h, and finding the average mass differences between the dried coating and the uncoated cores for the respective treatment times respectively.

The surface appearance of the coatings and the penetration depth into the cores were examined with Zeiss Stemi DV4 Stereo Microscope with LED Illumination. The measurements of proud layer thickness (coating deposit on the surface of the core) and the sub-surface layer (penetration depth) were made with image analysis software — *Image-Pro® Plus* version 6.0. Five measurements were made following the trace of the deposited and penetrated layers.

The casting process used was a sand casting process with the casting layout and core geometry shown in Fig. 1. The chemical composition of the grey iron melt is provided in Table 1. The charge was melted in an Inductotherm induction furnace operated at a frequency of 1000 Hz and a power of 125 kW. The casting was carried out when the furnace temperature was 1465 °C, measured with a thermocouple. The moulds contained uncoated PUCB cores and PUCB cores coated with sol–gel coating and two commercial coatings (alcohol-based and water-based coatings) with similar densities and viscosities as the sol–gel coating. The surface quality of the castings was elucidated by visual inspection, in which surface roughness and melt penetration into the cores were examined. The surface finish/quality can also be characterized quantitatively by average roughness (Ra) parameter [13]. The surface profile roughness, Ra of the castings was examined by using Alicona InfiniteFocus® G4 3D Optical Measuring Device (Germany). The operating principle is based on

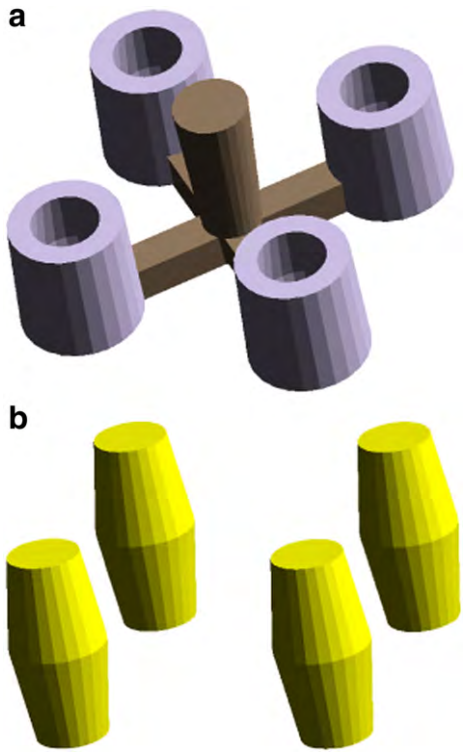

Fig. 1. 3D-CAD-Model of casting layout (a) the casting with Down sprue and runners (b) the cores.

Table 1
The melt composition.

Composition	Carbon	Silicon	Manganese	Phosphorus	Iron
Weight (%)	3.5	2.6	0.2	0.02	Bal.

Focus-Variation. A total number of 12 measurements were made on each surface of the castings. All measurements were made with 2.5× objective, a cut off length, Lc of 800 μm and an optical lateral resolution of 5.6 μm at a sampling distance of 3.52 μm. The Ra results were analysed by descriptive statistics, analysis of variance (ANOVA) and comparison of the means, to establish the influence of the coatings on the surface roughness of the castings. ANOVA was used to evaluate whether there is any indication that the group means differ. If the ANOVA results show that the group means differ, then multiple comparison tests is used to determine which of the mean(s) is/are different. The multiple comparison test used is Scheffe's Test. This test compares the difference between each pair of means with suitable adjustment for the multiple testing (in this study, 12 measurements for each surface).

3. Results

3.1. Refractory filler material particle size

The results from the particle size and size distribution analysis are presented in Fig. 2. It can be seen that the filler material has an average particle size of 15 μm. It is also clear that the bulk volume of the particles have sizes less than 100 μm.

3.2. Coating density

The coating density increases with the percentage solid content as shown in Fig. 3. This is attributed to the closure of the pore spaces in the matrix of the core by filter dust particles thereby reducing the pore-spaces. The result of this is shorter distances between filler particles reducing the volume of voids in the core and coating. Furthermore, this results in higher mass of particles per unit volume of coating matrix with increase in the percentage solid content. This is also expected to reflect in the viscosity of the coatings.

3.3. Coating viscosity

The coating viscosity as shown in Fig. 4 follows a similar trend with the coating density. The viscosity data presented is an average of 3 measurements and the error bars show 95% confidence interval. The viscosity increases with increase in the amount of solid content in the coating. This is due to the same reason stated for coating density. The

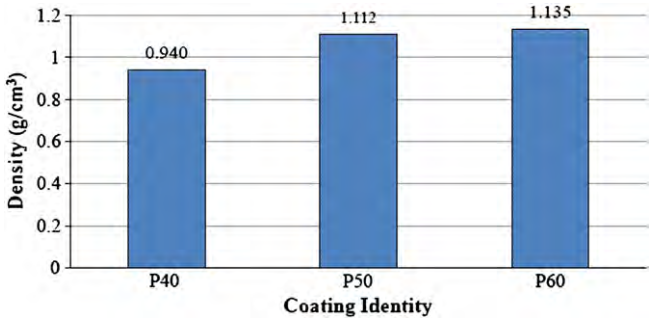

Fig. 3. Variation of sol–gel coating density with percentage solid content.

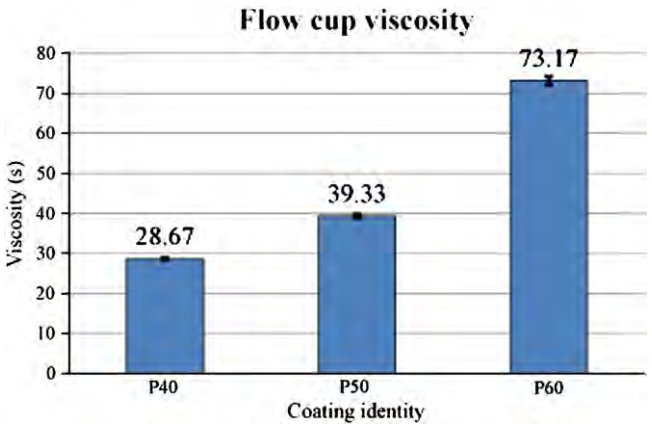

Fig. 4. Variation of sol–gel coating viscosity with percentage solid content. The error bars indicate a 95% confidence interval.

viscosity (s) from Ford Flow Cup measured for P40, P50 and P60 sol–gel coatings are 29, 39 and 73 respectively. The equivalent Stokes viscosity is 95, 155 and 285 centistokes respectively.

3.4. Mass of wet and dry coatings and moisture content

The results presented in this sub-section are for the respective dipping times 1, 3 and 5 s as can be seen from Fig. 5. The mass of wet coating on the cores after dipping increased with dipping time for all the percentage solid content as can be seen from Fig. 5(a)–(c). There is a deviation in the expected trend from the coating with 50% solid content dip-coated for 3 and 5 s (Fig. 5(b) and (c)). This unexpected behaviour of 50% solid content coating at these two dipping times is attributed to the fact that the density and viscosity of the coating could not allow further penetration of the coating into the core.

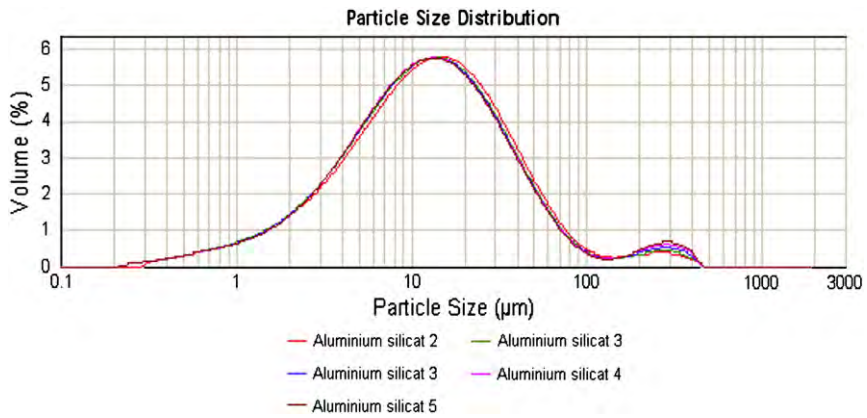

Fig. 2. Size distribution plot for the filter dust.

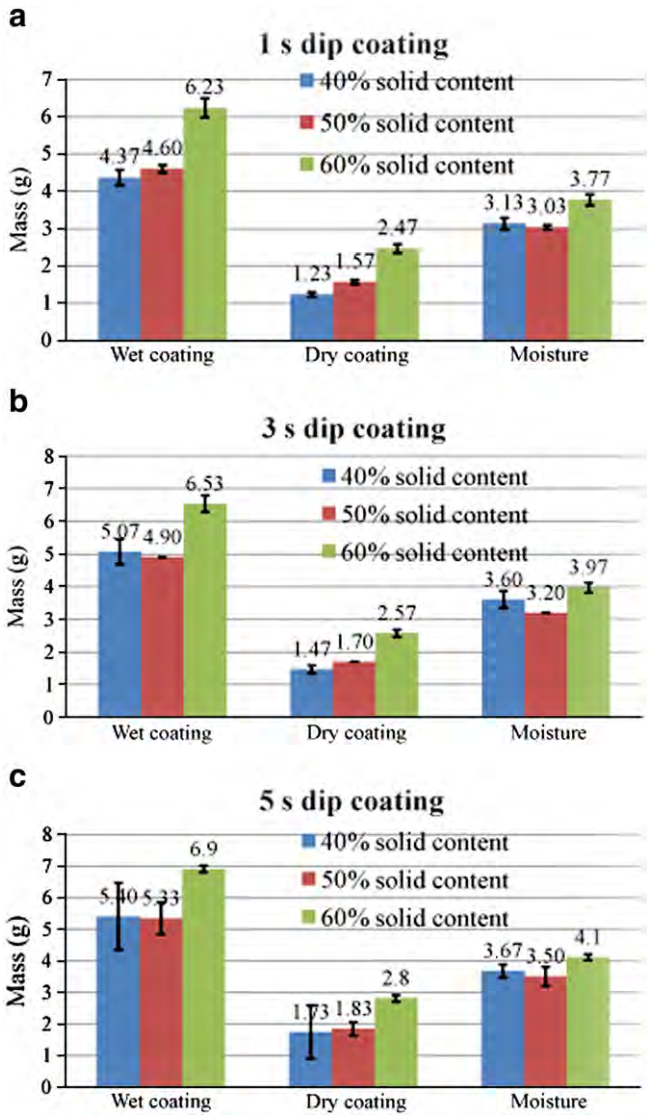

Fig. 5. Variation of mass of wet coating, dry coating and moisture on the cores after dipping and curing with dipping time and percentage solid content (a) 1 s dip coating (b) 3 s dip coating and (c) 5 s dip coating. The error bars indicate 95% confidence interval.

Therefore, less amount of coating penetrated into the core leaving just moderate amount of coating material adhering to the core unlike in the case of less viscous coating (40% solid content) where more penetration is likely to occur. In the case of 60% solid content coating, which has the highest density and viscosity, the coating penetrated less but significant amount of coating material is deposited on the surface.

After curing of the coating, the mass of the dry coating material left on the cores increases with dipping time as shown in Fig. 5(a)–(c). Furthermore, the mass of dry coating on the cores also increases with the percentage solid content for each dipping time. It seems that the variation in wet and dry coating masses is particularly high in the 40% coating, especially for longer dipping times. The wet coating mass depends on the amount of liquid carrier penetrating into the core. This is probably highly variable due to variable volume of pore spaces in the core and coating matrices.

As shown in Fig. 5(a)–(c), the moisture content of the coating on cores increases with the dipping time. However, at each dipping time, the coating with 50% solid content has lower moisture content relative to the other coatings. This means that less coating penetrated the cores and moderate amount of coating material with lower moisture relative to the other coatings deposited on the surface of the cores. The reason for this could be that the density and viscosity level of the coating controlled the penetration and also the amount of coating material deposited on the surface of the core. When there is high coating penetration depth and thick coating deposit on the surface of the cores, these cores are bound to have high moisture content as it is the case with 40 and 60% solid content respectively unlike the 50% solid content coating with lower moisture content. This lower moisture content is favourable to the permeability and strength of the PUCB cores.

3.5. Coating coverage and surface appearance

The surface appearance of uncoated PUCB core is presented in Fig. 6. The image shows that the sand grains are packed in a relatively open structure with a significant amount of pore space between the grains. The surface roughness is clearly determined by the sand grains. From Fig. 7, it is clear that the sol–gel coating completely covered the sand grains at all the percentage solid contents and dipping times as shown in Fig. 7(a)–(i). However, cracks are visible on the surface of the coatings. These cracks developed during the process of curing of the coating as the moisture is driven off from the coating. Furthermore, the coating contains bentonite as a suspension agent which swells on absorbing moisture. On drying, it cracks as the moisture is released [14]. These cracks increase in size with percentage solid content and dipping time. The cracks can also be initiated by the thermal stress induced in the coating system during the process of curing at a temperature of 140 °C for 1 h. In addition, there are also pinholes present in the coating layer; these are believed to have emanated from the escape of entrapped air during the dip-coating. These cracks and holes will reflect on the surface of the castings in contact with these cores, as the liquid metal will flow into the cracks and holes, forming veinings and metal penetration defects. Therefore, the cracks and holes are not favourable for the good surface quality of the castings. The coating with 40% solid content has cracks with negligible sizes on the surface of the cores while the 50 and 60% solid content coatings have cracks with relatively larger sizes. Since the surface deposit is refractory, both the coating and cracks will maintain their integrity during casting. Therefore, liquid metal will flow into these cracks forming rough surfaces. Hence, better surface quality is expected from casting made with cores coated with 40% solid content.

3.6. Influence of percentage solid content on coating penetration and deposit

The results of the influence of percentage solid content on coating penetration into the cores are presented in Fig. 8(a)–(c) for different percentage solid contents at 5 s dip-coating. The white horizontal lines on the micrographs separate approximately the deposited layer and the penetrated layer. The measurements show that 40% solid content coating has an average proud layer thickness of 0.17 ± 0.05 mm and penetrated an average of 1.18 ± 0.08 mm into the core (Figs. 8(a) and 9). The coating containing 50% solid content deposited

Fig. 6. Surface of uncoated PUCB core showing the sand grains.

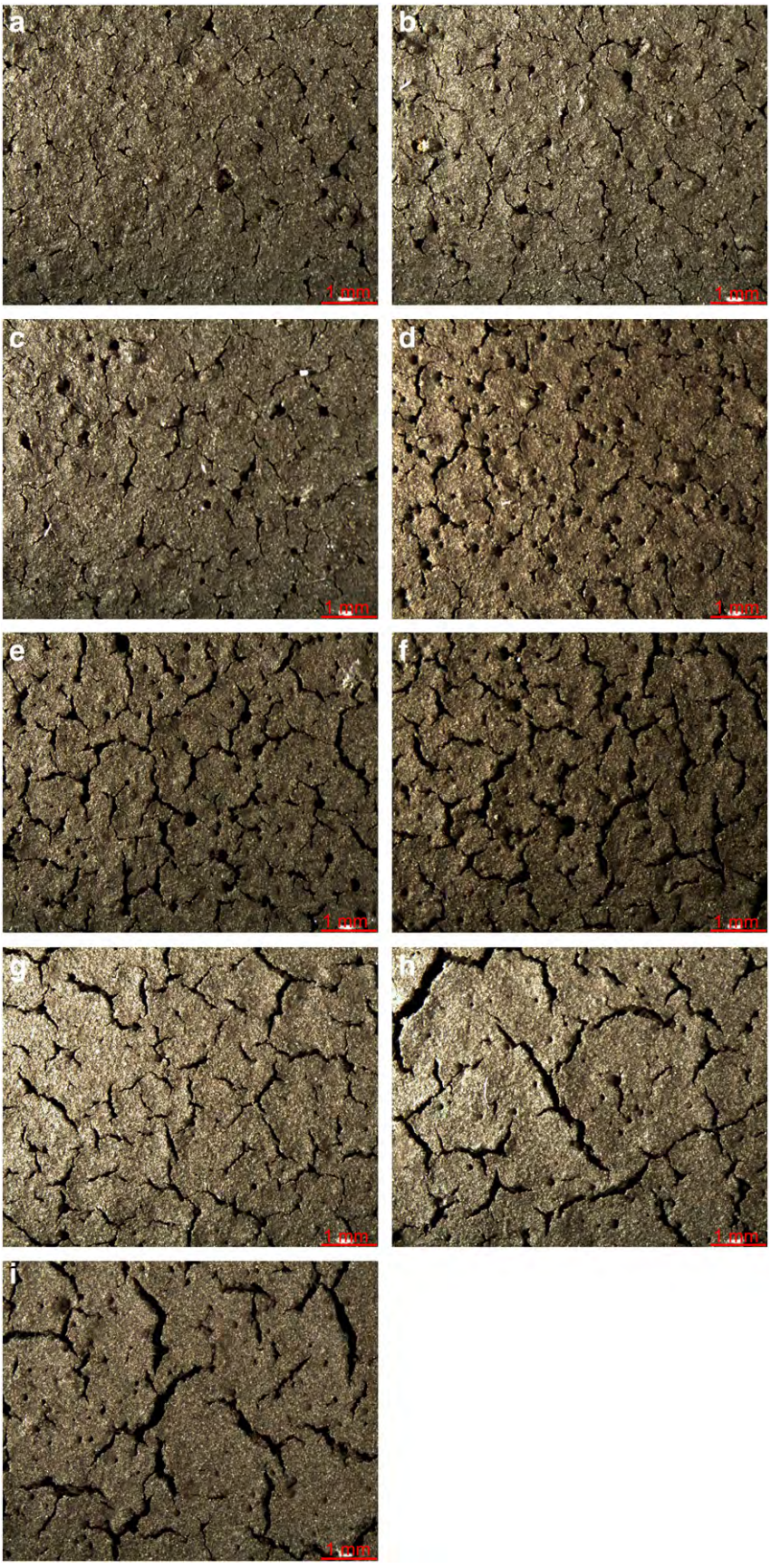

Fig. 7. Variation of coating coverage and surface appearance with dipping time and percentage solid content (a) P40D1 (b) P40D3 (c) P40D5 (d) P50D1 (e) P50D3 (f) P50D5 (g) P60D1 (h) P60D3 and (i) P60D5.

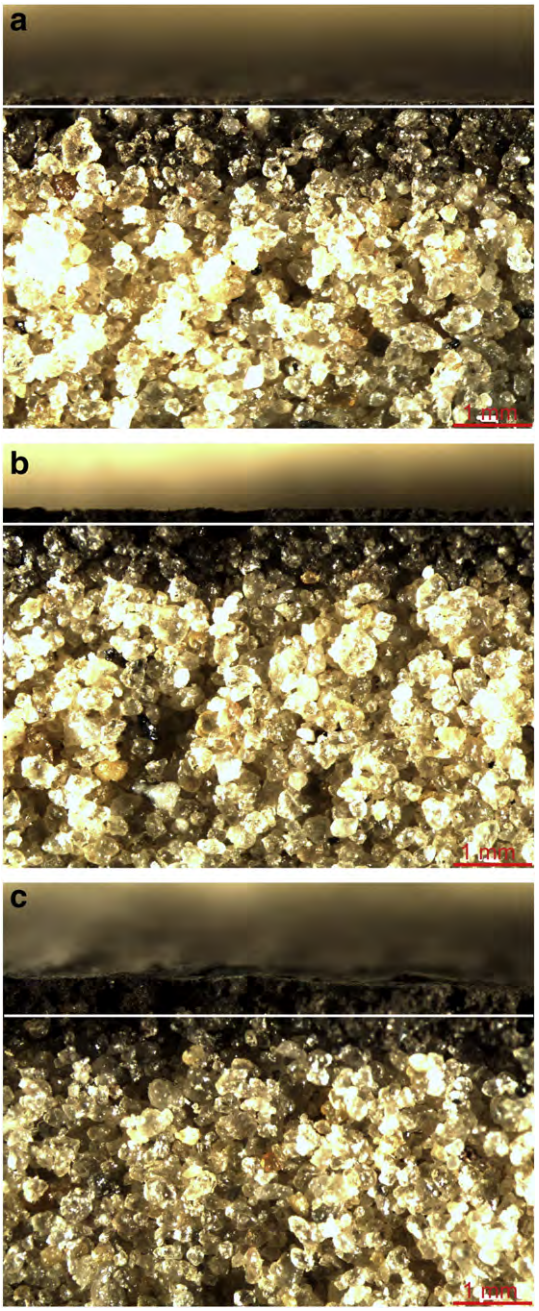

Fig. 8. Influence of percentage solid content on coating penetration using at 5 s dipping time for (a) 40% (b) 50% and (c) 60% solid content.

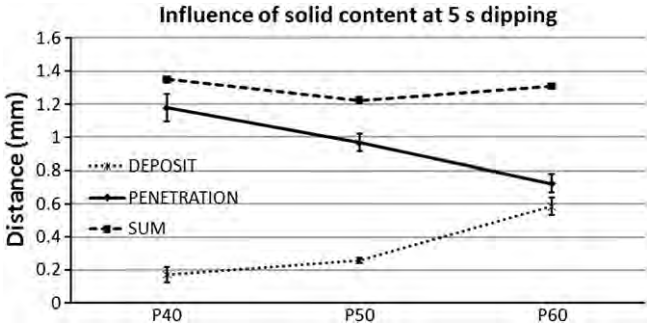

Fig. 9. Variation of deposit and penetration for various solid contents. The error bars indicate 95% confidence interval.

an average thickness of 0.26 ± 0.02 mm on the surface of the core and penetrated an average depth of 0.97 ± 0.05 mm (Figs. 8(b) and 9) while the coating with 60% solid content penetrated less into the core with an average of 0.72 ± 0.06 mm and deposited a thicker average proud layer of 0.58 ± 0.05 mm as shown in Figs. 8(c) and 9. From these results, it can be deduced that the more viscous the coating, the less it penetrates into the core and the more it deposits on the cores (e.g. a thicker layer). Therefore, it can be stated that increasing the percentage solid content of the coatings, higher thickness will be deposited on the surface of the cores and less will penetrate the cores. This is clearly seen in Fig. 9, however, the sum of the penetrated depth and the deposit for the various solid contents is not necessarily constant. From the data available, we cannot establish whether the sum should be constant or a reflection of natural variation in the pore volumes in the sand core.

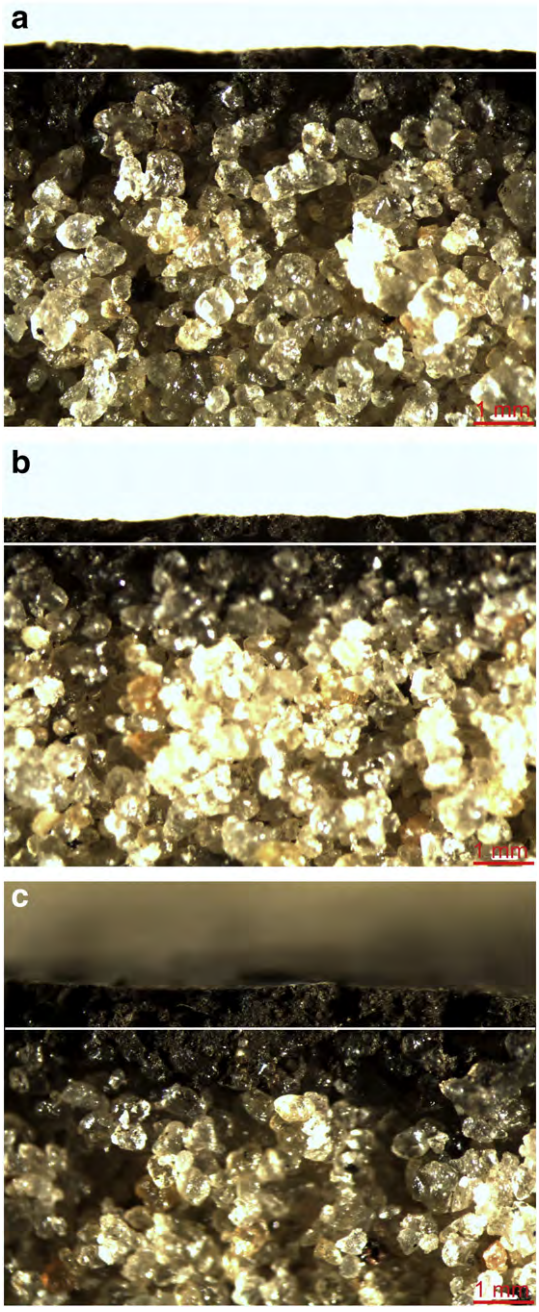

Fig. 10. Influence of dipping time on coating penetration using 60% solid content coating for (a) 1 s (b) 3 s and (c) 5 s (the scale bar is 1 mm).

3.7. Influence of dipping time on coating penetration and deposit

The same analyses performed in Section 3.6 was carried out for the different dipping times for 60% solid content coating to determine the influence of dipping time on the coating penetration and deposit on the surface of the cores. The results are presented in Fig. 10(a)–(c) (the white horizontal lines on the micrographs separate approximately the deposited layer and penetrated layer). The results showed a similar trend with the influence of percentage solid content as shown in Fig. 11. The 1 s dip-coating penetrated deepest into the core with an average depth of 1.14 ± 0.19 mm and deposited the lowest average proud layer thickness of 0.28 ± 0.02 mm (Figs. 10(a) and 11). The 3 s dip-coating penetrated an average of 0.83 ± 0.02 mm into the core and left an average deposit of 0.39 ± 0.07 mm thickness on the surface of the core (Figs. 10(b) and 11). Finally, the 5 s dip-coating produced the highest average thickness of 0.68 ± 0.10 mm in the proud layer and lowest subsurface average penetration of 0.73 ± 0.06 mm deep as shown in Figs. 10(c) and 11. Again in Fig. 11, the sum of the the penetrated depth and the deposit for the various dipping times is not constant for the same reason given in Section 3.6.

3.8. Casting surface quality

The casting surface referred to here is the surface of the casting (liquid metal) in contact with uncoated and coated PUCB cores during the casting process. The surface of the castings made with sol–gel coated and uncoated PUCB cores are shown in Fig. 12(a)–b). The presented casting surface was made with PUCB core dip-coated for 1 s in 40% solid content coating. This procedure was chosen based on the surface analysis, as this application procedure gave rise to smaller cracks and it was believed that it will have less negative effect on the surface quality of the castings produced unlike the cores with larger cracks. The features of these larger cracks were reproduced on the surface of the castings made with these cores. This is shown in Fig. 13 for a core dipped for 1 s in 50% solid content coating. This casting was not analysed further as a result of obvious poor surface quality. The surface quality of castings made with 60% solid content coating showed worse surface quality than the one shown in Fig. 13. From Fig. 12, it is clear that the sol–gel coated cores improved the surface quality of the castings compared to the surface of the casting made with the uncoated PUCB core. The surface of the castings from uncoated PUCB core has significant metal penetration (Fig. 12(a)). According to I. L. Svensson et. al [15], Draper and Gaindhar proposed a general definition of metal penetration accepted by the foundry industry, as the condition in which cast metal has entered into the pore spaces of the core or mould beyond the mid-point of the surface layer of sand grains. According to their definition, the expanding metal exerts a considerable pressure on the cores or mould walls causing metal penetration. This happens if the cores and mould walls are rigid and if the metal cannot be pushed back in the risers or the gates because they have solidified. It is quite evident that the cast

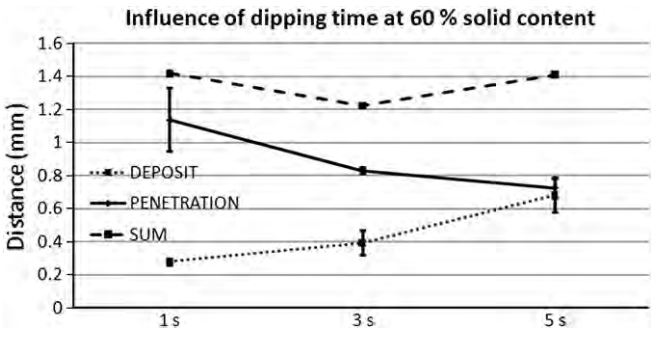

Fig. 11. Variation of deposit and penetration for various dipping times. The error bars indicate 95% confidence interval.

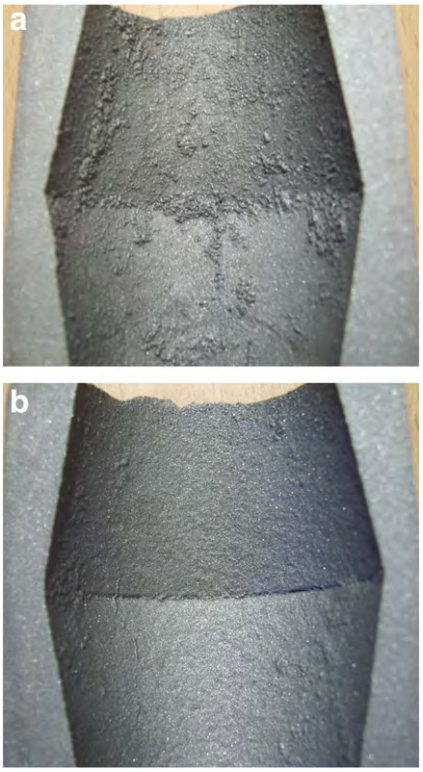

Fig. 12. The surface appearance of castings made with (a) uncoated and (b) sol–gel coated PUCB cores.

metal entered into the pore spaces of the core due to the exerted pressure from the liquid metal in the case of the uncoated core. Such features are not seen on the surface of the casting made with sol–gel coated PUCB core (Fig. 12(b)) because the coating withstood the pressure from the metal, consequently, inhibiting the metal penetration. To further elucidate the potential of sol–gel coating in foundry application, the results of the casting surfaces made with uncoated PUCB cores and PUCB cores coated with sol–gel, alcohol-based and water-based coatings are presented in Fig. 14(a)–(d). Alcohol-based and water-based coatings are commercial coatings used in the foundry. This comparison is made to ascertain the performance of sol–gel coating in improving the surface quality of castings relative to the commercial coatings. By visual inspection, the presented results show that the sol–gel coating has comparable performance in improving the surface quality of castings with the commercial coatings as can be seen in Fig. 14. It can also be seen that the castings made with water-based coating showed veins (marked feature, Fig. 14(c)), this is attributed to the higher viscosity of this coating

Fig. 13. The surface appearance of a casting made with 50% solid content.

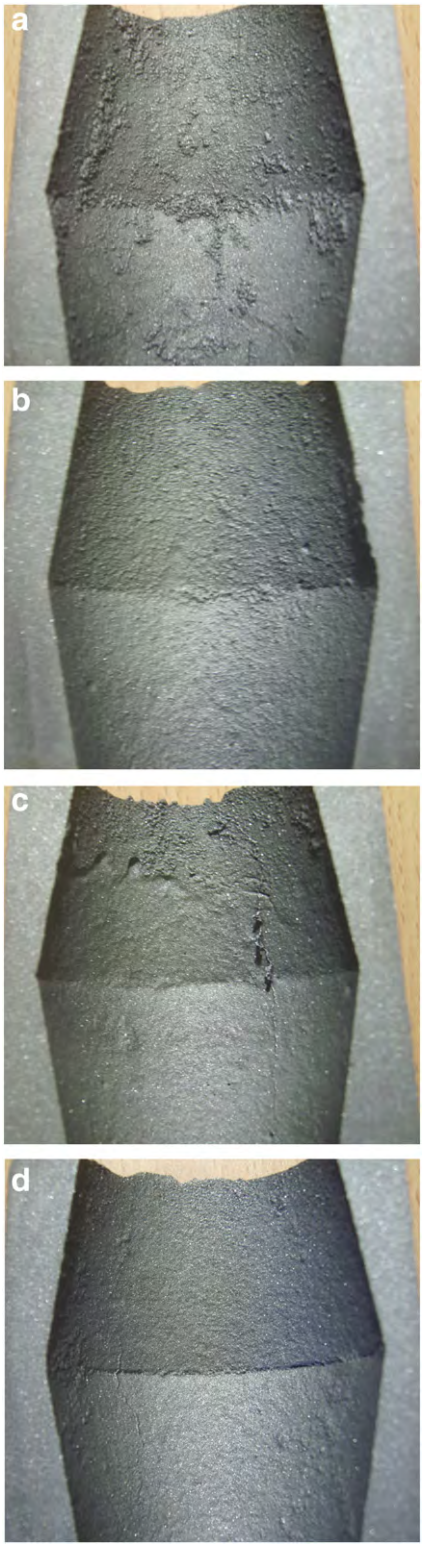

Fig. 14. The surface appearance of castings made with (a) uncoated (b) alcohol-based (c) water-based and (d) sol–gel coated PUCB cores.

compared to the other coatings [16]. However, apart from the veining defect, there was no penetration in the area in contact with coated core.

The results from the descriptive statistics of the surface profile measurements are presented in Fig. 15. The average surface roughness of the surfaces is expressed in Ra values. The results show that the castings made with coated cores have lower Ra values compared to

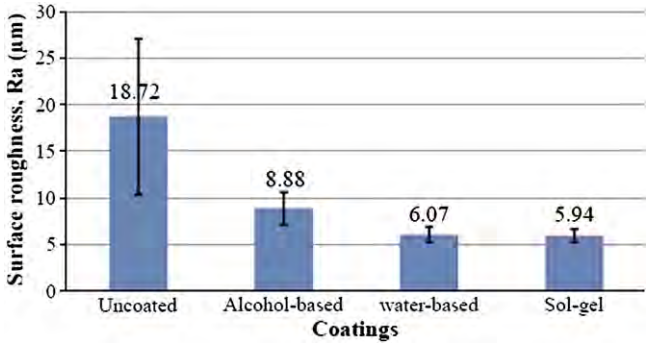

Fig. 15. The quantitative results of the surface roughness measurements from the Alicona InfiniteFocus® G4 3D Optical Measuring Device. The error bars indicate 95% confidence interval.

the Ra values of the casting made with uncoated core. From the results, it is evident that the use of coatings on moulding materials is important towards achieving a better surface finish. A One-Way ANOVA at 95% confidence level was used to establish this fact. The ANOVA result is shown in Table 2. From the ANOVA analysis, one or more of the means was significantly different based on the F- and P-values obtained (Table 2). So the larger the F value, the more important the coatings are in influencing the surface roughness [17]. In order to identify the mean(s) which is/are significantly different from the other means, a comparison of means using Scheffe's Test was performed at 95% level of confidence. The comparison shows that the mean of the casting from uncoated core was significantly different from the other means. The details of this comparison are presented in Table 3. The analogy drawn from the results show that the average surface finish of the casting made with sol–gel coated core is comparable to the average surface finish of the castings made with the commercial coatings but differ from the surface finish of the casting made with uncoated core.

4. Discussion

Refractory coatings have been used to aid casting surface finish improvements, reduce thermal expansion defects such as veining

Table 2
Analysis of variance (ANOVA) for the surface roughness.

Source variation	DoF	Sum of squares	Mean square	F value	P value	F crit.
Between Groups	3	1309.56	436.52	23.57	2.99×10^{-9}	2.82
Within Groups	44	814.81	18.52			

Table 3
Comparison of means for surface roughness using Scheffe´ Tests.

Test	Data set	Mean	Difference between means	Simultaneous confidence intervals		Significant at 0.05 level
				Lower limit	Upper limit	
Scheffe's	Uncoated	18.72				
	Alcohol-based	8.88	9.83	4.73	14.94	Yes
	Water-based	6.07	12.65	7.54	17.76	Yes
	Sol–gel	5.94	12.78	7.66	17.88	Yes
	Alcohol-based	8.88				
	Water-based	6.07	2.81	-2.29	7.92	No
	Sol–gel	5.94	2.95	-2.17	8.05	No
	Water-based	6.07				
	Sol–gel	5.94	0.13	-4.98	5.23	No

(finning) and un-bonded sand defects such as erosion. For a refractory coating to prevent metal penetration and veining defects, the refractory filler material should be able to fill the pore spaces between the sand grains and be able to protect the cores from local overheating while having suitable permeability for gas escape. When the pore spaces are closed by the refractory filler materials a smooth, refractory surface, that maintains its integrity and remains stable at elevated temperatures such as the casting temperature of cast iron, is provided. When casting in a sand mould or on sand core, the interfacial temperature between the melt and the mould or core is approximately equal to the liquidus temperature of the melt. Sand has a poor thermal conductivity; therefore, the solidification process is completely controlled by thermal conduction through the sand mould or core [18]. This is clearly expressed in the equation for the amount of heat that passes through the interface per unit area and unit time $(\frac{\partial q}{\partial t})$ in the negative direction into the mould or core, given by Eq. (2):

$$\frac{\partial q}{\partial t} = -\sqrt{\frac{K_{mould}\rho_{mould}c_p^{mould}}{\pi t}}(T_i - T_0) \quad (2)$$

where

K_{mould}	thermal conductivity of the mould
ρ_{mould}	density of the mould
c_p^{mould}	heat capacity of the mould at constant pressure
T_i	temperature between the melt and the mould
T_0	temperature of the surrounding
t	time

In order to stop the veining defects, the refractory material should improve the thermal conductivity of the system to enhance the extraction of heat from the melt and to avoid local overheating. This will reduce the effect of directional heating of sand composites (mould and core media) which generates anisotropic thermal gradients in the system. When sand composites come in contact with molten metal, the heat transferred causes thermo-chemical changes/reactions that result in the distortion of the sand composite. In the case of silica sand composite, which is the most commonly used sand in the foundry for sand casting process; the non-uniform heating of the silica sand is associated with the rapid expansion of silica when it reaches 573 °C. At this temperature, quartz, the main constituent of silica, undergoes a phase transformation from α-quartz to β-quartz. The α-phase is stable at lower temperature and has lower symmetry and smaller volume than the higher temperature stable β-phase. Atomistically, this phase transformation results in an increase in the dimensions in the a- and c-axes of the β-quartz crystal. As the temperature of the melt/core interface exceeds 600 °C, the surface of the core that has expanded starts to contract while the inner part of the core is still expanding. The thermal stresses induced as a result of this non uniform heating and differential expansion cause the core material and coating to crack before the first solidified skin of the melt is formed. Therefore, while the metal is still liquid, it flows into these cracks forming the veining defects. The depth of penetration is controlled by the freezing of the leading edge of the advancing metal when it reaches the freezing isotherm in the sand [19]. For this reason, the refractory coating material should be able to control the heating of the core for it to be effective in stopping the formation of the cracks and melt penetration. As a result, several coating properties will contribute to this. However, it was also reported in [20], that refractory coatings may also cause changes in thermo-mechanical behaviour of the core due to its pyrolysis. The percentage solid content of the coating increases the coating density and viscosity as illustrated in Fig. 16; this has significant influence on core surface coverage, coating permeability, the coating subsurface penetration and the proud layer thickness. As can be seen from the results of the microstructure of the surface of the coatings, the cores are completely covered by the sol–gel

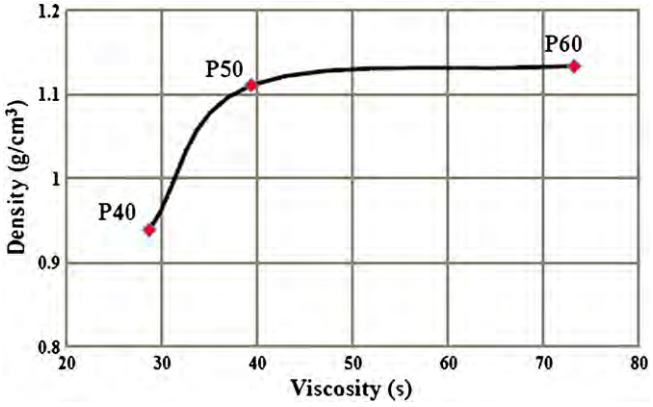

Fig. 16. Variation of coating density and coating viscosity for various percentage solid contents.

coating and had thicknesses that increased with percentage solid content and dipping times. It would have been expected that the longer the dipping time the more the coating penetrates into the core but from the results (Section 3.7), this is not the case. This is attributed to the thixotropic behaviour of the refractory coating during the dip coating process [21–23]. During the dip coating process, thixotropic behaviour was induced causing more coating to penetrate into the core in 1 s because there was only a very short time for recovery between the down-up shear applications in this system during the dipping. However, with increase in dipping time to 3 s, recovery of the coating increased thereby reducing coating penetration into the core. The reduction of coating penetration into the core increased with dipping time as observed for 5 s dip coating. Therefore, it can be suggested that the thixotropic behaviour of the coating and capillary forces existing in the porous core material favour coating penetration into the core. On the other hand, increasing the dipping time enhances the recovery of the coating due to the delay in-between the up–down shear applications during the dip coating. As a result more coating deposits are observed on the core surfaces (Figs. 8 and 9) making penetration into the cores difficult with uniform and smaller particle sizes of the filler material relative to that of the sand grains. The presence of big cracks on the surface of 50 and 60% solid content coatings and the reflection of these cracks on the surface of the casting made with these coatings reduced the interest in these coatings. However, the 40% solid content coating for PUCB cores dip-coated for 1 s proved significantly a suitable candidate for this application. The thickness of the proud layer was not as much as to induce big cracks and better surface quality was obtained.

It was also reported in [24,25] that coatings applied on cores significantly reduced the surface permeability of the cores. This claim was verified by the authors and the same results were obtained as reported in [16]. This could reasonably be the case, since the refractory material fills the pore spaces between the sand grains, thereby reducing or blocking the capillary channels. Although coatings by themselves are also porous and permeable materials due to their average particle sizes (for the sol–gel coating — 15 μm), their permeability is far lower than that of the sand material from which the cores were made since the sand grain size is more than 10 times higher than the refractory material particle size. This brings the pores in the dry coating one or two order of magnitude smaller than the pores between the sand grains. The reduced permeability could have been a problem with venting of the core during casting but this was circumvented by not coating the cores completely so the gas is forced to escape through uncoated core print to the sand mould where pressure gradient forces the gases out of the mould. Therefore, there was no sign of evolved gas defects on the surface of the castings. Considering that a high amount of gas is produced in iron casting, it is better to have a coating that prevents gas from penetrating into the melt by forcing the gas in the mould out through an uncoated

core print. This is achieved by using a lower solid content coating of optimum amount to give a better surface finish and good permeability.

The surface of the castings made with the sol–gel coated cores has proved that the sol–gel coating has a great tendency to improve the surface quality of castings. This was achieved by the refractory filler material being able to fill the pore spaces in between the sand grain and creating a smooth non-wetting surface [26] to the liquid metal and having high thermal stability. Non-wettability of the surface reduces the tendency of metal penetration as convex meniscus is created at the liquid metal/core interface. And due to low thermal expansion coefficient of the filler material, the coating maintained its integrity until the first solidified skin is formed at the liquid metal/core interface. As this was not the case for uncoated PUCB cores, the difference in the surface appearance is quite obvious.

The study has successfully applied the sol–gel technology in the preparation of a novel foundry coating which has comparable performance with the conventional commercial coatings. Moreover, it has opened a new area of research in the foundry coating technology. This process will save cost and energy in the casting cleaning shop because the surface defects (metal penetration and veining/finning) to be cleaned have been reduced or eliminated by the use of sol–gel coating on the cores. The sol–gel coating is also environmentally friendly being a water-based coating.

5. Conclusions

From the analyses carried out and presented here, it can be stated that the sol–gel coating is a potential area for foundry application. The sol–gel coating is environmentally friendly being water-based. The percentage solid content determines the density and viscosity of the coating. These properties in turn determine the sub-surface penetrated layer and the proud layer on the cores. The coating penetrates in two layers with the liquid carrier front advancing ahead follow by the refractory filler front. If the coating layer becomes too thick, it will crack on drying. Although this depends on the dipping time and the amount of filler material added. Cracks on coatings have negative impact on the surface quality of the castings made with coated cores. The sol–gel coating with 40% solid content showed better performance than the 50 and 60% solid content coatings. The refractory material size in the coating has a significant role to play to close the pore spaces on the cores creating the required smooth surface. The filter dust refractory filler material proved to have good thermal stability. The sol–gel coating has comparable performance with the commercial coatings.

Acknowledgements

The authors wish to thank the Danish Agency for Science, Technology and Innovation for financing the work. The authors are also grateful to the nine industrial partners to this project for their support.

References

[1] C.J. Brinker, G.W. Scherer, Sol–Gel Science, Academic Press, San Diego, 1990.
[2] L.L. Hench, J.K. West, Chem. Rev. 90 (1990) 33.
[3] P. Kiruthika, R. Subasri, A. Jyothirmayi, K. Sarvani, N.Y. Hebalkar, Surf. Coat. Technol. 204 (2010) 1270.
[4] A.L.K. Tan, A.M. Soutar, I.F. Annergreen, Y.N. Liu, Surf. Coating Technol. 198 (2005) 478.
[5] T. Hübert, S. Svoboda, B. Oertel, Surf. Coat. Technol. 201 (2006) 487.
[6] C. Viazzi, J.P. Bonino, F. Ansart, Surf. Coat. Technol. 201 (2006) 3889.
[7] K.–.H. Hass, S. Amberg-Schwab, K. Rose, G. Schottner, Surf. Coat. Technol. 111 (1999) 72.
[8] C. Guillén, A. Morales, J. Herrero, Surf. Coat. Technol. 132 (2000) 31.
[9] D.R. Uhlmann, T. Suratwala, K. Davidson, J.M. Boulton, G. Teowee, J. Non-Cryst. Solids 318 (1997) 113.
[10] A. Schrey, Foseco Foundry Pract. 246 (2007) 1.
[11] N. Hodgkinson, T. Birch, Foseco Foundry Pract. 240 (2003) 1.
[12] J.V. Koleske, Paint and Coatings Testing Manual 14th edition of the Gardner – Sward Handbook (ASTM manual series), ASTM International, 1995.
[13] K. Kadirgama, M.M. Noor, N.M. Zuki, M.M. Rahman, M.R.M. Rejab, R. Daud, K.A. Abou-El-Hossein, Jordan J. Mech. Ind. Eng. 2 (4) (2008) 209.
[14] F.W. Pursall, in: K. Strauss (Ed.), Applied Science in the Casting of Metals, Paragon Press, Oxford, 1970,, 361-304.
[15] I. Dugic, A. Diószegi, I.L. Svensson, Research Report, 1404-0018, 2006.
[16] U.C. Nwaogu, T. Poulsen, C. Bischoff, N.S. Tiedje, Proceedings of 69th World Foundry Congress, Hangzhou, China, , 2010, p. 648.
[17] V. Parashar, A. Rehman, J.L. Bhagoria, Y.M. Puri, Math. Appl. Sci. Technol. 1 (1) (2009) 27.
[18] H. Fredriksson, U. Åkerlind, Materials Processing During Casting, Wiley, Sussex, 2006.
[19] J. Campbell, Castings, Butterworth-Heineman, Oxford, 2000.
[20] S.N. Ramrattan, M. Rebros, M.K. Joyce, AFS Trans. 08–127 (04) (2008) 1.
[21] J.E. Wallevik, Annu. Trans. Nord. Rheol. Soc. 12 (2004) 21.
[22] A. Alessandrini, R. Lapasin, F. Sturzi, Chem. Eng. Commun. 17 (1982) 13.
[23] T.F. Tadros, Pure Appl. Chem. 64 (11) (1992) 1715.
[24] Y. Akbarzadeh, M. Rezaei, A.A. Babaluo, A. Charchi, H.R. Azimi, Y. Bahluli, Surf. Coat. Technol. 202 (2008) 4636.
[25] L. Winardi, R.D. Griffin, J.V. Grabel, AFS Trans. 08–047 (04) (2008) 1.
[26] P.L. Jain, Principles of Foundry Technology, 4th Ed.Tata McGraw-Hill, New Delhi, 2006.

SUPPLEMENT 3

U. C. Nwaogu, T. Poulsen, B. Gravesen, N.S. Tiedje,
“Using sol-gel component as additive to foundry coatings to improve casting quality”.

Published in International Journal of Cast Metals Research (2012)

DOI 10.1179/1743133611Y.0000000038

Using sol–gel component as additive to foundry coatings to improve casting quality

U. Nwaogu*[1], T. Poulsen[2], B. Gravesen[3] and N. Tiedje[1]

The improvement of foundry coatings to enhance performance is important. This paper investigates the effect of using sol–gel component as an additive to foundry coatings applied on chemically bonded sand cores. Three parameters at three levels each were investigated using Taguchi experimental parameter design. The effects of the sol–gel component on viscosity, density, °Baumé, core coverage and permeability are shown. Numerical simulations were used to predict defect areas. The thermal profiles of the core materials during casting were determined, and the surface quality of the castings was evaluated. The results show that the surface quality of castings obtained by adding the sol–gel component to the coatings for cold box cores has no significant difference from castings produced with coatings without sol–gel component. On the other hand, the addition of the sol–gel component in coatings for furan cores showed significant improvement on the surface quality of the castings compared to that obtained without sol–gel component.

Keywords: Foundry coatings, Dip coating, Surface roughness, Cast surface defects, Taguchi parametric design, Cold box cores, Furan cores, Numerical simulations

Introduction

The need for high surface quality castings is rising with the high demand of cast components for various applications, such as hydraulic applications, water and oil valves, etc. The improvement of the surface quality of castings has been made possible by fettling.[1] This is not an easy task for foundries; it delays production, consumes much energy and time and constitutes noise pollution. Furthermore, due to the intricate designs of some complex castings, cleaning by fettling may not be possible for example; it is not easy to use cleaning machines in the internal channels of an autoengine block. This limitation can be reduced using foundry coatings of different types with different refractory materials on the cores used to create the channels.[2] Therefore, it is important to direct research towards finding environmentally friendly ways of improving the existing foundry coatings.

Foundry servicing companies are carrying out research to improve their foundry coating products to satisfy their customers. This adoption of lean manufacturing will help keep these companies competitive. Foundries are really pushing coating manufacturing companies to improve their refractory coating performance in enhancing the surface quality of castings. Most times, the same coatings are used for different castings with different sizes and sections, while the coatings prove successful in some casting components; in others, they produce very poor surface finish with veining defects, scabs, sand burn-on, metal penetration or rough surfaces.[2,3] Therefore, research on how to improve foundry coatings is important, more especially in enhancing its thermal integrity to withstand the high temperature of liquid metal much longer without cracking or degrading. The ability of a coated core or mould to produce defect free surface is dependent on the thermal stability and integrity of the coating.[4] However, some coatings crack at elevated temperatures, and this is not favourable for good surface quality production.[5] Stefanescu *et al.*[6] classified the casting skin of iron into two groups: surface and subsurface. The surface feature is being described by surface roughness. However, in the case of defective castings, other features like metal penetration and sand burn-on may be found along surface roughness on the skin of castings. The subsurface features include graphite degradation, graphite depletion, pearlitic rim and ferritic rim.

This investigation will be limited to the study of the effect of the sol–gel additive to the foundry coatings on the surface features. The main surface feature of interest to elucidate the surface quality of the castings is the surface roughness parameter R_a defined according to ISO 4287/4288, as the arithmetic mean of the absolute values of the ordinate $z(x)$, within the sampling length L.[7,8] For discrete measurements, it is given by

$$R_a = \frac{1}{N}\sum_{i=1}^{N} |Z_i| \quad (1)$$

[1]Technical University of Denmark, Department of Mechanical Engineering, Institute of Process Technology, DK-2800 Kgs. Lyngby, Denmark
[2]Centre for Material Testing, Danish Technological Institute, Kongsvang Álle 29, Aarhus DK-8000, Denmark
[3]Santrol Europe ApS, Ågade 103, Pjedsted, Fredericia DK-7000, Denmark

*Corresponding author, email ugon@mek.dtu.dk

Received 1 November 2011; accepted 26 December 2011
DOI 10.1179/1743133611Y.0000000038

where N is the number of measured points in the sampling length.[7,9]

The R_a value measured over one sampling length is the average roughness. It is practically recommended to measure R_a values over a number of consecutive sampling lengths and to determine the average value to ensure that the R_a value obtained is typical of the surface investigated. R_a values are usually measured perpendicular to the lay of the surface.[7]

In this study, the sol–gel component is added in different amounts to a foundry coating. The suspension is characterised as it applies to the foundry industry. Chemically bonded sand core materials are dip coated, cured and characterised for casting purposes. Numerical simulations are used to predict defect areas in the model. Cast iron is produced by a sand casting process using a robust pattern, which eliminates the influence of differences in liquid metal, pouring temperature, pouring time, etc. The thermal behaviour of the coated cores will be measured using DASYLab Data Acquisition System.

Detailed surface quality studies will be performed on the surface of the castings to elucidate the influence of the sol–gel component additive in improving the surface quality of the castings.

Experimental

Coating formulation

A water based commercial coating (WCC) containing aluminium silicate refractory material and commonly used in the foundries was obtained from the manufacturer. The original density of the coating is 1·38 g cm^{-3}. The dilution was carried out as follows: to 400 g of the original coating, 40 (10), 100 (25) and 200 g (50%) of sol–gel components (SG) were added. For the sol–gel component, the sol–gel stock is produced by a controlled acid (HCl) catalysed hydrolysis with water of (3-glycidyoxypropyl)trimethoxysilane (Degussa) and aluminium (III)-s-butoxide, in 75% solution of s-butanol (ABCR) as the mutual co-solvent to form silanol group (Si–OH). The pH of this sol–gel solution is ~5. The hydroxide (≡Si–OH) from the hydrolysis is condensed with another silane, propyltrimethoxysilane (Evonik/Degussa), in a process called alkoxylation (condensation under release of alcohol) to form the siloxane bonds (≡Si–O–Si≡). The molar composition of the stock sol–gel solution is given by (3-glycidyoxypropyl)trimethoxysilane/aluminium (III)-s-butoxide/HCl/propyltrimethoxysilane as 385 : 3 : 1 : 95. After the addition of the sol–gel component to the foundry coating, the mixture is homogenised and diluted to the viscosities used in the foundries.

Coating characterisation

The coating density was determined according to method described by Nwaogu *et al.*[5] The Ford flow cup was used to determine the viscosity of the coatings according to the ASTM D1200 standard. This is a gravity device that measures the timed flow of a known volume of coating passing through an orifice located at the bottom of the cup. Under ideal conditions, the rate of flow would be proportional to the kinematic viscosity expressed in stokes or centistokes.[10] The °Baumé parameter was measured with a hydrometer. The hydrometer is floated in the sol–gel coating slurry, and the °Baumé reading is taken directly from the hydrometer scale when it has stopped sinking.

Coated core properties

The coverage of the core by the coating is elucidated using a stereomicroscope (Zeiss Stereo CL1500 ECO). The dried coated core materials were sectioned, and the coating penetrated areas of the core were carbon sputtered to make it conductive. The prepared samples were examined with a scanning electron microscope (SEM), JOEL JSM-5900, with LaB6 filament to investigate the interaction of the core materials and the refractory materials. The permeability of the cores was determined as an average of three measurements using a permeter.

Design of casting experiments

Taguchi experimental design was adopted and applied in this investigation to elucidate the effects of three parameters at three levels on the target performance response (surface roughness). The parameters/factors and their respective levels are presented in Table 1.

A key component to Taguchi's approach is the reduction in variability of design parameters by developing and understanding their effects using a minimum number of experiments. To analyse experimental data, Taguchi recommends analysing the mean response for each experimental run and also analysing the variation using the appropriate signal/noise S/N ratio measured in decibel. For the Taguchi method, there are three S/N ratios depending on the expected target performance response. These include 'small is better' (SB), 'nominal is best' and 'larger is better'. Since the target performance response is surface roughness, a surface with the lowest surface roughness value has better surface quality. Therefore, for higher surface quality, the S/N ratio for small is better (SB) is applied in this investigation, and it is given by[11–13]

$$\mathrm{SB} = -10\,log\left(\frac{1}{N}\sum_{i=1}^{N} y_i^2\right) \tag{2}$$

where N is the number of repeated observations in a run, y_i represents the observations (measure R_a values) and the subscript i represents the number 1, 2, 3, …, N.

In conducting experiments with Taguchi experimental design, orthogonal array (OA) is selected to organise the parameters and their respective levels affecting the target performance response.[7] Before selecting an OA, the following points are considered:[13]

(i) the number of parameters and interaction of interest
(ii) the number of levels for the parameters of interest.

Table 1 Design parameters/factors and their levels

		Level*		
Variables or factors	Units	1	2	3
Sol–gel component *S*	%	10	25	50
Viscosity *V*	s	11	13	15
Dipping time *D**	s	S	L	10

*S: short dipping time (1–2 s); L: long dipping time (3–5 s).

In this study, each parameter has three levels; therefore, each has 2 degrees of freedom *df* (i.e. number of levels−1). The total degrees of freedom for three parameters in each at three levels is 6=3 (number of parameters) × 2 (number of level−1). A three-level OA with nine experimental runs ($L_9 3^3$) is selected for this investigation. The OA is the shortest possible matrix of combinations in which all the parameters are varied at the same time, and their effect and performance interactions are investigated simultaneously.[14] An array name shows the number of rows and columns in it and also the number of levels in each of the columns. In this case, the array ($L_9 3^3$) has nine rows and three columns of three levels. The array is based on the 'theory of orthogonality'. It states that 'each and every level of each and every parameter is in combination with each and every level of every other parameter at least once'.[14] A well designed experiment can reduce significantly the number of experimental runs required.[15] With the selection of ($L_9 3^3$) OA, the number of experiments required is reduced to nine, which, in conventional full factorial experimental design, would require $3 \times 3 \times 3 = 27$ experiments to study the parameters at three levels. The OA for this investigation is given in Table 2. Analysis of variance (ANOVA) at 95% confidence interval was applied to the roughness data to determine how significantly different the means are.

Materials and casting process

At Frese Metal og Stålstøberi A/S, Slagelse, Denmark, the cores are made from silica sand with a chemical composition of 98·61%SiO_2–0·69%Al_2O_3–0·51%K_2O–0·05%Fe_2O–0·01%CaO–0·07%TiO_2–0·05%Na_2O, and two different binder systems were used. The regenerated sand cores are made from furan resin binders of phenol formaldehyde/furfuryl alcohol (PF/FA) type. Phenol formaldehyde/FA has FA contents in the regions of 30 and 70%. The cold box cores are made using the amine/phenol urethane process. The bond is based on the use of a two-part isocyanate: part one being a phenolic resin and the second part being an isocyanate contained in a solvent. The result, promoted by a reaction with triethylamine or dimethylethylamine vapour, is the formation of a solid polyurethane resin. Cylindrical cores of height 102 mm, middle section diameter of 50 mm and diameter of both ends being 33 mm are coated for short (S) (1–2 s), long (L) (3–5 s) and for 10 s (10) with the coating containing sol–gel component additive blended at Danish

Table 2 $L_9 3^3$ OA for three parameters at three levels each

	Variables or factors		
Standard number of experiments	Sol–gel component	Viscosity	Dipping time
1	10	11	S
2	10	13	L
3	10	15	10
4	25	11	10
5	25	13	S
6	25	15	L
7	50	11	L
8	50	13	10
9	50	15	S

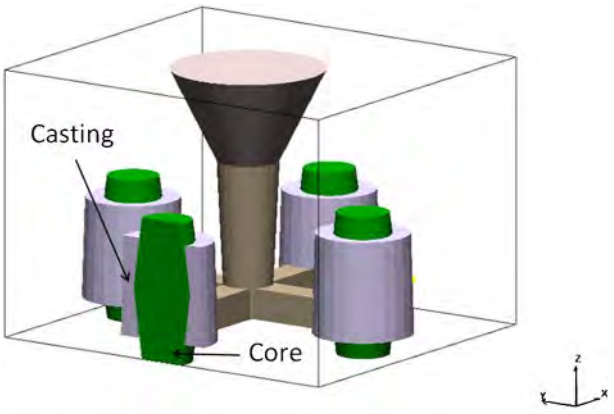

1 Computer aided design model of casting layout for simulation showing how cores sit within castings

Technological Institute, Aarhus, Denmark, by a dipping method.

The melt composition is Fe–3·5%C–2·6%Si–0·2% Mn–0·02%P. The charge was melted in an induction furnace operated at a frequency of 1000 Hz and a power of 125 kW. Casting was carried out when the temperature of the melt in the furnace was >1465°C to account for the delay during pouring so that a pouring temperature between 1400 and 1420°C is achieved.

The temperature profile of the cores when in contact with the melt was measured by using tungsten inert gas welded k-type thermocouples (Ø=0·2 mm) embedded in the cores up to the midsection. These thermocouples were connected to a PC with DASYLab data acquisition system laboratory software, version 8.

Numerical simulations

Numerical simulations were performed to study the temperature distributions in the cores and to predict likely defect areas in the model. For the casting simulations, MAGMAsoft version 5 software was used. The simulation parameters for filling and solidification were as follows: cast iron GJL 150 ($T_{liquidus}$=1173°C; $T_{solidus}$=1160°C). The cores are cold box and furan systems. Pouring temperature of 1400°C and heat transfer coefficient of 1000 W m^{-2} K^{-1} were specified. The pouring time was 5 s. Thermocouples were placed at the centre of each core for thermal profile measurement. The coating thickness on the cores was modelled by adding to the cores the proud layer thickness of the coatings reported by Nwaogu *et al.*[5] The numerical simulation results will be compared with the experimental results. The computer aided design model of the casting layout showing how the cores sit with the castings, for the numerical simulations, is shown in Fig. 1.

Surface quality evaluation

Surface roughness of various castings was measured using a three-dimensional (3D) Alicona Infinite Focus Microscope G4. The measurements were analysed using descriptive statistics [mean, standard deviation (SD) and standard error (SE)] and ANOVA with the analysis of the Taguchi experimental design parameters. With the combination of the mean target performance response, *S*/*N* ratio and descriptive statistics analyses, the optimal combination of the studied parameters can be predicted.

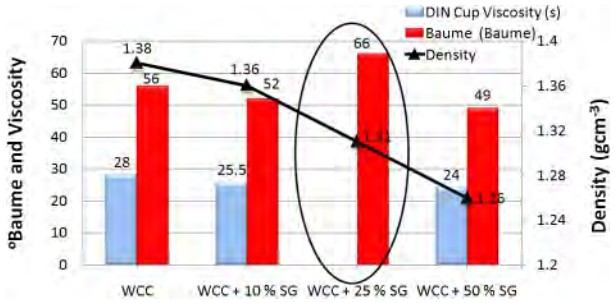

2 Wet characterisation of coating slurry immediately after addition of sol–gel component to WCC

Results and discussion

Wet coating characterisation

Density test is a quick test that enables deduction to be made about the total solid content and refractory component in the coatings.[16] The density or specific gravity results presented here show the effect of sol–gel component addition to the commercial coating on the coating slurry density. From the result presented in Fig. 2 and Table 3, the specific gravity decreases with increasing sol–gel component addition, which invariably means decreasing solid content. This is because the pore spaces are being increased by adding the sol–gel component to a fixed amount of solid material.

In the foundry, the coatings are usually diluted to the required consistency before application. In using sol–gel as an additive in a commercial foundry coating, the density, viscosity and °Baumé parameter in the undiluted condition are shown in Fig. 2. In this figure, it can be seen that the flow cup viscosity for the coating containing 25% sol–gel additive is missing in the chart (no blue column in the oval mark). This was due to the fact that the coating could not flow pass the orifice of the flow cup as a result of very high viscosity. However, the authors are of the opinion that strong chemical reaction(s) had taken place probably due to optimum or near optimum amount of sol–gel component, enhancing the polymerisation rate to form a high viscous gel with flow difficulty. Before this inference was drawn, the experiment was repeated for several times with fresh coating, and the observations remained consistent. Consequently, the °Baumé parameter was used to elucidate the viscosity of the coating and the result confirms the high viscosity of the coating with higher °Baumé parameter (Fig. 2). This result confirms the reason why the coating could not flow pass the orifice of the flow cup which is attributed to the higher rate of polymerisation taking place.

The coatings were diluted to 11, 13 and 15 s to reflect the operating viscosities in the foundry. Table 3 reveals that as the sol–gel component is increasing, the density is decreasing at each viscosity, while for each sol–gel additive, the density increases with increasing viscosity. This implies that at each viscosity, the solid content is fixed while the sol–gel component is added, thus creating more voids in the coating matrix. This is also the case with the °Baumé parameter, as shown in Table 3. The °Baumé parameter is commonly used in the foundries to control the coating consistency for various sizes of foundry applications because it is quick and easy to use. A higher °Baumé number indicates higher viscosity and vice versa.[17] Care should be taken to determine the optimum viscosity of coatings required for different casting sizes in order to avoid cracking of the coatings during curing, gas defects and poor permeability for high viscosity coatings. For low viscosity coatings, there will be poor core surface coverage and deeper and non-uniform penetration into the cores.[5] Both extremes produce defective castings; as a result, optimum coating viscosity for different castings becomes important.

Core–coating interaction

The coatings showed complete surface coverage, as presented in Fig. 3. Adding sol–gel component showed increasing glassy ceramic nature with increasing sol–gel component amount, as can be seen in the figure. This ceramic glassy nature may not be as porous as the coating without sol–gel component; hence; it is likely that these coated surfaces in Fig. 3 may have lower permeability relative to the surfaces of cores coated with coatings without sol–gel component. A cross-section of the coated core is examined with SEM, and the image is shown in Fig. 4. This micrograph reveals that the refractory filler materials filled the pore spaces between the sand grains and are deposited ~2 mm into the core substrate. Evidently, this will have effect on the core permeability.

Permeability

The permeability of the coated cores is significantly reduced by the coating.[5,18,19] This is due to the filling of intergranular pore spaces between the sand grains with the refractory materials, which have particle sizes very much smaller than the sand grains. In foundries, to vent big cores, holes are drilled into the cores to enhance venting, in order to avoid the tendency of formation of gas porosities and other gas related defects in the castings. For smaller cores, foundries rely on the core print for venting of the cores. Therefore, for the sol–gel coatings, this is not an exception. The permeability of the cores is significantly reduced due to the combined formation of a glass ceramic matrix and filling of the

Table 3 Wet characterisation of coatings after dilution with water to various viscosities (s) used in foundries

	Dilution viscosities					
	11 s		13 s		15 s	
Coatings	Density/g cm^{-3}	°Baumé	Density/g cm^{-3}	°Baumé	Density/g cm^{-3}	°Baumé
WCC + 10%SG	1·27	30	1·29	33	1·32	36
WCC + 25%SG	1·23	27	1·26	31	1·27	33
WCC + 50%SG	1·21	24	1·23	28	1·26	29

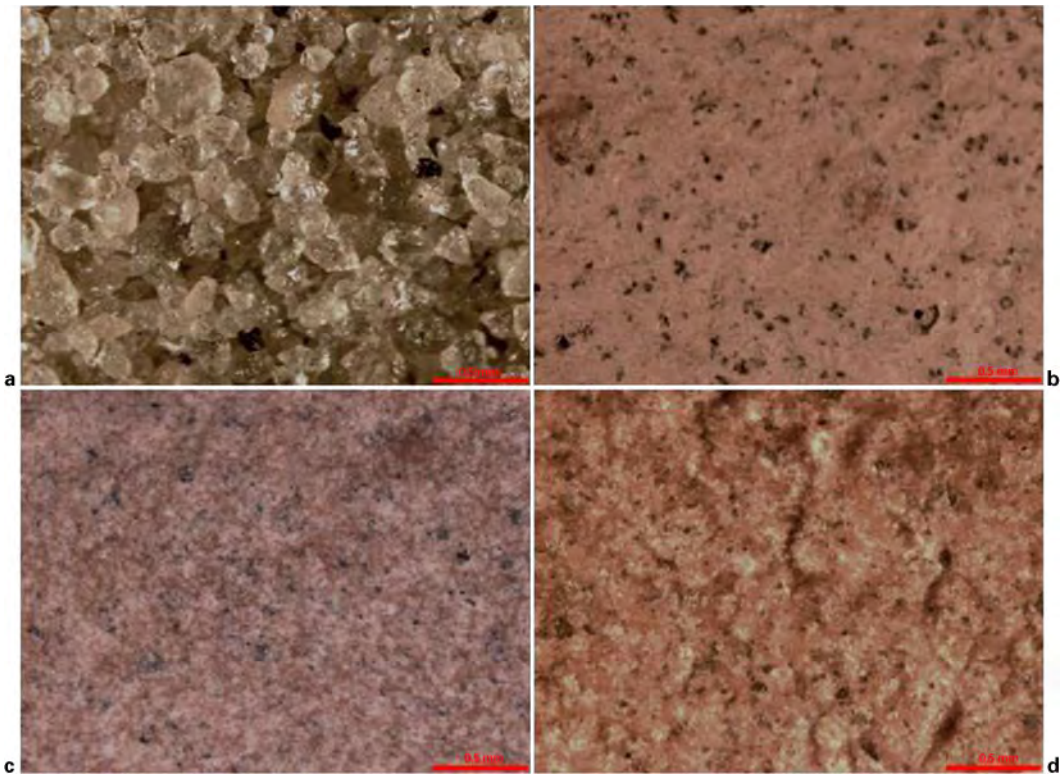

a uncoated core; *b* coating with 10% sol–gel component; *c* coating with 25% sol–gel component; *d* coating with 50% sol–gel component

3 Core surface coverage by coating slurry

pore spaces with the refractory materials. This is evident from the permeability results presented in Table 4 for the uncoated and coated cores. The coating significantly reduced the permeability of the cores. This reduction is slightly enhanced with the coating containing sol–gel components compared with the coating without sol–gel component additive.

Simulation results

Temperature distribution in cores

In these simulations, thermal data for silica sand cold box cores from the software database were used. Silica sand has a critical phase transformation temperature at 573°C, at which it expands rapidly because of the transformation from α-quartz to β-quartz. Therefore, it is expected that when the cores are heated up to this temperature, they will expand rapidly, causing thermal stresses in the cores due to non-uniform expansion. The core binder begins to degrade already at ~200°C.[20] This process continues up to 450°C. In combination, the two processes lead to cracking of the cores or complete degradation of the cores. The temperature distribution in the cores from simulations is shown in Fig. 5. Figure 5*a* shows the temperature distribution at completion of filling. It can be seen from the figure that the maximum temperature reached at the surface of the cores at the end of filling is between 300 and 400°C. This temperature is not critical for the cores but more than sufficient to, over some time, degrade the binder. However, as solidification progressed, the more heat diffused into the bulk of the cores, raising the temperature, as shown in Fig. 5*b*. From this simulation, it can be inferred that if at all there will be crack formation in the cores, it will occur at the end of filling and onwards when the melt temperature is still above the liquidus temperature and not during filling, which only took 5 s for this model. Therefore, to avoid the defects formed as a result of cracking of the core, the solidification should

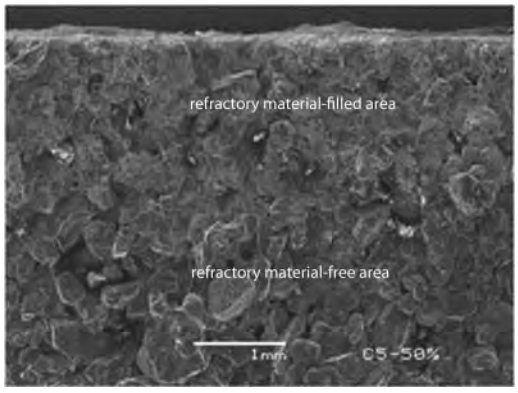

4 Image (SEM) showing core–coating refractory material interaction

Table 4 Permeability of uncoated and coated cores with WCC containing 10, 25 and 50% sol–gel component and WCC without sol–gel component

	Permeability			
Treatments	0 s	Short	Long	10 s
Uncoated	475±7	…	…	…
WCC	…	108±4	95±7	92±3
WCC+10%SG	…	85±7	75±7	67±2
WCC+25%SG	…	68±4	73±1	61±2
WCC+50%SG	…	53±4	50±3	39±2

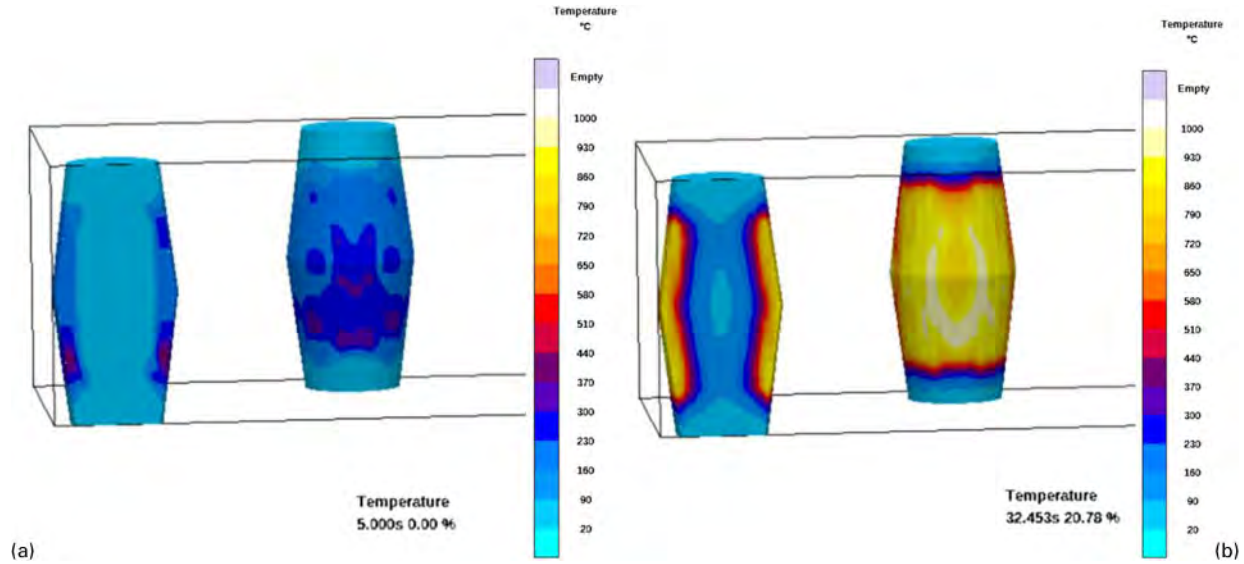

a at end of filling; *b* during solidification

5 Simulated temperature distribution in cores

start along with filling and continues after filling in order to form the first solidified metal skin (for some alloys) before cracking occurs.

The temperature profiles in the cores with varying thicknesses (modelled coating thickness) are shown in Fig. 6. The effect of the thickness of each core is clearly seen in these profiles. It takes longer time to reach the thermocouple in the core with the highest thickness. This trend continues until the lowest thickness, showing the shortest time as shown by the enlargement of region A at

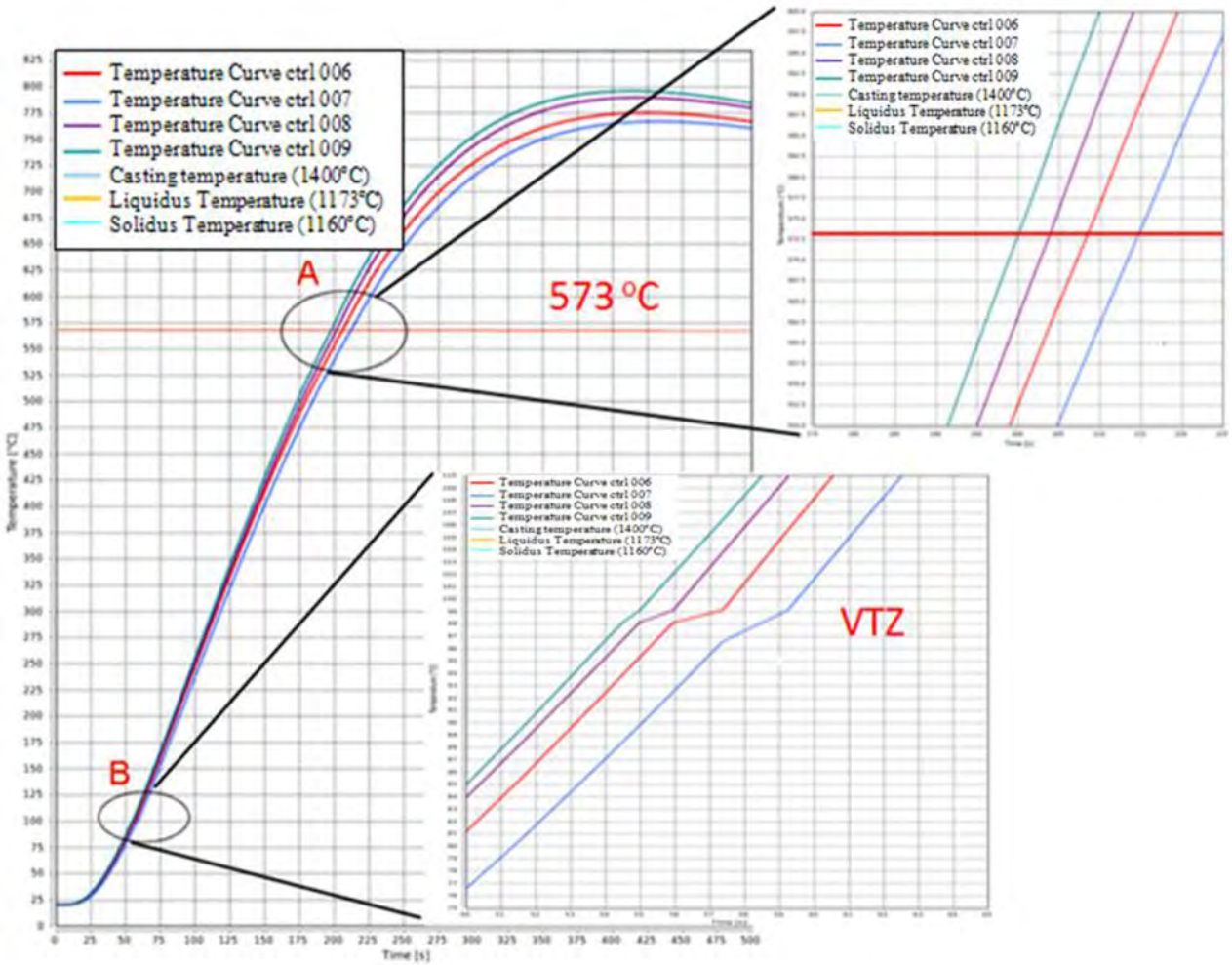

6 Simulated temperature profiles in cores showing silica sand transformation temperature zone (region A) and VTZ (region B)

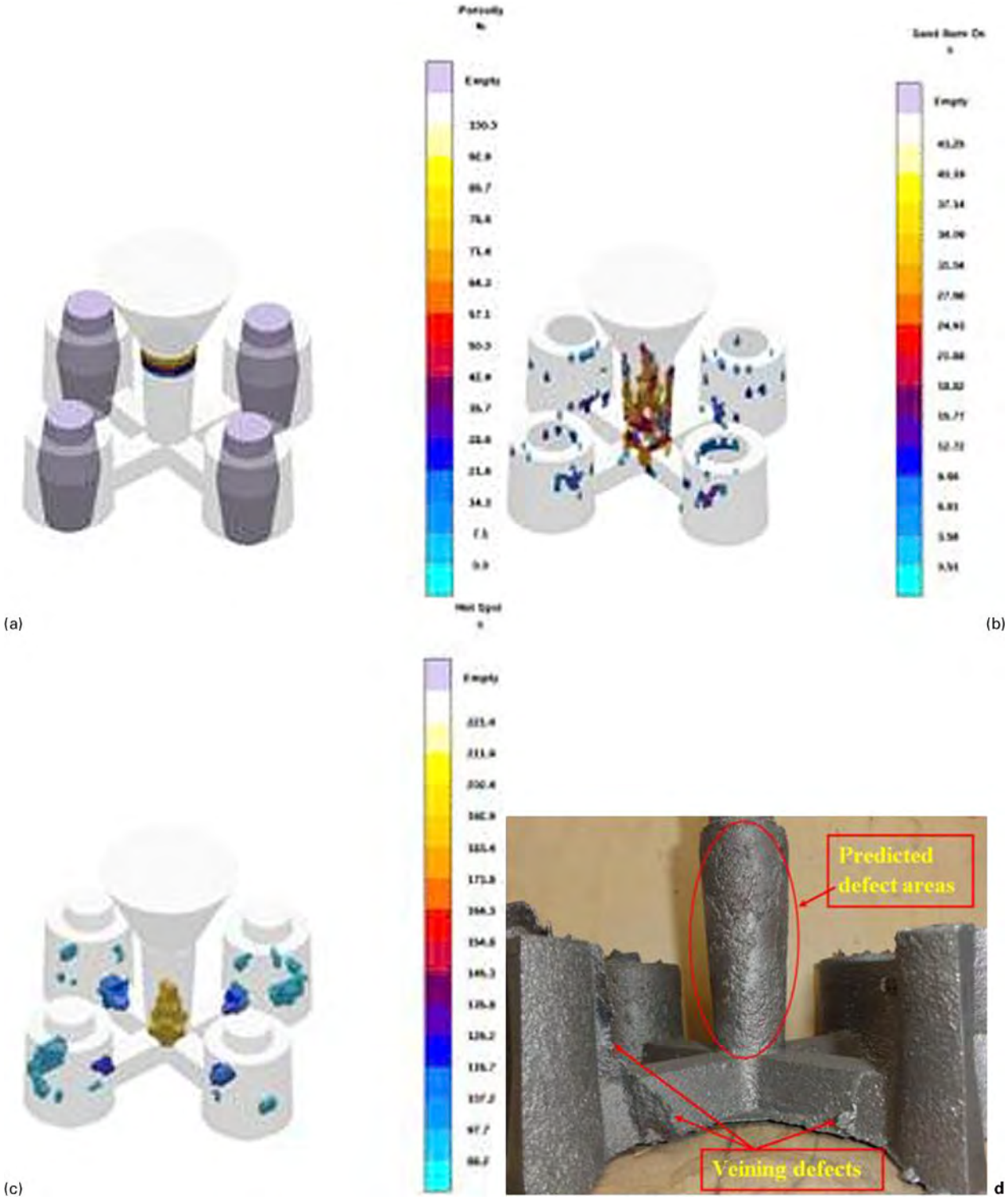

a simulated porosity; *b* simulated sand burn-on; *c* simulated hot spot; *d* experimental casting showing agreement with simulated results

7 Defect locations

573°C (transformation temperature zone). The time delay to reach this critical temperature is an advantage because it will allow for the first solidified skin of the casting to form before the critical temperature is reached, thereby creating a solid barrier between the cracks formed on cores at the critical temperature and the liquid metal. The situation prevails in alloys that form solid shell from the mould or core wall during solidification. Hence, liquid metal cannot flow back into the crack, thereby eliminating the formation of veining defects. At region B of the profile in Fig. 6, it can be seen from the enlargement of that region that the larger the thickness of the core, the larger the vapour transport zone (VTZ). This suggests that the moisture content in each of the cores increases with the thickness of the coating as more intergranular pores are created with higher coating thickness, giving more pore spaces for moisture to occupy. The simulated temperature profiles

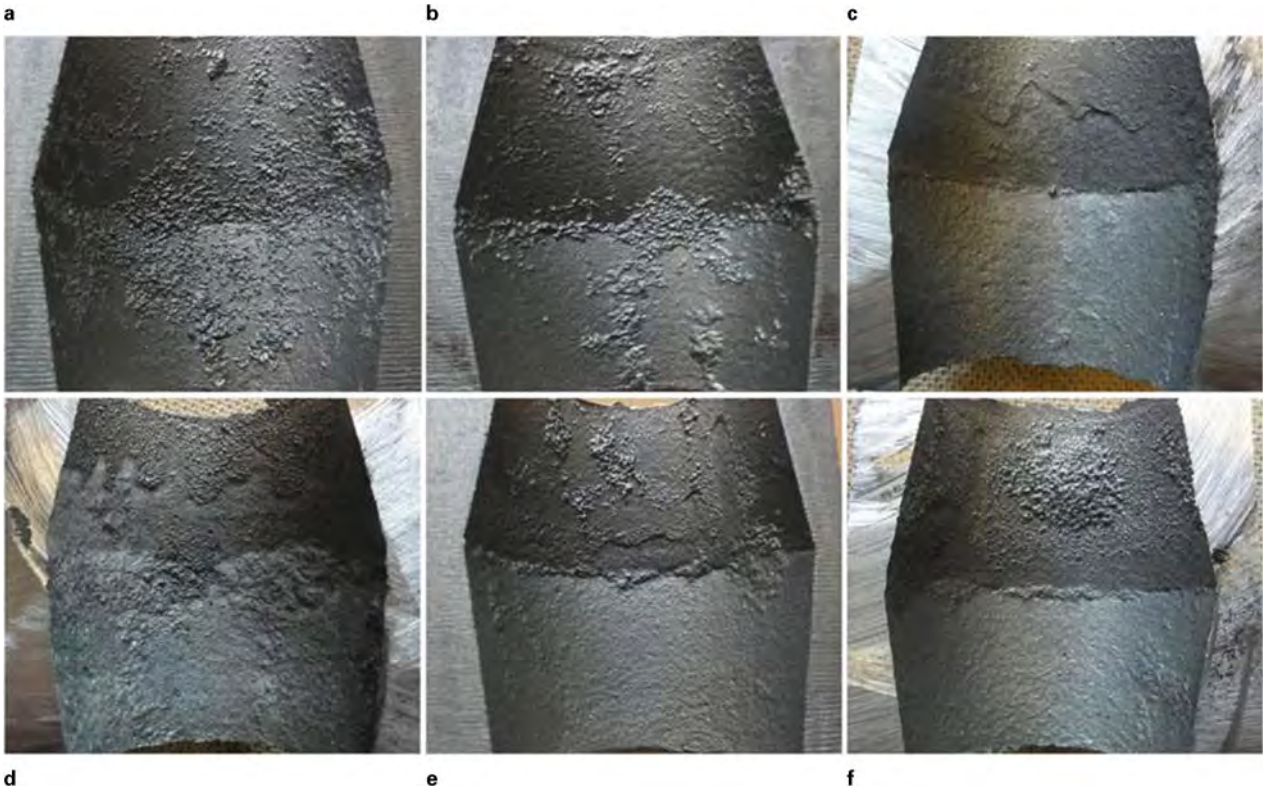

a uncoated cold box core; *b* uncoated furan core; *c* cold box core coated with WCC without sol–gel component; *d* furan core coated with WCC without sol–gel component; *e* cold box core coated with WCC + 25% sol–gel component; *f* furan core coated with WCC + 25% sol–gel component

8 Casting surfaces from cores with different coating treatments

show that the maximum temperature reached by each thermocouple is between 750 and 800°C under the specified simulation conditions. These conditions were replicated as much as possible in the casting experiments to ascertain the agreement of the numerically simulated results with the experimental results.

Prediction of defect areas

Defect prediction is one area of casting process numerical simulations that is very important because it provides information that will help in the optimisation of the process to reduce or eliminate the defects in castings. This saves money, time and energy for foundries. From the simulated results presented in Fig. 7, there is absence of porosities in the castings (Fig. 7*a*). The porosities are limited only to the downsprue. However, the results showed sand burn-on tendency and hot spot areas, which also enhance sand burn-on, as shown in Fig. 7*b* and *c*. From the colour scale, these are very low. Sand burn-on is caused by localised overheating of the mould or core, causing liquid metal at the mould/metal interface to penetrate shallowly into the mould or core. When the metal at the mould/metal interface stays hot enough to partially decompose the binder or coating material, while still remaining fluidy, burn-on will occur.[20] Considering the size of these castings, sand burn-on may not be a problem since from prediction, it is more severe in the downsprue and heavy section areas, as shown in Fig. 7*a–c*, and agrees with the experimental result shown in Fig. 7*d*.

Surface quality evaluation

Cast surface appearance

The penetration and fusion of molten alloy to the mould and core walls are considered to be two main factors governing the surface roughness of castings. The degree of penetration can be affected by the surface permeability of mould/core walls, the surface tension of molten alloy and the casting pressure to mould/core walls (metallostatic pressure).[21] In these experiments, metallostatic pressure and surface tension are ignored as possible factors to cause surface defects. This is because the castings are small. In the case of surface tension, since the casting time is too short (5 s) relative to the solidification time, the surface tension of molten alloy on contact with the mould/core walls was assumed to be uniform to result in significant deviation in the temperature and surface tension.[21] This leaves permeability of the mould/core walls as the likely factor to affect metal penetration. The lower permeability of moulding materials favours high quality casting surface finish.[22] The surfaces of the castings made from uncoated and some of the coated cores are presented in Fig. 8. For uncoated cores (Fig. 8*a* and *b*), the surfaces show poor surface appearance and evident metal penetration. Castings with these surfaces may not be acceptable by customers who are interested in surface aesthetics of their products and are not good for machining either. However, the application of coatings on the cores can circumvent this problem. By applying coatings, it means that finer refractory materials are deposited on the surface of the mould/core and may even penetrate a few millimetres into the pore spaces in

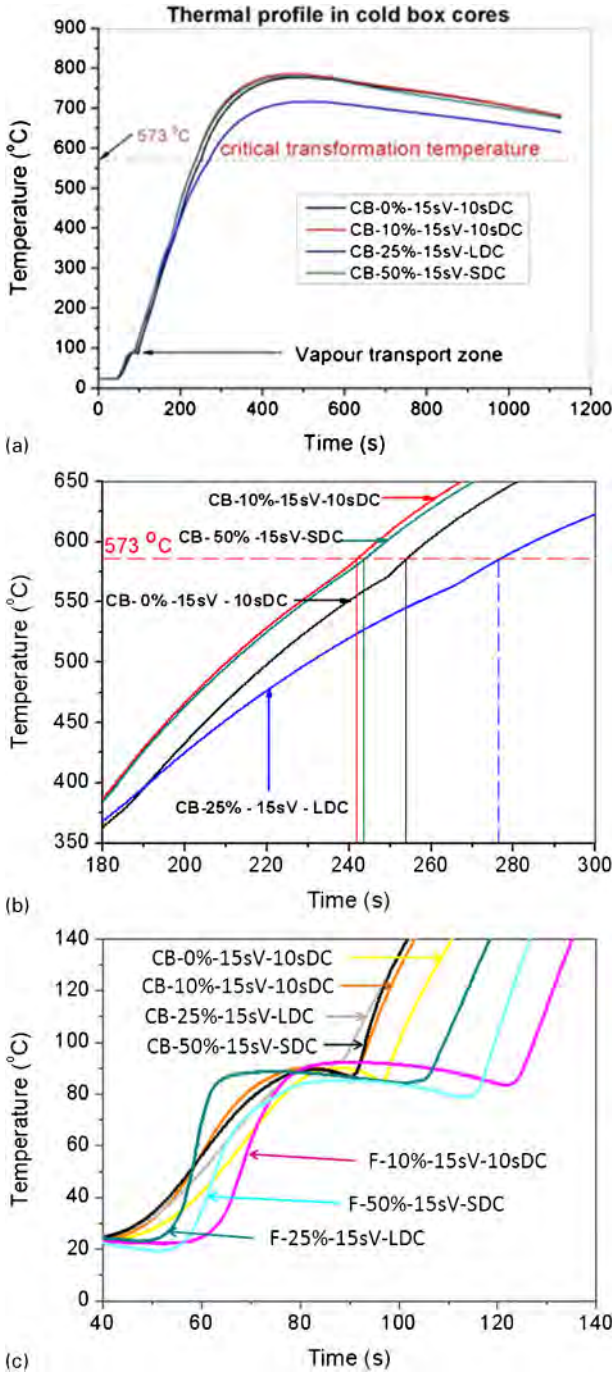

a full profile; *b* silica sand critical transformation zone; *c* vapour transport zone in cold box (CB) and furan (F) cores

9 Thermal profiles measured in cores during casting process

the substrate. As shown in Table 4, this reduces the permeability of the moulding material significantly. However, in agreement with Parkes,[23] it is expected that by applying coatings on the cores, the surface finish of castings will be enhanced because the surface fine details of the refractory materials will be reproduced on the surface of the castings.

A closer look at the surfaces of castings produced with coated cores shows an improved surface quality (Fig. 8*c*–*f*). The area of the cores that was not coated (top part) also showed its effect on the surface of the castings. The coatings on the cores enhanced the surface quality of the castings. However, no clear distinction is observable from the effect of sol–gel component additive in the presented results for castings produced with coated cold box cores, as can be seen from Fig. 8*c* and *e*. Therefore, addition of the sol–gel component to the coating may not be necessary for cold box applications as this means extra cost.

However, the addition of sol–gel component to the coating enhanced the performance of the coating in improving the surface quality of castings produced with furan cores. This is clearly seen from the surfaces of castings presented in Fig. 8*d* and *f*. The castings presented in this figure were produced from the same liquid metal, pouring temperature and pouring time because they were in the same mould. Therefore, it is evident that the variations that could have come from differences in these parameters may have been eliminated, giving room for level condition for the comparison of the surface quality of the castings. Application of WCC on furan cores may be questionable from these results (Fig. 8*d*); however, with the addition of sol–gel component to the coating, the performance and applicability of the coating on furan cores have been improved.

The results obtained from the experiments seem to agree with the numerically simulated results because there is no presence of surface defects like sand burn-on and metal penetration on the surface of the castings produced with the coated cores. The predicted results placed these defects at a very low level, which agrees with its absence on the surface of the castings. The areas of the castings where the prediction of the defects are significantly high, such as the downsprue, and heavy section areas of the castings are also where the defects occurred in the casting experiments, as shown in Fig. 7*d*. From the figure, the presence of veining defects around the heavy section and defects on the downsprue agrees with the simulated results. The veining defects at the heavy section areas occurred as a result of cracking of the mould around these areas due to local overheating of the moulding materials. This subjects the moulding materials to heavy thermal shock, leading to their premature failure. In the case of coated cores, the surfaces are free from these defects.

Furthermore, in the discussion on the agreement of the numerically simulated results and the experimental results, an examination of the thermal profiles (Fig. 9) shows that the cores in the casting experiments were heated up to 700–800°C as in the simulated results. It took ~200 s in both simulated results and experiments to heat the cores up to the silica sand critical transformation temperature (573°C). The thermal profiles in the simulated and experimental results showed evidence of delayed heating and the presence of VTZ at ~100°C.

The modelled coating thickness showed delayed heating of the cores, suggesting that the coating is thermally insulating. The delay is according to coating thickness with the highest thickness showing the largest delay. This is clearly shown in the inset (region A) in Fig. 6. In the experimental thermal profiles shown in Fig. 9*b*, thermal delays are also obvious and also according to coating thickness. The coating containing 25% sol–gel component additive showed the highest viscosity and °Baumé parameter; this coating deposited

the highest proud layer thickness on the core, thereby providing sufficient thermal barrier to the diffusing heat. This confirms the thermal insulating nature of the coating and also following the thermal property of the refractory material (aluminium silicate). The delay provided by the coating materials to the core substrate helps to protect the core from the heavy shock of the heat from the liquid metal. At the same time, it allows for the solidification of the skin before the critical transformation temperature is reached.

The VTZs for both cold box and furan core materials are presented in Fig. 9*c*. Closer observation shows that the furan cores have larger vapour transport zone than the cold box cores. This observation has been consistent, and it suggests that the furan cores have higher moisture content than the cold box cores.[18] This is attributed to the higher porosity of furan cores than cold box cores and the higher affinity of furan binder materials for moisture compared to cold box binder materials.[18]

Three-dimensional surface texture evaluation

The performance of the coatings in improving the surface quality of castings will reflect on the surface roughness of the castings. The lower the surface roughness values, the better the performance of the coatings. However, castings free from veining, scabs and metal penetration defects are also indications of the coatings' positive performance. From the Taguchi experimental design, the performance response refers to the mean surface roughness of the castings measured using the 3D Alicona Infinite Focus Microscope G4. The average (mean), SD and SE of five roughness measurements (R_a values) and their corresponding signal/noise (*S*/*N*) ratios for all the experimental runs were calculated and presented in Table 5. From this table, it can be seen that experiment 7 gave the lowest mean surface roughness (2·54 μm) and the highest *S*/*N* ratio (−8·14 dB). From this, one might be tempted to say that this experimental run appears to have the set experimental conditions with optimal parameters. However, by Taguchi method, this is not the fundamental way of selecting optimal experimental conditions.

In Taguchi experimental design, the *S*/*N* ratio in units of decibels is used to measure the quality characteristics deviating from the desired value.[24,25] The *S*/*N* ratio is a measure of the performance aimed at developing products and processes insensitive to noise factors. A high *S*/*N* ratio means that the signal is higher than the random effect of the noise factors. The part or process operation consistent with the highest *S*/*N* ratio normally gives optimal quality characteristics with minimum variance.[26] In this study, the performance response is the surface roughness, which should be minimised, so the required *S*/*N* ratio is the one characteristic to smaller the better.

The mean *S*/*N* ratio calculated from the effect of the parameters and the interactions at specified levels is the average of all *S*/*N* ratios of a set of parameters at a given level.[24] The mean *S*/*N* ratio, the difference in levels and the contribution for the parameters are presented in Table 6. The contribution of an experimental parameter was calculated from the ratio of the maximum difference in values between the mean *S*/*N* ratio at each level and the sum of the maximum difference in values between the mean *S*/*N* ratios for each of the parameters, expressed in percentage. From Table 6, the order of the influence of the parameters in terms of the reduction of surface roughness of castings is % sol–gel>viscosity>‴ dipping time. However, from the level of contributions of each parameter, they are quite important in reducing the surface roughness of castings.

The main effects of the various parameters when they change from lower to higher levels can be visualised from Fig. 10. A larger *S*/*N* ratio indicates a greater influence of the parameter at that level on the reduction of surface roughness of the castings. The numerical value of the maximum point in each graph indicates the optimum range of the experimental conditions.[24,27] It is clear from the figure that the surface roughness was

Table 5 Orthogonal array for L_9 with performance responses and *S*/*N* ratio

	R_a values/μm								
Number of experiment	1	2	3	4	5	Mean	SD	SE	*S*/*N* ratio
1	4·51	2·74	4·15	3·43	2·52	3·47	0·86	0·39	−11·02
2	3·43	2·78	3·56	3·25	3·29	3·26	0·30	0·13	−10·29
3	2·39	2·88	2·56	2·73	2·41	2·59	0·21	0·09	−8·30
4	2·83	3·57	3·26	2·60	2·11	2·87	0·57	0·25	−9·30
5	2·92	2·42	3·02	2·59	2·77	2·74	0·24	011	−8·80
6	2·53	2·67	2·88	2·44	2·49	2·60	0·18	0·08	−8·32
7	2·65	2·12	2·51	2·88	2·55	2·54	0·28	0·12	−8·14
8	2·67	3·18	3·42	3·26	3·91	3·29	0·45	0·20	−10·40
9	2·86	3·34	3·49	2·06	3·31	3·01	0·58	0·26	−9·71
No sol–gel	3·79	5·10	3·00	2·47	2·74	3·42	1·06	0·47	−11·00
Uncoated	2·39	11·08	6·00	7·37	5·46	6·46	3·16	1·41	−16·97

Table 6 Mean *S*/*N* ratio at given level, difference between two levels and contribution of parameters

	Levels mean *S*/*N* ratios			Difference			
Parameters	1	2	3	L_{2-1}	L_{3-1}	L_{3-2}	% Contribution
% sol–gel	−9·87	−8·81	−9·42	1·07	0·46	−0·61	35·07
Viscosity	−9·49	−9·83	−8·78	−0·34	0·71	1·06	34·74
Dipping time	−9·84	−8·92	−9·34	0·92	0·50	−0·41	30·19

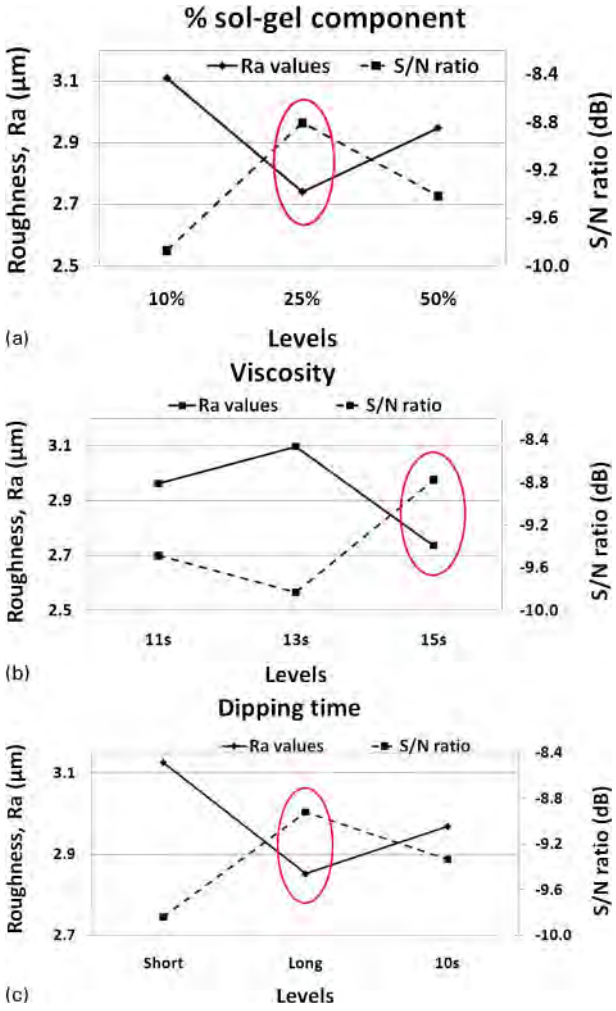

a per cent sol–gel component; *b* viscosity; *c* dipping time

10 Effects of parameter levels on performance response R_a and *S/N* ratio for cold box material

lowest at the second level for sol–gel component, third level for viscosity and second level for dipping time. These levels are circled in Fig. 10. Furthermore, the analysis of *S/N* ratio showed that the *S/N* ratio is highest for the same levels of parameters as the best level for obtaining the lowest values of surface roughness of the castings when using the sol–gel component as an additive to this coating.

The optimum value of the surface roughness can be predicted at the selected levels of the parameters. Identifying these parameters and their levels for mathematical purposes, let the sol–gel component at the second level be X_2, viscosity at the third level be Y_3 and dipping time at the second level be Z_2.

The predicted mean of the performance response MP can be computed as[13]

$$MP = \overline{X_2} + \overline{Y_3} + \overline{Z_2} - 2\overline{R} \quad (3)$$

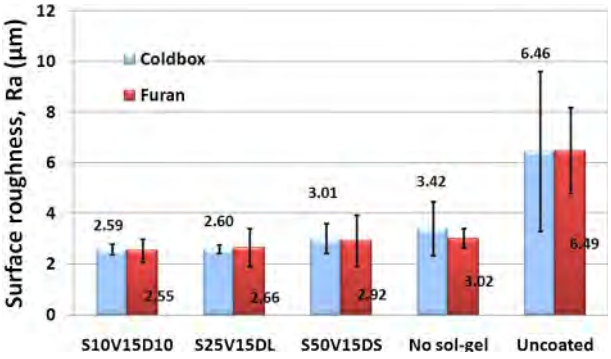

11 Comparison of surface roughness of cold box and furan cores with same treatment

where $\overline{R}$ is the overall mean of surface roughness (2·93 μm), $\overline{X_2}$ is the average surface roughness at the second level of the sol–gel component (2·74 μm), $\overline{Y_3}$ is the average surface roughness of the third level of viscosity (2·74 μm) and $\overline{Z_2}$ is the average surface roughness of the second level of dipping time (2·80 μm).

Therefore, substituting the values of various terms

$MP = (2{\cdot}74 + 2{\cdot}74 + 2{\cdot}8 - 2 \times 2{\cdot}93)$ μm $= 2{\cdot}42$ μm

The ANOVA results are presented in Table 7. From the data presented in the table, it can be seen that the calculated ratio F value is greater than F_{crit}, and the corresponding p value is very much lower than 0·05. Therefore, at 95% confidence level, these parameters had a significant effect on the reduction of the surface roughness of the castings.

A comparison of the surface roughness of the same treatments of cold box and furan cores is presented in Fig. 11. The results are comparable in all cases. However, this should not be the case with surfaces of castings produced without sol–gel component additive and uncoated cores when compared for both core systems. This is because visual surface inspection reveals that in the case of uncoated cores from both systems, the casting produced from cold box core should show higher roughness value than that of furan cores (Fig. 8*a* and *b*), although the scatter observed in the case of cold box cores is much higher than in furan (Fig. 11). Again, for castings produced with cores coated with coating without sol–gel component, it is expected from visual inspection that the furan casting should show higher roughness value. However, this is not the case. From these observations, it could be proposed that R_a, being a two-dimensional (2D) profile measurement, may not describe the surface roughness of castings accurately being that the surface of castings are not patterned. This is in line with the explanation by Leach[7] and Whitehouse[28] that a 2D profile does not necessarily indicate functional aspects of surfaces. This means possibly that two different surfaces can have the same R_a values but very different features and consequently very different functional properties. Leach further explained that with profile measurement and characterisation, it is

Table 7 Analysis of variance results for surface roughness data

Source of variation	Sum of squares	*df*	Mean square	*F* value	*p* value	F_{crit}
Between groups	60·82	10	6·08	5·14	0·00006	2·05
Within groups	52·07	44	1·18			

difficult to determine the exact nature of topographic features on surfaces. He suggested a more detailed surface texture parameter measurement in 3D. This is known as areal surface texture. This gives a more realistic representation of the whole surface and has more statistical significance.[7]

Conclusions

1. At 25% sol–gel content, a reaction led to the thickening of the coating with significant increase in °Baumé. This is attributed to increasing polymerisation rate, causing rapid gelation in the coating.

2. A glassy surface layer was observed to gradually build upon the cores with increasing sol–gel content.

3. The core permeability was reduced by the coatings and decreasing with increasing sol–gel content.

4. The sol–gel component additive to WCC coating applied on cold box cores showed no significant difference, as the surface quality of the castings is comparable.

5. A significant enhancement effect was observed on the surface of castings with the sol–gel component additive to WCC coating applied on furan cores.

6. The optimum coating performance can be obtained from 25%SG, 15 s DIN cup viscosity and 3–5 s dc for this case, and the expected mean surface roughness is 2·42 μm.

7. All the parameters (sol–gel component, viscosity and dipping time) contributed in the reduction of the surface roughness of the castings.

8. There is a positive potential in adding sol–gel component to foundry coatings; however, it requires optimum viscosity consideration as it changes the rheology of the coatings.

9. Finally, 2D surface texture characterisation may not be enough to describe the surface quality of cast components. A 3D areal surface texture measurement is suggested.

Acknowledgements

The authors wish to thank the Danish Agency for Science, Technology and Innovation for financing the work. They are also grateful to the two institutions and nine industrial partners to this project for their support and expertise.

References

1. in 'Metals handbook', 9th edn, Vol. 15, 'Casting'; 1998, Materials Park, OH, ASM International.
2. T. A. Burns (ed.): 'The Foseco foundryman's handbook', 9th edn; 1989, Oxford, Pergamon Press.
3. AFS: 'Analysis of casting defects'; 2007, Schaumburg, IL, American Foundry Society.
4. J. Campbell: 'Castings'; 1995, Oxford, Butterworth-Heinemann.
5. U. C. Nwaogu, T. Poulsen, R. K. Stage, C. Bischoff and N. S. Tiedje: 'New sol–gel refractory coatings on chemically-bonded sand cores for foundry applications to improve casting surface quality', *Surf. Coat. Technol.*, 2011, **205**, 4035–4044.
6. D. Stefanescu, S. Wills, J. Massone and F. Duncan: 'Quantification of casting skin in ductile and compacted graphite irons and its effect on tensile properties', *Int. J. Metalcast.*, 2008, 7–26.
7. R. K. Leach: 'Fundamental principles of engineering nanometrology'; 2010, London, Elsevier.
8. I. Asiltürk and M. Cunkas: 'Modelling and prediction of surface roughness in turning operations using artificial neural network and multiple regression method', *Expert Syst. Appl.*, 2011, **38**, 5826–5832.
9. A. Larena, F. Millan, M. Verdu and G. Pinto: 'Surface roughness characterisation of multilayer polymer films for graphitic arts applications', *Appl. Surf. Sci.*, 2001, **174**, 217–224.
10. 'BYK additives and instruments'. http://www.byk.com/physical-properties/viscosity-cups.html
11. D. C. Montgomery: 'Design and analysis of experiments', 3rd edn; 1991, New York, John Wiley & Sons.
12. Ö. Davaş and R. Kayikci: 'Application of Taguchi's methods to investigate some factors affecting microporosity formation in A360 aluminium alloy casting', *Mater. Des.*, 2007, **28**, 2224–2228.
13. S. Kumar, P. Kumar and H. S. Shan: 'Parametric optimization of surface roughness of castings produced by evaporative pattern casting process', *Mater. Lett.*, 2006, **60**, 3048–3053.
14. P. Vijian and V. P. Arunacalam: 'Optimization of squeeze cast parameters of LM6 aluminium alloy for surface roughness using Taguchi method', *J. Mater. Process. Technol.*, 2006, **180**, 161–166.
15. M. Alauddin, M. A. El Baradie and M. S. J. Hashmi: 'Computer aided analysis of a surface roughness model for end milling', *J. Mater. Process. Technol.*, 1995, **55**, 123–127.
16. Cast TIP: 'Controlling refractory coatings', 'Modern casting', 2010. http://www.docstoc.com/docs/56025950/Controlling-refractory-coatings (CAST-TIP-Technical-Information-and-Practice).
17. L. Winardi and R. D. Griffin: 'Effects of coating drying methods on LOI, gas evolution and core permeability', AFS Transactions paper, AFS, Schaumburg, IL, USA, Vol. 08-047, 2008.
18. U. C. Nwaogu, T. Poulsen, C. Bischoff and N. S. Tiedje: 'Influence of new sol–gel refractory coating on the casting properties of cold box and Furan cores for grey cast iron', Proc. 69th World Foundry Cong., Hangzhou, China, 648–653, October 2010, World Foundrymen Organization.
19. S. N. Ramrattan and M. K. Joyce: 'Final report – refractory coating control'. http://amc.aticorp.org/reports/wmu2009.pdf
20. Y. Wang, F. S. Cannon, M. Salama, J. Goudzwaard and A. J. Furness: 'Characterization of hydrocarbon emissions from green sand foundry core binders by analytical pyrolysis', *Environ. Sci. Technol.*, 2007, **41**, 7922–7927.
21. B. E. Brooks and C. Beckermann: 'Prediction of burn-on and mold penetration in steel casting using simulation', Proc. 60th SFSA Technical and Operating Conf., Chicago, IL, USA, December 2006, Steel Founders' Society of America, Paper 5·3.
22. T. Fusayama and M. Yamane: 'Surface roughness of castings made by various casting techniques', *J. Prosthet. Dent.*, 1973, **29**, (5), 529–535.
23. W. B. Parkes: 'Clay-bonded foundry sand'; 1971, London, Applied Science Publishers.
24. S. Kim, B. Yim, and Y. Park: 'Application of Taguchi experimental design for the optimization of effective parameters on the rapeseed methyl ester production', *Environ. Eng. Res.*, 2010, **15**, (3), 129–134.
25. K. Kandananond: 'Characterization of FDB sleeves surface roughness using the Taguchi approach', *Eur. J. Sci. Res.*, 2009, **33**, (2), 330–337.
26. N. M. Mehat and S. Kamaruddin: 'Optimization of mechanical properties of recycled plastic products via optimal processing parameters using Taguchi method', *J. Mater. Process. Technol.*, 2011, **211**, 1989–1994.
27. M. Altan: 'Reducing shrinkage in injection moldings via Taguchi, ANOVA and neural network methods', *Mater. Des.*, 2010, **31**, 599–604.
28. D. J. Whitehouse: 'Handbook of surface metrology'; 1994, London, IOP Publishing.

SUPPLEMENT 4

U. C. Nwaogu, K. S. Hansen, N.S. Tiedje,

“Design and production of a novel sand materials strength testing machine for foundry applications”.

Published in International Foundry Research 64 (2012) No. 2

Design and production of a novel sand materials strength testing machine for foundry applications

In the foundry, existing strength testing machines are used to measure only the maximum fracture strength of mould and core materials. With traditionally used methods, the loading history to ascertain deformation of the material is not available. In this paper, a novel moulding material strength testing machine was designed and built for both green sand and chemically-bonded sand materials. This machine measures and presents the loading response as a force-displacement profile from which the mechanical properties of the moulding materials can be deduced. The system was interfaced to a computer with a commercial PC based-control and data acquisition software. The testing conditions and operations are specified in the user interface and the data acquisition is made according to specifications. The force and displacements were calibrated to ensure consistency and reliability of the measurement data. The force was calibrated using an Amsler Hydraulic Press while the displacements were calibrated with and without loading using a displacement calibrator (Heidenhain Digitaler). The calibration results showed that the data obtained are stable and reliable and the machine can be used for the measurement of the strength of chemically-bonded sand materials.

Ugochukwu C. Nwaogu, Klaus S. Hansen and **Niels Skat Tiedje,** Lyngby, Denmark

Manuscript received 8 September 2011; accepted 13 October 2011

1 Introduction

The importance of knowing chemically-bonded moulding material's response to mechanical loading cannot be overlooked [1]. In the foundries, the practice of strength measurement on moulding materials is limited to greensand only. However, S. M. Strobl et al. [2] are of the opinion that foundries do not even go beyond measuring green compression strength thereby loosing important information from other strength parameters. This is due to the difficulty of obtaining reliable and repeatable tensile strength data. Meanwhile, the flexural strength (bending strength) is commonly used for brittle particulate materials. The stress at fracture in bending is known as the modulus of rupture, flexural strength, or transverse rupture stress [3]. It determines if the moulding or core material will withstand the metallostatic pressure from the incoming liquid metal without breaking leading to the production of castings with defects. However, research on the strengths of chemically-bonded sand core materials has been neglected for decades. Ademoh et al. [4] evaluated mechanical properties of local material-bonded moulding sand. They only examined tensile and compressive strengths which might be regarded as unreliable for chemically-bonded sand core materials.

For all the available measurements carried out so far, what has been determined is the maximum strength of the greensand moulding materials from either tensile or compression test or both of them using the Fischer universal strength machine (**Figure 1**).

In this machine, it is difficult to obtain a uniform rate of loading because the loading is operator dependent [5]. Therefore, it becomes imperative to have a machine for chemically-bonded moulding materials that can have uniform loading rate. This will enhance production of reliable and reproducible strength results. The strength machine shown in Figure 1 only shows the load at fracture neglecting the moulding materials elastic response to loading. It is on this note that the authors decided to design and build a new strength testing machine (new STM) that will have a uniform rate of loading and also show the loading profile. This machine was calibrated and used to make tensile and flexural tests on uncoated chemically-bonded moulding sand materials. It is run and controlled by a computer program that has been created for the device in a commercial PC based-control and data acquisition software. The program allows the user to apply a load to a specimen with choice

specifications. Depending on the particular test desired, the adaptor for that test can be fixed.

The machine generates the loading profile (force-displacement curve) from which the stress-strain curve is constructed. For many sand systems the stress-strain curve is a straight line or comparatively so, in that as the load is increased by equal increments, the sand system deforms by equal increments. In this article, a brief description of the theory of mechanical properties as it applies to moulding sand is given. The tensile and flexural strengths of chemically-bonded sand core materials were measured using the new STM.

2 Theory

The general theory of mechanical properties as it applies to foundry core materials will be discussed.

2.1 Tensile strength

The tensile test is the most common test for determining such mechanical properties of materials as strength, ductility, toughness, elastic modulus etc. [3]. The specimen is mounted between two jaws of a tension-testing machine and is loaded in a controlled manner while measuring the applied load and the elongation of the specimen over some distance. In the foundry, the maximum load is the only measurable property using the machine shown in Figure 1. The displacement cannot be determined from that instrument. The specimen for tensile measurement of moulding materials is shown in Figure 2. Typical results obtained by measuring the stress and strain under uniaxial loading until fracture occurs are presented in a Stress-strain curve. This curve gives a direct indication of the material properties. Typically, the specimen has an original length, l_0, and a cross-sectional area, A_0.

The engineering stress (nominal stress) is defined as the ratio of the applied load, F, to the original cross-sectional area, A_0, of the specimen:

$$\sigma = \frac{F}{A_0} \qquad (1)$$

The engineering strain is define as

$$\varepsilon = \frac{l - l_0}{l_0} \qquad (2)$$

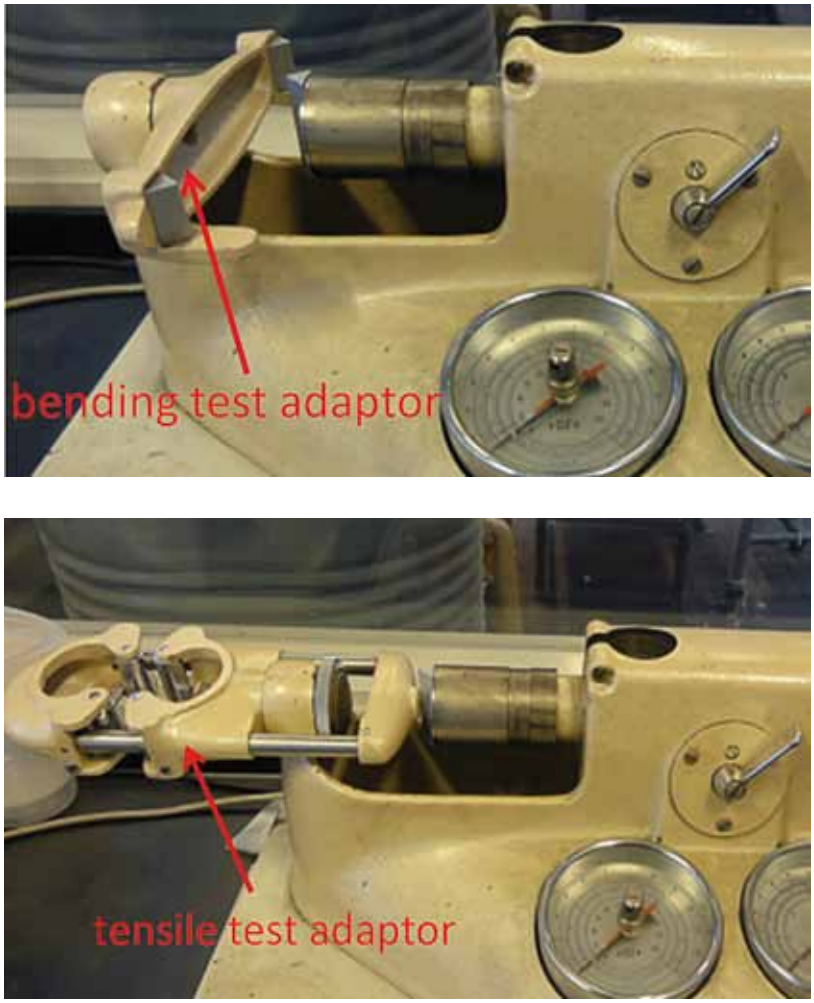

Figure 1: **Fischer universal strength machine (+GF+, Switzerland)**

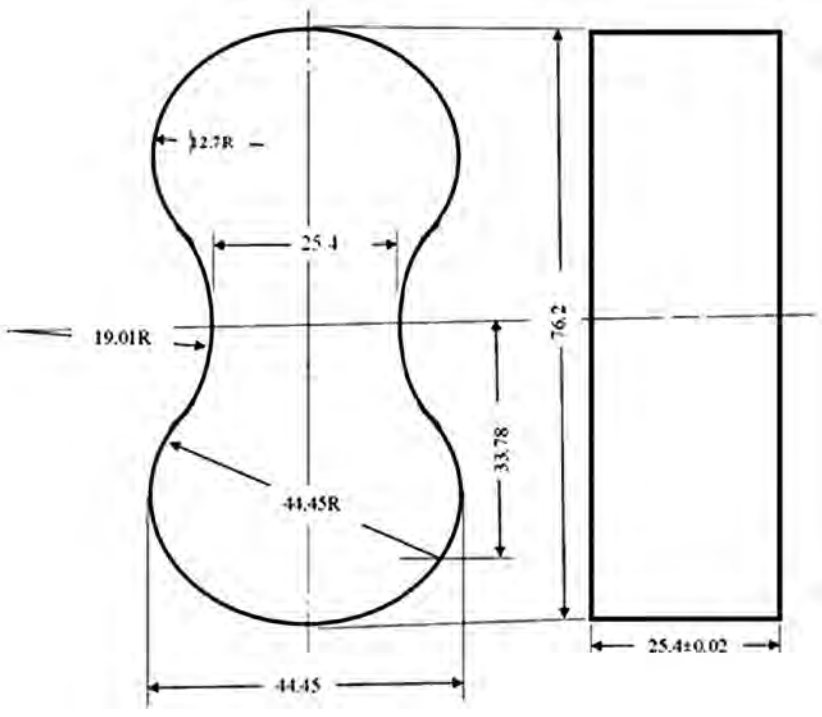

Figure 2: **The moulding material specimen for tensile strength measurement**

where l is the instantaneous length of the specimen. The engineering strain determines if the moulding or core material will withstand the metallostatic pressure from the incoming liquid metal.

In the case of brittle materials, the engineering stress and engineering strain are proportional in the elastic region until fracture, and there is no significant plastic deformation.

The initial portion of these curves for most materials used in engineering is linear. This is where elastic deformation takes place. The stress (σ) is directly proportional to the strain (ε). Therefore, for a specimen subjected to uniaxial loading, for the linear elastic portion it can be written.

$$\sigma = E\varepsilon \tag{3}$$

This relation is known as Hooke's law. The slope of the straight-line portion of the stress-strain diagram (E) is called Modulus of Elasticity or Young's Modulus. The modulus of elasticity may also characterize the "stiffness" or the ability of the material to resist deformation within the linear range. For brittle materials, like sand mould systems, the UTS is equal to the yield strength and their plastic deformation is almost null, because their failure does not involve significant deformation [3, 6].

2.2 Bending strength

A commonly used test method for brittle materials is the bend or flexure test [3]. It usually involves a specimen with a rectangular cross-section and is supported at its ends as shown in **Figure 3**. The longitudinal stresses in these specimens are tensile at their lower surface and compressive at their upper surfaces. The Flexural test measures the force required to bend a beam under three or four point loading conditions. The data obtained is often used to select materials for parts that will support loads without flexing. In the case of moulding materials, the three point bending test is used and it determines if the moulding or core material will withstand the metallostatic pressure from the incoming liquid metal without breaking. The stress at fracture in bending is known as the modulus of rupture, flexural strength, or transverse rupture stress [3].

Flexural modulus is used as an indication of a material's stiffness in bending. The load applied on the specimen and the displacements were measured until fracture occurred. The three point bending stress can be calculated by using the following equation [7, 8] (tension calculated positive).

$$\sigma_1 = \sigma_{max} = \frac{3L_0F}{2WT^2} \tag{4}$$

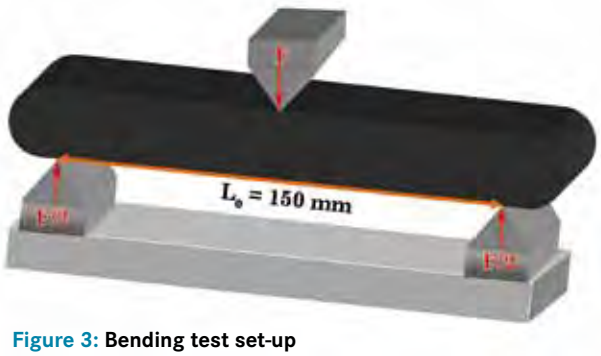

Figure 3: **Bending test set-up**

and the corresponding strain ε is calculated from equation (5) [8] (extension calculated positive)

$$\varepsilon_1 = \varepsilon_{max} = \frac{6T\Delta}{L_0} \tag{5}$$

where

L_0 distance between supports (mm)
F load (N)
W width of the specimen bar (mm)
T thickness of the specimen bar (mm)
Δ deflection at the loading point
$\varepsilon_1 = \varepsilon_{max}$ the maximum local strain
$\sigma_1 = \sigma_{max}$ the maximum local stress

Equations are only valid for a load placed in the middle of the support.

2.3 Compression strength

Compression is the reverse of tensile loading and involves pressing the material together. The test in the foundries is used to determine the bonding power of the binder systems. And subsequently, it is used to indicate the sand's shakeout characteristics when the sand system is subjected to the molten metal heat. If the dry compressive strength is high, the moulds and cores are stronger and difficult to shake out [9]. The compression test is usually carried out by subjecting a cylindrical specimen between two flat dies (platens) to compressive forces as shown in **Figure 4** [3]. Because of the friction between the specimen and the platens, the specimen being brittle will behave elastically to a certain load and then fails suddenly by splitting or cracking instead of bulging (barreling) [7]. A brittle material such as moulding sand is much weaker and less ductile in tension and shear than in compression [2, 3, 10]. J. W. Patrick et al. [11] and J. L. Amorós et al. [12] used diametrical-compression test to determine the tensile strength using the following equation:

$$\sigma = \frac{2W}{\pi DT} \tag{6}$$

where

W load (N)
D diameter (mm) of disc specimen
T thickness (mm) of disc specimen

Generally, failures in moulding materials under compression are essentially shear failures on planes because friction prevents the top and bottom of the specimen from expanding freely [3]. It is reported in [2], that a shear or cone of failure is typical of cylindrical moulding sand specimen when under compressive loading. The angle of inclination of the cone of failure is determined by the angle of friction which is typically 44 – 49 °. In the case of granular materials, the resistance to failure under shear stresses is a function of both the adhesion and the frictional resistance to the sliding of the ruptured surfaces. Therefore, it is expected that the compression strength of the coated cylindrical moulding specimens will be higher because both mechanisms apply than that of the uncoated specimen where only frictional resistance apply.

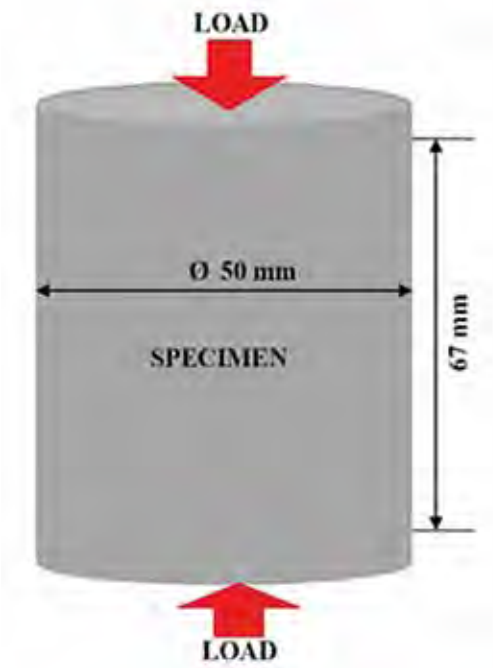

Figure 4: **Compression strength test specimen**

2.4 Brittle fracture

This is the mode of fracture observed in sand materials, brick, coal, concrete, gypsum, rocks and glass. The similarity in the cracking behaviour of different materials leads to the conclusion that there must be a common fundamental cause of fracture. Flaws, e. g. cracks, pores, voids and notches are present already in materials even prior to load application [13]. Brittle fracture occurs with little or no yielding. It is always sudden, extensive cleavage fracture with negligible distortion and low energy dissipation, under tensile or flexural stress usually at defects [10, 13]. In the early 1920s, Griffith postulated that crack extension in brittle materials occurs when there is sufficient elastic strain energy in the vicinity of a growing crack to form two surfaces. However, in 1950s, Irwin based on Griffith's work associated crack extension with an "energy release rate". This gave rise to a new parameter, K_{IC} – fracture toughness (MPa√m), or resistance to crack growth and is called the stress intensity factor [14]. The subscript I on the parameter K refers to mode I loading, i. e. the opening mode. Modern fracture mechanics relates the applied fracture stress at fracture origin, σ_f (MPa), to a flaw size, a (m) (= depth of surface crack, = ½ depth of embedded crack):

$$\sigma_f = \frac{K_{IC}}{Y\sqrt{a}} \qquad (7)$$

where Y is a dimensionless, material-independent constant, related to the flaw shape, location and stress configuration. For cracks extending to the surface as it is the case for sand materials, $Y = \sqrt{\pi} = 1.22$. As no material is perfectly homogeneous, all contain some sort of discontinuities or flaws on some scale. It can be seen from Equation (7) that the smallest strengths are associated with the largest flaws. In brittle materials, stress concentrations at specimen geometry changes, cracks, surface irregularities, pores and other intrinsic flaws are not relieved [14].

Brittle fracture initiates when $K_{IC} \leq Y\sigma_f\sqrt{a}$. Brittle fracture propagates at >1000 m/s if the driving force is present. K_{Ip} (propagation) < K_{Ic} (initiation) [14].

3 Materials and experimental procedure

3.1 Strength testing machine design, description of various parts and assemblage

The new Strength testing machine (new STM) with its identified parts is shown in Figure 5. The main functional parts of the new strength testing machine comprise of the following.

- servomotor (Motor) – JVL,
- linear axis – Bosch Rexroth,
- force transducer – Nordisk Transducer Teknik,
- mounting plates (base frame) – painted steel,
- tools (tensile and bending adaptors) – original machine.

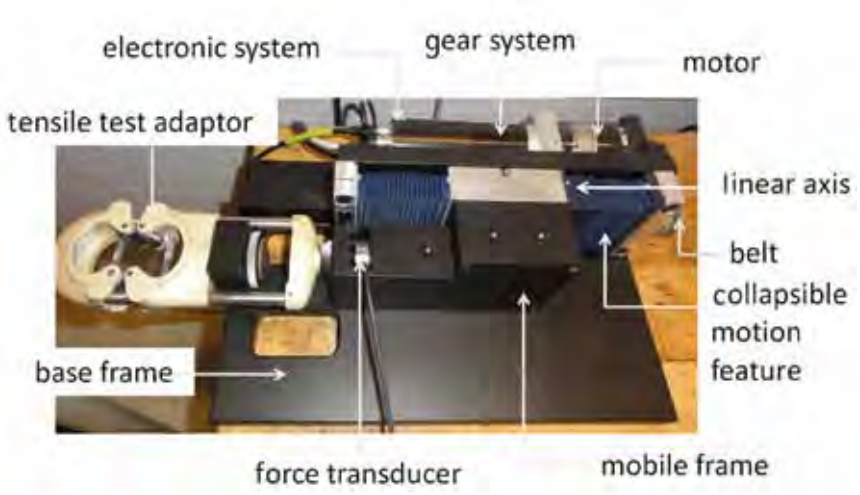

Figure 5: **The new strength testing machine (new STM) with the parts identified**

The motor is connected to the linear axis with a tooth-belt, which is tensioned to zero backlash. On the linear drive a mobile frame containing the force transducer is mounted on a block on the linear stage, and the counter part of the tool is mounted on a solid mount on the base-plate for the setup. Motor, gear, encoder and communication are done with an integrated servo drive from JVL, MAC-140 with a backlash-free planetary gear at 36 : 1.

The position of the tool is measured by an angular encoder on the motor, and then multiplied by the gearing to get the linear position. This gives room for a position error if there is backlash in any parts or connections, or if the stiffness of the machine is too low. The load

transducer does also deform a little during load/unload. This deformation can be corrected together with errors from the stiffness in the machine as long as the load is known.

The load transducer in the STM is a CM35 5000N, and has an accuracy of ±0.25 %, with a repeatability of ±0.10 % and a non-linearity of ±0.20 %. Since the load cell is calibrated against a known force in the whole range, the non-linearity, and accuracy decreases, and the maximum errors will be from lack of repeatability at ±0.10 %.

3.2 Calibration of the system

The force was calibrated using an AMSLER Hydraulic Press (Germany). The position/displacement was calibrated with and without loading using a displacement calibrator, HEIDENHAIN Digitaler Messtaster MI 25 (±0.0005 mm) (Germany). The set-up for the calibration without a load is shown in Figure 6. Later calibration curves with steel spring load are produced, and all measurements were subtracted, to remove the machines elastic response from the results.

Furthermore, the displacement curve from the system is compared with displacement curve from the Heidenhain calibration instrument. In same way, curves from load cell and Amsler press were compared.

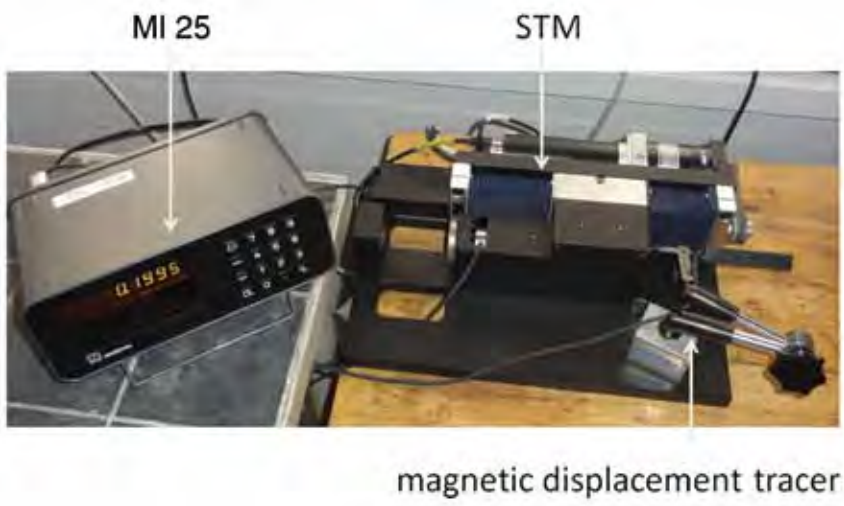

Figure 6: **The set-up for the calibration of the displacement**

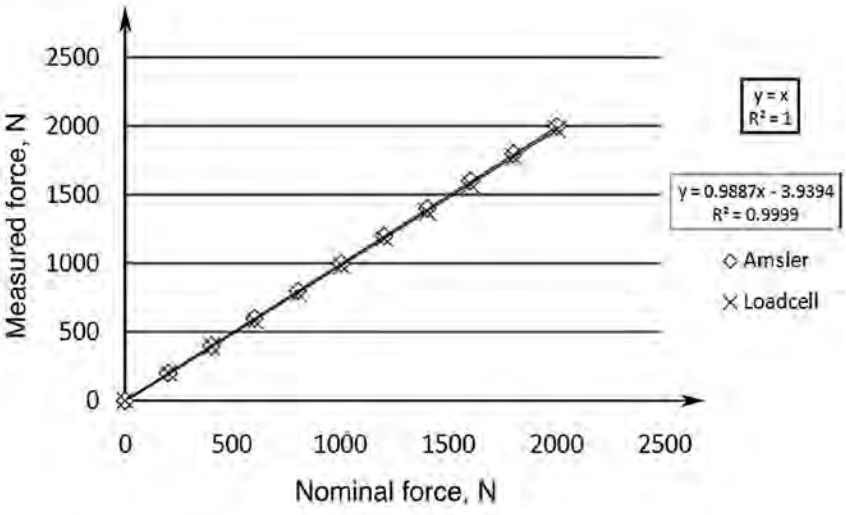

Figure 7: **Force calibration of the system with Amsler Hydraulic Press**

3.3 Preparation of core materials for strength tests

The chemically-bonded sand core specimens were made from silica sand with cold box and furan core making technologies. The dog bone specimens used for tensile tests have dimensions of 76.2 mm × 44.45 mm × 25.4 mm with a middle constriction length of 25.4 mm. The bending test is carried out with a bar of dimensions 172 mm × 22 mm × 22 mm.

3.4 Strength measurement

The tensile and bending tests were performed with the new STM. The proper adaptor for the specimens was fixed for each of the tests. The loading/measurement velocity was set at 0.05 mm/s. In these measurements, the loading profile was measured and presented as load-displacement curve. Three specimens with the same treatments were tested for both tensile and bending tests. Before, the processing of the data obtained from the new machine, the elastic behaviour of the system was taken into consideration so that the data presented only reflects the behaviour of the specimens.

4 Results and discussion

4.1 The calibration of the system

The force calibration results are shown in Figure 7 while the results from the calibration of displacements with and without loading are presented in Figure 8 respectively. Depending on the adaptor fitted to the machine, the tensile or flexural strength can be measured with a recorded profile. The data are linearly fitted using Regression analysis. From the figures, it can be seen that the data obtained from the system are in agreement with the data obtained from the references. From Figures 7 and 8, it can be seen that the coefficient of determination, R^2, obtained from the vertical deviations from the lines, is close to 1 and the slope of the lines is unity for the reference and approximately the same for the system. This means that the variability that will be observed from the system can be explained by the straight line model equation. This means that the measurement data obtained from the system will be reliable and can be used to charac-

terize the specimen material. The details of the least square method are explained elsewhere [16, 17]. When taking elasticity and other linear measurement errors into account the system shows excellent precision in measuring position and force. The remaining measurement errors are insignificant compared to the grain size of the sand used in the cores.

4.2 Mechanical properties

4.2.1 Tensile strength

A typical strength measurement specimen subjected to uniaxial tensile loading on the STM is shown in Figure 9. The specimen is pulled apart without any evident deformation. The typical loading profiles obtained from the new STM during tensile test are presented in Figure 10 for uncoated specimens. The screen dump of the Labview interface during measurement is shown in Figure 11.

From profiles presented in Figure 10, it can be seen that the loading part of the profiles is not uniform (not a straight line). This is due to the non uniformity of the specimens' density and also due to the slight movement of the specimen as it settles in the holder during loading. The difference in the maximum strengths of the specimens before fracture is due to the variation in density and surface quality (K_{IC}) which is inherent in granular materials. The reproducibility of the tensile strength of brittle materials is very low [6].

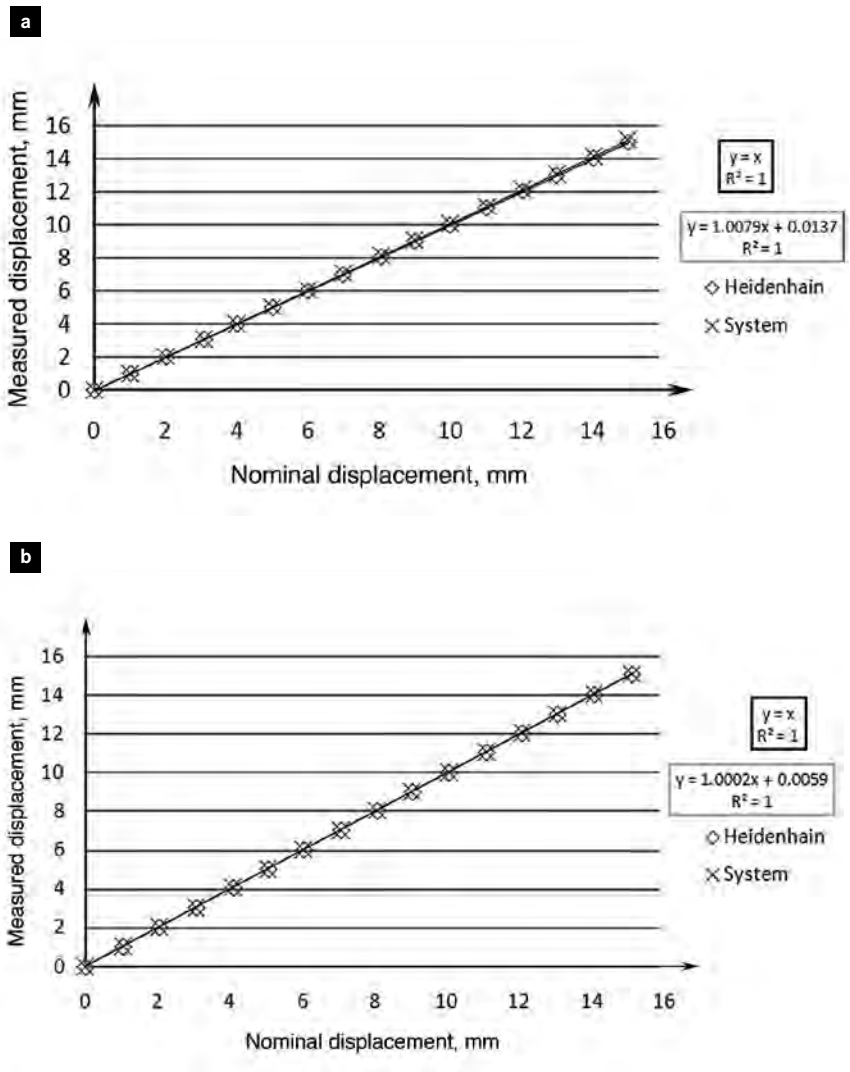

Figure 8: Displacement calibration on the system: a) with loading; b) without loading

Figure 9: Broken dog bone specimen subjected to uniaxial loading in new STM

4.2.2 Flexural strength

A typical strength measurement specimen subjected to flexural loading on the STM is shown in Figure 12. The specimen is subjected to three-point bending test on the new STM. The setup is shown in Figure 3. At the point of dynamic loading, the specimen experiences compressive stresses while tensile stresses are developed in the opposite side of the specimen. This leads to phenomenon known as simultaneous dual-stress-effect. The typical flexural loading profiles obtained from the new STM are presented in Figure 13 for uncoated specimens.

The profiles obtained are similar to the tensile test profiles. There are kinks observed between 50 and 75 N on the profile in Figure 13, this is due to the slight compaction of the sand grains at the point of loading. The presence of this effect is dependent on the porosity of the specimen around the loading point. The fracture strengths are much lower in flexural test and are also closer to each other. Due to the orientation of the specimen and the direction of the loading in bending test, the loading curves are more linear and re-

producible relative to the tensile test curves as can be seen in Figure 13. This suggests that the results obtained from the flexural tests may be more representative of the strength behavior of brittle materials. The is in agreement with the claim made in [3] that flexural tests are the most reliable test for the determination of the strength of brittles.

4.3 Confirmation of higher precision of the new strength testing machine (new STM) over the old strength testing machine (old STM)

The controlling software is made to acquire and present data as Force (N) vs. Time (s) during measurement. It automatically converts the data as Force (N) vs. Displacement (mm) during data saving.

The measurements with new strength testing machine (new STM) was done at a constant loading rate of 0.5 mms^{-1}, which is one of the advantages of the new STM. This is very clearly shown in

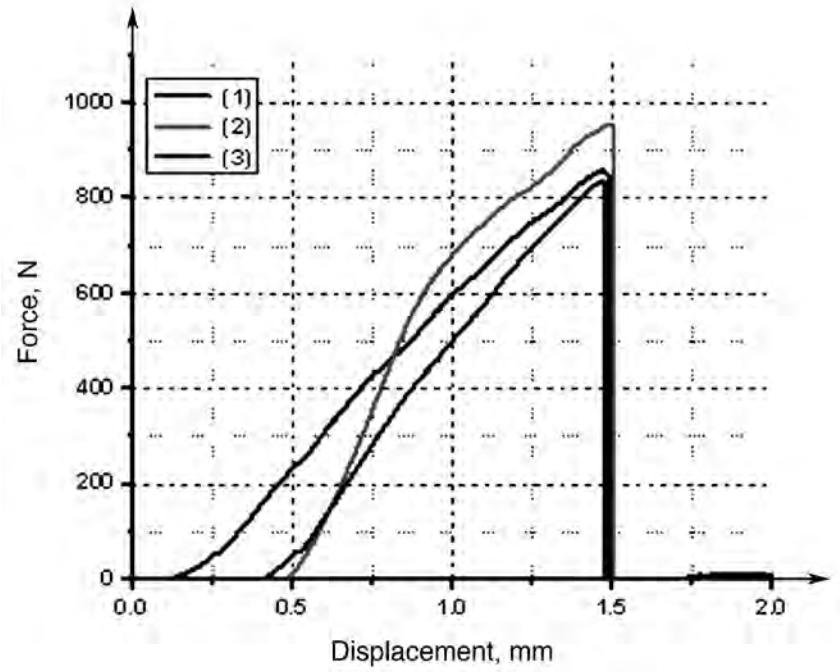

Figure 10: Tensile test – typical strength profiles from three uncoated dog bone specimens after fracture in new STM

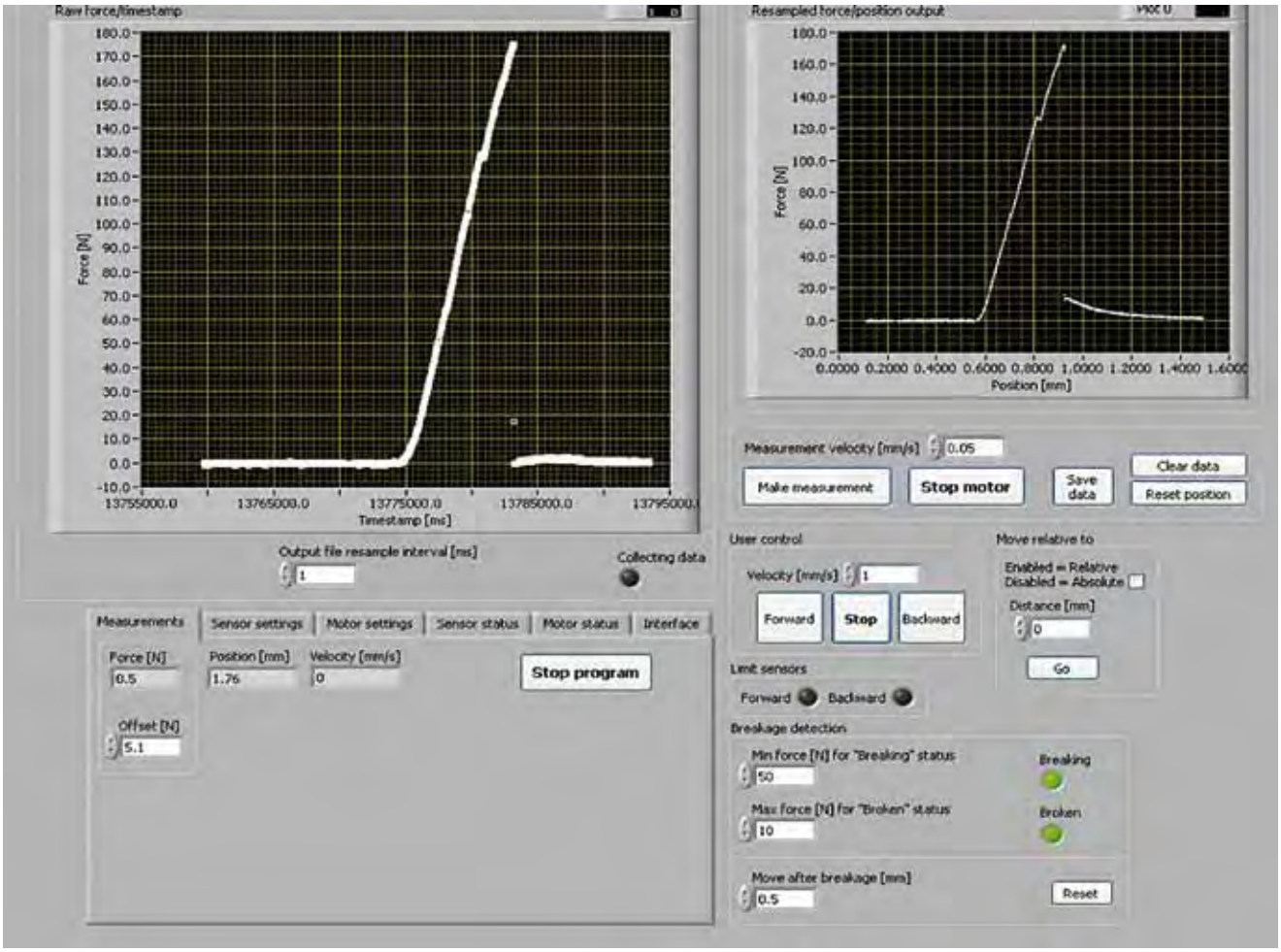

Figure 11: The screen dump of the data acquisition interface during measurement

Figure 14 with the smoothness of the curves. In the measurements with the old STM, the controlling software still assumes uniform loading rate in the data acquisition during measurement, even at this situation, it is clearly seen that the loading is not uniform because it is manually loaded, which is a limitation of the old STM. Furthermore, the old STM does not measure displacement, which is another limitation (the displacements seen here for old STM is as a result of the conversion of time to displacement by the system during data saving).

In the measurements presented in Figure 14, three measurements were made for both machines and the reproducibility of the new STM is obvious against the non reproducibility of the old STM. This confirms the higher precision and reliability of the new STM over the old STM.

5 Conclusions

A new moulding materials strength testing machine (new STM) was designed and built. The new STM was interfaced with a PC based-control and data acquisition software. The machine is designed to the standard that is normally used in laboratories to make tensile, compression and three-point-bend tests. The force and displacement of the new STM were calibrated to ensure reliability of the measurements. When taking elasticity and other linear measurement errors into account the system shows excellent precision in measuring position and force. The remaining measurement errors are insignificant compared to the grain size of the sand used in the cores. The tensile and bending strengths of chemically-bonded sand cores materials were successfully measured using the new STM and robust results were obtained.

In tensile tests, the profiles show the pulling tool and its point of contact with the specimens affected the linearity of the profile. Although, this depends on the position of the grip and the strength of the material at that point. In the bending test, the profiles are more reproducible and may be more reliable in the determination of the strength of brittle materials.

Figure 12: Broken bar specimen subjected to bending test in new STM

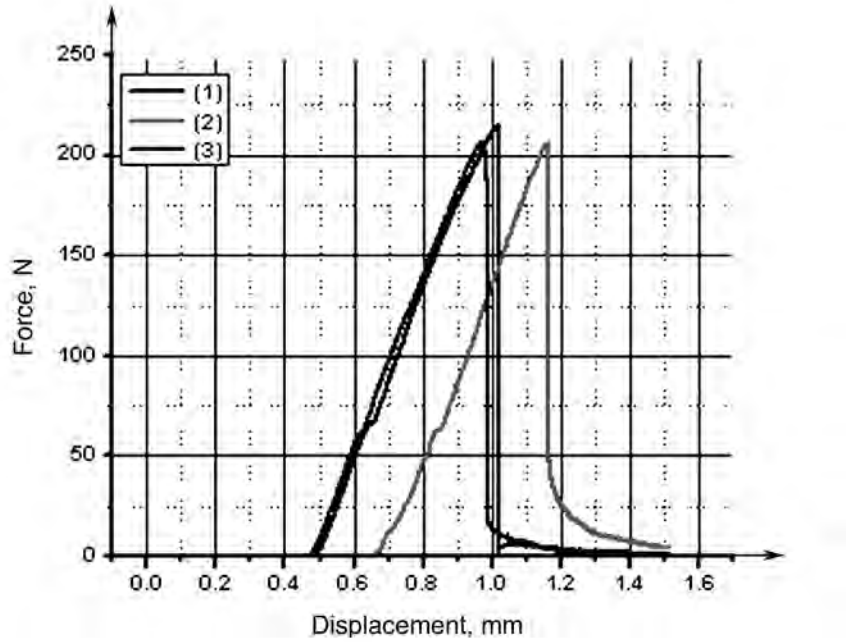

Figure 13: Three point bending test – typical strength profiles from three uncoated bar specimens after fracture in new STM

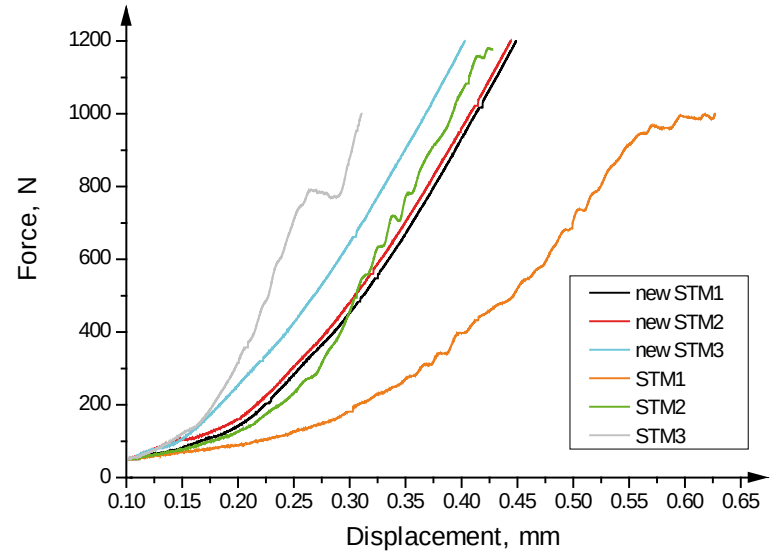

Figure 14: Force (N) vs. displacement – comparison between new strength testing machine (new STM) and old strength testing machine (old STM)

The authors wish to thank the Danish Agency for Science, Technology and Innovation for financing the work. The authors are also grateful to the nine industrial partners to this project for their support and expertise.

***U. C. Nwaogu**, Technical University of Denmark, Department of Mechanical Engineering, Institute of Production and Process Technology, DK2800 Kgs. Lyngby, Denmark, **K. S. Hansen**, IPU Technology Development, DK-2800 Kgs. Lyngby, Denmark, **N. S. Tiedje**, Technical University of Denmark, Department of Mechanical Engineering, Institute of Production and Process Technology, DK2800 Kgs. Lyngby, Denmark*

Literature

[1] Dietert, H. W.; Brewster, F. S.; Graham, A. L.: Load carrying power of moulding sand, moulding methods and materials. The American Foundrymen's Society, 1st ed., Illinois, 1962.
[2] Strobl, S. M.; Schuster, F. W.: Gauging green sand flowability helps predict mould quality. Modern Casting 87 (1997) no. 2, pp. 48-51.
[3] Kalpakjian, S.; Schmid, S. R.: Manufacturing engineering and technology. Pearson Prentice Hall, New Jersey, 2006.
[4] Ademoh, N. A.;. Abdullahi, A. T.: Evaluation of mechanical properties of expendable sand cores bonded with the Nigerian Gum Arabic Grade 4. American-Eurasian Journal of scientific Research 3 (2008) no. 2, pp. 199-204.
[5] Parkes, W. B.: Clay-bonded foundry sand. Applied Science Publishers, London, 1971.
[6] Van Vlack, L. H.: Materials science for engineers. Addison-Wesley, California, 1970.
[7] Mencik, J.: Strength and fracture of glass and ceramics. Glass Science and Technology 12 (1992), pp. 164-168.
[8] Ramrattan, S. N.; Paudel, A. M.; Makino, H.; Hirata, M.: Desirable green sand properties via aeration sand filling. AFS Transactions (2008), paper 08-128 (04).
[9] Fu, R.; Zhang, T.-Y.: Influences of temperature and electric field on the bending strength of lead zirconate titanate ceramics. Acta. Mater. 48 (2000), pp. 1729-1740.
[10] Ceriolo, L.; Tommaso, A. D.: Fracture mechanics of brittle materials: A historical point of view. 2nd Int. PhD Symposium in Civil Engineering, 1998, Budapest, Hungary.
[11] Patrick, J. W.; Stacey, A. E.; Wilkinson, H. C.: The strength of industrial cokes: Part 2. Tensile strength of foundry cokes. Fuel 51 (1972), pp. 174-179.
[12] Amorós, J. L.; Cantavella, V.; Jarque, J. C.; Felíu, C.: Green strength testing of pressed compacts: An analysis of the different methods. Journal of the European Ceramic Society 28 (2008), pp. 701-710.
[13] Wang, E. Z.; Shrive, N. G.: Brittle fracture in compression: mechanisms, models and criteria. Engineering Fracture Mechanics 52 (1995) no. 6, pp. 1107-1126.
[14] Quinn, J. B.; Quinn, G. D.: A practical and systematic review of Weibull statistics for reporting strengths of dental materials. Dental Materials 26 (2010), pp. 135-147.
[15] WTIA Technical note 10, WRC Bulletin no. 430; BS7910; AS/NZS 3788; API 579.
[16] Box, G. E. P.; Hunter, W. G.; Hunter, J. S.: Statistics for experimenters: An Introduction to design, data analysis, and model building. John Wiley & Sons, Canada, 1978.
[17] Montgomery, D. C.: Design and analysis of experiments. 3rd edition, John Wiley & Sons, Canada, 1991.

Keywords: Strength testing machine; mechanical properties; load transducer; linear displacements; calibration; cold box; furan

SUPPLEMENT 5

U. C. Nwaogu and N.S. Tiedje,

“Mechanical properties of chemically bonded sand core materials dipped in sol–gel coating impregnated with filter dust: novel approach to improve casting quality”.

Published in International Journal of Cast Metals Research (2012)

DOI 10.1179/1743133612Y.0000000013

Mechanical properties of chemically bonded sand core materials dipped in sol–gel coating impregnated with filter dust: novel approach to improve casting quality

U. Nwaogu* and N. S. Tiedje

A novel sol–gel coating impregnated with filter dust was applied on chemically bonded sand core materials by dipping. After curing, the strengths of the core materials were measured under uniaxial loading using a new strength testing machine (STM). The STM presents the loading history as a force–displacement curve from which the mechanical properties of the materials are deduced. The fracture surfaces were examined using a stereomicroscope and a scanning electron microscope. From the results, the strengths of the core materials were slightly reduced by the coating in tensile and flexural modes, while the strengths were increased under compression. The mode of fracture of the chemically bonded sand core materials was observed to be intergranular through the binder. The stiffness of the chemically bonded sand core materials was determined. For better understanding of the mechanical properties of the chemically bonded sand core materials, a combination of flexural and compression tests is suggested for improving the casting quality.

Keywords: Mechanical properties, Brittle fracture, ANOVA, Weibull statistics, Microscopy, Cold box, Furan, Linear regression analysis

Introduction

Knowledge of the strength of chemically bonded moulding materials cannot be overlooked.[1] Although, new technologies in core making, such as cold box, furan, hot box processes, etc., make presumably strong cores. However, there is a strong need to quantify the strength of moulding materials produced from these chemical systems, because some of them are coated with mould or core washes to enhance the surface finish of the castings produced from them.[2–6] Foundry experts believe that the application of refractory coatings on moulding materials reducess the strength, but to what extent is not known. This situation is worse with water based coatings compared to alcohol based coatings. It is well known that water degrades the strength of moulding materials made with sodium silicate/CO_2 process,[7,8] making the application of water based coating to sodium silicate cores difficult.

Above all these, in the foundries, the performance of strength measurement on moulding materials is limited to greensand materials. However, Strobl and Schuster[9] are of the opinion that foundries do not even go beyond measuring green compression strength. This leads to loss of important information from other strength parameters like flexural and tensile strengths. This is due to the difficulty in obtaining reliable and repeatable tensile strength data. Meanwhile, flexural strength (bending strength) is commonly used for brittle particulate materials.[10] The stress at fracture in bending is known as the modulus of rupture, flexural strength or transverse rupture stress.[9] It determines if the moulding or core material will withstand the metallostatic pressure from the incoming liquid metal without breaking and thus prevents the production of castings with defects. However, research on the strengths of chemically bonded sand core materials has been neglected for decades. Ademoh and Abdullahi[11] evaluated the mechanical properties of expendable sand cores bonded with gum Arabic (acacia species) grade 4. They only examined tensile and compressive strengths, which may be regarded as unreliable for chemically bonded sand core materials.

In this study, the tensile and flexural strengths of chemically bonded sand core materials were measured using a new strength testing machine (STM). The compression strength was measured with an Amsler hydraulic press. Descriptive statistics, analysis of variance (ANOVA) and Weibull statistical distribution were applied in the evaluation of data, and reliable deductions were made. The fracture surfaces were examined in detail, and deductions were made. The modulus of elasticity (stiffness) of the chemically bonded sand materials was also approximately quantified from the stress–strain curves.

Technical University of Denmark, Lyngby, Copenhagen, Denmark

*Corresponding author, email ugon@mek.dtu.dk

Received 9 November 2011; accepted 15 February 2012
DOI 10.1179/1743133612Y.0000000013

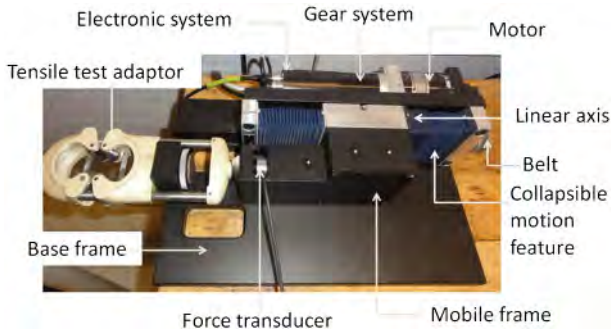

1 Strength testing machine used in this study

Experimental

Sol–gel coating formulation

The sol–gel coatings were formulated from a sol–gel stock solution prepared by acid (0·1N HCl) catalysed hydrolysis with water of (3-glycidyoxypropyl)trimethoxysilane (Degussa) and aluminium (III)-s-butoxide, 75% solution in s-butanol (AL, ABCR). After stirring the sol for 30 min, propyltrimethoxysilane (Evonik/Degussa) was added. Stirring continued for another 30 min. The molar composition of the sol–gel stock solution was 385 : 3 : 1 : 95 (3-glycidyoxypropyl)trimethoxysilane/aluminium (III)-s-butoxide/HCl/propyltrimethoxysilane). The sol–gel stock solution was mixed with 3% bentonite suspension in demineralised water, in the ratio of 6·7 : 1, for 30 min. The refractory filter dust was added, and the blend was stirred for ~2 h until a homogeneous suspension was obtained. The coatings were prepared with 40, 50 and 60 wt-% filter dust.

Preparation of core materials for strength tests

The chemically bonded sand core specimens were made from silica sand with cold box and furan core making technologies. The cold box cores were made from 100% new sand, while the furan cores were made from 80% regenerated sand with 20% new sand. The briquette or dog bone specimens used for tensile tests had a length of 76·2 mm, a rectangular reduced gauge section of 25·4 × 25·4 mm and enlarged shoulders at both ends of diameter 44·5 mm. The bending tests were carried out on a rectangular cross-section bar of dimension 172 × 22 × 22 mm and the compression tests on cylindrical specimens of height 67 mm and diameter 50 mm.[12] These specimens were dip coated with sol–gel coatings containing 40, 50 and 60% solid content for 1, 3 and 5 s. Three replicates were tested for each treatment condition.

Strength measurement

Tensile, bending and compression tests were performed in this study. Tensile and bending tests were performed with the custom built STM shown in Fig. 1. This machine was carefully calibrated. The loading/measurement velocity was set at 0·05 mm s^{-1}. Three uncoated specimens were tested for each of the three strength modes, whereas all the other specimens tested were coated. Three specimens at each level for each of the tests were dip coated in 40, 50 or 60% solid content solutions for 1, 3 or 5 s. Before processing the data obtained from the new machine, the elastic behaviour of the system (steel metal) was taken into consideration so that the data presented reflect only the actual behaviour of the specimens.

From the load–displacement curves obtained, the curves were converted to stress–strain curves accordingly. The tensile and bending strengths at fracture were determined. The curves obtained were linearly fitted to determine the elastic modulus (stiffness) of the moulding materials as the slope of the linear portion of the profiles.

The compression test was performed with an Amsler Hydraulic Press. In the Amsler Hydraulic Press, since only the lower punch moves, single end pressing was carried out. Moreover, the stress state in the sample was assumed to be homogeneous with the symmetry axis of the specimen.

Statistical evaluation

Descriptive statistical analysis was applied to the data from each set of three specimens to determine the means and standard deviations. Analysis of variance was applied to all the data in each test to determine the significance of the means. All statistical analyses were performed at a 95% confidence interval. A Weibull analysis[13–18] was performed on the data from the flexural strengths of the chemically bonded sand core materials.

Characterisation of the fracture surface

A stereomicroscope (Zeiss Stereo CL1500 ECO) was used to examine the fracture surface to elucidate the penetration depth of the coating into the substrates in order to evaluate the effect of the coating penetration on the mechanical properties of the core materials. Image-Pro Plus Version 6.2, an image analysis software, was used to measure the penetration depths from the stereomicrographs. Stereomicrographs with a calibration bar identifying a length of 0·5 mm were uploaded into Image-Pro Plus software, one at a time. The calibration bar was used to specify the length of 0·5 mm to the software using spatial calibration. After calibration of the image, a length measuring tool was used to measure the depth of the coating penetration into the cores, as identified by colour variations on the image from the coating penetrated area and the coating free area. For each stereomicrograph, five different measurements of the penetration depths were made. The averages and standard deviations of the data are presented.

The sand specimens are non-conducting; consequently, they were sputtered with carbon. After which, the fracture surfaces of the sand materials were examined using a scanning electron microscope (SEM) (JOEL JSM-5900 with LaB6) filament equipped with a INCA X Oxford Instruments EDS.

Results and discussion

Mechanical properties

Tensile strength

A typical briquet/dog bone specimen subjected to uniaxial tensile loading on the STM is shown in Fig. 2*a*. The specimen is pulled apart without any evident deformation. The typical loading profiles obtained from the STM during tensile test on three specimens are presented in Fig. 2*b*. It can be seen from Fig. 2*b* that two of the tensile strength profiles have

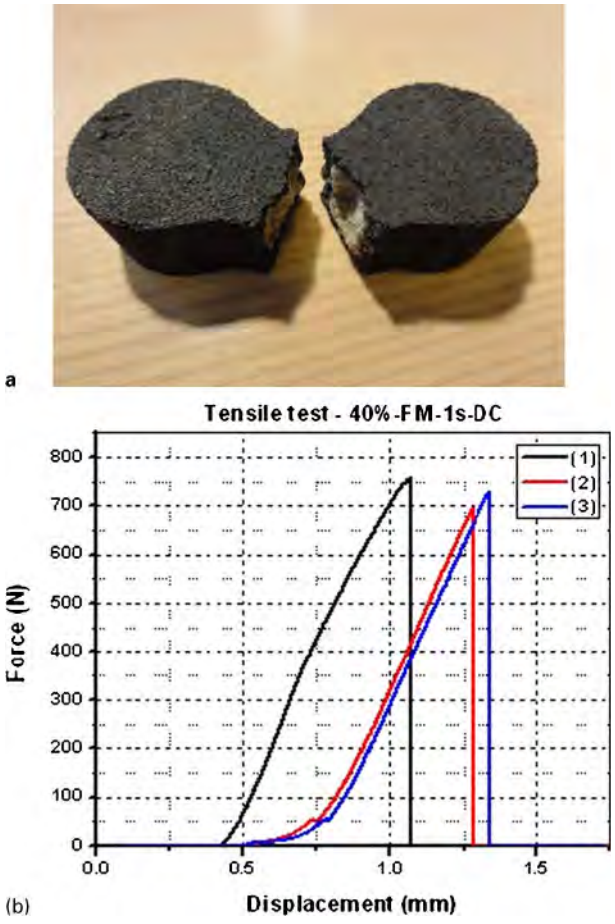

a broken dog bone specimen subjected to uniaxial loading on STM; *b* typical strength profiles from three dog bone specimens

2 Specimen and profiles obtained from tensile test

kinks of ~50 N loading; this is due to the adjustment of the specimens on the pulling fixtures of the STM. As can be seen from the profiles, after the adjustment, the profiles seem reasonably linear when firm grip is established until fracture.

From Fig. 2*b*, it is possible to determine the load at a corresponding displacement from the start of the loading until failure. The maximum strength at failure can also be determined, and as can be seen from the profiles, there is a scatter in the maximum strength values that is typical of brittle materials. This is attributable to the fact that granular materials have inherent pores, cracks, voids and fissures that are of different volumes and sizes in the various specimens. This means that it is difficult to assign a specific strength value to represent their mechanical behaviour.[19] Instead, the strength of chemically bonded sand core materials will be presented as an average with a 95% confidence interval to compensate for the variations.

From Fig. 3, it can be seen that the coating on the cores slightly reduced the strength of the core materials compared to the uncoated cores. This is attributed to the fact that the coating is aqueous in nature and as such may weaken the bonds formed by the binder with the sand grains, which suggests that the strength of the core materials may be determined by the bonding bridges between the sand grains. It can also be seen from Fig. 3 that the effect of the percentage solid content and the

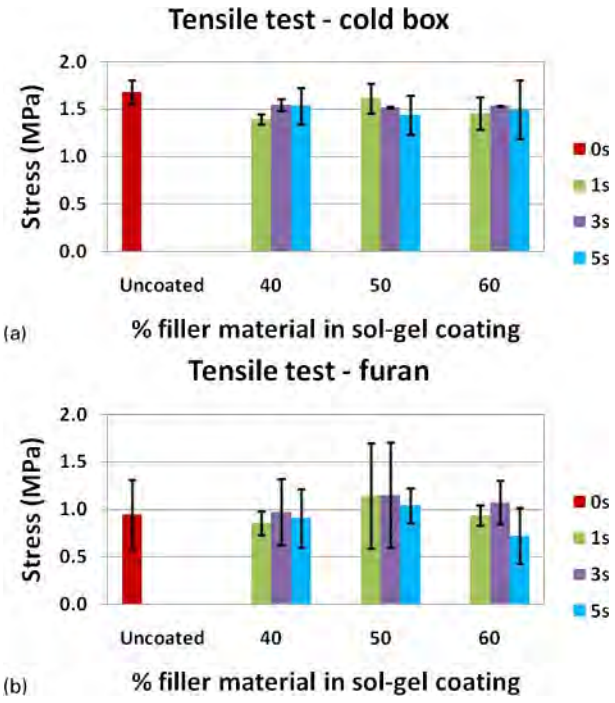

3 Tensile strengths of *a* cold box and *b* furan chemically bonded sand specimens

dipping time cannot be established due to the heterogeneity of the sand materials as a composite.

A comparison of the strengths of cold box (Fig. 3*a*) and furan (Fig. 3*b*) core materials shows that the cold box material has higher strength than the furan material in the tensile mode. This is expected because cold box binders, due to their chemistry, generally are stronger than furan binders. Since the cold box binder is used with fresh sand and the furan binder is used with partly regenerated sand, we should expect to see a difference in the mechanical properties of the two systems. Further analysis of Fig. 3 shows that the effect of the aqueous nature of the coating in strength reduction is less pronounced in the furan core material compared to the cold box core material. However, the scatter in the value of the strength in the furan core material is larger than in the cold box core material. This may be attributed to different influences such as the difference in the sand materials used (cold box, 100% new sand; and furan, 20% new sand and 80% regenerated sand), the chemicals and, most importantly, the core production process. The cold box core materials are made automatically, while the furan core materials are made manually. Therefore, in furan core materials, there may be inconsistencies in compaction, density, permeability, etc., which may vary from specimen to specimen. All these will affect the flaws that in turn will affect the strength values.

Flexural strength

A typical bar specimen subjected to bending/flexural loading on the STM is shown in Fig. 4*a*. The specimen is subjected to a three-point bending test according to ASTM standard D5934.[20] At the point of dynamic loading, the specimen experiences compressive stresses, while tensile stresses are developed in the opposite side of the specimen. This leads to a phenomenon known as simultaneous dual stress effect. The stress σ, strain ε and

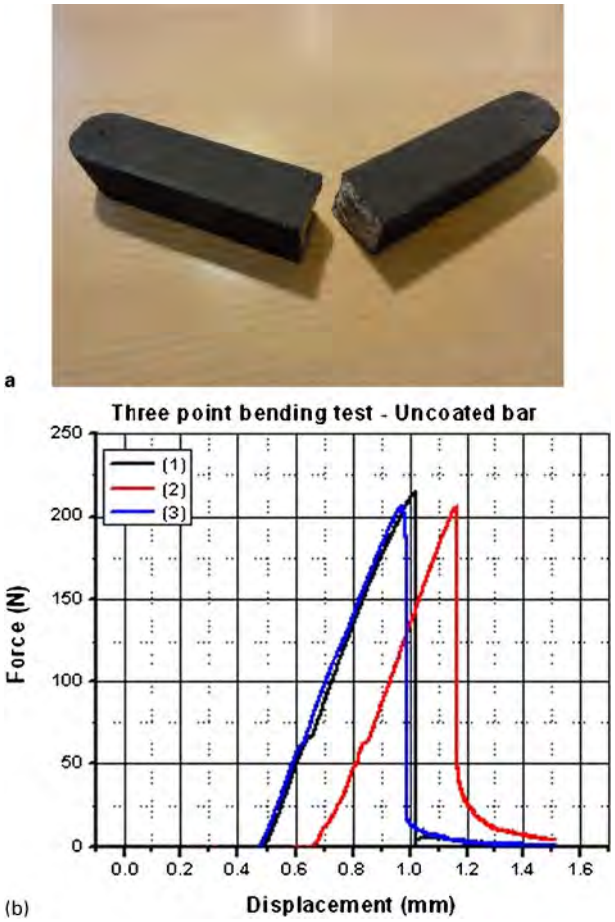

a bar specimen subjected to bending loading on STM; *b* typical strength profiles from three bar specimens

4 Specimen and profiles obtained from bending test

modulus of elasticity E can be calculated from the following flexural strength equations[21,22]

$$\sigma = \frac{3PL_0}{2lb^2} \tag{2}$$

and

$$\varepsilon = \frac{6db}{L_0^2} \tag{3}$$

Thus

$$E = \frac{\sigma}{\varepsilon} = \frac{L_0^3}{4lb^3}\left(\frac{P}{d}\right) \tag{4}$$

where P is the loading force, l is the cross-section length, b is the cross-section breadth, L_0 is the support span and d is the specimen displacement. The stresses presented in this study are calculated from equation (2).

The typical flexural loading profiles obtained from the STM are presented in Fig. 4*b* for three bar specimens. A closer look on the profiles reveals some kinks during loading; this time, it is as a result of cracking of the coating or compaction of the coating or sand (uncoated) at the loading point. It indicates that the force from the test fixture breaks the surface of the cores at a specific pressure.

The flexural strength is significant to assess the strength in the core print areas since the loading effect here during casting is bending. The loading effect can also be compression and bending, depending on the geometry of the castings, the locations of the core prints and the ingates.

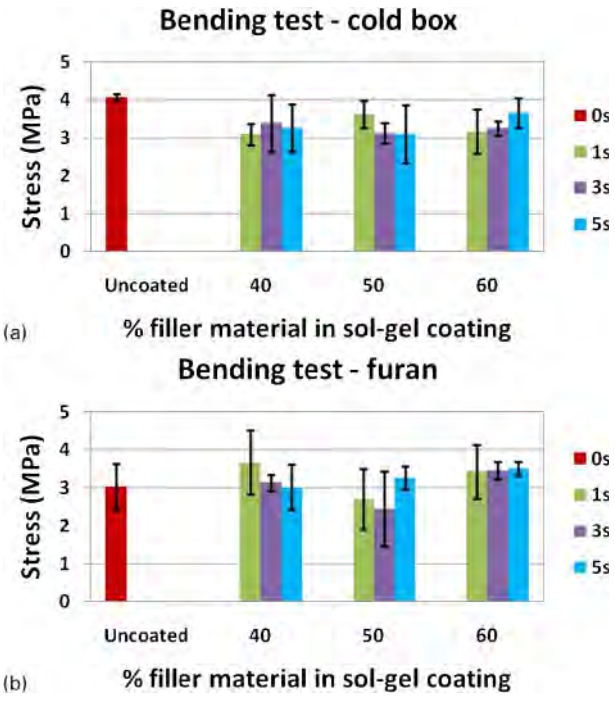

5 Flexural strengths with standard deviation of *a* cold box and *b* furan chemically bonded sand specimens subjected to different coating times

The profiles obtained are similar to the tensile profiles. The same deductions made from the tensile profiles are also applicable for the flexural profiles. For the uncoated bars, the profiles look consistent, and the maximum strength for the three specimens are quite close, as can be seen in Fig. 4*b*. However, with application of the coating to the core materials (Fig. 5), the results showed the influence of the coating on the strength. This is due to the coating weakening effect on the binder bonding bridge between the sand grains.

From Fig. 5, the absence of a trend with the percentage solid content and dipping time is also evident. The effect of the coating on strength reduction is also more obvious in the cold box core material (Fig. 5*a*) compared to the furan material (Fig. 5*b*). The furan materials also showed larger scatter in the measured values for the same reasons given above for the tensile test profiles.

Compression strength

Owing to the limited capacity of the load cell used for the STM as a result of the strength of the main frame, the compressive strength measurements were made with an Amsler hydraulic press. A specimen subjected to compressive testing is shown in Fig. 6. It is very clear to see the inclined fracture nature. This is referred to as conical, pyramidal or wedge shaped failure mode, which is frequently observed in uniaxial compression tests, as the normal type of fracture mode of granular materials. An inclination angle of 44–49° of the cone of failure, as suggested by Strobl and Schuster,[9] is evident. This happens due to the lateral confining effect of the loading platens of the test machine. Friction restricts lateral expansion of the specimen near both ends.[13,23] Consequently, under usual testing conditions, the stress

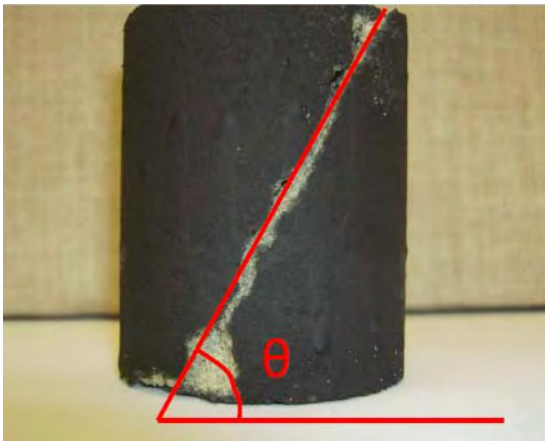

6 Broken cylinder specimen subjected to compression test on Amsler Press

distribution in the specimen is neither uniform nor uniaxial.[24]

From Fig. 7, a similar trend to tensile and flexural test results is also observed, with no justifiable trend on the influence of percentage solid content and dipping time on the strengths. However, it is obvious that the coated core materials in both systems demonstrated higher strength in compression than the uncoated specimens. Generally, brittle materials are stronger in compression than in tensile mode. From the results presented in Fig. 7, it can be seen that the coating enhanced the compression strength of the core material. This is attributable to the presence of the filler materials deposited into the pore spaces near and on the surface of the core material. These filler materials enhanced the resistance of the core material to compress by impeding the movement of the sand grains around the surface of the cores, hence the higher strength observed relative to the uncoated specimens. Larger scatters in the measurement values were also observed for the coated furan cores than in the cold box cores. The compression test results obtained from the Amsler hydraulic press showed a similar behaviour with the tensile and flexural strengths results obtained from the new STM. There is no observable trend on the effects of percentage solid content and dipping time. However, it is suggested that the compression test result can be used to determine the load carrying power of chemically bonded sand core materials.[1] This will show to a reasonable extent the amount of metallostatic weight the sand material can withstand for sound casting production.

Statistical analysis

The results of the descriptive statistics have been presented in the form of charts in Figs. 3, 5 and 7, showing the means and corresponding standard deviations. From the results presented in these figures, the influence of the percentage solid content and dipping

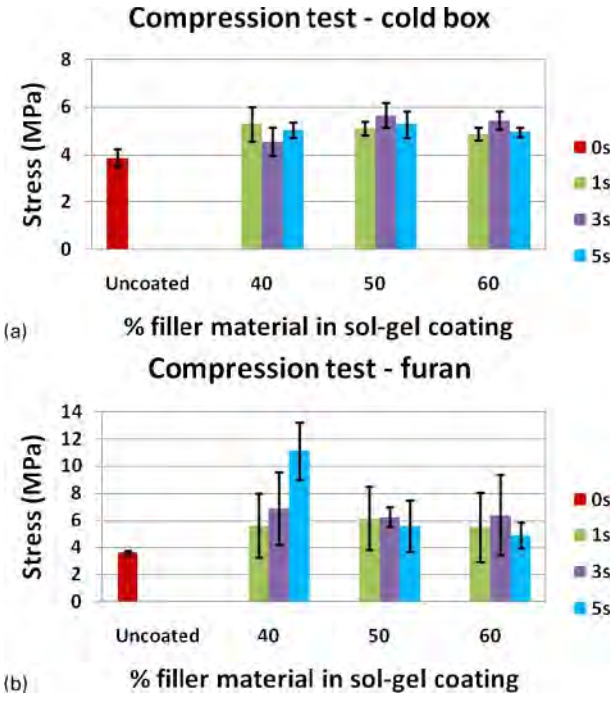

7 Compression strengths with standard deviation of *a* cold box and *b* furan chemically bonded sand specimens subjected to different coating times

times could not be established. The significance of the means was determined using ANOVA. The ANOVA results presented in Tables 1 and 2 for the two core systems show that the means are not significantly different for the tensile and flexural strengths at 95% confidence interval. This is clearly seen from the *P* values (*P* values >0·05), and the F values are less than the Fcrit. values, as shown in the tables.

On the other hand, for the compression strength of cold box and furan systems, ANOVA results show that the means are significantly different (*P* values <0·05), and the *F* values for both core systems are greater than the Fcrit. values, as shown in Table 3.

Kalpakjian and Schmid[10] stated that the flexural strength is the most reliable for brittle materials. Therefore, based on the ANOVA results for flexural strength, it can be stated that the average means of all the data for cold box and furan are not significantly different. Hence, to better understand the measured properties, Weibull statistical distribution is applied to model the mechanical properties of the cold box and furan core materials using flexural strength data. Since all the means are not significantly different, all the measurements of both coated and uncoated samples for each of the cold box and furan core materials were considered simultaneously. This gives a total of 30 measurements for each system. The results from the Weibull statistics are presented in Fig. 8. It is clear that

Table 1 Analysis of variance results of tensile strength of cold box and furan core materials

	Source of variation	DoF	Sum squares	Mean square	*F* value	*P* value	Fcrit.
Cold box	Between group	9	$1{\cdot}9 \times 10^{11}$	$2{\cdot}11 \times 10^{10}$	0·846	0·585	2·393
	Within group	20	$4{\cdot}98 \times 10^{11}$	$2{\cdot}49 \times 10^{10}$			
Furan	Between group	9	$4{\cdot}74 \times 10^{11}$	$5{\cdot}27 \times 10^{10}$	0·465	0·881	2·393
	Within group	20	$2{\cdot}27 \times 10^{12}$	$1{\cdot}13 \times 10^{11}$			

Table 2 Analysis of variance results of flexural strength of cold box and furan core materials

	Source of variation	DoF	Sum squares	Mean square	*F* value	*P* value	Fcrit.
Cold box	Between group	9	2·725	0·303	1·306	0·294	2·393
	Within group	20	4·637	0·232			
Furan	Between group	9	3·816	0·424	1·597	0·183	2·393
	Within group	20	5·310	0·265			

the experimental data fit with the predicted model for both cold box and furan core systems. The fitting showed a coefficient of determination $R^2=0{\cdot}98$ and 0·95 for the cold box and furan systems respectively.

The Weibull modulus (β) and characteristic strength (α) for the two core systems were determined from the Weibull statistical distribution and presented in Table 4. The Weibull modulus or shape parameter describes the variation in the distribution of the strength values from different materials and also establishes a direct relationship with the size and distribution of the defects present in a specific volume of a material. In this sense, high Weibull modulus indicates a smaller error range (narrow strength distribution) and potentially higher reliability.[22,24] Furthermore, the Weibull modulus (β) indicates whether the failure rate is increasing, constant or decreasing. A $\beta<1$ indicates that the materials have a decreasing failure rate, a $\beta=1$ indicates a constant failure rate and a $\beta>1$ indicates an increasing failure rate.[25] In both systems, the Weibull moduli are very much higher than unity, which indicates an increasing failure rate with increasing stress. With $\beta=7{\cdot}68$ and 6·14 for cold box and furan respectively, it means that these materials tends to fracture with higher probability for every unit increase in applied stress. From these values, cold box has a higher probability of fracturing than the furan core material. It can be seen from Fig. 8 that the Weibull moduli or the slopes are similar more or less. The similar slopes suggest that the same flaw types are operational in the core systems and are the cause of failure.[26] This suggestion will be verified by fractographic analysis. As a measure of the variability of strength in a material and its dependence on crack size distribution, a higher modulus is usually desirable, as materials with high Weibull moduli are more predictable and less likely to break at a stress much lower than the mean value.[22,24]

The characteristic strength or scale parameter represents the value of stress at which 63·2% of the material is expected to fail.[22,24] The reported Weibull characteristic strength values ($P_f=63{\cdot}2\%$, P_f is the probability of failure) are slightly greater than the mean strength values ($P_f=50\%$).[22] From the results presented in Table 4, it is clear that cold box has a higher characteristic strength than furan. This places cold box at an advantage over furan as core materials for cores with limited sizes in the foundry. Unknowingly to foundry men, the reason for the wide application of cold box core technology for smaller cores in the foundry can be justified by these analyses, which are rarely performed in the foundry routine tests.

The reliability analysis was performed for the two core systems using the data obtained from the Weibull analyses. The results are presented in Fig. 9. The term reliability is used for the probability of functional performance of a part under current service conditions and in a definite time period. This means that a material can be used without failure.[17] The reliability curve in Fig. 9 shows that between 1 and 2 MPa, the core materials show the highest reliability. However, for more certain assessment, between 2 and 4 MPa, the cold box core materials show higher reliability than the furan core material. The reliability decreases with increasing stress. Furthermore, at any of the reliability levels, the cold box core material has higher fracture strength than the furan core material. This is in consonance with the higher Weibull modulus and higher strength at which 62·3% of the data is expected to fail for the cold box core material, as presented in Table 4.

Fracture surface

Coating penetration depth on fracture surface

The coating penetration depths were examined with a stereomicroscope, and the penetration depths were measured with an Image-Pro Plus software. The stereofractographs showing the effects of solid contents on the coating penetration are shown in Fig. 10, while the coating penetration depths at 5 s dipping for different solid contents and at 60% solid content for different dipping times are presented in Fig. 11. From Figs. 10 and 11, it is clearly evident that the coating penetration depth into the cores decreases with increasing solid content and dipping time. The variation of surface layer deposition and penetration into the core material with solid content and dipping time was extensively investigated and discussed by Nwaogu *et al.*[2] From Figs. 3, 5 and 7, it is seen that the coating solid contents and dipping times have no obvious distinguishable effect on the strength of the core materials. This is attributed to the brittle nature of the refractory material of the coating. Both sand grains and refractory material are brittle in nature; however, the only difference is that the particle size of the refractory material is several orders of magnitude lower than the sand grains. As the cores are made with a binder before the application of the coating, the binder has already

Table 3 Analysis of variance results of compression strength of cold box and furan core materials

	Source of variation	DoF	Sum squares	Mean square	*F* value	*P* value	Fcrit.
Cold box	Between group	9	$1{\cdot}26\times10^{11}$	$1{\cdot}4\times10^{-10}$	3·748	0·007	2·393
	Within group	20	$7{\cdot}47\times10^{10}$	$3{\cdot}73\times10^{9}$			
Furan	Between group	9	$1{\cdot}89\times10^{12}$	$2{\cdot}1\times10^{11}$	2·647	0·033	2·393
	Within group	20	$1{\cdot}59\times10^{12}$	$7{\cdot}94\times10^{10}$			

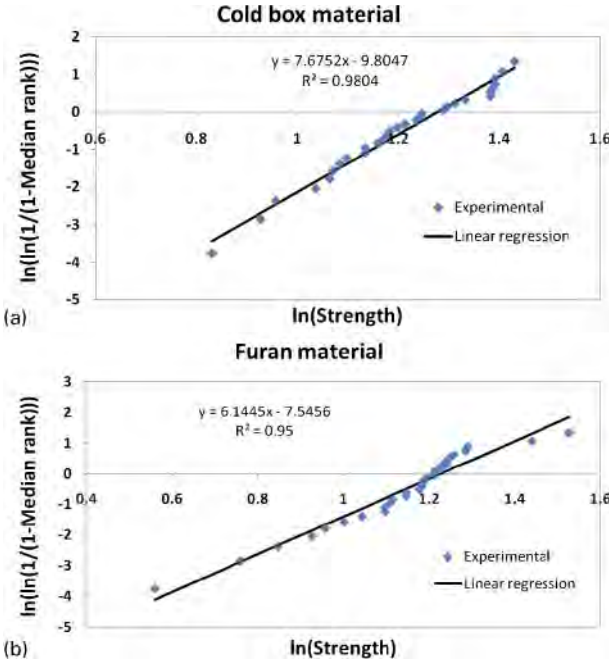

8 Regression analysis of flexural strength of *a* cold box and *b* furan core materials

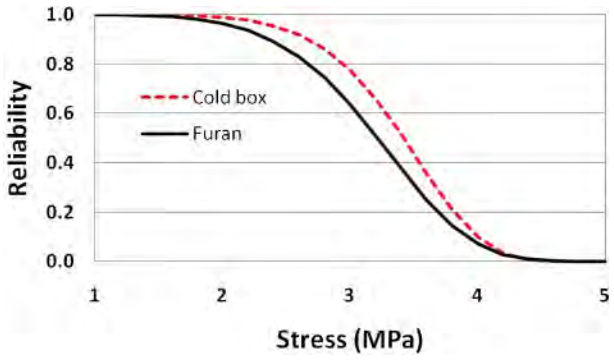

9 Weibull reliability curve for core materials

cured. By so doing, the sand grains are covered by the binder material. The slight reduction of the strength of the core material observed in tensile and flexural strengths is attributable to the aqueous reaction between the binder material and the moisture in the coating that weakens the bonding bridges formed by the binder system with the sand grains. If the core materials are dried immediately after coating, this effect may be reduced. When the coating on the core material is dried, the refractory materials are deposited in the pores or voids in the penetrated area. These deposited refractory materials are just sitting in the voids without any strong connection with the binder and therefore have no contribution to the bonding power. This is shown in Fig. 12*a* and *d*. However, in the case of compression, a different observation is made. Although the refractory material does not contribute to the bonding power, it enhances friction, which impedes the movement of the sand grains around the penetrated area. This means that the load on the coated surface is carried not only by the binder but also by the coating refractory grain. In this situation, the refractory material enhances the compression strength. This is in line with the ANOVA results for compression strength for both core systems, where the means are significantly different from the mean of the uncoated material.

It is worth noting that although the refractory materials in the coatings do not contribute to the strength of the moulding materials, they have a significant effect on permeability. Indeed, they may reduce the permeability of the moulding materials[2,3] to the extent that venting of the core gases is through the core prints. Binder constituents pyrolyse during casting, but diffusion of the gases produced into the melt is hindered by the sealing by the coating of the pores between sand grains, and the gas is redirected towards the core prints for venting. This helps to prevent gas related defects in the castings. Furthermore, the gas pressure built up in the cores may prevent metal penetration. In industrial practice, the cores are often not coated completely to provide a more rapid escape route for the generated gases. A fruitful subject for further studies may be to investigate the influence of foundry coatings on the formation of gases during casting. This will require improved understanding of coatings and binder chemistry, with good experimental design to study the effects of different factors.

Fracture surface examination

The SEM was used to study the fracture surface of the chemically bonded sand core materials in more detail in order to establish the cause of failure, and the SEM fractographs are presented in Figs. 12–14. From these micrographs presented, it could be suggested that the flaws present include pores or voids, cracks, micronotches and heterogeneities (caused by the filter dust) (Fig. 12*a*). Naturally, the moulding materials are porous. Therefore, the most important causes for failure among these flaws are pores or voids and micronotches. The sand grains are held together by the bonding bridges formed by the binder, as shown in Fig. 12*b*. The bonding bridges are only formed where the sand grains touch one another. These are at selected points, and voids are present in between bonding bridges. This is because the sand grains are not perfectly packed due to the variation in shapes and sizes (Fig. 12*c*). Some of the points of contact of the sand grains with one another are marked with arrows in Fig. 12*c*, and these are the failure points. To elucidate the fact that the refractory material does not contribute to the bonding power of the system, a closer look at Fig. 12*d* reveals that the powdery refractory filler material is only sitting on the sand grains without any evidence of bonding. From these analyses and as can be seen from the fractographs presented in Figs. 13 and 14, it is suggested that the fracture mode is intergranular through the binder. Therefore, the strength of the chemically bonded sand core materials

Table 4 Estimated Weibull parameters for two core systems

Identity	No. of specimens	Weibull moduli β	Characteristic stress α/MPa
Cold box	30	7·68	3·59
Furan	30	6·14	3·41

a 40% on cold box; *b* 40% on furan; *c* 50% on cold box; *d* 50% on furan; *e* 60% on cold box; *f* 60% on furan

10 Stereofractographs showing effects of solid content on penetration of cold box and furan at 5 s dip coating

is determined by the strength of the binder itself. This depends on the chemical composition as well as the number of bridges and their shapes.

Furthermore, the smoothness of the areas around the fracture points in Figs. 13 and 14 suggests the presence of voids between binder coated sand grains and directly confirms that one of the major reasons for the brittle nature of these sand systems is the presence of these voids. This has a weakening effect on the strength of the core materials.

Determination of Young's modulus or modulus of elasticity of chemically bonded sand core material

In the foundry, the primary interest is for the core materials to withstand metallostatic pressure from the incoming melt and still be easily shaken out after casting; otherwise, defective castings will be produced, thereby increasing the scrapping rate. This is not what the foundries want. The sand core material should have limited movement or deformation to insure that the molten metal will solidify in a solid mass with the right dimensions and free from internal porosity or shrinkage around it. Therefore, it becomes important to quantify the stiffness and load carrying power of the core materials. The maximum load that the sand core material will carry at a point of collapse is called the ultimate strength. At this point is also found the ultimate deformation, which is often used in defining the elasticity of a sand material. A value that has greatly helped engineers in evaluating the load carrying power of metals is the modulus of elasticity. For sand

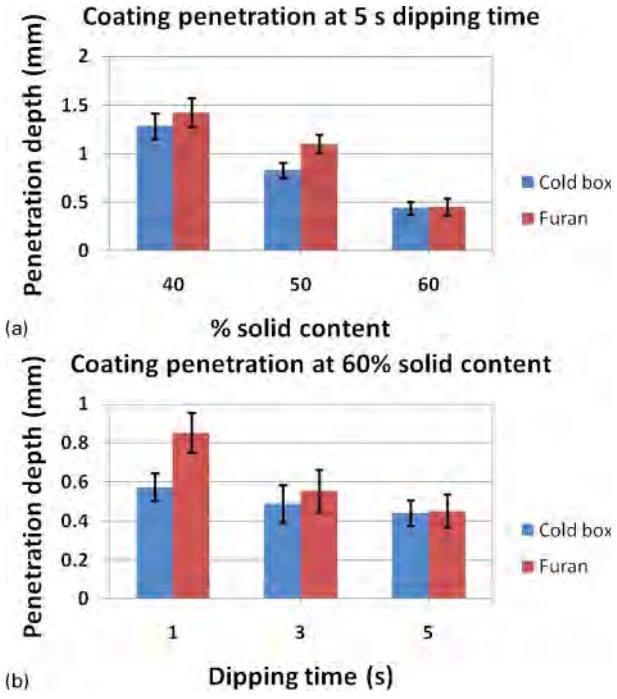

11 Coating penetration depth in core materials at *a* 5 s dipping time for different solid contents and *b* 60% solid content at different dipping times

materials, it is proposed to use a similar factor.[1] The modulus of elasticity of sand materials is a measure of the rigidity of the sand and may be used to express the load carrying power of sand materials in that it is the ratio of stress/strain at any load below the yield point. This increases as the sand material becomes more rigid. The more rigid a sand material is, the steeper or greater the angle of the stress–strain curve. As the angle increases, the deformation will be lower for a given load.[1]

As the bending or flexural test is commonly used to test brittle materials,[10] the modulus of elasticity or stiffness of the chemically bonded sand materials investigated in this study is determined using the bending test data. The elastic (linear) portion of the load–displacement curves is converted to stress–strain curves. Typical stress–strain curves obtained from this study are presented in Fig. 15. For sand materials, this region is known as the proportional range. A long proportional range is a good attribute in that the sand material will resist movement, breakage or enlargement over a wide loading.[1] The curves in the figure were linearly fitted, and the slope of the linear portion was taken to represent the stiffness of the specimens.[21] The deduced stiffness of all the specimens studied and the corresponding determination coefficients (regression coefficients) are presented in Table 5. From the results presented in the table, it can be inferred that the coating, the dipping time and the percentage solid content have negligible effect on the stiffness of the chemically bonded sand core materials. It is also observed that the coating has no effect on the stiffness obtained from the comparison of the results from the coated and uncoated chemically bonded core materials. This means that the sol–gel filter dust coating has no significant effect on the stiffness of the moulding materials. This could probably

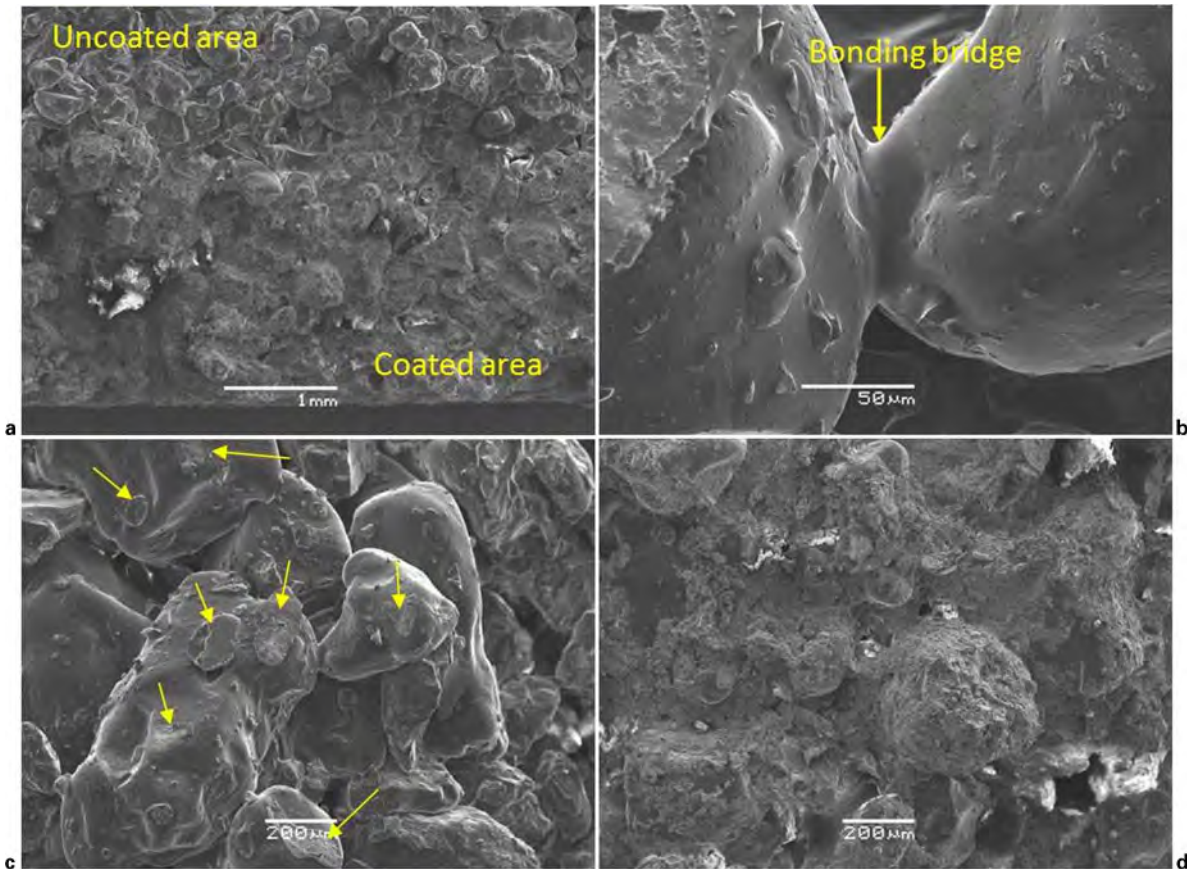

12 Fractographs of cold box cores from SEM showing *a* coated and uncoated area, *b* interparticle bonding bridge, *c* fracture point in uncoated area and *d* coated area containing filler particles

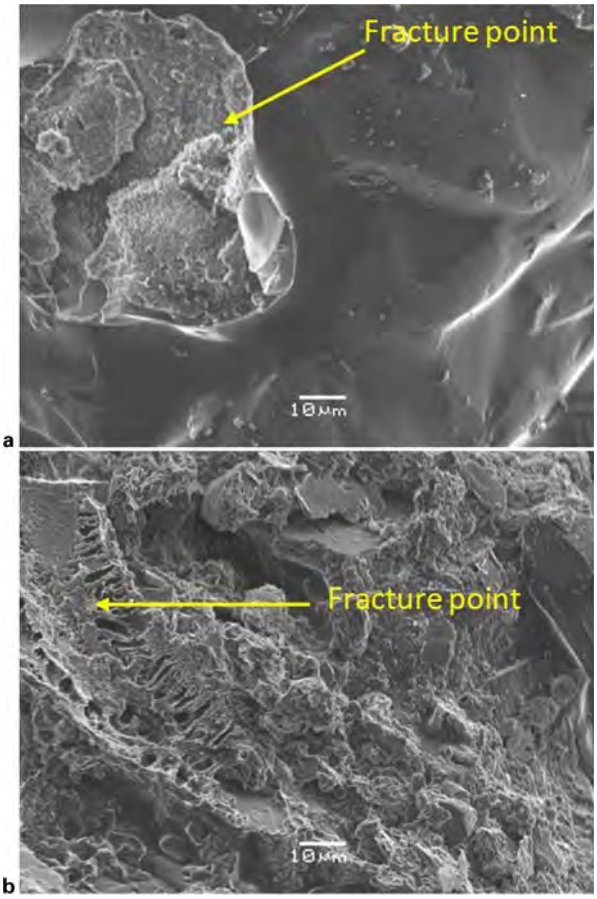

13 **Fractographs showing fracture points at failure during test of cold box cores: *a* sand grain covered by binder and *b* sand grain covered by refractory materials**

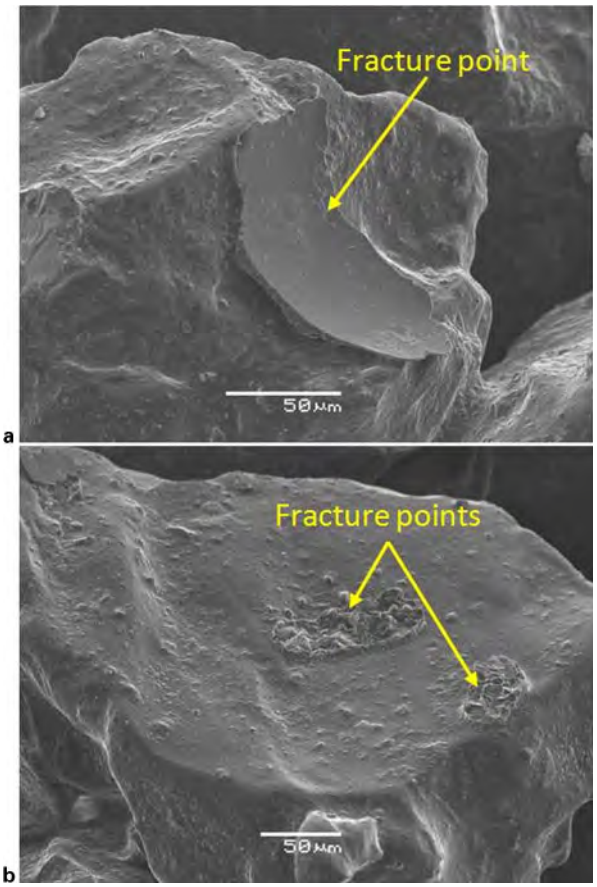

14 **Fractographs showing fracture points at failure during test of furan cores: *a* spalling of sand grain at a bonding bridge and *b* breakage of bonding bridges at grain contacts**

be attributed to the fact that the filler materials in the coating are brittle like the sand system itself and do not contribute to the bonding power. This invariably confirms the fact that the refractory materials are loosely sitting in the voids. It could also be as a result of insignificant coating penetration depth, which is evident in Fig. 10. From the profiles in Fig. 15*a* and *b* for the uncoated and coated core materials, there is little or no plastic deformation shown during the period under stress. This is typical of the brittle material due to large number of various flaws in the materials.

Conclusions

The tensile and bending strengths of chemically bonded sand core materials were measured using a new STM, and the compression strength of the same materials was measured with an Amsler hydraulic press. From the detailed studies and analyses, the following conclusions are drawn.

1. The novel sol–gel filter dust refractory coating has no significant effect on the strength and stiffness of the chemically bonded sand core materials.
2. Chemically bonded sand core materials have no specific strength but a range of strengths at ambient temperature. However, from Weibull statistical distribution, 63·2% of the materials tested are expected to fail in a three-point bending test at 3·59 and 3·41 MPa for cold box and furan core respectively.
3. The Weibull modulus for cold box is larger than that of furan, making cold box a stronger core material

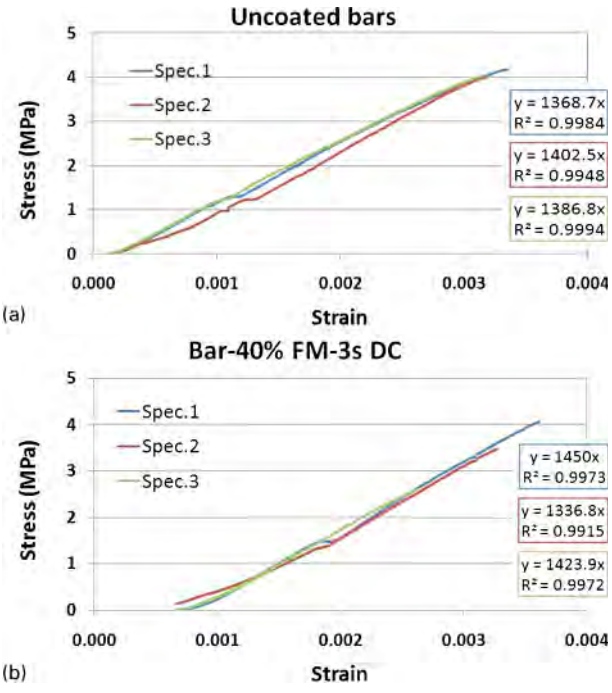

15 **Typical stress–strain curves: three *a* uncoated and *b* coated chemically bonded sand core materials showing curve fitting details**

Table 5 Deduced stiffness and corresponding determination coefficient for cold box and furan core material

		Cold box		Furan	
Dip coating	ID	Stiffness/MPa	R^2	Stiffness/MPa	R^2
0 s	Uncoated	1386 (±17)	0·998	1339 (±438)	0·9855
1 s	40%	1540 (±190)	0·995	1302 (±226)	0·9665
	50%	1427 (±364)	0·998	1198 (±325)	0·9758
	60%	1220 (±285)	0·994	1071 (±421)	0·9579
3 s	40%	1404 (±59)	0·995	1095 (±356)	0·9641
	50%	1335 (±141)	0·981	1440 (±78)	0·9679
	60%	1142 (±231)	0·987	1274 (±194)	0·9699
5 s	40%	1289 (±29)	0·989	1572 (±132)	0·9972
	50%	1373 (±221)	0·9927	1218 (±126)	0·9919
	60%	1051 (±291)	0·9798	1278(±261)	0·9266

in tensile and flexural modes. Furan is a stronger material than cold box under compression.

4. The reduction in strength of the materials with coating under tensile and flexural loading may be caused by the chemical reaction between the moisture in the coating and the chemicals of the binder. This reaction may be reduced by drying the core immediately after coating.

5. The extent of strength reduction by the coating can be considered negligible as suggested by the ANOVA results for tensile and flexural strengths. However, for compression, the coating refractory material enhanced the strength of the materials.

6. A combination of the flexural and compressive tests will give a better understanding of the strength condition of chemically bonded sand core materials for effective foundry applications.

7. The mode of fracture for the chemically bonded sand core materials is established to be intergranular through the binder. Therefore, the binder determines the strength of the core materials.

8. The moduli of elasticity of the chemically bonded sand core materials were determined in the range of 1000–1500 MPa for cold box and 1000–1600 MPa for the furan core material at ambient temperature. The binder remains the determinant.

9. The deduced modulus of elasticity for the chemically bonded sand core materials may find application in expressing the rigidity of the materials. This can also be extended to the moulding materials.

10. The compression test can be termed the 'load carrying test', which measures the movement of the sand system under a selected load at various time intervals. This will offer foundries a new tool to enhance the production sound castings.

Acknowledgements

The authors wish to thank the Danish Agency for Science, Technology and Innovation for financing the work. The authors are also grateful to the nine industrial partners to this project for their support.

References

1. H. W. Dietert, F. S. Brewster and A. L. Graham: 'Load carrying power of moulding sand, moulding methods and materials', 1st edn; 1962, Illinois, The American Foundrymen's Society.
2. U. C. Nwaogu, T. Poulsen, C. Bischoff and N. S. Tiedje: ;Influence of new sol–gel refractory coating on the casting properties of cold box and furan cores for grey cast iron', Proc. 69th World Foundry Cong., Hangzhou, China, October 2010, Foundry Institution of Chinese Mechanical Engineering Society, 648–653.
3. U. C. Nwaogu, T. Poulsen, R. K. Stage, C. Bischoff and N. S. Tiedje: 'New sol–gel refractory coatings on chemically-bonded sand cores for foundry applications to improve casting surface quality', *Surf. Coat. Technol.*, 2011, **205**, 4035–4044.
4. A. Schrey: 'Noracel* W100 – a new technology to prevent veining defects', Foseco foundry practice 246, Staffordshire, 2007.
5. T. B. N. Hodgkinson: 'Improving foundry profitability through the use of Rheotec* XL', Foseco foundry practice 240, Staffordshire, 2003.
6. T. Birch and D. Bell: 'Improved iron casting quality through application of advanced coating technology', Foseco foundry practice 243, Staffordshire, 2005.
7. P. D. Webster: 'Fundamentals of foundry technology'; 1980, Surrey, Portcullis Press.
8. Y. A. Owusu: 'Physical–chemical study of sodium silicate as a foundry binder', *Adv. Colloid Interface Sci.*, 1982, 18.
9. S. M. Strobl and F. W. Schuster: 'Gauging green sand flowability helps predict mould quality', *Modern Cast.*, 1997, 48–50.
10. S. Kalpakjian and S. R. Schmid: 'Manufacturing engineering and technology'; 2006, Upper Saddle River, NJ, Pearson Prentice Hall.
11. N. A. Ademoh and A. T. Abdullahi: 'Evaluation of mechanical properties of expendable sand cores bonded with the nigerian gum arabic grade 4', *Am.–Eurasian J. Sci. Res.*, 2008, 3.
12. American Foundrymen's Society: 'Foundry sand handbook', 7th edn; 1963, Des Plaines, IL, American Foundrymen's Society.
13. WTIA Technical note 10, WRC bulletin no. 430; BS7910; AS/NZS 3788; API 578.
14. M. H. Dirikolu, A. Aktas and B. Birgoren: 'Statistical analysis of fracture strength of composite materials using Weibull distribution', *Turkish J. Eng Env. Sci.*, 2002, **26**, 45–48.
15. B. Basu, D. Tiwari, D. Kundu and R. Prasad: 'Is Weibull distribution the most appropriate statistical strength distribution for brittle materials?', *Ceram. Int.*, 2009, **35**, 237–246.
16. Y. Xu, L. Cheng, L. Zhang, D. Yan and C. You: 'Optimization of sample number for Weibull function of brittle materials strength', *Ceram. Int.*, 2001, **27**, 239–241.
17. R. Sakin and I. Ay: 'Statistical analysis of bending fatigue life data using Weibull distribution in glass–fiber reinforced polyester composites', *Mater. Des.*, 2008, **29**, 1170–1181.
18. A. Saghafi, A. R. Mirhabibi and G. H. Yari: 'Improved linear regression method for estimating Weibull parameters', *Theor. Appl. Fract. Mech.*, 2009, **52**, 180–182.
19. E. M. Schulson, M. C. Gies, G. J. Lasonade, W. A. Nixon, E. Z. Wang and N. G. Shrive: 'Brittle fracture in compression: mechanisms, models and criteria', *Eng. Fract. Mech.*, 1995, **52**, (6), 1107–1126.
20. ' Standard test method for determination of modulus of elasticity for rigid and semi-rigid plastic specimens by controlled rate of loading using three-point bending', ASTM Standard D5934:2002, ASTM International, West Conshohocken, PA, USA, 2002.
21. J. Thole and C. Beckermann: 'Measurement of elastic modulus of PUNB bonded sand as a function of temperature', *Int. J. Metalcast.*, 2010, **4**, (4).
22. S. A. Rodrigues Junior, J. L. Ferracane and Á. D. Bona: 'Flexural strength and Weibull analysis of a microhybrid and a nanofill composite evaluated by 3- and 4- point bending test', *Dent. Mater.*, 2008, **24**, 426–431.
23. A. M. Neville: 'Properties of concrete', 3rd edn; 1981, London, Pitman.
24. J. B. Quinn and G. D. Quinn: 'A practical and systematic review of Weibull statistics for reporting strengths of dental materials', *Dent. Mater.*, 2010, **26**, 135–147.
25. W. W. Dorner: 'Using Microsoft Excel for Weibull analysis', http://www.qualitydigest.com/jan99/html/body_weibull.html.
26. N. G. Shrive: 'Compression testing and cracking of plain concrete', *Mag. Concrete Res.*, 1983, **35**, 27–39.

SUPPLEMENT 6

U. C. Nwaogu and N.S. Tiedje,

“Foundry Coating Technology: A Review”

Published in Materials Sciences and Applications, 2 (2011).

DOI 10.4236/msa.2011.28155

Materials Sciences and Application, **2011, 2, 1143-1160**
doi:10.4236/msa.2011.28155 Published Online August 2011 (http://www.SciRP.org/journal/msa)

Foundry Coating Technology: A Review

U. C. Nwaogu*, N. S. Tiedje

Technical University of Denmark, Department of Mechanical Engineering, Institute of Production and Process Technology, Kgs. Lyngby, Denmark.
Email: ugon@mek.dtu.dk

Received April 27th, 2011; revised May 16th, 2011; accepted May 31st, 2011

ABSTRACT

The importance of foundry coating in improving the surface quality of castings cannot be over emphasized. The application of mould and core washes creates a high thermal integrity barrier between the metal and the mould resulting in the reduction of the thermal shock experienced by the sand system. These thermal shock leads to series of surface defects such as veining/finning, metal penetration, burn-on/in, scab, rat tail, erosion etc. The use of coatings reduces the tendency of occurrence of these defects. However, the understanding of the coating, its components, characteristics and mechanism of action is important. In this review, a detailed description of these topics and examples are provided where necessary. A potential area of research in foundry coating development, using sol-gel process is suggested. The application of sol-gel technology in the development of foundry coatings is a novel approach.

Keywords: *Coating, Refractory Materials, Application Methods, Characterization, Sol-Gel Technology*

1. Introduction

Research in coatings for various applications such as aesthetics, corrosion protection, wear resistance, thermal barrier, self-cleaning, antifouling etc. have been very wide spread but not much is going on in the area of foundry coatings in recent times. The use of foundry coatings for moulds and cores during casting is very necessary as a means of achieving high quality surface finish of castings more especially in complex internal channels created by use of cores. This is despite the considerable advances that have taken place over the recent years in binder and sand technology giving the foundries greater opportunity to choose and control these basic foundry raw materials. Since casting surface finish depends largely on sand particle grading, it might be supposed that a proper selection of a particular grade of sand would be the only requirement to achieve the desired casting surface quality. However, there are other factors to be considered, such as the ability to vent off the gases produced during casting, economic use of a binder, non availability of sand with required grading, etc., these make the use of coatings the more practicable approach [1].

In filling a mould with liquid metal its surface is subjected to thermal, mechanical and physicochemical actions. The oxidation products of the metal, reacting with the mould material, form low-melting materials such as silicates, which lubricate the grains of the quartz sand well. This promotes penetration of the metal into the inter-granular spaces and the formation of mechanical pick-up which is difficult to remove from the casting surface. Considering that the sand moulds and cores are highly porous, the production of castings in these materials without pick-up and other surface defects is possible only with protection of the surfaces of moulds and cores with refractory coatings. The fundamental requirements for the refractory coatings are minimum porosity, high refractoriness and reduction of the physicochemical reaction at the metal-coating interface (lubrication, solution, penetration) [2]. These refractory coatings are used to make better castings and to reduce costs. Castings surface quality is improved because the coating produces smoother metal surfaces, either by filling the spaces between the sand grains or by providing, to the metal, a surface smoother than the mould surface itself. Further improvement from the coatings is due to the cleaner and better peel of sand at shakeout and elimination of certain defects such as metal penetration, veining, erosion, sand burn-in etc [3,4].

Controlling casting quality and increasing productivity are top priorities for foundries to become more competitive in a global casting market and coatings can help to provide the required remedy. Addressing the issue of mould/core moisture can lead to improvements in productivity and help keep foundries competitive. Identify-

ing problems like poor mould/core density and moisture in the both core and mould is challenging, but advancement in coating technology enhances the engineering of refractory coatings as a quality-control tool to help identify these issues. The presence of moisture can lead to a scrapped casting, but coatings that indicate when drying is complete can address this issue. Coating technologies that change colour offer visual confirmation that the coating is dry. This confirmation may also indicate poor sand compaction in a core or mould, as these areas will absorb more moisture from the coating and take longer time to dry. Therefore, a visually obvious colour change based on moisture content permits these new refractory coatings to act not only as a barrier between the metal and the mould or core but also as a quality diagnostic [5].

The objective of this paper is to collate as much as possible the significant works and results on foundry coatings in the past and to give insight to a novel technology for the production of foundry coatings with greater potential towards improving the surface quality of castings from readily available raw materials at a cheaper cost. This paper provides a detailed understanding of the constitution of foundry coatings while providing alternatives to the foundry coating components depending on the metal to be cast and their properties and compatibility with sand properties such as grain size and grain size distribution and binder properties.

2. Groups of Foundry Coatings

Foundry coatings may be divided into two groups, those applied dry and those applied wet.

2.1. Coatings for Dry Application

For dry application, the most widely used is Plumbago. Other dry coatings used to a lesser extent include mica, white talc and wheat flour. These materials are either shaken or blown onto mould or core surfaces from open-mesh cloth bags. Plumbago is a finely ground blend of graphite containing 80% to 90% of particles that will pass through a 200-mesh (75 micron). The graphite may be amorphous (no definite crystal structure) or crystalline (having definite particle shape or flaky). Graphite will not melt at the highest foundry temperatures but its carbon is driven off by oxidation at these temperatures depending on the air (containing oxygen) available at the metal-mould interface. Amorphous graphite oxidizes easier than does crystalline graphite. Plumbago is applied dry only on green sand moulds [3].

2.2. Coatings for Wet Application

Mould and core coatings for wet application are of two types, carbon-base and carbon-free coatings. Both types are sold in either powder or paste form. The adherence of the coating on the mould or core surface depends on the moisture in the sand. Carbon-based coatings may contain several types of graphite, coke, anthracite or any of the numerous combinations that can be made from these materials. Carbon-free coatings may contain silica, mica, zircon flour, magnesite, olivine, clays, talc or a combination of these materials. Many coatings formulations contain both carbonaceous and non-carbonaceous raw materials to take the advantage of the synergistic characteristics of both types [3]. Foundry coatings for wet application are also classified into two, based on their carrier systems. Those employing an aqueous carrier and those in which organic solvent carriers are used. The former must be dried after application while the later are self-drying or can be ignited and dried by their own combustion. Both classes of coating make use of the refractory materials [6].

3. Components of a Coating (Coating Materials)

A refractory coating on the mould or core should have the following characteristics:

- Sufficient refractory properties to cope with the metal being poured
- Good adhesion to the substrate to prevent spalling
- Be permeable to minimize air entrapment
- Be fast in drying
- No tendency to blistering, cracking or scaling on drying
- Good suspension and remixing properties
- Minimize core strength degradation
- Provide adequate protection against metal penetration
- Good stability in storage
- Good covering power
- Good application properties by the method chosen
- Leveling well and minimizing runs and tear drops

For a coating to achieve these characteristics, the coating will consists of

- Refractory filler
- Liquid carrier
- Suspension agents (Rheology control system)
- Binder agents
- Additives as shown in **Figure 1.**

3.1. Refractory Filler (Filler Materials)

Refractory materials are substances or minerals that have high melting points and are difficult to fuse except at very high temperatures. They are processed at high temperature and/or intended for high temperature applications [7,8]. Refractoriness has been defined by Committee C-8 of the American Society for Testing and Materials (ASTM) as "...the capability of maintaining the de-

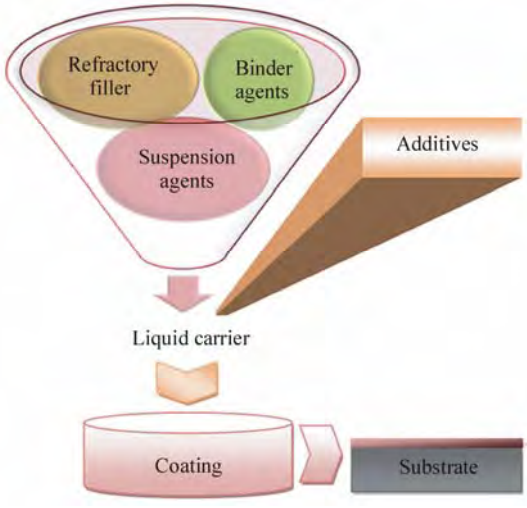

Figure 1. Coating components.

sired degree of chemical and physical identity at high temperatures and in the environment and conditions of use." The melting temperature of refractory materials is an important characteristic showing the maximum temperature of use and represents fundamental point in phase diagrams used in high temperature chemistry, metallurgy, ceramics etc [9].

In coatings, refractory materials are dispersed in the binder and constitute the skeleton of the coating film. They increase the density, viscosity and hardness of the coating film and reduce the permeability.

There are characteristics other than resistance to high temperatures that refractory materials should exhibit. These include:

- Suitable particle shape, particle size (PS) and particle size distribution (PSD),
- Chemically inert with molten metal,
- Not be readily wetted by molten metal,
- Not contain volatile elements that produce gas on heating,
- Have consistent cleanliness and pH
- Be compatible with new chemical binders as they are developed

The significance of particle shape, PS and PSD are elaborated below in the following paragraphs. The other factors are readily understood.

At a given refractory material loading, particle shape determines the mechanical properties of the coating matrix. The particle shape is usually described by a dimensionless parameter, the aspect ratio–this is the ratio between the average diameter and average thickness of the particle. The higher the aspect ratio of the particle of refractory material, the higher the reinforcing effect on the coating matrix will be.

The particle size distribution (PSD) of a refractory material is usually given as a cumulative curve, indicating the amount per volume or weight of particles (%), which are smaller than a given size. PSD can be adjusted by grinding and classification. The coarsest particles act as points of highest stress concentration, where crack or fractures occur under loading. Impact strength is significantly improved by using finer particles [10].

It is generally assumed that a sieve analysis sharply defines between the different sizes of particles comprising aggregate materials. According to [3], such is not the case. On any particular sieve one finds particles ranging from those just able to pass through the preceding sieve to those just unable to pass through to the following sieve. As a result of this lack of sharp differentiation between the particle sizes on adjacent sieves, it is difficult to simply screen aggregate material and secure particles of uniform size on each of two successive sieves (**Figure 2**).

From a practical aspect, the refractory material should be available in large quantities at reasonable prices [8]. In foundry coatings, refractory materials determine the efficiency of the coating. The refractory filler may be either a single material or a blend of materials selected for specific applications. They make up 50% to 70% of the coating. Fillers are chosen for their particle size and shape, density, sintering point, melting point, thermal conductivity, thermal expansion and reactivity towards the metal being cast and the mould or core material on which it is applied [11]. These refractory materials include Plumbago, silica, graphite, coke, anthracite, zircon flour, magnesite, Chalmette, olivine, clays, talc, chromite, alumina, mica [3,12,13]. The material of which sand moulds and cores are made generally exert influence upon the surface quality of the castings formed from these moulds and cores. This is because they have a high degree of porosity to the extent that the pores tend to be filled with molten metal causing high surface roughness on the castings.

Therefore, with the application of refractory coatings on the surface of the moulds and cores that will be in contact with the molten metal, the refractory particles tend to fill these pores on drying, thereby creating a smooth inert surface on the moulds and cores. These refractory materials have different properties and are selected depending on the metal to be cast. The more common refractory materials are discussed below.

Silica flour is a commonly used refractory filler, particularly in steel foundries. The silica flour should contain minimum 98% silica and not more than 1% moisture [11]. The fusion point of silica flour is 1734˚ [9]. At approximately 650˚C (1100˚F), silica refractory filler has an expansion of 1.6%. Silica fillers are well known for use as pigments, reinforcing agents and the like.

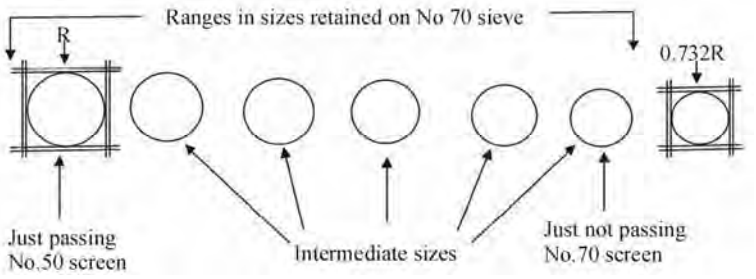

Figure 2. Schematic portrayal of range in sizes of sand aggregate retained on No 70 sieve to demonstrate non-uniformity on any sieve [3].

Commercially available silica and other metals oxides are often derived from burning volatile metal halides with various fuels and oxidants. Silica filler has been produced by direct combustion of silicon powder as reported in [14]. Silica flour does not excessively increase viscosity [15]. However, it is reported in [16] that as the content of silica filler increased the coefficient of thermal expansion of the composite decreased while the viscosity increased.

Zircon flour is a highly refractory material and is primarily used for coatings in steel foundries. Good quality zircon flour suitable for foundry work should contain minimum 64% zircon oxide (ZrO_2), 30 to 35.5% silica and maximum of 0.5% TiO_2 + Fe_2O_3. Refractory uses of zircon require low interstitial water content. This translates into low loss on ignition. Excessive internal radiation damage to zircon crystals (metamict zircon) can cause an increase in the loss on ignition of a zircon product. The desire of the refractory market for a low loss on ignition implies that a low picocurie/gram requirement is placed on zircon products [8].

It has a specific gravity of about 4.5 and a pH value of the water-based coating of not more than 9 [11].The melting temperature is 2727 ± 10˚C [9]. The high heat conductivity, about double that of silica, promotes quick formation of a solidified metal layer and helps in producing castings with a fine grained structure. Its higher density than that of silica prevents metal penetration [17].

Graphite refractory materials are most commonly used for coatings in iron foundries and for non-ferrous castings. Molten metal does not wet graphite and sand grains coated with graphite coatings resist metal penetration. This is the reason why graphite, Plumbago and carbon are usually used in mould and core coatings except those for steel [6]. Mould and core coatings containing carbonaceous ingredients are not used for steel, particularly low-carbon steels. The reason for this is because steel is sensitive to the carbon content and if there is carbon pick-up, the properties of the steel will change [3]. The graphite used is naturally flaky type, silvery white in appearance, of a fine powder form and free from gritty particles. Good quality graphite for foundry use should have ash content of about 12 to 15% maximum; volatile matter 3% maximum; and moisture content 1% maximum [11]. Graphite inclusion in mould and core coatings also improves stripping during shakeout. A highly useful, desirable, substantially non-porous, smooth, non-spalling mould surface can be produced on porous moulds by subjecting them to a treatment with a controlled amount of colloidal graphite suspended in a volatile carrier or vehicle followed by a drying after the treatment and finally baking at a relatively high temperature. The mould surfaces prepared in this manner possess substantially no pores, at least those of a size which can be penetrated by molten metal. With the presence of pores which cannot be penetrated by molten metal it is considered to be substantially non-porous. The treatment, it is believed, introduces colloidal graphite particles into the mould pores and the subsequent baking fixes or anchors them in such a way as to prevent removal unless the mould surface itself is worn or cut away [18].

Olivine is orthosilicate of magnesium and iron $(MgFe)O.SiO_2$ and it˚Ccurs as forsterite and fayalite. Its density, conductivity and refractoriness are higher than those of silica. Its fusion point is high—about 1800˚C- and as such it is favoured for heavy sections of alloy steel casting. Its resistance to slag reaction makes it suitable for the casting of high manganese steels. Olivine refractory material can also be used for the casting of non ferrous castings of intricate nature [17]. Olivine is used in preference to silica sand to overcome the silicosis hazard [19] (**Silicosis** is a form of respiratory disease caused by inhalation of silica dust, and is marked by inflammation in the upper lobes of the lungs).

Talc is a hydrous magnesium silicate mineral with the chemical formula ($Mg_3Si_4O_{10}.(OH)_2$) and the softest mineral on Mohr's scale of hardness. Talc is widely used as a filler material [20]. Talc Mohr's hardness is 1 and density of 2.6 - 2.8 g/cm^3. It is used in many industries because of its characteristics—low hardness, adhesion capability (surface coating), high melting temperature, chemical inertness, hydrophobic, organophilic, platy, low

electrical and high thermal conductivity [20,21]. The inert and lamellar platy natures of talc improve its cracking resistance, adhesion and barrier properties. Talc is practically insoluble in water and weak acids and alkalis. Above 900˚C, talc progressively loses its hydroxyl groups and above 1050˚C, it recrystallizes into different forms of enstatite (anhydrous magnesium silicate). Talc's melting point is at 1500˚C [22].

Mica is a plate-like crystalline aluminosilicate and has been widely used as reinforcing filler in polymer matrix due to its excellent mechanical, electrical and thermal properties as well as lower cost than carbon or glass fibres [23]. Chemically they contain complex silicate of aluminium and alkalis with hydroxyl. They crystallize in monoclinic system. Some varieties may contain iron, magnesium, lithium. There are seven important mica minerals: Muscovite or potassium mica, $H_2KAl_3(SiO_4)_3$; Paragonite or sodium mica, $H_2NaAl_3(SiO_4)_3$; Lepidolite or lithium mica, K Li $Al(OH, F)_2Al(SiO_4)_3$; Phlogopite or magnesium mica , $H_2KMg_3Al(SiO_4)_3$; Biotite or magnesium iron mica , $(H_2K)(Mg, Fe)_3Al(SiO_4)_3$; Zinnwaldite or lithium iron mica, $Li_2K_2Fe_2Al_4Si_7O_{24}$; and Lepidomelane or iron mica , $(H, K)_2(Fe, Al)_4(SiO_4)_5$. Muscovite is the commonest of all and whenever the word mica is used it is understood to mean muscovite. No other natural substance has been found to possess the properties equal to those of mica. Of all the known varieties of mica only muscovite and phlogopite are of commercial importance. Muscovite finds the largest use while phlogopite has a limited application. On the other hand phlogopite is superior to muscovite in heat resistance. Muscovite can withstand temperatures up to 700˚C, and phlogopite up to about 1000˚C. Phlogopite is, therefore, preferred where a high temperature is required [24]. Mica can be used as refractory filler in foundry core and mould coatings to eliminate or reduce finning defect in castings because of its lamellar plate-like nature [8].

Clays used for the manufacture of refractory fillers are the kaolinites. In the kaolinites there are equal numbers of silica and alumina sheets and equal numbers of silicon and aluminium atoms. The basic composition is $Al_2O_3.2SiO_2.2H_2O$ [25]. Kaolinite crystals are normally hexagonal disks which are built up by laying double sheets of alumina˚Ctahedral and silica tetrahedral on top of one another [26]. Kaolin clay is the most extensively used particulate mineral in the filling of coating of paper [27,28]. Since kaolin clay is fine and refractory and has found application in coating for papers, it also has potential application in foundry coating technology.

Other filler materials and their properties are provided in **Table 1**.

Different filler materials and their functions in the matrix depending on their various particles sizes are presented in **Figure 3.**

3.2. Liquid Carrier

The liquid career is the medium containing the coating constituents and also serves as the vehicle to transport the filler materials onto the sand substrate [11]. Therefore, the coatings are typically suspensions of high melting point refractories in a liquid carrier. Liquid carrier constitutes about 20 to 40% of the coating. After application, it is necessary to dry the coating to prevent gas formation when the hot metal is poured into the mould. The formation of gases may cause casting defects. After the liquid carrier is removed by evaporation or combustion, a protective refractory layer is deposited on the surface of the mould or core [29,30]. This layer prevents or minimizes the penetration of molten metal into the sand, reduces or prevents "burn-on" and erosion of the sand, and generally improves the quality of a casting surface. However, there are many factors to consider with carrier selection, including: compatibility of carrier with sand binder and/or refractory, method of drying, flammability and "burning" characteristics; toxicity and odour; application; labour and floor space. The most commonly used carrier are water-based (aqueous) and spirit-based (organic solvent) [29].

Table 1. Other filler materials and their respective properties [17].

Data	Chamotte	Chromite	Magnesite	Chrome-Magnesite
Availability	abundant	Good	Good	Good
Refractoriness℃ (approx.)	1780	1850	1850	1850
Thermal expansion (×1000 mm/m)	0.0052	0.007	0.014	0.012
Thermal conductivity ($WK^{-1}m^{-1}$)	6-9.5	9-15	20-30	13-20
Wettability with molten metal	No wetting	No wetting	No wetting	No wetting

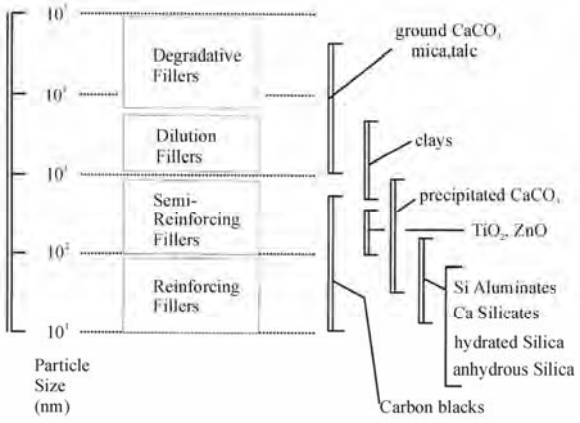

Figure 3. Classification of fillers according to average particle size [31].

3.2.1. Aqueous-Based Carrier

In this class, water is used as the carrier. Water is cheap and readily available but drying in an oven is usually necessary to remove it before casting [11,12,29]. Water is non flammable and non toxic. It has no flash point. Water is the safest of the carriers. From environmental view point, the use of water-based coatings is highly recommended. However, apart from requiring heat to dry water-coatings, complete drying of deep pockets in a reasonable time can be difficult. It has greater tendency for tears or runs compared to organic-based coatings. It reduces the tensile strength of urethane no-bakes, cold box and silicate sands. It increases the potential for core breakage. There is also possible degradation during core storage. Moreover, aqueous-based coatings can freeze [29].

3.2.2. Organic Solvent-Based Carrier

Organic solvent-based or spirit-based coating usually contains isopropanol (isopropyl alcohol) as liquid carrier for coating constituents, and the coating is dried by igniting and burning off the isopropanol [12]. This is typical of organic solvent-based carriers which also include methanol, ethanol, hydrocarbons and chlorinated hydrocarbons. They dry very fast. Isopropanol is recommended for use on large moulds and cores [11]. Isopropanol has good combustion characteristics with slow burning front and a moderate hot flame. This reduces the chance of over-heating the sand surface and subsequent problems of sand friability. Isopropanol is also technically acceptable because it is compatible with a wide range of suspension agents and resin binders also used in the formulation of these coatings. Most of the organic solvent-based carriers are referred to as air-drying carrier. These include carbon tetrachloride, methylenechloride, chloroethene and chloroform. They rely for efficiency on a rapid rate of evaporation which places them in a more hazardous category than isopropanol. They are also not versatile as isopropanol in the formation of foundry coatings. In many cases, they call for specialized forms of gelling media and resin binders [6]. The use of organic solvent-based coatings is threatened by environmental issues because they are toxic and flammable [30].

3.3. Suspension Agents (The Rheology Control System)

There is no difficulty in keeping solid particles in permanent suspension in a liquid if both have the same specific gravity. This is not the case with foundry sand coatings. The maintenance of solid particles in suspension is achieved by addition of suspension agents. These agents provide the suspension system that prevents the filler particles from agglomerating and separating out during storage of the coating over extended periods. It ensures that the coating is homogeneous and ready for application with the minimum of agitation. It also controls the flow properties of the coating and is designed to suit the application method that is used [11,12]. The suspension agent makes up 1 to 5% of the coating.

When water is used as the carrier liquid, bentonite clay is used as a suspension agent. Bentonite swells and forms a gel when mixed with water. Time must be allowed for gelling to proceed to completion. Two kinds of bentonite are in common use, one linked with calcium and the other with sodium ions. As a suspension agent bentonites initially of the sodium type are preferred. Calcium bentonite is converted to sodium bentonite by treatment with sodium carbonate. This treatment affects the swelling power of the clay and makes control of the viscosity of the coating unpredictable. Apart from the difficulties with quality control of the bentonite, it has the disadvantage of tending to induce shrinkage cracks in the coating when dried. In view of the drawbacks associated with bentonite, substitutes are found in polysaccharide and certain forms of carboxymethyl cellulose. Polysaccharides require special mixers, which few foundries possess, to obtain optimum suspension [6]. The cellulose type does not require this special mixers and do not induce shrinkage cracks as does dried bentonite as shown in **Figure 4** below.

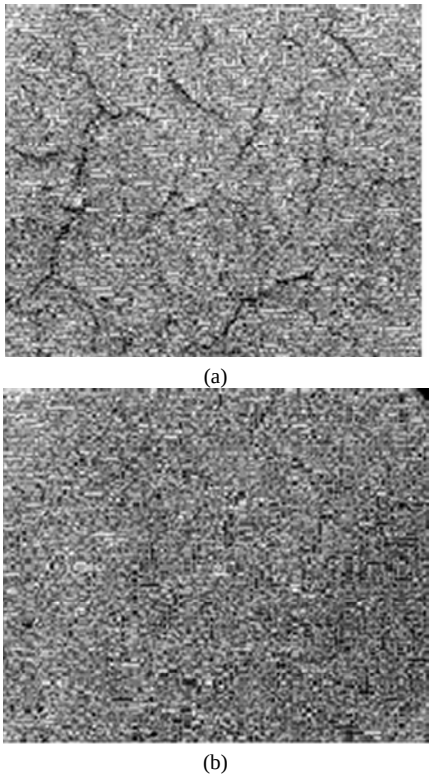

(a)

(b)

Figure 4. Surfaces of coated cores (a) cracking of coating induced by bentonite and (b) cracking eliminated by using carboxymethyl cellulose [6]

With organic solvent-based carrier systems, different suspension agents are used. Modified bentonite known also as organic bentonite or bentone will gel and increase the viscosity of organic liquids such as alcohols and solvents. Bentones result from a base exchange of the inorganic Ca and Na cation for an organic one which is quaternary ammonium. Examples of suitable suspension agent for organic solvent-based carrier are hydrogenated castor oil and quaternary alkyl ammonium montmorillonite gels [12].

3.4. Binding Agents

Binding agents are various materials which act to hold the particles of refractories together and attach them to the sand surface. The quantity of binder required for this purpose increases a little as the particle size of the refractory decreases, thereby increasing the surface area for a given ratio in the coating. However, it makes up to 1 to 5% of the coating. It is important to determine the minimum quantity of the binding agent, because too little results in poor adhesion but, excess produces brittle coating which may crack on drying and spall off during casting. Furthermore, resins and similar organic binders evolve gas on heating. Thus, any undispersed binder collected in partially dried areas of moulds or cores will cause local concentration of gas generation. In this way, defects such as porosity and lapping can result. It is also worthy to note that most organic binders and many suspension agents used in water suspensions are subject to biological degradation. For longer storage of the coating, precautions must be taken to suppress these reactions. Such reactions do not occur with spirit-based coatings.

Binders used for water suspensions include sulphite lye, various clays (bentonite and kaolin), dextrin, molasses, sugars, silica ester and resins (furan and phenol) soluble or miscible with water. For spirit-based suspensions, natural or synthetic resins are required. These include furan, phenol, urea formaldehyde, phenol formaldehyde, novolac and natural wood resins.

4. Coating Application Methods

Several variables dictate the choice of application method. Part geometry and size, appearance of the coating finish, and production rate, allinfluence the type of application method. Facility constraints will also determine the choice of application method. The configuration of the application equipment is dependent on space or climate. Systems can be manually or automatically controlled. Other systems may require extra equipment, such as holding tanks or outside air supply to operate properly.

Similar application systems may operate at widely varying parameters. The viscosity of the coating material, the desired thickness of the final coating, and the complexity of the part will determine the best operating-parameters for the application method. Thus, part temperatures, dip times or number of coats are put into consideration.

One factor that is important to all application methods is the transfer efficiency of coating material onto the part. Transfer efficiency is the percentage of solid coating material used that actually deposited on the surface of the part. The amount of solvent in the coating material is irrelevant. The higher the transfer efficiency, the better, as more coating material adheres to the part and less is wasted. Transfer efficiency ranges from 25% to 40% for conventional spray systems to almost 100% for dip and powder coating methods. Much of the pollution and waste created from organic finishing operations can be minimized or eliminated by improving the transfer efficiency of the application system. If the transfer efficiency cannot be improved, pollution control technology and waste handling measures must be employed [32]. The following are different methods of applying foundry coating on cores or moulds.

1) Brushing and swabbing
2) Spraying
3) Dip coating
4) Flow coating

4.1. Brushing and Swabbing

Brushing and swabbing methods of applying coatings are used in many foundries. The effort imparted by brushing helps to force the refractory particles into the pores of the sand surface, which is a desirable feature. The swab is a most useful aid in coating interior of difficult pockets and re-entrant angles. Both methods give uneven thickness and strives from brush motion is visible on casting. They also depend on the skills of the operator. There is also the risk of sand-coating mixture due to frothing and this initiates metal penetration [6].

4.2. Spraying

Spraying is a much faster means of application widely used in foundries of all types. It is important to pay greater attention to the coating composition because less mechanical effort is available to force the particles into the pores between the sand grains. Selection of the solid constituents and the overall viscosity is more critical for sprayed coating than for brushing and swabbing. Spray methods use specially designed guns to atomize the coating into a fine spray. This method along with brushing suffers the disability of not being able to coat deep recesses thoroughly. One reason for this is the back pressure of air which prevents refractory deposition in the cavity. The system of airless spraying provides a means of overcoming this disadvantage. Airless Spray has higher

transfer efficiency and lower chance of blowback. Again, it is more efficient when a flat surface is involved which is also placed vertically during spraying [6,33].

The above discussion refers to liquid coating mixtures; however, a group of researchers from Austria developed a new method of spraying dry coating on substrates overcoming the inherent disadvantages of the use of wet coating. The process is called electrostatic or tribostatic powder spraying method, also designated as EPS method. In this process, the surfaces of the substrate is first made conductive (if it is not a conducting material) by spraying electrically conducting polymer solutions on them. Then the powder coatings can be applied. According to the developers, this novel coating process has been tested on all popular binder systems—from cold box, through hot box and furan to inorganic types [34].

4.3. Dip Coating

Dip coating techniques can be described as a process where the substrate to be coated is immersed in the liquid or coating and then withdrawn with a controlled speed under controlled temperature and atmospheric conditions. Coating thickness increases with a faster withdrawal speed. The deposited thickness is determined by the balance of forces at the stagnation point on the coating suspension surface as shown in **Figure 5**. The faster the withdrawal speed the more coating suspension is pulled up onto the substrate surface because there is no time for the suspension to flow back down to the coating pool. During sol-gel dip coating, the coating suspension is rapidly concentrated on the surface of the substrate by gravitational draining with associated evaporation and condensation reactions. Dip coating is usually used for cores and is well suited for automatic applications. Dip coating enhances a high production rate and high transfer efficiency (almost 100%) and relatively little labour is required. The effectiveness of dip coating depends greatly on the viscosity of the coating, which thickens with exposure to air unless it is carefully managed. The viscosity of the coating must remain practically constant if the deposited film quality is to remain high and the same. To maintain viscosity, solvent must be routinely added as makeup. This results in high volatile organic compounds (VOC). Dip coating is not suitable for objects with hollows or cavities [33]. Other factors that determine the effectiveness of dip coating include coating density and surface tension. Better surface penetration is obtained than with spraying because of the head pressure of the coating in the dip tank. Even thickness of surface is necessary so as to maintain dimensional accuracy and true reproduction of contour. Uneven coating is at its worst when it runs down as tears. This defect can be encouraged by the nature of the surface to be coated but is mainly due to the kind of

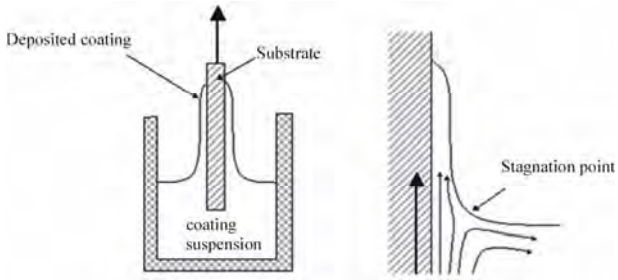

Figure 5. A schematic diagram of dip-costing process [35].

the suspension agent used in the coating. Tears and similar coating faults are sources of high gas evolution and casting defects may result [6]. The coating can be cured by a number of methods such as conventional thermal, UV, or IR techniques depending on the coating formulation [35].

4.4. Flow Coating

Flow coating is a method of applying a refractory coating that can be described as wetting the moulds or heavy cores with a garden hose at low pressure. With flow coating the mould or core is maneuvered so it is at an angle (20 to 40˚ to the vertical) in front of the operator [35] and coating applied through a hose as seen in **Figure 6**, starting at the top and in lateral movements progressively working down to the bottom. Flow coating is usually used for large or oddly shaped parts that are difficult or impossible to dip coat. Coatings applied by flow coating have only a poor to fair appearance unless the parts are rotated during drippage. Flow coating is fast and easy, requires little space, involves relatively low installation cost, requires low maintenance, and has a low labour requirement. Required operator skill is also low. Flow coating achieves a high coating transfer efficiency, often 90% and higher. Principal control of dry-film thickness depends on the coating viscosity [33]. Flow coating can eliminate all the various problems associated with the other coating techniques such as spraying, dipping or brushing. For flow coating to

Figure 6. Flow coating method, it is seen that the mould is inclined at an angle.

be effective, it must create a surface and sub-surface coating. Surface coating provides a barrier to the metal and improves surface finish. The sub-surface coating penetrates the surface of a mould or core to fill the voids between the sand grains. This reduces the possibility of metal penetration and veining [36].

5. Drying of Coating

After coating application, each coating must be 'dried', which means that the suspension agent (water, alcohol or volatile agents) must be completely removed. These substances do penetrate the mould or core material and do not have any protective effect for the mould or core. On the contrary, it can cause severe problems of gas formation, blows, slag entrapment, porosity, blistering, and penetration and drastically reduce the strength of the mould or core. The methods of removal are different depending on the type of coating [30,37-39].

5.1. Drying Organic Solvent-Based Coatings

In the past, foundries typically used solvent-based carriers because they dry quickly without external heating (air drying). They are also referred to as self-drying coatings. This takes a lot of time [30,37,38]. Consequently, flame torching became the accepted means of drying coated cores and moulds. However, workplace environmental, health and safety concerns, as well as economic considerations emanating from the rapidly increasing cost of petrochemicals based solvent, continue to enhance the development and use of water-based coating technologies [39].

5.2. Drying water-based coatings

The trend today is towards water-based coatings. But they require longer drying times using air drying and conventional ovens compared to organic solvent-based coatings. The drying temperature must exceed 100˚C, but lower than the temperature at which the binder system is destroyed (mostly 250˚C) [37]. Different drying techniques such as high intensity lights, microwave, drying tunnels and infrared ovens can be applied to water-based coatings. It was reported in [40] that the high intensity lights and drying tunnels did not dry fast enough as expected to prevent coatings from dripping and losing thickness uniformity. Microwave drying used non-selective heat that penetrated the sand cores and caused them to disintegrate. Infrared ovens, however, dry the coated cores or moulds quickly without damaging the sand bodies. Application of infrared heating for mould and core coating can reduce drying time by 85%. The energy saving comes from the controllability of the infrared unit, which brings the mould surface to the desired temperature and then cycles off in a predetermined time sequence. Less heat is dissipated to the surroundings. The infrared elements direct the heat more effectively at the mould and can dry deep cavities and mould pockets – thus contributing to better casting quality. The sub-surface of the mould is not affected. An additional advantage of using infrared heating is that only 25% of the floor space occupied by the resistance oven was required [41]. A significant development in water-based coatings is the feature in which there is a distinctive colour change as the coating dries and transitions from the wet to the dry state as shown in **Figure 7**. This change in colour offers visual confirmation that the coating is dry. Not only that this shows when drying is complete, it can also serve as a quality control tool. When drying takes longer time than necessary it will mean that the moisture content is high and can be adjusted. This feature saves energy used in drying thereby saving cost [39].

6. Characterization of Coatings

In order to understand the behaviour of coatings containing refractory materials, there is need for characterization of the coatings. The parameters that characterize foundry coatings are discussed below.

6.1. Specific Gravity

Specific gravity is the unit weight per unit volume. Specific gravity is a quick test that allows inferences to be drawn about the total solids and refractory components present in the coating [42]. The knowledge of the specific gravity of the suspension agent and that of the refractory material is critical. There would be no difficulty in keeping the refractory material in permanent suspension in the suspension agent if they have similar specific gravity [6]. The specific gravity also gives a fair idea of the refractory material content of the coating. Water has a lower specific gravity of 1. When it used to dilute a

Figure 7. Colour changing Zircon Foundry Coatings changes colour from Yellow to Pink, Pink to Yellow on drying or ignition. Available both in Water and Solvent based [43].

coating with relatively higher specific gravity component; the specific gravity of the coating is reduced.

6.2. Viscosity

Viscosity, a measurement of material flow properties, is the best test for evaluating coatings because of its high correlation with the dried deposit on the core. There are several different methods of measuring viscosity. The most commonly applied in foundries is the flow cup method as shown in **Figure 8**. The flow cup measure of viscosity requires the use of a cup with a specific size of hole in the bottom to match the material being used. A stopwatch is used as the cup is lowered into the coating and then taken from the surface of the coating after it has filled. The time it takes the coating to drain through the hole is the viscosity in number of seconds [44].

6.3. Baume´ Parameter

The Baume´ test is the most common test used in foundries to control coating because it is quick and easy. The test is performed with a hydrometer. It usually consists of a thin glass tube closed at both ends, with one end enlarged into a bulb that contains fine lead shot or mercury. The glass tubular end contains a calibrated scale in degrees Baume. The Baume scale of numbers relates to the specific gravity and body of a coating. After mixing the coating sample thoroughly, the hydrometer is immediately floated in the coating slurry. When it stops sinking, the degrees Baume is read directly from the hydrometer scale [44]. Baume is a simple test to help measure dilution consistency. However, there is a potential for operator variability, and test parameters must be carefully controlled. Operator consistency in placing the hydrometer into the coating and length of test time are critical. When Baume test is used in combination with the specific Gravity measured by Gravimetric method, the combined results can be a more useful diagnostic tool. Many metal casting facilities also include viscosity test in their refractory coating control test procedures [42]. L. Winardi *et al*. [46], reported that coating viscosity is typically reported in degree Baume. Higher Baume´ number indicates higher viscosity.

It was also reported in [47] that Baume when performed in a controlled laboratory environment tracks well certain coating properties, but fails to identify the coating property that must be controlled during application. They suggested that it must therefore be used with one or more additional tests, such as, Hercules surface tension and % solid content. Measurement of Baume´ is shown in **Figure 9.**

6.4. Solid content

The solids in the coating must be measured because they are the refractory materials that provide protection to the core or mould. The higher the percent solids, the more protection the coating offers. The solid content of a coating determines some other important parameters of the coating such as the density, viscosity, thickness, coverage etc [48]. Therefore, the knowledge of the amount of solid in the coating is very important for reproducibility of these properties. The percent solid content can be determined by dividing the weight of the dried coating by the original weight and multiplying by 100.

6.5. Colloidal Stability

Colloidal stability is describing the formation of uniform suspension of the particles in the coating matrix. The stability of particles is determined by their resistance to aggregation.

The formation of uniform suspensions of particles can be understood by calculation of the sedimentation rates assuming that the particles are spherical so that Stokes's Law may be applied. Equating gravitational and frictional forces:

$$\text{Sedimentation rate}, \frac{dx}{dt} = \left[\left(\frac{4\pi r^3}{3}\right)\left(\rho' - \rho\right) g\right] / 6\pi r\eta = \left[2r^2\left(\rho' - \rho\right) g\right] / 9\eta \quad (1)$$

Figure 8. Measurement of viscosity with a Flow cup [45].

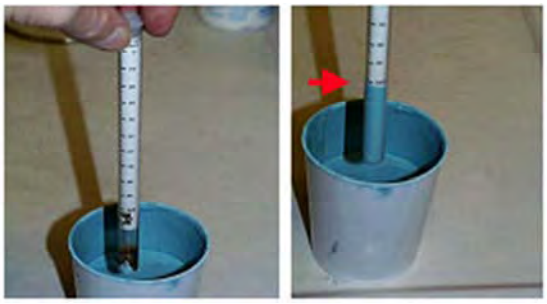

Figure 9. Measurement of °Baume´ [45].

Figure 10. Measuring the wet thick layer of a coating [45].

where

η = viscosity of coating

ρ = density of coating

ρ' = density of refractory particle material

r = radius of the refractory particle (assuming a spherical particle)

g = acceleration due to gravity

The stability of small particles is surprising, since surface tension leads to very high pressure differences across surfaces with small radii of curvature. For a particle of radius r, density ρ, and relative molar mass M, with surface tension γ, the pressure difference across the curved surface, p_r, compared to that across a flat surface, p_o, is given by the Kelvin equation.

$$\mathrm{RT}\ln\left(\frac{p_r}{p_o}\right)=\frac{2\gamma}{\rho r}\mathrm{M} \qquad (2)$$

Thus small particles should tend to dissolve while larger particles should grow as observed in Oswald ripening of precipitates [49].

6.6. Coating Thickness

Coating thickness is usually measured using a destructive test. To date no reliable non-destructive test is being applied by the foundry industry to measure the consistency of the coating layer thickness applied on the cores or moulds. In some tests, the cores are sectioned and the measurements were taken using a microscope [47,48].

In some other methods, the coating is removed from a flat surface on a core and the difference in the cored surface and the coated surface is measured.

The amount of surface deposit can be used as a reference for future comparisons and making decisions about coating allowance in casting design. There is a strong correlation between the viscosity of the coating and the coating thickness [44,48]. However, coating dry thickness has proved difficult to measure, so what is generally done is to measure the wet coating layer thickness using the elcometer wet film "comb" as shown in Figure 10. The elcometer wet film combs can be used in accordance with following standards; ISO 2808-7B, ASTM D 4414-A, BS 3900-C5-7B and NF T30-125. The film combs have various lengths on their sides. These standards specify that wet film comb be perpendicular to the substrate and the thickness of the coating lies between the biggest value wet tooth and the smallest value dry tooth values [50]. The wet coating layer thickness will be correlated to the dry coating thickness, if the volume to solids ratio of the coating is known [37,50]. As a rule of thumb dry coating thickness is 50% of the wet coating thickness [50].

In dip coating, the coating thickness is mainly defined by the withdrawal speed, the solid content (density), the surface tension and the viscosity of the liquid. The coating thickness can be calculated from landau-Levich equation [35]. This equation gives the wet coating layer

thickness on a vertically withdrawn flat plate.

$$h_w = 0.944\left(\frac{\eta\upsilon}{\rho g}\right)^{\frac{1}{2}}\left(\frac{\eta\upsilon}{\gamma_{LV}}\right)^{\frac{1}{6}} \quad (3)$$

Where h_w = Wet coating thickness
υ = withdrawal speed
ρ = density
γ_{LV} = Liquid-vapour surface tension
g = acceleration due to gravity

To calculate the dry film thickness these equations need to be modified. It was reported in [51], that Yan *et al*. derived Eq. (4) for dry film thickness, h_d.

$$h_d = Q\xi\left(\frac{\eta-\eta_s}{\eta_o}\right)^{0.84}\left(\frac{\eta\upsilon}{g\rho_s}\right)^{0.5} \quad (4)$$

here Q is called a dimensionless flux and is given b

$$Q = T\left(1-\frac{1}{3}T^2\right) \quad (5)$$

T is absolute temperature. ξ is defined as:

$$\xi = \frac{\rho_s}{\rho_p} \quad (6)$$

where ρ_s is the solvent density and ρ_p is the particle density. η_o is obtained from the viscosity of the solution as a function of the matrix concentration C_m, and according to Eq. (7)

$$\eta = \eta_s + \eta_o C_m \quad (7)$$

In Eq. (7), η is the viscosity of the particle solution with concentration C_p, and the viscosity of the solvent is η_s.

6.7. Coating Penetration Depth

The distance the coating penetrates the core is an important feature to a coating's success. A coating that lies entirely on the surface of the cores is not anchored well and will most likely spall away. A coating that penetrates too much will over degrade the core. Coating penetration is also a function of core density. A core that is blown too tightly resists coating penetration, while one blown softly acts like a sponge and absorbs much water. Therefore, any evaluation of coating penetration should be done on a core that is of normal production quality. It is also note worthy that core release agents may waterproof the core and affect coating penetration. Coating penetration is evaluated by cutting a coated dried core and observing how far the coating penetrates the core. The usual reference is sand grain penetration. A normal level of penetration is 2 – 4 sand grains [44]. It was reported in [47], that this is not the most precise methodology because sand grain sizes differ from one foundry to the other. Moreover, a batch of foundry sand has a known distribution of a variety of grain sizes within it, which also makes using sand grain count as a measuring system inadequate. Lower surface tension increases the depth of coating penetration. As coating penetration increases, the thickness of the proud layer decreases while the reverse is the case if the proud layer increases [48]. Thermal expansion increases with the thickness of the proud coating layer (the layer on the surface of the substrate) [47]. Therefore, an optimum proud layer thickness is needed to reduce the expansion defects on the casting made with these cores. This requires that the coating penetration depth is controlled.

6.8. Coating permeability

Coating permeability is the amount of gas that can pass through the coating. The level of permeability is detected by both the type and amount refractory materials that are used in the coating formulation and the dry film thickness deposit on the core. The permeability of the coating on the core is measured using a laboratory permmeter. A coating with low permeability is desirable when directing evolved gases to vent through specific areas of the core. A high permeability coating is best when the goal is the evacuation of core gases through the coating. The permeability of the coating at the coating-metal interface may be different than that measured on the core. Some constituents of the coating may quickly thermally decompose leaving voids that result in higher permeability. Some may soften and flux resulting in lower permeability [44]. High permeability coating will reduce the time required for removing the degradation products and will increase the metal fill velocity, often leading to blister and fold defects. Low permeability coating will slow down the metal velocity, which causes the molten metal to lose the adequate thermal energy required for complete pyrolysis, traps the degradation products and leads to misrun or partial fill. It has been reported in [51] that mould filling times decreased with permeability of the coatings. A standard approach to characterize the permeability of porous materials is to use Darcy's law (Eq. 8), which relates volumetric flow and pressure gradients with the properties of the fluid and porous materials.

$$K = \frac{\mu Q L}{A(\Delta P)} \quad (8)$$

where
K = permeability value in units of Darcys;
μ = viscosity of the fluid in centipoises;
Q = volumetric flow rate measured in cm^3/sec;
L = length of specimen in cm in the flow direction;
A = cross-sectional area of the specimen perpendicular the direction of gas flow in cm^2,

$\Delta P = (P_2 - P_1)$ = pressure drop over the specimen length

P_2 = pressure at outlet side of the specimen in atmospheres

P_1 = pressure at inlet side of specimen in atmospheres

Eq. (8) is valid when KA/μL is a constant in the laminar flow region (slow viscous flow) [52,53][*i.e.* for very small Reynolds number (Re) [54]. The upper limit is at a value of Re between 1 and 10. At a high Reynolds number, the deviation from Darcy's law will be observed. The Darcian permeability coefficient K indicates the capability of the porous medium to transmit fluids. Theoretically, the permeability coefficient only depends on the porous medium's properties. At high pressures, the turbulent and inertia flow become more dominant so that Darcy's law is no longer valid. The transition from the linear (Darcy's law) to the nonlinear regime˚Ccurs gradually as the Reynolds number increases. Therefore, the classical approach to macroscopically characterize the effect of inertia and turbulence on flow through real porous media is to use Forchheimer's equation (Eq. 9), which includes parabolic parts in the equation considering the influence of inertia and turbulence [51,54].

$$-\frac{\Delta P}{L} = \frac{\mu}{K}V + \beta\rho V^2 \quad (9)$$

where V = fluid velocity averaged over the total cross-section of the porous specimen (Q/A)

β = inertial parameter

ρ = density of the fluid

This equation macroscopically quantifies the non-linear effect [55]. Research [51] has shown that the deviation from Darcy's law (which occurs at Re = 1 – 10) cannot be attributed to turbulence, and inertia forces are more appropriate to explain the deviation. The role of inertial effects over such a transition at high Re from linear to nonlinear flow in the pore space was successfully simulated in the laminar regime without including turbulence effects [55]. However, the random aspect of the pore distribution induces a highly heterogeneous local flow which becomes turbulent at high Reynolds' regimes [56].

6.9. Core Degradation

Core degradation varies from coating to coating. The longer a core stays wet, the more core degradation will take place. So, it is the best practice to put cores into an oven heat zone as quickly as possible after the core is coated. Most coatings use surfactants as wetting agents to allow the coating to penetrate the proper depth. These surfactants change the surface tension of the water, making it worse for core degradation. To evaluate the effect refractory coating on core strength, dip one set of cores and leave the other set undipped. Place both sets in the drying oven until dry and allow them to cool to ambient temperature approximately one hour. Then, when cool, evaluate both sets of cores for strength. The comparative loss in strength of coated cores will most likely be substantial [44]. It was reported in [37] that the strength of core and mould material will decrease about 30% with alcohol based coatings and 50% for water based coatings. This is in agreement with the authors' findings in the investigation of the strength of core materials. The publication of these results is on the way.

6.10. Wettability and Surface Tension

The deposition of a coating on a solid substrate generates new interface between dissimilar materials and involves considerations of wettability, spreading, interface evolution and adhesion. The wettability of a solid by a liquid is characterized in terms of the angle of contact that the liquid makes on the solid [57]. The basic law governing the equilibrium of a liquid drop on a surface was formulated by Thomas Young σ.

The drop is shaped by the resultant forces pulling at the three-phase contact line of the drop, where the solid/liquid, liquid/gas and solid/gas interfaces meet, in the plane of the solid as shown in **Figure 11**. The forces (per unit length) acting at this line are the surface tensions and their balance yields the famous Young's equation.

$$\sigma_{SG} = \sigma_{SL} + \sigma_{LG}\mathrm{Cos}\theta_c \quad (10)$$

where σ_{SG} , σ_{SL} and σ_{LG} are solid/gas, solid/liquid and liquid/gas surface tensions, respectively [57,58].

According to Taylor's depiction of liquid droplet shape on solid surface, the droplet height, h = 2asin ($\theta^*/2$), where a is the capillary length ($a = (\sigma/\rho g)^{1/2}$, σ, the liquid surface tension and ρ, its density, a = 2.7 mm for water). It shows that gravity g can affect drop shape besides the three phase forces. Only if the drop is small enough that the effect of gravity is negligible, which typically is the case for drops of millimetre size down to micrometres, the drop will have the shape of a spherical cap and the liquid/gas interface meets the solid surface at an angle θ_c, which is called the contact angle of a flat

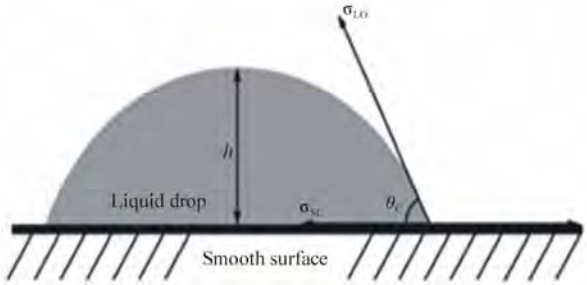

Figure 11. Shape of droplet on a smooth surface [57].

surface [58]. The condition $\theta < 90^{\circ}$ indicates that the solid is wetted by the liquid, such a surface is referred to as a hydrophilic surface and $\theta > 90^{\circ}$ indicates nonwetting, and the surface is called a hydrophobic surface. Wettability of a solid surface is governed by the chemical properties and the microstructure of the surface. Wettability is mainly determined by its interfacial free energy (σ_{SG}). The greater, the free surface energy, the easier, the liquid can spread upon and vice versa.

Young's equation applies to ideal surfaces that are perfectly smooth and devoid of all chemical and structural inhomogeneities. The contact angle measured on a rough surface (called the Wenzel angle, θ_w) does not obey Young's equation; it is related to the equilibrium (Young's) angle θ_y [59], by Eq. 11

$$\mathrm{Cos}\theta_w = r\cos\theta_y \tag{11}$$

where r is the ratio of true wetted area to the apparent area. Equation 11 is called the Wenzel equation.

Wenzel's equation applies to equilibrium angles on rough surfaces and not to advancing and receding angles of a droplet on a rough solid surface that give rise to contact-angle hysteresis. Hysteresis, H, is defined as the difference of the advancing and receding angles (*i.e.*, $H = \theta_a - \theta_r$) and arises because the liquid-vapour interface does not retrace its original path when it recedes on the solid, so that spreading is thermodynamically irreversible. Because roughness hinders the contact line motion by creating energy barriers, the system can reside in any of the potential wells accessible to it that are commensurate with the vibrational (or thermal) energy of the droplet [58].

In many industrial processes like that found in foundries, the substrate (core in foundries) is immersed in a liquid coating material, and then withdrawn to leave a liquid film on the substrate. The film (coating) thickness depends upon the surface tension, withdrawal speed, substrate geometry, roughness, and viscosity. The dispersion of fine, granular solids in a liquid vehicle is a basic step in preparing paints and other coating materials and involves particle transfer across a gas-liquid interface. The transfer of non-wettable solids into liquids requires the solid to overcome a surface energy barrier at the liquid-gas interface, and energy must be expended to assist the transfer of non-wettable solids. Once the solid enters the liquid, the capillary (attractive) forces and gas bridges between solids control such phenomena as agglomeration, dispersion, and air entrapment. The inter-particle forces between dispersed solids are due to liquid surface tension and pressure difference across the curved liquid-vapour boundary between contacting solids. The maximum inter-particle force, F, due to capillary forces between two touching spheres is

$$F = 2(2)^{\frac{1}{2}}\sigma_{LG}\frac{\mathrm{Cos}\theta}{R} \tag{12}$$

where R is the radius of the sphere. The force increases with increasing liquid surface tension and decreasing contact angle and particle radius. These forces affect the viscosity, density, and sedimentation behaviour of the suspension and the properties of the coating deposited using the suspension [58].

7. Potential Area of Exploitation in Foundry Coating Development: the Sol-Gel Technology

7.1. Introduction

Sol-gel technology is discovered in the late 1800s and extensively studied since the early 1930s. Various steps in the sol-gel process to control the morphology of the final product for particular properties meant for specific applications are shown in **Figure 12**. Coating production is one of the techniques for controlling the morphology of the product. Sol-gel coating technology has been applied to various areas of coating production for corrosion protection [60,61], wear resistance [62], thermal barrier [63][, anti-soiling [64], anti reflective [65,66] etc but has not been applied to the foundry industry. A literature survey reveals that surprisingly little research [67-69] is carried out on a topic that is of great importance for the surface quality of castings. The application of sol-gel technology in the production of foundry coatings is a novel research area undertaken by our research group.

The technology gained much of its popularity in the glass and ceramics production. Sol-gel technology is an area of materials science. It denotes a process by which largely inorganic polymers are synthesized through the formation of a colloidal suspension (sol) and gelation of the sol to form a network in a continuous liquid phase (gel). A "sol" is a dispersion of colloidal particles. A "gel" is an interconnected polymeric network formed by assembly of the sol. The gelation proceeds through stages by which the product's rigidity is increased. The final material produced in a room temperature synthesis is a porous glasslike solid, which is termed a xerogel [70]. This xerogel is the sol-gel component of the coating being produced and tested for foundry application. The precursors for synthesizing the colloids consist of a metal or metalloid element surrounded by various reactive ligands. Metal alkoxides are the most popular because they react readily with water.

The most widely used metal alkoxides are the alkoxysilanes, such as tetramethoxysilane (TMOS) and tetraethoxysilane (TEOS). The sol-gel process offers many advantages over other methods of producing coatings and films. For example, the low processing temperature; the possibility of changing the sol composition, thereby producing a change in film and coating microstructure and

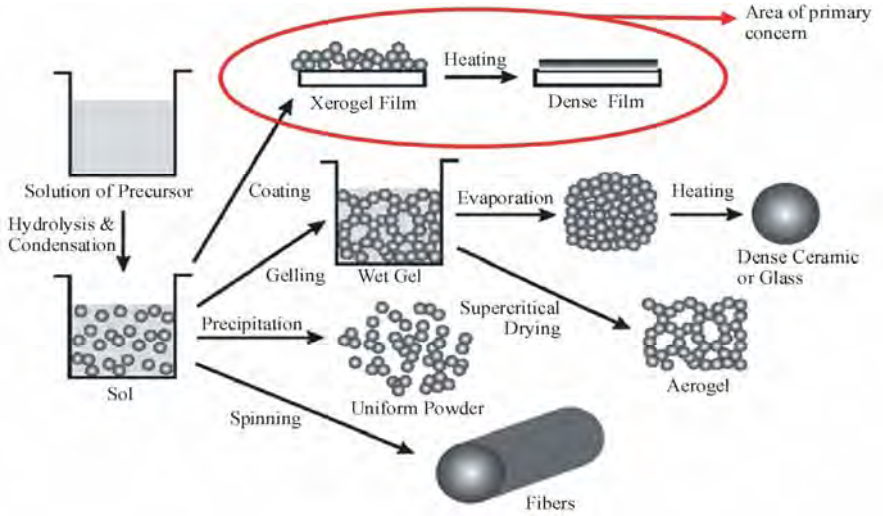

Figure 12. Various steps in the sol-gel process to control the final morphology of the product [71].

low processing cost compared to some other competitive process such as ceramic (powder) method, chemical deposition process etc [72].

7.2. Sol-Gel Reactions

The characteristics and properties of a particular sol-gel inorganic network are related to a number of factors that affect the rate of hydrolysis and condensation reactions, such as, pH, temperature and time of reaction, reagent concentrations, catalyst nature and concentration, H_2O/Si molar ratio (R), aging (structure modifications with time depending on time and temperature, solvent and pH conditions) temperature and time, and drying. Of the factors listed above, pH, nature and concentration of catalyst, H_2O/Si molar ratio (R), and temperature have been identified as the most important. Thus controlling these factors, it is possible to vary the structure and properties of the sol-gel derived inorganic network over wide ranges. At the functional group level, three reactions are used to describe the sol-gel process: hydrolysis, water condensation and alcohol condensation.

Generally speaking, the hydrolysis reaction, through the addition of water, replaces alkoxides groups (-OR) with hydroxyl groups (OH). Subsequent condensation reactions involving the silanol groups (Si-OH), which are hydroxylated species, produce siloxane bonds (Si-O-Si) under release of water (oxolation), whereas the reaction between a hydroxide and an alkoxide leads to siloxane bonds (Si-O-Si) under release of an alcohol (alkoxolation).

$\equiv Si - OR + H_2O \longrightarrow \equiv Si - OH + ROH$ This process is called hydrolysis

$\equiv Si - OH + HO - Si \equiv \longrightarrow \equiv Si - O - Si \equiv + H_2O$ This condensation process is called oxolation

$\equiv Si - OR + HO - Si \equiv \longrightarrow \equiv Si - O - Si \equiv +$ ROH This condensation process is called alkoxolation

Under most conditions, condensation starts before hydrolysis is complete. However, conditions such as, pH, H_2O/Si molar ratio (R), and catalyst can force completion of hydrolysis before condensation begins. Additionally, because water and alkoxides are immiscible, a mutual solvent such as an alcohol is utilized. With the presence of this homogenizing agent, alcohol, hydrolysis is facilitated due to the miscibility of the alkoxides and water. As the number of the siloxane bonds increases, the individual molecules are bridged and jointly aggregate in the sol. When the sol particles aggregate, or inter-knit into a network, a gel is formed. Upon drying, trapped volatiles (water, alcohol, etc.) are driven off and the network shrinks as further condensation can occur.

The first step of the hydrolysis of the Silicon alkoxides can occur by acid-catalysed or base-catalysed processes. Mineral acids (HCl) and ammonia are most generally used; however, other catalysts are acetic acid, KOH, amines, KF and HF. It can generally be said that sol-gel derived silicon oxide networks, under acid catalysed conditions, yield primarily linear or randomly branched polymers which entangle and form additional branches resulting in gelation. On the other hand, silicon oxides networks derived under base-catalysed conditions yield more highly branched clusters which do not interpenetrate prior to gelation and thus behave as discrete clusters having larger sol particles and large pores between the interconnected particles. Hence the choice of acid or base catalysis has a substantial influence on the nature of the gel which is formed [49,73].

7.3. Application of Sol-Gel Process in Foundry Coating Formulation

The application of sol-gel coating process in foundry

coating production is a novel area of research undertaken by the authors at Technical University of Denmark, DTU and the coating producers at Danish Technological Institute, DTI along with the expertise of the industrial partners [48,74]. Chemically bonded sand cores are dip coated with the sol-gel coatings containing different filler materials. The core-coating interactions are investigated using advanced microscopy and spectroscopy. During casting, the thermal behaviour of the coated cores is monitored using a data acquisition soft ware. The modeled results for commercial casting modeling and simulating soft ware are correlated to experimental results accordingly. After casting, the surface and subsurface quality of the castings are examined with a 3 D optical surface roughness measuring microscope and a scanning electron microscope respectively. The results so far obtained show a significant potential in the sol-gel process towards, improvement of the surface quality of casting.

8. Conclusions

This is a review about foundry coating technology. It includes but not limited to the coating components, methods of application and characterization parameters. New area of innovation for further development and improvement of foundry coating technology was also introduced. Following the ongoing discussions, this review has thrown more light in the foundry coating technology. The information in this report will help foundries to identify the right parameters to enhance the performance of their coatings to produce castings with excellent surface finish. On the other hand foundry coating manufacturers will find this report highly resourceful for the improvement of their various existing products.

9. Acknowledgements

The authors wish to acknowledge the Danish Agency for Science, Technology and Innovation for their financial support for the ongoing project.

REFERENCES

[1] T. A. Burns, “The Foseco Foundryman's Hanbook,” Pergamon Press, Staffordshire, 1986.

[2] I. D. Kascheev, N. Yu. Novozhilov, E. V. Tsarevskii, V. A. Perepelitsyn, V. A. Ryabin and N. F. Seliverstov, “Refractory Coatings for Foundry Moulds and Cores,” *Journal of Refractories and Ceramics*, Vol. 23, 1982, pp. 36-139.

[3] AFS, “Moulding Methods and Materials,” 1st Edition, The Ameriacan Foundrymen’s Society, Illonois, 1962.

[4] S. D. Chastain, “A Sand Casting Manual for the Small Foundry,” Jacksonvile Publishers, Florrida, Vol. 1, 2004.

[5] L. Horvath, “Coatings Go Beyond Appearance to Provide Quality Control,” 2010. Http://www.Foundrymag.com/Classes/Article/articledraw.Aspx.

[6] F. W. Pursall, “Coatings for Moulds and Cores,” K. Straus, Ed., Applied Science in the Casting of Metals, Pergamon Press, Oxford, 1970.

[7] R. E. Moore, “Refractories, Structure and Properties,” *Encyclopedia of Materials: Science and Technology*, 2001, pp. 8079-8099.

[8] F. L. Pirkle, D. A. Podmeyer, “Zircon: Origin and Uses,” *Society for Mining, Metallurgy and Exploration*, Vol. 292. http://cam.usf.edu/CAM/exhibitions/1998_12_McCollum/supplemental_didactics/62.Zircon.pdf

[9] J. Hlavac, “Melting Temperatures of Refractory Oxides,” *Pure and Applied Chemistry*, Vol. 54, No. 3, 1982, pp. 681-688. doi:org/10.1351/pac198254030681

[10] C. E. Houssa, “Minerals in Plastics,” *Bulletin de la Societe Royale des sciences de liege*, Vol. 72, 2003, pp. 71-80.

[11] J. R. Brown, “The Foseco Foundryman’s Handbook”, Pergamon Press, Oxford, 2000.

[12] S. Derbyshire, “Coating Composition,” US patent, 4279, 946, 1981. http://www.freepatentsonline.com/4279946

[13] J. J. Horak, “Core and Mould Wash,” US patent 075, 1990. http://www.freepatentsonline.com/1990075

[14] G. D. Ulrich and D. W. Molesky, “Silica Fillers from Silicon Powder,” US patent 4, 755, 368, 1988. http://www.osti.gov/energycitations/product.biblio

[15] N. A. Waterman, R. Trubshaw and A. M. Pye, “Filled thermoplastic Materials Part 1: Fillers and Compounds,” *International journal of Materials in Engineering Applications*, Vol. 1, No. 2, 1978, pp. 74-79. doi:org/10.1016/S0141-5530(78)90036-5

[16] K. W. Jang, W. S. Kwon, M. J. Yim and K. Paik, “Effects of Silica Filler and Diluent on Materials Properties of Non-Conductive Paste and thermal Cycling reliability of Flip Chip Assembly,” *Microelectronics and packaging Society*, Vol. 10, 2003, pp. 1-9.

[17] P. L. Jain, “Principle of Foundry Technology,” 4th Edition, McGraw-Hill, New Delhi, 2006.

[18] F.O. Traenkner, “Surface Treatments of Moulds,” US Patent 2,618,032, 1952. http://www.freepatentsonline.com/2618032

[19] J. W. G. Wells, “Olivine Uses and Beneficiation Methods,” NCSU Minerals Laboratoty Bull, Vol. 2, 1959. http://www.p2pays.org/ref/49/48621

[20] M. Yekeler, U. Ulusoy and C. Hicyilmaz, “Effect of Particle Shape and Roughness of Talc Mineral Around by Different Mills on the Wettability and Floatability,” *Powder Technology*, Vol. 140, No. 12, 2004, pp. 68-78. doi:org/10.1016/j.powtec.2003.12.012

[21] Z. S. Aćimović-Pavlović, A. K. Prstić and L. D. Andrić, “The Characterization of Talc-Based Coating for Application for Al-Si Alloy Casting,” *Chemical Industry and Chemical Engineering Quarterly*, Vol. 13, No. 1, 2007, pp. 38-40.

[22] K. S. Ariffin, “Talc and Pyrophylite Group–2:1 Phyllosilicate,” EBS 425–Mineral Perindustria, pp. 1-21, 2000.

http://mineral.eng.usm.my/web%20halaman%20mineral/Talc%20and%20pyrohyllite

[23] D. Gan, S. Lu, C. Song and Z. Wang, "Physical Properties of Poly(ether ketone ketone)/Mica Composites: Effect of Filler Content," *Materials Letters*, Vol. 48, No. 5, 2001, pp. 299-302. doi:org/10.1016/S0167-577X(00)00318-9

[24] M. Zone, "Mica," 2010. Http://www.Mineralszone.com/minerals/mica.Html.

[25] W. B. Parkes, "Clay-Bonded Foundry Sand," ASP, England, 1971.

[26] A. Astruc, E. Joliff, J. F. Chailan, E. Aragon, C. O. Petter and C. H. Sampaio, "Incorporation of Kaolin Fillers into an Epoxy/Polyamidoamine Matrix for Coatings ," *Progress in Organic Coatings*, Vol. 65, No. 1, 2009, pp. 158-168. doi:org/10.1016/j.porgcoat.2008.11.003

[27] W. M. Bundy and J. N. Ishley, "Kaolin in paper filling and coating," *Scholars Portal Journals*, Vol. 5, No. 1, 1991, pp. 397-420. doi: 10.1016/0169-1317(91)90015-2

[28] B. W. Rowland, "Modified Clay," US patent 2,307,239, 2006. http://www.google.com/patents?

[29] M. Swartzlander, "Refractory Coating: Making the Right Choice," *Modern Casting*, 1992. http://www.allbusiness.com/manufacturing/fabricated-metal-product-manufacturing/340970-1.html

[30] J. Koller and B. Schmitt, "The Challenge: Decrease the Drying Time for Wash Coatings on Sand Moulds and Cores," The EPRI Center for Materials Production. CMP-091. http://www.p2pays.org/ref/09/08993

[31] J. L. Leblane, "Rubber-Filler Interactions and Rheological Properties in Filled Compounds," *Progress in Polymer Scence*, Vol. 27, No. 4, 2002, pp. 627-687. doi:org/10.1016/S0079-6700(01)00040-5

[32] EPA "Self-Audit and Inspection Guide: Organic Finishing of Metals," 2010. Http://www.Paintcenter.org/ctc/applimeth.Cfm.

[33] C. J. Brinker, G. C. Frye, A. J. Hurd and C. S. Ashley, "Ashley Fundamentals of Sol-Gel Dip Coating," *Thin Solid Films*, Vol. 201, No. 5, 1991, pp. 97-108. doi:org/10.1016/0040-6090(91)90158-T

[34] A. C. Psimenos and G. Eder, "PCT-Pure Coating Technology," 2011. http://kongre.tudoksad.org.tr/assets/Uploads/31.GunterEder-word.pdf.

[35] YTCA's, "Anti-reflection coating technology," 2010. http://www.ytca.com/dip_coating.

[36] S. Brannon, M. McElrath, R. Reddy and S. R. Counselor, "Navigating the Ripples of Flow Coating," *Modern Casting*, pp. 29-31, 2009.

[37] Gietech BV ir Henderieckx, "Coatings for Chemical Bounded Sand," 2005. http://www.gietech.be/LinkClick.aspx?fileticket=l6MCLoftoMI%3D&tabid=111&mid=539

[38] Y. P. Yakunin, G. A. Ponomarevn and E. V. Shtyrenkov, "Experience in the Preparation of Self-Drying Sand-Burning Resistant Coatings for Foundry Moulds and Cores," US Patent UDC 678.026.3.

[39] J. Kroker, "Casting solutions," 2010. http://www.ductile.org/magazine/2003_3/nbriefs.htm

[40] Case Study, "Aluminium Foundry replaces TCA with Water-based Coatings," 2010 http://www.p2pays.org/ref/05/04239.htm.

[41] Canadian Foundry Association, "Guide to Energy Efficiency Opportunities in Canadian Foundries," 2003. http://oee.rncan.gc.ca/cipec/ieep/newscentre/foundry/2/2_3_5.cfm?attr=29.

[42] Cast TIP, "Controlling Refractory Coatings," *Modern Casting*, 2010. http://www.thefreelibrary.com/Controlling+refractory+coatings.-a022

[43] Shamlax Meta-chem Private, "Colour Changing Zircon Foundry Coatings," 2003. http://www.tradeindia.com/fp442828/Color-Changing-Zircon-Foundry-Coatings.html

[44] S. G. Baker, "Evaluating Refractory Coatings: a Practical Approach," *Modern Casting*, Vol. 92, 2002, pp. 21-23.

[45] N. Hodgkinson, "Improved Ductile Iron Casting Quality Through Optimized Coating Technology," *The Ductile Iron News*, 2004. http://www.ductile.org/magazine/2004_1/coating.htm

[46] L. Winardi and R. D. Griffin, "Effects of Coating Drying Methods on LOI, Gas Evolution and Core Permeability,"*AFS Transactions Paper*, Vol. 08-047, 2008.

[47] S. N. Ramrattan and M. K. Joyce, "Final Report-Refractory Coating Control," http://amc.aticorp.org/reports/wmu2009.pdf.

[48] U. C. Nwaogu, T. Poulsen, R. Stage, C. Bischoff and N. S. Tiedje, "New sol-gel Refractory Coatings on Chemically-Bonded Sand Cores for Foundry Applications to Improve Casting Surface Quality," *Science and Coatings Technology*, Vol. 205, No. 16, 2011. doi:10.1016/j.surfcoat.2011.02.042

[49] J. D. Wright and N. A. J. M. Sommerdijk, "Sol-Gel Materials Chemistry and Applications," CRC Press, London, 2001.

[50] BAMR (Pty), "Elcometer Wet Film Combs," 2011. http://www.bamr.co.za/elcometer%203238%20long%20edge%20wet%20film%20comb.shtml.

[51] X. Chen, "Permeability Measurement and Numerical Modelling for Refractory Porous Materials," A*merican Foundry Society Transactions Paper*, Vol. 08-133, 2008.

[52] W. A. Anderson, "Permeability Relationships Using Darcy Permeability, Vacuum Decay, Pressure Decay, and Pore Size Distribution Methods on Graphitic Materials," *Carbon*, Vol. 4, No. 1, 1966, pp. 107-114. doi:org/10.1016/0008-6223(66)90015-7

[53] T. Sogabe, M. Inagaki and T. Ibuki, "Coating of graphite by polyimide and its gas permeability," *Carbon*, Vol. 30, No. 3, 1992, pp. 513-516. doi:org/10.1016/0008-6223(92)90051-W

[54] X. H. Wang and Z. Liu, "The Forchheimer Equation in Two-Dimensional Percolation Porous Media," *Physical A*:

Statical and Theoretical Phycics, Vol. 337, No. 3-4, 2004, pp. 384-388. doi:org/10.1016/j.physa.2004.01.047

[55] U. M. S. Costa, J. S. Andrade Jr, H. A. Makse and H. E. Stanley, "The Role of Inertia on Fluid Flow through Disordered Porous Media," *Physical A*: *Statistical Mechanics and Its Applications*, Vol. 266, No. 1-4, 1999, pp. 420-424. doi:org/10.1016/S0378-4371(98)00624-4

[56] H. H. Macedo, U. M. S. Costa and M. P. Almeida, "Turbulent Effects on Fluid Flow through Disordered Porous Media," *Physical A*: *Statistical Mechanics and Its Applications*, Vol. 299, No. 1-4, 2001, pp. 371-377. doi:org/10.1016/S0378-4371(01)00257-6

[57] A. W. Neumann and R. J. Good, *Surface and Colloid Science*, Vol. 2, 1979.

[58] Z. Lijun, W. Xuedong, L. Zeng and W. Dan, "Superhydrophobicity from Microstructured Surface," *Chinese science Bulletin*, Vol. 49, No. 17, 2004, pp. 1779-1787. doi:10.1007/bf03183400

[59] R. Asthana and S. S. T. Mileiko, "Wettability and Interfacial Considerations in Advanced Heat-Resistant Ni-base Composites," *Bulletin of the Polish Academy of Sciences, Technical Sciences*, Vol. 54, 2006.

[60] P. Kiruthika, R. Subasri, A. Jyothirmayi, K. Sarvani and N. Y. Hebalkar, "Effect of Plasma Surface Treatment on Mechanical and Corrosion Protection Properties of UV-Curable sol-gel based GPTS-ZrO_2 Coatings on Mild Steel," S*urface and Coatings Technology*, Vol. 204, No. 6, 2010, pp. 1270-1276. doi:org/10.1016/j.surfcoat.2009.10.017

[61] A. L. K. Tan, A. M. Soutar, I. F. Annergreen and Y. N. Liu, "Multilayer sol-gel Coatings for Corrosion Protection of Magnesium," *Surface and Coatings Technology*, Vol. 198, No. 1-3, 2005, pp. 478-482. doi:10.1016/j.surfcoat.2004.10.066

[62] T. Hübert, S. Svoboda and B. Oertel, "Wear Resistant Alumina Coatings Produced by a sol-gel Process," *Surface and Coatings Technology*, Vol. 201, No. 1-2, 2006, pp. 487-491. doi:10.1016/j.surfcoat.2005.11.014

[63] C. Viazzi, J. P. Bonino and F. Ansart, "Synthesis by sol-gel Route and Characterization of Yttria Stabilized Zircinia Coatings for Thermal Barrier Applications," S*urface and Coatings Technology*, Vol. 201, No. 7, 2006, pp. 3889-3893. doi:org/10.1016/j.surfcoat.2006.07.241

[64] K. H. Hass, S. Amberg-Schwab, K. Rose and G. Schottner, "Functionalized Coatings based on Inorganic-Organic Polymers (ORMOCER ®s) and Their Combination with vapor Deposited Inorganic Thin Films," *Surface and Coatings Technology*, Vol. 111, No. 1, 1999, pp. 72-79. doi:org/10.1016/S0257-8972(98)00711-7

[65] C. Guillén, A. Morales and J. Herrero, "Performance of sol-gel SiO_2 Coatings onto Glass/SnO_2 Superstrates," S*urface and Coating Technology*, Vol. 132, No. 1, 2000, pp. 31-35. doi:org/10.1016/S0257-8972(00)00727-1

[66] D. R. Uhlmann, T. Suratwala, J. K. Davidson, M. Boulton and G. Teowee, "Sol-gel coatings on Glass," *Journal of Non-Crystalline Solids*, Vol. 318, 1997, pp. 113-122. doi:org/10.1016/S0022-3093(97)00162-2

[67] T. B. N. Hodgkinson, "Improving Foundry Profitability through the Use of Rheotec* XL Coating," *Foseco Foundry Practice*, Vol. 240, 2003.

[68] T. Birch and D. Bell, "Improved Iron Casting Quality through Application of Advanced Coating Technology," *Foseco Foundry Practice*, Vol. 243, 2005.

[69] A. Schrey, "NORACEL* w100 - A New Technology to Prevent Veining Defects," *Foseco Foundry Practice*, Vol. 246, 2007.

[70] J. B. Laughlin, J. L. Sarquis, V. M. Jones and J. A. Cox, "Using Sol-Gel Chemistry to Synthesize a Material with properties Suited for Chemical Sensing," *Journal of Chemical Education*, Vol. 77, No. 1, 2000, pp. 77-79. doi:10.1021/ed077p77

[71] M. Niederberger and N. Pinna, "Metal Oxide Nanoparticles in Organic Synthesis," *Formation, Assembly and Application*, Vol. XIII, No. 217, 2009.

[72] S. M. Tracey, S. N. B. Hodgson, A. K. Ray and Z. Ghassemlooy, "The Role and Interactions of Process Parameters on the Nature of Alkoxides Derived sol-gel Films," *Journal of Materials Processing Technology*, Vol. 77, No. 1-3, 1998, pp. 86-94. doi:org/10.1016/S0924-0136(97)00399-3

[73] K. Mauritz, "Sol-Gel Chemistry," http://www.psrc.usm.edu/mauritz/solgel.html.

[74] U. C. Nwaogu, T. Poulsen, C. Bischoff and N. S. Tiedje, "Influence of New sol-Gel Refractory Coating on the Casting Properties of Cold Box and Furan Cores for Grey Cast Iron," The Proceedings of 69th World Foundry Congress, Hangzhou, 16-20 October 2010, pp. 648-653.

SUPPLEMENT 7

A Technical Report

U. C. Nwaogu and N.S. Tiedje,

“A new approach to surface texture characterization of castings”, 2011.

A Technical Report

A new approach to surface texture characterization of castings

U. C. Nwaogu
N.S. Tiedje

Casting Technology Group,
Department of Mechanical Engineering,
Technical University of Denmark.

2011

Contents

List of Figures

List of Tables

1 Introduction

Surface characterization, the nature of surfaces, and the measurement of surfaces cannot be separated from each other. A deeper understanding of the surface geometry produced by better instrumentation often produces a new approach to characterization. Surface characterization means the breakdown of the surface geometry into basic components based usually on some functional requirements. These components have various shapes, sizes, distribution in space, and can be constrained by a multiplicity of boundaries in height and position [1]. Surface roughness is that part of the irregularities left on the surface after manufacture. In the study of roughness, the word lay is used to describe the direction of the predominant surface pattern. Surface roughness is generally examined in plane i.e., areal view with the aid of optical and electron microscopes, in cross-sections normal to the surface with stylus instruments and, in oblique cross-section, by optical interference methods [1].

The surface topography or roughness is the most important parameter describing surface integrity of a component. It has great importance in specifying the function of a surface, as a significant proportion of component failure, starts at the surface due to either discontinuity or deterioration of the surface quality. In the manufacturing industry, the surface must be within a certain limit of roughness. Consequently, measuring surface roughness is important for quality control. Surface finish has also important role in aesthetics and corrosion resistance and may translate to improved performance and reduced life cycle cost [2].

The surface roughness of castings is influenced by the manufacturing process (expendable mould process, permanent mould process, etc.), the moulding materials used (sand, binder, coatings, etc.), the equipment available, and the alloy cast, etc. [3, 4, 5]. Figure 1 shows a detailed list of all the factors influencing the surface roughness of cast components. The controlling parameters are so many that the problem becomes a complex situation. To control the surface roughness of castings, these factors must be selected in a proper way most suitable. However, in measuring the cast surface roughness, the following issues are considered [6]:

1. Compliance with standards
2. Suitability for random pattern
3. Repeatability (or reproducibility)
4. Latitude to accommodate rough and smooth surface and a variety of shapes
5. Easy operation
6. Dependence on human judgement

In the foundries the measurement of surface roughness of castings have been neglected for decades, due to the inability of the mechanical surface roughness testing instruments such as stylus instruments, to reproduce the exact surface texture of casting surfaces. Probably, the single factor causing the most difficulty in devising a means of measuring surface roughness is that the surface characteristic has three

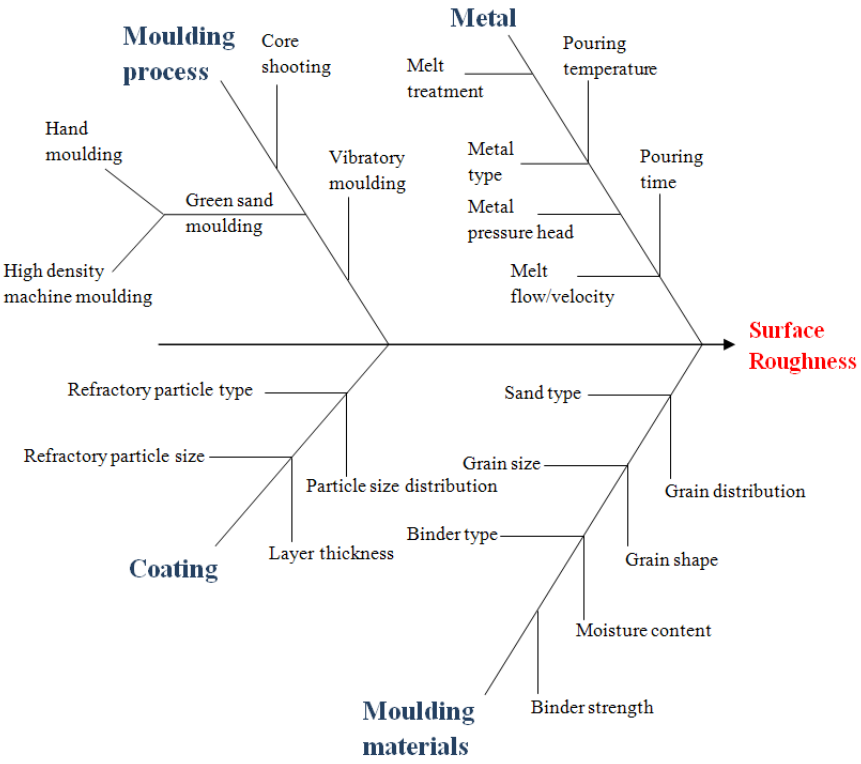

Fig. 1: Fish-bone cause-effect diagram with the factors that affect surface roughness of cast components in expendable moulds.

dimensions. Therefore, it becomes necessary to average a multitude of readings for the third dimension to be included. Another important factor is that the roughness definition was established to accommodate machined surfaces. Machined surfaces have a definite, regular, repetitive, directional pattern. Defining a cross-section of a machined surface defines the surface. In contrast, the cast surfaces have an irregular, random pattern, and there can be a wide latitude in the mathematical value within an area [6]. It is also reported in [3] that since cast surfaces do not exhibit the same cyclic character as machined surfaces, it is difficult to evaluate their roughness using conventional mechanical, optical, or pneumatic devices. Consequently, visual tactile standards are used, to describe the surface of castings. Purchasers of castings can specify and assess surface quality and surface texture more accurately and definitively using tactile comparators developed by Casting Technology International (CTI) [7]. These provide a practical and functional alternative to photographic representation of casting surfaces in standards such as MSS SP-55-2001. Two set of comparators are in widespread use:

- SCRATA comparators for the definition of surface quality of steel and cast iron castings, from Casting Technology International, Sheffield, UK.
- BNIF 359 Recommendation technique du Bureau de Normalisation des Industries de la Fonderie, Sèvres, France.

Typical SCRATA tactile surface comparators from CTI are shown in Figure 2. These comparators are among the five A series comparators used to describe the

surface texture of castings. The A series comparators form the part of a larger set of comparators defining different surface defects of castings and apply to ISO 11971:2008 Steel and Iron Castings-Visual examination of surface quality; BS EN 1370:1997 Founding - Surface roughness inspection by visual tactile comparators; BN EN 12454:1998 Founding - Visual examination of surface discontinuities [3]. Figure 3 shows another standard from Swecast, Sweden, which describes the surface of castings after shot blasting. All these standards are tactile and do not have high reproducibility as their interpretation depends on the operator. Therefore, there are lots of variations from different individuals.

On this note, this paper presents a detailed approach to surface roughness characterisation of cast components and its application in the foundry industry. This novel method applies a non-contact technique using a 3D optical system to measure the surface roughness of sand cast components. A Scanning Probe Image Processor (SPIP) was used to process and evaluate the data for the surface roughness. Two different standard surface roughness tactile comparators used in the foundry industry were also evaluated for the foundries to know the level of roughness of those comparators in numbers. These values will serve as the reference for the cast components and for order specifications in the foundry industry. Profile and areal parametric analyses were performed on the roughness data of the standards to establish the relationship between various parameters and their variations. From the results, it is intended to determine which of profile and areal parameters are more informative for sand cast components since sand cast components have no surface structural pattern like machined surfaces. The results from selected castings were compared with the roughness values of the standards.

2 Surface Characterization

Surface characterization involves [8]:

- Defining the parameters to quantify the geometrical features of surfaces,
- selecting the parameters relating to functional properties of the surface,
- Generating a surface profile for given parameters.

2.1 Types of Surfaces

Surface:

A surface is a boundary that separates a solid object from another object or substance [9].

Nominal Surface:

A nominal surface is the intended surface. The shape and extent of a nominal surface are usually shown and dimensioned on a drawing. The nominal surface does not include intended surface roughness.

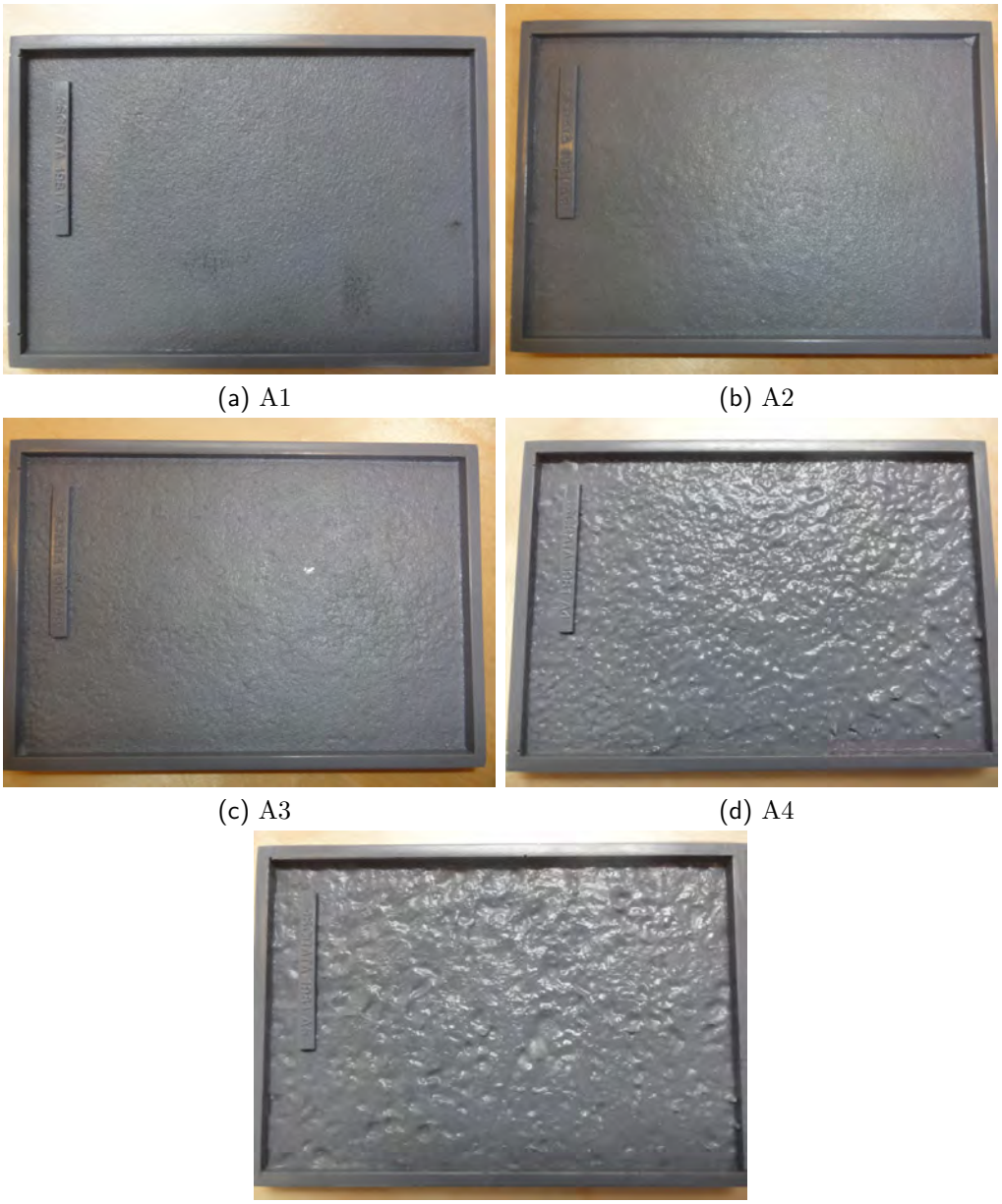

(a) A1 (b) A2

(c) A3 (d) A4

(e) A5

Fig. 2: SCRATA comparators for casting surface roughness (UK).

Fig. 3: Tactile comparators for casting surface roughness after shot blasting (Sweden).

Real Surface:

A real surface is the actual boundary of an object. It deviates from the nominal surface as a result of the process that created the surface. The deviation also depends on the properties, composition, and structure of the material the object is made of [1, 9, 10, 11].

Measured Surface:

A measured surface is a representation of the real surface obtained with some measuring instruments. This distinction is made because no measurement will give the exact real surface.

Form:

Form refers to the intentional shape of a surface which differs from a flat line [9, 11].

2.2 Surface Texture

Surface texture is the combination of fairly short wavelength deviations of a surface from the nominal surface. Texture includes roughness, waviness, and lay, that is, all of the deviations that are shorter in wavelength than form error deviations.

Roughness:

Roughness includes the finest (shortest wavelength) irregularities of a surface. Roughness generally results from a particular production process or material condition.

Waviness:

Waviness includes the more widely spaced (longer wavelength) deviations of a surface from its nominal shape. Waviness errors are intermediate in wavelength between roughness and form error. The distinction between waviness and form error is not always made in practice, and it is not always clear how to make it. New standards are emerging that define this distinction more rigorously.

Lay:

Lay refers to the predominant direction of the surface texture. Ordinarily lay is determined by the particular production method and geometry used. Turning, milling, drilling, grinding, and other cutting tool machining processes usually produce a surface that has lay: striations or peaks and valleys in the direction that the tool was drawn across the surface. Other processes produce surfaces with no

characteristic direction: sand casting, spark erosion and grit blasting. Sometimes these surfaces are said to have a non-directional, particulate, or protuberant lay. Several different types of lay are possible depending on the manufacturing and machining processes [1, 9, 11, 10, 12].

2.3 Filtering

Filter:

A filter (for purposes of surface finish measurement) is an electronic, mechanical, optical, or mathematical transformation of a profile to attenuate (remove) wavelength components of the surface outside the range of interest for a measurement. Filters select (or reject) the structure according to its scale in the x-axis, that is in terms of wavelengths or spatial frequencies. A filter that rejects short wavelength while retaining longer ones is called a low-pass filter since it preserves (or lets pass) the low frequencies. A high-pass preserves the shorter wave-length features while rejecting longer ones [9, 11].

Waviness Profile:

The waviness profile includes medium wavelength deviations of the measured profile from the nominal profile. The waviness is the modified profile obtained by filtering a measured profile to attenuate the longest and shortest wavelength components of the measured profile (i.e. the filter removes form error and roughness).

Texture Profile:

The texture profile is the sum of the waviness profile and the roughness profile, i.e. the remaining medium and short wavelength deviations of the measured profile from the nominal profile after form error has been subtracted from the primary profile. Measurement of texture is the primary domain of traditional surface finish analysis.

Roughness Profile:

The roughness profile includes only the shortest wavelength deviations of the measured profile from the nominal profile. The roughness profile is the modified profile obtained by filtering a measured profile to attenuate the longer wavelengths associated with waviness and form error. Optionally, the roughness may also exclude (by filtering) the very shortest wavelengths of the measured profile which are considered noise or features smaller than those of interest. Roughness is of significant interest in manufacturing because it is the roughness of a surface (given reasonable waviness and form error) that determines its friction in contact with another surface. The roughness of a surface defines how that surface feels, how it looks, how it behaves in a contact with another surface, and how it behaves for coating or sealing. For moving parts the roughness determines how the surface will wear, how well it will retain lubricant, and how well it will hold a load [9, 10, 11].

3 Optical Systems

Optical systems apply the light reflection method in measuring surface roughness and this involves illuminating the surface and the relative amounts of reflected light are observed [6]. This is a non contact and non destructive method. Generally, roughness measurement is done using stylus instruments. The major disadvantage of using stylus profilometry is that it requires direct physical contact, which limits the speed of the measurement. In addition, the instrument measurements are based on a limited number of line samplings, which may not represent the real characteristics of the surface. Due to these drawbacks, contact-type instruments are not suitable for high high-speed automated inspection [13]. Furthermore, contact-type instruments are not applicable on sand cast surfaces because of high surface roughness encountered. For non-contact surface roughness measurement, white light interferometry, interference microscopy, phase-shifting interferometry, coherence scanning microscopy, and Fourier transform method (FTM) are used to measure the surface roughness [13]. These principles are applied in Areal optical techniques. There are many different types of optical instruments applying these principles, for measuring surface topography [11]. These include atomic force microscope (AFM), scanning electron microscope (SEM), total integrated scattering (TIS), interferometric methods and specular reflection methods [14, 15, 16, 17].

New breakthroughs by the instrumentations have been made in the recent years, to establish high-tech instruments which can acquire a 3D surface structure of components [18]. Danzl et al. [19] presented a method to measure the three-dimensional structure of complex objects using an optical principle called focus-variation technology. This technology has been recently added to a new ISO standard [20].

3.1 Focus-Variation

The optical technology Focus-Variation, developed by Alicona and added in the latest draft of the upcoming ISO standard 25178, provides high resolution 3D surface metrology even at complex topographies [21]. The technique of Focus-Variation combines the small depth of focus of an optical system with vertical scanning to provide topographical and colour information from the variation of focus [11, 22]. The main characteristics of the system are that it delivers high resolution measurements of even complex surfaces, that it is able to measure surfaces with steep flanks up to 80°, with strongly varying reflection properties and greatly varying roughness. In addition to 3D and colour information, a repeatability measure is analytically estimated for each measurement point. Focus-Variation is used to perform high resolution 3D surface measurement for industrial quality assurance as well as research and development activities [22]. Figure 4 shows a schematic diagram of a focus-variation instrument.

The main component of the system is a precision optic containing various lens systems that can be equipped with different objectives, allowing measurements with different resolution. With a beam splitting mirror, light emerging from a white light source is inserted into the optical path of the system and focused onto the specimen via the objective. Depending on the topography of the specimen,

the light is reflected into several directions as soon as it hits the specimen via the objective. If the topography shows diffuse reflective properties, the light is reflected equally strong into each direction. In case of specular reflections, the light is scattered mainly into one direction. All rays emerging from the specimen and hitting the objective lens are bundled in the optics and gathered by a light sensitive sensor behind the beam splitting mirror. Due to the small depth of field of the optics only small regions of the object are sharply imaged. To perform a complete detection of the surface with full depth of field, the precision optic is moved vertically along the optical axis while continuously capturing data from the surface. This means that each region of the object is sharply focused. Algorithms convert the acquired sensor data into 3D information and a true colour image with full depth of field. This is achieved by analysing the variation of focus along the vertical axis [11, 22].

Using the 3D measurement device Alicona InfiniteFocus (Figure 5) based on the operating principle of Focus-Variation, the following technical specifications emerge: The vertical resolution depends on the chosen objective and can be as low as 10 nm. The vertical scan range depends on the working distance of the objective and ranges from 3.2 to 22 mm. The XY range is determined by the used objective and typically ranges from 0.14 x 0.1 mm to 5 x 4 mm for a single measurement. By using special algorithms and a motorized XY stage the XY range can be exceeded up to 100 x 100 mm.

In contrast to other optical techniques that are limited to coaxial illumination, the maximum measurable slope angle is dependent on the numerical aperture of the objective. Focus-Variation can be used with a large range of different illumination sources (such as a ring light) which allows the measurement of slope angles exceeding 80°. Basically, Focus-Variation is applicable to surfaces with a large range of different optical reflectance values. As the optical technique is very flexible in terms of using light, typical limitations such as measuring surfaces with strongly varying reflection properties even within the same field of view can be avoided. Specimen can vary from shiny to diffuse reflecting, from homogeneous to compound material and from smooth to rough surface properties. Focus-Variation overcomes the aspect of limited measurement capabilities in terms of reflectance by a combination of modulated illumination, controlling the sensor parameters and integrated polarization. Modulated illumination means that the illumination intensity is not constant, but varying. The complex variation of the intensity can be generated by a signal generator. Through the constantly changing intensity far more information is gathered from the specimens´ surface.

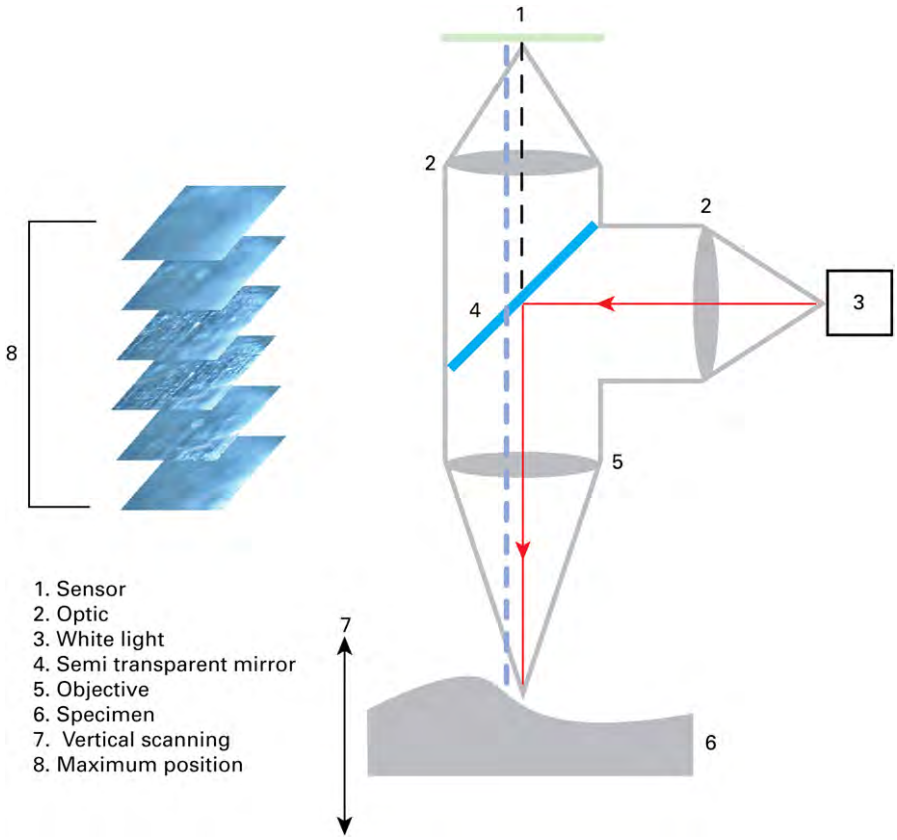

Fig. 4: Schematic of focus-variation instrument [11].

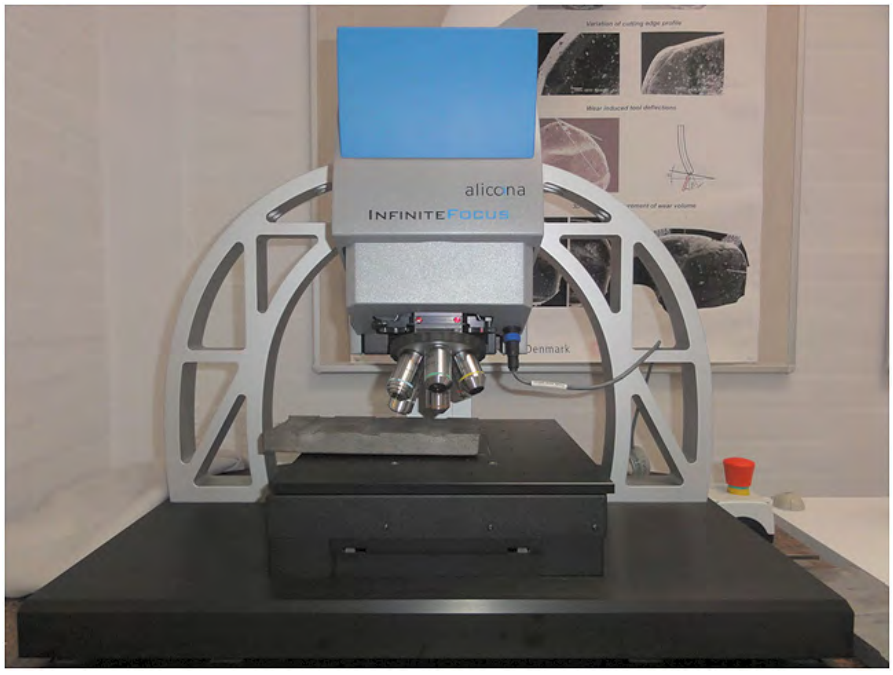

Fig. 5: IFM G4 laboratory system.

4 Definition of Parameters for Roughness Characterisation

4.1 Profile Parameters

Table 1 gives the definitions of the 2D height parameters. The centre line average parameter (Ra) is the most common of all the parameters. It is defined in ISO 4287 as the arithmetic mean deviation of the assessed profile [12, 23, 24]. There will be normally five Ra values (Ra1 to Ra5) over an evaluation length. The root-mean-square (RMS) parameter (Rq) is another sample length average parameter. It is defined in ISO 4287 as the root square deviation of the assessed profile. There will normally be five Rq values: Rq1 to Rq5. There are also other parameters as shown in Table 1, but the two most widely used parameters are Ra and Rq [11, 12, 25]. Average parameters suffer several disadvantages, they do not distinguish between a peak and a valley, they do not respond to a redistribution of material above and below the mean line, they are unrelated to wavelength and do not describe the form or shape of the unit event. Their advantage is that they can monitor averages and drifts from the average [12]. There are inherent limitations with 2D surface measurement and characterization. A fundamental problem is that a 2D profile does not necessarily indicate functional aspects of the surface. With profile measurement and characterization it is also often difficult to determine the exact nature of a topographic feature [11, 28]. With respect to the parameters that measure extremes rather than averages, the Rt parameter is the real extreme parameter in that it measures the vertical distance from the highest peak to the lowest valley within the evaluation length.

Tab. 1: Profile amplitude parameters [12].

Parameter			Description
Ra	Centre line average	SL	$Ra = \frac{1}{N}\sum_{i=1}^{N} \mid Y_i \mid$
Rq	RMS Roughness	SL	$Rq = \sqrt{\frac{1}{N}\sum_{i=1}^{N} Y_i^2}$
Rp	Maximum peak height	SL	$Rp = Z_{max}$
Rv	Maximum valley depth	SL	$Rv = Z_{min}$
Rt	Maximum peak to valley height	EL	$Rt = Z_{max} - Z_{min}$
Rz	Maximum peak to valley height	SL	$Rz = Z_{max} - Z_{min}$

4.2 Surface Parameters

In many instances, the parameters determined from a single 2D trace are unable to define a surface satisfactorily because surfaces interact in three-dimensions and not two [12, 26]. All 3D parameters are defined in one sampling area, which is contrary to most 2D parameters which are defined in one evaluation length consisting of several sampling lengths [26]. 3D height parameters and their mathematical description are presented in Table 2. The average parameter Sa is the arithmetic mean of the absolute value of the height within a sampling area. The Sa parameter is the closest relative of the Ra parameter. The Sq parameter is defined as the root-mean-square value of the surface departures within the sampling area [12, 11, 26, 27]. The equation for Sq is the double summation of heights in the two horizontal directions, as shown in Table 2. An extreme parameter, Sz, the ten-point height, is a 3D equivalent of 2D Rz. It is the difference between the average of the five highest peaks and the five lowest valleys, within the sampling area as shown in Table 2. 3D measurements allow improved functional correlation in the calculation of volume for fluid retention, amount of wear on a surface, number and percentage of particle distribution in a surface, and many more surface finish characteristics. ISO 4288 provides a standard procedure for dealing with this problem [20]. This specification states that it is acceptable for 16% of the finish measurements to be beyond the specified finish tolerance and still consider the part to meet the specification. During early development of the three-dimensional measurement process, it was anticipated that finish data developed utilizing three-dimensional surface characteristics would provide improved consistency of readings [28]. Comparison of the number of readings required to keep the parameter value within ±10% at the 95% confidence level utilizing 2D and 3D surface measuring techniques is shown in Figure 6.

Tab. 2: Surface amplitude parameters [9].

	Parameter	**Description**
Sa	Average roughness	$Sa = \frac{1}{MN}\sum_{i=1}^{M-1}\sum_{j=1}^{N-1} \mid z(x_i, y_j) - \mu \mid$
Sq	RMS roughness	$Sq = \sqrt{\frac{1}{MN}\sum_{i=1}^{M-1}\sum_{j=1}^{N-1} [z(x_i, y_j) - \mu]^2}$
Sp	Maximum peak height	$Sp = Z_{max}$
Sv	Maximum valley height	$Sv = Z_{min}$
St	Maximum peak to valley height	$St = Z_{max} - Z_{min}$
Sz	Ten point height	$Sz = \frac{\sum_{i=1}^{5}(z_{pi}-\mu)+\sum_{i=1}^{5}(z_{vi}-\mu)}{5}$

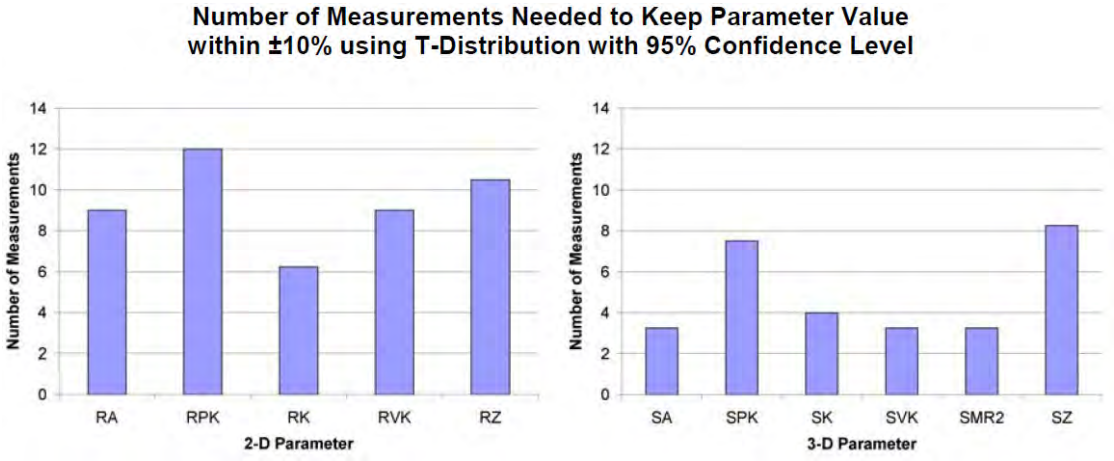

Fig. 6: Number of measurements needed to keep parameter value within ±10% using T-Distribution with 95% Confidence Level [28].

Figure 6 shows although the use of three dimensional finish measurement techniques can reduce the number of readings by some amount as compared with two-dimensional data, multiple readings are still required if statistical confidence is to be developed with respect to the finish parameter being measured [28].

4.3 Bearing Area Ratio Curve

This is the ratio of the total contacting area, obtained by truncating the surface summits by a plane parallel to the mean plane at a given truncation level, over the sampling area. The material ratio curve formally called surface bearing area ratio curve, or surface Abbot-Firestone curve, is a function of truncation level. The vertical axis of the material ratio curve is normalised in accordance with the RMS deviation i.e. Rq or Sq for profile and areal respectively. The origin is placed at the mean plane. A material plane which is above the mean plane is scaled in the positive axis, whereas a material plane which is below the mean plane is scaled in the negative axis [11, 26, 29]. A topographical model that captures the essential characteristics of the bearing area curve using a very limited set of parameters is the linearised five-parameter models that are shown in Figure 7 for profile and areal measurements.

Surface bearing area ratio curve provides information about the height distribution and material volume and void volume of surface topography, hence it is useful for defining functional parameters [26]. The material volume is defined as the material portion enclosed in a truncation plane parallel to the mean plane and the interfacial surface above the plane. A void volume is a complementary function of the material volume. It is the air volume enclosed between a truncation plane at a given level parallel to the mean plane and the interfacial surface beneath the plane. Figure 8 shows a section of the material volume, Vm(h), and the void volume Vv(h). The volumes are functions of the truncation depth, h. At the highest point, i.e. $h = h_{max}$ the material volume is 0 and the void volume is the maximum. Whilst at the lowest point, i.e. $h = h_{min}$, the material volume is maximum and the void volume is 0 [26].

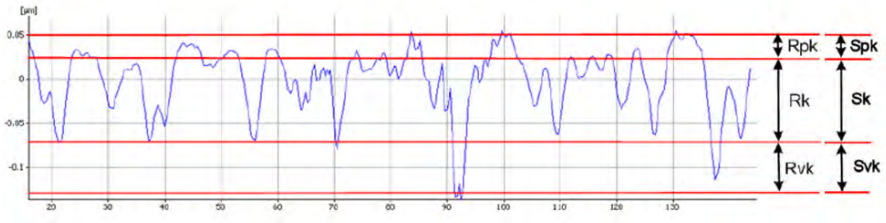

(a) Isometric plot of the profile (R) and surface (S)

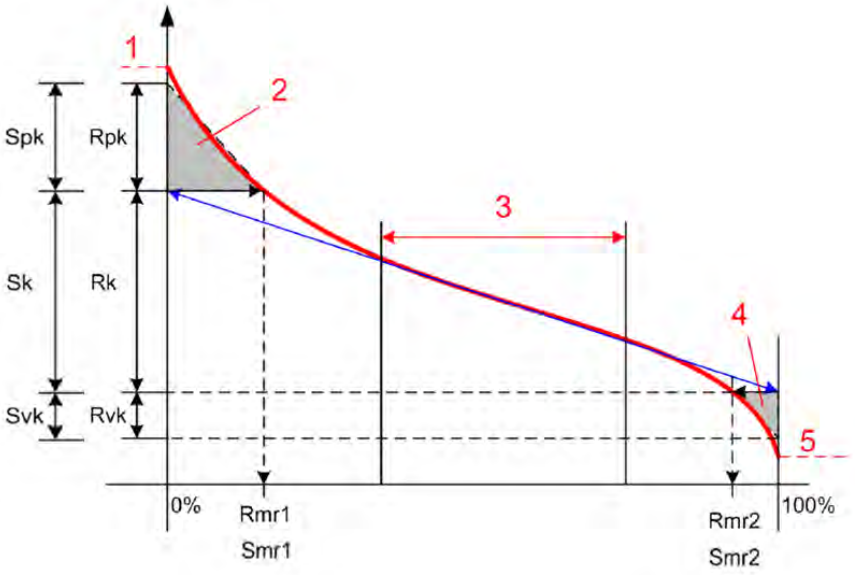

(b) Bearing area curve

Fig. 7: Profile and surface bearing area curve characterized by five profile and corresponding surface parameters: Rk, Sk, Rpk, Spk, Rvk, Svk, Rmr1, Smr1 and Rmr2, Smr2 [29].

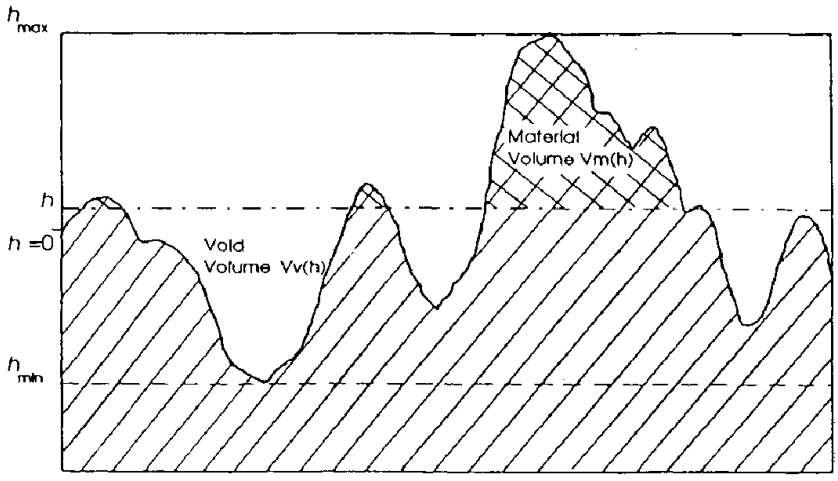

Fig. 8: Schematic diagram of the material volume and the void volume from isometric plot of the surface [26].

European instrument manufacturers devised height distribution parameters such as Rpk, Rk, Rvk, Rmr1 and Rmr2 for profile parameters as shown in Figure 7.

These are ISO parameters. The parameters Rpk, Rk and Rvk are expressed in microns, whereas Rmr1 and Rmr2 are expressed in percentages. The parameter Rpk is the reduced peak height and is defined in ISO 13565-2 (1996) as the mean height of the peaks above the roughness core profile. It represents the top portion of the surface that is easily worn out. The parameter Rk is the core roughness depth and is defined in ISO 13565-2 (1996) as the height of the roughness core profile. It characterizes the long-term running surface that will influence the performance and life of the part. The parameter Rvk is the reduced valley depth and is defined in ISO 13565-2 (1996) as the mean depth of the profile valleys below roughness core profile. It characterizes the oil-retaining capacity of the surface provided by the deep valleys. The parameters Rmr1 and Rmr2 are material portions. They are defined in ISO 13565-2 (1996) as the material portion determined for the intersection line which separates the profile peaks from the roughness core profile and the materials portion determined for the intersection line which separates the deep valleys from the roughness core profile respectively [26, 31]. All these parameters have their 3D counterparts as Spk, Sk, Svk, Smr1 and Smr2 [1, 11, 29] as shown in Figure 7. These 3D or areal parameters are included in ISO 25178-2 [20].

Characteristic analysis of surface bearing area ratio curve

Three parameters were extracted from the bearing area ratio curve. The peak roughness was defined as the range of heights embracing 2-25% of the bearing length, the medial or core roughness covers the range 25-75% while the valley roughness was defined to cover 75-98% of the bearing length. The topography feature from typical electric discharge machining (EDM) or sand blast surfaces show a height distribution that approximates to a Gaussian. A typical example of such surface is shown in Figure 10. From figure 10b, two horizontal lines were drawn in the surface of the bearing ratio curve. one intersects with the 5% bearing area denoted by $h_{0.05}$, the other intersects with the 80% bearing area denoted by $h_{0.8}$. Then the curves are classified into three zones similar to that of DIN 4776, i.e. peak zone, core zone and valley zone [26, 31]. The material volume per unit sampling area of each zone is actually the area enclosed beneath the surface Abbott-Firestone curve and the horizontal line of this zone. The void volume per unit sampling area of each zone is the area enclosed beneath the top horizontal line of this zone and above the surface Abbott-Firestone curve [26]. A comparative analysis of 2D and 3D Bearing area curves made by Cellery et al. [31], shows a very poor agreement. they are of the opinion with other researchers that more useful information about the surface properties can be achieved by using 3D analysis.

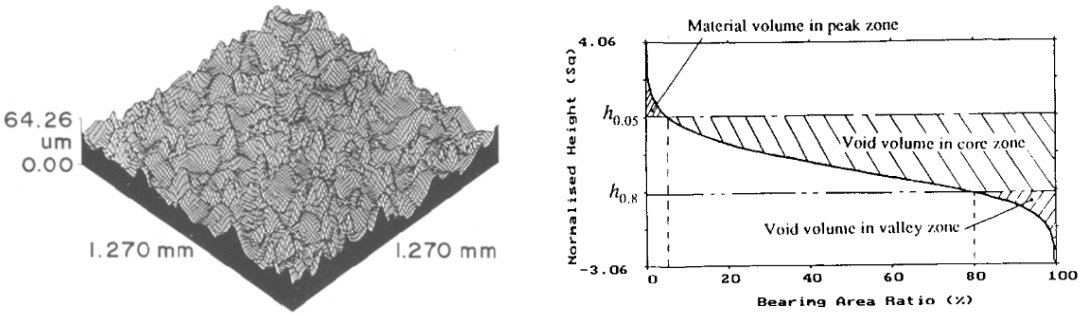

(a) Isometric plot of the surface (b) Surface bearing ratio

Fig. 9: Bearing area ratio and the height distribution of an EDM surface [26].

5 Approach used for the Measurements

Alicona InfiniteFocus microscope (IFM) G4 (Figure 5) was used to acquire the surface topography information on all the surfaces of standard comparators and the castings. The objective used is 5× giving a vertical resolution of 410 nm. For this objective the XY range is 2.8392 mm × 2.1538 mm and a spot diameter of 6 mm. After the data acquisition with Alicona InfiniteFocus Microscope, the image was analysed with Scanning Probe Image Processor (SPIP) software. Plane correction was performed on the entire image to level the surface and to remove primary profile. The surfaces were filtered to separate roughness and waviness using Gaussian filter according to ISO 11562. These sequence of operations was followed consistently for all the measurements. Typical example of processed surfaces are shown in Figure 10.

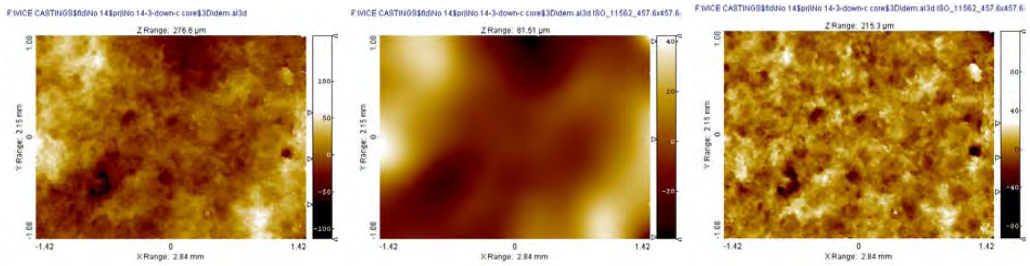

(a) Original surface (b) Filtering-waviness (c) Filtering-roughness

Fig. 10: Surface processing in Scanning Probe Image Processor (SPIP).

The reason for filtering the surfaces is to remove the dominance of waviness over the surface roughness. This reason is shown in Figure 11. As can be seen, the actual surface roughness is obvious in Figure 11d. A typical 3D surface texture of an analyzed surface is presented in Figure 12.

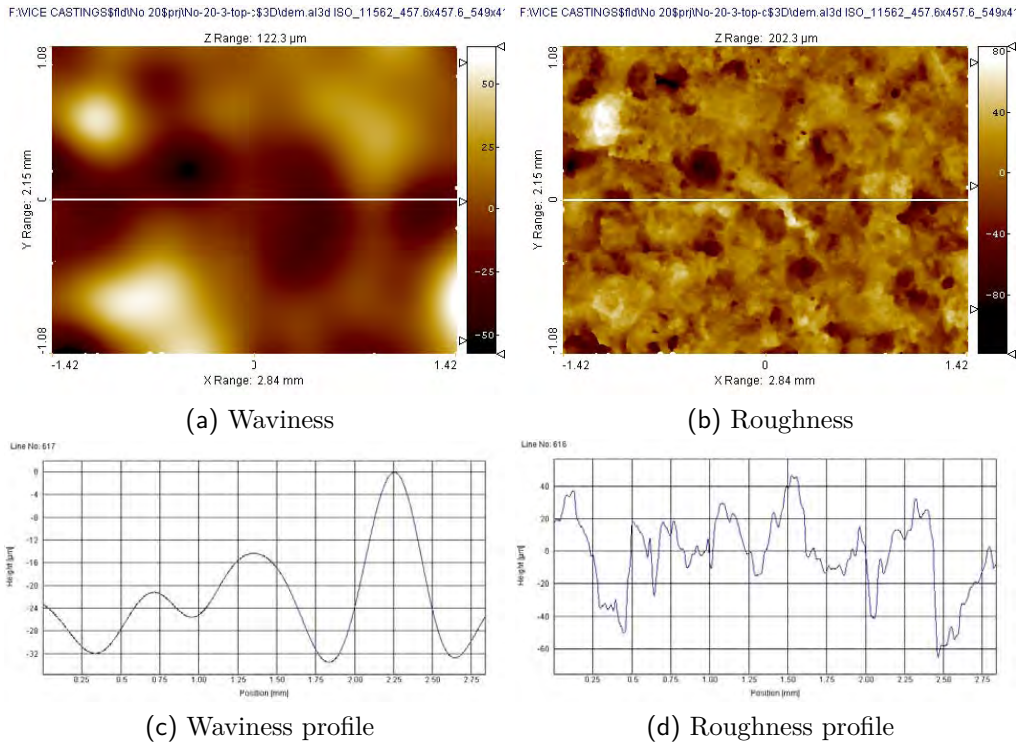

(a) Waviness (b) Roughness

(c) Waviness profile (d) Roughness profile

Fig. 11: The difference between waviness and roughness. The reason for filtering.

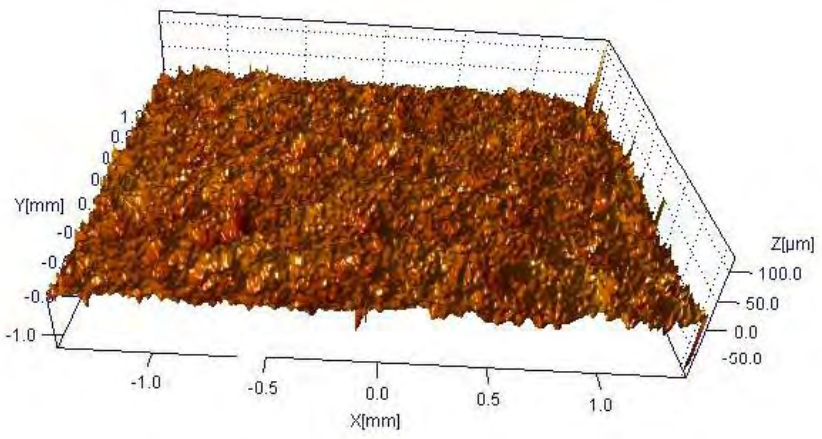

Fig. 12: A typical 3D surface texture of a processed casting surface for roughness measurement in SPIP.

For the tactile standard comparators from CTI, A1 and A2, 20 scans were made on each surface while 6 scans were made on each of the 6 standards (S25, S40, S63, S100, S160, and S250) from Swecast.

6 Results from Standard Roughness Comparators

The roughness characterization of two standard comparators (A1 and A2) from the CTI series (Figure 2) and the Swecast standards (Figure 3) was performed.

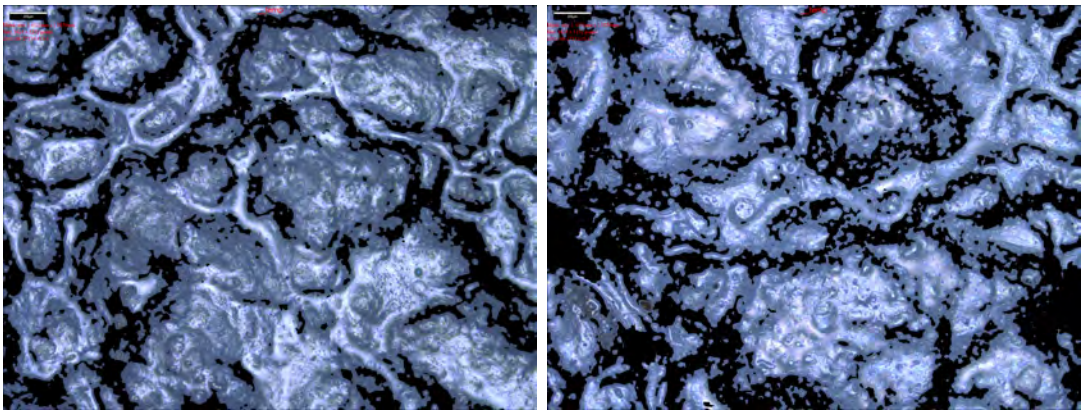

(a) A1 (b) A2

Fig. 13: Surface structure of A1 and A2 comparators from measuring system.

Figure 13 shows the typical microstructure of the surfaces of A1 and A2 of the CTI standard comparators. It is from typical surfaces like these that the profile and surface parameters are determined. The surfaces of A1 and A2 proved measurable unlike the other three surfaces (A3, A4 and A5, Figure 2) whose surface texture were way out of the right objective of the measuring system. From measurement observations on these three surfaces, the surfaces show smoother texture than those of A1 and A2, which is not suppose to be the case. This means that the system measures smoothness on a rough surface, implying that the surface topography is out of the capacity of the system. This was observed with objective higher than 5×, increasing the objective reduces the spot size which means reduced field of view. Therefore, the right surface texture evaluation is not obtained from these surfaces. Consequently, the measurements were limited to A1 and A2 which gave reasonable data in the micron range instead of data in the nano-range (not real). This abnormality in the measurements is attributable to wrong surface features on the surfaces and also on the type of material (polymer) of the surface.

The profiles of different single point measurements and their statistical descriptions are presented in Figure 14. From the figure, it can be seen that the amplitude profile parameters (peak to valley): Rt, Rz, R10z, Rv, and Rp; show the highest inconsistency in the measurements. This is evident in the scatter in each of the profiles in Figure 14a and in the large standard deviations shown in Figure 14b. The amplitude parameters (average of ordinates): Ra and Rq and the bearing area curve parameters: Rpk, Rk, and Rvk show more consistent measurement data with little scatter in the profiles and smaller standard deviations as can be seen from Figure 14.

Based on these observations, most of the analyses will be made on the amplitude and bearing area curve parameters. However, all the parameters were also analysed on the surface measurement data obtained. The single point measurement profiles and their corresponding statistical distribution are shown in Figure 15. It can be seen that there is presence of scatter in the profiles and large standard deviations for the amplitude surface parameters (St, Sz, S10z, Sv and Sp) like in the profile parameters. However, it can be obviously observed from Figure 15, that the scatter in the profile and the deviations are not as large as it is in the profile measurements.

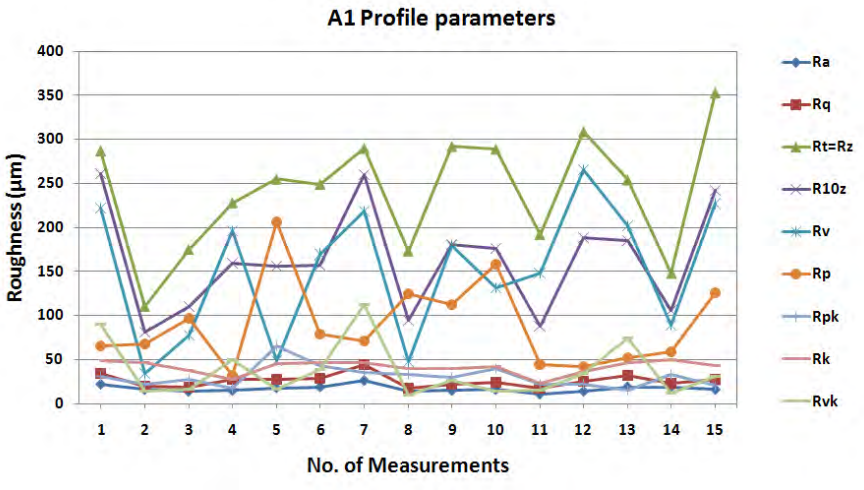

(a) Single point plot

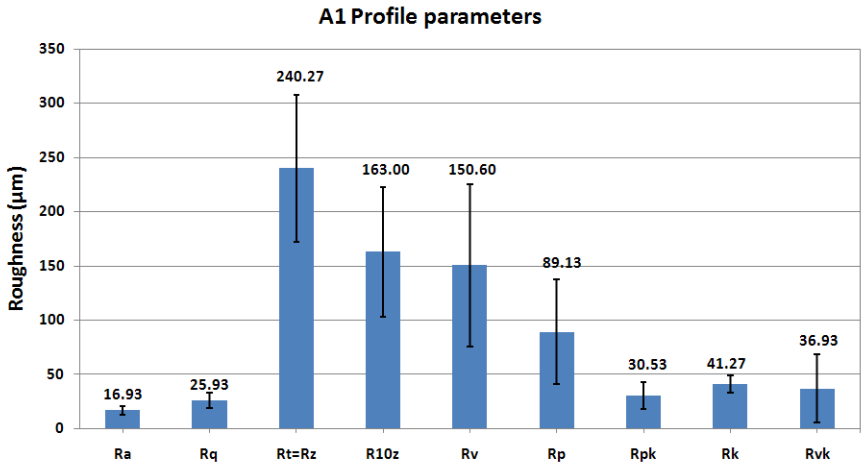

(b) Descriptive statistics

Fig. 14: Profile roughness of A1 comparator showing various parameters.

The surface average amplitude (Sa and Sq) and the bearing area curve (Spk, Sk and Svk) parameters also showed little scatter in the profile and lower standard deviations than their profile counterparts. This points to the fact that the surface (areal) measurements may be more consistent and reliable than the profile measurements which are sectional. The emergence of commercial 3D measurement systems has emphasized the importance of 3D surface topography in science and engineering applications, and an advent of measurement and characterization of surface topography in three dimensions. It is recognised that 3D surface topography greatly affects not only the mechanical and physical properties of contacting parts, but also the optical and coating properties of some non-contacting components. The amplitude and spatial characteristics of 3D surface topography dominate the functional applications in fields like wear, friction, lubrication, fatigue, sealing, jointing, reflectance, painting, bearing, etc. [26]. However, problems still exist in establishing the relationship between functional properties of engineering surfaces and the characterization of surface topography [32].

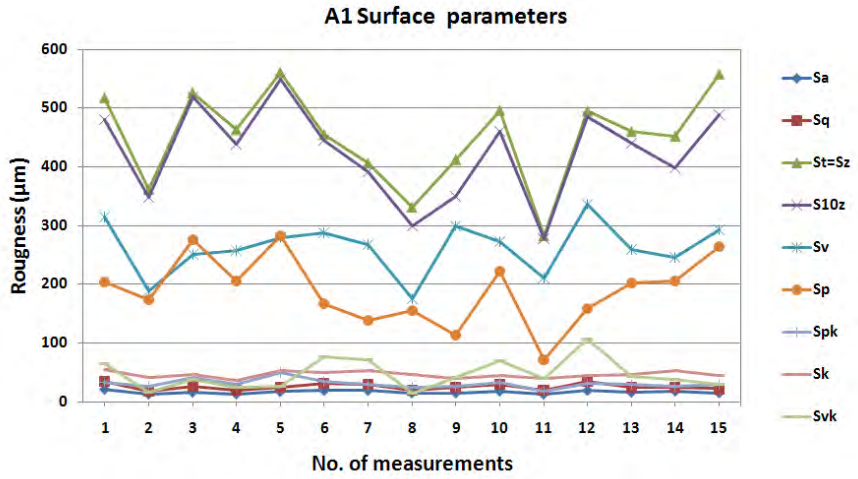

(a) Single point plot

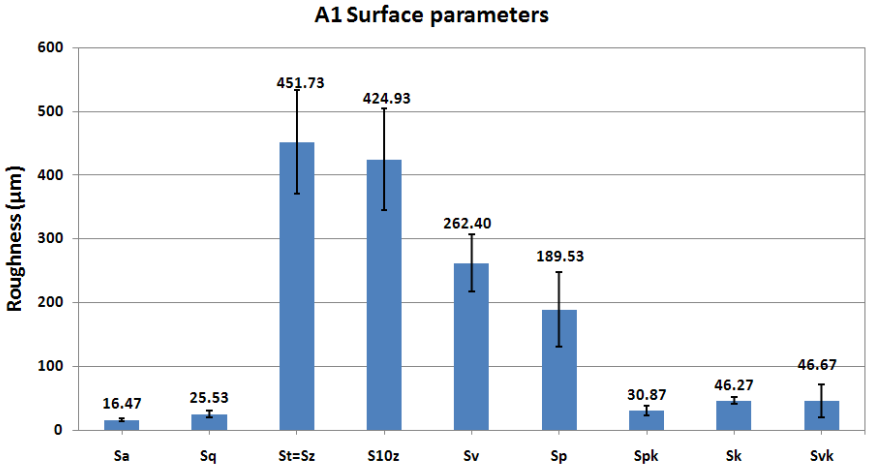

(b) Descriptive statistics

Fig. 15: Surface (Areal) roughness of A1 comparator showing various parameters.

The statistical description of the selected parameters from the amplitude average and bearing area curve parameters for profile and areal measurements on A2 series standard comparator is presented in Figure 16. From the figure, it also evident that the standard deviations are higher in the profile measurements than in the surface measurement data. These observations support the question raised by W. P. Dong et al. [33], on how effective are the parameters calculated from a profile, at representing the surface character?. Although, Thomas and Charlton [34] are of the opinion that variation of 50% are not uncommon on machined surfaces. If this is the case with machined surfaces, then sand casting surfaces are bound to have higher variations based on their higher surface roughness. In this regard, the parameter that minimizes these variations will be more applicable and reliable in the characterization of the surface quality of castings. Both profile and areal roughness data with their corresponding standard deviations are presented in Tables 3 and 4 respectively. These show the average roughness of the standards in various parameters and the observed variations in these parameters.

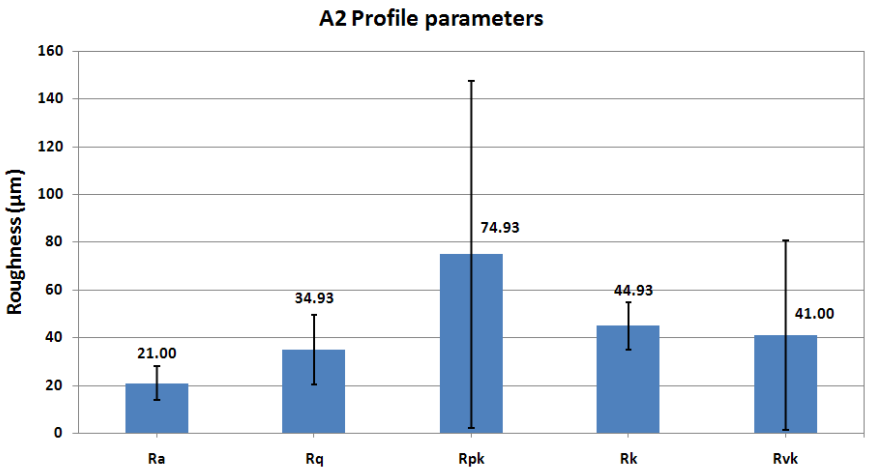

(a) Profile roughness

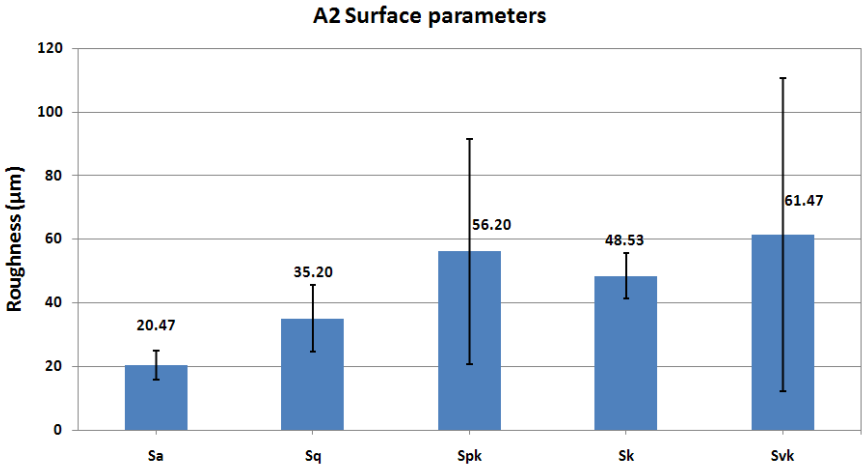

(b) Surface roughness

Fig. 16: Roughness of A2 comparator with selected parameters.

Tab. 3: Profile parameters for A1 and A2 standards of A series comparators.

Standards	Profile parameters (µm)				
	Ra	Rq	Rpk	Rk	Rvk
A1	16.9±3.7	25.9±6.9	30.5±12.7	41.3±7.8	36.9±31.6
A2	21±7.1	34.9±14.7	74.9±72.7	44.9±10.1	41.0±39.6

Tab. 4: Surface parameters for A1 and A2 standards of A series comparators.

Standards	Surface parameters (µm)				
	Sa	Sq	Spk	Sk	Svk
A1	16.5±2.5	25.5±5.5	30.9±7.6	46.3±5.3	46.7±25.9
A2	20.5±4.5	35.2±10.4	56.2±35.4	48.5±5.3	61.5±49.2

Similar detailed analyses were also performed on the data obtained from one of the Swecast standard comparators, S250, which has the highest roughness, in order to track data variations of all the parameters. Typical microstructures showing the surface texture of all the S series standard comparators (S25, S40, S63, S100, S160 and S250) are shown in Figure 17. The growth of the texture of the surface is obvious and is expected to reflect on the measured surface roughness accordingly.

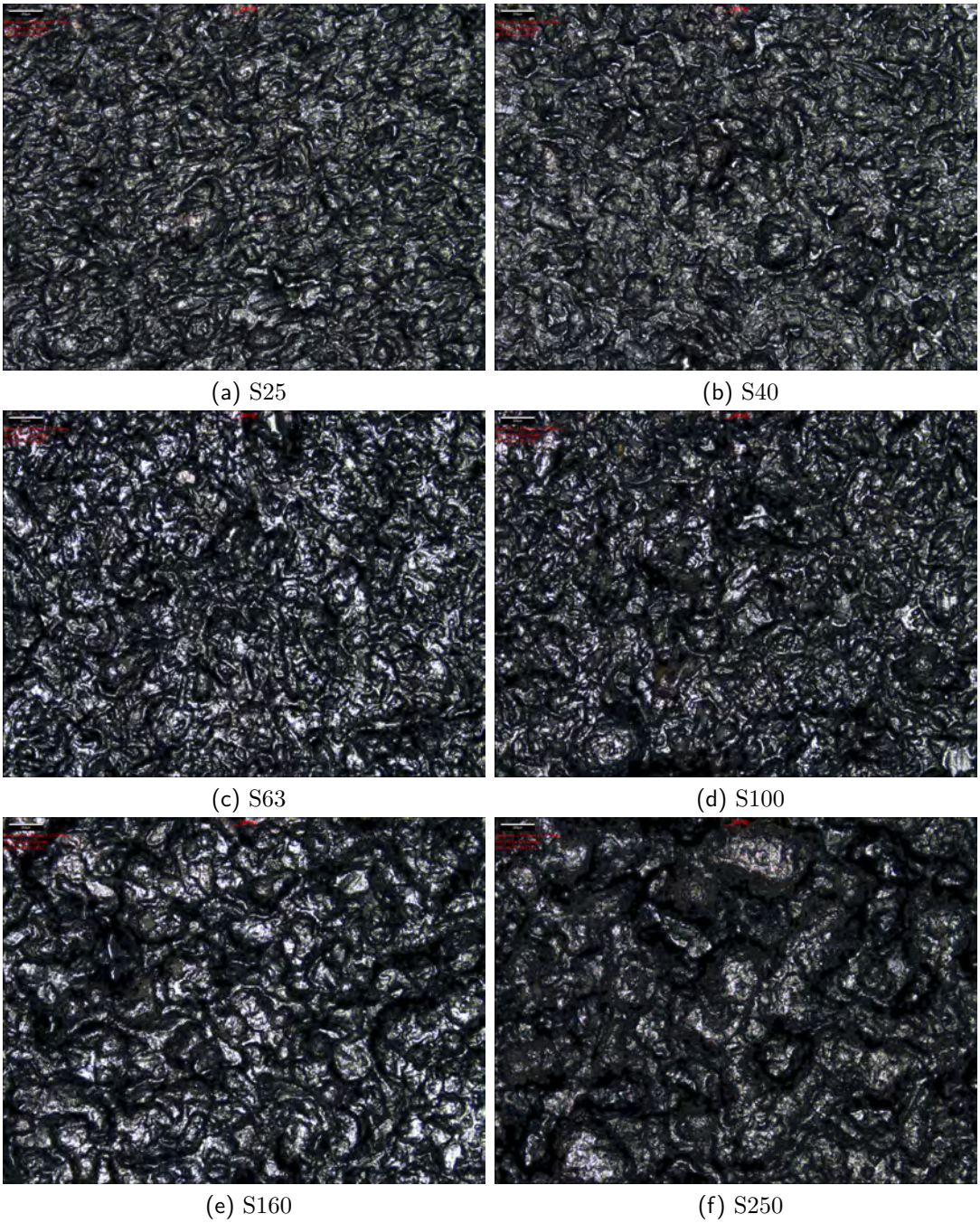

(a) S25 (b) S40

(c) S63 (d) S100

(e) S160 (f) S250

Fig. 17: Surface texture of S25-S250 from the measuring system.

Similar observations are made on S series standard comparators like in the case of the A series standard comparators discussed above. From Figures 18 and 19, there are also the presence of scatter in the profiles and larger standard deviations for

the amplitude data of both profile and surface measurements as can be seen from Figures 18 and 19. Although the scatter and standard deviations are larger for profile measurement data relative to surface measurement data. The amplitude average parameters showed lower scatter and lower standard deviations. These observations are consistent with the earlier observations for A series standard comparators. Therefore, applying amplitude average parameters in the description of the surface texture of casting is reasonable as more reproducible results will be obtained. However, this still requires a couple of measurements (but less than that required by profile measurements) [28] in order to apply some statistics to the measurement data, to determine the central tendency.

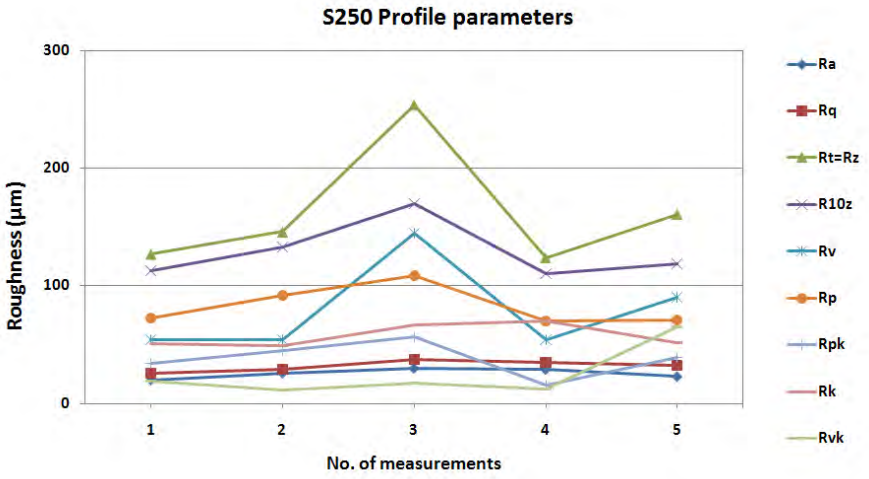

(a) Single point plot

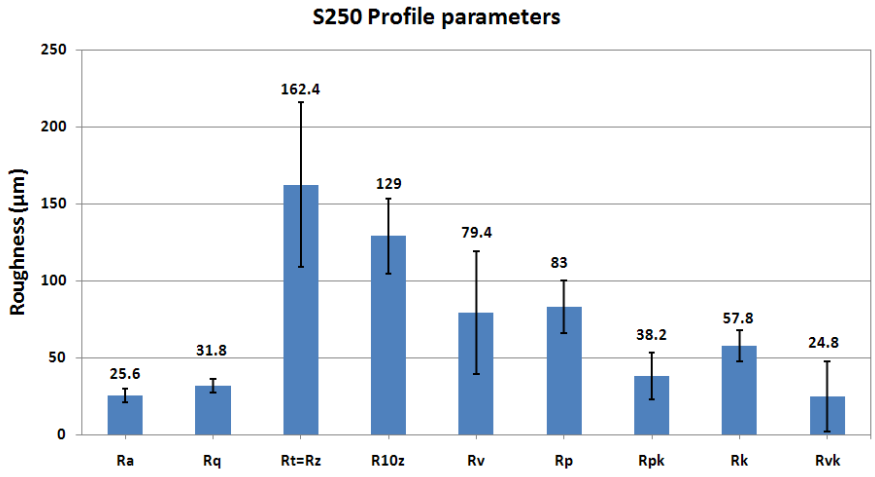

(b) Descriptive statistics

Fig. 18: Profile roughness of S250 comparator showing various parameters.

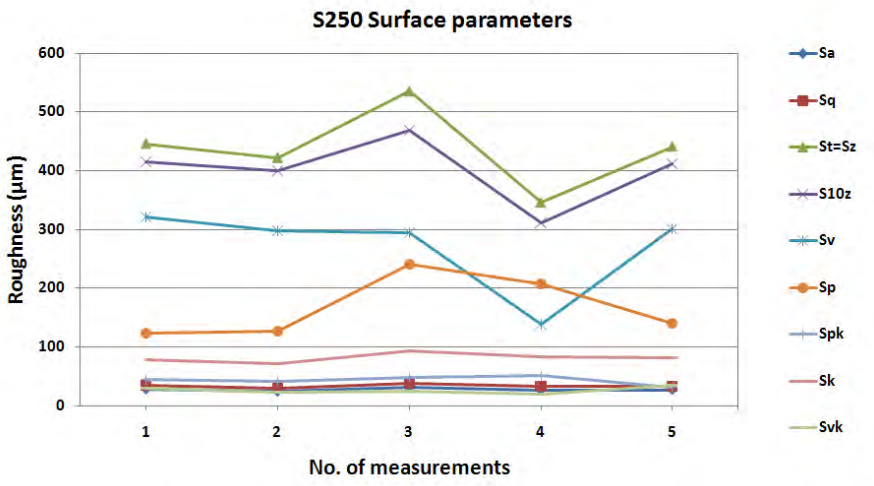

(a) Single point plot

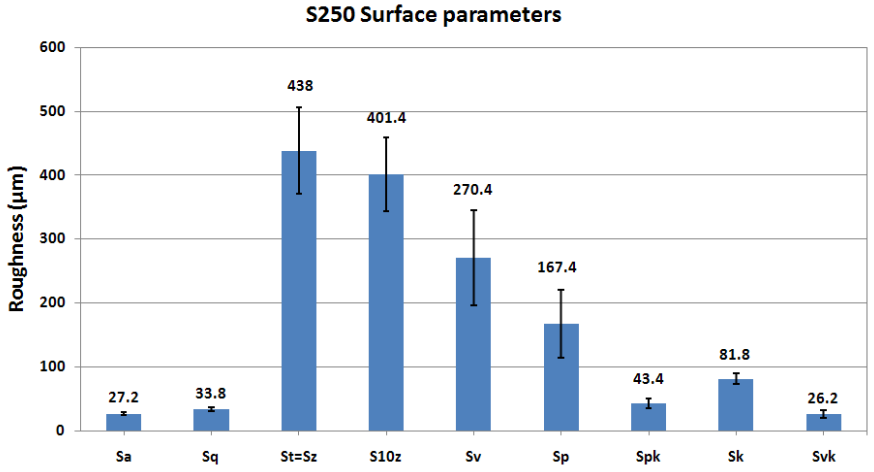

(b) Descriptive statistics

Fig. 19: Surface (Areal) roughness of S250 comparator showing various parameters.

The roughness results of all the measurements made on the surface of the S series standard comparators for profile and surface data with higher reproducibility are presented in Tables 5 and 6 respectively. From the tables, it can be seen that the standard deviations of the parameters are larger with the profile parameters. In line with the previous arguments, the surface parameters seem to produce data with less scatter.

Comparing Ra and Sa values from the A (Tables 3 and 4) and S (Tables 5 and 6) series standard comparators, it can be seen that their respective values are comparable in each case. Both Ra and Sa reflect the arithmetic mean of the absolute values of the surface point departures from the mean plane within the sampling area. This implies that with profile evaluation, larger number of measurements are required to make the data reproducible. This invariably places Sa measurements at advantage over Ra measurements because more time is required for the higher number of Ra measurements needed. Sa, being an areal measurement covers a larger field thereby becoming more representative. Furthermore, Sa showed lower

deviation from the mean than the Ra from all the tables. Therefore, as a generalization, Sa parameter can be adopted as a parameter for the characterization of the surface of castings. Furthermore, Sk from the surface bearing area curve showed lower variation than its counterpart, Rk from the profile bearing area curve. This will further be discussed in the bearing area curve section.

Tab. 5: Profile parameters for all the S series standards.

Standards	**Profile parameters (µm)**				
	Ra	**Rq**	**Rpk**	**Rk**	**Rvk**
S25	7.4±1.7	9.8±2.2	8.6±1.7	19.4±5.6	13.2±4.1
S40	8.2±1.3	10.6±1.1	13.6±3.3	24.0±4.2	8.2±2.2
S63	11.2±1.6	13.8±2.4	15.8±7.9	31.2±7.8	7.8±3.7
S100	15.0±2.4	18.6±2.3	21.2±4.4	42.4±9.9	11.8±5.6
S160	20.2±4.1	24.0±4.2	20.4±6.2	59.4±16.8	17.2±8.3
S250	25.6±4.2	31.8±4.4	38.2±15.1	57.8±9.9	24.8±22.7

Tab. 6: Surface parameters for all the S series.

Standards	**Surface parameters (µm)**				
	Sa	**Sq**	**Spk**	**Sk**	**Svk**
S25	7.6±0.6	10.0±1.0	15.0±4.1	22.8±2.3	13.8±1.3
S40	8.2±1.1	10.6±1.3	16.6±2.3	27.0±1.9	10.0±2.4
S63	11.0±0.7	13.4±1.1	18.6±2.8	34.4±2.1	12.0±1.0
S100	14.4±0.6	18.2±0.8	23.8±2.3	44.6±2.7	15.4±1.8
S160	18.6±2.9	23.8±4.0	34.6±9.6	57.4±6.2	18.4±2.3
S250	27.2±2.6	33.8±2.9	43.4±7.3	81.8±8.1	26.2±5.9

Having reasonably established the reliability of the surface measurements over profile measurements and the reproducibility of the Sa data over Ra data, a comparison of the surface roughness of the A series and of the S series standard comparators using the Sa values and their various deviations are shown in Figure 20. This is done to avoid “parameter rash”, [26, 34] therefore just one reliable parameter

suffices to characterize the surface of castings. As can be seen from the figure, the measurement results on various standards followed the expected trend which is observable from visual inspection from Figures 2 and 3. This indicates that the measuring system is applicable to casting surfaces. Following these discussions, to a reasonable level, these standards have been quantified and these values can be used to specify the roughness level of castings. It must be emphasized that, before these values are quoted any where, the measuring system, the cut-off length, and the objective used, must be specified in order to ensure reproducibility. The results presented in this figure will be compared with the results obtained from real casting surfaces after shot blasting.

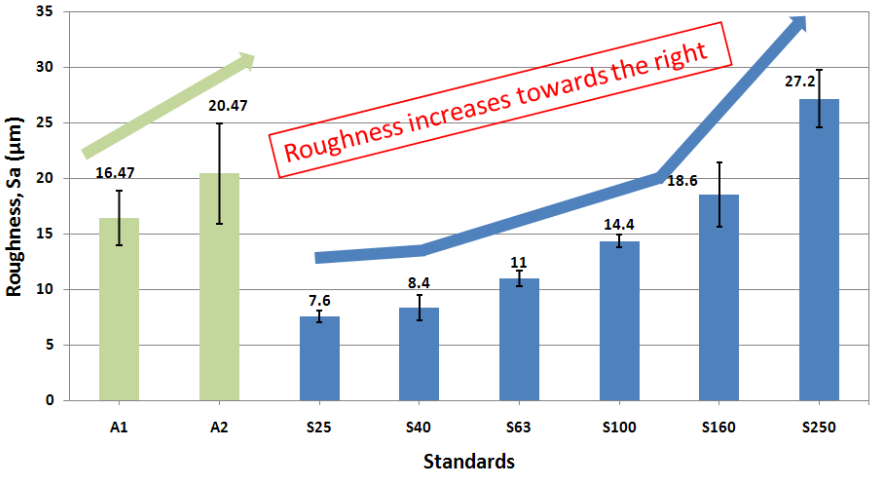

Fig. 20: Comparison of the roughness (Sa) of A and S series standard comparators.

7 Roughness Description by Bearing Area Ratio Curve

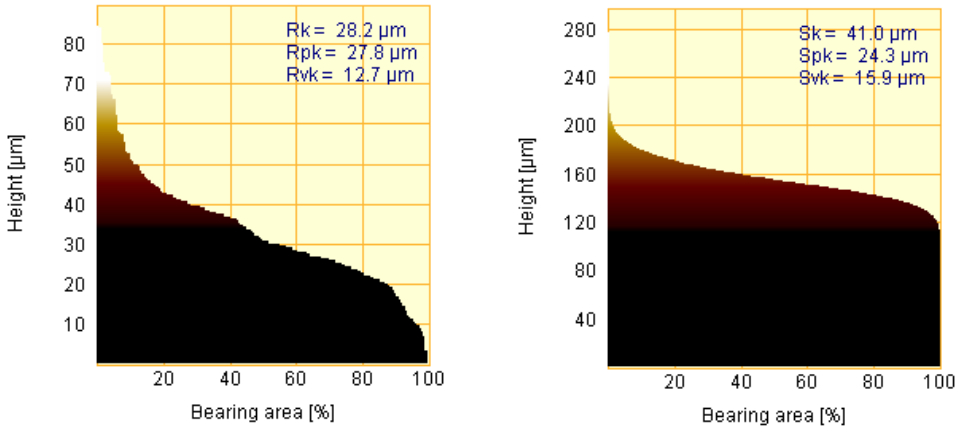

(a) Profile (b) Surface

Fig. 21: Typical bearing area ratio curves from the same surface.

The three most commonly used parameters to describe roughness of a surface from the bearing area curve are the Rk, Rpk and Rvk for profile measurements and Sk,

Spk and Svk for surface measurements. Typical bearing area curves are shown in Figure 21. The roughness parameters are shown in each curve and the variations in the parameters are obvious in both cases. The details of bearing area curve have been provided in the subsection 4.3 with definition of the various parameters encountered in the bearing area curve. In bearing curve, the core roughness for profile and surface is described by the Rk and Sk values respectively. However, for all the standard measured, the three parameters for profile and surface were also quantified and presented in Tables 3, 4, 5 and 6. As can be seen from the tables, the parameters that describe the surface of the standards according to the roughness level are the Rk and Sk values which showed consistent rise with increasing roughness. These parameters quantifies the surface roughness while the other two parameters describe the effect of peaks and valleys on the surface. A large Spk implies a surface cokmposed of high peaks providing small initial contact area and thus high areas of contact stresses (force/area) when the surface is contacted. Svk is a measure of the valley depths below the core roughness and may be related to the lubricant retention and debris entrapment [35]. Due to the associated variations in these parameters, they alone cannot be used to describe the surface quality of castings. However, a wear model was proposed [28] based on these parameters for contacting surfaces as given by the following equation:

Wear = $(\mathrm{Sk} + \mathrm{Spk})_{before\,test}$ - $(\mathrm{Sk} + \mathrm{Spk})_{after\,test}$

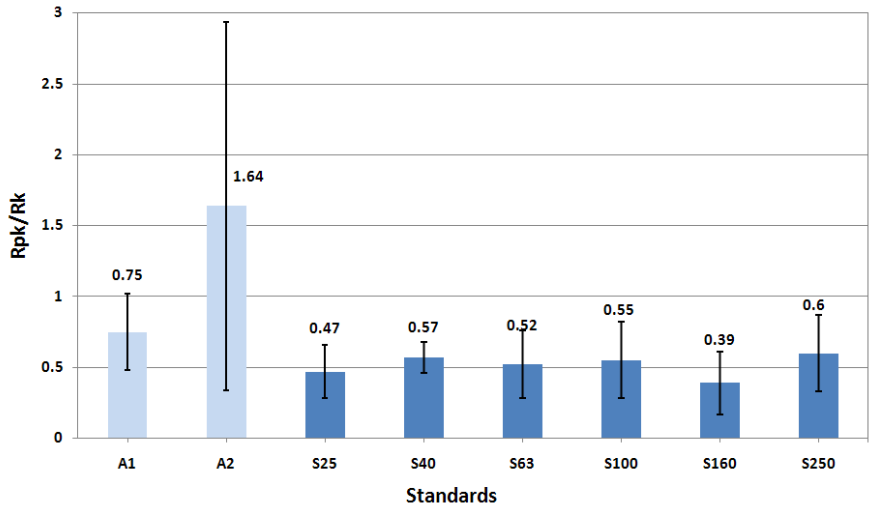

(a) Rpk/Rk

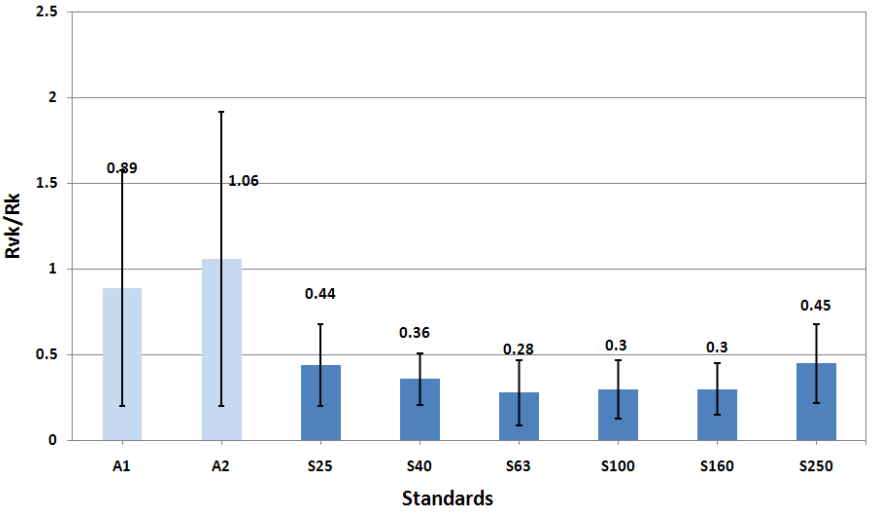

(b) Rvk/Rk

Fig. 22: Profile reduced peak height and valley depth to core roughness ratio.

Furthermore, they can be used to determine the symmetry of the surface texture of the surface i.e is the surface dominated by peak or by valleys?. For the right standards it is expected that the surface texture will be symmetrical around the mean. By applying this dimension of the analyses, it can be deduced which of the standards have symmetrical surface texture. This may be relevant to the intended function of the surface [2]. From the bearing area curve analysis, the ratios of Rpk/Rk and Spk/Sk indicate the peak heights above the core texture normalized by the magnitude of the core texture height [36]. Therefore, larger Rpk/Rk and Spk/Sk values indicate surfaces that tend too be dominated by peaked structures than surface with lower Rpk/Rk and Spk/Sk values. As demonstrated in Figures 22 and 23 for profile bearing area curve and surface bearing area curve respectively, it can be seen that there is strong variation in the values of the ratios from the A series comparators unlike their S series counterparts.

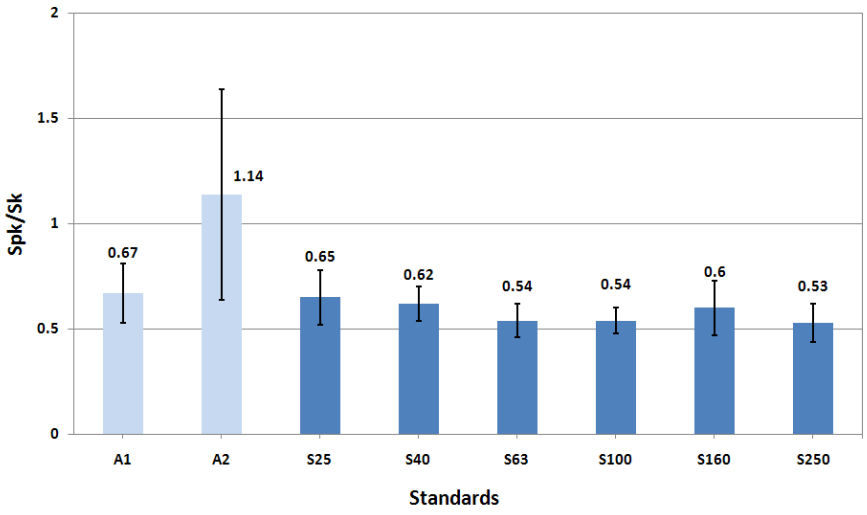

(a) Spk/Sk

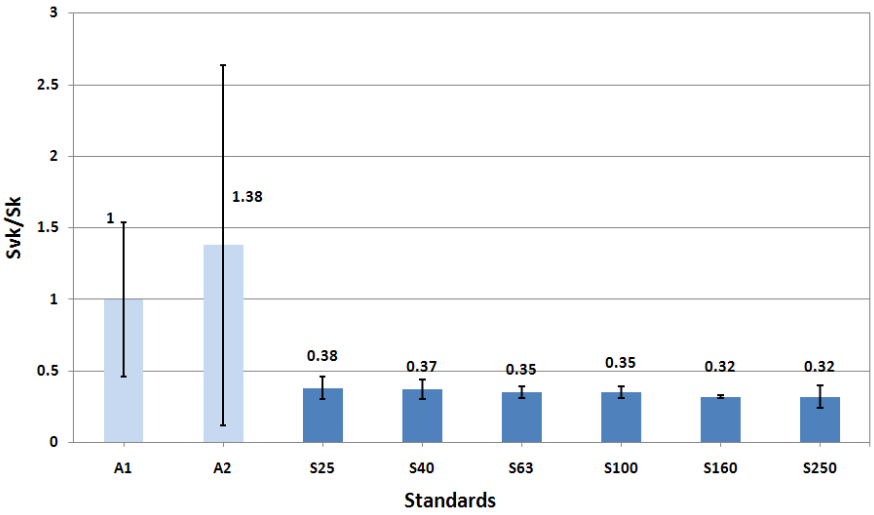

(b) Svk/Sk

Fig. 23: Surface reduced peak height and valley depth to core roughness ratio.

The ratios Rvk/Rk and Svk/Sk, also derived from the bearing area curve analysis illustrated in Figures 22 and 23 for profile bearing area curve and surface bearing area curve respectively, are measures of the dominant valley depths below the core texture relative to the core texture height forming the surface. Higher Rvk/Rk and Svk/Sk values may be characteristic of more plateau-like structures suggestive of a higher real area of contact with other surfaces. Higher Rvk/Rk and Svk/Sk values may also be indicative of crevice-like structures related to potential fatigue wear sites [2]. Again, from the figures it can be seen that the A series standard comparators showed larger variations compared to the S series comparators with symmetrical surface features. Areal data of the S series comparators are more consistent with the expected symmetry to the core texture as shown in Figure 23. This also confirms the reliability of the surface measurements. From these analyses, it can be proposed that the S series standard comparators have more

homogeneously distributed and symmetrical surface features than the A series standard comparators. Hence, show a better description of the surfaces.

8 Results from Castings

A description of the casting geometry is provided in Figure 24 for the vertically-parted moulds. Prints 2 and 4 were spray-coated while prints 1 and 3 are left uncoated. This pattern also helps in the investigation of the influence of metal-lostatic pressure on the surface finish of the vice castings. For each of the prints in a mould, the top and down of the front face (Figure 24c) and top and down of the reverse face (Figure 24d) were scanned for roughness measurement. Six measurements were made on each face and then averaged.

The castings are vice casting made by spraying foundry coatings containing sol-gel component as an additive. The castings examined are castings identified with the mould numbers as 10, 11, 14, 20, and 22. The description of the treatments given to the prints in the mould is as follows:

- Mould no.10: Print 1+3: No coating, Print 2+4: W230, dilution of W230: 30% addition of water.
- Mould no. 11: Print 1+3: No coating, Print 2+4: W230 + 4% Sol-Gel, dilution of W230: 25% addition of water.
- Mould no. 14: Print 1+3: No coating, Print 2+4: W230 + 20% Sol-Gel, dilution of W230: 25% addition of water with Multilayer application. Moulds poured after 1 hour extra waiting time
- Mould no. 20: Print 1+3: No coating, Print 2+4: W226 + 4% Sol-Gel, dilution of W226: 30% addition of water.
- Mould no. 22: Print 1+3: No coating, Print 2+4: W226, dilution of W226: 30% addition of water with Multilayer application

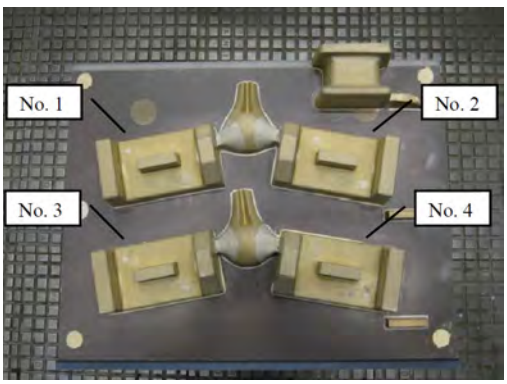

(a) Casting layout-SP showing the prints

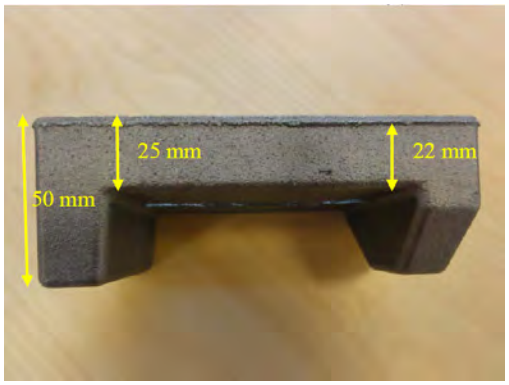

(b) Vice - side view

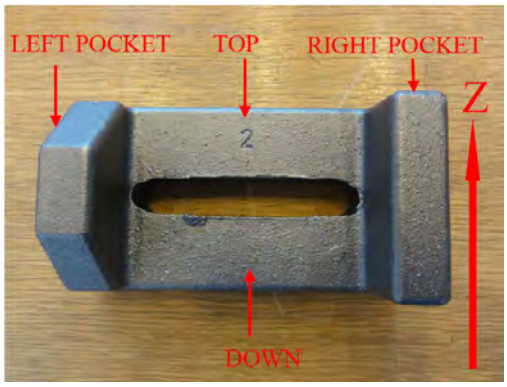

(c) Vice-front face

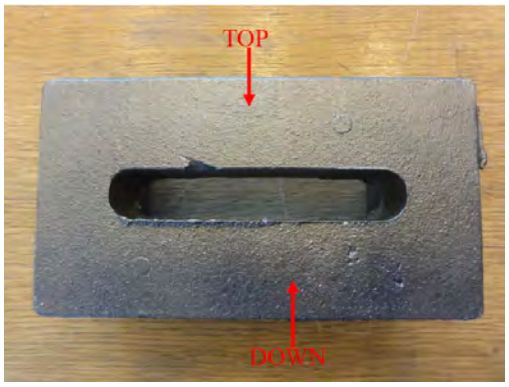

(d) Vice-reverse face

Fig. 24: Casting layout and descriptions.

In the investigation of real casting surfaces, measurements were carried out with the same measuring system and with the same conditions used for the standards. This will provide the level ground for comparison of the results. Although, the results that will be compared with the standards are those obtained from the best coating conditions for the moulds which are expected to give the best casting surface quality. The main stay of this investigation is verify the applicability of the measuring system in the characterization of the surface quality of castings. The measuring system is a new break through in the area of optical surface metrology. Meanwhile, the system has been applied successfully to machined surfaces [18, 22]. Therefore, the authors thought it is worthwhile to apply the system to castings surfaces after shot blasting. The success of this study on sand cast surfaces will definitely confirm its applicability on castings made on permanent moulds and other casting with better surface quality than those of sand castings. The surface roughness of the castings described by Sa values measured with the new measuring system, Alicona InfiniteFocus optical microscope and the corresponding standard deviations are presented in Table 7. The results show that it is possible to use the new optical microscope to measure the surface texture of cast components. However, considering the surface roughness of the sand castings, higher objectives should not be used in order to have a field of view representative of the surface. From Table 7, the coating prints (2 and 4) in Moulds 10, 11 and 14 showed reduction in surface roughness relative to prints (3 and 4) without coatings for W230 coating unlike for moulds 20 and 22 for W226 coating. The best surface quality from the lowest roughness value is observed from the coated prints of Mould 14, which had multilayer application. This indicates the sensitivity of the measuring

system on the changes of the surface features.

Tab. 7: Surface roughness results of the castings.

Mould no.	**Prints**	**Front face (µm)**		**Reverse face (µm)**	
		Top	**Down**	**Top**	**Down**
10	1	14.3±1.0	15.9±1.7	15.0±3.8	16.0±1.2
	2	9.8±1.1	13.2±1.8	13.2±1.3	9.8±1.1
	3	17.3±1.1	18.6±3.1	17.1±1.1	20.4±4.3
	4	11.6±2.3	15.1±1.4	14.7±2.1	9.7±1.6
11	1	13.2±1.6	15.3±1.3	11.2±1.7	13.3±0.8
	2	9.6±2.3	14.0±2.5	9.9±3.2	13.9±1.0
	3	18.3±3.1	18.8±2.0	17.3±1.7	18.7±0.6
	4	15.2±4.3	17.4±1.6	13.3±2.4	9.6±2.7
14	1	13.5±1.6	12.1±1.9	12.1±1.0	15.3±1.4
	2	7.5±0.9	12.9±1.3	5.6±0.9	5.6±0.3
	3	13.8±1.3	17.6±1.4	17.1±2.5	19.2±2.1
	4	8.4±1.8	7.5±0.8	5.8±0.2	7.7±2.2
20	1	16.1±1.9	16.3±1.5	15.4±0.6	16.4±0.9
	2	11.9±1.5	16.3±1.0	15.2±1.4	17.8±1.2
	3	15.9±2.0	20.0±2.2	17.8±1.0	19.7±2.4
	4	17.0±2.9	20.8±1.8	12.4±0.6	11.7±0.5
22	1	11.1±1.1	16.7±1.3	11.8±1.7	15.3±0.8
	2	11.4±1.2	13.8±1.8	12.5±1.0	16.2±2.1
	3	14.6±2.1	16.5±2.1	14.5±1.0	17.8±1.6
	4	16.4±1.6	19.8±1.9	16.6±1.4	17.2±1.2

In the analysis of the single measurement points and their variations from one another, Figure 25 shows the profiles and their variations with one another for prints

1 and 2 (Figure 25a) and prints 3 and 4 (Figure 25b) for Mould 14 with multilayer coating application of W230 coating. The lower roughness of the castings in Prints 2 and 4 is obvious by the clear separation of of their profiles from those of Prints 1 and 3. This points to the sensitivity of the measuring system to the changes with the features on the surface being measured. This simply means that the system is able to track effectively changes on the surfaces. Therefore, it can be used for the characterization of castings produced by different production processes. Basically, parameter variation is the product inherent surface topography features emanating from manufacturing methods. Take for instance, the surface of sand castings after shot blasting is difficult to measure with stylus instrument, because of non-homogeneity of the surface features and material pick-up. These, were observed from previous trials with stylus profilometry. Consequently, foundries resorted to tactile comparators.

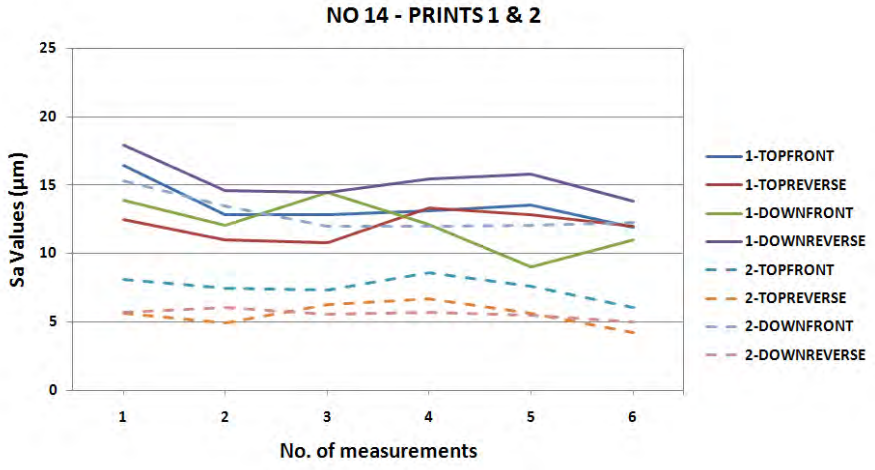

(a) Prints 1 & 2

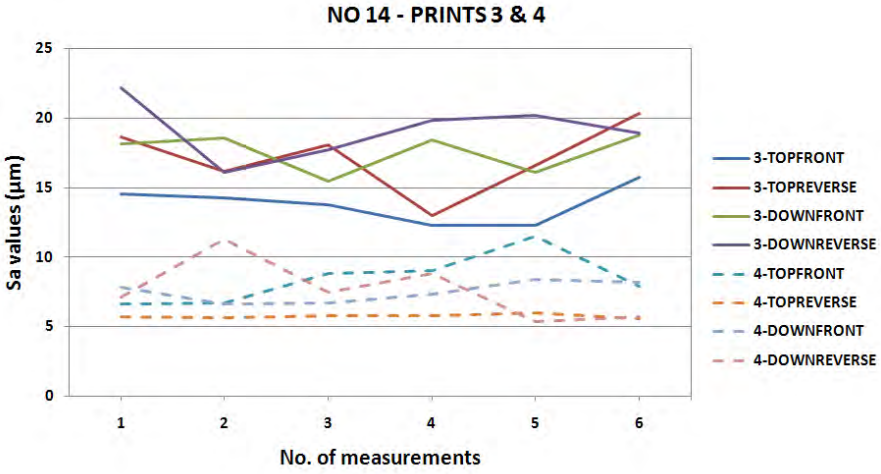

(b) Prints 3 & 4

Fig. 25: Single point roughness of casting made with W230 + 20% sol-additive with multilayer application.

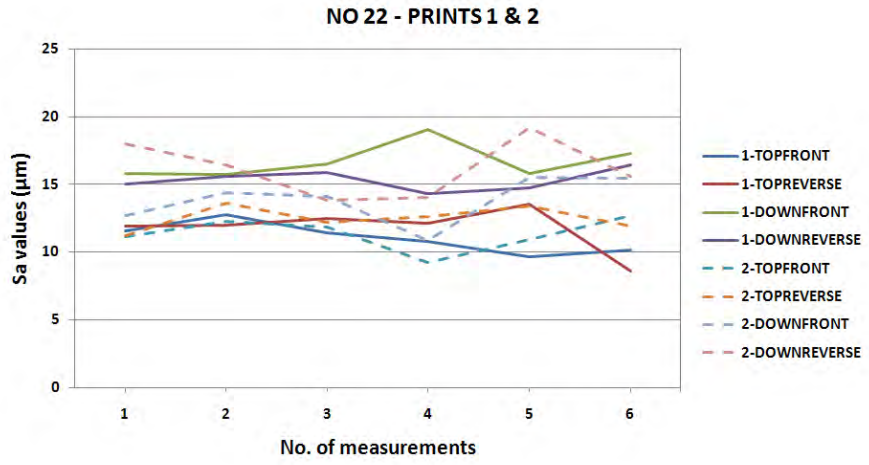

(a) Prints 1 & 2

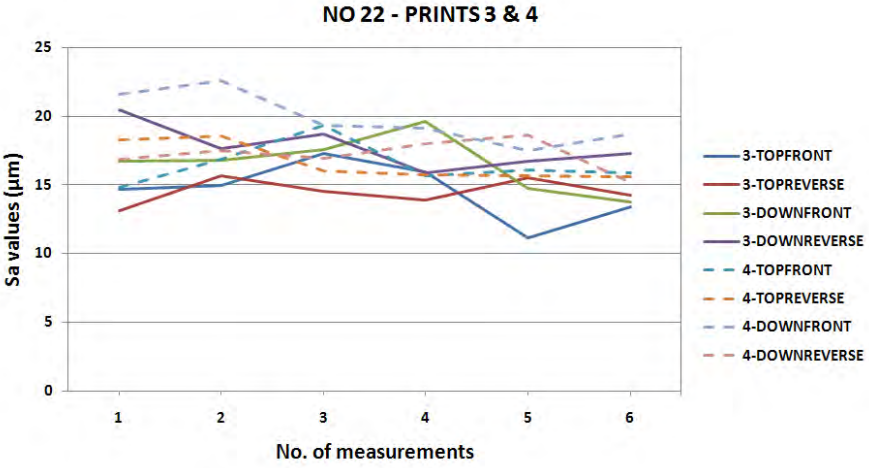

(b) Prints 3 & 4

Fig. 26: Single point roughness of casting made with W226 with multilayer application.

In furtherance of the discussion of the sensitivity of the system with changes in surface features measured, Figure 26 shows profiles and their variations with one another for prints 1 and 2 (Figure 26a) and prints 3 and 4 (Figure 26b) for Mould 22 with multilayer coating application of W226 coating. As can be seen from the figure, it is clear that due the poor surface quality of the castings, the machine measured the features on the surface accordingly. By hand feeling and visual inspection of the castings, they felt sharp to touch and look rough visually. There was no difference from the surface of castings made in coated moulds and those made in uncoated moulds. This means that the coating on the moulds did not improve the surface quality of the castings. This is evident from the high roughness values obtained from the surface of these castings.

In another context, the surface roughness of selected castings were compared with those of the standards and the results are shown in Figures 27 and 28. Figure 27 shows the comparison of the surface roughness of castings made in Mould 10 with

Prints 2 and 4 mould cavity coated with W230 coating and those of the standard comparators. A closer examination of the figure shows that for the castings, both the front face (Figure 27a) and reverse face (Figure 27b) are lower than the surface roughness of A1 standard comparator while falling between S40 and S160 for the S series standard comparators.

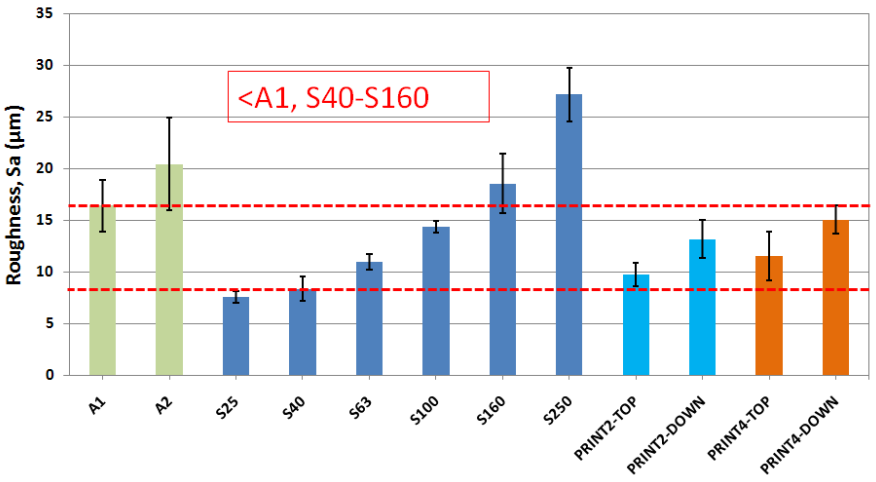

(a) No. 10 Front face

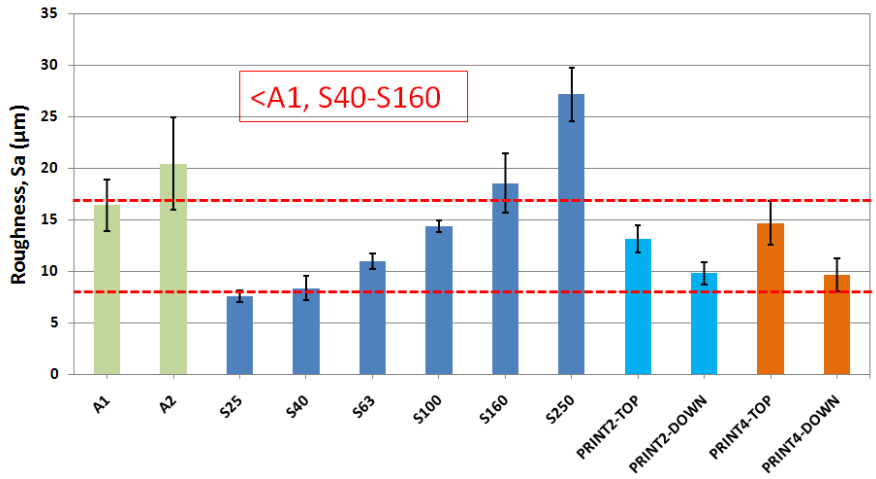

(b) No. 10 Reverse face

Fig. 27: Comparison of roughness of castings made with W230 and roughness of standards.

The comparison of the surface roughness of the castings made in Mould 14 with multilayer application of W230 coating on the mould cavity for Prints 2 and 4 with the roughness values of the standard comparators is shown in Figure 28. The results shows that the surface roughness of both the front face (Figure 28a) and reverse face (Figure 28b) are lower that the roughness level of A1 standard comparator while the surface roughness of the front face of the casting falls between S25 and S100 and that of the reverse face of the casting falls between S25 and S63 of the S series standard comparators. From the level of reduction of the surface

roughness in the two moulds with different treatments, it can be deduced that the mould with multilayer application of the coating improved the surface quality of the castings more than the one with single layer coating application. The multilayer coating application is more effective in closing the pore spaces on the surface of the mould walls with the coating refractory materials. Furthermore, it is also observed that the reverse face of most of the casting had better surface finish based on their lower surface roughness. The is attributed to the effective of of the mould wall at the reverse face since this particular part of the mould is only 3 mm into the mould unlike the front face which is 22 mm into the mould as shown in Figure 24b. Due to the depth of the mould cavity in the front face, back pressure will resist effective deposition of the coating refractory materials in those areas [37].

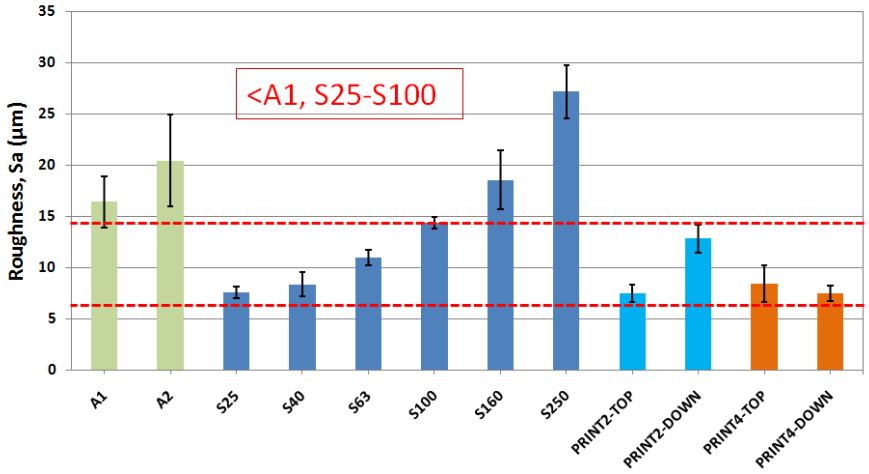

(a) No. 14 Front face

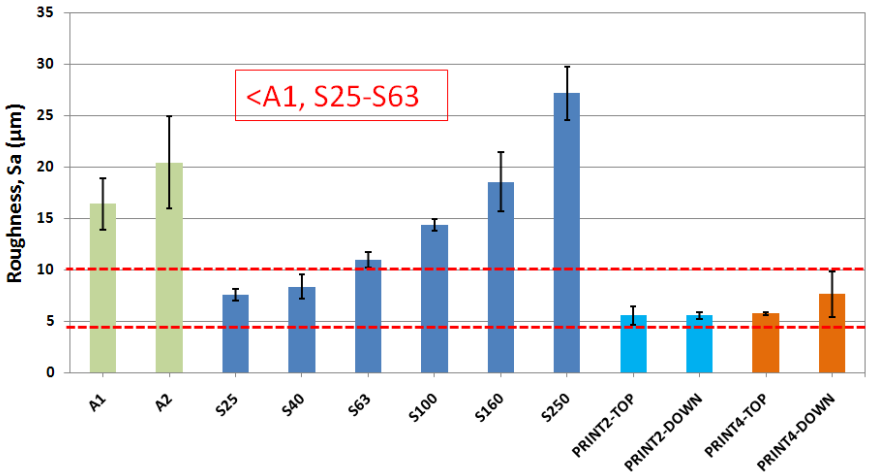

(b) No. 14 Reverse face

Fig. 28: Comparison of roughness of castings made with W230 + 20% sol-gel additive + multilayer application and roughness of standards.

9 Conclusions

The surface texture characterization of cast components is an area of surface metrology in manufacturing that has been neglected for ages due to the inability of the existing mechanical and optical roughness measuring systems to measure the surface roughness of castings. This is due to the peculiar nature of the surface of castings with its associated higher roughness level, especially with sand cast components.

In this study, considering the new breakthroughs by instrumentations in the recent times, to establish high-tech instruments which can acquire 3D surface structure of surfaces in Manufacturing Engineering, the authors thought it is time to try these new technologies in the characterization of surface texture of castings. One of the new technologies adopted for this investigation is the InfiniteFocus optical metrology device produced by Alicona, which is based on Focus-Variation technology. In this study, the authors have been able to make the following findings and assertions:

- The surface texture of castings can be characterized by using the new InfiniteFocus Optical Metrology Microscope.
- The roughness of tactile standard surface comparators was evaluated.
- S series comparators described the surface texture of castings better than the A series comparators
- The measuring system is non-destructive.
- Higher objectives should be avoided, working with 5× is suggested for sand castings but lower objective, 2.5× can still be used.
- Parameter rash should be avoided in the foundries to avoid complications in data interpretation.
- 3D surface parameters give more precise reflection of the surface and more precision than their 2D counterparts.
- Ra and Sa have close values. However, larger number of measurements are required for Ra, to get this closeness. Therefore, the measurement of Sa parameter save time and energy.
- The surface average amplitude parameters, Sa and Sq and the bearing area curve parameter, Sk can be used to characterize the surface texture of castings. However, Sa suffices for the evaluation of casting surface texture.
- The variation in extreme parameters (Peak-Valley height) is larger than the variation in the average parameters. As a result, average parameters are more sensitive to the changes in surface topography features.
- The variations observed in the parameters is mainly due to the nature of the surface feature resulting from the manufacturing processes.

- To understand the symmetry of the surface texture of standards and surfaces as a whole, the normalized surface bearing area curve parameters can be used i.e. Spk/Sk and Svk/Sk.

References

[1] D. J. Whitehouse, Handbook of Surface and Nanometrology, 2nd ed., CRC Press, Florida, 2011.

[2] O. Hatamleh, J. Smith, D. Cohen and R. Bradley, Surface roughness and friction coefficient in peened friction stir welded 2195 aluminium alloy, Applied Surface Science 255 (2009) 7414-7426.

[3] British Standard-Founding-Surface roughness inspection by visual tactile comparators, BS EN 1370:1997. http://bbs.6jc.cn/pdf/o/EN%201370-1997.pdf

[4] U. C. Nwaogu, T. Poulsen, R. K. Stage, C. Bischoff, N.S. Tiedje, New sol-gel refractory coatings on chemically-bonded sand cores for foundry applications to improve casting surface quality, Surface & Coatings Technology 205 (2011) 4035-4044.

[5] E. Konstantoulakis, H. Nakajima, R. D. Woody and A. W. Miller, Marginal fit and surface roughness of crowns made with an accelerated casting technique, The Journal of Prosthetic Dentistry, Vol. 80 No. 3(1998)337-345

[6] E. Swing, Methods of Surface Roughness Measurement, Transactions of the American Foundrymen's Society, Proceedings of the Sixty-Seventh Annual Meeting, May 6-10, 1963, Volume 71, Illinois, 1964.

[7] http://www.castingstechnology.com/

[8] V. M. huynh and Y. Fan, Surface Texture Measurement and Characterisation with Applications to Machine-Tool Monitoring, Int. J. Adv. Manuf. Technol. 7 (1992) 2-10.

[9] U. Işleyici, Effect of Surface Roughness on Ultrasonic Testing, A Thesis submitted to the Department of Mechanical Engineering, Middle east Technical University, 2005.

[10] L. D. Chiffre, Geometrical Metrology and Machine Testing Textbook, DTU Mekanik, CGM, 2011.

[11] R. Leach, Fundamental Principles of Engineering Nanometrology, Elsevier, Oxford, 2010.

[12] B. Griffiths, Manufacturing Surface Technology, Butterworth Heinemann, 2001.

[13] C. -L. Tien, H. -M. Yang and M. -C. Liu, The measurement of surface roughness of optical thin films based on fast Fourier transform, Thin Solid Films, 517 (2009) 5110-5115.

[14] B. Dhanasekar, N. Mohan, B. Bhaduri and B. Ramamoorthy, Evaluation of surface roughness based on monochromatic speckle correlation using image processing, Precision engineering 32 (2008) 196-206.

[15] E. kayahan, H. Oktem, F. Hacizade, H. Nasibov and O. Gundogdu, Measurement of surface roughness of metals using binary speckle image analysis, Tribology International 43 (2010) 307-311.

[16] C. -C. Kuo, and C. -S. Chao, Rapid optical measurement of surface roughness of polycrystalline thin films, Optics and Lasers in Engineering 48 (2010) 1166-1169.

[17] C. -C. Kuo and Y. -R. Chen, A new method of characterizing surface roughness of TiO_2 thin films, Optics and Laser Engineering 49 (2011) 410-414.

[18] P. Demircioglu and M. N. Durakbasa, Investigations on machined metal surface through the stylus type and optical 3D instruments and their mathematical modelling with the help of statistical techniques, Measurements 44 (2011) 611-619.

[19] R. Danzl, F. Helmli and S. Scherer, 3D Measurement of complex structures using focus variation: http://www.focusonmicroscopy.org/2007/PDF/106_Danzl.pdf

[20] ISO 25178-6: Geometrical product specifications (GPS) – Surface texture: Areal – Part 6: Classification of methods for measuring surface texture.

[21] O. Huber, Focus-Variation - A New Technology for High Resolution Optical 3D Surface Metrology in the Micro- and Nano-meter Range, Geophysical Research Abstracts, Vol. 11 (2009) 8417.

[22] R. Danzl, F. Helmli and S. Scherer, Focus-Variation - A New Technology for High Resolution Optical 3D Surface Metrology, The 10th International Conference of the Slovanian Society for Non-Destructive Testing, Application of Contemporary Non-Destructive Testing in Engineering, September 1-3, 2009, Ljubljana, Slovenia.

[23] I. Asiltürk and M. Çunkaş, Modelling and prediction of surface roughness in turning operations using artificial neural network and multiple regression method, Expert Systems with Applications 38 (2011) 5826-5832.

[24] C. Y. Poon and B. Bhushan, Surface roughness analysis of glass-ceramic substrates and finished magnetic disks, and Ni-P coated Al-Mg and glass substrate, Wear 190 (2995) 89-109.

[25] S. Chandrasekaran and S. Sundararajan, Effect of micro-fabrication processes on surface roughness parameters of silicon surfaces, Surface and Coating Technology 188-189 (2004) 581-587.

[26] W. P. Dong, P. J. Sullivan and K. J. Stout, Comprehensive study of parameters for characterizing three-dimensional surface topography III: Parameters for characterizing amplitude and some functional properties, Wear 178 (1994) 29-43.

[27] J. Järnström, P. Ihalainen and J. Peltonen, Roughness of pigment coatings and its influence on gloss, Applied Surface Science 254 (2008) 5741-5749.

[28] H. McCormick and K. Duho, A brief History of the Development of 2-D Surface Finish Characterization and More Recent Developments in 3-D Surface Finish characterization, C-K Engineering, Inc: http://www.c-kengineering.com/files/3-D%20Surface%20Measurement.pdf.

[29] Alicona InfiniteFocus, IFM Manual, IFM 3.1.1.2 EN 26.02.2009, Alicona Imaging GmbH.

[30] U. Sellgren, S. Björklund and S. Andersson, A finite element-based model of normal contact between rough surfaces, Wear (2003) 1180-1188.

[31] A. Cellary, M. Wieczorowski and K. F. Ehmann, A comparative analysis of 2D and 3D Bearing area curves, S. M. Wu Symposium, Vol. II (1996)196-200.

[32] W. P. Dong, P. J. Sullivan and K. J. Stout, Comprehensive study of parameters for characterizing three-dimensional surface topography II: Statistical properties of parameter variation, Wear 167 (1993) 9-21.

[33] W. P. Dong, P. J. Sullivan and K. J. Stout, Comprehensive study of parameters for characterizing three-dimensional surface topography I: Some inherent properties of parameter variation. Wear, 159 (1992) 161-171.

[34] T. R. Thomas and G. Charlton, Variation of roughness parameters on some typical manufactured surfaces, Precision Engineering (1981) 91-96.

[35] 3D Functional Parameters - Michigan Metrology http://www.michmet.com/3d_s_functional_parameters.htm

[36] ISO 13565-2:1996, Geometrical product specifications (GPS) - Surface texture: Profile method; surfaces having stratified functional properties - Part 2: Height characterization using the linear material ratio curve.

[37] U. C. Nwaogu, N. S. Tiedje, Foundry Coating Technology: A Review, Materials Science and Applications, 2 (2011) 1143-1160.